BEILSTEIN JOURNAL OF NANOTECHNOLOGY

Advances in nanomaterials II

Edited by Horst Hahn, Mario Ruben and Herbert Gleiter

Generated on 09 August 2026, 07:47

Imprint

Beilstein Journal of Nanotechnology
www.bjnano.org
ISSN 2190-4286
Email: journals-support@beilstein-institut.de

The *Beilstein Journal of Nanotechnology* is published by the Beilstein-Institut zur Förderung der Chemischen Wissenschaften.

Beilstein-Institut zur Förderung der Chemischen Wissenschaften
Trakehner Straße 7–9
60487 Frankfurt am Main
Germany
www.beilstein-institut.de

The copyright to this document as a whole, which is published in the *Beilstein Journal of Nanotechnology*, is held by the Beilstein-Institut zur Förderung der Chemischen Wissenschaften. The copyright to the individual articles in this document is held by the respective authors, subject to a Creative Commons Attribution license.

BEILSTEIN JOURNAL OF NANOTECHNOLOGY

Influence of grain size and composition, topology and excess free volume on the deformation behavior of Cu–Zr nanoglasses

Daniel Şopu*[1,2] and Karsten Albe[1]

Full Research Paper

Open Access

Address:
[1]Institut für Materialwissenschaft, Technische Universität Darmstadt, Petersenstr. 32, D-64287 Darmstadt, Germany and [2]Currently at: IFW Dresden, Helmholtzstr. 20, 01069 Dresden, Germany

Email:
Daniel Şopu* - d.sopu@ifw-dresden.de

* Corresponding author

Keywords:
enhanced plasticity; metallic glasses; nanoglasses; shear bands

Beilstein J. Nanotechnol. **2015,** *6,* 537–545.
doi:10.3762/bjnano.6.56

Received: 18 June 2014
Accepted: 02 February 2015
Published: 24 February 2015

This article is part of the Thematic Series "Advances in nanomaterials II".

Guest Editor: H. Hahn

© 2015 Şopu and Albe; licensee Beilstein-Institut.
License and terms: see end of document.

Abstract

The influence of grain size and composition on the mechanical properties of Cu–Zr nanoglasses (NGs) is investigated by molecular dynamics simulations using two model glasses of different alloy composition, namely $Cu_{64}Zr_{36}$ (Cu-rich) and $Cu_{36}Zr_{64}$ (Zr-rich). When the grain size is increased, or the fraction of interfaces in these NGs is decreased, we find a transition from a homogeneous to an inhomogeneous plastic deformation, because the softer interfaces are promoting the formation shear transformation zones. In case of the Cu-rich system, shear localization at the interfaces is most pronounced, since both the topological order and free volume content of the interfaces are very different from the bulk phase. After thermal treatment the redistribution of free volume leads to a more homogenous deformation behavior. The deformation behavior of the softer Zr-rich nanoglass, in contrast, is only weakly affected by the presence of glass–glass interfaces, since the interfaces don't show topological disorder. Our results provide clear evidence that the mechanical properties of metallic NGs can be systematically tuned by controlling the size and the chemical composition of the glassy nanograins.

Introduction

A nanoglass (NG) is a nanostructured material produced via cold compaction of glassy nanoparticles [1]. It consists of glassy grains separated by glass–glass interfaces. Indirect experimental evidence for the existence of interfaces in NGs have been provided by Gleiter et al. [2-7]. The recent work of Chen et al. [8], supports Gleiter's results on the structural model of a NG. The microstructure of a metallic nanoglass consisting of glassy grains and glass–glass interfaces has been experimentally revealed by electron microscopy, small-angle X-ray scattering and positron annihilation spectroscopy [9], while molecular dynamics studies showed that glass–glass interfaces exhibit an excess free volume and a modified local order [10,11].

If plastically deformed, the soft glass in the interfaces promotes shear band nucleation similar to the effect of residual shear bands in pre-deformed metallic glasses [11]. Consequently, the NG exhibits a more homogeneous plastic deformation carried by a pattern of multiple shear bands [12] as compared to the bulk metallic glass (BMG), where plastic deformation is well localized in a few dominant shear bands. The influence of interfaces on the deformation behavior of nanoglasses has been shown both in computer simulation [11,13,14] and experiment [9,15], where also an enhanced plasticity under compression was observed indicating that not critical shear bands occur. Recent experiments on sputtered nanograined Au-based glasses also showed high hardness and a low elastic modulus as compared to their bulk counterparts [8].

In light of these interesting results, further studies on the mechanical properties of this new type of material seem to be mandatory. Critical questions are, if and how mechanical properties of NGs change by varying the grain size and grain composition. Moreover, it is unclear how thermal treatment or mechanical pre-deformation affect the plasticity of NGs.

Recently, Adibi et al. [14,16] showed for 2D perodic systems that the plasticity of Cu–Zr NGs of different composition will improve with decreasing grain sizes. In these simulations, however, free surfaces were present that promote the activation of shear transformation zones [17]. Thus, these results are representative for samples on the nanoscale, where surfaces and glass–glass interfaces are competing heterogeneities, but don't give necessarily a clear picture on the situation in bulk NGs.

In this work, we study the influence of grain size and chemical composition on mechanical properties of Cu–Zr NGs by means of molecular dynamics simulations. First, we investigate whether by varying the grain size the plastic deformation of NGs changes. Second, we investigate if the plastic behavior of NGs changes with glass composition. Finally, the impact of the thermal relaxation of the glass–glass interface is studied. For this, two model glasses of different alloy composition are used, namely $Cu_{64}Zr_{36}$ (Cu-rich) and $Cu_{36}Zr_{64}$ (Zr-rich). All simulations are carried out in 3D periodic arrangements and thus surface effects are deliberately excluded.

Methods

Molecular dynamics simulations are carried out with the program package LAMMPS [18]. The modified Finnis–Sinclair type potential for Cu–Zr proposed by Mendelev et al. [19] was applied for describing the atomic interactions. For all simulations a constant integration time step of 2 fs was used. In the first step, two homogeneous amorphous alloys consisting of 8000 atoms were generated by quenching from the melt. Initially, the melts were relaxed at 2000 K for 2 ns to ensure chemical homogeneity. The $Cu_{64}Zr_{36}$ and $Cu_{36}Zr_{64}$ glassy alloys have been cooled to 50 K with a cooling rate of 0.01 K/ps.

The Cu-centered full icosahedral (FI) short range order (SRO) and free volume content was analyzed using the Voronoi tessellation method [20]. We have focused the characterization of topological SRO on the population of Cu-centered FI [0,0,12,0] because this polyhedron is known to be the key structural motif in amorphous Cu–Zr alloy, characterized by a high packing density [21] and high shear resistance [22].

For modeling the NG microstructure, a 2D array of columnar grains with a hexagonal cross section is used. The grains with diameters of 4 nm, 10 nm and 16 nm have been cut from the glassy bulk structure, respectively. The nanoglass was then generated by compacting the columnar grains under external hydrostatic pressure of 3 GPa at 50 K. An overview of the NGs is presented in Table 1.

Table 1: Number of glassy grains, average grain diamater and total number of atoms used for the construction of NGs.

Composition	Grains	<*d*> (nm)	N_{atoms}
$Cu_{64}Zr_{36}$	81	4	$\approx 8.0 \cdot 10^5$
	18	10	$\approx 5.5 \cdot 10^5$
	18	16	$\approx 2.0 \cdot 10^6$
	BMG		$\approx 1.3 \cdot 10^6$
$Cu_{36}Zr_{64}$	18	10	$\approx 1.0 \cdot 10^6$
	BMG		$\approx 1.3 \cdot 10^6$

We simulated the deformation of these NGs and compared to the case of homogeneous BMGs by deforming in uniaxial tension parallel to the *z*-direction with a constant strain rate of $4 \cdot 10^7\ s^{-1}$ at $T = 50$ K. 3D periodic boundary conditions were applied to exclude surface effects. The pressure in *x* and *y* direction was kept at 0 kbar allowing for lateral contraction. The atomic scale deformation mechanisms were analyzed by visualizing the local atomic shear strain [23], calculated with the OVITO analysis and visualization software [24]. A quantitative interpretation of strain localization has been realized by using the strain localization parameter defined by Cheng et al. [25],

$$\psi = \sqrt{\frac{1}{N}\sum_{i=1}^{N}\left(\eta_i^{Mises} - \eta_{ave}^{Mises}\right)^2}.$$

A larger ψ value indicates larger fluctuations in the atomic strain and a more localized deformation mode.

Results

Grain size effects

For studying the effect of grain size on the mechanical properties, we simulated the deformation of Cu-rich glasses with grain sizes of $<d> = 4$, 10 and 16 nm (see Table 1). All NGs and a BMG ($\approx 1.3 \cdot 10^6$ atoms) were deformed in tension following the procedure described above. The stress–strain curves of all three NGs and the BMG under tensile deformation are plotted in Figure 1. Up to a strain of about 2%, all four curves show a similar slope and, thus, the fraction of interfaces does not have a strong influence on the elastic deformation. In contrast, the yield stress and maximum stress decrease considerably with decreasing grain size or increasing the glass–glass interface density. In the past, we have shown that these planar interfaces have a lower fraction of densely packed FI clusters [11]. As the FI clusters have a high shear resistance [21,22], a decrease in the total amount of FI clusters by increasing the fraction of interfaces in the NG can explain the decrease in yield stress. Therefore, an increased number of interfaces results in a softer NG. In addition, an increase of the volume fraction of interfaces in the NG results in an improved plastic behavior. As shown in our previous work [12], a large number of interfaces causes a more homogeneous deformation of the NG in a highly organized pattern of multiple shear bands, in contrast to the BMG which exhibits localized deformation in one dominant shear band.

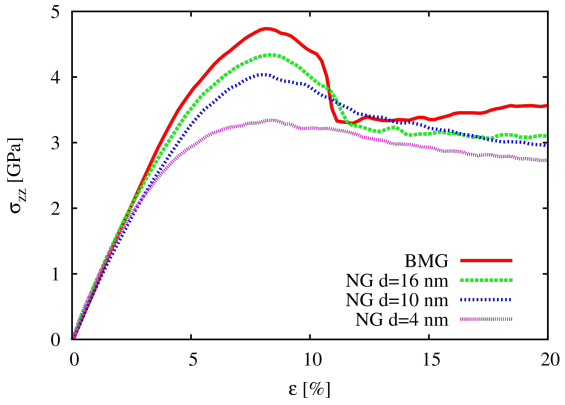


Figure 1: Tensile stress–strain curves for a BMG in comparison to three NGs with grain sizes of 4 nm, 10 nm and 16 nm, respectively, at a constant strain rate of $4 \cdot 10^7$ s^{-1}.

In order to study how the deformation mechanism of NGs changes by varying the glassy grain size the local atomic shear strain was calculated for each of these NGs and BMG (Figure 2). Up to a strain of 8% in all three NGs, the shear transformation zones (STZs) are mostly activated in the soft interface regions. Although the shear band nucleation process is similar in all three NGs, the shear band propagation in case of the NG with the largest grain size strongly differs from to the other two NGs. It can be seen in Figure 2 that the plastic deformation is more localized at a strain of 16% in case of the NG with a grain size of 16 nm. This can be explained by the lower fraction of soft interfaces with respect to the NG volume. Up to a strain of 8%, the elastic energy is released locally in embryonic shear bands formed by precipitation of the STZs along the interfaces (see Figure 2).

After a strain of 8% the local energy released is sufficient to accelerate one of these embryonic shear bands, so that it goes critical. The propagation of one single shear band leads to a stress drop, which is not observed for the other two NGs with smaller grains, as it can be seen in Figure 1. Nevertheless, this stress drop is not as pronounced as in the case of the BMG. This means that even for a NG constructed with bigger glassy grains, the deformation deviates from the well localized deformation found in the BMG. Together with a dominant shear band, many secondary shear bands mediate the plastic deformation of the NG (see Figure 2). This observation is supported by the calculated strain localization parameter ψ. The ψ values for all three NGs and BMG at a strain of 16% are plotted in Figure 3. It can be seen that the ψ value of the NG with a grain size of 16 nm is higher than for the other two NGs, but still lower than for the BMG. For the other two NGs with smaller glassy grains the ψ values are much lower indicating a more homogeneous deformation mode. Figure 2 shows that both NGs undergo plastic deformation mediated by multiple shear bands uniformly distributed over the whole sample.

At this point, it is interesting to compare our results obtained for 3D periodic systems with those reported for 2D periodic nanoglasses with free surfaces by Adibi et al. [14,16]. In their simulations the presence of a surfaces clearly promotes strain localization and the formation of critical shear bands, which leads to massive stress drops in the stress–strain curve. In our data for fully periodic systems the strain is obviously more delocalized and the stress drop is less pronounced. For the smallest grain sizes <5 nm, however, our data and those of Adibi et al. [14,16] agree, both showing plastic stable flow up to a large strain. This can be explained by the high fraction of interfaces, which dominate over surface effects. In a NG with a grain size smaller than 4 nm the percentage of atoms located in the soft interfaces is higher than 70%. Basically the NG structure resemble the one of a soft BMG. Similar, a transition in the deformation mechanism of a BMG form a localized deformation in shear bands to a homogeneous plastic flow was observed when increasing the casting cooling rate [26]. Here the softening of the glassy structure is due to the faster quenching, while in our case the NGs with very small grains get softer due to the high fraction of interfaces.

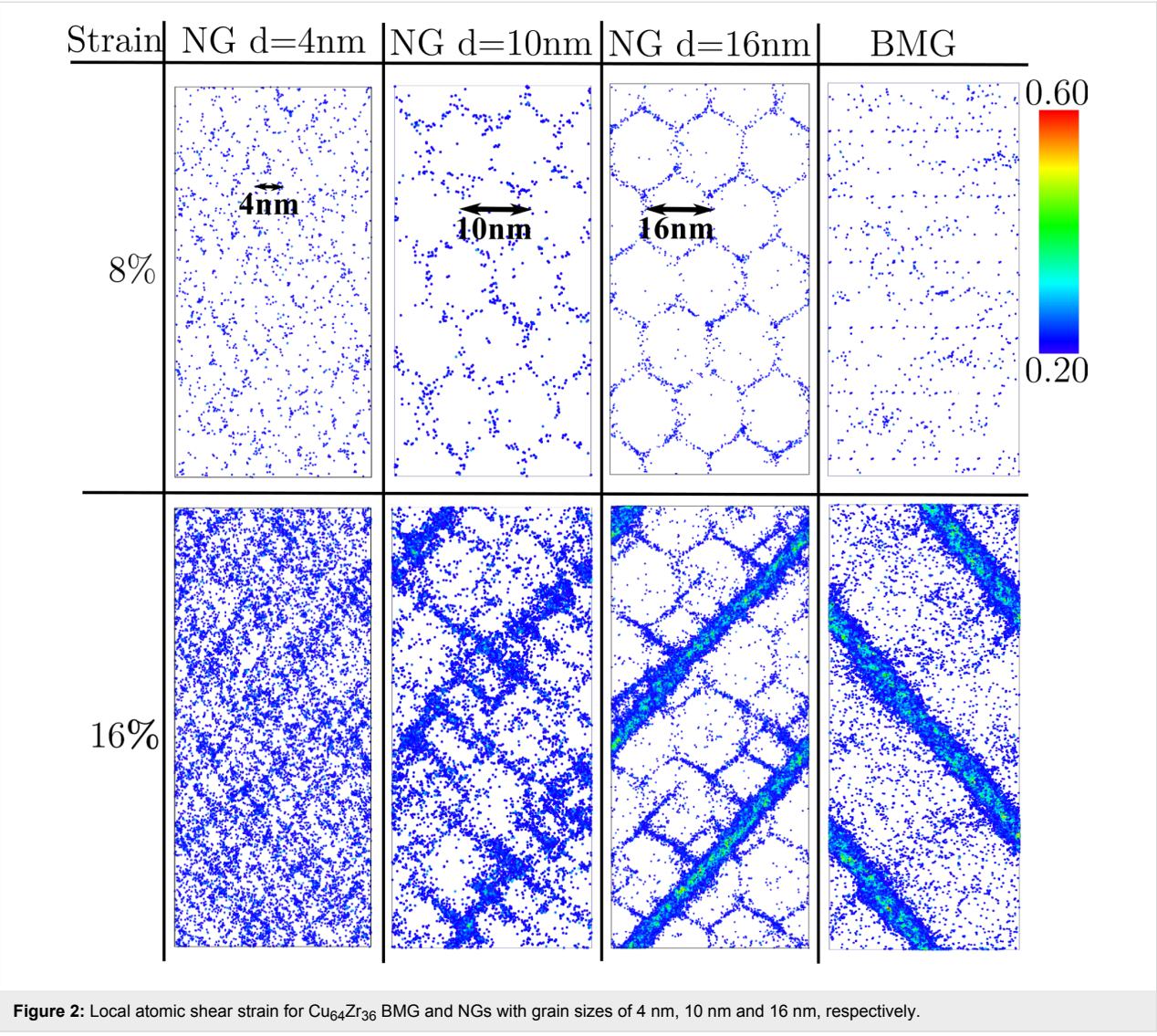


Figure 2: Local atomic shear strain for $Cu_{64}Zr_{36}$ BMG and NGs with grain sizes of 4 nm, 10 nm and 16 nm, respectively.

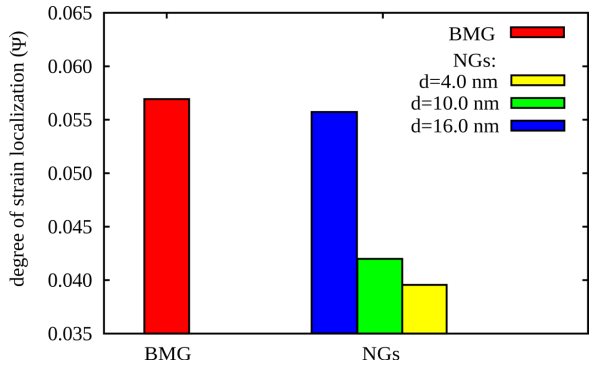


Figure 3: The ψ values for a BMG in comparison to three NGs with grain sizes of 4 nm, 10 nm and 16 nm, respectively, after plastic deformation to an overall strain of 16%.

Chemical composition effects

Next we test if the results on the NG mechanical properties are transferable to other Cu–Zr alloys. It is known that the short-to-medium-range structural order varies with alloy composition [27], and is assumed to play a major role in controlling the macroscopic properties of metallic glasses, particularly the plastic deformation [22,28].

Therefore, the influence of chemical composition on the plastic behavior of NGs was investigated by using two alloy compositions: a Zr-rich NG ($Cu_{36}Zr_{64}$) and the Cu-rich NG ($Cu_{64}Zr_{36}$) studied also in [12]. Both types of NGs have an average grain size of 10 nm. The operating deformation mechanisms in these NGs and the corresponding BMGs (≈10^6 atoms) was analyzed under tensile deformation. In Figure 4 it can be observed that the Zr-rich BMG shows a lower yield stress compared to the yield stress of the Cu-rich BMG. In [25] it was reported that

FI-clusters have a high packing density and high shear resistance and determine the plasticity of Cu–Zr glasses [21]. We found a population of Cu-centered FI in the Cu-rich alloy of about 22% compared to only 5% in the Zr-rich alloy. This can explain the corresponding variation of yield stress and plastic strain. On the other hand, it can be seen in Figure 5 that also the plastic behavior of the $Cu_{36}Zr_{64}$ BMG differs completely from the one of the Cu-rich BMG. The Cu-rich BMG exhibits localized deformation in one dominant shear band, while the Zr-rich BMG exhibits a homogeneous deformation. The difference in the short-to-medium structural order for these two alloy compositions can serve as an explanation. In the $Cu_{36}Zr_{64}$ alloy the low fraction of FI-clusters leaves space for the formation of a high fraction of Voronoi polyhedra characterized by a low packing density and low shear resistance. Hence, Zr-rich BMGs should produce more STZs and can carry more strain. On the other hand, the Cu-rich BMG contains a high fraction of FI-clusters and, therefore, a high degree of MRO formed from the interconnection of FI-units. Due to the smaller flow region within this alloy, $Cu_{64}Zr_{36}$ is unable to mediate large plastic strains. Consequently, the plastic deformation is localized in one dominant shear band. If open surface are present [14,16] both types of BMGs deform in one dominant shear band and the compositional effect is less pronounced. We repeated the deformation process of $Cu_{36}Zr_{64}$ BMG under free surface conditions and observed similar localized deformation in one dominant shear band.

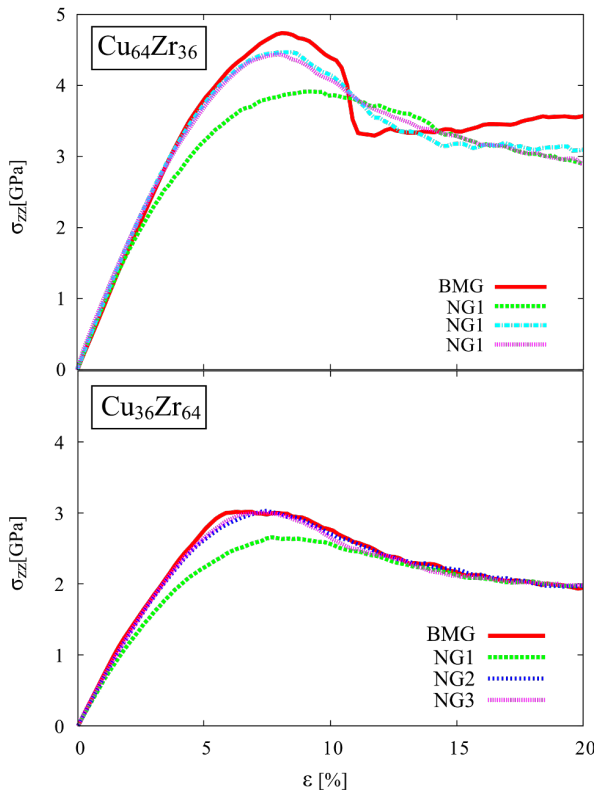


Figure 4: Tensile stress–strain curves for $Cu_{64}Zr_{36}$ and $Cu_{36}Zr_{64}$ BMGs and as-prepared (NG1), annealed (NG2), annealed and pre-deformed (NG3) NGs with the same chemical composition and a grain size of 10 nm, at a constant strain rate of $4 \cdot 10^7$ s^{-1}.

Further, the impact of the glass–glass interface structure on the plastic behavior of Cu-rich and Zr-rich NGs is investigated in comparison. First, the stress–strain curves show a lower maximum stress for both as-prepared NGs (NG1) when compare to the BMG. In Figure 4 it can be seen that in case of as-prepared $Cu_{64}Zr_{36}$ NG the maximum stress is lower (about 4.0 GPa) compared to the BMG (about 4.7 GPa). The same trend is found for the maximum stress of NG1 $Cu_{36}Zr_{64}$ (about 2.6 GPa) compared to 3.0 GPa in case of the BMG with the same chemical composition. This can be explained by the lower activation barrier for STZs in the soft interfaces of nanoglasses [12]. This observation is supported when calculating the local atomic shear strain. Up to a strain of 8%, the STZs are only activated in the soft interface regions of both as-prepared NGs (see Figure 5, the NG1 case). Increasing the strain to 16%, embryonic shear bands are formed along the interfaces and propagate through the grain interiors. In all cases, the embryonic shear bands are blocked and no dominant shear band is formed. A more homogeneous deformation of the as-prepared $Cu_{64}Zr_{36}$ NG compared to the well localized deformation of the BMG in one dominant shear band is also supported when calculating the strain localization parameter (see Figure 6). On the other hand the Zr-rich BMG exhibits a homogeneous deformation. Therefore, in case of $Cu_{36}Zr_{64}$ NG, a more localized deformation confined in these embryonic shear bands results in a slightly higher ψ value for the NG1 compared to the BMG (see Figure 6).

The NGs studied in [14,16] have been structurally relaxed at a low temperature of 50 K. Due to the limited atoms mobilities, at this low temperature, interfaces still contain a frozen amount of excess volume. Therefore, in line with our previous studies [12] it is worth to investigate how thermal annealing affects the structure of glass–glass interfaces and the plastic deformation mechanisms in the Zr-rich NG in comparison to the Cu-rich NG. The NGs were annealed at 800 K (≈0.85 T_g of the bulk glass) for 2 ns. After annealing, the NGs were quenched to 50 K and deformed in uniaxial tension. In case of annealed Cu-rich NG (NG2) the plastic deformation no longer takes place in a network of multiple shear bands, and one dominant shear band is formed (see Figure 5 lower panel). Nevertheless, as it was already shown in [12] the plastic deformation of the NG2 deviates from what has been observed for the BMG. In contrast, the deformation mechanisms of the annealed Zr-rich NG (NG2)

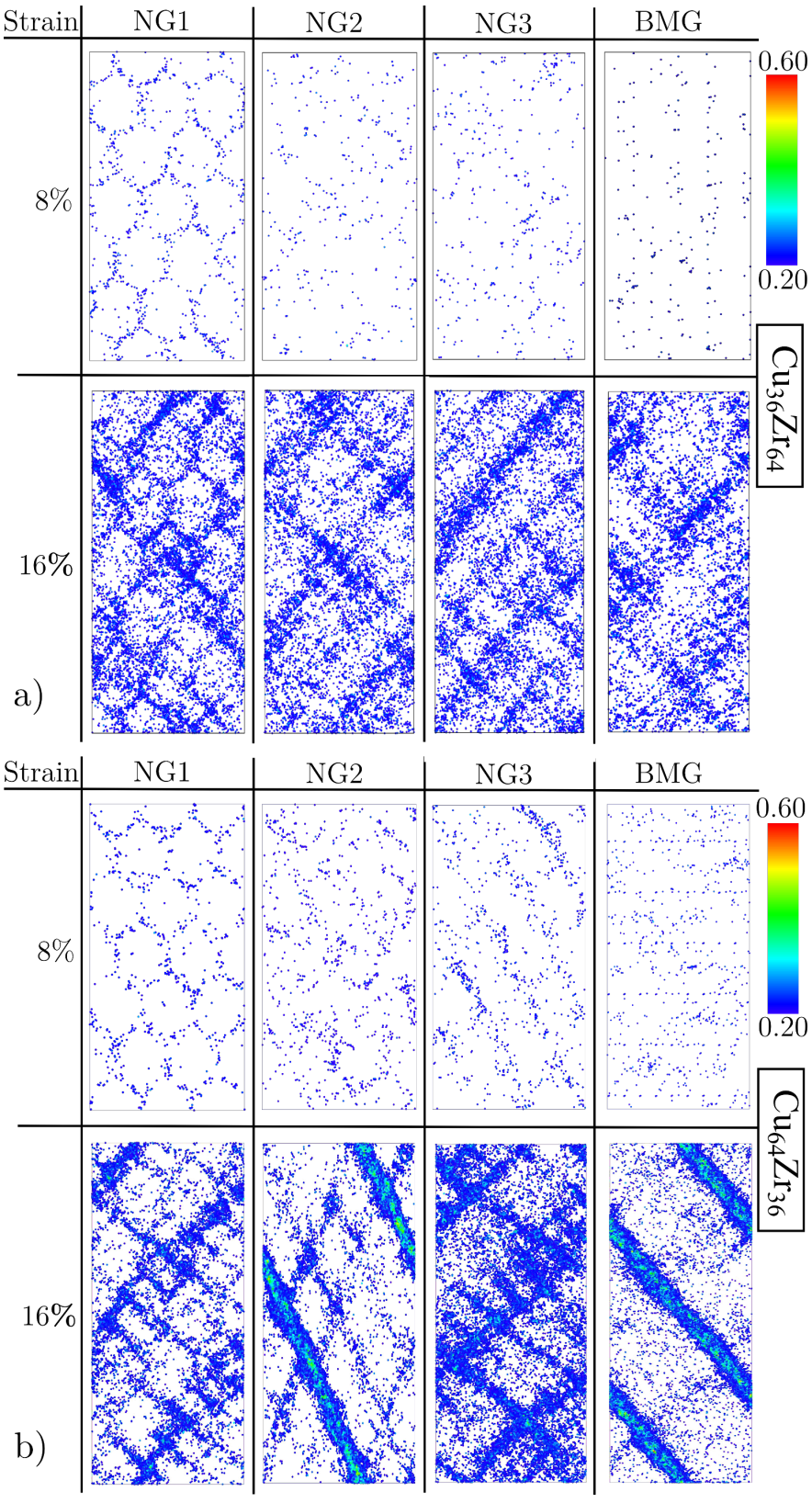


Figure 5: Local atomic shear strain for (a) $Cu_{36}Zr_{64}$ and (b) $Cu_{64}Zr_{36}$ BMGs and as-prepared (NG1), annealed (NG2), annealed and pre-deformed (NG3) NGs with a grain size of 10 nm.

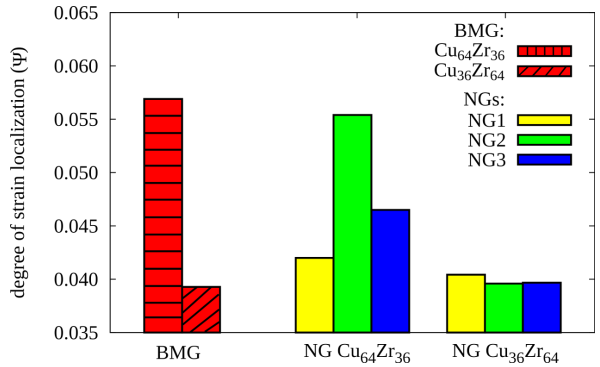


Figure 6: The ψ values for $Cu_{64}Zr_{36}$ and $Cu_{36}Zr_{64}$ BMGs and as-prepared (NG1), annealed (NG2), annealed and pre-deformed (NG3) NGs after plastic deformation to an overall strain of 16%.

observed at a strain of 8% and 16%, respectively, are similar to the ones in the BMG, as can be seen in Figure 5 upper panel. The anomalous plastic behavior observed for the annealed Zr-rich NG can be attributed to the structure of the interfaces for this alloy composition.

In order to understand how the alloy composition affects the interface structure, we constructed a simple model of a planar glass–glass interface in a Cu-rich and Zr-rich glass, respectively. The interfaces were prepared by joining two planar relaxed glass surfaces. The planar interface is located at $x = 0$ parallel to the yz-plane. The geometry and the total number of atoms is about the same for both alloy compositions ($16 \times 7 \times 12$ nm^3, ≈95,000 atoms). In the case of $Cu_{64}Zr_{36}$ the planar interface of about 1 nm width shows an excess free volume and a defective FI SRO. In Figure 7, upper, it can be seen that in the planar interface the FI-density is decreased by 70% from the bulk value. The fraction of Cu-centered FIs is as low as 10% in the interface compared to average FI value of the bulk glass of about 22% (with respect to the number of Cu atoms in the system). From the defective FIs SRO results approximately 1–2% excess free volume in the interface. In Figure 7, upper, the free volume through the system is plotted together with the Cu-centered FI cluster. When the Cu-rich glass with one planar interface is annealed at a temperature of 800 K for 2 ns, the fraction of FIs in the interface increases to 16% from the initial value of 10% leaving a difference between bulk glass and interface of about 2% [11]. At the same time, the excess free volume observed initially in the interfaces delocalizes completely under annealing. However, after annealing the planar interfaces in Cu-rich alloys are still characterized by a defective SRO. This explains why glass–glass interfaces in the annealed $Cu_{64}Zr_{36}$ nanoglass still have an impact on plastic deformation, as can be seen in Figure 5 upper panel.

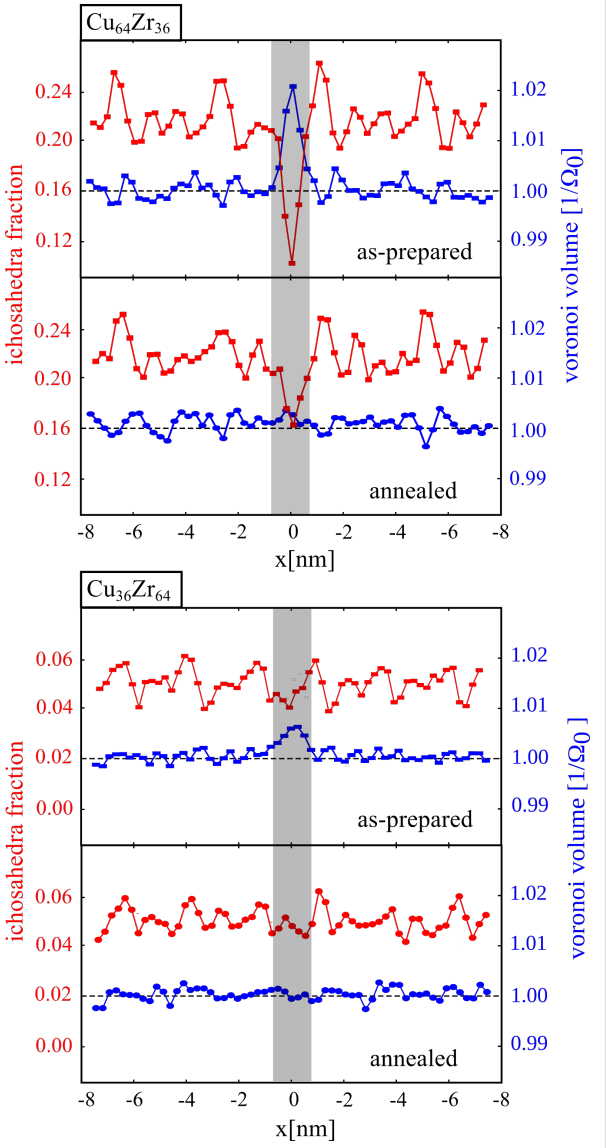


Figure 7: The fraction of Cu-centered full icosahedra and Voronoi volume in the $Cu_{64}Zr_{36}$ and $Cu_{36}Zr_{64}$ metallic glasses with a planar glass–glass interface.

On the other hand, in case of the $Cu_{36}Zr_{64}$ alloy the FI density is constant in the whole sample, and we do not see a deviation at the position of the interface (see Figure 7). We found that the population of Cu-centered FIs in case of the Zr-rich glass is only 5%. This value is similar to the one found in other studies [17,22]. Surprisingly, in Figure 7 it can be seen that the density in the interface is decreased although the FI density is not affected. However, the fraction of about 0.7% excess free volume detected for the interface in Zr-rich glass is much lower compared to the case of Cu-rich metallic glass (≈2%). Similar results have been found by Ritter et al. in the case of shear bands in $Cu_{36}Zr_{64}$ glass [17]. Here, the increase in the free volume in the shear band was not related to the decrease of

densely packed FI cluster inside the shear bands as found for the case of Cu-rich metallic glass. In [17] it has been shown that the volume expansion inside the shear band is related to the creation of new FI clusters which show a lower packing density. The creation of these new less densely packed FI clusters fully compensate the destruction of the original icosahedra SRO. In the case of a planar interface in Zr-rich glass the increase in the free volume is related also to the destruction and formation of FI clusters. This time, the FI clusters are damaged when cutting the planar surfaces. When the interface is prepared by joining the resulting glassy surfaces a new set of FI clusters form. These new FIs show a lower packing density than the FIs in the bulk glass which leads to an increased volume inside the interface. Although the excess free volume of the planar interface in the Zr-rich glass is below 1%, it can be seen in Figure 5 lower panel that also the plastic behavior of $Cu_{36}Zr_{64}$ NG deviates from the homogeneous BMG.

Finally, we also examined, the structure of the planar interface in the Zr-rich metallic glass after thermal annealing. The system with one planar interface is annealed following the same procedure as in the case of Cu-rich glass. Also, in this case the excess free volume of the glass–glass interface in Zr-rich glass delocalizes, completely. Therefore, the planar interface in the annealed Zr-rich glass has the same FI fraction and atomic density as the bulk glass. This observation explains the similarity between the plastic behavior of the annealed Zr-rich NG and the homogeneous BMG. Without interfaces, the plasticity of the annealed NG could not be tuned by pre-deforming to strain levels below the yield stress. It can be seen in Figure 5 that even at a strain of 16% the plastic behavior of the annealed and pre-deformed NG (NG3) is almost similar to the one of the annealed NG and BMG. This observation is supported when analyzing the stress–strain curves for NG2 and NG3 in comparison the BMG. In Figure 4, it can be seen that the curves of these three structures are very similar. In addition, the degree of strain localization parameters ψ for NG2, NG3, and BMG have almost same values (see Figure 6).

Conclusion

In the present study we investigated the influence of grain size and composition on the deformation behavior of Cu–-Zr NGs. We find that as-prepared NGs show a homogeneous plastic deformation in a pattern of multiple shear bands. For the case of $Cu_{64}Zr_{36}$ a transition from a more homogeneous to inhomogeneous plastic deformation can be observed, when the grain size is increased from 4 nm to 16 nm. Even for the largest grain size the deformation behavior of the NG differs from the well localized plastic deformation observed in the BMG. However, after a thermal annealing step, the excess free volume is equilibrating and only topological disorder can still be found in the glass–glass interfaces, which is having a minor influence on the formation of shear transformation zones. In the Zr-rich system ($Cu_{36}Zr_{64}$), in contrast, there is no appreciable difference in the topological order of the glassy matrix and the glass–glass interfaces. Thus, only the as prepared state, where some excess volume is localized in the glass–glass interfaces, shows a slightly enhanced shear localization as compared to the bulk glass.

In summary, our results show that the mechanical properties of a nanoglass can be tuned by varying the initial grain sizes, if the glass–glass interfaces have an excess free volume and are distinct in their topology from the homogeneous bulk phase.

Acknowledgements

The authors acknowledge the financial support of the Deutsche Forschungsgemeinschaft (DFG) through project Al-578-15. A DAAD-PPP travel grant with University of Helsinki is also acknowledged. Computing time was made available at HHLR Frankfurt and Darmstadt, as well as by the Gauss Centre for Supercomputing (GCS) through the John von Neumann Institute for Computing (NIC). The authors acknowledge Dr. Yvonne Ritter for fruitful discussions.

References

1. Gleiter, H. *Beilstein J. Nanotechnol.* **2013,** *4,* 517–533. doi:10.3762/bjnano.4.61
2. Jing, J.; Krämer, A.; Birringer, R.; Gleiter, H.; Gonser, U. *J. Non-Cryst. Solids* **1989,** *113,* 167–170. doi:10.1016/0022-3093(89)90007-0
3. Weissmüller, J.; Birringer, R.; Gleiter, H. *Key Eng. Mater.* **1993,** *77–78,* 161–170. doi:10.4028/www.scientific.net/KEM.77-78.161
4. Weissmüller, J.; Schubert, P.; Franz, H.; Birringer, R.; Gleiter, H., Eds. *Proceedings of the 7th National Conference on the Physics of Non-Crystalline Solids,* Cambridge, England, Aug 4–9, 1991; .
5. Weissmüller, J.; Birringer, R.; Gleiter, H. In *Proceedings of the TMS Annual Meeting New Orleans;* 1991; pp 291 ff.
6. Ghafari, M.; Hahn, H.; Gleiter, H.; Sakurai, Y.; Itou, M.; Kamali, S. *Appl. Phys. Lett.* **2012,** *101,* 243104. doi:10.1063/1.4769816
7. Witte, R.; Feng, T.; Fang, J. X.; Fischer, A.; Ghafari, M.; Kruk, R.; Brand, R. A.; Wang, D.; Hahn, H.; Gleiter, H. *Appl. Phys. Lett.* **2013,** *103,* 073106. doi:10.1063/1.4818493
8. Chen, N.; Frank, R.; Asao, N.; Louzguine-Luzgin, D. V.; Sharma, P.; Wang, J. Q.; Xie, G.; Ishikawa, Y.; Hatakeyama, N.; Lin, Y. C.; Esashi, M.; Yamamoto, Y.; Inoue, A. *Acta Mater.* **2011,** *59,* 6433–6440. doi:10.1016/j.actamat.2011.07.007
9. Fang, J. X.; Vainio, U.; Puff, W.; Würschum, R.; Wang, X. L.; Wang, D.; Ghafari, M.; Jiang, F.; Sun, J.; Hahn, H.; Gleiter, H. *Nano Lett.* **2012,** *12,* 458–463. doi:10.1021/nl2038216
10. Sopu, D.; Albe, K.; Ritter, Y.; Gleiter, H. *Appl. Phys. Lett.* **2009,** *94,* 191911. doi:10.1063/1.3130209
11. Ritter, Y.; Şopu, D.; Gleiter, H.; Albe, K. *Acta Mater.* **2011,** *59,* 6588–6593. doi:10.1016/j.actamat.2011.07.013
12. Şopu, D.; Ritter, Y.; Gleiter, H.; Albe, K. *Phys. Rev. B* **2011,** *83,* 100202. doi:10.1103/PhysRevB.83.100202

13. Albe, K.; Ritter, Y.; Şopu, D. *Mech. Mater.* **2013,** *67,* 94–103. doi:10.1016/j.mechmat.2013.06.004
14. Adibi, S.; Sha, Z.-D.; Branicio, P. S.; Joshi, S. P.; Liu, Z.-S.; Zhang, Y.-W. *Appl. Phys. Lett.* **2013,** *103,* 211905. doi:10.1063/1.4833018
15. Franke, O.; Leisen, D.; Gleiter, H.; Hahn, H. *J. Mater. Res.* **2014,** *29,* 1210–1216. doi:10.1557/jmr.2014.101
16. Adibi, S.; Branicio, P. S.; Zhang, Y.-W.; Joshi, S. P. *J. Appl. Phys.* **2014,** *116,* 043522. doi:10.1063/1.4891450
17. Ritter, Y.; Albe, K. *J. Appl. Phys.* **2012,** *111,* 103527. doi:10.1063/1.4717748
18. Plimpton, S. *J. Comput. Phys.* **1995,** *117,* 1–19. doi:10.1006/jcph.1995.1039
19. Mendelev, M. I.; Sordelet, D. J.; Kramer, M. J. *J. Appl. Phys.* **2007,** *102,* 043501. doi:10.1063/1.2769157
20. Voronoi, G. *J. Reine Angew. Math.* **1908,** *134,* 198–287. doi:10.1515/crll.1908.134.198
21. Lee, J.-C.; Park, K.-W.; Kim, K.-H.; Fleury, E.; Lee, B.-J.; Wakeda, M.; Shibutani, Y. *J. Mater. Res.* **2007,** *22,* 3087–3097. doi:10.1557/JMR.2007.0382
22. Cheng, Y. Q.; Cao, A. J.; Sheng, H. W.; Ma, E. *Acta Mater.* **2008,** *56,* 5263–5275. doi:10.1016/j.actamat.2008.07.011
23. Shimizu, F.; Ogata, S.; Li, J. *Mater. Trans.* **2007,** *48,* 2923–2927. doi:10.2320/matertrans.MJ200769
24. Stukowski, A. *Modelling Simul. Mater. Sci. Eng.* **2010,** *18,* 015012. doi:10.1088/0965-0393/18/1/015012
25. Cheng, Y. Q.; Cao, A. J.; Ma, E. *Acta Mater.* **2009,** *57,* 3253–3267. doi:10.1016/j.actamat.2009.03.027
26. Xiao, Q.; Sheng, H. W.; Shi, Y. *MRS Commun.* **2012,** *2,* 13–16. doi:10.1557/mrc.2011.26
27. Sheng, H. W.; Luo, W. K.; Alamgir, F. M.; Bai, J. M.; Ma, E. *Nature* **2006,** *439,* 419–425. doi:10.1038/nature04421
28. Lee, M.; Lee, C.-M.; Lee, K.-R.; Ma, E.; Lee, J.-C. *Acta Mater.* **2011,** *59,* 159–170. doi:10.1016/j.actamat.2010.09.020

License and Terms

This is an Open Access article under the terms of the Creative Commons Attribution License (http://creativecommons.org/licenses/by/2.0), which permits unrestricted use, distribution, and reproduction in any medium, provided the original work is properly cited.

The license is subject to the *Beilstein Journal of Nanotechnology* terms and conditions: (http://www.beilstein-journals.org/bjnano)

The definitive version of this article is the electronic one which can be found at: doi:10.3762/bjnano.6.56

BEILSTEIN JOURNAL OF NANOTECHNOLOGY

Polymer blend lithography for metal films: large-area patterning with over 1 billion holes/inch^2

Cheng Huang[1,2], Alexander Förste[1,2], Stefan Walheim[*1,2] and Thomas Schimmel[1,2]

Full Research Paper

Open Access

Address:
[1]Institute of Applied Physics and Center for Functional Nanostructures (CFN), Karlsruhe Institute of Technology (KIT), 76128 Karlsruhe, Germany and [2]Institute of Nanotechnology (INT), Karlsruhe Institute of Technology (KIT), 76021 Karlsruhe, Germany

Email:
Stefan Walheim[*] - stefan.walheim@kit.edu

* Corresponding author

Keywords:
localized surface plasmonic resonance; metal islands; metal nanostructures; metal polymer blend lithography (metal PBL); nano-patterned template; nanoscale discs; optical transmission; perforated metal film; polymer phase separation; poly(methyl methacrylate) (PMMA); polystyrene (PS); self-assembly; spin-coating; surface plasmons

Beilstein J. Nanotechnol. **2015,** *6,* 1205–1211.
doi:10.3762/bjnano.6.123

Received: 10 August 2014
Accepted: 22 April 2015
Published: 26 May 2015

This article is part of the Thematic Series "Advances in nanomaterials II".

Guest Editor: H. Hahn

© 2015 Huang et al; licensee Beilstein-Institut.
License and terms: see end of document.

Abstract

Polymer blend lithography (PBL) is a spin-coating-based technique that makes use of the purely lateral phase separation between two immiscible polymers to fabricate large area nanoscale patterns. In our earlier work (Huang et al. 2012), PBL was demonstrated for the fabrication of patterned self-assembled monolayers. Here, we report a new method based on the technique of polymer blend lithography that allows for the fabrication of metal island arrays or perforated metal films on the nanometer scale, the metal PBL. As the polymer blend system in this work, a mixture of polystyrene (PS) and poly(methyl methacrylate) (PMMA), dissolved in methyl ethyl ketone (MEK) is used. This system forms a purely lateral structure on the substrate at controlled humidity, which means that PS droplets are formed in a PMMA matrix, whereby both phases have direct contact both to the substrate and to the air interface. Therefore, a subsequent selective dissolution of either the PS or PMMA component leaves behind a nanostructured film which can be used as a lithographic mask. We use this lithographic mask for the fabrication of metal patterns by thermal evaporation of the metal, followed by a lift-off process. As a consequence, the resulting metal nanostructure is an exact replica of the pattern of the selectively removed polymer (either a perforated metal film or metal islands). The minimum diameter of these holes or metal islands demonstrated here is about 50 nm. Au, Pd, Cu, Cr and Al templates were fabricated in this work by metal PBL. The wavelength-selective optical transmission spectra due to the localized surface plasmonic effect of the holes in perforated Al films were investigated and compared to the respective hole diameter histograms.

Introduction

Research on micro-/nano-sized island arrays and perforated films has drawn wide interest due to their applications in various fields, such as optical devices [1,2], DNA or protein electrophoresis [3,4], and catalysis [5,6]. Varieties of techniques have been developed to achieve metal or semiconductor nanopatterns, such as electron beam lithography [7-9], nanosphere lithography [10-13], laser interference lithography [14,15], AFM-based dip-pen lithography [16], and more. Masuda and his colleagues used anodic porous alumina as lithographic mask for the fabrication of both ordered gold or silver nanodot arrays and ordered nanohole arrays in a gold film [17,18]. Lithographic methods incorporated with self-assembled block copolymers are also promising ways to fabricate sub-100 nm metal nanodots or perforated films, however these processes are often complicated or time consuming, e.g., as vapor annealing for block-copolymers takes days to complete and UV radiation or reactive ion etching (RIE) is required for the lift-off process [19,20].

Here, we introduce a very rapid and cost-effective way to fabricate metal island arrays or perforated metal films via metal polymer blend lithography (metal PBL). The polymer blend lithography was applied in our earlier reports to fabricate self-assembled monolayer (SAM) patterns (monolayer PBL) [21], which were used, e.g., for the selective growth of ZnO nanostructures [22]. Instead of silicon wafers, other materials such as glass or metal can also be used as substrates. For example iron was used as substrate for the fabrication of nanoporous gold mesoflower arrays, which served afterwards for surface-enhanced Raman scattering [23]. With the metal PBL technique it is possible to fabricate more than one billion metal islands or holes on a substrate with a size of 1 inch × 1 inch.

Results and Discussion

Metal polymer blend lithography (metal PBL) for metal islands or perforated films

The metal polymer blend lithography method (metal PBL) is schematically demonstrated in Figure 1. The spin casting of the polystyrene (PS)/poly(methyl methacrylate) (PMMA) blend film from a blend solution ends with a purely lateral phase separation between the two immiscible polymers under controlled spin-coating parameters (see Figure 1a). As reported in our earlier publication, the ambient atmosphere (humidity), the molar mass of the polymers and the mass ratio between the two polymers in the blend solution play important roles in the determination of the structure of the formed films [21,24]. In this study cyclohexane was used as the selective solvent for removing PS while acetic acid for removing PMMA. Via selective dissolution, either the PMMA matrix (see Figure 1b, PMMA marked in red) or the PS droplets (see Figure 1g, PS marked in blue) can be kept on the substrate for the lithographic application.

After the deposition of metal by thermal evaporation, the desired metal covers the whole surface of the sample (see in Figure 1c and Figure 1h, metal is marked in gold). Finally the snow jet method is applied for the lift-off of the polymer mask and a nano-patterned metal structure (either a perforated film as shown in Figure 1i or islands as shown in Figure 1d) remains on the substrate. This metal pattern is an exact replica of the selectively dissolved polymer.

Figure 1e,f,j,k show the SEM images of the polymer lithographic masks and the gold islands together with the perforated gold film respectively, which were fabricated applying these masks. The density of the holes shown in Figure 1k is about 130 million/cm^2. Figure 1e is an SEM image taken at a tilting angle of 45° of a polymer lithographic mask, which is schematically shown in Figure 1b. After the polymer blend film was rinsed in cyclohexane, the PS droplets were dissolved and a perforated PMMA film with holes was left on the silicon substrate. The diameters of these holes range from 200 to 800 nm. The metal islands deposited into the holes are stable and resist the snow-jet treatment that is used for the lift-off of the PMMA mask. For some metals such as gold and silver, an adhesion enhancing interlayer of metal, e.g., titanium or chromium is necessary between the desired metal and the substrate. The SEM top view image of the gold islands with a thickness of 20 nm is shown in Figure 1f. The islands have the same size (200–800 nm) as the holes in the polymer film (see Figure 1e).

For the fabrication of a perforated metal film, the polymer blend must be rinsed in acetic acid instead of cyclohexane. In this case, consisting PS droplets is left on the substrate. A smooth and clean silicon surface can be seen in the SEM image taken at a tilting angle of 45°. The “Go stone”-like PS droplets are ideal for the following lift-off process (see Figure 1j). Consequently the fabricated perforated gold film (see Figure 1k) has holes with perfectly round shapes and smooth edges. The diameters of these holes range also from 200 to 800 nm, which is in accordance with the PS lithographic mask. To demonstrate the feasibility of the reported lithographic technique to form patterns of various metals, we used the process described in Figure 1g–i to fabricate 20 nm thick films of gold, palladium, copper and chromium (see Figure 2).

Sub-100 nm holes and islands

By using polystyrene with very low molecular weight (9.58 kg/mol), it is possible to obtain a polymer blend film with very small PS droplets. This offers the possibility to fabricate

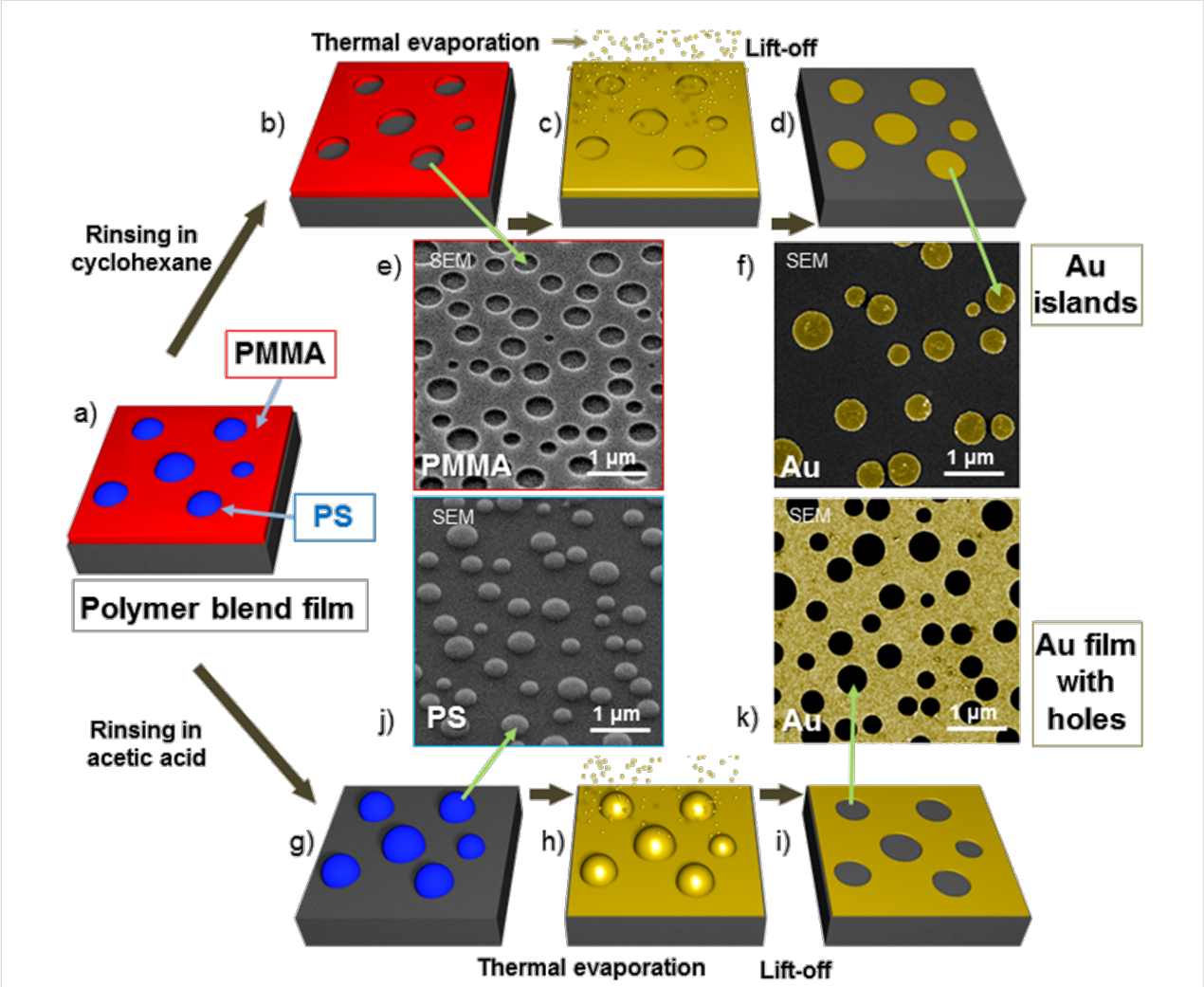


Figure 1: Schematic drawing and experimental results of the metal PBL process for the fabrication of metal nano-patterns. a) A blend film (PS/PMMA 3:7 mass ratio) is formed through spin-coating. PS droplets are formed in a PMMA matrix, and both phases have contact to the substrate as well as to the air. b) PS droplets are selectively dissolved by cyclohexane. c) Deposition of metal via thermal evaporation. d) After lift-off via snow-jet treatment, a negative metal copy of the PMMA mask is formed. e) SEM image of a perforated PMMA film (taken at a tilting angle of 45°). f) SEM image of gold islands. g) The PMMA matrix is selectively dissolved by acetic acid. h) Deposition of metal via thermal evaporation. i) After lift-off via snow jet, a negative metal copy of the PS mask is formed. j) SEM image of PS droplets (taken at a tilting angle of 45°). k) SEM image of a perforated gold film.

sub-100 nm metal islands or sub-100 nm holes in metal films, which is comparable, e.g., to the size of viruses. Figure 3a is an AFM image of a perforated Cu film with a thickness of 20 nm. The diameters of the holes range from 50 to 250 nm and have an average size of about 150 nm (see Figure 3c). The (sub-)100 nm holes are homogeneously distributed over the samples (about 14%). Figure 3b is an SEM image of the gold islands together with the PMMA lithographic mask, which was also covered with gold. The gold islands have statistically the same size as the holes in Figure 3a. In general, metal PBL is a good supplementary to the conventional lithographic methods for fabrication of structures in hundreds of nanometer or even sub-100 nanometer range in a versatile and up-scalable way.

Localized surface plasmonic resonance of perforated Al films

The size of the holes in the fabricated perforated metal films is in the range of the wavelength of visible light. Therefore it is interesting to investigate their optical transmission properties. It has been published in 2003 by Barnes et al. that ordered hole arrays fabricated by e-beam lithography can be used as wavelength-selective optical filters [25]. The photons couple to surface plasmons on the incident side of a nanohole film. These surface plasmons convert back to photons after they propagate through the holes to the opposite side of the film [26]. In recent years, also the colloidal lithography method has been used to study the surface plasmonics of random nano-hole arrays in metal films [26,27].

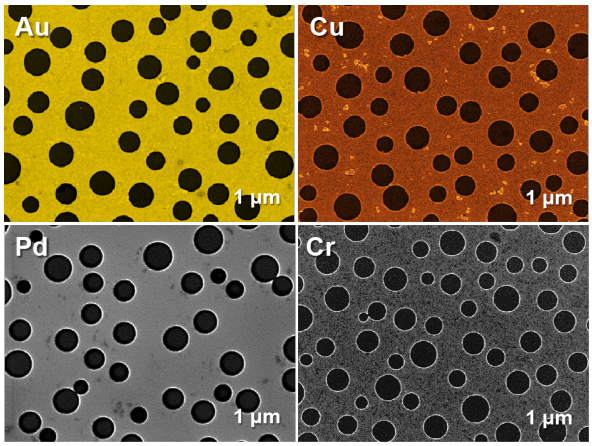


Figure 2: SEM images of perforated Au, Pd, Cu, and Cr films fabricated by metal PBL. Aluminum films are shown below in Figure 4.

Since the skin depth, and therefore the transmission of thin films, of Cu, Au and Ag is relatively high, we selected aluminum, which shows a high reflectivity in the range of 220 to 650 nm (about 90%) already at a thickness below 30 nm [28]. Our result, using templates produced according to the process described in Figure 1g–i is shown in Figure 4. A transmission difference of 13% can be observed (see Figure 4a,b) due to the hole coverage area difference between the two samples (see Figure 4c,d). A red shift of the transmission peak can be observed from 1200 to 1450 nm when the average size of the nano-holes in the perforated aluminum film increases from 400 to 500 nm (see Figure 4a,b). This red shift is expected as the surface plasmonic effect in perforated metal films can be tuned by the size of the sub-wavelength holes [22,29,30]. Compared with colloidal lithography, which requires extra process steps to charge the substrate and the colloidal spheres, metal PBL brings a more convenient way to fabricate nano-hole arrays in various kinds of metal films with the potential to be applied on the square meter scale.

Hole density in perforated films

As shown in Figure 4c and Figure 4d, the hole density of the perforated Al film which was fabricated with 3:7 PS/PMMA solution (mass ratio) is about 400 holes/225 µm^2 (180 million/cm^2) and for film fabricated with 4:6 PS/PMMA

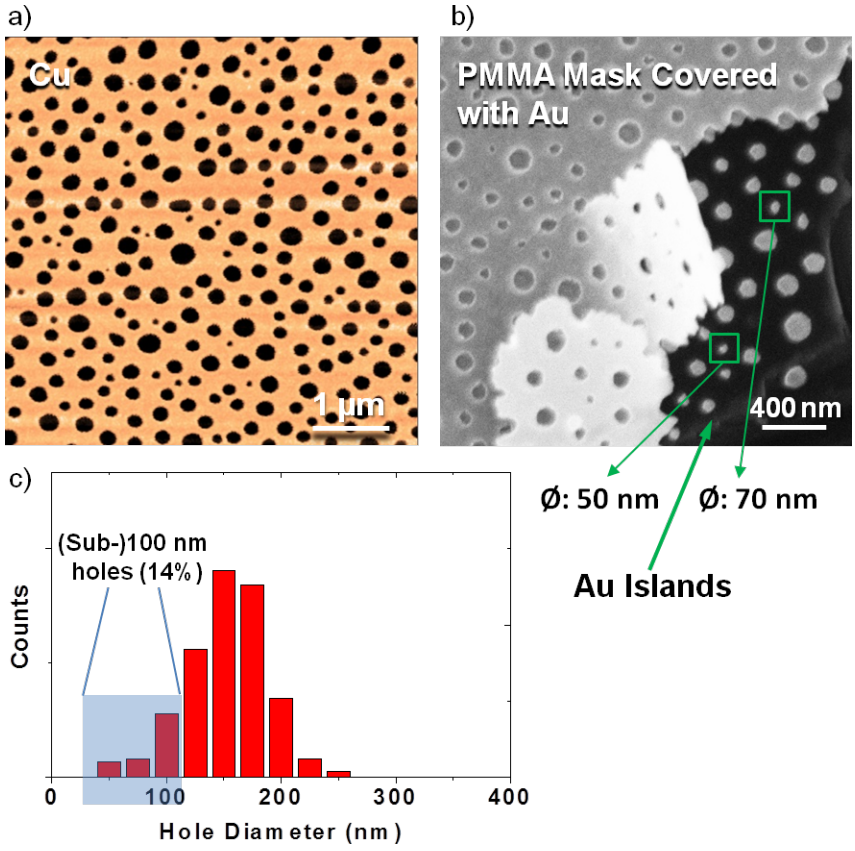


Figure 3: Sub-100 nm holes in a Cu film (left) and gold islands (right) fabricated by metal PBL. a) AFM image of a perforated Cu film with a thickness of 20 nm. b) SEM image of gold islands (with a thickness of 20 nm) with PMMA lithographic mask covered with gold. c) Diameter distribution of the holes in Figure 3a. The holes have an average diameter of about 150 nm and there are holes found in the (sub-)100 nm range (about 14%).

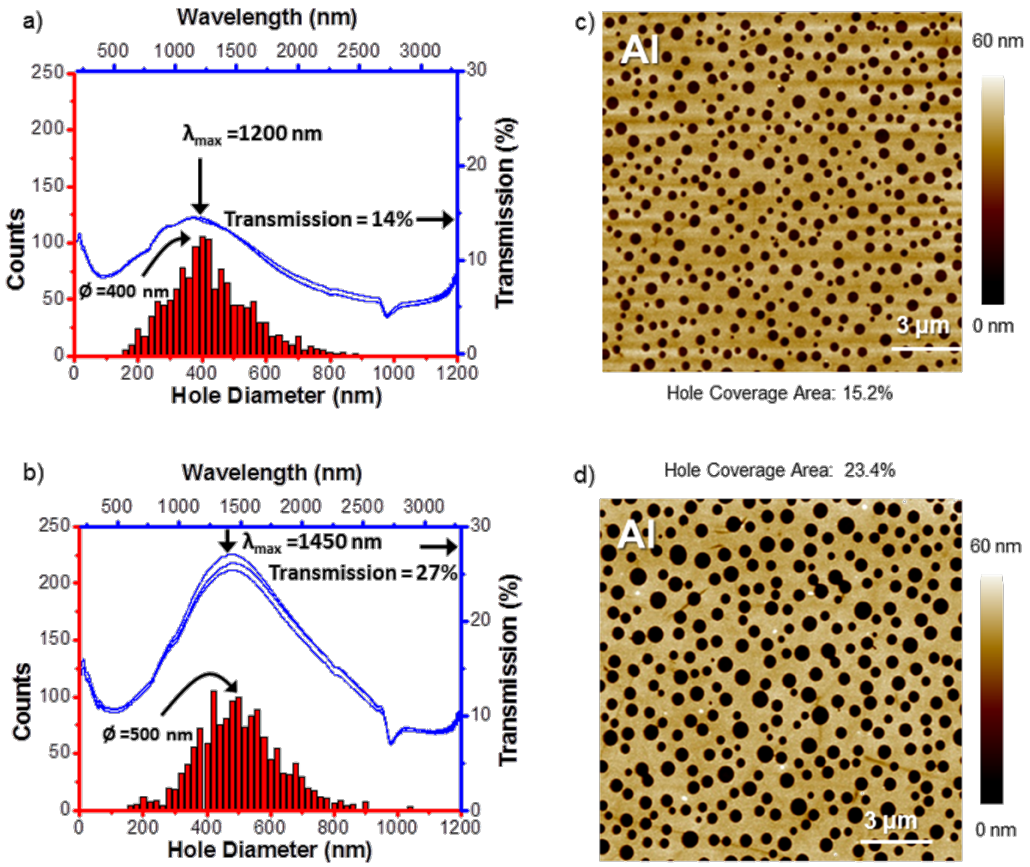


Figure 4: Optical transmission due to localized surface plasmonic resonance (blue) of perforated aluminum films with two different hole size distributions (red). Top: smaller holes (PS/PMMA mass ratio 3:7) with a hole coverage area of 15.2%, bottom: larger holes (PS/PMMA mass ratio 4:6) with a hole coverage area of 23.4%. a) and b): The hole size distributions are shown with red columns, the data are the summarization of five 15 µm × 15 µm AFM images taken at randomly selected positions. The optical transmission spectra, taken at various sample positions, are plotted as blue line graphs. The representative AFM topography (tapping mode) of the samples is shown in c) and d).

solution is about 300 holes/225 µm^2 (130 million/cm^2). Another sample, a perforated Cr film (see Figure 2), shows a hole density of 220 million/cm^2.

Perspectives

The metal nano-disc arrays have a variety of potential applications such as the localized growth of ZnO nano wires or rods [31,32] or plasmonic applications [23]. The surface of the metal can be selectively modified with molecules such as thiols and used for immobilization of biomaterials [33]. The perforated metal films, which can be fabricated on large areas based on spin-coating and physical vapor deposition (PVD), have the potential to be used as wavelength-selective optical filters. In the case of our examples they let NIR light pass and block photons with longer wavelengths. It is also possible to combine the perforated metal films with micelle lithographic technique [34,35] to implant gold dots with diameter of 10 nm into the holes to form hierarchical micro–nano structures for applications such as cell-adhesion studies [36,37]. Metals like Cr, Au or Cu are good etching resists. Therefore the metal masks could be used to amplify the topographic contrast by anisotropic etching into the substrate with techniques such as reactive ion etching [38,39].

Conclusion

Polymer blend lithography (PBL) makes use of the purely lateral phase separation of two immiscible polymers during spin-casting at controlled humidity. A metal copy of either of the polymer components can be fabricated by the selective dissolution of one component, followed by metal deposition and the final lift-off of the lithographic mask. Metal PBL starts with spin-coating of a polymer blend (PS/PMMA in MEK) film onto a substrate. A purely lateral phase separation occurs at the selected adequate conditions. Either of the components can be selectively dissolved and the other used as a lithographic mask. After the evaporation of metal and the lift-off process by snow jet treatment, a negative metal copy of the polymer mask is achieved.

The diameter of the metal islands or the holes in the metal films can be tuned by changing the molecular weight of polystyrene [21]. The typical diameter ranges from 200 to 800 nm with an average of about 400 nm (achieved by using 96 kg/mol PS and PS/PMMA mass ratio of 3:7). By using PS with a molar mass of 9.56 kg/mol, we obtained nano-islands and nano-holes with diameters ranging from 50 to 250 nm. Both the island arrays and the perforated films could be used for various applications, e.g., in cell adhesion studies, for the immobilization of biomaterials, for plasmonics such as optical filters or as resist layers for anisotropic reactive ion etching. The wavelength-selective optical transmission of our perforated films due to the localized surface plasmonic resonance was clearly demonstrated. In general, metal polymer blend lithography (metal PBL) is a new up-scalable and time-efficient method for the fabrication of functional micro/nanosized metal island arrays or nano-perforated metal films.

Large area applications in the square meter range could be realized, e.g., by using slot dye coating in a roll to roll process followed by large scale metal evaporation which is already used in the food packaging industry.

Experimental

Polymer solution

Poly(methyl methacrylate) (PMMA) (M_w = 9.56 kg/mol PDI = 1.05) and poly(styrene) (PS) (M_w = 96 kg/mol PDI = 1.04) were purchased from Polymer Standards Service GmbH (PSS) and dissolved directly in methyl ethyl ketone (MEK, Aldrich). The combined concentration of the two polymers was 15 mg/mL and the mass ratio between PS and PMMA was 3:7. (Exception: Figure 4b,d with PS/PMMA 4:6). For fabrication of templates with sub-100 nm structures (Figure 2) PS with a molecular weight of 9.58 kg/mol (PDI = 1.03, also purchased from PSS) was used to prepare the lithographic mask. All other parameters were kept constant.

Cleaning of Si and quartz glass substrates

Silicon substrates were used as delivered with their native oxide layer. Both silicon and quartz glass substrates were cleaned by the snow jet method [21]: The wafers were exposed to a jet of CO_2 ice crystals, which were produced by expanding CO_2 stream through a nozzle. In this way, surface contaminants are removed either by mechanical impact or by dissolution in CO_2.

Preparation of a polymer blend lithographic mask (humidity)

The polymer blend films were spin-casted at a speed of ca. 1500 revolutions per minute (rpm) under a relative humidity of 40% onto silicon substrates cleaned by snow jet treatment (at least 20 s for a 2 cm × 2 cm substrate). The humidity was controlled by venting the chamber (about 1 L volume) with a mixture of nitrogen and water-saturated nitrogen (total flow rate approximately 40 standard cubic centimeters per minute (sccm)). The humidity in the chamber was measured by a hygrometer (Testo 635). For the optical transmission test, quartz glass was used as the substrate.

Fabrication of metal islands and perforated films

For the fabrication of metal islands PS was selectively dissolved by cyclohexane, as shown in Figure 1b. Samples were rinsed in the solvent three times, each time for about 30 s with constant movement of the samples and then dried in nitrogen flow. The metal was deposited by a custom-built e-beam thermal evaporation machine. The distance between the evaporation source and the sample was about 60 cm. The thickness of the deposited metal film was measured by a quartz balance. For the deposition of gold, a Ti film with a thickness of 1.5 nm was deposited first in order to ensure the adhesion of the gold to the silicon substrate. The lift-off of PMMA on silicon substrates was done by snow-jet treatment. For a complete lift-off it is important that the CO_2 gas cylinder is at room temperature and has a proper filling level. The lift-off process can also be done by using a good solvent as THF for the remaining polymer. This was done, e.g., for PMMA on quartz glass. These samples were processed by sonication in tetrahydrofuran (THF) (30 min).

For the fabrication of perforated metal films the PMMA was selectively dissolved by acetic acid as shown in Figure 1g. The metal film was then deposited the same way and the PS droplets were removed by snow-jet treatment for silicon substrate and by sonication in THF for quartz glass.

Sample characterization

The metal patterns were characterized by scanning electron microscopy (SEM). SEM images were taken at 10 kV with a LEO 1530 SEM using a secondary electron detector. The SEM images of the metal islands and perforated films were taken at 10 kV using an in-lens detector while the AFM image was taken in tapping mode with a Bruker ICON and a custom-built AFM equipped with an Asylum MFP-3D controller. The transmission spectra were measured by a Varian Cary 500 Scan UV–vis spectrometer with open reference beam.

Acknowledgements

This work was supported by the Deutsche Forschungsgemeinschaft (DFG) within the Center for Functional Nanostructures (CFN) and by the Baden-Württemberg Stiftung within the Network of Excellence “Functional Nanostructures”.

References

1. Chalamala, B. R.; Wei, Y.; Gnade, B. E. *IEEE Spectrum* **1998,** *35,* 42. doi:10.1109/6.666960
2. Kim, T. J.; Thio, T.; Ebbesen, T. W.; Grupp, D. E.; Lezec, H. J. *Opt. Lett.* **1999,** *24,* 256. doi:10.1364/OL.24.000256
3. Volkmuth, W. D.; Austin, R. H. *Nature* **1992,** *358,* 600. doi:10.1038/358600a0
4. Volkmuth, W. D.; Duke, T.; Wu, M. C.; Austin, R. H.; Szabo, A. *Phys. Rev. Lett.* **1994,** *72,* 2117. doi:10.1103/PhysRevLett.72.2117
5. Bright, R. M.; Ealter, D. G.; Musick, M. D.; Jackson, M. A.; Allison, K. J.; Natan, M. J. *Langmuir* **1996,** *12,* 810. doi:10.1021/la950429h
6. Pan, J. H.; Dou, H.; Xiong, Z.; Xu, C.; Ma, J.; Zhao, X. S. *J. Mater. Chem.* **2010,** *20,* 4512. doi:10.1039/b925523k
7. Ishikawa, T.; Kohmoto, S.; Asakawa, K. *Appl. Phys. Lett.* **1998,** *73,* 1712. doi:10.1063/1.122254
8. Schaal, P. A.; Simon, U. *Beilstein J. Nanotechnol.* **2013,** *4,* 336. doi:10.3762/bjnano.4.39
9. Trasobares, J.; Vaurette, F.; François, M.; Romijn, H.; Cordron, J.; Vuilaume, D.; Théron, D.; Clément, N. *Beilstein J. Nanotechnol.* **2014,** *5,* 1918. doi:10.3762/bjnano.5.202
10. Sun, F.; Cai, W.; Li, Y.; Cao, B.; Lu, F.; Duan, G.; Zhang, L. *Adv. Mater.* **2004,** *16,* 1116. doi:10.1002/adma.200400006
11. Gonçalves, M. R.; Makaryan, T.; Enderle, F.; Wiedemann, S.; Plettl, A.; Marti, O.; Ziemann, P. *Beilstein J. Nanotechnol.* **2011,** *2,* 448. doi:10.3762/bjnano.2.49
12. Herr, U.; Kuerbanjiang, B.; Benel, C.; Papageorgiou, G.; Goncalves, M.; Boneberg, J.; Leiderer, P.; Ziemann, P.; Marek, P.; Hahn, H. *Beilstein J. Nanotechnol.* **2013,** *4,* 306. doi:10.3762/bjnano.4.34
13. Zhao, J.; Frank, B.; Neubrech, F.; Zhang, C.; Braun, P. V.; Giessen, H. *Beilstein J. Nanotechnol.* **2014,** *5,* 577. doi:10.3762/bjnano.5.68
14. Riedel, S.; Schmotz, M.; Leiderer, P.; Boneberg, J. *J. Appl. Phys.* **2010,** *101,* 309. doi:10.1007/s00339-010-5822-x
15. Kim, D. S.; Ji, R.; Fan, H. J.; Bertram, F.; Scholz, R.; Dadgar, A.; Nielsch, K.; Krost, A.; Christen, J.; Gösele, U.; Zacharias, M. *Small* **2007,** *3,* 76. doi:10.1002/smll.200600307
16. Maynor, B. W.; Li, Y.; Liu, J. *Langmuir* **2001,** *17,* 2575. doi:10.1021/la001755m
17. Masuda, H.; Fukuda, K. *Science* **1995,** *268,* 1466. doi:10.1126/science.268.5216.1466
18. Masuda, H.; Yasui, K.; Nishio, K. *Adv. Mater.* **2000,** *12,* 1031. doi:10.1002/1521-4095(200007)12:14<1031::AID-ADMA1031>3.0.CO;2-R
19. Park, M.; Chaikin, P. M.; Register, R. A.; Adamson, D. H. *Appl. Phys. Lett.* **2001,** *79,* 257. doi:10.1063/1.1378046
20. Shin, K.; Leach, K. A.; Goldbach, J. T.; Kim, D. H.; Jho, J. Y.; Tuominen, M.; Hawker, C. J.; Russell, T. P. *Nano Lett.* **2002,** *2,* 933. doi:10.1021/nl0256560
21. Huang, C.; Moosmann, M.; Jin, J.; Heiler, T.; Walheim, S.; Schimmel, T. *Beilstein J. Nanotechnol.* **2012,** *3,* 620. doi:10.3762/bjnano.3.71
22. Bauermann, L. P.; Gerstel, P.; Bill, J.; Walheim, S.; Huang, C.; Pfeifer, J.; Schimmel, T. *Langmuir* **2010,** *26,* 3774. doi:10.1021/la903636k
23. Tian, C.; Liu, Z.; Jin, J.; Lebedkin, S.; Huang, C.; You, H.; Liu, R.; Wang, L.; Song, X.; Ding, B.; Walheim, S.; Schimmel, T.; Fang, J. *Nanotechnology* **2012,** *23,* 165604. doi:10.1088/0957-4484/23/16/165604
24. Walheim, S.; Böltau, M.; Mlynek, J.; Krausch, G.; Steiner, U. *Macromolecules* **1997,** *30,* 4995. doi:10.1021/ma9619288
25. Barnes, W. L.; Dereux, A.; Ebbesen, T. W. *Nature* **2003,** *424,* 824. doi:10.1038/nature01937
26. Reilly, T. H., III; Tenent, R. C.; Barnes, T. M.; Rowlen, K. L.; van de Lagemaat, J. *ACS Nano* **2010,** *4,* 615. doi:10.1021/nn901734d
27. Schwind, M.; Kasemo, B.; Zorić, I. *Nano Lett.* **2013,** *13,* 1743. doi:10.1021/nl400328x
28. Hass, G.; Waylonis, J. E. *J. Opt. Soc. Am.* **1961,** *51,* 719. doi:10.1364/JOSA.51.000719
29. Bulatov, V.; Abraham, F. F.; Kubin, L.; Devincre, B.; Yip, S. *Nature* **1998,** *391,* 669. doi:10.1038/35577
30. Genet, C.; Ebbesen, T. W. *Nature* **2007,** *445,* 39. doi:10.1038/nature05350
31. Fan, H. J.; Lee, W.; Hauschild, R.; Alexe, M.; Rhun, G. L.; Scholz, R.; Dadgar, A.; Nielsch, K.; Kalt, H.; Krost, A.; Zacharias, M.; Gösele, U. *Small* **2006,** *2,* 561. doi:10.1002/smll.200500331
32. Fan, H. J.; Werner, P.; Zacharias, M. *Small* **2006,** *2,* 700. doi:10.1002/smll.200500495
33. Ariga, K.; Nakanishi, T.; Michinobu, T. *J. Nanosci. Nanotechnol.* **2006,** *6,* 2278. doi:10.1166/jnn.2006.503
34. Spatz, J. P.; Mössmer, S.; Hartmann, C.; Möller, M.; Herzog, T.; Krieger, M.; Boyen, H.-G.; Ziemann, P.; Kabius, B. *Langmuir* **2000,** *16,* 407. doi:10.1021/la990070n
35. Glass, R.; Möller, M.; Spatz, J. P. *Nanotechnology* **2003,** *14,* 1153. doi:10.1088/0957-4484/14/10/314
36. Cavacanti-Adam, E. A.; Aydin, D.; Hirschfeld-Warneken, V. C.; Spatz, J. P. *HFSP J.* **2008,** *2,* 276. doi:10.2976/1.2976662
37. Geiger, B.; Spatz, J. P.; Bershadsky, A. D. *Nat. Rev. Mol. Cell Biol.* **2009,** *10,* 21. doi:10.1038/nrm2593
38. Calvert, J. M.; Chen, M.-S.; Dulcey, C. S.; Georger, J. H.; Peckerar, M. C.; Schnur, J. M.; Schoen, P. E. *J. Vac. Sci. Technol., B* **1991,** *9,* 3447. doi:10.1116/1.585820
39. Özdemir, B.; Seidenstücker, A.; Plettl, A.; Ziemann, P. *Beilstein J. Nanotechnol.* **2013,** *4,* 886. doi:10.3762/bjnano.4.100

License and Terms

This is an Open Access article under the terms of the Creative Commons Attribution License (http://creativecommons.org/licenses/by/2.0), which permits unrestricted use, distribution, and reproduction in any medium, provided the original work is properly cited.

The license is subject to the *Beilstein Journal of Nanotechnology* terms and conditions: (http://www.beilstein-journals.org/bjnano)

The definitive version of this article is the electronic one which can be found at: doi:10.3762/bjnano.6.123

BEILSTEIN JOURNAL OF NANOTECHNOLOGY

In situ observation of deformation processes in nanocrystalline face-centered cubic metals

Aaron Kobler[1,2], Christian Brandl[3], Horst Hahn[1,2] and Christian Kübel[*1,4,§]

Full Research Paper

Open Access

Address:
[1]Institute of Nanotechnology (INT), Karlsruhe Institute of Technology (KIT), Hermann-von-Helmholtz-Platz 1, 76344 Eggenstein-Leopoldshafen, Germany, [2]Joint Research Laboratory Nanomaterials (KIT and TUD), Technische Universität Darmstadt (TUD), Jovanka-Bontschits-Straße 2, 64287 Darmstadt, Germany, [3]Institute for Applied Materials (IAM-WBM), Karlsruhe Institute of Technology (KIT), Hermann-von-Helmholtz-Platz 1, 76344 Eggenstein-Leopoldshafen, Germany, and [4]Karlsruhe Nano Micro Facility (KNMF), Karlsruhe Institute of Technology (KIT), Hermann-von-Helmholtz-Platz 1, 76344 Eggenstein-Leopoldshafen, Germany

Email:
Christian Kübel[*] - christian.kuebel@kit.edu

* Corresponding author
§ Tel.: +49 721 608 28970

Keywords:
ACOM-STEM; deformation mechanisms; in situ straining; nanocrystalline metals; orientation mapping; quantitative crystallographic analysis

Beilstein J. Nanotechnol. **2016,** *7,* 572–580.
doi:10.3762/bjnano.7.50

Received: 26 November 2015
Accepted: 29 March 2016
Published: 19 April 2016

This article is part of the Thematic Series "Advances in nanomaterials II".

Associate Editor: P. Ziemann

© 2016 Kobler et al; licensee Beilstein-Institut.
License and terms: see end of document.

Abstract

The atomistic mechanisms active during plastic deformation of nanocrystalline metals are still a subject of controversy. The recently developed approach of combining automated crystal orientation mapping (ACOM) and in situ straining inside a transmission electron microscope was applied to study the deformation of nanocrystalline Pd_xAu_{1-x} thin films. This combination enables direct imaging of simultaneously occurring plastic deformation processes in one experiment, such as grain boundary motion, twin activity and grain rotation. Large-angle grain rotations with ≈39° and ≈60° occur and can be related to twin formation, twin migration and twin–twin interaction as a result of partial dislocation activity. Furthermore, plastic deformation in nanocrystalline thin films was found to be partially reversible upon rupture of the film. In conclusion, conventional deformation mechanisms are still active in nanocrystalline metals but with different weighting as compared with conventional materials with coarser grains.

Introduction

Nanocrystalline (NC) metals and alloys with grain size below 100 nm exhibit outstanding mechanical properties, in particular, superior hardness, strength and fatigue properties as compared to their coarse grained counterparts [1-5]. Modified or even unexpected deformation mechanisms are ascribed to the increasing influence of grain boundaries (GBs) on mechanical

properties [3,4,6-20]. GB-mediated deformation mechanisms, such as GB sliding and migration, grain growth and rotation [21] have been discussed (Figure 1a). Dislocation-mediated plasticity in the grain interior is reported to be based on dislocation nucleation at GBs, propagation and eventual absorption in the surrounding GB network, as well as twin nucleation, migration and detwinning (Figure 1a). Such twin activity and dislocation-driven grain rotation can still be attributed to dislocation formation, propagation and adsorption [13,22]. The understanding of the active deformation mechanisms is essential to support the application of NC metals, for example, in micro-electrical mechanical systems (MEMS) [23], hydrogen storage materials [24], radiation-resistant materials for nuclear reactors [25], applications for wear and corrosion protection [6,26] and for flexible electrical components [27].

Beside simulations [12-14,17,28,29], only few experimental methods are capable to measure in situ structural signatures of the deformation mechanisms in NC metals during mechanical deformation. X-ray diffraction (XRD) is one of the experimental methods [4,11,26,30]. However, XRD cannot directly image and spatially resolve deformation processes (e.g., grain growth or twinning); it measures the global structural signatures of the diffracting volume, which is encoded in the diffraction pattern and peak profile. For a local analysis, NC metals are traditionally investigated using bright/dark field transmission electron microscopy (BF/DF-TEM) [31-33] or high resolution TEM (HRTEM) [34]. In situ BF/DF-TEM deformation experiments are even more challenging to uniquely interpret local changes of nanometer-sized grains because of varying image contrast due to bending or tilting of the whole sample as well as lattice (grain) rotation within the sample during testing. The electron-transparent thin films necessary for TEM might also show more surface effects in comparison to bulk techniques. On the micrometer scale and for ultra-fine grained materials, local crystal orientations at the sample surface can be quantitatively tracked in a scanning electron microscope (SEM) by electron back scatter diffraction (EBSD) [35]. However, NC metals are beyond the spatial resolution limits of EBSD (>20 nm) [36].

Here, we demonstrate a combination of automated crystal orientation mapping (ACOM) in scanning TEM (STEM) modus with in situ straining [37-39] of NC metals to follow the GB-mediated processes (GB sliding and grain growth) and dislocation-mediated intragranular formation of twins to provide real space evidence for the active deformation mechanisms. Contrary to conventional TEM investigations, the crystal orientation of all grains within the investigated area are tracked quantitatively, which allows sample bending/tilting effects to be separated from real local crystallographic changes [38].

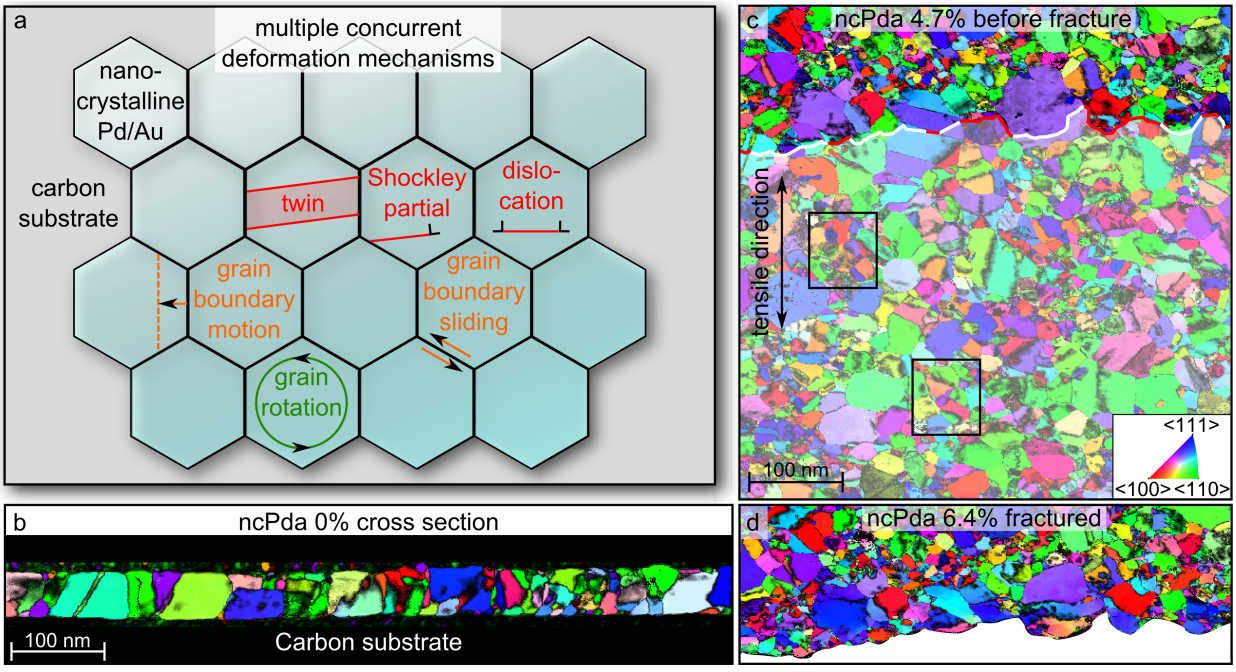


Figure 1: (a) Sketch showing multiple concurrent deformation mechanisms. (b) ACOM-STEM orientation maps overlaid with the reliability and the cross-correlation index of a cross-section of ncPda at 0% strain. (c,d) ACOM-STEM orientation maps overlaid with the reliability of the fracture morphology of ncPda before (c) and after fracture (d). The crack line of (d) is overlaid in (c) to reveal the crack behavior. Red parts of the crack line indicate fracture along grains boundaries and white lines indicate cracks passing through grains. The projection direction is along the tensile direction and the color code is given in (c). The black boxes in (c) indicate the areas of the detailed analysis in Figure 2 and Figure 3.

In situ ACOM-STEM is applied to magnetron-sputtered NC thin film samples exhibiting a predominately columnar grain structure. In the following, we concentrate on results from an annealed NC Pd (ncPda) thin film with ≈50 nm thickness supported by a thin (≈20 nm) carbon film (Figure 1b). An additional experiment using an annealed NC AuPd (ncAuPda) thin film was also conducted and the results are compared with the ncPda results at the end of the paper.

In this study, a distinction between crystallites and grains is made. Crystallites are defined as the smallest volume with one crystal orientation within a disorientation tolerance of 3° and grains are either single crystallites or multiple crystallites connected by twin boundaries.

Results and Discussion

All presented ACOM-STEM orientation maps (color coding according to the inverse pole figure, inset in Figure 1c) are superimposed with the reliability values in black, which constitute a measure for the unambiguousness of the orientation determination during the orientation assignment to the diffraction pattern. The evolution of the local orientation is tracked in a tensile experiment until fracture (Figure 1d). This procedure allows the assignment of the fracture site to the microstructural features (i.e., grain boundaries) (Figure 1c). The direct overlay reveals that the crack behavior is a combination of intragranular fracture with the crack path through a crystallite (white lines in Figure 1c) and intergranular fracture with the crack path along grain boundaries (red lines in Figure 1c). The observation of grain growth, fragmentation and recrystallization next to the crack path (Figure 1c,d) suggests that the deformation is both a result of intragranular deformation (related to dislocation-mediated processes in grains) and intergranular deformation by GB-mediated deformation mechanisms.

Focusing on a single grain level, Figure 2 shows details of the orientation map in Figure 1c for selected straining states to visualize the grain's structural changes during tensile loading and subsequent unloading by fracture. The overall size of the encircled grain (white line) continuously decreases during the tensile loading until 4.7%, directly showing GB motion during mechanical loading. However, upon fracture, the initial grain shape and grain size is almost recovered. The neighboring grains on the lower right hand side indicated in purple/blue and orange show similar recovery processes. The recovery of the grain shape indicates that the GB motion is the result of an external driving force rather than the reduction of GB area as in the case of conventional grain growth. Moreover, the pre-existing orientation gradient (orange to red color in Figure 2; lattice perturbations along a ≈15 nm section across the boundary shown in Supporting Information File 1, Figure S11a) at 0% strain is subsequently condensed (red and orange crystallite at 1.1% strain in Figure 2, ≈15° disorientation Supporting Information File 1, Figure S11b). The high Schmid factor (≈0.5) of the orange crystallite (Supporting Information File 1, Figure S8) in conjunction with the decreasing reliability (amount of black pixels increases) from 0% to 4.7% strain is consistent with the creation and accumulation of mobile and/or sessile dislocations in the grain during the tensile load [40-42], which can condense around the boundary and can leave the orange crystallite with reduced defect concentration in the grain upon fracture (see the disorientation to mean orientation plot, Supporting Information File 1, Figure S11a). Previous in situ X-ray diffraction studies revealed reversible diffraction peak broadening in a

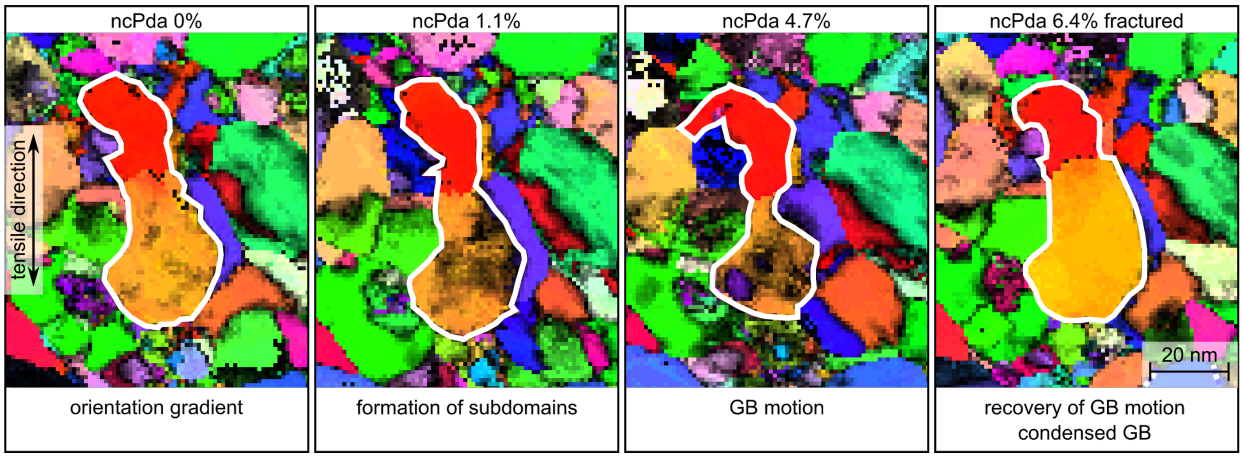


Figure 2: Grain fragmentation of the center grain (white boundary) during the tensile deformation (0–4.7% strain) of ncPda and grain recovery after fracture (6.4% strain) of the sample. The ACOM-STEM orientation maps overlaid with the reliability are shown for selected straining states with the projection direction along the tensile direction and the color code is given in Figure 1c.

loading–unloading cycle in NC Ni, which indicates the suppression of a build-up of a residual dislocation network during deformation in the nanograins [30]. Here the accumulation of defects into a sharp small angle GB (Figure 2, 6.4%) upon unloading by fracture is, however, consistent with the accumulation of a residual dislocation network in the nanograin during deformation, which condenses into a small angle grain boundary. Moreover, the reversible GB motion observed here can also explain the previously reported extraordinary strain recovery in NC Al and NC Au thin films [43].

Figure 3 shows a sequence of detwinning (0–1.1% purple red grain), twin nucleation (1.1–2.5%) and twin growth (2.5–4.7%). The twin activity is accompanied by substantial structural changes in the surrounding grains (e.g., white/grey crystallite at the bottom grows with straining). In general, the twin activity correlates with local plastic strain manifested in the structural changes. Since Shockley partial dislocations of the fcc lattice have the same Burgers vectors as the intrinsic crystallographic structure elements of twin (Σ3) boundaries [44], the twin motion indicates the operation of Shockley partial dislocations entering the grain from the boundary or moving along the preexisting twin planes.

The twin activity associated with heterogeneous distribution of the plastic strain indicates the necessity of accommodating processes to suppress fracture by local plastic strain incompatibilities. Grain-to-grain level ACOM-STEM measurements are used to follow the change of lattice orientation relative to the tensile loading direction. The absolute orientation change of the individually tracked grains through the straining series with respect to the initial state is displayed in a rotation map (Figure 4a and Figure 5a). This map allows the heterogeneous deformation in NC metals to be separated from an overall sample bending or tilting. Figure 4a shows the crystallite rotations in the range 0–65° and clearly indicates individual grains with ≈39° and ≈60° rotations (red and black), which are consistent with Σ3 and Σ9 misorientation relations, respectively. Additionally, Figure 5a highlights the crystallite rotations in the range 0–12° and uncovers the heterogeneous deformation in the small angle rotations, which are accommodated along GBs. Our observations are in line with previous work on NC Pt [34] and NC Ni [45].

Focusing on the large angle crystallite rotations (0–65°), Figure 4b shows the coalescence of two Σ3 boundaries (white/blue dashed lines at 0%) to one Σ9 boundary (white/red dashed line at 1.1%; a detailed analysis is shown in Supporting Information File 1, Figure S12). In Figure 4c, another example for twin boundary movement is shown. The triple line at 1.1% strain formed by two twin boundaries (white/blue dashed lines) and one Σ9 boundary (red/blue dashed line) originating from a grain boundary at 0% strain and the migration of the triple line half way through the grain during tensile loading. Since the Σ9 misorientation can be generated by a sequence of two distinct twin variants [46,47], Figure 4d illustrates schematically possible twin morphologies in one grain: the upper schematic shows a single twin domain (T1) in a grain. The twin-in-twin morphology, a secondary twin (T2) developed in the primary twin domain (T1), is shown in the middle schematic. The lower schematic shows the coalescence of two twin boundaries of two distinct twin variant disorientations, T1 and T2, creating a triple line with a Σ9 boundary. Generalized, the observed Σ9 boundary in the NC system is a signature of subsequent or multiple twinning in a grain (as shown in Figure 4d, middle and lower schematic), and the nucleation as

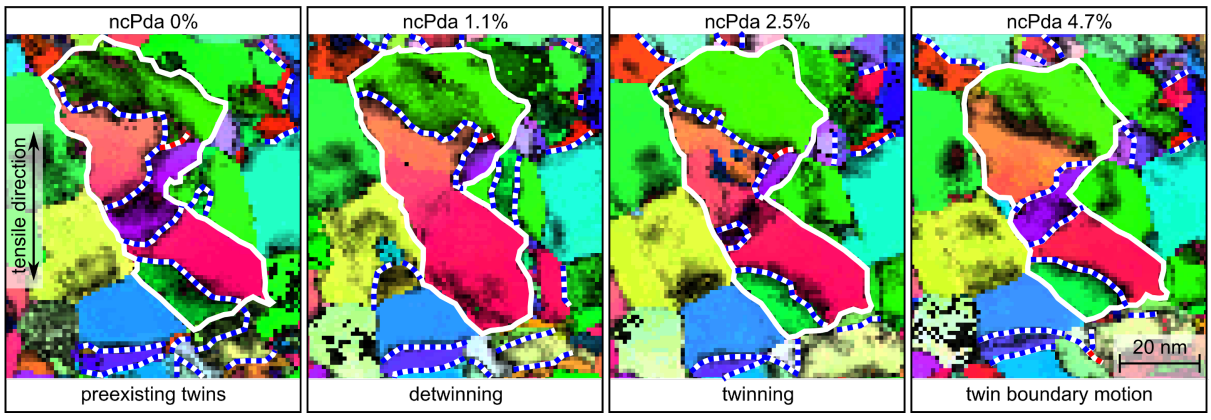


Figure 3: Twinning, twin boundary migration and detwinning of the center grain (white boundary) during the tensile deformation (0-4.7% strain) of ncPda. The ACOM-STEM orientation maps overlaid with the reliability are shown for selected straining states with the projection direction along the tensile direction and the color code is given in Figure 1c. The Σ3 disorientations are marked with white/blue dashed lines and the Σ9 disorientations with white/red dashed lines.

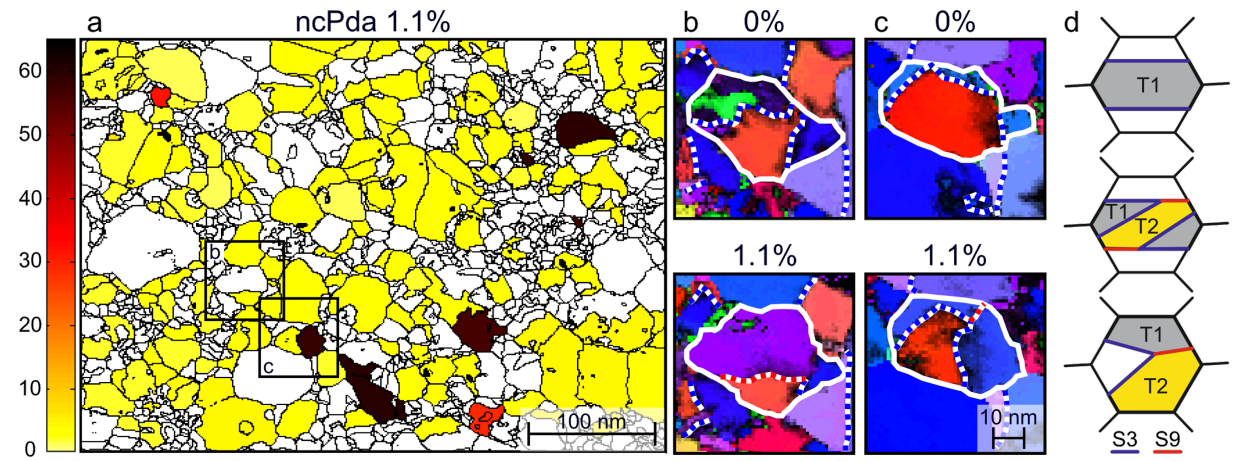


Figure 4: Analysis of the crystallite rotations in the range 0–65° for ncPda: (a) Crystallite boundary map overlaid with the rotation of selected and tracked crystallites for the 1.1% strain state. The color code is displayed on the left. (b,c) ACOM-STEM orientation maps of selected areas marked in (a). Σ3 disorientations marked with white/blue dashed lines and Σ9 disorientations marked with white/red dashed lines; the white boundary outlines the grain of interest. Projection direction: normal to the paper plane; color code is given in Figure 1c. (b) Details of a twin boundary activity. (c) Details of a grain that shows the creation of a triple line with two Σ3 and one Σ9 disorientation. (d) Schematic of the formation of Σ3 and Σ9 disorientations. The twin domains are labeled as grey/yellow areas, and the twin boundaries are indicated by the blue solid lines. The combination of two distinct twin variants (T1 in grey and T2 in yellow) results in a triple lines of two Σ3 (blue) and one Σ9 (red) boundary, which is equivalent to a chain of twin disorientation [46].

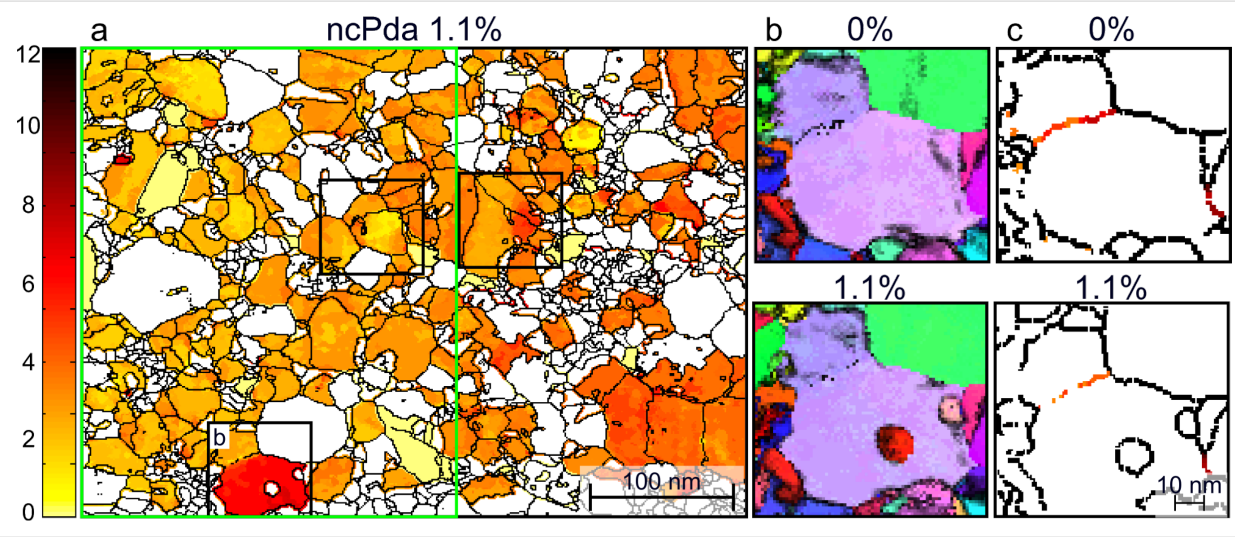


Figure 5: Analysis of the crystallite rotations in the range 0–12° for ncPda: (a) Crystallite boundary map of ncPda overlaid with the rotation of each pixel of individually tracked crystallites for the 1.1% strain state. The color code for the overlaid rotation of the crystallites is displayed on the left. (The green frame is the area which is evaluated in Figure 6 and additional black boxes indicate local deviations from the sample bending) (b) ACOM-STEM orientation maps of a selected area marked in (a). Projection direction: along the tensile direction; color code is given in Figure 1c. (c) Boundary disorientation plot of (b) with color coding according to (a).

well as migration of Σ9 boundaries is a result of two different sets of lattice partial dislocation motions associate with the coalesced Σ3 boundaries [22].

Concentrating now on the small angle crystallite rotations (0–12°), Figure 5a displays an overall bending of the thin TEM film during deformation that appears as a rotation gradient (left to right). Figure 5a shows additional local deviations from the sample bending, which appear as local, distinct rotations within the crystallites and in the vicinity of the grain boundaries (examples indicated by black boxes). A mismatch of the relative lattice rotation of neighboring grains needs to be accommodated as a shear deformation across the GB between the crystallites. The small angle rotation discontinuity at the grain boundary directly shows the operation of GB deformation processes, such as GB sliding and/or shear coupled GB motion.

The small angle crystallite rotation highlighted in Figure 5b,c even shows the partial coalescence of two crystallites with an initial disorientation of ≈4–7° at 0% strain. During deformation (at 1.1% strain), the disorientation between the crystallites partially disappears predominantly by the ≈4° rotation of the lower grain relative to its environment (Figure 5c). Grain boundary migration can be excluded, since a residual disorientation remains approximately at the same location of the former small angle grain boundary. The reduction of the disorientation is, therefore, associated with dislocations pushed from the small angle grain boundary into the crystallite or dislocations from the crystallite annihilate the small angle grain boundary dislocations. Both processes effectively reduce the dislocation content of the small angle grain boundary.

Figure 6 shows the signatures of the previously spatially resolved crystallite rotations versus the crystallite size for the tracked crystallites of ncPda (d_A = 25 nm) and ncAuPda (d_A = 26 nm). Both systems have a multimodal distribution with peaks in the small angle regime (<10°), a ≈39° regime (Σ9-rotation), and a ≈60° twin regime (Σ3-rotation) (a similar distribution has been found in two other Pd–Au systems not shown here). The small angle regime is a convolution of film bending (indicated by the green line in the histogram) and crystallite rotation due to heterogeneous intergranular deformation, which is accommodated by GB-mediated processes (Figure 5). Twin and multiple twin activity (Σ3 and Σ9 activity) are observed in all Pd–Au alloys investigated here. No significantly different behavior (within the statistical limitations) was observed for the different alloy systems, although molecular dynamics simulations suggest different dislocation and stacking fault densities with increasing strain as well as different grain boundary migration behavior for different alloy compositions [28,48]. In situ XRD studies also showed evidence on the concentration-dependent deformation behavior in the Pd–Au alloy [49]. Despite the good grain statistics of ACOM-TEM in comparison to HRTEM, synchrotron-based in situ XRD studies offer better temporal resolution in comparison to ACOM-TEM with far better grain statistics. Both good statistics and temporal resolution are necessary to reveal small differences in the deformation mechanism with the alloy content. With ACOM-TEM, the multiple concurrent mechanisms in all alloy systems are apparent. The twin activity does not reveal any statistically significant crystallite size dependence within the grain size distribution of the samples. This is a contradiction to previous observations on a grain size dependence of twinning in NC fcc metals [20]. Changing the alloy content and the sputter parameter can also increase the internal stresses and eventually the dislocation and twin density [50,51]. Besides the dislocation content and growth twins, the grain size and structure as well as texture at the beginning of straining are expected to influence the strength, the detailed interplay and transition of multiple concurrent mechanisms with increasing strain. The two presented systems were comparable in grain size and twin density (Supporting Information File 1, Figure S7, S18, Table S1), which allows a direct comparison. However, more measurements and better grain statistics are needed and may eventually reveal the transition and strength of the active deformation mechanisms in nanocrystalline material.

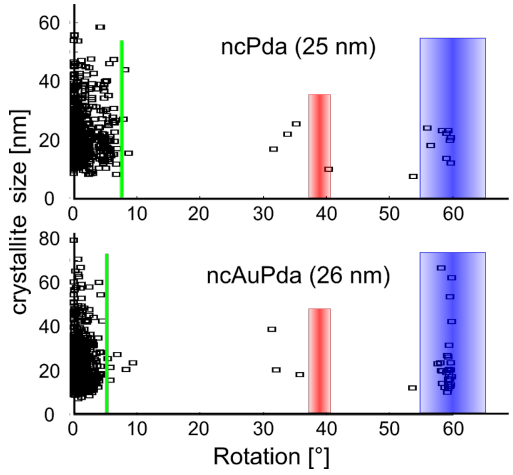


Figure 6: Crystalllite size versus lattice rotation plot of all tracked crystallites: (a) ncPda (d_A = 25 nm) (the green area of Figure 5a is evaluated), (b) ncAuPda (d_A = 26 nm). The green line indicates the rotation due to sample bending during straining. The Σ9 (39 ± 1.7°) and Σ3 (60 ± 5°) disorientations are marked in red and blue, respectively.

Conclusion

In summary, the utilization of ACOM-STEM in combination with in situ straining of ncPda and ncAuPda inside the TEM revealed the spatial–temporal interaction of intergranular and intragranular proccesses, which are operated by GB-mediated and dislocation-mediated deformation mechanisms. Moreover, the insights gained here reveal that GB and dislocation-based deformation mechanisms are still operational at grain sizes as low as 10 nm (number averaged) in the Pd–Au system. Our observations question the absolute statements on the exclusive operation of one class of deformation mechanisms at the nanoscale and favor the explanation of multiple concurrent mechanisms and with different overall weighting between them compared to their coarse-grained counter parts.

Experimental

Metal thin films were deposited by radio frequency (RF) magnetron sputtering using 2" diameter planar targets with 99.95% purity. TEM grids (holycarbon R2/1 + 2 nm C, Quantifoil) were used as a substrate. The nominal thickness between the holes is 22 nm. Pd was sputtered in 5 cycles of 50.38 s at 60 W

constant sputtering power under a working gas pressure (Ar) of 0.005 mbar at room temperature. Au (72 atom %) Pd (28 atom %) was sputtered for 102.5 s at 60 W constant sputtering power (for both Pd and Au) under a working gas pressure (Ar) of 0.0055 mbar at room temperature. The root mean squared (RMS) roughness between the holes was measured by AFM to be 1.3 nm for the ncPda film (Supporting Information File 1, Figure S2). The thickness of the films (ncPda ≈50 nm; ncAuPda ≈50 nm) was measured from FIB cross sections. The ncPda metal films were annealed in situ for ≈1 min at 300 °C and ≈18 min at 300 °C plus an additional ≈22 min at 350 °C for ncAuPda (plus the cooling down time of the holder) using a Gatan TEM heating holder during continuous STEM imaging for a fine adjustment of the grain size. After the annealing step, the grain size and twin density was measured using ACOM-STEM (Supporting Information File 1, Table S1).

A FEI Strata 400S dual beam FIB was used to transfer the metal C films to the push-to-pull (PTP) device (Hysitron) (Supporting Information File 1, Figure S1c,d) and to cut the films using an acceleration voltage of 30 kV and a beam current of 980 nA. The final shaping of the dog bone straining sample was performed at 30 kV and 1.5 nA beam current.

A Philips Tecnai F20 ST TEM operated at 200 kV in µp-STEM mode using spot size 7, gun lens 6, an extraction voltage of 4.5 kV and a 50 µm C2 aperture and equipped with the NanoMEGAS ASTAR system was used for ACOM-STEM data acquisition. A camera length of 100 mm was used to acquire the diffraction patterns.

A Hysitron Picoindenter PI95 with a push-to-pull (PTP) device (Supporting Information File 1, Figure S1a,b) operated under load control (0.1 µN/s) was used for the in situ straining experiments and was operated similar as described in [37]. The displacement was continuously monitored by the live µp-STEM imaging until a load holding segment was reached, which was necessary to acquire the ACOM-STEM orientation maps (Supporting Information File 1, Figures S5 and S12). Before and after the loading ramps, high quality µp-STEM overview images were acquired as reference for determining the strain (all strain values in this paper are giving relative to the initial dog bone length) and the spring constant of the PTP device was measured with the film ruptured to subtract the PTP device related forces from the measured stress–strain curve (Supporting Information File 1, Figures S3 and S13) [52]. Digital image correlation and tracking (DICT) was used to measure the strain during the loading ramps [53]. DICT was done twice per data set, once on the edges of the PTP to subtract the force coming from the PTP spring, and once on the edges of the dog bone to reveal the strain close to the area of interest.

The acquired ACOM-STEM data has been processed by the evaluation routine described in [37] to reduce the noise and to track crystallites through the straining series for the analysis of crystallite rotation, grain growth and twin activity. The evaluation routine used here differs from the one cited only in the noise filtering. Two new noise filters were developed: an "ambiguity filter" and a "minimum distance filter" [54]. The data processing parameters can be found in Supporting Information File 1.

Supporting Information

Supporting Information File 1

Additional experimental results.
[http://www.beilstein-journals.org/bjnano/content/supplementary/2190-4286-7-50-S1.pdf]

Acknowledgements

The authors would like to acknowledge Florian Bachmann, TU Bergakademie Freiberg, and Ralf Hielscher, TU Chemnitz, for their support with Mtex and Prof. David Mastronarde, University of Colorado, Boulder for the special IMOD version to align orientation images. We acknowledge Stefan Hengsbach, Karlsruhe Institute of Technology (KIT) for the production of sample transfer frames. Furthermore, we would like to thank Karsten Albe, Technische Universität Darmstadt (TUD) and Edgar Rauch, Laboratoire de Science et Ingénierie des Matériaux et Procédés (SIMAP laboratory) for inspiring discussions and feedback. We thank Paul Vincze, Karlsruhe Institute of Technology (KIT) for the AFM measurements and Torsten Scherer as well as Robby Prang, Karlsruhe Institute of Technology (KIT) for their help with the FIB. Financial support by the German Science Foundation (DFG) as part of the research group FOR714 "Plastic deformation of nanocrystalline metals", support by the Karlsruhe Nano Micro Facility (KNMF), a large scale Helmholtz research infrastructure operated at Karlsruhe Institute of Technology (KIT) and support by the Robert Bosch Foundation in the framework of the Endowed Chair on Nanostructured Functional Materials at KIT is gratefully acknowledged.

References

1. Gleiter, H. *Acta Mater.* **2000,** *48,* 1–29. doi:10.1016/S1359-6454(99)00285-2
2. Valiev, R. Z.; Alexandrov, I. V.; Zhu, Y. T.; Lowe, T. C. *J. Mater. Res.* **2002,** *17,* 5–8. doi:10.1557/JMR.2002.0002
3. Zehetbauer, M. J.; Zhu, Y. T. *Bulk Nanostructured Materials;* Wiley: Berlin, Germany, 2009. doi:10.1002/9783527626892
4. Van Swygenhoven, H.; Weertman, J. R. *Mater. Today* **2006,** *9,* 24–31. doi:10.1016/S1369-7021(06)71494-8

5. Kumar, K. S.; Van Swygenhoven, H.; Suresh, S. *Acta Mater.* **2003,** *51,* 5743–5774. doi:10.1016/j.actamat.2003.08.032
6. Suryanarayana, C.; Koch, C. C. *Hyperfine Interact.* **2000,** *130,* 5–44. doi:10.1023/A:1011026900989
7. Qi, Z.; Jiang, J.; Meletis, E. I. *J. Nanosci. Nanotechnol.* **2009,** *9,* 4227–4232. doi:10.1166/jnn.2009.M37
8. Hahn, H.; Mondal, P.; Padmanabhan, K. A. *Nanostruct. Mater.* **1997,** *9,* 603–606. doi:10.1016/S0965-9773(97)00135-9
9. Tjong, S. C.; Chen, H. *Mater. Sci. Eng., R* **2004,** *45,* 1–88. doi:10.1016/j.mser.2004.07.001
10. Hemker, K. J. *Science* **2004,** *304,* 221–223. doi:10.1126/science.1097058
11. Lohmiller, J.; Grewer, M.; Braun, C.; Kobler, A.; Kübel, C.; Schüler, K.; Honkimäki, V.; Hahn, H.; Kraft, O.; Birringer, R.; Gruber, P. A. *Acta Mater.* **2014,** *65,* 295–307. doi:10.1016/j.actamat.2013.10.071
12. Yamakov, V.; Wolf, D.; Phillpot, S. R.; Mukherjee, A. K.; Gleiter, H. *Nat. Mater.* **2004,** *3,* 43–47. doi:10.1038/nmat1035
13. Van Swygenhoven, H.; Derlet, P. M.; Frøseth, A. G. *Nat. Mater.* **2004,** *3,* 399–403. doi:10.1038/nmat1136
14. Van Swygenhoven, H. *Science* **2002,** *296,* 66–67. doi:10.1126/science.1071040
15. Brandl, C.; Derlet, P. M.; Van Swygenhoven, H. *Philos. Mag.* **2009,** *89,* 3465–3475. doi:10.1080/14786430903313690
16. Bitzek, E.; Brandl, C.; Derlet, P. M.; Van Swygenhoven, H. *Phys. Rev. Lett.* **2008,** *100,* 235501. doi:10.1103/PhysRevLett.100.235501
17. Yamakov, V.; Wolf, D.; Phillpot, S. R.; Mukherjee, A. K.; Gleiter, H. *Nat. Mater.* **2002,** *1,* 45–49. doi:10.1038/nmat700
18. Yamakov, V.; Wolf, D.; Phillpot, S. R.; Gleiter, H. *Acta Mater.* **2002,** *50,* 61–73. doi:10.1016/S1359-6454(01)00329-9
19. Meyers, M. A.; Mishra, A.; Benson, D. J. *Prog. Mater. Sci.* **2006,** *51,* 427–556. doi:10.1016/j.pmatsci.2005.08.003
20. Zhu, Y. T.; Liao, X. Z.; Wu, X. L. *Prog. Mater. Sci.* **2012,** *57,* 1–62. doi:10.1016/j.pmatsci.2011.05.001
21. Cahn, J. W.; Mishin, Y.; Suzuki, A. *Acta Mater.* **2006,** *54,* 4953–4975. doi:10.1016/j.actamat.2006.08.004
22. Wang, Y. M.; Sansoz, F.; LaGrange, T.; Ott, R. T.; Marian, J.; Barbee, T. W., Jr.; Hamza, A. V. *Nat. Mater.* **2013,** *12,* 697–702. doi:10.1038/nmat3646
23. Baghbanan, M.; Erb, U.; Palumbo, G. *Phys. Status Solidi* **2006,** *203,* 1259–1264. doi:10.1002/pssa.200566155
24. Oelerich, W.; Klassen, T.; Eigen, N.; Bormann, R. Nanocrystalline Metal Hydrides for Hydrogen Storage. In *Functional Materials;* Grassie, K.; Teckhoff, E.; Wegner, G.; Hausselt, J.; Hanselka, E., Eds.; Wiley: Berlin, Germany, 2006; Vol. 13, pp 141–145. doi:10.1002/3527607420.ch24
25. Chang, Y.-Q.; Guo, Q.; Zhang, J.; Chen, L.; Long, Y.; Wan, F.-R. *Front. Mater. Sci.* **2013,** *7,* 143–155. doi:10.1007/s11706-013-0199-3
26. Koch, C. C. *Nanostructured Materials: Processing, Properties and Potential Applications;* William Andrew Publishing: Norwich, NY, U.S.A., 2002.
27. Koo, J. H.; Seo, J.; Lee, T. *Thin Solid Films* **2012,** *524,* 1–19. doi:10.1016/j.tsf.2012.10.001
28. Schäfer, J.; Stukowski, A.; Albe, K. *Acta Mater.* **2011,** *59,* 2957–2968. doi:10.1016/j.actamat.2011.01.036
29. Lee, S.; Im, J.; Yoo, Y.; Bitzek, E.; Kiener, D.; Richter, G.; Kim, B.; Oh, S. H. *Nat. Commun.* **2014,** *5,* 3033. doi:10.1038/ncomms4033
30. Budrovic, Z.; Van Swygenhoven, H.; Derlet, P. M.; Van Petegem, S.; Schmitt, B. *Science* **2004,** *304,* 273–276. doi:10.1126/science.1095071
31. Rupert, T. J.; Gianola, D. S.; Gan, Y.; Hemker, K. J. *Science* **2009,** *326,* 1686–1690. doi:10.1126/science.1178226
32. Legros, M.; Gianola, D. S.; Hemker, K. J. *Acta Mater.* **2008,** *56,* 3380–3393. doi:10.1016/j.actamat.2008.03.032
33. Jin, M.; Minor, A. M.; Stach, E. A.; Morris, J. W., Jr. *Acta Mater.* **2004,** *52,* 5381–5387. doi:10.1016/j.actamat.2004.07.044
34. Wang, L.; Teng, J.; Liu, P.; Hirata, A.; Ma, E.; Zhang, Z.; Chen, M.; Han, X. *Nat. Commun.* **2014,** *5,* 4402. doi:10.1038/ncomms5402
35. Yang, K.; Fecht, H.-J.; Ivanisenko, Y. *Adv. Eng. Mater.* **2014,** *16,* 517–521. doi:10.1002/adem.201300413
36. Zaefferer, S. *Cryst. Res. Technol.* **2011,** *46,* 607–628. doi:10.1002/crat.201100125
37. Kobler, A.; Kashiwar, A.; Hahn, H.; Kübel, C. *Ultramicroscopy* **2013,** *128,* 68–81. doi:10.1016/j.ultramic.2012.12.019
38. Kobler, A.; Kübel, C. *Imaging Microsc.* **2014,** No. 1, 40–43. http://www.imaging-git.com/science/electron-and-ion-microscopy/situ-straining-analysis-acom-tem
39. Kobler, A.; Hodge, A. M.; Hahn, H.; Kübel, C. *Appl. Phys. Lett.* **2015,** *106,* 261902. doi:10.1063/1.4923398
40. Colla, M.-S.; Amin-Ahmadi, B.; Idrissi, H.; Malet, L.; Godet, S.; Raskin, J.-P.; Schryvers, D.; Pardoen, T. *Nat. Commun.* **2015,** *6,* 5922. doi:10.1038/ncomms6922
41. Wu, X. L.; Zhu, Y. T.; Wei, Y. G.; Wei, Q. *Phys. Rev. Lett.* **2009,** *103,* 205504. doi:10.1103/PhysRevLett.103.205504
42. Wang, L.; Han, X.; Liu, P.; Yue, Y.; Zhang, Z.; Ma, E. *Phys. Rev. Lett.* **2010,** *105,* 135501. doi:10.1103/PhysRevLett.105.135501
43. Rajagopalan, J.; Han, J. H.; Saif, M. T. A. *Science* **2007,** *315,* 1831–1834. doi:10.1126/science.1137580
44. Brandl, C.; Germann, T. C.; Perez-Bergquist, A. G.; Cerreta, E. K. *Mater. Res. Lett.* **2013,** *1,* 220–227. doi:10.1080/21663831.2013.830993
45. Wang, Y. B.; Li, B. Q.; Sui, M. L.; Mao, S. X. *Appl. Phys. Lett.* **2008,** *92,* 011903. doi:10.1063/1.2828699
46. Cayron, C. *Acta Crystallogr., Sect. A: Found. Crystallogr.* **2007,** *63,* 11–29. doi:10.1107/S0108767306044291
47. Reed, B. W.; Kumar, M. *Scr. Mater.* **2006,** *54,* 1029–1033. doi:10.1016/j.scriptamat.2005.11.045
48. Schäfer, J.; Albe, K. *Scr. Mater.* **2012,** *66,* 315–317. doi:10.1016/j.scriptamat.2011.11.031
49. Lohmiller, J.; Kobler, A.; Spolenak, R.; Gruber, P. A. *Appl. Phys. Lett.* **2013,** *102,* 241916. doi:10.1063/1.4811743
50. Castrup, A.; Kübel, C.; Scherer, T.; Hahn, H. *J. Vac. Sci. Technol., A* **2011,** *29,* 021013. doi:10.1116/1.3554265
51. Kobler, A.; Castrup, A.; Lohmiller, J.; Schäfer, J.; Kerber, M.; Kashiwar, A.; Scherer, T.; Gruber, P. A.; Albe, K.; Hahn, H.; Kübel, C. *Beilstein J. Nanotechnol.* **2013,** *4,* 554–566. doi:10.3762/bjnano.4.64
52. Oh, Y.; Cyrankowski, E.; Shan, Z.; Syed Asif, S. A. Micromechanical testing system employing tensile test holder with push-to-pull transformer. U.S. Patent 8,434,370, May 7, 2013.
53. Eberl, C.; Thompson, R.; Gianola, D.; Sharpe Jr., W.; Hemker, K. Digital image correlation and tracking. MatLabCentral, Mathworks file exchange server, FileID, 12413, 2006.
54. Kobler, A.; Kübel, C. *Ultramicroscopy*, in press.

License and Terms

This is an Open Access article under the terms of the Creative Commons Attribution License (http://creativecommons.org/licenses/by/2.0), which permits unrestricted use, distribution, and reproduction in any medium, provided the original work is properly cited.

The license is subject to the *Beilstein Journal of Nanotechnology* terms and conditions: (http://www.beilstein-journals.org/bjnano)

The definitive version of this article is the electronic one which can be found at: doi:10.3762/bjnano.7.50

BEILSTEIN JOURNAL OF NANOTECHNOLOGY

Phenalenyl-based mononuclear dysprosium complexes

Yanhua Lan*[1,2], Andrea Magri[1], Olaf Fuhr[1,3] and Mario Ruben*[1,4]

Full Research Paper

Open Access

Address:
[1]Institut für Nanotechnologie, Karlsruher Institut für Technologie (KIT), Postfach 3640, D-76344 Karlsruhe, Germany (Tel: +49 721-608-28948), [2]Institut Néel, CNRS, Nanosciences Department, BP 166, 25 rue des Martyrs, 38042 GRENOBLE Cedex 9, France, [3]Karlsruhe Nano Micro Facility (KNMF), Karlsruher Institut für Technologie (KIT), Postfach 3640, D-76344 Karlsruhe, Germany and [4]Université de Strasbourg, Institut de Physique et de Chimie des Materiaux de Strasbourg, Campus de Cronenbourg, 23 Rue du Loess, 67034 Strasbourg Cedex 2, France

Email:
Yanhua Lan* - yanhua.lan@kit.edu;
Mario Ruben* - mario.ruben@kit.edu

* Corresponding author

Keywords:
coordination complexes; dysprosium; magnetism; mononuclear; phenalenyl-based

Beilstein J. Nanotechnol. **2016,** *7,* 995–1009.
doi:10.3762/bjnano.7.92

Received: 03 March 2016
Accepted: 24 June 2016
Published: 08 July 2016

This article is part of the Thematic Series "Advances in nanomaterials II".

Guest Editor: H. Hahn

© 2016 Lan et al.; licensee Beilstein-Institut.
License and terms: see end of document.

Abstract

The phenalenyl-based dysprosium complexes [Dy(PLN)$_2$(HPLN)Cl(EtOH)] (**1**), [Dy(PLN)$_3$(HPLN)]·[Dy(PLN)$_3$(EtOH)]·2EtOH (**2**) and [Dy(PLN)$_3$(H$_2$O)$_2$]·H$_2$O (**3**), HPLN being 9-hydroxy-1*H*-phenalen-1-one, have been synthesized. All compounds were fully characterized by means of single crystal X-ray analysis, paramagnetic ^{1}H NMR, MALDI-TOF mass spectrometry, UV–vis spectrophotometry and magnetic measurements. Both static (dc) and dynamic (ac) magnetic properties of these complexes have been investigated, showing slow relaxation of magnetization, indicative of single molecule magnet (SMM) behavior. Attempts to synthesize sublimable phenalenyl-based dysprosium complexes have been made by implementing a synthetic strategy under anhydrous conditions. The sublimed species were characterized and their thermal stability was confirmed. This opens up the possibility to deposit phenalenyl-based lanthanides complexes by sublimation onto surfaces, an important prerequisite for ongoing studies in molecular spintronics.

Introduction

In the pioneering studies of next-generation information processing devices, single-molecule magnets (SMMs) are often regarded as building blocks for realizing spintronic devices at the molecular scale [1]. Out of thousands of SMMs available, the class of the LnPc$_2$ (Ln = Tb, Dy) complexes is the most popular example. It has been successfully assembled into different molecular schemes of spintronic quantum devices such as spin valve, spin transistor and spin resonator [2-5]. The fasci-

nating experimental results obtained from these quantum devices foster a bright future in the field of nanospintronics.

In order to fabricate spintronic devices with molecular units, an essential step is to investigate the magnetic properties of the molecules on the surface of or close to conducting electrodes. So far, depositing and addressing individual molecules of SMMs on surfaces [2] was explored only for very few complexes such as $TbPc_2$, Fe_4 and Mn_{12}. With the successful experience in utilizing $TbPc_2$ [6], our earnest attention in searching new SMMs with enhanced properties has led to the preparation of mononuclear lanthanide complexes. Indeed the mononuclear lanthanide complexes could allow for the study of controlled entanglement of spins on neighboring spin carriers [7], because there is no decoherence of individual spins through dipolar exchange in such a simple molecular unit. As highlighted recently in many work [8-14], the determining factor in the construction of SMMs and single-ion magnets (SIMs) and in the control of the single-axial anisotropy is related to the symmetry at the individual Ln sites along with the nature of the ligand field. Owing to a very strong Ising-type uniaxial anisotropy of the metal ion, dysprosium containing compounds are extensively studied and have been found to have the most promising slow-relaxation behavior. Typical examples are $[Dy(acac)_3(H_2O)_2]$ [8] and known organometallic compounds such as $[Li(THF)_4][(Ph_2PNPh)_4Dy]$ and $[Dy\{N(PPh_2)_2\}_3]$ [15], Dy-$(N(SiMe_3))_3$ [16] and $[\{Cp'_2Dy(\mu\text{-}SSiPh_3)\}_2]$ (Cp'= η^5-C_5H_4Me) [17], $[Dy(1,4\text{-}(Me_3Si)_2\text{-}C_8H_6)_2]$ [18], and $[Dy(COT'')_2Li(THF)(DME)]$ (COT'' = 1,4-bis(trimethylsilyl)cyclooctatetraenyl dianion) [19] showing interesting magnetic relaxation properties.

A phenalenyl unit can be considered as an aromatic variation of β-diketonates (Figure S1, Supporting Information File 1) formed by the fusion of three benzene rings. As a consequence of the extended aromatic system, enhanced interactions with carbon-based surfaces such as HOPG, graphene and CNT substrates are expected [20]. The significance of the phenalenyl unit in the diverse research areas ranging from chemistry and materials chemistry to device physics is closely linked to its essential role as an electronic reservoir that has driven the development of the best organic single-component conductor and has led to the creation of spin memory devices [21]. Indeed, a neutral planar phenalenyl-based molecule namely zinc methyl phenalenyl has recently been utilized as non-innocent building block for the construction of a spin memory device by Raman and co-workers [22]. Upon deposition of these molecules onto a ferromagnetic surface, a hybridized organometallic supramolecular magnetic layer can be formed. This interface layer exhibits a spin-dependent resistance leading to an interface magnetoresistance (IMR) effect. These findings suggest that phenalenyl-based molecules could potentially be utilized in building molecular-scale quantum spin memory and processors.

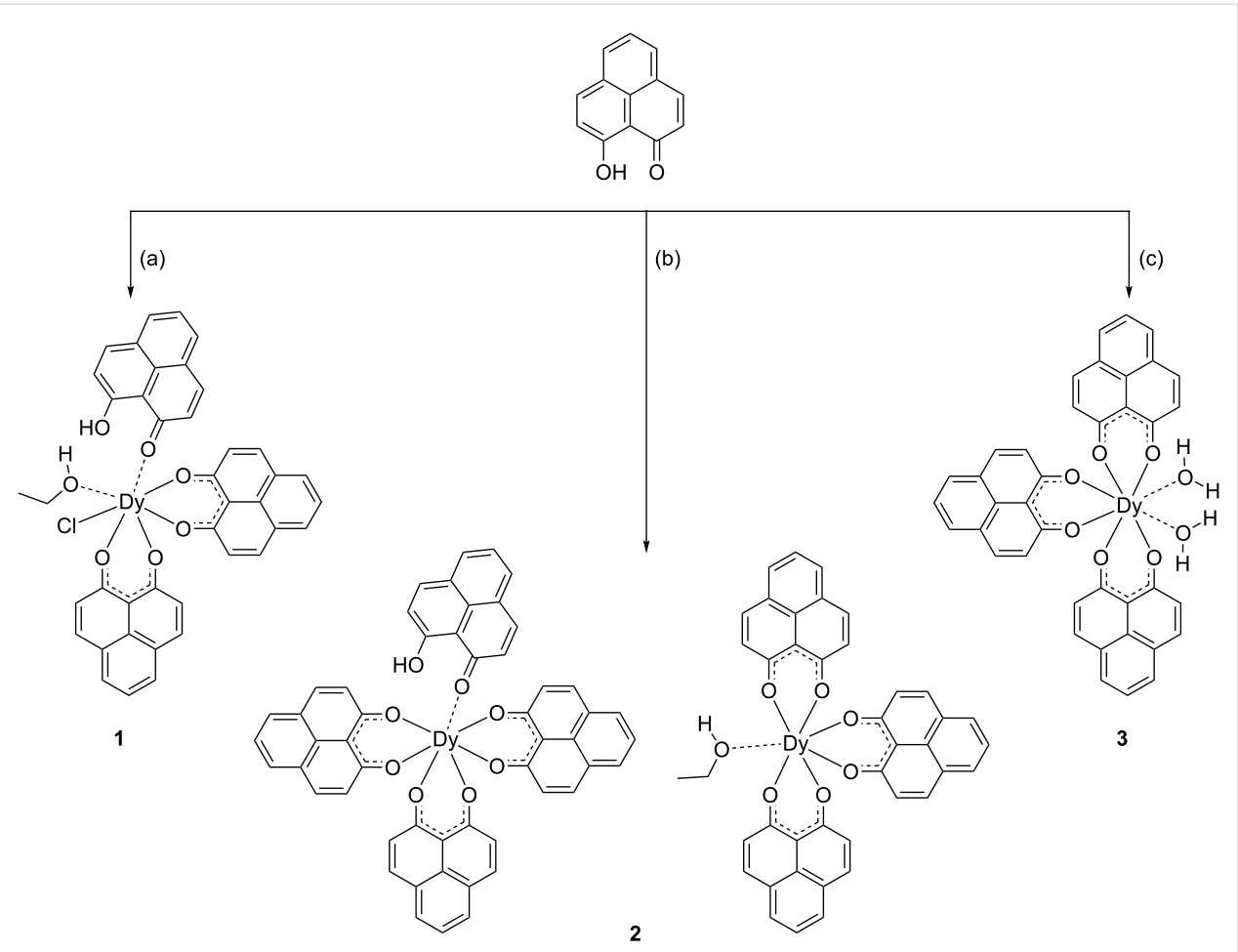
Taking all these points into consideration, one idea would be to step further and to introduce anisotropic lanthanide ions into these phenalenyl-based complexes with the focus on their interesting magnetic properties. In this regard, the 9-hydroxy-1*H*-phenalen-1-one (HPLN) ligand has previously been utilized for the preparation of mononuclear lanthanide complexes [23,24] to study the near-infrared luminescence upon excitation with visible light. However, this work, carried out by our group, aimed to study gas-phase dispersed photoluminescence spectra [25,26]. In this paper we report on the synthesis of three mononuclear dysprosium complexes $[Dy(PLN)_2(HPLN)Cl(EtOH)]$ (**1**), $[Dy(PLN)_3(HPLN)]\cdot[Dy(PLN)_3(EtOH)]\cdot 2EtOH$ (**2**) and $[Dy(PLN)_3(H_2O)_2]\cdot H_2O$ (**3**) with the focus on studying their magnetic properties. In addition, these complexes have been characterized by means of single crystal X-ray analysis, paramagnetic ^1H NMR, MALDI–TOF spectrometry and UV–vis spectrophotometry. Furthermore, attempts to synthesize sublimable phenalenyl-based dysprosium complexes **4** have been made. The sublimed species **4'** was characterized confirming its thermal stability.

Results and Discussion

Synthesis

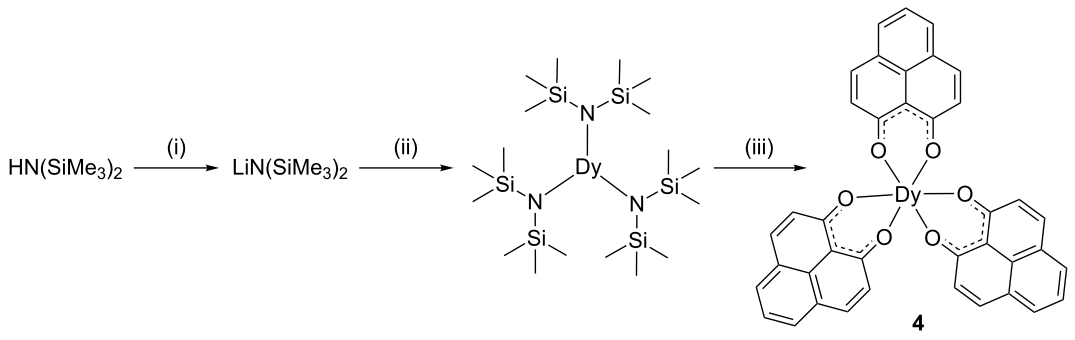
Van Deun et al. [23,24] synthesized 1:3 metal-to-ligand complexes using ammonia as a base and 1:4 metal-to-ligand complexes using the stronger base NaOH. In addition, phenalenyl-based europium and gadolinium nonanuclear complexes [26] were obtained by using $(Et)_3N$ as base in a 1:1.8 metal-to-ligand ratio. The synthetic procedures reported in our work are illustrated in Scheme 1. Instead of ammonia or NaOH as a base [23,24], we used NaH or diisopropyl amine to deprotonate the HPLN ligand. In order to obtain neutral complexes and to make them sublimable, we carried out the reactions only in a 1:3 Dy/HPLN stoichiometry. In general, the reaction is maintained at room temperature and then refluxed for 3 h. The crystals are grown through slow evaporation from the filtrate. Complex $[Dy(PLN)_2(HPLN)Cl(EtOH)]$ (**1**) was formed in a mixed solvent of $CHCl_3$/EtOH (1:5) in the presence of NaH, while complex $[Dy(PLN)_3(HPLN)]\cdot[Dy(PLN)_3(EtOH)]\cdot 2EtOH$ (**2**) was obtained in pure EtOH using diisopropyl amine as a base. Since two mononuclear species are co-crystallized in **2**, the volume of EtOH is then scaled up to the 1.5-fold, resulting in $[Dy(PLN)_3(H_2O)_2]\cdot H_2O$ (**3**).

Due to the presence of non-depronated ligands and solvent molecules in the coordination sphere, all these complexes decomposed at ca. 350 °C during the sublimation process in



Scheme 1: Synthesis of complexes **1**–**3**. (a) NaH, 1/3$DyCl_3 \cdot 6H_2O$, EtOH, reflux then stirring at RT overnight. (b) Diisopropylamine, 1/3$DyCl_3 \cdot 6H_2O$, EtOH, reflux then stirring at RT overnight. (c) Diisopropylamine, 1/3$DyCl_3 \cdot 6H_2O$, big volume of EtOH, reflux then stirring at RT overnight.

high vacuum (10^{-6} mbar). Sublimable lanthanides quinolinates have been prepared by Katkova et al. by using bis(trimethylsilyl)amino complexes as precursor [27-29]. With this experience, a sublimable phenalenyl-based dysprosium complex **4** was synthesized as illustrated in Scheme 2. The synthesis was carried out under anhydrous conditions implementing standard Schlenk techniques, carefully distilled THF, anhydrous starting materials and oven-dried glassware. So far, single crystals of the complex **4** were not obtained, thus its exact structure remains unknown yet. Nevertheless, the product was fully char-



Scheme 2: Synthesis of complex **4** under anhydrous conditions. The proposed structure of the complex is based on the characterizations. (i) *n*-BuLi, THF, 0 °C, 1 h. (ii) 1/3$DyCl_3$, THF, stirring at RT overnight. (iii) 3HPLN, THF, reflux overnight.

acterized by NMR spectroscopy, mass spectrometry and UV–vis spectrophotometry in comparison to the complexes **1**–**3**. In addition, complex **4** was successfully sublimated at about 300 °C in high vacuum (10^{-6} mbar). To confirm the thermal stability, the compound was also characterized after the sublimation process.

X-ray crystal structures

Single crystals of the complexes **1**–**3** were grown through the slow evaporation from the respective reaction filtrate and their structures were determined by single crystal X-ray diffraction. The refinement data are summarized in Table S1 (Supporting Information File 1) and the bond lengths and angles are listed in the caption of Figures **1**–**3**. The molecular structure of [Dy(PLN)$_2$(HPLN)Cl(EtOH)] (**1**) is illustrated in Figure 1. The central dysprosium atom is coordinated by seven donor atoms, six oxygen and one chlorine, resulting in a mono-capped trigonal prism geometry with a symmetry lower than D_{5h}. The bond lengths Dy-O1, Dy-O2, Dy-O3 and Dy-O4 (of the deprotonated phenalenyl) are between 2.25 and 2.28 Å. In addition, the bond angles Dy-O1-C1, Dy-O2-C3, Dy-O3-C14, and Dy-O4-C16, range between 136.8 and 138.8°. The bond length of Dy-Cl is 2.70 Å, which is longer than the Dy-O bod lengths. Although the molecule itself is asymmetric, the two deprotonated phenalenyls are virtually identical. On the contrary, compared to those of the deprotonated phenalenyls, the bond length Dy-O5 of the protonated phenalenyl of 2.38 Å is considerably longer and the angle Dy-O5-C27 of 148.3° is wider. There are two intramolecular hydrogen bonds between O6H6 and O2 (2.52 Å) and between O6H6 and O5 (1.90 Å) associated with the non-depronated phenalenyl, and an intermolecular hydrogen bond between O7H7 and Cl1 (2.49 Å) involving EtOH. Clearly, the intermolecular hydrogen bonds, together with the π–π stacking (ca. 3.45 Å) between the phenalenyl moieties, aid the molecular packing in the crystal lattice (Figure S2, Supporting Information File 1).

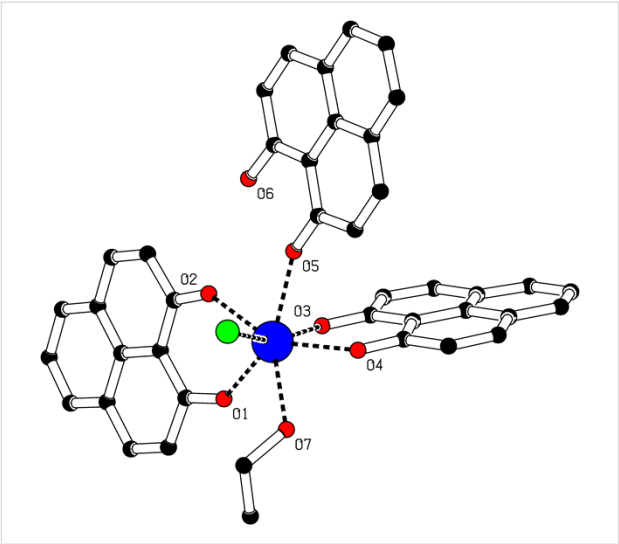


Figure 1: Molecular structure of complex **1** obtained by single crystal X-ray diffraction. Hydrogen atoms are omitted for clarity.
Selected bond lengths [Å], angles [°]: Dy-Cl1 2.6983(5), Dy-O1 2.2517(18), Dy-O2 2.2647(14), Dy-O3 2.2802(15), Dy-O4 2.2599(16), Dy-O5 2.3756(16), Dy-O7 2.4215(17); Cl-Dy-O1 108.38(4), O2-Dy-O3 85.95(5), Cl-Dy-O2 92.92(4), O2-Dy-O4 149.03(6), Cl-Dy-O3 161.85(4), O2-Dy-O5 72.01(6), Cl-Dy-O4 99.30(4), O2-Dy-O7 139.73(6), Cl-Dy-O5 84.30(4), O3-Dy-O4 73.69(5), Cl-Dy-O7 79.19(4), O3-Dy-O5 78.12(5), O1-Dy-O2 73.31(5), O3-Dy-O7 112.98(5), O1-Dy-O3 88.68(6), O4-Dy-O5 80.97(6), O1-Dy-O4 127.84(5), O4-Dy-O7 70.92(6), O1-Dy-O5 143.56(5), O5-Dy-O7 144.33(6), O1-Dy-O7 72.06(6).

In an asymmetric unit of complex **2**, two mononuclear dysprosium moieties [Dy(PLN)$_3$(HPLN)] **2a** and [Dy(PLN)$_3$(EtOH)] **2b** are co-crystallized together with two EtOH lattice molecules as illustrated in Figure 2. In both moieties the central dysprosium is coordinated by seven oxygen atoms in a mono-capped trigonal prism geometry. Compared with those of the protonated and deprotonated phenalenyls, the bond lengths and angles are down to the same trend as that described for complex **1**, in which those for the deprotonated phenalenyls are longer and wider than those of the protonated ones. On the other hand, compared to those around each dysprosium atom in the two moieties of **2a** and **2b**, the bond lengths and angles are very similar. The bond lengths between the dysprosium and the oxygen atoms of the protonated phenalenyls vary from 2.280 to 2.309 Å for **2a** and 2.249 to 2.324 Å for **2b**; and the bond angles range from 135.3 to 139.1° for **2a** and from 137.5 to 139.1° for **2b**. It is noteworthy that the bond distances between the dysprosium atom and the oxygen atoms of the HPLN ligands can be compared to those reported in other dysprosium–oxygen compounds [30-36]. Additionally, two intramolecular hydrogen bonds are formed: O8H8-O4 (2.39 Å) and O8H8-O7 (1.86 Å) in **2a**, but three are formed in **2b**. The intermolecular hydrogen bond, O15H15-O16 (2.06 Å) involves the EtOH bonded to the dysprosium and one EtOH in the crystal lattice. Two more hydrogen bonds, O16H16-O9 (2.06 Å) and O17aH17a-O12 (2.23 Å), take place between the deprotonated phenalenyls and one EtOH in the crystal lattice. As clearly depicted in Figure S3 (Supporting Information File 1), the presence of EtOH molecules in the crystal lattice forming intermolecular hydrogen bonds packs the molecules together and drives the co-crystallization. Additionally, weak π–π stacking (ca. 3.61 Å) between the phenalenyl moieties of **2a** and **2b** might be also responsible for the co-crystallization of the complexes in one asymmetric unit.

Compound [Dy(PLN)$_3$(H$_2$O)$_2$]·H$_2$O (**3**) crystallizes in a monoclinic system in contrast to the triclinic one of **1** and **2**. The central dysprosium is surrounded by three anionic phenalenyls and two water molecules (Figure 3), in which the eight chela-

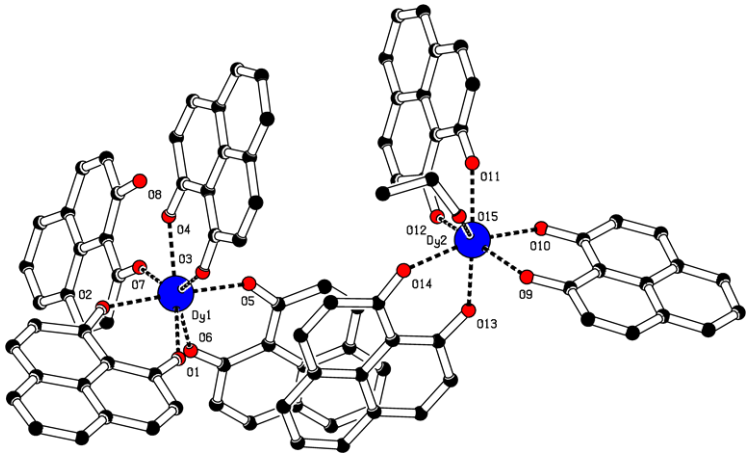


Figure 2: Molecular structure of complex **2** obtained by single crystal X-ray diffraction. Hydrogen atoms are omitted for clarity.
Selected bond lengths [Å], angles [°] for **2a**: Dy1-O1 2.290(3), Dy1-O2 2.286(3), Dy1-O3 2.280(3), Dy1-O4 2.280(3), Dy1-O5 2.289(3), Dy1-O6 2.309(3), Dy1-O7 2.381(3); O1-Dy1-O2 73.25(11), O3-Dy1-O4 72.93(12), O1-Dy1-O3 73.37(12), O3-Dy1-O5 86.47(12), O1-Dy1-O4 142.63(12), O3-Dy1-O6 137.28(11), O1-Dy1-O5 105.15(11), O3-Dy1-O7 144.34(12), O1-Dy1-O6 77.00(12), O4-Dy1-O5 88.42(11), O1-Dy1-O7 138.78(11), O4-Dy1-O6 140.20(12), O2-Dy1-O3 95.61(12), O4-Dy1-O7 71.55(12), O2-Dy1-O4 94.47(11), O5-Dy1-O6 72.33(11), O2-Dy1-O5 176.83(12), O5-Dy1-O7 95.51(11), O2-Dy1-O6 104.56(11), O6-Dy1-O7 75.94(12), O2-Dy1-O7 84.20(11).
Selected bond lengths [Å], angles [°] for **2b**: Dy2-O9 2.324(3), Dy2-O10 2.268(3), Dy2-O11 2.249(3), Dy2-O12 2.288(3), Dy2-O13 2.290(3), Dy2-O14 2.261(3), Dy2-O15 2.444(3); O9-Dy2-O10 72.83(12), O11-Dy2-O12 73.47(12), O9-Dy2-O11 117.23(11), O11-Dy2-O13 154.72(12),O9-Dy2-O12 156.73(12), O11-Dy2-O14 112.83(12), O9-Dy2-O13 82.10(11), O11-Dy2-O15 72.58(13), O9-Dy2-O14 107.08(12), O12-Dy2-O13 82.82(12), O9-Dy2-O15 73.15(12), O12-Dy2-O14 85.15(12),O10-Dy2-O11 82.04(12), O12-Dy2-O15 129.87(12), O10-Dy2-O12 89.34(12), O13-Dy2-O14 72.88(12), O10-Dy2-O13 89.16(11), O13-Dy2-O15 131.41(12), O10-Dy2-O14 161.72(12), O14-Dy2-O15 75.44(12), O10-Dy2-O15 120.73(12).

ting oxygen atoms result in a distorted square antiprismatic arrangement. The bond lengths between the dysprosium and the oxygens of the deprotonated phenalenyls are in the range of 2.317 and 2.347 Å. These distances are relatively longer than those observed in **1**, **2a** and **2b**, in which the dysprosium atom is in a mono-capped trigonal geometry. Moreover, the bond lengths of the dysprosium and the oxygen atoms from the coordinated water molecules are 2.396 Å (Dy-O7) and 2.439 Å (Dy-O8), respectively, which are comparable to that for the protonated phenalenyl in $[Dy(PLN)_2Cl(HPLN)(EtOH)]$ **1** (Dy-O5) and in $[Dy(PLN)_3(HPLN)]$ **2a** (Dy1-O7) and that for the coordinated EtOH molecule in $[Dy(PLN)_2Cl(HPLN)(EtOH)]$ **1** (Dy-O7) and in $[Dy(PLN)_3(EtOH)]$ **2b** (Dy2-O15). Lastly, due to the presence of three water molecules, several inter- (O9H9A-O2 3.02 Å , O9H9A-O5 3.06 Å and O9H9B-O9 2.99 Å) and intra-molecular (O7H7A-O1 2.89 Å, O7H7B-O1 2.79 Å, O7H7B-O6 2.73 Å, O8H8A-O3 2.72 Å and O8H8B-O2 2.98 Å) hydrogen bonds occur in the crystal lattice (Figure S4, Supporting Information File 1).

MALDI–TOF studies

The MALDI–TOF spectra (positive mode) of complexes **1**–**4** and the sublimed product **4'** are illustrated in Figure S5 (Supporting Information File 1). In all the spectra, the highest intensity peak corresponds to the $[Dy(PLN)_2]^+$ fragment (m/z = 554),

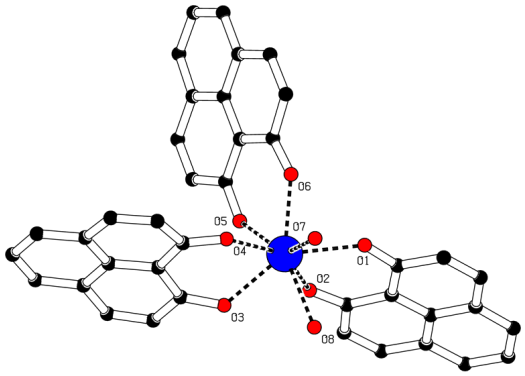


Figure 3: Molecular structure of complex **3** obtained by single crystal X-ray diffraction. Hydrogen atoms are omitted for clarity.
Selected bond lengths [Å], angles [°]: Dy1-O1 2.347(3), Dy1-O2 2.332(4), Dy1-O3 2.337(3), Dy1-O4 2.339(4), Dy1-O5 2.317(4), Dy1-O6 2.323(3), Dy1-O7 2.396(3), Dy1-O8 2.439(4); O1-Dy-O2 70.56(12), O3-Dy-O5 74.38(12), O1-Dy-O3 143.35(12), O3-Dy-O6 134.79(13), O1-Dy-O4 139.12(11), O3-Dy-O7 122.26(11), O1-Dy-O5 116.79(12), O3-Dy-O8 75.98(12), O1-Dy-O6 79.60(12), O4-Dy-O5 89.53(13), O1-Dy-O7 72.29(11), O4-Dy-O6 80.61(12), O1-Dy-O8 76.93(12), O4-Dy-O7 68.10(12), O2-Dy-O3 79.57(12), O4-Dy-O8 101.23(13), O2-Dy-O4 149.73(12), O5-Dy-O6 71.05(12), O2-Dy-O5 76.36(13), O5-Dy-O7 141.52(12), O2-Dy-O6 118.31(12), O5-Dy-O8 142.94(11), O2-Dy-O7 136.96(13), O6-Dy-O7 74.55(11), O2-Dy-O8 76.84(13), O6-Dy-O8 145.39(12), O3-Dy-O4 70.80(11), O7-Dy-O8 74.29(11).

in which the cation is formed by the elimination of one anionic ligand. This is an indication that all the complexes at least have two phenalenyls around the dysprosium atom. The trace peak observed at m/z = 572 is relative to the fragment $[Dy(PLN)_2(H_2O)]^+$. The absorption of water molecules during the preparation of the samples is usual. However, in the spectra of the sublimed complex, which was prepared under anhydrous conditions, the relative intensity of the fragment $[Dy(PLN)_2(H_2O)]^+$, both before and after the sublimation process, is considerably lowered. Other three small fragments in the spectra are observed for a neutral $Dy(PLN)_3$ core plus a metal cation of Li^+ or Na^+ ($[Dy(PLN)_3Li]^+$, m/z = 756; $[Dy(PLN)_3Na]^+$, m/z = 772) and for a neutral $Dy(PLN)_3$ core plus a protonated phenalenyl $[H_2PLN]^+$ cation $[Dy(PLN)_3(H_2PLN)]^+$ (m/z = 945). The fact that these fragments are present in the spectra of complex **4** and its sublimed species **4'** suggests that the sublimable dysprosium complex contains three deprotonated phenalenyl ligands as structurally proposed in Scheme 2.

NMR experiments

The paramagnetic ^1H NMR spectra of complexes **1**–**4** obtained in deuterated DMSO are shown in Figure S6 (Supporting Information File 1). The set of resonances between 16 and 6 ppm in the low-ppm range of the spectrum of **1** clearly originates from the free non-deprotonated ligand. This is confirmed by comparison with the ^1H NMR spectrum obtained for the pure ligand, which lacks two observations: (i) The peaks are not shifted to high ppm and broadened (the H–H coupling is still visible) by the paramagnetic dysprosium, and (ii) the peak at about 16 ppm is characteristic of the extremely de-shielded proton, which is involved in a strong intramolecular hydrogen bond with the α,β-conjugated carbonyl group of the phenalenyl rings. A set of peaks between 28 and 38 ppm shown in all the three spectra can be assigned to protons of the deprotonated phenalenyls, which are common to all the dysprosium complexes. However, two peaks between 40 and 50 ppm are observed only in the spectra of complexes **1** and **2**, but not for **4**, which is synthesized in the absence of EtOH. Thus these peaks are attributed to EtOH coordinated to the dysprosium in complexes **1** and **2**. In addition, the resonances between 18 and 24 ppm, which are noticeable in the spectra of complex **2** and of the sublimed species, could be assigned to the protonated ligand. Probably, they are not detected for complex **1** due to the low intensity of the spectrum, or due to a partial decomposition of the complex in DMSO. At last, the spectrum of **4** is characterized by a set of resonances between 6 and 10 ppm. These resonances cannot be assigned to unreacted free ligands, because the peaks are broadened and the characteristic peak at about 16 ppm is missing. However, they are in region of aromatic proton signals and are not shifted at high chemical shift from the paramagnetic Dy(III) ion.

UV–vis experiments

To further characterize the phenalenyl-based SMMs we have measured at room temperature the absorption spectra of the diluted DMSO solutions of complexes **1**–**4** and of the sublimed product **4'**. For comparison, UV–vis spectra were recorded for the free HPLN ligand in parallel. The spectra of the three dysprosium compounds present a similar pattern, as illustrated in Figure 4. Two main absorption bands, which derive from the characteristic α,β-conjugated carbonyl group of the ligand [37], are visible: one between 375 and 475 nm and another one between 300 and 375 nm. Both absorptions take place in the ligands. The former is related to n→π* transitions, while the latter is associated to π→π* transitions. Interestingly, there is no evidence of bands arising from charge or energy transfers between ligands and metal. Due to the limited contribution of the metal, the absorption peaks, which are listed in Table 1, display minimal shifts in comparison to the free ligand. In contrast, the extinction coefficients of the dysprosium complexes are about fourfold compared to those of the free ligand. This is expected since the complexes are formed by two, three or four ligands. In addition to that, the complexes **2** and **3** are characterized by an additional peak at 457–458 nm. The origin of this peak can be ascribed to the common feature in the structures of these two complexes: Complexes **2** and **3** are both formed by a $Dy(PLN)_3$ core but there is a $Dy(PLN)_2Cl$ core in complex **1**.

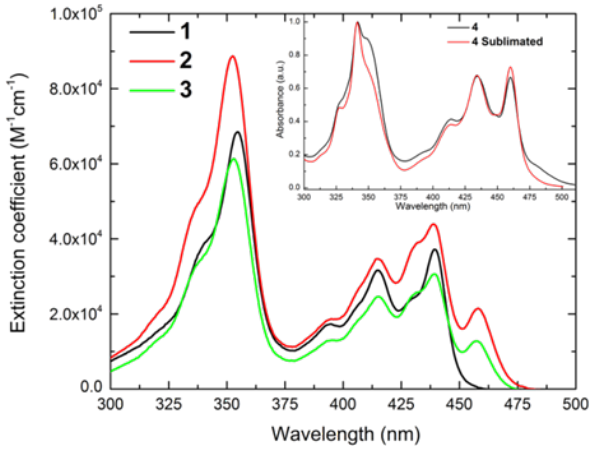


Figure 4: Absorption spectra of the three dysprosium complexes in diluted (2×10^{-6} M) DMSO solutions of **1–4** at room temperature.

The correspondent maximum of 349 nm of **1**–**3** is found at 341 nm in complex **4** both before and after the sublimation. Nevertheless, the spectrum of **4**, before the sublimation, has a shoulder at 349 nm, which is less pronounced after the sublimation process. Considering that the bands between 300 and 375 nm are associated to π→π* transitions centered on the phenalenyl ligands, the shift of the bands can result from slight

Table 1: List of the absorption peaks with their extinction coefficients.

compound	λ_{abs}^{max} (nm)	ε_λ ($M^{-1}\cdot cm^{-1}$)	compound	λ_{abs}^{max} (nm)	ε_λ ($M^{-1}\cdot cm^{-1}$)
9-HPLN [38,39]	440.0	9700	**1**	439.5	37200
	414.5	8300		415.0	31600
	394.5	4600		394.5	17294
	355.0	17600		354.5	68500
2	458.0	21500	**3**	457.5	12800
	439.0	43900		439.0	30600
	414.5	34700		415.5	24600
	395.0	18700		395.5	13000
	352.5	88700		353.0	61300

differences in the structures of the complexes. As a consequence of the few milligrams of material obtained by the sublimation process, we were unable to compare the extinction coefficients of the complexes. As observed previously in the absorption spectra, the ligand dominates the photophysical properties of the dysprosium complexes. As a result, the emission spectra of the three complexes are almost identical (Figure S7, Supporting Information File 1). Moreover, no sensitization of dysprosium is observed. A complete photophysical analysis is necessary to investigate the effect of the structure on the photoluminescence of those complexes.

Magnetic studies

Both static (dc) and dynamic (ac) magnetic properties have been investigated of the complexes **1**–**3**, but not for **4**. The single crystal structure of complex **4** is not available up to now and the sublimed product **4'** has been obtained only in a small quantity. Therefore, the magnetic studies on this compound were not feasible yet.

Static magnetic properties

The temperature dependence of the dc magnetic susceptibility has been measured in an applied magnetic field of 1000 Oe in the temperature range between 1.8 and 300 K for all three complexes. At 300 K, the product χT of **1**–**3** is 14.11, 13.56 and 14.19 $cm^3\cdot K\cdot mol^{-1}$, respectively, which are all in good agreement with the expected value of 14.17 $cm^3\cdot K\cdot mol^{-1}$ for one Dy(III) metal ion ($S = 5/2$, $L = 5$, $^6H_{15/2}$, $g = 4/3$) [40]. Decreasing the temperature, the product χT continuously falls to 8.78, 10.90 and 8.00 $cm^3\cdot K\cdot mol^{-1}$ at 1.8 K for **1**–**3**, respectively (see Figures in Supporting Information File 1). The gradual decrease of χT vs T is indicative of the type of paramagnetic behavior resulting from the thermal depopulation of the Stark sublevels of the $^6H_{15/2}$ ground state or of low-lying excited states of the Dy(III) ion while decreasing the temperature [41-47]. The field dependence of the magnetization at low temperatures has been measured at 2, 4 and 5 K. At 2 K and 70 kOe the magnetization approaches about 5.17 μ_B, 5.22 μ_B and 6.35 μ_B for **1**–**3**, respectively. However, due to the incomplete saturation of the magnetization, a residual slope is observed at high fields indicating the presence of magnetic anisotropy in the material [48,49]. Moreover, no hysteresis effect is observed in all three cases under these conditions.

Dynamic magnetic properties

As a consequence of the presence of magnetic anisotropy, the slow relaxation of magnetization has been probed by measuring ac susceptibilities as a function of the temperature at different frequencies as well as a function of frequency at different temperatures. The plots are illustrated in Supporting Information File 1 and the results are summarized in Table 2.

The ac susceptibilities of compound **1** under zero dc field show that a frequency-dependent in-phase and out-of-phase signal is

Table 2: Magnetization dynamics of compounds **1**–**3**.

compound	χ″ in zero dc field	pre-exponential factor τ_0 (s), energy gap Δ (K)	width of distribution α
1	approx. 13 K at 1500 Hz	3.3×10^{-6}, 43.8 (0 Oe) 2.9×10^{-6}, 49.4 (200 Oe)	0.073–0.279 0.111–0.471
2	no signal	7.1×10^{-6}, 14.1 (1500 Oe) 3.0×10^{-5}, 7.6 (3000 Oe)	0.179–0.476 0.266–0.368 (3.0–5.5 K)
3	no maxima	2.3×10^{-4} (0 Oe) 2.0×10^{-6}, 36.5 (500 Oe)	0.103–0.179 0.117–0.468

detected below 20 K suggesting a slow relaxation of the magnetization. At a frequency of 1500 Hz, the out-of-phase component first reaches a maximum at 13 K and then steadily increases rather than declining to zero while decreasing the temperature. This indicates a transition from a thermally activated to a temperature-independent regime in the relaxation process [36,50,51]. Shape and frequency dependence of the out-of-phase component in ac susceptibilities suggests that **1** might be a SMM. The relaxation time plotted in Figure 5 was extracted with an Arrhenius law by fitting the frequency sweeping data between 11 and 13 K. In doing so, we estimated the characteristic energy gap Δ for the thermally activated relaxation process to be 43.8 K, and the respective pre-exponential factor τ_0 to have a value of 3.3×10^{-6} s. Additionally, a saturation of about 5×10^{-4} s, relative to the quantum-tunneling process, is obtained below 5 K.

In relaxation processes of SMMs that are to a certain extent subjected to quantum effects, the application of a small dc field can remove the state degeneracy, and accordingly also the probability of quantum tunneling. Aiming to explore the relaxation process and to evaluate the quantum tunneling effect, the frequency dependence of the ac susceptibility was estimated at 1.8 K under a small external dc field. The characteristic frequency for compound **1** is 315 Hz at 1.8 K under zero field, whereas it decreases to 180 Hz under a dc field of 200 Oe. Thus, similar to what has been observed for some SMMs earlier, a small external dc field indeed slows down the relaxation due to the suppressed quantum tunneling of the magnetization (QTM) [52].

Lastly, ac susceptibilities as a function of the temperature have been measured under a dc field of 200 Oe to estimate the effec-

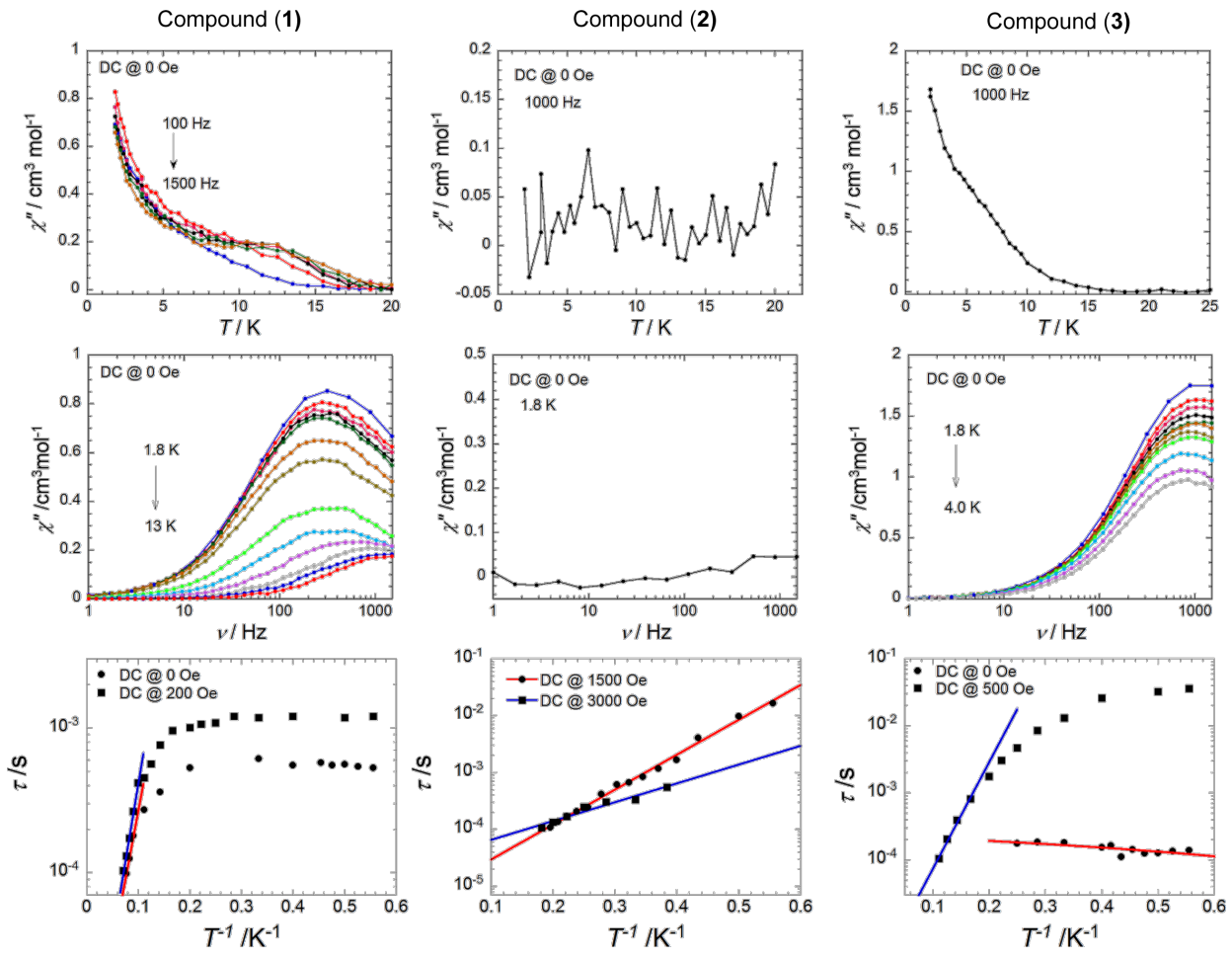


Figure 5: (Top) Temperature dependence of out-of-phase component of ac magnetic susceptibility under zero dc field. (Middle) Frequency dependence of out-of-phase component of ac magnetic susceptibility under zero dc field. (Bottom) Arrhenius semi-log plots of the relaxation time, τ vs 1/*T* from ac susceptibility measurements under a zero dc field and applied dc field. The solid lines represent a linear fit in the thermally activated range of temperature. The parameters are discussed in the text. Sample codes are indicated in the insets of the figures.

tive relaxation time (Figure 5). The data were fitted with an Arrhenius law function in the temperature range between 10 and 14 K. The characteristic SMM energy gap Δ is 49.4 K and the pre-exponential factor is τ_0 is 2.9×10^{-6} s. Additionally, a quantum relaxation time of 1×10^{-3} s is observed below 7 K. Compared to the data calculated in zero-field, the energy gap Δ and its corresponding pre-exponential factor τ_0 are fairly similar, suggesting that the quantum tunneling effect in **1** is not pronounced. However, the quantum relaxation time at low temperatures under 200 Oe is twice as high as that obtained under zero dc field.

For compound **2**, at a zero dc field, no out-of-phase component of ac susceptibility was detected at 1000 Hz suggesting the possible presence of an energy barrier to the relaxation of the magnetization, but it is short-cut by a fast tunneling relaxation process at zero dc field (Figure 5). In such a case, ac susceptibility measurements in the presence of a weak dc field could slow down the tunneling process which enables one to further investigate the dynamic magnetic properties of **2**. Indeed compound **2** shows a field-induced slow relaxation of the magnetization. The intensity of the out-of-phase component of the ac susceptibility is dramatically increased when a dc field is applied confirming the cooperation between a slow magnetic relaxation and a rapid quantum tunneling. The relaxation process immediately slows down to 40Hz when the applied field reaches 500 Oe, in contrast, it becomes faster at ca. 10 Hz up to 1500 Oe. This behavior points to the fact that this compound, concerning its relaxation dynamics, is characterized by a very fast tunneling process at zero dc field.

When the applied dc field is increased from 1500 Oe upwards, the relaxation process oscillates to a higher frequency and subsequently slows down again at 3000 Oe. This observation implies that there is more than one relaxation process in the system. That is not surprising if we correlate this behavior with the X-ray crystal structure of this compound. As there are two isolated Dy(III) centers present in this compound, the presence of multiple relaxation processes is likely to be correlated to the different individual ion anisotropies around the two Dy(III) centers. However, it is not possible to distinguish them based on the present data.

Then, the frequency sweeping ac susceptibility measurements are performed under a dc field of 1500 and 3000 Oe, respectively. Under a dc field of 1500 Oe, one set of peaks is observed in the out-of-phase component of the ac susceptibility. Conversely, under a dc field of 3000 Oe, two sets of peaks are clearly visible in the plot of the frequency dependence of the out-of-phase component of the ac susceptibility, indicating the presence of more than one relaxation pathway. Moreover, as a stronger dc field is applied, the smaller peak at lower frequencies increases at the expense of the larger peak beyond the window of the measurements. The energy barrier Δ and the pre-exponential factors τ_0 of the relaxation pathways are calculated by plotting the relaxation time τ vs $1/T$ (Figure 5). At 1500 Oe, the relaxation time deduced from the data between 1.8 and 5.1 K approximately follows an activated behavior with an energy gap Δ of 14.1 K and a pre-exponential factor τ_0 of 7.1×10^{-6} s. At 3000 Oe, the relaxation time Δ of the relaxation pathway located at higher frequencies in the temperature range between 2.6 and 5.5 K is 7.6 K and its pre-exponential factor τ_0 is 3.0×10^{-5} s. The characteristic parameters obtained under a dc field of 1500 Oe and 3000 Oe are roughly in the same order of magnitude, indicating that the mechanism of the two relaxation processes, corresponding to the two isolated Dy(III) ions in **2**, is most probably the same.

The dynamics of the magnetization of compound **3** was studied by the same methods applied for compounds **1** and **2** described as above. The ac out-of-phase component is clearly observed up to 20 K under zero dc field, but no maximum could be observed in the χ'' component indicating that the blocking temperature is below 1.8 K. As demonstrated in Supporting Information File 1, the relaxation time retains its value of ca. 2.3×10^{-4} s, being nearly temperature-independent between 1.8 K and 4.0 K. Above 1.8 K, the constraint set by the low-temperature limit of our magnetometer, the peaks of χ'' signals could only be detected in the frequency range above 1000 Hz. This phenomenon is attributable to temperature-independent zero-field fast quantum tunneling of the magnetization, whereby the degeneracy of the m_S states can be removed and the probability of the zero-field QTM between the $\pm m_S$ states lowered by the effect of a weak external field [52]. Then the frequency dependence of the ac susceptibility data at 1.8 K has been studied by applying a small dc field up to 3 kOe. As expected, the zero-field QTM is partially suppressed. A field of 500 Oe is applied to investigate the frequency and temperature dependence of the ac susceptibility leading to a relaxation time Δ of the relaxation pathway in the temperature range between 7 and 10 K of 36.5 K and its pre-exponential factor τ_0 of 2.0×10^{-6} s. Below 7 K, the relaxation time increases non-exponentially and is substantially curved. This curvature indicates that the moment of **3** has access to multiple pathways for spin reversal, which means that the Orbach thermally activated relaxation process and quantum-tunneling process (Raman or direct processes) coexist in this temperature regime.

Discussion

The program Magellan [53] was used to extract information about the magnetic easy axis in complexes **1**–**3** (Figure 6). On the basis of the Magellan output, we found that in all three cases

the axis of preferred alignment extends along with the planes of deprotonated phenalenyls defined by the aromatic rings. The co-ligands such as the Cl^- anion, H_2O and EtOH molecules act as weak ligands that interact with the dysprosium ion in the hard plane where the biggest contribution to tunneling would be expected. The weak ligand fields imposed on the dysprosium ion by these co-ligands lead to non-negligible transverse components that induce the quantum tunneling effect so as to be suppressed with the application of external dc field. On the other hand, the presence of these co-ligands in these systems reduces the three-fold symmetry of the whole molecule. Indeed, low-symmetry elements present in such a ligand field play an important role in facilitating tunneling or other magnetic relaxation processes [54]. This effect is consistent with the observation of true thermally activated relaxation resulting in a highly curved relaxation time down to the low temperature regime (Figure 5). The foregoing results obtained from this calculation well explain the tunneling dynamics of magnetization discussed in the earlier section. Finally, it is worthwhile to point out that the anisotropy axes of two dysprosium atoms in compound **2** are symmetrically twisted in a torsion angle of 40.7° (Figure 6b and Supporting Information File 1). As mentioned in the structural description, this molecule is rich of hydrogen bonding and the π–π stacking. With such a narrow torsion angle calculated from Magellan, one can think that the two magnetic centers could be strongly interacting through the π orbitals of the condensed rings so that the single-ion anisotropy between the two molecules is probably canceled out leading to a zero overall anisotropy so that no out-of-phase signal could be observed under zero dc field. In principle the effect of the intermolecular interaction could be evaluated by preparing a diamagnetically doped system, but it is too much work compared to the importance of the information that can be extracted.

To see if it is possible to further study the relaxation process and to better characterize the time distribution for relaxation, a Cole–Cole plot of the out-of-phase vs in-phase susceptibilities at low temperatures was constructed. The width of distribution quantified by a parameter α indicates how significantly the relaxation process is distributed, i.e., when a single relaxation process is active, a semicircular shape would be anticipated in the Cole–Cole plot with the α being close to zero. The χ'' vs χ' data (Figure 7) under zero or dc different fields were fitted by the extended Debye Model [55]. All derived parameters are summarized in Supporting Information File 1, Tables S2–S7. For compound **1**, under zero dc field, the width of distribution α varies from 0.073 to 0.279 in the entire temperature range of 1.8–13 K. From 7.0 to 13 K, the small α values below 0.16 are compatible with the SMM behavior. The process within this observed temperature range is thermally activated and leads to the exponential temperature dependence of the relaxation time of 3.3×10^{-6} s, which is a characteristic value observed for typical SMMs [56,57]. Under a dc field of 200 Oe, α varies from 0.111 to 0.471 between 1.8 and 13 K. Below 6 K, α is down to the range of 0.400–0.471 suggesting that there is likely to be more than one relaxation process operating at these temperatures. Indeed, as seen from Figure 5, a transition from a thermally activated to a temperature-independent regime is detected in the relaxation rates. For compound **2**, under a dc field of 1500 Oe, the width of distribution α varies from 0.179 to 0.476 up to 5.5 K but is not greater than 0.366 above 3.9 K. However, under a dc field of 3000 Oe, two obvious sets of Argand plots corresponding to two relaxation processes are observed below 3.5 K, which is consistent with the experimental results discussed in the dynamic properties of **2**. With the increase of temperature up to 5.5 K, the width of distribution α is determined to be 0.266–0.368. Within this temperature range the relaxation time

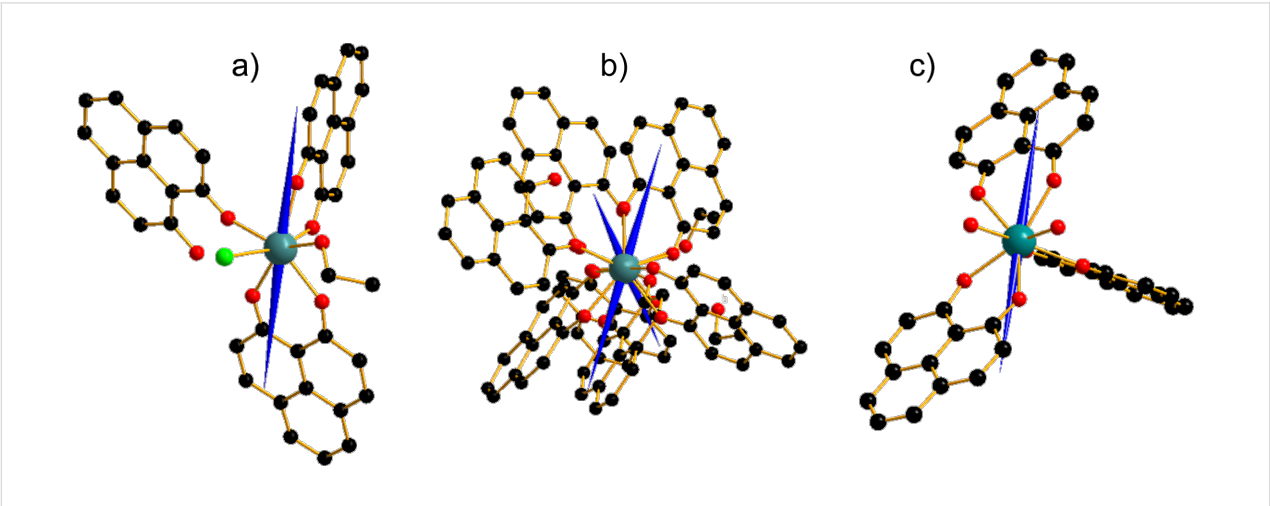


Figure 6: Orientation of the main anisotropy axis in complexes **1**–**3** indicated as blue arrows (a, b and c) calculated using the Magellan Software. Coordinates are taken from the crystal structures depicted in Figures 1–3.

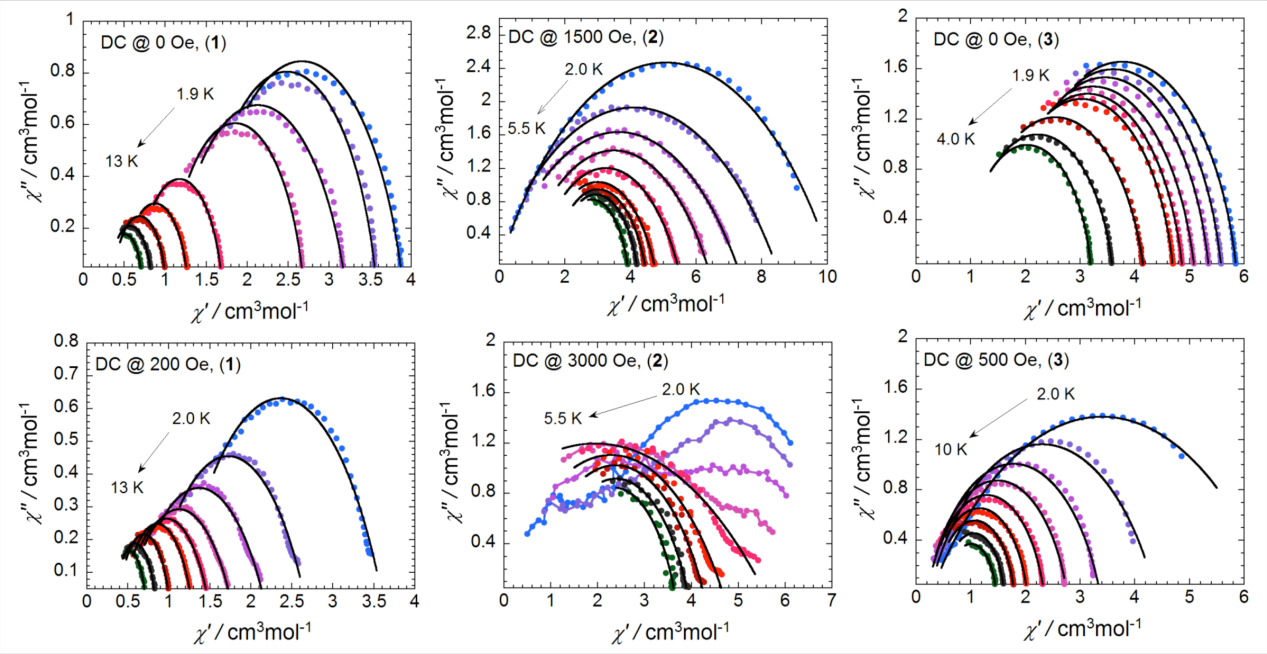


Figure 7: Cole–Cole plots under zero or different dc fields in the given temperature ranges. Sample codes are indicated in the graphs. The black solid lines represent the least-squares fit obtained with a generalized Debye model. The parameters are discussed in the text. In the figure for **2** under a dc field of 3000 Oe, the colored solid lines are guided to eyes.

obeys the Arrhenius law. For compound **3**, the relaxation rate under zero field is almost independent from the temperature indicating that the relaxation process remains in the quantum tunneling regime with a quantum time of 2.3×10^{-4} s. The width of distribution is very narrow with α of 0.103–0.179. Under a dc field of 500 Oe, the relaxation slows down so that it could be detected up to a high temperature of 9 K. The width of distribution varies from 0.117 to 0.468, which is very similar to the values obtained for compound **1** under a dc field of 200 Oe. Again the relaxation process encounters a crossover from a thermally activated (4.0–10 K) to a temperature-independent regime (1.8–4.0 K).

Conclusion

Three phenalenyl-based mononuclear dysprosium complexes have been synthesized from the reaction of 9-hydroxy-1*H*-phenalen-1-one with hexahydrous $DyCl_3$ in a 3:1 molar ratio in the presence of NaH or diisopropylamine. Single crystals in reasonable yields were obtained by slow evaporation of the solvents. All compounds were characterized by standard spectroscopic and analytical techniques and their solid-state structures were established by single crystal X-ray crystallography.

The magnetic properties of complexes **1**–**3** were studied in detail suggesting that these complexes are SMMs with fast zero-field quantum tunneling of the magnetization. The presence of co-ligands reduces the three-fold symmetry of the molecules so that non-negligible transverse anisotropy is imposed on the single dysprosium ion. The relaxation processes present in these complexes were discussed elaborately with the analysis of the width of distribution in the Cole–Cole plots. The energy barriers and its corresponding pre-exponential factors associated with the relaxation processes are determined under both zero and external dc fields. In particular, the relaxation process of **1** under zero dc field is a characteristic of an energy gap Δ of 43.8 K and a pre-exponential factor τ_0 of 3.3×10^{-6} s.

Furthermore, a sublimable phenalenyl-based dysprosium complex **4** has been made by implementing a synthetic strategy under anhydrous conditions. The sublimed species **4'** was preliminary characterized, confirming its thermal stability. However, growing single crystals of these complexes is fundamental to elucidate their exact structures so as to study their magnetic properties. There are two concerns regarding the exploration of this system. First of all, these molecules can be grafted by sublimation onto surfaces for a variety of studies, which further offers the potential to be used for device. Another important point is that a higher blocking temperature could be expected in compound **4** than those observed in compounds **1**–**3** as a consequence of the removal of coordinated solvents. In the cases of **1**–**3**, the Magellan output reveals that the presence of coordinated solvents or anions invokes a transverse anisotropy facilitating tunneling pathways. Based on the design criteria proposed by Chilton et al. [58,59] for the two-coordinate complexes of Dy(III), large values of the effective energy barrier, U_{eff}, are immediately diminished if axial ligation is disrupted by

solvent coordination. Considering this assumption, an increase of the magnetic relaxation barrier so as to blocking temperatures could be expected if such complexes could be obtained in the absence of a coordinating solvent. Therefore, our further efforts will be to isolate and structurally characterize the complexes **4** and **4'** and their respective magnetic properties, in particular after being sublimed onto surfaces. This work is currently in progress. During the submission of this work, a few interesting Dy(III)-SIMs with D_{5h} symmetry have been reported [60-62]. The three examples all show a fascinating anisotropic barrier over 500 K as a result of the higher order symmetry around Dy(III) ion. This is related to the concept that we discussed in our introduction.

Experimental

Instrumentation

Elemental analysis of carbon and hydrogen, were carried out in a Vario Micro Cube. Infrared spectra were recorded using KBr pressed pellets with a Perkin-Elmer Spectrum GX FTIR spectrometer (MAGNA FTIR 750, Nicolet) in the region of 4000–400 cm^{-1} region. Paramagnetic ^1H NMR spectra were recorded in a Bruker FT-NMR Avance III 500 MHz with deuterated solvents as internal standards. Matrix-assisted laser desorption/ionization-time of flight (MALDI–TOF) mass spectrometric data were acquired on a MALDI–TOF Synapt G2-S HDMS without additional matrix compound other than the sample itself. The absorption spectra were acquired at room temperature for diluted (2.0×10^{-6} M) DMSO (spectrophotometric grade) solutions on a Cary 500 Scan UV–vis–NIR spectrophotometer using a 1 cm quartz cell. Emission spectra were recorded at room temperature for diluted (2.0×10^{-6} M) DMSO (spectrophotometric grade) solutions on a Cary Eclipse Fluorescence spectrophotometer using a 1 cm quartz cell.

X-ray crystallography

Single crystal X-ray diffraction data were collected on a STOE IPDS II diffractometer with graphite monochromated Mo Kα radiation (λ = 0.71073 Å). Structure solution and refinement against F^2 were carried out using shelxs and shelxl software. Refinement was performed with anisotropic temperature factors for all non-hydrogen atoms (disordered atoms were refined isotropically); hydrogen atoms were calculated on idealized positions. Crystallographic data are summarized in Table S1 (Supporting Information File 1).

Magnetic studies

Magnetic measurements were obtained with a Quantum Design SQUID magnetometer MPMS-XL. Direct current (dc) susceptibility measurements were carried out over the temperature range of 1.8–300 K under an applied dc field of 1000 Oe. Magnetization measurements were made at low temperatures with applied dc fields from 0 to 70 kOe. Alternating current (ac) susceptibility measurements were measured under zero dc field with an oscillating ac field of 3 Oe and ac frequencies ranging from 1 to 1500 Hz. Measurements were performed on polycrystalline samples. The ground powder was restrained in Apiezon grease. The magnetic data were corrected for the sample holder.

Synthesis

All the purchased chemicals and solvents were used as received without any further purification unless otherwise stated. The reactions involving water-sensitive materials were carried out with distilled THF (over Na) and implementing standard Schlenck techniques; the glassware was kept in an oven at 80 °C, evacuated and flushed with argon prior to use.

Synthesis of [Dy(PLN)$_2$(HPLN)Cl(EtOH)] (**1**)

To a yellow solution of 9-hydroxy-1*H*-phenalen-1-one (117.7 mg, 0.6 mmol, 3 equiv) of $CHCl_3$ (5 mL) was added dropwise a colorless solution of NaH (14.4 mg, 0.6 mmol, 3 equiv) in ethanol, leading to a yellow suspension. After stirring for 5 min, a solution of $DyCl_3{\cdot}6H_2O$ (75.4 mg, 0.2 mmol, 1 equiv) in ethanol (15 mL in total) was added dropwise to afford a homogeneous solution, which was left to stir at room temperature for 2 h and then brought to reflux for 3 h. The reaction solution was then left to stir overnight at room temperature. After filtration, the filtrate was allowed to evaporate slowly. Red blocks were formed over two weeks. Yield (single crystals) based on Dy: 20.8 mg, 13%. Elemental analysis (%) calculated ($C_{41}H_{28}ClDyO_7$, 830.58 g/mol): Anal. calcd for $C_{41}H_{28}ClDyO_7$: C, 59.29; H 3.40; found: C, 59.87; H 3.67; FTIR (KBr) ν (cm^{-1}): 3369, 2924, 1631, 1583, 1561, 1521, 1482, 1428, 1346, 1257, 1241, 1181, 1152, 1047, 986, 960, 851, 806, 745, 694, 644, 553, 483, 451, 432; MALDI–TOF (CH_2Cl_2, positive) *m*/*z* (%): 554 ([M-HL-Cl-C_2H_5O]$^+$, 100); ^1H NMR (500 MHz, DMSO, δ) 49.23, 40.63, 36.40, 33.58, 28.49, 16.27, 8.33, 7.77 ppm.

Synthesis of [Dy(PLN)$_3$(HPLN)] (**2a**)·[Dy(PLN)$_3$(EtOH)]·2EtOH (**2b**)

To a yellow suspension of 9-hydroxy-1*H*-phenalen-1-one (117.7 mg, 0.6 mmol, 3 equiv) of ethanol (5 mL) was added dropwise a colorless solution of diisopropylamine (60.6 mg, 0.6 mmol, 3 equiv) in ethanol, leading to no obvious color change. After stirring for 5 min, a solution of $DyCl_3{\cdot}6H_2O$ (75.4 mg, 0.2 mmol, 1 equiv) in ethanol (20 mL in total) was added dropwise, in which the reaction mixture remained as a yellow suspension, which was left it to stir at room temperature for 2 h and then brought it to reflux for 3 h. The reaction mixture was then left to stir overnight at room temperature. Upon filtration, the yellow filtrate was allowed to evaporate slowly.

Red needles are formed over two weeks. Yield (single crystals) based on Dy: 18.3 mg, 10%. Elemental analysis (%) calculated ($C_{194}H_{136}O_{34}Dy_4$, 3661.03 g/mol): Anal. calcd for $C_{194}H_{136}O_{34}Dy_4$: C, 63.64; H 3.74; found: C, 63.51; H 3.66; FTIR (KBr) ν (cm^{-1}): 3432, 3047, 2969, 1627, 1582, 1560, 1522, 1421, 1412, 1345, 1252, 1241, 1222, 1177, 1140, 1045, 985, 957, 851, 804, 745, 698, 643, 545, 482, 450, 419; MALDI–TOF (CH_2Cl_2, positive) *m*/*z* (%): 554 ($[M - HL - L]^+$, or $[M - L - C_2H_5O]^+$, 100).

Synthesis of $[Dy(PLN)_3(H_2O)_2]\cdot H_2O$ (3)

This complex is synthesized based on the same procedure as that of preparation of complex **2**. The modification is that the volume of ethanol used in this reaction is scaled up from 20 to 30 mL. The crystals of **3** as red/orange needles were grown from the slow evaporation of the yellow filtrate. Yield (single crystals) based on Dy: 12.1 mg, 8%. Elemental analysis (%) calculated ($C_{39}H_{27}DyO_9$, 802.10 g/mol): Anal. calcd for $C_{39}H_{27}DyO_9$: C, 58.40; H, 3.39; found: C, 58.69; H, 3.43; MALDI–TOF (CH_2Cl_2, positive) *m*/*z* (%): 554 ($[M - L - 2H_2O]^+$, 100).

Synthesis of complex 4 in anhydrous conditions [63]

A solution of hexamethyldisilazide (16.5 mL, 78.0 mmol) in 40 mL of freshly distilled THF was cooled to 0 °C. To the ice-cold solution *n*-butyllithium (1.6 M in hexane, 50.0 mL, 80.0 mmol) was slowly added and the mixture was stirred for 1 h. Then anhydrous $DyCl_3$ (6.45 g, 24.0 mmol) was carefully added and the mixture was allowed to warm up to room temperature overnight under stirring. The resulting mixture was then purified by sublimation in high vacuum (2×10^{-6} mbar, 90 °C). Subsequently, a solution of HPLN (0.46 g, 2.4 mmol) in 20 mL in freshly distilled THF was added to the sublimed product (0.50 g, 0.8 mmol). The mixture was further refluxed at 65 °C overnight. The yellow precipitate was filtered and washed with fresh THF (0.28 g).

X-ray crystallographic studies of 1–3

Suitable crystals of compounds **1**–**3** were covered with perfluoroether oil and mounted onto a glass fiber. The crystal was transferred directly to the −93 °C N_2 cold stream of a Stoe IPDS 2T diffractometer. Data were corrected for absorption effects using indexed faces of the crystals [64].

All structures were solved by using the program SHELXS-97 [65]. The remaining non-hydrogen atoms were located from successive difference Fourier map calculations. The refinements were carried out by using full-matrix least-squares techniques on F^2, minimizing the function $(F_o - F_c)^2$, where the weight is defined as $4F_0^2/2(F_o^2)$ and F_o and F_c are the observed and calculated structure factor amplitudes using the program SHELXL-97 [63]. The hydrogen atom contributions of all compounds were calculated, but not refined. The locations of the largest peaks in the final difference Fourier map calculation as well as the magnitude of the residual electron densities in each case were of no chemical significance. The graphics of crystal structures were generated by PLATON software.

Crystal data of 1

$C_{41}H_{28}ClDyO_7$, M = 830.58 g/mol, triclinic, a = 10.4482(7) Å, b = 12.5823(8) Å, c = 13.2433(8) Å, α = 93.446(5)°, β = 112.211(5)°, γ = 95.762(5)°. V = 1594.55(18) $Å^3$, T = 180.15 K, space group $P-1$, Z = 2, 10913 reflections measured, 5790 unique (R_{int} = 0.0169), which were used in all calculations. The final R_1 values were 0.0172. The final $wR(F^2)$ was 0.0441 (all data). The goodness of fit on F^2 was 1.047.

Crystal data of 2

$C_{194}H_{136}O_{34}Dy_4$, M = 3661.03 g/mol, triclinic, a = 11.0591(8) Å, b = 17.2521(8) Å, c = 19.8266(10) Å, α = 92.328(4)°, β = 104.285(5)°, γ = 95.206(5)°. V = 3642.9(4) $Å^3$, T = 180.15 K, space group $P-1$, Z = 1, 29552 reflections measured, 13592 unique (R_{int} = 0.0444), which were used in all calculations. The final R_1 values were 0.0336. The final $wR(F^2)$ was 0.0639 (all data). The goodness of fit on F^2 was 0.914.

Crystal data of 3

$C_{39}H_{27}O_9Dy$, M = 802.10 g/mol, monoclinic, a = 29.9539(9) Å, b = 10.5596(2) Å, c = 22.9909(6) Å, β = 120.106(2)°, V = 6291.0(3) $Å^3$, T = 180.15 K, space group $C2/c$, Z = 8, 17247 reflections measured, 5879 unique (R_{int} = 0.0289), which were used in all calculations. The final R_1 values were 0.0349. The final $wR(F^2)$ was 0.0813 (all data). The goodness of fit on F^2 was 1.046.

CCDC deposit

Crystallographic data (excluding structure factors) for the structures reported in this paper have been deposited with the Cambridge Crystallographic Data Centre as a supplementary publication no. CCDC-1055828 (**1**), 1055829 (**2**) and 1055830 (**3**). Copies of the data can be obtained free of charge on application to CCDC, 12 Union Road, Cambridge CB21EZ, UK (fax: (+(44)1223-336-033; email: deposit@ccdc.cam.ac.uk).

Supporting Information

Supporting Information File 1

Additional experimental data.
[http://www.beilstein-journals.org/bjnano/content/supplementary/2190-4286-7-92-S1.pdf]

Acknowledgements

This work was supported by MoQuaS FP7-ICT-2013-10, No. 610449 and the DFG TR88 "3Met". We thank Prof. Annie K. Powell and Dr. Valeriu Mereacre for the allocation of and the assistance with technical equipment.

References

1. Rocha, A. R.; García-Suárez, V. M.; Bailey, S. W.; Lambert, C. J.; Ferrer, J.; Sanvito, S. *Nat. Mater.* **2005,** *4,* 335–339. doi:10.1038/nmat1349
2. Lan, Y.; Klyatskaya, S.; Ruben, M. Bis(phthalocyaninato) Lanthanide(III) Complexes - From Molecular Magnetism to Spintronic Devices. In *Lanthanides and Actinides in Molecular Magnetism;* Layfield, R.; Murugesu, M., Eds.; Wiley-VCH: Weinheim, 2015. doi:10.1002/9783527673476.ch8
3. Thiele, S.; Balestro, F.; Ballou, R.; Klyatskaya, S.; Ruben, M.; Wernsdorfer, W. *Science* **2014,** *344,* 1135–1138. doi:10.1126/science.1249802
4. Vincent, R.; Klyatskaya, S.; Ruben, M.; Wernsdorfer, W.; Balestro, F. *Nature* **2012,** *488,* 357–360. doi:10.1038/nature11341
5. Ganzhorn, M.; Klyatskaya, S.; Ruben, M.; Wernsdorfer, W. *Nat. Nanotechnol.* **2013,** *8,* 165–169. doi:10.1038/nnano.2012.258
6. Lodi Rizzini, A.; Krull, C.; Balashov, T.; Kavich, J. J.; Mugarza, A.; Miedema, P. S.; Thakur, P. K.; Sessi, V.; Klyatskaya, S.; Ruben, M.; Stepanow, S.; Gambardella, P. *Phys. Rev. Lett.* **2011,** *107,* 177205. doi:10.1103/PhysRevLett.107.177205
7. Woodruff, D. N.; Winpenny, R. E. P.; Layfield, R. A. *Chem. Rev.* **2013,** *113,* 5110–5148. doi:10.1021/cr400018q
8. Jiang, S.-D.; Wang, B.-W.; Su, G.; Wang, Z.-M.; Gao, S. *Angew. Chem., Int. Ed.* **2010,** *49,* 7448–7451. doi:10.1002/anie.201004027
9. Blagg, R. J.; Muryn, C. A.; McInnes, E. J. L.; Tuna, F.; Winpenny, R. E. P. *Angew. Chem., Int. Ed.* **2011,** *50,* 6530–6533. doi:10.1002/anie.201101932
10. Liu, J.-L.; Lin, W.-Q.; Chen, Y.-C.; Leng, J.-D.; Guo, F.-S.; Tong, M.-L. *Inorg. Chem.* **2012,** *52,* 457–463. doi:10.1021/ic302349f
11. Ungur, L.; Chibotaru, L. F. *Phys. Chem. Chem. Phys.* **2011,** *13,* 20086–20090. doi:10.1039/c1cp22689d
12. Klemm, R. A.; Efremov, D. V. *Phys. Rev. B* **2008,** *77,* 184410. doi:10.1103/PhysRevB.77.184410
13. Yamashita, A.; Watanabe, A.; Akine, S.; Nabeshima, T.; Nakano, M.; Yamamura, T.; Kajiwara, T. *Angew. Chem., Int. Ed.* **2011,** *50,* 4016–4019. doi:10.1002/anie.201008180
14. Feltham, H. L. C.; Lan, Y.; Klöwer, F.; Ungur, L.; Chibotaru, L. F.; Powell, A. K.; Brooker, S. *Chem. – Eur. J.* **2011,** *17,* 4362–4365. doi:10.1002/chem.201100438
15. Völcker, F.; Lan, Y.; Powell, A. K.; Roesky, P. W. *Dalton Trans.* **2013,** *42,* 11471–11475. doi:10.1039/c3dt51078f
16. Zhang, P.; Zhang, L.; Wang, C.; Xue, S.; Lin, S.-Y.; Tang, J. *J. Am. Chem. Soc.* **2014,** *136,* 4484–4487. doi:10.1021/ja500793x
17. Tuna, F.; Smith, C. A.; Bodensteiner, M.; Ungur, L.; Chibotaru, L. F.; McInnes, E. J. L.; Winpenny, R. E. P.; Collison, D.; Layfield, R. A. *Angew. Chem., Int. Ed.* **2012,** *51,* 6976–6980. doi:10.1002/anie.201202497
18. Le Roy, J. J.; Jeletic, M.; Gorelsky, S. I.; Korobkov, I.; Ungur, L.; Chibotaru, L. F.; Murugesu, M. *J. Am. Chem. Soc.* **2013,** *135,* 3502–3510. doi:10.1021/ja310642h
19. Jeletic, M.; Lin, P.-H.; Le Roy, J. J.; Korobkov, I.; Gorelsky, S. I.; Murugesu, M. *J. Am. Chem. Soc.* **2011,** *133,* 19286–19289. doi:10.1021/ja207891y
20. Müller, S.; Steil, S.; Droghetti, A.; Grossmann, N.; Meded, V.; Magri, A.; Schäfer, B.; Fuhr, O.; Sanvito, S.; Ruben, M.; Cinchetti, M.; Aeschlimann, M. *New J. Phys.* **2013,** *15,* 113054. doi:10.1088/1367-2630/15/11/113054
21. Mukherjee, A.; Sen, T. K.; Ghorai, P. K.; Mandal, S. K. *Sci. Rep.* **2013,** *3,* 2821. doi:10.1038/srep02821
22. Raman, K. V.; Kamerbeek, A. M.; Mukherjee, A.; Atodiresei, N.; Sen, T. K.; Lazić, P.; Caciuc, V.; Michel, R.; Stalke, D.; Mandal, S. K.; Blügel, S.; Münzenberg, M.; Moodera, J. S. *Nature* **2013,** *493,* 509–513. doi:10.1038/nature11719
23. Van Deun, R.; Nockemann, P.; Fias, P.; Van Hecke, K.; Van Meervelt, L.; Binnemans, K. *Chem. Commun.* **2005,** 590–592. doi:10.1039/b414703k
24. Van Deun, R.; Fias, P.; Nockemann, P.; Van Hecke, K.; Van Meervelt, L.; Binnemans, K. *Inorg. Chem.* **2006,** *45,* 10416–10418. doi:10.1021/ic0616277
25. Greisch, J.-F.; Harding, M. E.; Schäfer, B.; Rotter, M.; Ruben, M.; Klopper, W.; Kappes, M. M.; Schooss, D. *J. Phys. Chem. A* **2014,** *118,* 94–102. doi:10.1021/jp4086624
26. Greisch, J.-F.; Harding, M. E.; Schäfer, B.; Ruben, M.; Klopper, W.; Kappes, M. M.; Schooss, D. *J. Phys. Chem. Lett.* **2014,** *5,* 1727–1731. doi:10.1021/jz500614x
27. Katkova, M. A.; Kurskii, Yu. A.; Fukin, G. K.; Averyushkin, A. S.; Artamonov, A. N.; Vitukhnbovsky, A. G.; Bochkarev, M. N. *Inorg. Chim. Acta* **2005,** *358,* 3625–3632. doi:10.1016/j.ica.2005.07.017
28. Katkova, M. A.; Ilichev, V. A.; Konev, A. K.; Bochkarev, M. N.; Vitukhnovsky, A. G.; Parshin, M. A.; Pandey, L.; Van der Auweraer, M. *J. Appl. Phys.* **2008,** *104,* 053706. doi:10.1063/1.2968541
29. Katkova, M. A.; Ilichev, V. A.; Konev, A. N.; Bochkarev, M. N. *Russ. Chem. Bull.* **2008,** *57,* 2281–2284. doi:10.1007/s11172-008-0321-3
30. Gao, Y.; Xu, G.-F.; Zhao, L.; Tang, J.; Liu, Z. *Inorg. Chem.* **2009,** *48,* 11495–11497. doi:10.1021/ic901806g
31. Prasad, T. K.; Ralasekharan, M. V. *Inorg. Chem.* **2009,** *48,* 11543–11550. doi:10.1021/ic901066v
32. Feng, X.; Zhao, J.; Liu, B.; Wang, L.; Ng, S.; Zhang, G.; Wang, J.; Shi, X.; Liu, Y. *Cryst. Growth Des.* **2010,** *10,* 1399–1408. doi:10.1021/cg901391y
33. Rinck, J.; Novitchi, G.; Van den Heuvel, W.; Ungur, L.; Lan, Y.; Wernsdorfer, W.; Anson, C. E.; Chibotaru, L. F.; Powell, A. K. *Angew. Chem., Int. Ed.* **2010,** *49,* 7583–7587. doi:10.1002/anie.201002690
34. Ke, H.; Xu, G.-F.; Guo, Y.-N.; Gamez, P.; Beavers, C. M.; Teat, S. J.; Tang, J. *Chem. Commun.* **2010,** *46,* 6057–6059. doi:10.1039/c0cc01067g
35. Wang, Z.-L.; Fang, W.-H.; Yang, G.-Y. *Chem. Commun.* **2010,** *46,* 8216–8218. doi:10.1039/c0cc02131h
36. Liang, L.; Peng, G.; Li, G.; Lan, Y.; Powell, A. K.; Deng, H. *Dalton Trans.* **2012,** *41,* 5816–5823. doi:10.1039/c2dt30175j
37. Turro, N. J. *Modern Molecular Photochemistry;* University Science Book, 1991.
38. Haddon, R. C.; Rayford, R.; Hirani, A. M. *J. Org. Chem.* **1981,** *46,* 4587–4588. doi:10.1021/jo00335a060

39. Magri, A.; Friederich, P.; Schäfer, B.; Fattori, V.; Sun, X.; Strunk, T.; Meded, V.; Hueso, L. E.; Wenzel, W.; Ruben, M. *Beilstein J. Nanotechnol.* **2015,** *6,* 1107–1115. doi:10.3762/bjnano.6.112
40. Benelli, C.; Gatteschi, D. *Chem. Rev.* **2002,** *102,* 2369–2388. doi:10.1021/cr010303r
41. Kahn, M. L.; Sutter, J.-P.; Golhen, S.; Guionneau, P.; Ouahab, L.; Kahn, O.; Chasseau, D. *J. Am. Chem. Soc.* **2000,** *122,* 3413–3421. doi:10.1021/ja994175o
42. Kahn, M. L.; Ballou, R.; Porcher, P.; Kahn, O.; Sutter, J.-P. *Chem. – Eur. J.* **2002,** *8,* 525–531. doi:10.1002/1521-3765(20020118)8:2<525::AID-CHEM525>3.0.CO;2-L
43. Lin, P.-H.; Burchell, T. J.; Clérac, R.; Murugesu, M. *Angew. Chem., Int. Ed.* **2008,** *47,* 8848–8851. doi:10.1002/anie.200802966
44. Xu, G.-F.; Wang, Q.-L.; Gamez, P.; Ma, Y.; Clérac, R.; Tang, J.; Yan, S.-P.; Cheng, P.; Liao, D.-Z. *Chem. Commun.* **2010,** *46,* 1506–1508. doi:10.1039/B920215C
45. Rinehart, J. D.; Fang, M.; Evans, W. J.; Long, J. R. *Nat. Chem.* **2011,** *3,* 538–542. doi:10.1038/nchem.1063
46. Long, J.; Habib, F.; Lin, P.-H.; Korobkov, I.; Enright, G.; Ungur, L.; Wernsdorfer, W.; Chibotaru, L. F.; Murugesu, M. *J. Am. Chem. Soc.* **2011,** *133,* 5319–5328. doi:10.1021/ja109706y
47. Guo, Y.-N.; Xu, G.-F.; Wernsdorfer, W.; Ungur, L.; Guo, Y.; Tang, J.; Zhang, H.-J.; Chibotaru, L. F.; Powell, A. K. *J. Am. Chem. Soc.* **2011,** *133,* 11948–11951. doi:10.1021/ja205035g
48. Osa, S.; Kido, T.; Matsumoto, N.; Re, N.; Pochaba, A.; Mrozinski, J. *J. Am. Chem. Soc.* **2004,** *126,* 420–421. doi:10.1021/ja037365e
49. Tang, J.; Hewitt, I.; Madhu, N. T.; Chastanet, G.; Wernsdorfer, W.; Anson, C. E.; Benelli, C. B.; Sessoli, R.; Powell, A. K. *Angew. Chem., Int. Ed.* **2006,** *45,* 1729–1733. doi:10.1002/anie.200503564
50. Car, P.-E.; Perfetti, M.; Mannini, M.; Favre, A.; Caneschi, A.; Sessoli, R. *Chem. Commun.* **2011,** *47,* 3751–3753. doi:10.1039/c0cc05850e
51. Watanabe, A.; Yamashita, A.; Nakano, M.; Yamamura, T.; Kajiwara, T. *Chem. – Eur. J.* **2011,** *17,* 7428–7432. doi:10.1002/chem.201003538
52. Gatteschi, D.; Sessoli, R.; Villain, J. *Molecular Nanomagnets;* Oxford University Press: Oxford, 2006. doi:10.1093/acprof:oso/9780198567530.001.0001
53. Chilton, N. F.; Collison, D.; McInnes, E. J. L.; Winpenny, R. E. P.; Soncini, A. *Nat. Commun.* **2013,** *4,* 2551. doi:10.1038/ncomms3551
54. Demir, S.; Zadrozny, J. M.; Long, J. R. *Chem. – Eur. J.* **2014,** *20,* 9524–9529. doi:10.1002/chem.201403751
55. Cole, K. S.; Cole, R. H. *J. Chem. Phys.* **1941,** *9,* 341–351. doi:10.1063/1.1750906
56. Hewitt, I. J.; Lan, Y.; Anson, C. E.; Luzon, J.; Sessoli, R.; Powell, A. K. *Chem. Commun.* **2009,** 6765–6767. doi:10.1039/b908194a
57. Abbas, G.; Lan, Y.; Kostakis, G. E.; Wernsdorfer, W.; Anson, C. E.; Powell, A. K. *Inorg. Chem.* **2010,** *49,* 8067–8072. doi:10.1021/ic1011605
58. Chilton, N. F. *Inorg. Chem.* **2015,** *54,* 2097–2099. doi:10.1021/acs.inorgchem.5b00089
59. Chilton, N. F.; Goodwin, C. A. P.; Mills, D. P.; Winpenny, R. E. P. *Chem. Commun.* **2015,** *51,* 101–103. doi:10.1039/C4CC08312A
60. Gupta, S. K.; Rajeshkumar, T.; Rajaraman, G.; Murugavel, R. *Chem. Sci.* **2016,** in press. doi:10.1039/C6SC00279J
61. Chen, Y.-C.; Liu, J.-L.; Ungur, L.; Liu, J.; Li, Q.-W.; Wang, L.-F.; Ni, Z.-P.; Chibotaru, L. F.; Chen, X.-M.; Tong, M.-L. *J. Am. Chem. Soc.* **2016,** *138,* 2829–2837. doi:10.1021/jacs.5b13584
62. Liu, J.; Chen, Y.-C.; Liu, J.-L.; Vieru, V.; Ungur, L.; Jia, J.-H.; Chibotaru, L. F.; Lan, Y.; Wernsdorfer, W.; Gao, S.; Chen, X.-M.; Tong, M.-L. *J. Am. Chem. Soc.* **2016,** *138,* 5441–5450. doi:10.1021/jacs.6b02638
63. Magri, A. Multifunctional Complexes for Molecular Devices. Ph.D. Thesis, Université de Strasbourg, France, 2015.
64. *Stoe&Cie X-AREA and X-RED32;* STOE: Darmstadt, Germany, 2006.
65. Sheldrick, G. M. *Acta Crystallogr., Sect. A* **2008,** *64,* 112–122. doi:10.1107/S0108767307043930

License and Terms

This is an Open Access article under the terms of the Creative Commons Attribution License (http://creativecommons.org/licenses/by/2.0), which permits unrestricted use, distribution, and reproduction in any medium, provided the original work is properly cited.

The license is subject to the *Beilstein Journal of Nanotechnology* terms and conditions: (http://www.beilstein-journals.org/bjnano)

The definitive version of this article is the electronic one which can be found at: doi:10.3762/bjnano.7.92

BEILSTEIN JOURNAL OF NANOTECHNOLOGY

In situ characterization of hydrogen absorption in nanoporous palladium produced by dealloying

Eva-Maria Steyskal*[1], Christopher Wiednig[2], Norbert Enzinger[2] and Roland Würschum[1]

Letter

Open Access

Address:
[1]Institute of Materials Physics, Graz University of Technology, Petersgasse 16, A-8010 Graz, Austria and [2]Institute of Materials Science and Welding, Graz University of Technology, Kopernikusgasse 24, A-8010 Graz, Austria

Email:
Eva-Maria Steyskal* - steyskal@tugraz.at

* Corresponding author

Keywords:
dealloying; dilatometry; hydrogen storage; nanoporous palladium; resistometry

Beilstein J. Nanotechnol. **2016,** *7,* 1197–1201.
doi:10.3762/bjnano.7.110

Received: 14 June 2016
Accepted: 08 August 2016
Published: 17 August 2016

This article is part of the Thematic Series "Advances in nanomaterials II".

Guest Editor: H. Hahn

© 2016 Steyskal et al.; licensee Beilstein-Institut.
License and terms: see end of document.

Abstract

Palladium is a frequently used model system for hydrogen storage. During the past few decades, particular interest was placed on the superior H-absorption properties of nanostructured Pd systems. In the present study nanoporous palladium (np-Pd) is produced by electrochemical dealloying, an electrochemical etching process that removes the less noble component from a master alloy. The volume and electrical resistance of np-Pd are investigated in situ upon electrochemical hydrogen loading and unloading. These properties clearly vary upon hydrogen ad- and absorption. During cyclic voltammetry in the hydrogen regime the electrical resistance changes reversibly by almost 10% upon absorbing approximately 5% H/Pd (atomic ratio). By suitable loading procedures, hydrogen concentrations up to almost 60% H/Pd were obtained, along with a sample thickness increase of about 5%. The observed reversible actuation clearly exceeds the values found in the literature, which is most likely due to the unique structure of np-Pd with an extraordinarily high surface-to-volume ratio.

Findings

The knowledge about the remarkable hydrogen absorption properties of palladium dates back to the mid-nineteenth century [1] and has been studied intensively ever since. Even though palladium itself does not possess technical relevance as a hydrogen storage material due to its high price and rather low achievable H storage densities, it is a frequently used model system. During the past few decades particular interest was placed on nanostructured Pd, which exhibits superior absorption properties due to a high surface-to-volume ratio, and its application potential in important fields of technology such as energy storage, sensing and catalysis [2].

One attractive method to produce nanostructured metals with macroscopic dimensions is dealloying, an (electro-)chemical

process, which removes the less noble component from an alloy by selective etching [3]. Nanoporous palladium (np-Pd) produced by free corrosion [4] as well as potential-assisted dealloying [5] has been studied recently with regards to actuation upon electrochemical hydrogenation [4] as well as hydrogen solubility from the gas phase [6]. In the present study np-Pd is produced by electrochemically dealloying a Co–Pd master alloy and investigated upon electrochemical H absorption in an alkaline aqueous electrolyte. Volume and electrical resistance of the sample, two qualities both known to sensitively depend on the H content of Pd [4,7-11], are monitored in situ during electrochemical hydrogenation and compared to literature data.

The Co–Pd master alloy (80 wt % Co–20 wt % Pd) was prepared by electron beam melting (EBM) high purity wires of Co and Pd (ChemPur, 99.99%). The resulting alloy droplet was rolled to a thickness of 280 µm in several steps. Between each rolling step, the alloy was annealed for 1 h at 800 °C. From this master alloy sample platelets were cut for dealloying and subsequent charging experiments.

The resistometric measurements were set up similar to our work on nanoporous platinum [12,13]. To sum up briefly, the rectangular sample (ca. 12 × 3 mm^2) was immersed into the electrolyte hanging on five Pd wires, glued onto the platelet. The mid-positioned wire served as working-electrode contact connected to a PGZ-100 potentiostat (Radiometer Analytical), the other wires were connected to a Keithley 2400 Source Meter for four-point resistometry.

For dilatometry a square shaped sample platelet (ca. 5 × 5 mm^2) was placed under the pushrod of a Linseis L75 vertical dilatometer applying a constant pressure of 100 mN. A well-annealed, flattened Pd wire served as working electrode contact to an Autolab PGSTAT204 potentiostat.

Electrochemical charging was performed at room temperature using commercial Ag/AgCl (saturated KCl) reference electrodes, related to which all potentials $U_{Ag/AgCl}$ will be stated. Co–Pd was dealloyed in 0.1 M H_2SO_4 under the same conditions as in [5], which were shown to yield porous structures with pore diameters of 5–20 nm [5] and very low residual Co concentrations [6]. Correspondingly hydrogen concentrations were calculated assuming Co-free samples in the following. With this assumption a specific surface area of about 30 m^2/g was determined electrochemically for np-Pd from monolayer adsorption of oxygen, following a procedure presented in detail in reference [14]. All electrochemical experiments subsequent to dealloying were performed in a 1 M solution of KOH, a highly porous carbon fabric contacted by a Pd wire served as counter electrode. The property variations of np-Pd upon electrochemical charging were calculated with respect to the sample resistance R_0 and thickness L_0 in the electrochemical double layer regime.

Nanoporous metals freshly prepared by dealloying are in a strongly oxidized condition, associated with particular physical properties [12,13,15,16]. By suitable treatment, i.e., repeated cyclic voltammetry (CV) in a wide potential range, the sample can be reduced until finally a metallic CV behavior is reached in a steady state. Figure 1a shows a steady-state CV performed with a scan rate of 1 mV/s between potentials $U_{Ag/AgCl}$ of −1000 mV and +400 mV. As the potential varies triangularly,

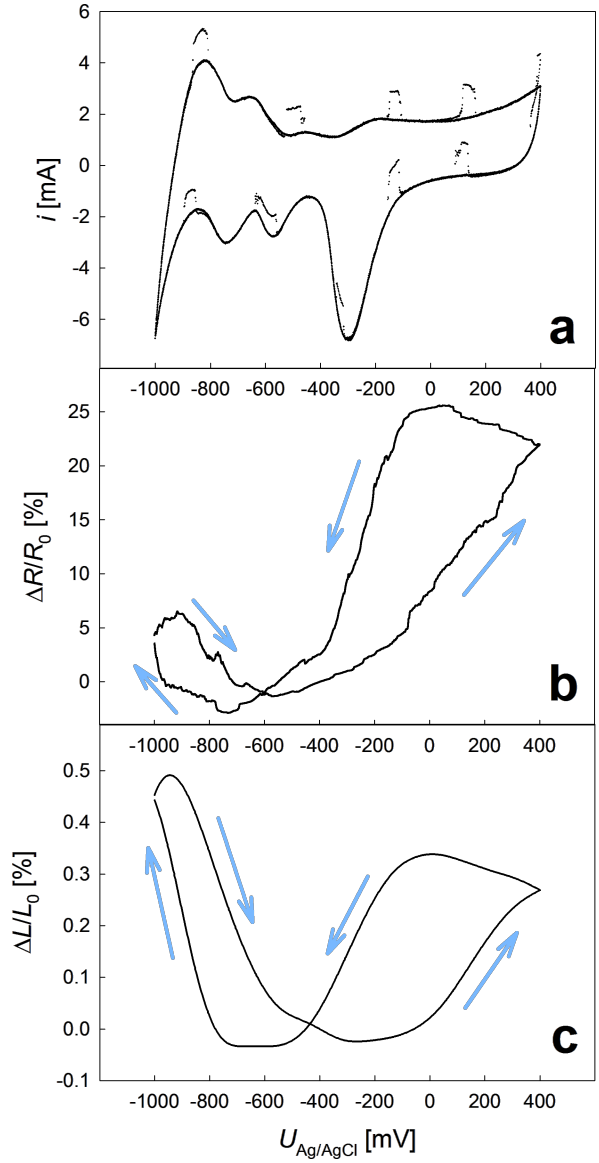


Figure 1: Cyclic voltammetry of np-Pd with a scan rate of 1 mV/s, recorded between potentials $U_{Ag/AgCl}$ of −1000 mV and +400 mV (a) with concommitant relative variations in electrical resistance (b) and sample thickness (c).

the CV curve is run through clockwise, while resistance changes up to almost 30% (Figure 1b) and thickness variations of about 0.5% (Figure 1c) occur. Occasionally visible spikes in the otherwise smooth cyclic voltammogram are caused by coinciding resistometric measuring pulses, which have to be sufficiently high for accurate resistance results. This causes certain irregularities in the CV curve, yet does not interfere with the property-tuning experiment.

In the double layer and oxygen regime (potentials between −550 mV and +400 mV) the property variations are similar to previous observations for porous nanophase metals: Increasing sample thicknesses and resistances upon positive scan are considered to be caused by charging-induced modifications in the atomic bindings [17-20] and charge-carrier scattering [13,16,21] at the metal surface, respectively. The hydrogen regime, situated at potentials between −1000 mV and −550 mV, which is particularly interesting due to the extraordinary H-absorption properties of Pd, is associated with resistance variations $\Delta R/R_0$ of approximately 7% and a thickness increase $\Delta L/L_0$ of about 0.5%.

This regime was investigated in more detail by cyclic voltammetry at a very slow scan rate of 0.1 mV/s. Figure 2 shows the relative variations of electrical resistance and sample thickness as functions of the imposed charge Q, determined by continuously integrating the charging current, corrected for minor leakages by subtracting a constant factor determined from the cycle to cycle offset. Resistance and length changes reveal remarkable similarities, both exhibiting two regions of different slope, attributed to hydrogen adsorption followed by hydrogen absorption at higher imposed charges. For dilatometry (Figure 2b) these results agree fairly well with the behavior of consolidated palladium nanoparticles, which was discussed within an electrocapillary coupling model by Viswanath and co-workers [8].

For the resistance variation (Figure 2a), the total charge flow of about −1.2 A·s arises from a transfer of about −0.3 A·s in the adsorption and −0.9 A·s in the absorption regime. Converting the latter into the absorbed hydrogen concentration c yields a H/Pd atomic ratio of about 5%, associated with a variation of R of about 9.6%. At such low hydrogen concentrations, the electrical resistance of bulk Pd is particularly sensitive to hydrogen absorption. Values for the resistance coefficient $(\Delta R/R_0)/c$ deduced from literature data range from 1.8 [9] to 2.3 [10].

The matching of these values with the present resistance coefficient $(\Delta R/R_0)/c$=1.9 of np-Pd is, however, surprising: Since nanoporous metals possess a high initial resistance, governed by surface scattering processes [16], a lower sensitivity to additional scattering centers inside the crystal due to absorbed hydrogen would be expected. An additional resistance contribution by adsorbates might arise in the present case, in analogy to the oxygen regime of porous nanophase metals [16,21].This is, however, unlikely as the variations of R during adsorption are small. The striking similarities between $\Delta R/R_0$ and $\Delta L/L_0$ suggest that actuation might influence R: An expansion during hydrogenation may disconnect electrical contacts in the nanoporous network, leading to a resistance increase. Such a mechanical effect would also explain the noisy R-signal due to immediate resistance changes caused by opening/closing connections.

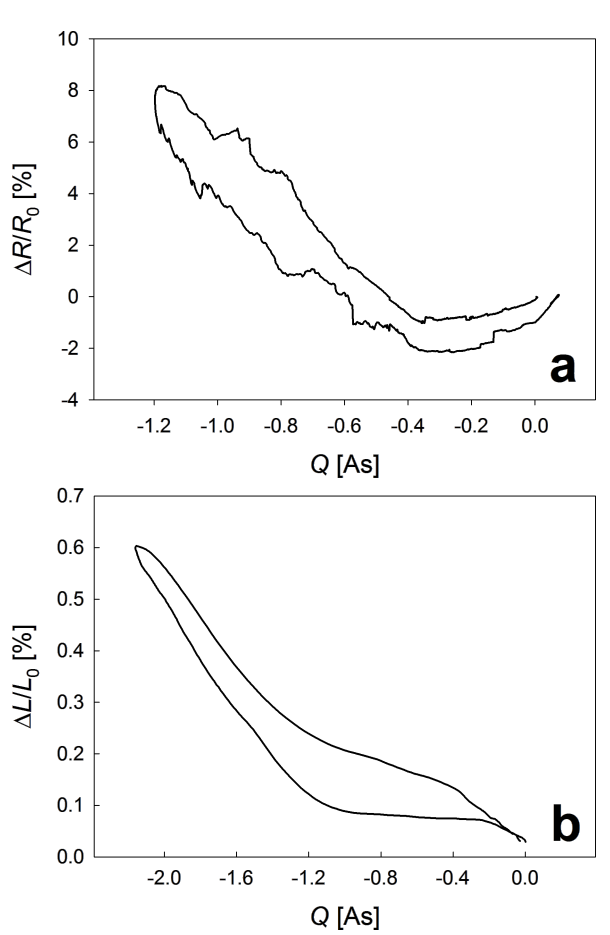


Figure 2: Charge dependence of relative electrical resistance (a) and sample thickness (b) upon cyclic voltammetry in the hydrogen regime at potentials $U_{Ag/AgCl}$ between −1000 mV and −550 mV.

Since extraordinarily strong actuation properties were reported quite recently for nanoporous Pd produced by free corrosion [4], the dilatometric measurements were extended to higher hydrogen concentrations by employing different charging parameters (Table 1). Before each loading experiment, the sample was activated by a CV similar to Figure 1. Hydrogen was absorbed either voltage-controlled at constant potentials between −900 mV and −1050 mV, or current-controlled by

Table 1: Dilatometrically monitoring hydrogen absorption upon voltage-controlled charging procedures at quoted voltages $U_{Ag/AgCl}$ or current-controlled charging at quoted currents, resulting in a final H/Pd atomic ratio c_f associated with a final thickness increase $(\Delta L)_f/L_0$ (see Figure 3).

parameters	time [min]	c_f	$(\Delta L)_f/L_0$ [%]
−900 mV	60	0.12	0.49
	120	0.11	0.42
−950 mV	60	0.14	0.54
	120	0.14	0.55
−1000 mV	60	0.35	2.90
	120	0.45	4.05
−1050 mV	60	0.51	4.71
	120	0.57	5.11
−5 mA	60	0.58	5.35
−2 mA	150	0.58	5.06

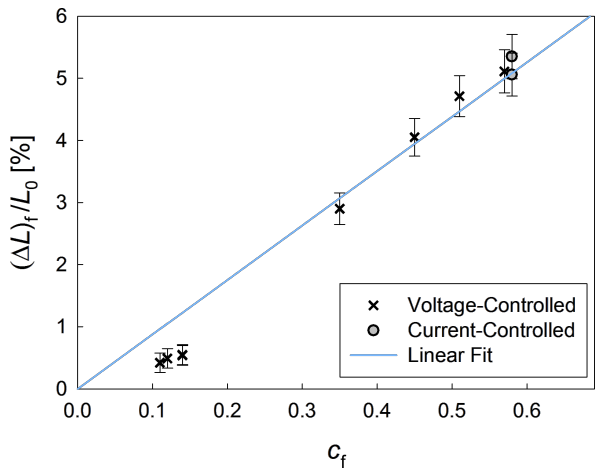


Figure 3: Thickness variations $(\Delta L)_f/L_0$ of np-Pd upon loading experiments up to different final hydrogen concentrations characterized by the H/Pd atomic ratio c_f (see Table 1).

applying a constant current and in both cases subsequently desorbed at a constant potential of −400 mV for 120 min. The stored amount of hydrogen was determined by integrating the discharging current. The length changes measured along with the hydrogen charging are plotted in Figure 3.

Upon charging to a H/Pd ratio of almost 60%, a thickness increase of about 5% was observed, representing the highest electrochemically induced actuation reported for a dealloyed material so far. This variation is not only significantly higher than predicted by literature data for bulk Pd [7], according to which an approximately linear variation of only about 3.5% would be expected at this concentration, but also exceeds the maximum hydrogen solubility as well as the relative sensitivity of actuator response to hydrogen loading of recently investigated nanoporous palladium produced by free corrosion of an Al–Pd master alloy [4].

While the maximum hydrogen solubilities show a strong variation with the charging parameters, such as the chosen electrolyte and applied potential, the strong sample expansion upon hydrogenation is directly related to the nanoporosity of np-Pd, i.e., its high surface-to-volume ratio. Since nanoporous Pd possesses very fine pore sizes of 5–20 nm [5,22,23], which strongly depend on the dealloying parameters, a significant fraction of the total H absorption takes place on sites close to the surface. Being subjected to significantly lower constraints than atomic layers inside the bulk, superficial planes may show stronger outward relaxation during hydrogen uptake, similar to the surface-chemistry-driven actuation behavior known for nanoporous gold, which is caused by alterations in the atomic bindings in superficial atomic layers [19].

In conclusion, resistometry and dilatometry represent two efficient, independent methods to characterize the hydrogen concentration in nanoporous palladium. The volume expansion of nanoporous palladium upon hydrogen absorption is stronger than predicted by literature data, which might be due to the high surface-to-volume ratio in the nanoporous samples. Resistance variations of almost 10% could be achieved upon absorbing approximately 5% H/Pd during cyclic voltammetry. Besides scattering processes also a resistance contribution by actuation in the nanostructure was discussed. To give a brief outlook, the H absorption behavior of np-Pd should be studied systematically with regards to different master alloy compositions and dealloying parameters. Moreover the experiments might be extended to higher hydrogen concentrations by using acidic electrolytes in future experiments.

References

1. Graham, T. *Proc. R. Soc. London* **1867,** *16,* 422–427. doi:10.1098/rspl.1867.0090
2. Pundt, A.; Kirchheim, R. *Annu. Rev. Mater. Res.* **2006,** *36,* 555–608. doi:10.1146/annurev.matsci.36.090804.094451
3. Erlebacher, J.; Aziz, M. J.; Karma, A.; Dimitrov, N.; Sieradzki, K. *Nature* **2001,** *410,* 450–453. doi:10.1038/35068529
4. Zhang, J.; Bai, Q.; Zhang, Z. *Nanoscale* **2016,** *8,* 7287–7295. doi:10.1039/C6NR00427J
5. Hakamada, M.; Mabuchi, M. *J. Alloys Compd.* **2009,** *479,* 326. doi:10.1016/j.jallcom.2008.12.078
6. Hakamada, M.; Nakano, H.; Furukawa, T.; Takahashi, M.; Mabuchi, M. *J. Phys. Chem. C* **2010,** *114,* 868–873. doi:10.1021/jp909479m
7. Feenstra, R.; Griessen, R.; de Groot, D. G. *J. Phys. F: Met. Phys.* **1986,** *16,* 1933. doi:10.1088/0305-4608/16/12/008
8. Viswanath, R. N.; Weissmüller, J. *Acta Mater.* **2013,** *61,* 6301–6309. doi:10.1016/j.actamat.2013.07.013
9. Fischer, F. *Ann. Phys.* **1906,** *325,* 503–526. doi:10.1002/andp.19063250804

10. Flanagan, T. B.; Lewis, F. A. *Trans. Faraday Soc.* **1959,** *55,* 1400–1408. doi:10.1039/TF9595501400
11. Vertova, A.; Rondinini, S.; Busca, G. *J. Appl. Electrochem.* **2002,** *32,* 661–670. doi:10.1023/A:1020149306968
12. Steyskal, E.-M.; Besenhard, M.; Landgraf, S.; Zhong, Y.; Weissmüller, J.; Pölt, P.; Albu, M.; Würschum, R. *J. Appl. Phys.* **2012,** *112,* 073703. doi:10.1063/1.4755808
13. Steyskal, E.-M.; Qi, Z.; Pölt, P.; Albu, M.; Weissmüller, J.; Würschum, R. *Langmuir* **2016,** *32,* 7757–7764. doi:10.1021/acs.langmuir.6b01734
14. Fang, L.-l.; Tao, Q.; Li, M.-f.; Liao, L.-w.; Chen, D.; Chen, Y.-x. *Chin. J. Chem. Phys.* **2010,** *23,* 543–548. doi:10.1088/1674-0068/23/05/543-548
15. Jin, H.-J.; Parida, S.; Kramer, D.; Weissmüller, J. *Surf. Sci.* **2008,** *602,* 3588. doi:10.1016/j.susc.2008.09.038
16. Wahl, P.; Traußnig, T.; Landgraf, S.; Jin, H.-J.; Weissmüller, J.; Würschum, R. *J. Appl. Phys.* **2010,** *108,* 073706. doi:10.1063/1.3490789
17. Weissmüller, J.; Viswanath, R. N.; Kramer, D.; Zimmer, P.; Würschum, R.; Gleiter, H. *Science* **2003,** *300,* 312–315. doi:10.1126/science.1081024
18. Viswanath, R. N.; Kramer, D.; Weissmüller, J. *Electrochim. Acta* **2008,** *53,* 2757. doi:10.1016/j.electacta.2007.10.049
19. Biener, J.; Wittstock, A.; Zepeda-Ruiz, L. A.; Biener, M. M.; Zielasek, V.; Kramer, D.; Viswanath, R. N.; Weissmüller, J.; Bäumer, M.; Hamza, A. V. *Nat. Mater.* **2009,** *8,* 47–51. doi:10.1038/nmat2335
20. Jin, H.-J.; Weissmüller, J. *Adv. Eng. Mater.* **2010,** *12,* 714–723. doi:10.1002/adem.200900329
21. Steyskal, E.-M.; Topolovec, S.; Landgraf, S.; Krenn, H.; Würschum, R. *Beilstein J. Nanotechnol.* **2013,** *4,* 394–399. doi:10.3762/bjnano.4.46
22. Chen, Q.; Sieradzki, K. *Nat. Mater.* **2013,** *12,* 1102–1106. doi:10.1038/nmat3741
23. Cao, Y. K.; Ma, X. Y.; Chen, Y. Z.; Shan, G. B.; Liu, F. *Scr. Mater.* **2016,** *123,* 1. doi:10.1016/j.scriptamat.2016.05.040

License and Terms

This is an Open Access article under the terms of the Creative Commons Attribution License (http://creativecommons.org/licenses/by/4.0), which permits unrestricted use, distribution, and reproduction in any medium, provided the original work is properly cited.

The license is subject to the *Beilstein Journal of Nanotechnology* terms and conditions: (http://www.beilstein-journals.org/bjnano)

The definitive version of this article is the electronic one which can be found at: doi:10.3762/bjnano.7.110

BEILSTEIN JOURNAL OF NANOTECHNOLOGY

Mesoporous hollow carbon spheres for lithium–sulfur batteries: distribution of sulfur and electrochemical performance

Anika C. Juhl[1], Artur Schneider[2], Boris Ufer[1], Torsten Brezesinski[2], Jürgen Janek[*2,3] and Michael Fröba[*1]

Full Research Paper

Open Access

Address:
[1]Institute of Inorganic and Applied Chemistry, University of Hamburg, Martin-Luther-King-Platz 6, 20146 Hamburg, Germany, [2]Battery and Electrochemistry Laboratory, Institute of Nanotechnology, Karlsruhe Institute of Technology, Hermann-von-Helmholtz-Platz 1, 76344 Eggenstein-Leopoldshafen, Germany and [3]Institute of Physical Chemistry, Justus-Liebig-University Giessen, Heinrich-Buff-Ring 17, 35392 Giessen, Germany

Email:
Jürgen Janek[*] - juergen.janek@phys.chemie.uni-giessen.de;
Michael Fröba[*] - michael.froeba@chemie.uni-hamburg.de

* Corresponding author

Keywords:
carbon/sulfur composites; cycling stability; distribution of sulfur in pores; hollow carbon spheres; lithium–sulfur batteries

Beilstein J. Nanotechnol. **2016,** *7,* 1229–1240.
doi:10.3762/bjnano.7.114

Received: 15 June 2016
Accepted: 18 August 2016
Published: 30 August 2016

This article is part of the Thematic Series "Advances in nanomaterials II".

Guest Editor: H. Hahn

© 2016 Juhl et al.; licensee Beilstein-Institut.
License and terms: see end of document.

Abstract

Hollow carbon spheres (HCS) with a nanoporous shell are promising for the use in lithium–sulfur batteries because of the large internal void offering space for sulfur and polysulfide storage and confinement. However, there is an ongoing discussion whether the cavity is accessible for sulfur. Yet no valid proof of cavity filling has been presented, mostly due to application of unsuitable high-vacuum methods for the analysis of sulfur distribution. Here we describe the distribution of sulfur in hollow carbon spheres by powder X-ray diffraction and Raman spectroscopy along with results from scanning electron microscopy and nitrogen physisorption. The results of these methods lead to the conclusion that the cavity is not accessible for sulfur infiltration. Nevertheless, HCS/sulfur composite cathodes with areal sulfur loadings of 2.0 mg·cm^{-2} were investigated electrochemically, showing stable cycling performance with specific capacities of about 500 mAh·g^{-1} based on the mass of sulfur over 500 cycles.

Introduction

In the past 20 years, rechargeable lithium–ion batteries have proven to be superior energy storage devices and have been subject of intensive research [1-3]. However, being limited by a theoretical specific capacity of the active materials of approximately 300 mAh·g^{-1}, their storage capacity is not sufficient to serve as the primary energy source of domains such as long-

range automotive transport [4,5]. Due to the high theoretical specific capacity (1675 mAh·g^{-1}) and specific energy (2600 Wh·kg^{-1}) of sulfur the lithium–sulfur (Li–S) battery is a promising candidate to overcome this limitation and, thus, replace the Li–ion system [4,6]. Besides, sulfur offers the advantages of being naturally abundant, non-toxic and of low cost.

Nevertheless, the Li–S cell is facing several problems that have to be settled for industrial application. One is the insulating nature of sulfur and its discharge product lithium sulfide (Li_2S), which leads to a low utilization of active material [7-9]. Another problem is the solubility of the lithium polysulfides (Li_2S_x, $3 \leq x \leq 8$) formed as intermediate products during charge and discharge in the commonly used organic electrolytes. The dissolved polysulfides shuttle between the cathode and anode and cause the deposition of insoluble Li_2S_2 and Li_2S on both upon further reduction at the end of discharge. In consequence, the cell suffers from low Coulombic efficiency and short cycle life [8,10,11]. The third drawback is a volume expansion of about 80% during discharge, resulting from the lower density and thus higher molar volume of lithium sulfide (28.0 cm^3·mol^{-1} compared to 15.5 cm^3·mol^{-1} for sulfur) [12]. This can lead to the loss of electrical contact of Li_2S with the conducting additive or the current collector [9].

Cathode materials composed of porous carbon and sulfur show promising results with regard to overcoming these problems. Thus, a lot of research has been carried out on nanostructured carbon hosts for sulfur storage including carbon fibers [13,14], carbon nanotubes [15,16], graphene/graphene oxide [17-19] as well as micro-/mesoporous carbons [20-22]. Among the porous carbons, especially hollow carbon spheres (HCS) have attracted significant attention because sulfur and the resulting polysulfides can be confined in the shell while the large cavity offers room for sulfur storage and volume expansion during discharge [23-31].

However, there is an ongoing discussion on the location of sulfur in the hollow spheres. It remains unclear at present, whether the cavity and the micro- or mesopores of the shell are both accessible for sulfur infiltration. The analysis of sulfur distribution in the literature is usually conducted by energy dispersive X-ray spectroscopy (EDX) measurements using either a transmission electron microscope (TEM) or a scanning electron microscope (SEM). Although revealing similarities in the main characteristics, the conclusions being drawn are rather contradictory [24-31]. A problem may arise from the high spatial mobility of sulfur species under vacuum conditions. Raiß et al. examined the behavior of sulfur in the presence of carbon in high vacuum and found that sulfur is redistributing rapidly. They concluded that for this reason, the analysis of carbon/sulfur composites by means of vacuum-based methods can be misleading [32].

In this work, we present the analysis of sulfur distribution in hollow carbon spheres with a mesoporous shell by combining the results from non-vacuum methods, namely X-ray diffraction (XRD) and Raman spectroscopy, with those from vacuum-based ones (SEM and nitrogen physisorption). Moreover, we examined the influence of the pressure during melt impregnation on the distribution of sulfur and compared the resulting loading and distribution with composites obtained by impregnation from a solution of sulfur in carbon disulfide. Finally, the electrochemical performance of HCS/sulfur composite cathodes with a sulfur areal loading of 2.0 mg·cm^{-2} was investigated.

Results and Discussion

Silica template and hollow carbon spheres

Hollow carbon spheres with a mesoporous shell were obtained by impregnation of silica spheres with a core–shell structure with phenol and formaldehyde (first step in Figure 1). Carbonization under inert atmosphere and etching of the template yielded the hollow spheres (second and third step in Figure 1).

The employed silica spheres with a solid core and mesoporous shell (SCMS silica) were synthesized in two steps by modified literature methods [33,34]. Solid silica spheres were synthesized by the Stöber method [35]. In the second step a mesoporous shell was grown on the spheres by employing tetraethyl orthosilicate in presence of cetyltrimethylammonium bromide (CTAB) as a structure-directing agent. Combustion of CTAB in

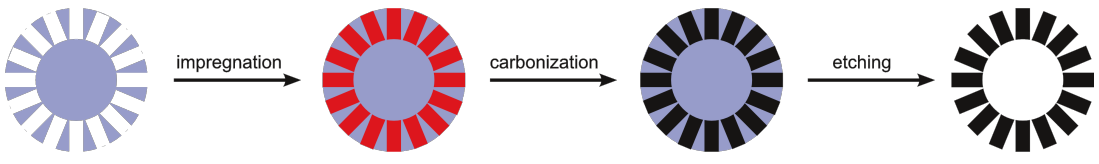


Figure 1: Synthesis of the hollow carbon spheres via impregnation of silica spheres with solid core and mesoporous shell, followed by carbonization and etching of silica.

air generated the core–shell silica spheres. The diameter of the solid core was determined to be 380 nm by dynamic light scattering, while the diameter of the core–shell particles was about 515 nm. From SEM images (Figure S1 in Supporting Information File 1) a diameter of about 490 nm was determined for the core–shell spheres. Further characterization of the SCMS silica can be found in Supporting Information File 1 (Figure S2).

SEM and TEM images of HCS synthesized from SCMS silica (Figure 2) show that the particle size is uniform with an outer diameter of approximately 400 nm, an inner diameter of about 300 nm and a shell thickness of roughly 40 to 50 nm. Moreover, the shell of the HCS has an appearance typical of a material composed of disordered mesopores. The disordered structure is supported by the small-angle X-ray diffraction pattern of the hollow spheres (Figure 3a), which does not show any reflections between $2\theta = 0.5°$ and $2\theta = 10°$.

The wide-angle X-ray diffraction pattern (Figure 3b) shows two broad reflections that result from the interlayer and intralayer scattering of graphene sheets. From the fact that they are broad and little pronounced it can be concluded that the degree of graphitization is low and the carbon is mainly amorphous [36,37]. This is confirmed by the Raman spectrum (Figure 3c), which shows two bands centered at 1597 cm^{-1} (G band) and 1340 cm^{-1} (D band) typical of carbon with small graphitic domains. The G band results from the in-plane stretching of sp^2-bonded (graphitic) carbon atoms, while the D band is induced by defects and disorder in the carbon structure [38].

From the nitrogen physisorption isotherm (Figure 4a) of the HCS a Brunauer–Emmet–Teller (BET) surface of 1123 $m^2 \cdot g^{-1}$ can be determined. The pore size distribution (Figure 4b) was calculated by a quenched solid density functional theory (QSDFT) model from the adsorption branch and shows that the mesopore diameter of the spheres is approximately 5 nm. The adsorbed volume of nitrogen gas is not reaching a plateau at high relative pressures but is increasing steeply at a pressure of p/p_0 higher than 0.9. This is because of the large inner cavity of the hollow spheres, the volume of which cannot be determined

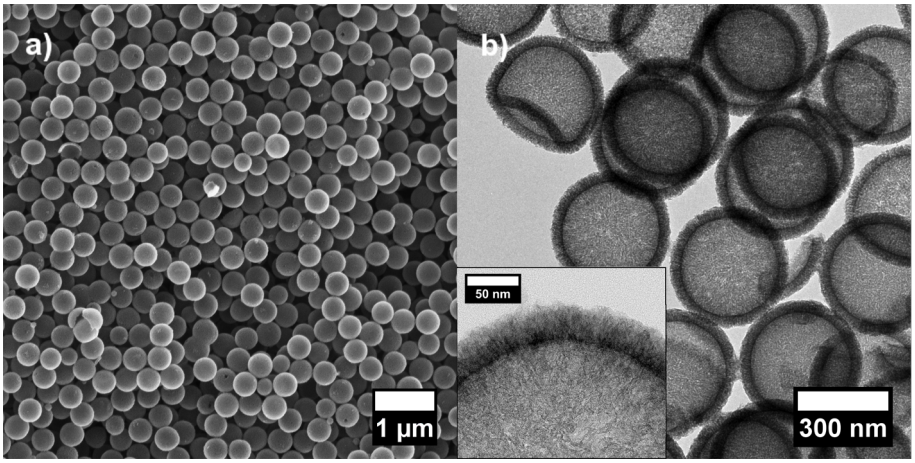


Figure 2: a) SEM and b) TEM images of mesoporous hollow carbon spheres. Inset: larger magnification of the shell of a hollow sphere.

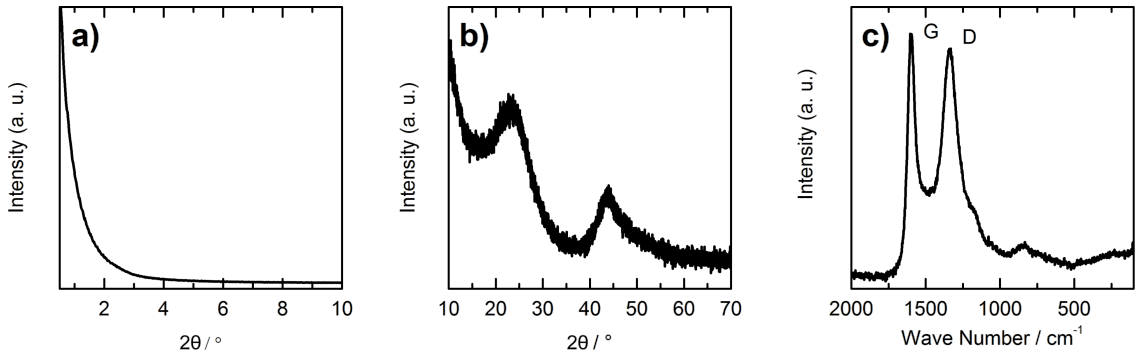


Figure 3: a) Small-angle and b) wide-angle XRD patterns as well as c) Raman spectrum of hollow carbon spheres.

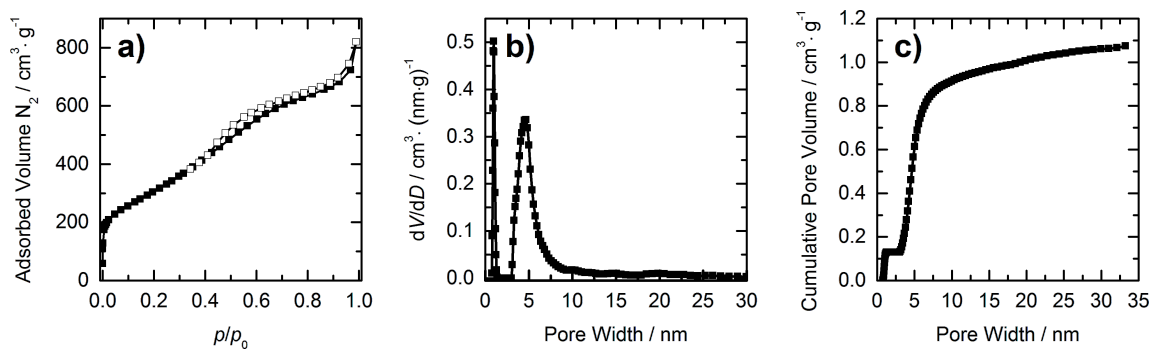


Figure 4: a) Nitrogen physisorption isotherm (measured at 77 K), b) pore size distribution and c) cumulative pore volume of hollow carbon spheres. Pore size distribution and cumulative pore volume were obtained from the isotherm by QSDFT analysis.

by nitrogen physisorption. And this in turn makes it impossible to determine the total pore volume of the HCS [39]. To assess the pore volume of the shell, however, the cumulative pore volume (Figure 4c) of pores in the meso-range can be used as an estimate. As the shell thickness is about 40 nm, it can be assumed that the pore volume of the shell originates from pores smaller than that. To be sure not to take into account too much of the cavity volume, the pore volume of the shell was estimated from the cumulative pore volume of pores up to 30 nm, which adds up to 1.06 $cm^3 \cdot g^{-1}$. The micropores (pores smaller than 2 nm) contribute 0.13 $cm^3 \cdot g^{-1}$ to this volume.

The microporosity of carbonaceous materials can be determined more appropriately by carbon dioxide physisorption. From carbon dioxide physisorption measurements (see Figure S3 in Supporting Information File 1 for the isotherm, pore size distribution and cumulative pore volume) it can be concluded that the HCS contain a considerable amount of pores smaller than 1.5 nm. The cumulative pore volume of these small pores is as high as 0.26 $cm^3 \cdot g^{-1}$, which is significantly higher than the 0.13 $cm^3 \cdot g^{-1}$ determined by nitrogen physisorption for pores smaller than 2 nm.

Carbon/sulfur composites

To get an impression of how much sulfur can be loaded into the pores and the cavities of the hollow carbon spheres, we calculated which sulfur loadings can be reached by either filling only the pores of the shell of the HCS or by filling the pores of the shell and the cavity.

The maximum mass of sulfur m_{sulfur} that can be incorporated into the shell by melt impregnation can be calculated by multiplication of the pore volume V_{pores} of the shell (1.06 cm^3 for 1 g HCS) with the density of liquid sulfur (ρ_{sulfur} = 1.819 $g \cdot cm^{-3}$) [12].

$$m_{sulfur} = V_{pores} \cdot \rho_{sulfur} \quad (1)$$

This means, that by filling just the shell of HCS, 1.93 g sulfur can be loaded into 1 g of HCS, corresponding to a sulfur loading w_{sulfur} of 65 wt %. The latter value was calculated by using Equation 2, where m_{HCS} is the mass of the hollow carbon spheres.

$$w_{sulfur} = \frac{m_{sulfur}}{m_{sulfur} + m_{HCS}} \quad (2)$$

The maximum sulfur loading for the case that both the cavity and the shell of HCS are filled by sulfur can also be calculated when considering the pore volume of the shell V_{pores} and the volume of the cavities by taking into account the geometry of a sphere. The derivation of the resulting Equation 3 can be found in Supporting Information File 1. The constant C is given by Equation 4.

$$w_{sulfur} = \frac{C \cdot \rho_{sulfur}}{C \cdot \rho_{sulfur} + m_{HCS}} \quad (3)$$

$$C = \left(\frac{m_{HCS}}{\rho_{carbon}} + V_{pores} \right) \frac{r_i^3}{r_o^3 - r_i^3} + V_{pores} \quad (4)$$

In Equation 4, ρ_{carbon} represents the density of carbon without pores, r_i is the radius of the cavity (the inner radius of the hollow sphere) and r_o is the outer radius of the sphere.

Because the maximum sulfur loading by melt impregnation is calculated, the density of liquid sulfur is used again. The density of the carbon is unknown, but as the HCS are obtained

by carbonization at 900 °C and the XRD pattern indicates mainly amorphous carbon, the density of amorphous carbon ($\rho_{amorphousC}$ = 1.8 g·cm^{-3}) [12] is assumed. This way a sulfur loading of 81 wt % is obtained. For comparison, the possible sulfur loadings were also determined using the densities of graphite ($\rho_{graphite}$ = 2.30 g·cm^{-3}) [12] and charcoal ($\rho_{charcoal}$ = 0.56 g·cm^{-3}) [12]. These calculations led to values of 80 wt % and 86 wt %, respectively. Consequently, it can be concluded that a sulfur loading between 80 wt % and 86 wt % can be reached by filling both the shell and the cavity of HCS with sulfur.

To monitor the filling of the hollow spheres, they were loaded with sulfur in mass ratios of carbon to sulfur ranging from 70:30 to 30:70 by a melt impregnation method at 155 °C. For comparison, samples with sulfur loadings of 60 wt % and 70 wt % were also prepared in vacuum and under increased pressure. Moreover, impregnation of HCS with sulfur from a solution containing sulfur in carbon disulfide was carried out repeatedly so that sulfur loadings close to 60 and 70 wt % were obtained. The mass fractions of carbon and sulfur in the composites were determined by thermogravimetric measurements (see Figure S5 in Supporting Information File 1) and the corresponding values are given in Table 1. Samples are denoted as HCS-*x*-*method*, where *x* indicates the exact amount of sulfur and *method* specifies the impregnation method. The term "melt" stands for melt impregnation at ambient pressure, "vac" for melt impregnation in vacuum, "press" indicates impregnation under increased pressure and "sol" stands for the impregnation from solution. It is worth noting that even the composite with the highest fraction of sulfur (HCS-76-sol) contains less sulfur than can theoretically be filled into the pore volume of cavity and shell, which would be at least 80 wt % (see calculations above).

X-ray diffraction

The HCS/sulfur composites were investigated by powder X-ray diffraction (pXRD). The wide-angle XRD patterns of the samples impregnated at ambient pressure (Figure 5a) show that up to a sulfur content of 60 wt % there are only the broad reflections of amorphous carbon visible. In the literature this behavior is attributed to sulfur being dispersed in mesopores, thereby losing its crystallinity [22,40]. For a sulfur content of 70 wt % however, reflections of crystalline sulfur can be seen. For the samples impregnated with sulfur in vacuum (Figure 5b), under increased pressure (Figure 5c) and from solution (Figure 5d), the XRD patterns look similar: For a sulfur content of less than 60 wt % no reflections are visible, while diffraction peaks of crystalline sulfur can be observed when the sulfur content is approximately 70 wt %.

There are two possible explanations for the existence of crystalline sulfur in the composites. The first is that sulfur fills the cavities of the HCS leading to larger crystallites than in the mesopores of the shell. The second explanation is that sulfur accumulates on the outside of the hollow spheres, thus showing bulk-like behavior. Given that no broadening of the sulfur reflections due to nano-sized crystallites can be observed, we conclude that the crystalline sulfur is only present on the outside of HCS.

Table 1: Water, sulfur and carbon content of HCS, HCS/sulfur composites and elemental sulfur determined by thermogravimetric measurements as well as the residual mass after thermogravimetry.[a]

sample	water content / %	sulfur content / %	carbon content / %	residual mass / %
HCS	2.3	—	96.0	2.0
elemental sulfur	—	99.5	—	0.6
HCS-29-melt	1.0	29.2	68.3	1.9
HCS-38-melt	0.6	37.9	60.6	0.8
HCS-49-melt	—	48.6	50.5	0.5
HCS-59-melt	0.2	59.1	39.2	1.5
HCS-68-melt	—	68.3	30.1	1.6
HCS-58-vac	—	58.0	41.2	1.0
HCS-67-vac	—	66.5	31.7	2.3
HCS-59-press	—	58.8	39.5	1.2
HCS-67-press	—	67.2	31.2	2.2
HCS-53-sol[b]	—	53.0	45.4	1.2
HCS-76-sol[b]	—	76.0	23.0	1.7

[a]Values that add up to more than 100% are due to the measuring inaccuracy of thermogravimetry.
[b]Mass ratios obtained by impregnation from solution differ from those obtained by the other methods because carbon disulfide evaporated fast, thus changing the concentration of the solution.

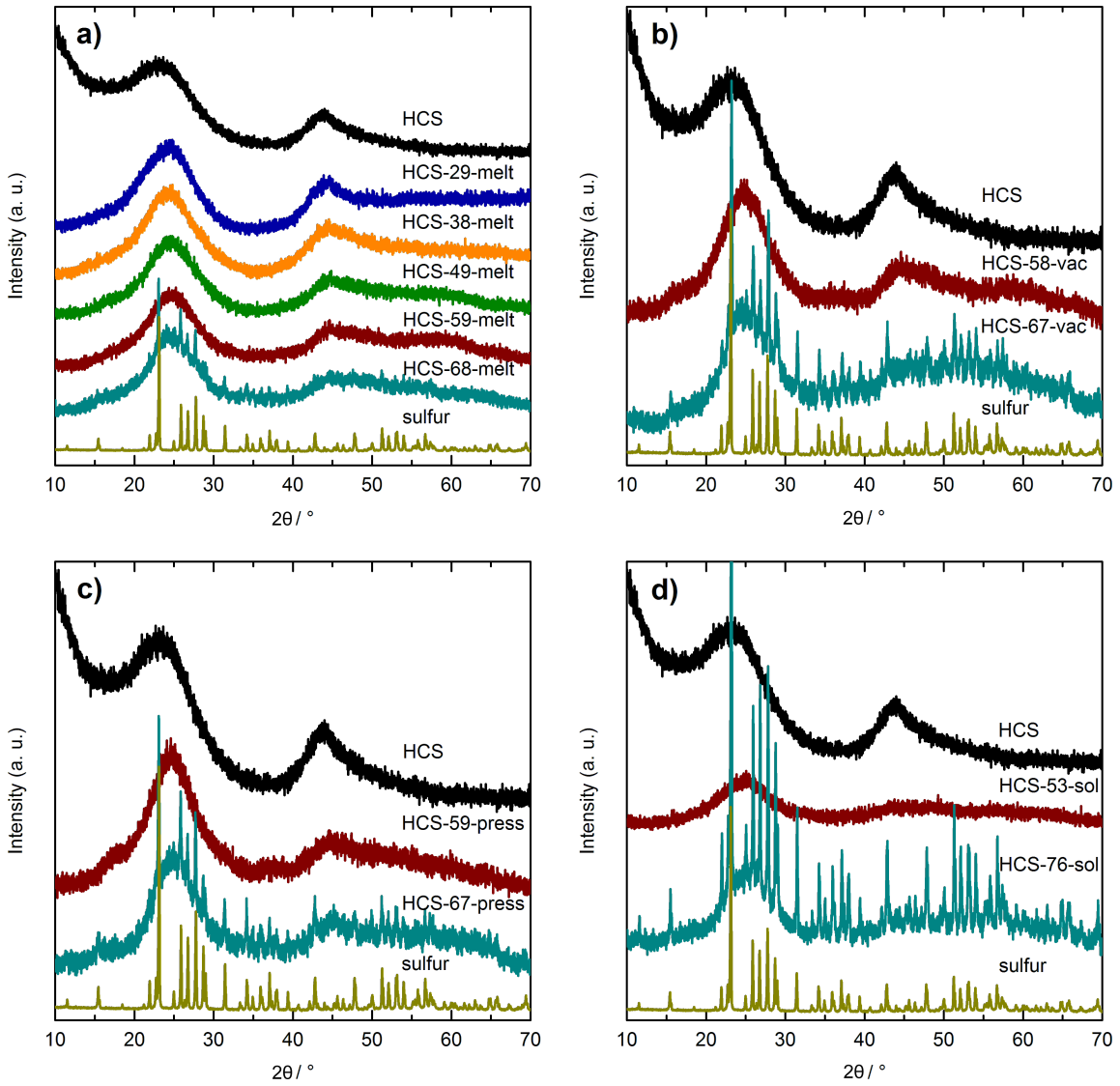


Figure 5: Powder X-ray diffraction patterns of HCS loaded with different amounts of sulfur by a) melt impregnation at ambient pressure, b) melt impregnation in vacuum, c) melt impregnation under increased pressure and d) impregnation from a solution of sulfur in carbon disulfide.

Raman spectroscopy

Raman spectroscopy (Figure 6) shows results similar to those obtained by pXRD measurements. For carbon/sulfur composites with sulfur contents below 60 wt %, the characteristic bands resulting from the vibrations of S_8 cannot be observed, while they are visible at least in some of the composites containing more than 60 wt % sulfur. This behavior has also been reported in the literature [41-43] but could not yet be explained satisfactorily. However, as these observations are in good agreement with the results from pXRD, it can be assumed, that the lack of Raman bands might also be due to confinement effects. Thus, the appearance of bands at high sulfur loadings could also be explained either by sulfur filling the cavities of HCS or by sulfur accumulating on the outside of the spheres.

SEM and EDX

SEM images of HCS-58-vac and HCS-67-vac (Figure 7a,b) which can be seen as representative examples of the composites studied here (see Figure S6 and Figure S7 in Supporting Information File 1 for the others), show that the sample morphology is significantly different depending on the sulfur content. SEM images of samples containing less than 60 wt % sulfur only show carbon spheres regardless of the impregnation method. SEM images of the composites containing 67 wt % sulfur or more indicate the presence of a second phase. This phase is darker than the spheres and is extended over large areas. Exemplary, EDX measurements of the hollow spheres and the second phase in HCS-67-vac are shown in Figure 7c; the measured areas and corresponding EDX spectra are marked

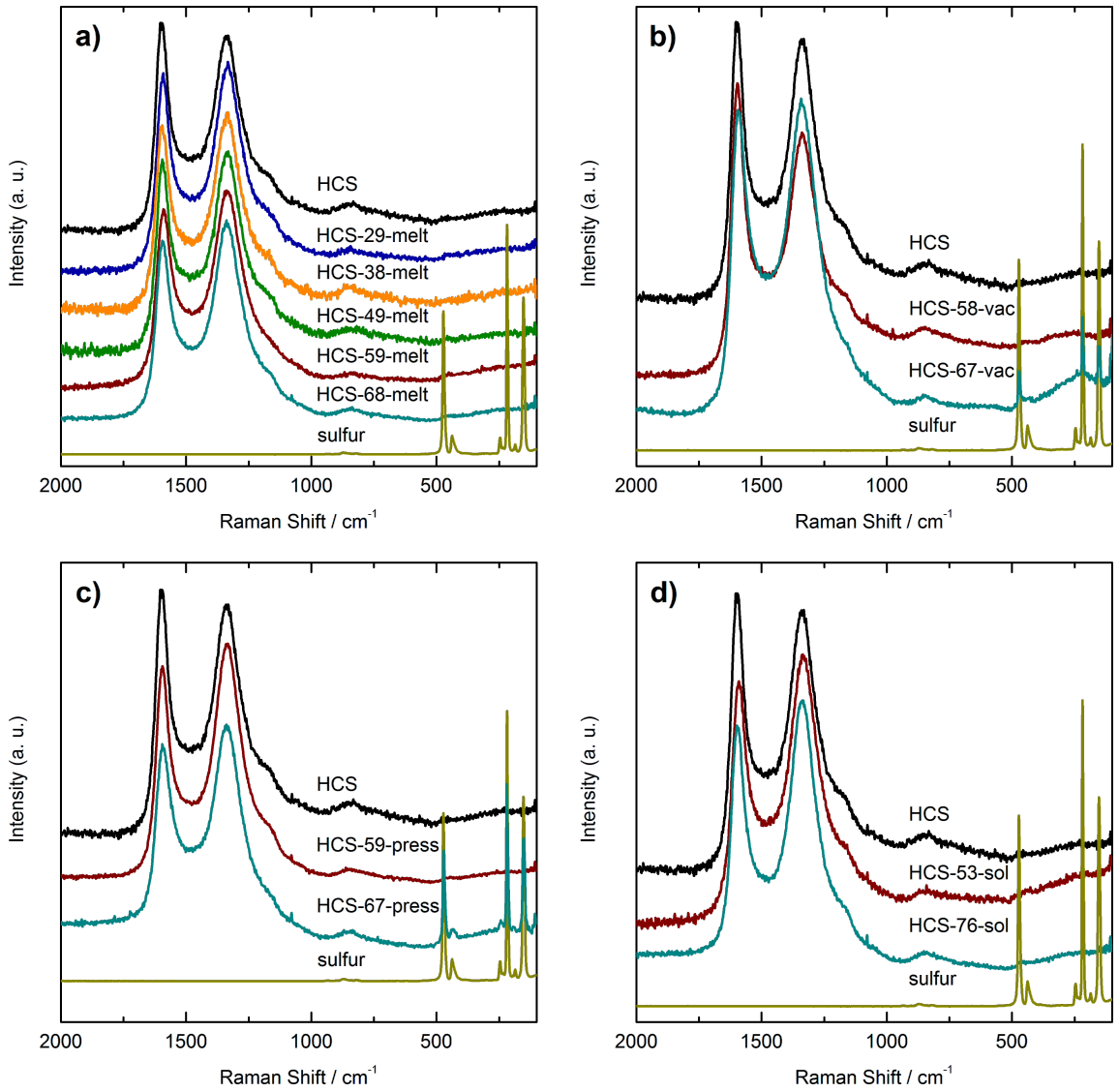


Figure 6: Raman spectra of HCS loaded with different amounts of sulfur by a) melt impregnation at ambient pressure, b) melt impregnation in vacuum, c) melt impregnation under increased pressure and d) impregnation from a solution of sulfur in carbon disulfide.

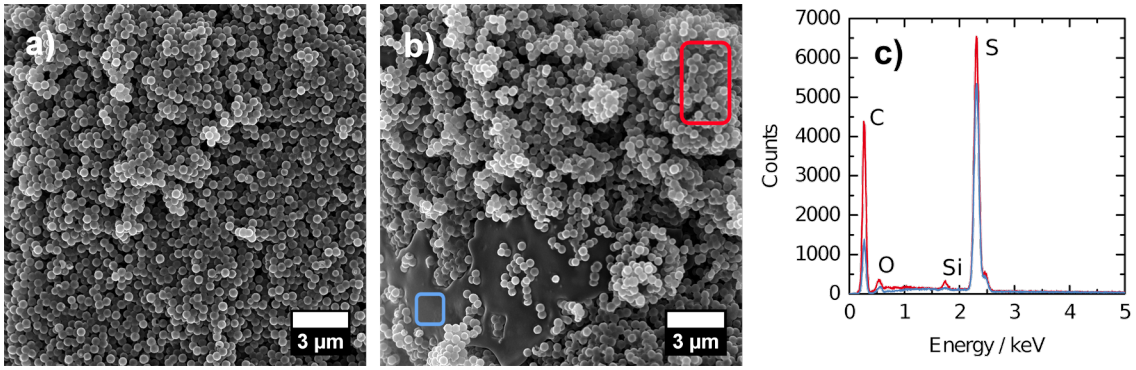


Figure 7: SEM images of a) HCS-58-vac, b) HCS-67-vac, and c) EDX spectra of HCS-67-vac (measured areas are marked red and blue, respectively).

in red and blue. When comparing the EDX peaks of sulfur and carbon in both areas, it can be clearly seen that there is a larger amount of sulfur present in the darker areas than in the sulfur-loaded HCS. Thus, it can be assumed that the second phase consists of molten and recrystallized sulfur. The amount of carbon that is still measureable in this area is due to the deposition of an additional carbon layer onto the samples prior to EDX analysis. EDX spectra for HCS-68-melt, HCS-67-press and HCS-76-sol can be found in Supporting Information File 1 (Figure S7). As these large accumulations of sulfur can only be found in samples with the highest sulfur contents, we assume that this result is not due to sulfur redistribution in vacuum during the SEM/EDX analysis. It also helps to explain the appearance of sulfur reflections in pXRD and characteristic sulfur bands in the Raman spectra. Keeping in mind that the shell of HCS is supposed to hold about 66 wt % sulfur while the complete hollow spheres should be able to contain as much as 80 wt % sulfur, we conclude from the results with pXRD, Raman spectroscopy and SEM/EDX that only the shell of HCS can be filled by sulfur. Using more sulfur to eventually fill the cavity leads to crystalline sulfur on the outside of HCS.

Nitrogen physisorption

Nitrogen physisorption measurements of the composites also confirm the inaccessibility of the HCS cavity for sulfur. Nevertheless, the results have to be handled with care because of the vacuum applied while degassing and measuring the samples. From the physisorption isotherms the pore volume of the shell of the HCS/sulfur composites can be determined in the same way as that of the pure hollow spheres (see Figure S8 in Supporting Information File 1 for the physisorption isotherms and plots of cumulative pore volumes). For comparison, a theoretical pore volume can be calculated from the pore volume of HCS and the volume of the impregnated sulfur according to Equation 5 (for the derivation see Supporting Information File 1). The density of liquid sulfur was used for the calculation of the theoretical pore volumes because both the state and structure of sulfur in nanopores are unknown.

$$V_{\text{pores,C–S}} = \frac{V_{\text{pores,HCS}} \cdot m_{\text{HCS}} - \frac{m_{\text{sulfur}}}{\rho_{\text{sulfur}}}}{m_{\text{HCS}} + m_{\text{sulfur}}} \quad (5)$$

The calculation was carried out for all samples containing less than 60 wt % sulfur as the others contain a sulfur volume higher than the pore volume of the shell. Table 2 gives the pore volumes of HCS and HCS/sulfur composites determined from nitrogen physisorption and the calculated pore volumes. Interestingly, the measured pore volume is always lower than the calculated value. This might be due to the fact that some pores are blocked by sulfur and thus, are no longer accessible for nitrogen gas during the measurements. We believe that the strong capillary forces on liquids/melts in the mesopores are responsible for the pore blocking effect. Once sulfur has filled the mesopores there is no further driving force for filling of the cavities, and only the mesoporous shell is filled with sulfur.

Electrochemical characterization

Since we could show that, for a HCS/sulfur ratio of approximately 40:60, the sulfur is completely incorporated in the porous carbon, electrochemical testing was performed on coin-type cells using HCS/sulfur composite containing 61 wt % sulfur as cathode material. The voltage range was 2.5–1.7 V with respect to Li/Li^+. Representative charge–discharge curves for the first, 100th and 500th cycles of a cell with areal sulfur loading of 2.0 $mg \cdot cm^{-2}$ are shown in Figure 8a. This intermediate loading was chosen in order to ensure competitive areal capacities. Moreover, electrodes with higher sulfur loadings, especially with increased electrode thickness are prone to severe degradation, as the mechanical stress and the interfacial resistance are increased. Two distinct plateaus at about 2.3 V and 2.1 V are clearly visible upon discharge, corresponding to the reduction of elemental sulfur to higher-order lithium polysulfides (Li_2S_x with $6 \leq x \leq 8$) and formation of lower-order lithium polysulfide species (Li_2S_y with $2 \leq y \leq 6$) and Li_2S, respectively. The plateau at 1.8 V in the first discharge cycle at C/50

Table 2: Pore volume of HCS and HCS/sulfur composites measured by nitrogen physisorption and theoretical pore volume of the composites calculated from the pore volume of HCS and the volume of the impregnated amount of sulfur.

sample	measured pore volume / $cm^3 \cdot g^{-1}$	theoretical pore volume / $cm^3 \cdot g^{-1}$
HCS	1.06	—
HCS-29-melt	0.57	0.58
HCS-38-melt	0.39	0.44
HCS-49-melt	0.23	0.27
HCS-59-melt	0.08	0.09
HCS-58-vac	0.07	0.12
HCS-59-press	0.08	0.10
HCS-53-sol	0.17	0.19

rate can be ascribed to lithium nitrate decomposition at the cathode side [44]. The charge curve shows two plateaus at about 2.2 V and 2.4 V, indicating the reoxidation of lithium polysulfides to sulfur. Figure 8b presents data on the long term performance at C/5. As can be seen, the specific capacity (areal capacity) levels off at about 500 mAh·g^{-1} (1 mAh·cm^{-2}) after 60 cycles, and the cell exhibits rather stable performance for 500 cycles with a fade rate of 0.06% per cycle (between the 2nd and 500th cycle at C/5). Also, the Coulombic efficiency stabilizes above 99.5%, thereby indicating good reversibility.

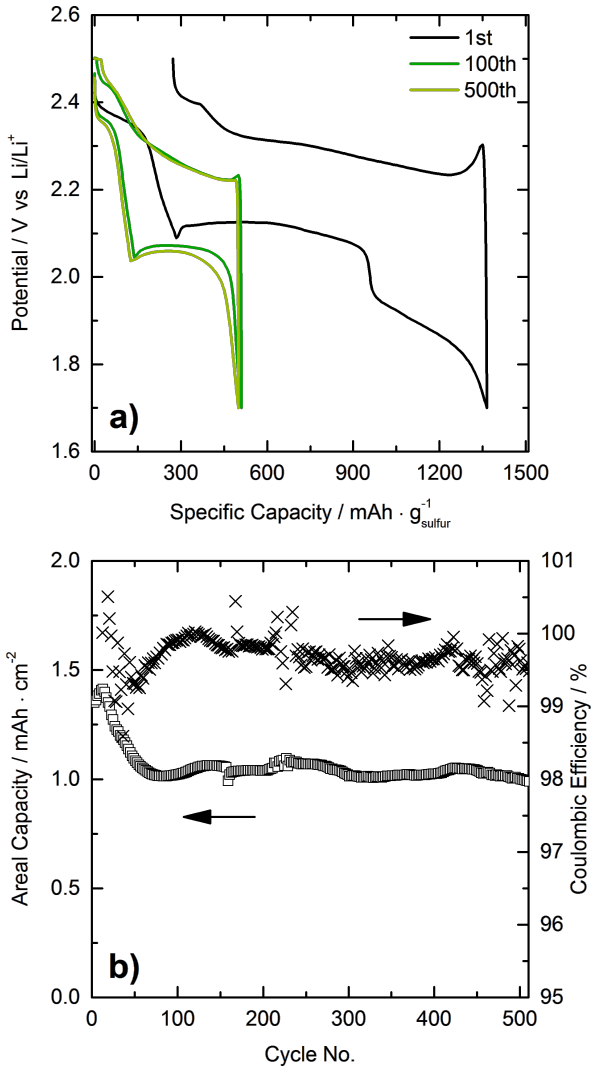


Figure 8: a) Voltage profiles of a Li–S cell with areal sulfur loading of 2.0 mg·cm^{-2}. After the formation cycle at C/50, the rate was increased to C/5. b) Areal capacity and Coulombic efficiency versus the cycle number. The 1st cycle areal capacity was about 2.8 mAh·cm^{-2}.

The measured areal capacities are comparable with those calculated from literature data [24,27,29]. Nevertheless, due to differences in cell type, electrode and electrolyte composition as well as electrolyte/sulfur ratio, a precise comparison is not possible. Even more, as necessary information for this comparison like the electrolyte/sulfur ratio and partly also the areal sulfur loading are often not given.

Overall, the data in Figure 8 demonstrate that Li–S cells based on HCS/sulfur composite show good cyclability, with moderate specific capacities at C/5 rate. Given that the results were obtained on non-optimized cathodes, this is a good starting point for future research in this direction.

Conclusion

Hollow carbon spheres with a mesoporous shell were loaded with different amounts of sulfur by melt impregnation at ambient pressure, in vacuum and under increased pressure as well as from a solution of sulfur in carbon disulfide. By combining calculations considering the mesopore volume of the shell and the size of the cavity with results from pXRD, Raman spectroscopy and SEM, it could be concluded that the cavity of HCS is not filled by sulfur regardless of the impregnation method. This is an important result as the analysis of HCS/sulfur composites is usually carried out by EDX measurements during which sulfur can redistribute due to the vacuum applied. Although the cavity of the HCS remains empty during sulfur loading, batteries using HCS/sulfur composite with 61 wt % sulfur and with reasonably high sulfur loading of 2.0 mg·cm^{-2} showed stable electrochemical performance over 500 cycles. It seems possible that the empty cavity has a positive effect on polysulfide confinement. In summary, the HCS employed in this work are a promising system capable of storing and retaining significant amounts of sulfur, thus ensuring stable performance upon prolonged cycling.

Experimental details

Synthesis of hollow carbon spheres

Synthesis of silica template

Silica spheres with a solid core and mesoporous shell were synthesized according to a modification of literature methods in a two-step procedure [33,34]. For synthesis of the core, 536 mL of ethanol were mixed with 45 mL of aqueous ammonia (32%) and 6.8 mL of deionized water. After stirring for 30 min, 24 mL of tetraethyl orthosilicate (TEOS) were added and the mixture was stirred at room temperature for 18 h. The resulting suspension was diluted with 1200 mL of deionized water and 180 mL of a solution of cetyltrimethylammonium bromide (0.11 mol/L in a 2:1 mixture of water and ethanol) was added. The suspension was stirred at room temperature for one hour before 13.5 mL of TEOS were added dropwise. After stirring for another 18 h at room temperature, the suspension was neutralized with hydrochloric acid (32%) to precipitate the core–shell

particles. The precipitate was centrifuged and dried at 60 °C before removing the surfactant by calcination at 550 °C for 6 h in air.

Synthesis of hollow carbon spheres

The synthesis of hollow carbon spheres was carried out by a combination and modification of literature methods [45,46]. Phenol (3.52 g) was melted at 45 °C and 615 µL of a 20 wt % sodium hydroxide aqueous solution were added to the liquid phenol. The solution was stirred for 15 min (with a KPG stirrer). After adding 5.6 mL of formalin (37 wt % formaldehyde) and further stirring for 5 min, 9.59 g of ground silica template were added. The mixture was heated to 75 °C and stirred for 1.5 h. The polymer/silica composite was dried in vacuum and polymerized in an oven at 100 °C for 24 h. The particles were washed with water and dried at 60 °C. Carbonization was carried out in a tubular furnace under argon atmosphere in two steps: The sample was heated to 350 °C for 5 h (heating rate: 1 °C/min) and 900 °C for 2 h (heating rate: 5 °C/min). The silica template was removed by washing with hydrofluoric acid (10%). The samples were washed with deionized water and ethanol and dried at 100 °C. The removal of the silica template was assured by thermal combustion of the carbon in air. The template was considered removed when the residual mass was less than 2 wt %.

Preparation of carbon/sulfur composites

Carbon/sulfur composites were prepared in four different ways.

1. Melt impregnation: HCS and sulfur were ground together in distinct weight ratios, sealed in a flask and heated to 155 °C for 12 h.
2. Melt impregnation in vacuum: HCS and sulfur were ground together in distinct weight ratios, sealed in a flask, evacuated to a pressure of $1.1 \cdot 10^{-4}$ bar and heated to 125 °C for 12 h at this pressure.
3. Melt impregnation under pressure: HCS and sulfur were ground together in distinct weight ratios and placed in a Teflon lined steel autoclave filled to 90% capacity with water. The autoclave was sealed and the sample was heated to 155 °C for 12 h. This temperature and degree of filling with water creates a pressure of approximately 7 bar (measured by heating water in a microwave and monitoring the resulting pressure).
4. Impregnation from solution: HCS were ground for several minutes with a 0.62 M solution of sulfur in carbon disulfide. The volume of solution was chosen in accordance to the absolute pore volume of the applied amount of carbon. After drying the composite at room temperature the procedure was repeated until the desired amount of sulfur was achieved.

Electrode processing, cell assembling and electrochemical testing

A mixture of the carbon/sulfur composite powder (83 wt %), Super C65 (Timcal, 6 wt %), Printex XE2 (Orion, 6 wt %) and poly(vinyl alcohol) Selvol 425 (Sekisui, 5 wt %) in water, isopropanol and 1-methoxy-2-propanol (65:30:5 weight ratio) was prepared to form a homogeneous slurry. The slurry coating and drying procedure are described elsewhere [47,48]. 50–60 µm thick electrodes with a sulfur loading of approx. 2.0 $mg \cdot cm^{-2}$ were used for testing. Sulfur cathode, polyethylene membrane (Toray Tonen, 15 mm) and lithium foil (Chemetall Foote Corp., 50 µm) were assembled in coin-type cells inside an argon-filled glovebox from MBraun. The electrolyte used was a solution of lithium bis(trifluoromethanesulfonyl)imide (Aldrich, 99.95%, 8 wt %), lithium nitrate (Merck, 99.995%, 4 wt %), 1,2-dimethoxyethane (Alfa Aesar, >99%, 44 wt %), and 1,3-dioxolane (Acros, 99.8%, 44 wt %). The volume of electrolyte used in the cell was 10 $\mu L/mg_{sulfur}$. Galvanostatic measurements were performed at 25 °C in the potential range of 2.5–1.7 V versus Li/Li^+ using a MACCOR Series 4000 (Tulsa, Oklahoma) multichannel battery cycler. A constant voltage step was applied at the end of charging until a current drop of 90% was achieved. Capacity values in the manuscript were calculated on the basis of the sulfur mass. After the formation cycle at a C/50 rate (with 1C = 1672 mA/g_{sulfur}) was completed, the cells were charged and discharged at C/5.

Characterization methods

Dynamic light scattering was measured with a Malvern Nano ZS using a HeNe gas laser with a wavelength of 633 nm.

X-ray diffraction patterns were recorded with a PANalytical X'Pert Pro MPD using Cu Kα radiation (λ = 1.5406 Å, 45 kV, 40 mA).

Thermogravimetric measurements of the samples were carried out on a Netzsch STA 409 at a heating rate of 5 °C/min in air.

Nitrogen physisorption measurements were performed on a Quantachrome Quadrasorb-SI-MP instrument at 77.4 K. Pore size distributions were calculated from the adsorption branch by a non-local density functional theory (NLDFT) model assuming cylindrical pores for silica samples and by a quenched solid density functional theory model assuming slit pores for pores smaller than 2 nm and cylindrical pores for pores larger than 2 nm for carbon samples. The specific surface area was calculated from the adsorption branch in a relative pressure interval from 0.07 to 0.30 by the BET method. Carbon dioxide physisorption was conducted on a Quantachrome Autosorb-iQ-MP instrument at 273.15 K. The pore size distribution was calcu-

lated by an NLDFT model assuming slit pores with a moving point average of three. Degassing prior to the physisorption measurements was carried out in vacuum at 120 °C for 20 h for carbon samples and at room temperature for 20 h for carbon/sulfur composites.

Scanning electron microscopy images were taken on a Zeiss Leo 1525 microscope operated at 5 kV and 20 kV for EDX analysis. A carbon layer of approximately 20 nm was deposited onto the samples prior to EDX measurements.

Transmission electron microscopy was carried out using a JEOL JEM 2200 FS operated at 200 kV.

Raman spectra were recorded on a Bruker Senterra Raman microscope (λ = 532 nm, P = 2 mW).

Supporting Information

Supporting Information contains characterization of the silica template (SEM, pXRD, nitrogen physisorption), CO_2 physisorption of HCS as well as thermal analysis, SEM/EDX analysis and nitrogen physisorption of HCS/sulfur composites and derivation of Equation 3 and Equation 4.

Supporting Information File 1

Additional Information.
[http://www.beilstein-journals.org/bjnano/content/supplementary/2190-4286-7-114-S1.pdf]

Acknowledgements

We thank Dr. Frank Hoffmann and Carl-Philipp Elverfeldt for helpful discussions and proof reading as well as Renate Walter for SEM and EDX measurements. This research was supported by the BASF International Scientific Network for Electrochemistry and Batteries.

References

1. Tarascon, J.-M.; Armand, M. *Nature* **2001,** *414,* 359–367. doi:10.1038/35104644
2. Aricò, A. S.; Bruce, P.; Scrosati, B.; Tarascon, J.-M.; van Schalkwijk, W. *Nat. Mater.* **2005,** *4,* 366–377. doi:10.1038/nmat1368
3. Bruce, P. G.; Scrosati, B.; Tarascon, J.-M. *Angew. Chem., Int. Ed.* **2008,** *47,* 2930–2946. doi:10.1002/anie.200702505
4. Bruce, P. G.; Freunberger, S. A.; Hardwick, L. J.; Tarascon, J.-M. *Nat. Mater.* **2011,** *11,* 19–29. doi:10.1038/nmat3191
5. Scrosati, B.; Garche, J. *J. Power Sources* **2010,** *195,* 2419–2430. doi:10.1016/j.jpowsour.2009.11.048
6. Ji, X.; Nazar, L. F. *J. Mater. Chem.* **2010,** *20,* 9821–9826. doi:10.1039/b925751a
7. Yamin, H.; Gorenshtein, A.; Penciner, J.; Sternberg, Y.; Peled, E. *J. Electrochem. Soc.* **1988,** *135,* 1045–1048. doi:10.1149/1.2095868
8. Cheon, S.-E.; Ko, K.-S.; Cho, J.-H.; Kim, S.-W.; Chin, E.-Y.; Kim, H.-T. *J. Electrochem. Soc.* **2003,** *150,* A796–A799. doi:10.1149/1.1571532
9. Cheon, S.-E.; Ko, K.-S.; Cho, J.-H.; Kim, S.-W.; Chin, E.-Y.; Kim, H.-T. *J. Electrochem. Soc.* **2003,** *150,* A800–A805. doi:10.1149/1.1571533
10. Shim, J.; Striebel, K. A.; Cairns, E. J. *J. Electrochem. Soc.* **2002,** *149,* A1321–A1325. doi:10.1149/1.1503076
11. Mikhaylik, Y. V.; Akridge, J. R. *J. Electrochem. Soc.* **2004,** *151,* A1969–A1976. doi:10.1149/1.1806394
12. Haynes, W. M., Ed. *CRC Handbook of Chemistry and Physics;* CRC Press: Boca Raton, 2015.
13. Ji, L.; Rao, M.; Aloni, S.; Wang, L.; Cairns, E. J.; Zhang, Y. *Energy Environ. Sci.* **2011,** *4,* 5053–5059. doi:10.1039/c1ee02256c
14. Elazari, R.; Salitra, G.; Garsuch, A.; Panchenko, A.; Aurbach, D. *Adv. Mater.* **2011,** *23,* 5641–5644. doi:10.1002/adma.201103274
15. Han, S.-C.; Song, M.-S.; Lee, H.; Kim, H.-S.; Ahn, H.-J.; Lee, J.-Y. *J. Electrochem. Soc.* **2003,** *150,* A889–A893. doi:10.1149/1.1576766
16. Yuan, L.; Yuan, H.; Qiu, X.; Chen, L.; Zhu, W. *J. Power Sources* **2009,** *189,* 1141–1146. doi:10.1016/j.jpowsour.2008.12.149
17. Wang, J.-Z.; Lu, L.; Choucair, M.; Stride, J. A.; Xu, X.; Liu, H.-K. *J. Power Sources* **2011,** *196,* 7030–7034. doi:10.1016/j.jpowsour.2010.09.106
18. Wang, H.; Yang, Y.; Liang, Y.; Robinson, J. T.; Li, Y.; Jackson, A.; Cui, Y.; Dai, H. *Nano Lett.* **2011,** *11,* 2644–2647. doi:10.1021/nl200658a
19. Ji, L.; Rao, M.; Zheng, H.; Zhang, L.; Li, Y.; Duan, W.; Guo, J.; Cairns, E. J.; Zhang, Y. *J. Am. Chem. Soc.* **2011,** *133,* 18522–18525. doi:10.1021/ja206955k
20. Wang, J. L.; Yang, J.; Xie, J. Y.; Xu, N. X.; Li, Y. *Electrochem. Commun.* **2002,** *4,* 499–502. doi:10.1016/S1388-2481(02)00358-2
21. Ji, X.; Lee, K. T.; Nazar, L. F. *Nat. Mater.* **2009,** *8,* 500–506. doi:10.1038/nmat2460
22. Chen, S.-R.; Zhai, Y.-P.; Xu, G.-L.; Jiang, Y.-X.; Zhao, D.-Y.; Li, J.-T.; Huang, L.; Sun, S.-G. *Electrochim. Acta* **2011,** *56,* 9549–9555. doi:10.1016/j.electacta.2011.03.005
23. Jayaprakash, N.; Shen, J.; Moganty, S. S.; Corona, A.; Archer, L. A. *Angew. Chem., Int. Ed.* **2011,** *50,* 5904–5908. doi:10.1002/anie.201100637
24. He, G.; Evers, S.; Liang, X.; Cuisinier, M.; Garsuch, A.; Nazar, L. F. *ACS Nano* **2013,** *7,* 10920–10930. doi:10.1021/nn404439r
25. Zhang, C.; Wu, H. B.; Yuan, C.; Guo, Z.; Lou, X. W. D. *Angew. Chem., Int. Ed.* **2012,** *51,* 9592–9595. doi:10.1002/anie.201205292
26. Böttger-Hiller, F.; Kempe, P.; Cox, G.; Panchenko, A.; Janssen, N.; Petzold, A.; Thurn-Albrecht, T.; Borchardt, L.; Rose, M.; Kaskel, S.; Georgi, C.; Lang, H.; Spange, S. *Angew. Chem., Int. Ed.* **2013,** *52,* 6088–6091. doi:10.1002/anie.201209849
27. Wang, Z.; Li, X.; Cui, Y.; Yang, Y.; Pan, H.; Wang, Z.; Qian, G. *J. Electrochem. Soc.* **2014,** *161,* A1231–A1235. doi:10.1149/2.0341409jes
28. Liu, S.; Xie, K.; Chen, Z.; Li, Y.; Hong, X.; Xu, J.; Zhou, L.; Yuan, J.; Zheng, C. *J. Mater. Chem. A* **2015,** *3,* 11395–11402. doi:10.1039/C5TA00897B
29. Zhou, W.; Xiao, X.; Cai, M.; Yang, L. *Nano Lett.* **2014,** *14,* 5250–5256. doi:10.1021/nl502238b

30. Zhou, W.; Wang, C.; Zhang, Q.; Abruña, H. D.; He, Y.; Wang, J.; Mao, S. X.; Xiao, X. *Adv. Energy Mater.* **2015,** *5,* 1401752. doi:10.1002/aenm.201401752
31. Zhou, G.; Zhao, Y.; Manthiram, A. *Adv. Energy Mater.* **2015,** *5,* 1402263. doi:10.1002/aenm.201402263
32. Raiß, C.; Peppler, K.; Janek, J.; Adelhelm, P. *Carbon* **2014,** *79,* 245–255. doi:10.1016/j.carbon.2014.07.065
33. Haffer, S.; Tiemann, M.; Fröba, M. *Chem. – Eur. J.* **2010,** *16,* 10447–10452. doi:10.1002/chem.201000643
34. Yoon, S. B.; Kim, J.-Y.; Kim, J. H.; Park, Y. J.; Yoon, K. R.; Park, S.-K.; Yu, J.-S. *J. Mater. Chem.* **2007,** *17,* 1758–1761. doi:10.1039/b617471j
35. Stöber, W.; Fink, A.; Bohn, E. *J. Colloid Interface Sci.* **1968,** *26,* 62–69. doi:10.1016/0021-9797(68)90272-5
36. Fujimoto, H. *Carbon* **2003,** *41,* 1585–1592. doi:10.1016/S0008-6223(03)00116-7
37. Li, Z. Q.; Lu, C. J.; Xia, Z. P.; Zhou, Y.; Luo, Z. *Carbon* **2007,** *45,* 1686–1695. doi:10.1016/j.carbon.2007.03.038
38. Pimenta, M. A.; Dresselhaus, G.; Dresselhaus, M. S.; Cançado, L. G.; Jorio, A.; Saito, R. *Phys. Chem. Chem. Phys.* **2007,** *9,* 1276–1290. doi:10.1039/B613962K
39. Thommes, M.; Kaneko, K.; Neimark, A. V.; Olivier, J. P.; Rodriguez-Reinoso, F.; Rouquerol, J.; Sing, K. S. W. *Pure Appl. Chem.* **2015,** *87,* 1051–1069. doi:10.1515/pac-2014-1117
40. Wang, J.; Liu, L.; Ling, Z.; Yang, J.; Wan, C.; Jiang, C. *Electrochim. Acta* **2003,** *48,* 1861–1867. doi:10.1016/S0013-4686(03)00258-5
41. Balakumar, K.; Kalaiselvi, N. *RSC Adv.* **2015,** *5,* 34008–34018. doi:10.1039/C5RA01436K
42. Dong, Y.; Liu, S.; Wang, Z.; Liu, Y.; Zhao, Z.; Qiu, J. *Nanoscale* **2015,** *7,* 7569–7573. doi:10.1039/C5NR01015B
43. Li, C.; Yin, L. *Part. Part. Syst. Charact.* **2015,** *32,* 756–763. doi:10.1002/ppsc.201400259
44. Jozwiuk, A.; Sommer, H.; Janek, J.; Brezesinski, T. *J. Power Sources* **2015,** *296,* 454–461. doi:10.1016/j.jpowsour.2015.07.070
45. Yoon, S. B.; Sohn, K.; Kim, J. Y.; Shin, C.-H.; Yu, J.-S.; Hyeon, T. *Adv. Mater.* **2002,** *14,* 19–21. doi:10.1002/1521-4095(20020104)14:1<19::AID-ADMA19>3.0.CO;2-X
46. Meng, Y.; Gu, D.; Zhang, F.; Shi, Y.; Yang, H.; Li, Z.; Yu, C.; Tu, B.; Zhao, D. *Angew. Chem., Int. Ed.* **2005,** *44,* 7053–7059. doi:10.1002/anie.200501561
47. Schneider, A.; Weidmann, C.; Suchomski, C.; Sommer, H.; Janek, J.; Brezesinski, T. *Chem. Mater.* **2015,** *27,* 1674–1683. doi:10.1021/cm504460p
48. Kulisch, J.; Sommer, H.; Brezesinski, T.; Janek, J. *Phys. Chem. Chem. Phys.* **2014,** *16,* 18765–18771. doi:10.1039/C4CP02220C

License and Terms

This is an Open Access article under the terms of the Creative Commons Attribution License (http://creativecommons.org/licenses/by/4.0), which permits unrestricted use, distribution, and reproduction in any medium, provided the original work is properly cited.

The license is subject to the *Beilstein Journal of Nanotechnology* terms and conditions: (http://www.beilstein-journals.org/bjnano)

The definitive version of this article is the electronic one which can be found at: doi:10.3762/bjnano.7.114

BEILSTEIN JOURNAL OF NANOTECHNOLOGY

Fabrication and characterization of branched carbon nanostructures

Sharali Malik*[1], Yoshihiro Nemoto[2], Hongxuan Guo[2], Katsuhiko Ariga[2] and Jonathan P. Hill[2]

Full Research Paper

Open Access

Address:
[1]Institute of Nanotechnology, Karlsruhe Institute of Technology (KIT), D-76131 Karlsruhe, Germany and [2]WPI-Center for Materials Nanoarchitectonics, National Institute for Materials Science (NIMS), Namiki 1-1, Tsukuba, Japan

Email:
Sharali Malik* - sharali.malik@kit.edu

* Corresponding author

Keywords:
branched multiwalled carbon nanotubes; carbon nanostructures; carbon nanotubes; graphene nanoribbons; multiwalled carbon nanotubes

Beilstein J. Nanotechnol. **2016,** *7,* 1260–1266.
doi:10.3762/bjnano.7.116

Received: 04 May 2016
Accepted: 15 August 2016
Published: 05 September 2016

This article is part of the Thematic Series "Advances in nanomaterials II".

Guest Editor: H. Hahn

© 2016 Malik et al.; licensee Beilstein-Institut.
License and terms: see end of document.

Abstract

Carbon nanotubes (CNTs) have atomically smooth surfaces and tend not to form covalent bonds with composite matrix materials. Thus, it is the magnitude of the CNT/fiber interfacial strength that limits the amount of nanomechanical interlocking when using conventional CNTs to improve the structural behavior of composite materials through reinforcement. This arises from two well-known, long standing problems in this research field: (a) inhomogeneous dispersion of the filler, which can lead to aggregation and (b) insufficient reinforcement arising from bonding interactions between the filler and the matrix. These dispersion and reinforcement issues could be addressed by using branched multiwalled carbon nanotubes (b-MWCNTs) as it is known that branched fibers can greatly enhance interfacial bonding and dispersability. Therefore, the use of b-MWCNTs would lead to improved mechanical performance and, in the case of conductive composites, improved electrical performance if the CNT filler was better dispersed and connected. This will provide major benefits to the existing commercial application of CNT-reinforced composites in electrostatic discharge materials (ESD): There would be also potential usage for energy conversion, e.g., in supercapacitors, solar cells and Li-ion batteries. However, the limited availability of b-MWCNTs has, to date, restricted their use in such technological applications. Herein, we report an inexpensive and simple method to fabricate large amounts of branched-MWCNTs, which opens the door to a multitude of possible applications.

Introduction

Lighter, stronger materials such as nanocarbon composites offer benefits for applications such as transport, energy storage/conversion and bone/tooth replacement. Hence, the mechanical properties of CNTs are utilized in reinforcing polymer composites [1-4], and their electrical conductivity is utilized for conducting polymers [4-6]. Under tensile load only the outermost

layers of MWCNTs are involved as the relatively weak (van der Waals) bonding between the outer layers and the inner layers leads to slippage – the so called "sword in sheath" failure mechanism, which reduces the load-bearing capacity [1,7]. However, under compressive load this slippage leads to the very useful elastic deformation of MWCNTs [8,9].

For all nanoscale reinforcing component materials (NRCMs) including nanocarbons such as graphene, there remain two well-known, long standing issues which are widely recognized as being critical for the development of mechanically efficient nanocomposites: a) inhomogeneous dispersion of the filler [10] and (b) insufficient strength of the interphase between the filler and the matrix [11]. However, these issues can be addressed by utilizing branched multiwalled carbon nanotubes (b-MWCNTs). It is known from theory and simulation experiments [12-14] that branched fibers can greatly enhance interfacial bonding and dispersability. Such an approach is exemplified by the process of adding straw (branched plant fibers) to mud to make stronger bricks which has been used since the Neolithic period, i.e., before 3400 BC [15]. More recently, Masselter et al. have correlated the functional morphology of branching in plants with mechanical behavior and concluded that the concepts generated have a high potential for implementation in the development of branched fiber-reinforced technical composites [16]. With respect to electrical and electronic properties, it is well known that in carbon nanotube networks the junction resistance controls the overall performance [17]. Therefore, in addition to b-MWCNTs/composite applications, the enhanced electrical properties of networks arising within this new material has major potential benefits for design, development and production of supercapacitors, solar cells and Li-ion batteries.

The first experimental observation of branched carbon nanotubes appears to have been in 1995, when after using an arc-discharge method L-, Y- and T-shaped MWCNTs were produced [18]. Subsequently, branched CNTs have been fabricated using a variety of methods, which include pyrolysis of metallocenes [19,20], nanowelding [21], catalytic CVD [22,23], carbon infiltration of MWCNTs [24], templating [25] and chemical functionalization [26]. However, none of these methods are easily industrially scalable. Herein, we report a cheap and simple method to fabricate large amounts of branched MWCNTs in order to address the well-known problems of adequate dispersion and sufficiently strong interfacial bonding required for large-scale applications.

As a starting material it was decided to use the commercially available MWCNTs, namely Baytubes©. Other workers have shown using high resolution transmission electron microscopy (HRTEM) that Baytubes© are parallel-walled in long closed sections and that they are strong and relatively pure [27]. They form around a catalyst and are supplied as loosely agglomerated pellets (Figure 1), which has advantages regarding health, safety and environment. According to the data sheet Baytubes© belong to the category of short, thin tangled MWCNTs for which no "fibre-like" pathogenic behaviour is expected based on the available data. The MWCNTs used in this research were Baytubes© C 150P (Bayer Material Science A.G., Leverkusen, Germany).

Results and Discussion

The idea of this work is to "unzip" the MWCNTs and to allow them to re-roll and form branched MWCNTs. This works for MWCNTs like Baytubes©, because they have parallel sides [27] and so they can unzip to form layered nanoribbons. Since they are in long closed sections (Figure 1d) we can assume that the end of these sections acts like a "rip-stop" so that the unzipped tubes can re-roll from these points to form branched structures (Figure 2a–c). The Raman spectra of the as-received MWCNTs (bottom spectrum) and of the branched-MWCNTs (top spectrum) are shown in (Figure 2d). Both sets of spectra are typical of MWCNTs and the I_D/I_G values [28,29] of the as-received MWCNTs and the b-MWCNTs are 1.26 and 1.43, respectively. This indicates that they both have very similar defect densities.

The mechanism of unzipping MWCNTs to form graphene nanoribbons is well known from research by Hirsch [30] and Dai et al. [31] but the procedure is complex and the yield is low [32-34]. However, as we show here, if the aim is to make branched-MWCNT then the procedure is much simpler. Thus, as-received MWCNTs were heated to 500 °C, which results in the introduction of defects that later act as the "unzipping" points. The procedure has the additional benefit of cleaning the tubes as substantiated from the Raman (Figure 2d) and HRTEM data (Figure 3) confirming the absence of carbon impurities or residual catalyst material. The heated MWCNTs were then sonicated in ethanol which causes the MWCNTs to unzip and re-roll. Figure 4 shows a suggested schematic sequence in agreement with observations by Kaner et al. [35] and Geim [36] indicating that nanoribbons tend to re-roll unless prevented from doing so.

Dispersions of the starting MWCNTs and b-MWCNTs were compared by dispersing 1 mg of each material in 4 mL of ethanol. These dispersions were then centrifuged at 3500*g* for 2 h and then left to stand for 24 h. The liquid suspensions are shown in Figure 5. The b-MWCNTs clearly show better dispersability compared to the starting MWCNTs.

As no surfactants or expensive polymers are needed for this process, it can be described as inexpensive and easy and it

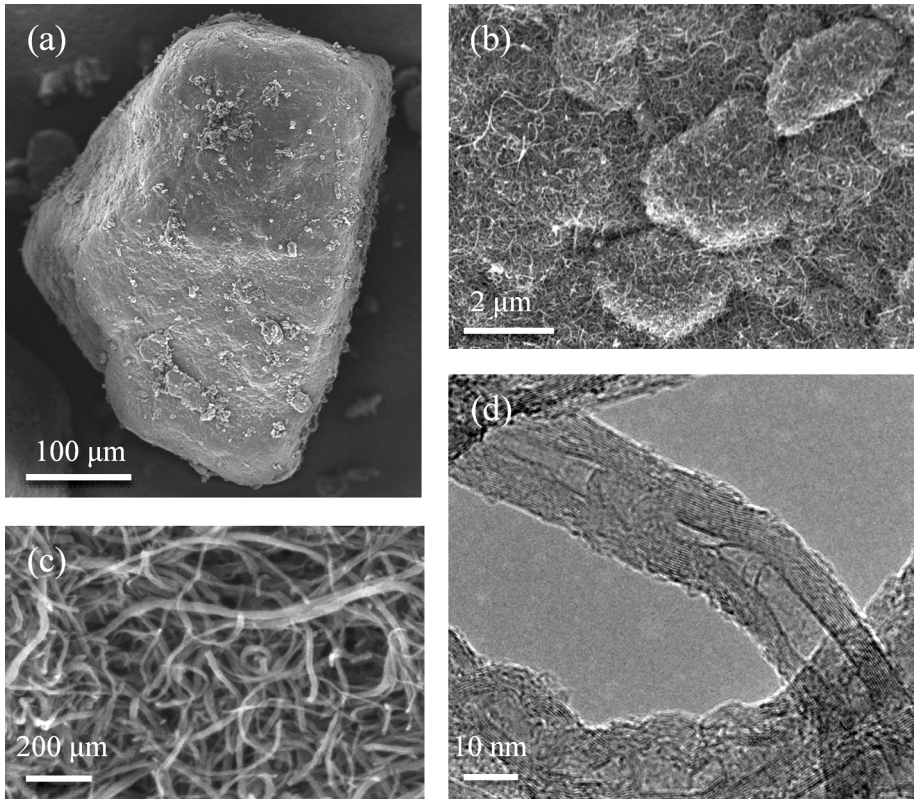


Figure 1: a) SEM overview of a Baytubes agglomerated pellet; b, c) SEM details of the MWCNTs; d) TEM detail of typical MWCNTs.

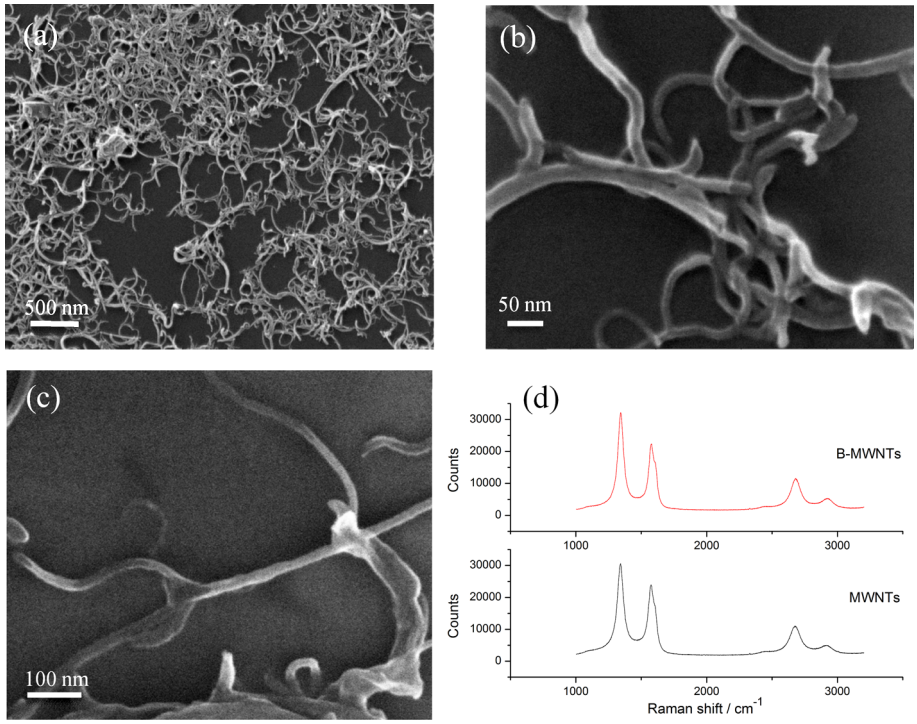


Figure 2: a) Helium ion microscope (HeIM) overview of b-MWCNTs and b) HeIM detail of b-MWCNTs; c) SEM detail of unzipped and branched-MWCNTs; d) Raman spectra of as received MWCNTs (bottom spectrum) and b-MWCNTs (top spectrum) – both at 532 nm.

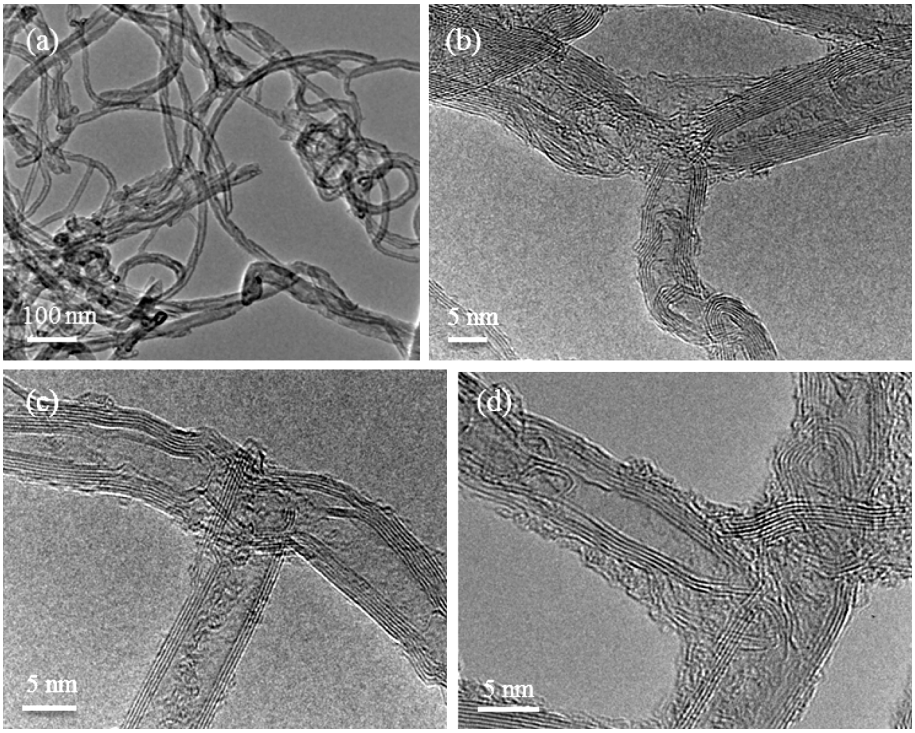


Figure 3: a) HRTEM overview of branched-MWCNTs and b) HRTEM detail of Y-pattern b-MWCNTs; c, d) HRTEM detail of T-pattern b-MWCNTs.

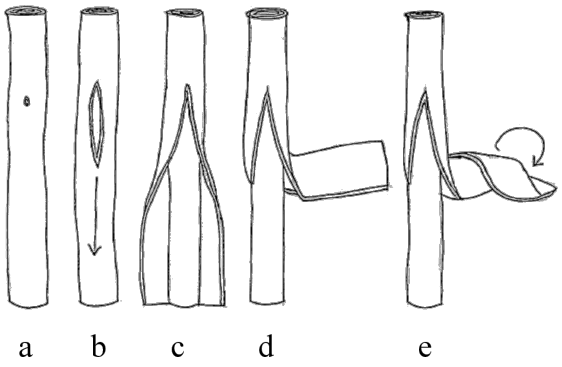


Figure 4: A schematic diagram of the suggested "unzipping" and "re-rolling" sequence: a) formation of unzipping point; b) onset of unzipping; c) unzipping and onset of peeling of inner parallel tubes; d) outer layers peeling out as a sheet; e) onset of re-rolling of outer layers.

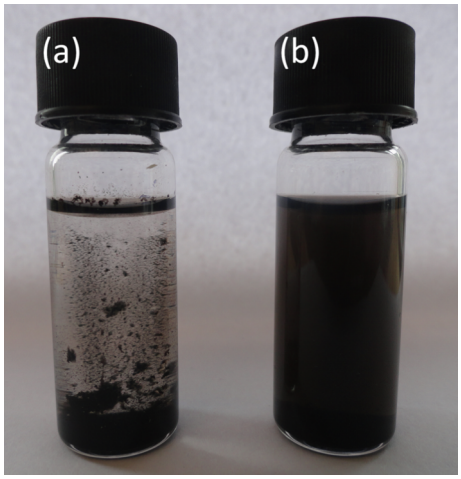


Figure 5: (a) Dispersion of MWCNTs starting material; (b) dispersion of b-MWCNTs.

results in clean b-MWCNTs (Figure 3). The yield is estimated (using the methodology by Dai et al. [31]) to be about 60% branched MWCNTs. The Y-branched MWCNTs fabricated here (Figure 3b) obey geometric conservation laws that are consistent with earlier theory [37] in that the angle between two neighboring branches should be 120°. Therefore, in this instance theory and experiment are in agreement, even though this agreement is not "perfect" as in practice defects will certainly be present.

The unzipping and re-rolling process appears to reduce the number of walls on the MWCNTs compared to those for the as-received tubes (Figure 1d) and it is also possible that some of the tubes re-roll to form carbon nano-scrolls (CNS) [35,38-40]. This possibility is evidenced in Figure 3c where the number of walls of the three parts of the "T" pattern does not meet the "Russian Doll" MWCNTs requirement of N (left) = N (right) +

N (down) or *N* (right) = *N* (left) + *N* (down). The Raman spectra show that the b-MWCNTs have a similar defect density as the starting material, which shows that the material has not been damaged by the fabrication procedure. The EDX analysis of the MWCNTs starting material is 100% carbon (the data sheet indicates a carbon purity of over 95%). The EDX analysis of the branched-MWNTs is 96% carbon and 4% oxygen. This is consistent with the initial heating in air, which removes amorphous impurities and etches/oxidizes the MWCNTs at defect sites without damaging the sidewalls [31]. In many nanocarbon material applications the presence of residual surfactant or organic residues can be a problem, but this is not the case here.

The experimental procedure produces b-MWCNTs when using thick MWCNTs (more than a few walls). However, when the same procedure is used with thin MWCNTs (e.g., triple-walled MWCNTs, Figure 6a), synthesised by a "water-assisted" CVD method [41], graphene nanoribbons are produced in small yields (Figure 6b) which is consistent with earlier works by Hirsch [30] and Dai et al. [31].

Conclusion

In summary, we have described herein a new, simple and cheap route to fabricate large amounts of branched MWCNTs using widely available commercial MWCNTs. We have demonstrated a facile procedure for making clean branched nanostructures and this opens promising avenues for the development and manufacturing of nanocarbon composites for a variety of commercial applications. The fabrication and testing of composite materials with branched MWCNTs as well as measurements of electrical conductivity are currently in progress.

Experimental

The MWCNTs used in this research were Baytubes© C 150P (Lot-No E0009AA007, Drum-No 033), supplied by Bayer Material Science A.G. (Leverkusen, Germany).

Preparation of b-MWCNTs

Commercial MWCNTs were heated in air to 500 °C for 2 h to give the "stage I"-modified MWCNTs. Then a small amount of these were sonicated in ethanol (30 mL) for 8 h (ultrasonic denerator, model GSCVP 150 at ca. 80% power). The dispersion was centrifuged at 3500*g* for 90 min to give the "stage II"-modified MWCNTs, which are the b-MWCNTs. The supernatant was spotted onto lacey carbon Cu TEM grids and onto polished Si chips for subsequent characterization.

Preparation of graphene nanoribbons

A "water-assisted" CVD process as reported earlier [41,42] was used to fabricate thin walled MWCNTs (ca. three walls), which were subsequently heated in air to 500 °C for 2 h. Subsequently, ca. 10 mg of this material was sonicated (UP200s Dr. Hielscher, 200 W, 24 Hz, 0.5 cycles, 60% amplitude) in ethanol (4 mL) for 1 h. The resultant dispersion was spotted onto plain Cu TEM grids and polished Si chips for subsequent characterization.

Characterization

Quality and morphology of the fabricated branched nanostructures were scrutinised by Raman spectroscopy (Renishaw inVia), TEM (Tecnai F20 ST at 200 kV), HRTEM (Jeol ARM at 120 kV), SEM (Zeiss Ultra-Plus at 5 kV), SEM (Zeiss Leo 1530 at 10 kV with Oxford X-Max 50 EDX) and helium ion microscopy (HeIM, Zeiss Orion at 30 kV).

Acknowledgements

This paper is dedicated to Professor Herbert Gleiter on the occasion of his 75th birthday. S. M. acknowledges the continuing support of Prof. Dr. M. M. Kappes. This work was partly supported by World Premier International Research Center Initiative (WPI Initiative) from MEXT, Japan and we thank Dr. Daisuke Fuijita and Dr. Kiyotaka Iiayma for their support. We acknowledge Dr. Tony D. Keene, Southampton University, for his support. We also thank Bayer Material Science A.G. for

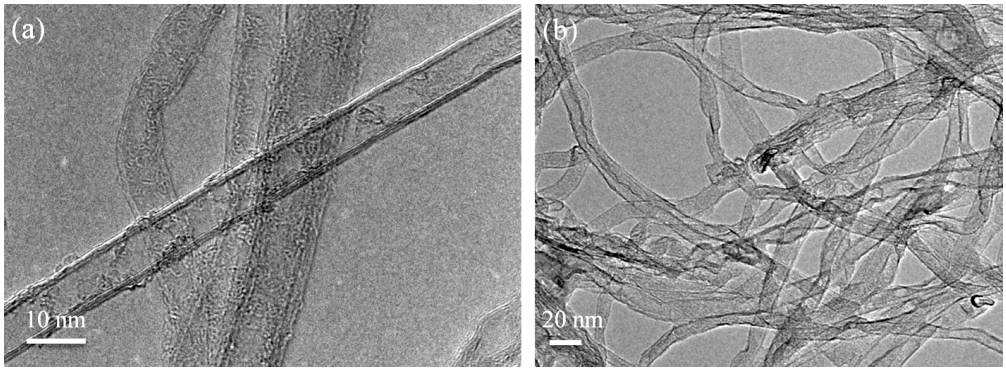


Figure 6: TEM overview of a) thin MWCNTs starting material and b) graphene nanoribbons after treatment.

supply of MWCNTs. The authors would like to acknowledge networking support by the COST Action CA15107 (Multi-Comp).

References

1. Yu, M.-F.; Lourie, O.; Dyer, M. J.; Moloni, K.; Kelly, T. F.; Ruoff, R. S. *Science* **2000,** *287,* 637–640. doi:10.1126/science.287.5453.637
2. Peng, B.; Locascio, M.; Zapol, P.; Li, S.; Mielke, S. L.; Schatz, G. C.; Espinosa, H. *Nat. Nanotechnol.* **2008,** *3,* 626–631. doi:10.1038/nnano.2008.211
3. Wong, E. W.; Sheehan, P. E.; Lieber, C. M. *Science* **1997,** *277,* 1971–1975. doi:10.1126/science.277.5334.1971
4. Hernández-Pérez, A.; Avilés, F.; May-Pat, A.; Valadez-González, A.; Herrera-Franco, P. J.; Bartolo-Pérez, P. *Compos. Sci. Technol.* **2008,** *68,* 1422–1431. doi:10.1016/j.compscitech.2007.11.001
5. Gojny, F. H.; Wichmann, M. H. G.; Fiedler, B.; Kinloch, I. A.; Bauhofer, W.; Windle, A. H.; Schulte, K. *Polymer* **2006,** *47,* 2036–2045. doi:10.1016/j.polymer.2006.01.029
6. Bauhofer, W.; Kovacs, J. Z. *Compos. Sci. Technol.* **2009,** *69,* 1486–1498. doi:10.1016/j.compscitech.2008.06.018
7. Ganesan, Y.; Peng, C.; Lu, Y.; Loya, P. E.; Moloney, P.; Barrera, E.; Yakobson, B. I.; Tour, J. M.; Ballarini, R.; Lou, J. *ACS Appl. Mater. Interfaces* **2011,** *3,* 129–134. doi:10.1021/am1011047
8. Schadler, L. S.; Giannaris, S. C.; Ajayan, P. M. *Appl. Phys. Lett.* **1998,** *73,* 3842–3844. doi:10.1063/1.122911
9. Wagner, H. D.; Ajayan, P. M.; Schulte, K. *Compos. Sci. Technol.* **2013,** *83,* 27–31. doi:10.1016/j.compscitech.2013.04.017
10. Qian, D.; Dickey, E. C.; Andrews, R.; Rantell, T. *Appl. Phys. Lett.* **2000,** *76,* 2868–2870. doi:10.1063/1.126500
11. Wagner, H. D.; Lourie, O.; Feldman, Y.; Tenne, R. *Appl. Phys. Lett.* **1998,** *72,* 188–190. doi:10.1063/1.120680
12. Fu, S.; Zhou, B.; Lung, C. *Compos. Sci. Technol.* **1993,** *47,* 245–250. doi:10.1016/0266-3538(93)90033-D
13. Suzuki, T.; Miyajima, T.; Sakai, M. *Compos. Sci. Technol.* **1994,** *51,* 283–289. doi:10.1016/0266-3538(94)90197-X
14. Liu, L.; Zhang, L.; Lua, J. *Appl. Phys. Lett.* **2012,** *101,* 161907. doi:10.1063/1.4761936
15. Brownell, W. E. *Applied Minerology;* Structural Clay Products, Vol. 9; Springer: Vienna, 1976; pp 1–23. doi:10.1007/978-3-7091-8449-3_1
16. Masselter, T.; Eckert, S.; Speck, T. *Beilstein J. Nanotechnol.* **2011,** *2,* 173–185. doi:10.3762/bjnano.2.21
17. Nirmairaj, P. N.; Lyons, P. E.; De, S.; Coleman, J. N.; Boland, J. J. *Nano Lett.* **2009,** *9,* 3890–3895. doi:10.1021/nl9020914
18. Zhou, D.; Seraphin, D. S. *Chem. Phys. Lett.* **1995,** *238,* 286–289. doi:10.1016/0009-2614(95)00406-T
19. Deepak, F. L.; John, N. S.; Govindaraj, A.; Kulkarni, G. U.; Rao, C. N. R. *Chem. Phys. Lett.* **2005,** *411,* 468–473. doi:10.1016/j.cplett.2005.06.076
20. Wei, Q.; Liu, Y.; Zhang, L.; Huang, S. *Nano-Micro Lett.* **2013,** *5,* 124–128. doi:10.1007/BF03353739
21. Rodríguez-Manzo, J. A.; Wang, M.-S.; Banhart, F.; Bando, Y.; Golberg, D. *Adv. Mater.* **2009,** *21,* 4477–4482. doi:10.1002/adma.200901321
22. Heyning, O. T.; Bernier, P.; Glerup, M. *Chem. Phys. Lett.* **2005,** *409,* 43–47. doi:10.1016/j.cplett.2005.04.097
23. Romo-Herrera, J. M.; Sumpter, B. G.; Cullen, D. A.; Terrones, H.; Cruz-Silva, E.; Smith, D. J.; Meunier, V.; Terrones, M. *Angew. Chem., Int. Ed.* **2008,** *47,* 2948–2953. doi:10.1002/anie.200705053
24. Jin, Y.; Zhang, Y.; Zhang, Q.; Zhang, R.; Li, P.; Qian, W.; Wei, F. *Nanoscale* **2013,** *5,* 6181–6186. doi:10.1039/c3nr01069d
25. Meng, G.; Han, F.; Zhao, X.; Chen, B.; Yang, D.; Liu, J.; Xu, Q.; Kong, M.; Zhu, X.; Jung, Y. J.; Yang, Y.; Chu, Z.; Ye, M.; Kar, S.; Vajtai, R.; Ajayan, P. M. *Angew. Chem., Int. Ed.* **2009,** *48,* 7166–7170. doi:10.1002/anie.200901999
26. Balaban, T. S.; Balaban, M. C.; Malik, S.; Hennrich, F.; Fischer, R.; Rösner, H.; Kappes, M. M. *Adv. Mater.* **2006,** *18,* 2763–2767. doi:10.1002/adma.200600138
27. Tessonnier, J.-P.; Rosenthal, D.; Hansen, T. W.; Hess, C.; Schuster, M. E.; Blume, R.; Girgsdies, F.; Pfänder, N.; Timpe, O.; Su, D. S.; Schlögl, R. *Carbon* **2009,** *47,* 1779–1798. doi:10.1016/j.carbon.2009.02.032
28. Ouyang, Y.; Cong, L. M.; Chen, L.; Liu, Q. X.; Fang, F. *Physica E* **2008,** *40,* 2386–2389. doi:10.1016/j.physe.2007.11.008
29. Dresselhaus, M. S.; Jorio, A.; Souza Filho, A. G.; Saito, R. *Philos. Trans. R. Soc. London, Ser. A* **2010,** *368,* 5355–5377. doi:10.1098/rsta.2010.0213
30. Hirsch, A. *Angew. Chem., Int. Ed.* **2009,** *48,* 6594–6596. doi:10.1002/anie.200902534
31. Jiao, L.; Wang, X.; Diankov, G.; Wang, H.; Dai, H. *Nat. Nanotechnol.* **2010,** *5,* 321–325. doi:10.1038/nnano.2010.54
32. Li, X.; Wang, X.; Zhang, L.; Lee, S.; Dai, H. *Science* **2008,** *319,* 1229–1232. doi:10.1126/science.1150878
33. Kosynkin, D. V.; Higginbotham, A. L.; Sinitskii, A.; Lomeda, J. R.; Dimiev, A.; Price, B. K.; Tour, J. M. *Nature* **2009,** *458,* 872–876. doi:10.1038/nature07872
34. Jiao, L.; Zhang, L.; Wang, X.; Diankov, G.; Dai, H. *Nature* **2009,** *458,* 877–880. doi:10.1038/nature07919
35. Viculis, L. M.; Mack, J. J.; Kaner, R. B. *Science* **2003,** *299,* 1361. doi:10.1126/science.1078842
36. Geim, A. K. *Science* **2009,** *324,* 1530–1534. doi:10.1126/science.1158877
37. Yin, Y.; Chen, Y.; Yin, J.; Huang, K. *Nanotechnology* **2006,** *17,* 4941–4945. doi:10.1088/0957-4484/17/19/027
38. Braga, S. F.; Coluci, V. R.; Legoas, S. B.; Giro, R.; Galvão, D. S.; Baughman, R. H. *Nano Lett.* **2004,** *4,* 881–884. doi:10.1021/nl0497272
39. Mpourmpakis, G.; Tylianakis, E.; Froudakis, G. E. *Nano Lett.* **2007,** *7,* 1893–1897. doi:10.1021/nl070530u
40. Shi, X.; Pugno, N. M.; Gao, H. *Acta Mech. Solida Sin.* **2010,** *23,* 484–497. doi:10.1016/S0894-9166(11)60002-5
41. Kiowsky, O.; Lebedkin, S.; Hennrich, F.; Malik, S.; Rösner, H.; Arnold, K.; Sürges, C.; Kappes, M. M. *Phys. Rev. B* **2007,** *75,* 075421. doi:10.1103/PhysRevB.75.075421
42. Hata, K.; Futuba, D. N.; Mizuno, K.; Namai, T.; Yumura, M.; Iijima, S. *Science* **2004,** *306,* 1362–1364. doi:10.1126/science.1104962

License and Terms

This is an Open Access article under the terms of the Creative Commons Attribution License (http://creativecommons.org/licenses/by/4.0), which permits unrestricted use, distribution, and reproduction in any medium, provided the original work is properly cited.

The license is subject to the *Beilstein Journal of Nanotechnology* terms and conditions: (http://www.beilstein-journals.org/bjnano)

The definitive version of this article is the electronic one which can be found at: doi:10.3762/bjnano.7.116

BEILSTEIN JOURNAL OF NANOTECHNOLOGY

The self-similarity theory of high pressure torsion

Yan Beygelzimer[1,2], Roman Kulagin[*3], Laszlo S. Toth[1,4] and Yulia Ivanisenko[3]

Full Research Paper

Open Access

Address:
[1]Laboratory of Excellence on Design of Alloy Metals for low-mAss Structures (DAMAS), Université de Lorraine, Île du Saulcy, Metz, F-57045, France, [2]Donetsk Institute for Physics and Engineering named after O.O. Galkin, National Academy of Sciences of Ukraine, pr. Nauki 46, Kyiv 03028, Ukraine, [3]Institute of Nanotechnology (INT), Karlsruhe Institute of Technology (KIT), Hermann-von-Helmholtz-Platz 1, Eggenstein-Leopoldshafen, 76344, Germany and [4]Laboratoire d'Etude des Microstructures et de Mécanique des Matériaux (LEM3), Université de Lorraine, UMR 7239, Metz, F-57045, France

Email:
Roman Kulagin* - roman.kulagin@kit.edu

* Corresponding author

Keywords:
deformation mechanisms; high pressure torsion; nanocrystalline metals; self-similarity; severe plastic deformation

Beilstein J. Nanotechnol. **2016,** *7,* 1267–1277.
doi:10.3762/bjnano.7.117

Received: 15 June 2016
Accepted: 25 August 2016
Published: 07 September 2016

This article is part of the Thematic Series "Advances in nanomaterials II".

Guest Editor: H. Hahn

© 2016 Beygelzimer et al.; licensee Beilstein-Institut.
License and terms: see end of document.

Abstract

By analyzing the problem of high pressure torsion (HPT) in the rigid plastic formulation, we show that the power hardening law of plastically deformed materials leads to self-similarity of HPT, admitting a simple mathematical description of the process. The analysis shows that the main parameters of HPT are proportional to β^q, with β being the angle of the anvil rotation. The meaning of the parameter q is: $q = 0$ for velocity and strain rate, $q = 1$ for shear strain and von Mises strain, $q = n$ for stress, pressure and torque (n is the exponent of a power hardening law). We conclude that if the hardening law is a power law in a rotation interval β, self-similar regimes can emerge in HPT if the friction with the lateral wall of the die is not too high. In these intervals a simple mathematical description can be applied based on self-similarity. Outside these ranges, the plasticity problem still has to be solved for each value of β. The results obtained have important practical implications for the proper design and analysis of HPT experiments.

Introduction

High pressure torsion (HPT) is a severe plastic deformation process, which is widely used for producing nanocrystalline metals and alloys [1-3]. The generally accepted theory of HPT is based on the assumptions of uniformity of simple shear deformation along the height of the specimen and that there is no slippage between the sample and the anvils. This theory gives a simple expression for the shear strain

$$\gamma = \beta r / H , \qquad (1)$$

where β is the torsion angle of the anvil, r is the radial position and H is the height of the disc.

However, a number of recent experiments and numerical simulations show that the true plastic flow during HPT can differ

significantly from the theoretical predictions given by the simple scheme above. In particular, in [4,5] a problem of coupled phase transformations and plastic flows under torsion at high pressure in a rotational diamond anvil cell was investigated. It has been shown that not only the stress, but the strain state of the sample are strongly dependent on the rheological properties of the material. In addition, it has been shown that the assumption of no slippage between the sample and the anvils is too simple in some cases, and leads to significant errors in the description of phase transformations. A correct approach to take into account the slippage in finite element simulations has been developed in [4,5]. A simple analytical model taking into account the slippage has been offered in [6]. It leads to an equation similar to Equation 1 for shear strain with a factor decreasing the angle of rotation of the sample due to slippage. The same result was obtained experimentally in [7].

The effect of the elasticity of the anvils on the geometry of the sample and the distribution of the shear strain has been investigated in [8-10]. In particular, it was shown in [10] that the samples are further deformed during unloading of the anvils and this produces a peak in the strain in the central region of the disc.

Finite element modeling is used in [11,12] to show variations of the stress–strain state along the height of the specimen. In particular strong shear strain localization near the contact surface between sample and anvil was quantified in [12]. In [13] a dead zone is found along the border of the specimen. A double-swirl pattern in the plane perpendicular to the torsion axis is experimentally shown in [14].

The above results point out the fact that plastic flow during HPT may have a fairly complex behavior, which should be taken into account when investigating materials obtained by this method. Thus, the following question can be raised: Under what conditions can HPT be modeled in a simple manner?

We will call an HPT process *simple* if the shear strain in every point of the specimen is a linear function of the torsion angle of the anvil, i.e.,

$$\gamma = \beta \Phi(r,z), \tag{2}$$

where $\Phi(r,z)$ is a differentiable function of r and z, and z is the coordinate along the specimen axis as shown below in Figure 1. This relationship generalizes Equation 1 by inheriting its main property: the separation between the dependency on β and the dependency on r and z. According to Equation 2, once we have $\Phi(r,z)$, we have a tool for calculating γ at every point of the specimen, for any value of the torsion angle. This is exactly what makes HPT simple. If, on the other hand, one cannot separate the β-dependence from the dependence on the coordinates, i.e., $\gamma = \Gamma(r,z,\beta)$, then, in order to compute γ, one has to solve a plasticity problem for every angle β. This is what makes the process complex in terms of its mathematical description.

The question what makes a complex physical process simple to describe emerges naturally, and the answer often has to do with the self-similarity of the process [15]. Self-similarity makes a complex process simple to describe because the process just repeats itself at different scales of time or space. For example, the self-similarity of powerful blast waves has allowed G. I. Taylor to predict damage from nuclear explosions even before such damage was observed for the first time. These results were obtained at the beginning of 1941 but were declassified only in 1950 [16]. Many other examples of simple descriptions of complex processes based on their self-similarity are given in [15].

In this work we investigate plastic flow during constrained HPT. We show that, within the rigid plastic framework, the problem we are considering has a self-similar solution if the deformed material satisfies a power hardening law. In this case, the shear strain is a linear function of the torsion angle of the anvil and can be described by Equation 2. We analyze different properties of self-similar regimes of HPT, and show that the self-similarity of HPT at the macro-level is connected to the self-similarity of the structure of the material at the micro-level hypothesized in [17].

Model

1 Rigid plastic flow formulation for HPT

Figure 1 schematically shows the constrained HPT process [2].

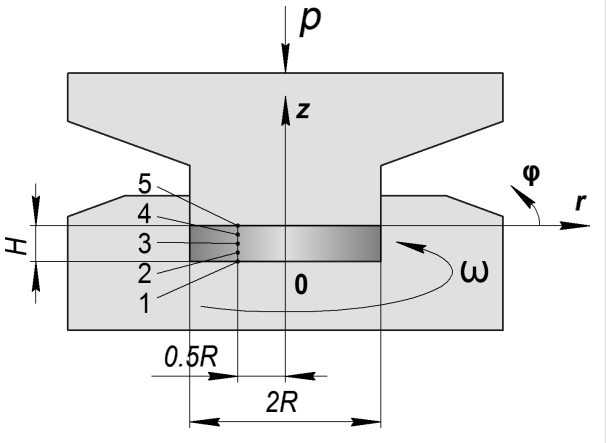


Figure 1: Schematic geometry of the constrained HPT process (the notation is defined in the main text).

Within the rigid plastic flow framework [18], the definition of the stress–strain state (SSS) during HPT is reduced to solving a set of equations in the cylindrical coordinate system, r, φ, z (see Figure 1), including (a) the equilibrium equations obtained from $\mathrm{div}(\sigma) = 0$:

$$\begin{aligned}
&\frac{\partial \sigma_{rr}}{\partial r}+\frac{1}{r}\frac{\partial \sigma_{r\varphi}}{\partial \varphi}+\frac{\partial \sigma_{rz}}{\partial z}+\frac{\sigma_{rr}-\sigma_{\varphi\varphi}}{r}=0 \quad (a),\\
&\frac{\partial \sigma_{r\varphi}}{\partial r}+\frac{1}{r}\frac{\partial \sigma_{\varphi\varphi}}{\partial \varphi}+\frac{\partial \sigma_{\varphi z}}{\partial z}+\frac{2\sigma_{r\varphi}}{r}=0 \quad (b),\\
&\frac{\partial \sigma_{rz}}{\partial r}+\frac{1}{r}\frac{\partial \sigma_{\varphi z}}{\partial \varphi}+\frac{\partial \sigma_{zz}}{\partial z}+\frac{\sigma_{rz}}{r}=0 \quad (c),
\end{aligned} \tag{3}$$

(b) the relations between the components of the strain rate tensor and the velocity vector:

$$\begin{aligned}
&\dot{e}_{rr}=\frac{\partial v_r}{\partial r}, && \dot{e}_{\varphi z}=\frac{1}{2}\left(\frac{\partial v_\varphi}{\partial z}+\frac{1}{r}\frac{\partial v_z}{\partial \varphi}\right),\\
&\dot{e}_{\varphi\varphi}=\frac{1}{r}\left(\frac{\partial v_\varphi}{\partial \varphi}+v_r\right), && \dot{e}_{rz}=\frac{1}{2}\left(\frac{\partial v_r}{\partial z}+\frac{\partial v_z}{\partial r}\right),\\
&\dot{e}_{zz}=\frac{\partial v_z}{\partial z}, && \dot{e}_{r\varphi}=\frac{1}{2}\left(\frac{\partial v_\varphi}{\partial r}-\frac{v_\varphi}{r}+\frac{1}{r}\frac{\partial v_r}{\partial \varphi}\right),
\end{aligned} \tag{4}$$

(c) the von Mises plasticity condition:

$$\bar{\sigma}=\sigma_s\left(e_M\right), \tag{5}$$

(d) the associated flow rule:

$$\dot{e}_{ij}=\frac{3}{2}\frac{\dot{e}_M}{\bar{\sigma}}\left(\sigma_{ij}-\sigma\delta_{ij}\right) \text{ with } i=r,\varphi,z;\ j=r,\varphi,z, \tag{6}$$

and (e) the constant volume condition:

$$\dot{e}_{rr}+\dot{e}_{\phi\phi}+\dot{e}_{zz}=0, \tag{7}$$

where σ_{ij} and e_{ij} with $i = r,\varphi,z$; $j = r,\varphi,z$ are the components of the stress and strain rate tensors respectively; v_i with $i = r,\varphi,z$ are the components of the velocity vector; $\sigma = 1/3\cdot\sigma_{ij}\cdot\delta_{ij}$ is the hydrostatic stress,

$$\bar{\sigma}=(3/2)^{1/2}\left(\left(\sigma_{ij}-\frac{1}{3}\sigma\delta_{ij}\right)\left(\sigma_{ij}-\frac{1}{3}\sigma\delta_{ij}\right)\right)^{1/2}$$

is the equivalent stress, $\dot{e}_{\mathrm{M}}=(2/3)^{1/2}\left(\dot{e}_{ij}\dot{e}_{ij}\right)^{1/2}$ is the von Mises strain rate, and $\sigma_s(e_{\mathrm{M}})$ is the flow stress of the material that depends on the von Mises strain:

$$e_{\mathrm{M}}=\int_0^t \dot{e}_{\mathrm{M}}dt\,. \tag{8}$$

The set of Equations 3–7 is solved under the following boundary conditions:

$$\begin{aligned}
&v_r=v_\varphi=v_z=0, \text{ when } z=H,\ 0\le r\le R\\
&v_r=0,\ \sigma_{\varphi r}=m\sigma_s, \text{ when } r=R,\ 0<z<H,\\
&v_r=v_z=0,\ v_\varphi=r\omega, \text{ when } z=0,\ 0\le r\le R,
\end{aligned} \tag{9}$$

where m is the friction coefficient and ω is the torsion rate of the anvil.

Under the terms of Equation 9 we believe there is no slippage in the contact between the sample and the surface planes of the anvils. According to the experiments in [7] this can always be achieved by applying a sufficiently high pressure. In subsection 2, we will show that under certain conditions, the HPT problem has a self-similar solution both with and without slippage.

The torsion angle β does not explicitly appear in Equations 3–7 but the problem is time-dependent because the flow stress σ_s depends on the von Mises strain e_{M}, which in turn increases with β according to Equation 8.

The global solution of Equations 4–9 has the following form:

$$\sigma_{ij}=\sigma_{ij}\left(\mathbf{x},\beta\right),\ \ v_i=v_i\left(\mathbf{x},\beta\right), \tag{10}$$

where $\mathbf{x}$ is the position vector.

2 A self-similar solution of the rigid plastic flow problem for HPT

Let $y = f(x,t)$ describe the spatial distribution of a quantity y as a function of time t, where x is the spatial coordinate. The process is called self-similar, if the spatial distribution of y at any time t can be obtained from a reference solution at time t_0 by a simple similarity transformation:

$$f\left(x,t\right)=T\left(t\right)f\left(x,t_0\right), \tag{11}$$

where $T(t)$ is time-dependent.

Thus, the spatial distribution of y varies with time while remaining always geometrically similar to itself. This definition generalizes the concept of similarity in geometry where

two figures are called similar if one can be obtained from the other by uniformly scaling along all dimensions [15].

It can be shown [15] that a self-similar process satisfies the following scaling law:

$$f\left(x,t\right)=\left(\frac{t}{t_0}\right)^k f\left(x,t_0\right), \tag{12}$$

where k is a parameter.

This scaling law suggests that a self-similar solution to the HPT problem should have the following form:

$$\sigma_{ij}=\left(\frac{\beta}{\beta_0}\right)^g \sigma'_{ij}\left(\mathbf{x},\beta_0\right),\ \nu_i=\left(\frac{\beta}{\beta_0}\right)^q \nu'_i\left(\mathbf{x},\beta_0\right), \tag{13}$$

where g and q are parameters to be defined, and $\sigma'_{ij}\left(\mathbf{x},\beta_0\right)$ and $\nu'_i\left(\mathbf{x},\beta_0\right)$ represent a solution to the problem for a given torsion angle β_0.

In the following it will be shown that, under certain conditions, the relationships in Equation 13 satisfy the set of Equations 3–7 and the boundary conditions in Equation 9, i.e., the HPT problem has a self-similar solution.

We look for a self-similar velocity field in the following form:

$$v_r\equiv 0;\ v_z\equiv 0;\ v_\varphi=\left(\frac{\beta}{\beta_0}\right)^q v'_\varphi\left(r,z;\beta_0\right). \tag{14}$$

It can be readily seen that such a velocity field automatically satisfies the condition of constant volume (Equation 7) and also the boundary conditions (Equation 9) for v_r and v_z. According to Equation 9, when $z = 0$, the value of v_φ does not depend on β. This implies that $q = 0$, i.e., a self-similar velocity field under HPT should not depend on the torsion angle of the anvil. In this case, the components of the strain-rate tensor have the following form:

$$\dot{e}_{rr}=\dot{e}_{\varphi\varphi}=\dot{e}_{zz}=\dot{e}_{rz}=0, \tag{15}$$

$$\dot{e}_{\varphi z}=\frac{1}{2}\frac{\partial v'_\varphi}{\partial z}, \tag{16}$$

$$\dot{e}_{r\varphi}=\frac{r}{2}\frac{\partial}{\partial r}\left(\frac{v'_\varphi}{r}\right). \tag{17}$$

Under these conditions the von Mises strain rate is defined by:

$$\dot{e}_{\mathrm{M}}=\frac{1}{\sqrt{3}}\sqrt{\left(\frac{\partial v'_\varphi}{\partial z}\right)^2+\left(r\frac{\partial}{\partial r}\left(\frac{v'_\varphi}{r}\right)\right)^2}. \tag{18}$$

Inserting this expression into Equation 8 it can be seen that if HPT is self-similar, the von Mises strain in every point of the specimen is a linear function of the torsion angle β:

$$e_{\mathrm{M}}=\frac{\beta}{\sqrt{3}\omega}\sqrt{\left(\frac{\partial v'_\varphi}{\partial z}\right)^2+\left(r\frac{\partial}{\partial r}\left(\frac{v'_\varphi}{r}\right)\right)^2}. \tag{19}$$

Now we determine the components of the stress tensor for self-similar flow. They should satisfy the set of equilibrium equations (Equation 3), the von Mises plasticity condition (Equation 5) and the associated flow rule (Equation 6). The latter, with Equations 15–17, gives:

$$\sigma_{rr}=\sigma_{\varphi\varphi}=\sigma_{zz}=\sigma, \tag{20}$$

$$\sigma_{rz}=0, \tag{21}$$

$$\sigma_{\varphi z}=\sigma_s\left(e_{\mathrm{M}}\right)\frac{\frac{\partial v'_\varphi}{\partial z}}{\sqrt{3}\sqrt{\left(\frac{\partial v'_\varphi}{\partial z}\right)^2+\left(r\frac{\partial}{\partial r}\left(\frac{v'_\varphi}{r}\right)\right)^2}}, \tag{22}$$

$$\sigma_{r\varphi}=\sigma_s\left(e_{\mathrm{M}}\right)\frac{r\frac{\partial}{\partial r}\left(\frac{v'_\varphi}{r}\right)}{\sqrt{3}\sqrt{\left(\frac{\partial v'_\varphi}{\partial z}\right)^2+\left(r\frac{\partial}{\partial r}\left(\frac{v'_\varphi}{r}\right)\right)^2}}. \tag{23}$$

It can be readily seen that the right hand sides of Equation 22 and Equation 23 scale with β only when the material hardens according to a power law (where von Mises strain is a linear function of β in Equation 19):

$$\sigma_s\left(e_{\mathrm{M}}\right)=Ae_{\mathrm{M}}^n, \tag{24}$$

where A and n are parameters. Inserting Equation 24 and Equation 19 into Equation 22 and Equation 23, we get:

$$\sigma_{r\varphi} = \sigma'_{r\varphi}\left(r, z, \beta_0\right)\left(\frac{\beta}{\beta_0}\right)^n, \tag{25}$$

$$\sigma_{\varphi z} = \sigma'_{\varphi z}\left(r, z, \beta_0\right)\left(\frac{\beta}{\beta_0}\right)^n, \tag{26}$$

where

$$\sigma'_{\varphi z} = \frac{A\beta_0^n}{3\omega}\left(\frac{1}{\sqrt{3}\omega}\sqrt{\left(\frac{\partial v'_\varphi}{\partial z}\right)^2 + \left(r\frac{\partial}{\partial r}\left(\frac{v'_\varphi}{r}\right)\right)^2}\right)^{n-1}\frac{\partial v'_\varphi}{\partial z}, \tag{27}$$

$$\sigma'_{r\varphi} = \frac{A\beta_0^n}{3\omega}\left(\frac{1}{\sqrt{3}\omega}\sqrt{\left(\frac{\partial v'_\varphi}{\partial z}\right)^2 + \left(r\frac{\partial}{\partial r}\left(\frac{v'_\varphi}{r}\right)\right)^2}\right)^{n-1} r\frac{\partial}{\partial r}\left(\frac{v'_\varphi}{r}\right). \tag{28}$$

Comparing Equation 25 and Equation 26 with Equation 13, we obtain: $g = n$.

According to Equation 20 and Equation 21, and using the torsional symmetry (derivatives with respect to φ are 0), Equation 3a and Equation 3c have the following form:

$$\frac{\partial\sigma}{\partial r} = 0,\ \frac{\partial\sigma}{\partial z} = 0. \tag{29}$$

Thus, according to Equation 20, the normal stresses do not depend on the coordinates. We obtain:

$$\sigma_{rr} = \sigma_{\varphi\varphi} = \sigma_{zz} = P, \tag{30}$$

where P is the pressure applied in HPT.

By virtue of the torsional symmetry and using Equation 25 and Equation 26, Equation 3c becomes:

$$\frac{\partial\sigma'_{r\varphi}}{\partial r} + \frac{\partial\sigma'_{\varphi z}}{\partial z} + \frac{2\sigma'_{r\varphi}}{r} = 0. \tag{31}$$

Inserting this into Equation 27 and Equation 28, and after some algebraic manipulations, a second order partial differential equation is obtained:

$$\frac{\partial}{\partial r}\left(\Phi\frac{\partial u}{\partial r}\right) + \frac{\partial}{\partial z}\left(\Phi\frac{\partial u}{\partial z}\right) = 0, \tag{32}$$

where

$$\Phi = r^{n+2}\left(\left(\frac{\partial u}{\partial z}\right)^2 + \left(\frac{\partial u}{\partial r}\right)^2\right)^{\frac{n-1}{2}} \text{ and } u = \frac{v'_\varphi}{r}.$$

Equation 32 is a steady-state diffusion equation [19], where u represents the concentration, and the function Φ, which depends on the absolute value of the gradient of the concentration and on the radius r, serves as the diffusion coefficient. According to Equation 9, the boundary conditions for Equation 32 are the following:

$$u = 0,\ \text{when}\ \ z = H,\ 0 \le r \le R, \tag{33}$$

$$u = \omega,\ \text{when}\ \ z = 0,\ 0 \le r \le R. \tag{34}$$

The equation gives another boundary condition for $\sigma_{r\varphi}$ when $r = R$, $0 < z < H$ (see Equation 9). After inserting Equation 23 and doing some algebraic operations, we get:

$$\frac{\partial u}{\partial r} = \sqrt{3}m\sqrt{\left(\frac{\partial u}{\partial z}\right)^2 + \left(\frac{\partial u}{\partial r}\right)^2}\ \ \text{when}\ \ r = R,\ 0 < z < H. \tag{35}$$

In [19] it is shown that the problem defined by Equations 32–35 has a unique solution. Thus, if the hardening law has a power form, the problem of rigid plastic flow in HPT has a self-similar solution, according to which the following relations hold for the velocity vector

$$v_r = v_z = 0,\quad v_\varphi = ur, \tag{36}$$

for the strain rate tensor

$$\dot{e}_{rr} = \dot{e}_{\varphi\varphi} = \dot{e}_{zz} = \dot{e}_{rz} = 0,\ \dot{e}_{\varphi z} = \frac{r}{2}\frac{\partial u}{\partial z},\ \dot{e}_{r\varphi} = \frac{r}{2}\frac{\partial u}{\partial r}, \tag{37}$$

the von Mises strain

$$e_{\mathrm{M}} = \frac{\beta r}{\sqrt{3}\omega}\sqrt{\left(\frac{\partial u}{\partial z}\right)^2 + \left(\frac{\partial u}{\partial r}\right)^2}, \tag{38}$$

and the shear stress

$$\sigma_{r\varphi} = \left(\frac{\beta}{\beta_0}\right)^n \frac{A\beta_0^n r^n}{3^{\frac{n+1}{2}}\omega^n}\left(\sqrt{\left(\frac{\partial u}{\partial z}\right)^2+\left(\frac{\partial u}{\partial r}\right)^2}\right)^{n-1}\frac{\partial u}{\partial z},$$
$$\sigma_{\varphi z} = \left(\frac{\beta}{\beta_0}\right)^n \frac{A\beta_0^n r^n}{3^{\frac{n+1}{2}}\omega^n}\left(\sqrt{\left(\frac{\partial u}{\partial z}\right)^2+\left(\frac{\partial u}{\partial r}\right)^2}\right)^{n-1}\frac{\partial u}{\partial r}, \quad (39)$$

where the exponent n is equal to the exponent in the hardening law of the material, while the function $u = u(r,z)$ is the solution of Equations 32–35.

It follows from Equation 39 that if the evolution of the process is self-similar, the torque $M(\beta)$ during HPT satisfies a power law, i.e.,:

$$M(\beta) = M(\beta_0)\left(\frac{\beta}{\beta_0}\right)^n. \quad (40)$$

If the hardening law does not satisfy a power law form, there is no self-similar solution.

When there is no friction on the cylindrical surface of the anvil ($m = 0$) a solution of Equations 32–35 can be readily obtained for an ideally plastic material ($n = 0$). This case is of interest because due to saturation in strain hardening, metals are perfectly plastic in the high strain regime [20,21]. One can verify by direct substitution that when $n = 0$ and $m = 0$, the function $u = [(H - z)/H]\cdot\omega$ satisfies the differential Equation 32 and the boundary conditions (Equations 33–35). In this case, the sample is deformed by a simple shear pattern and the fields of velocity, strain rate and stress do not depend on the rotation angle. Furthermore, Equation 38 for the von Mises strain simplifies to the well-known formula

$$e_M = \frac{\beta r}{\sqrt{3}H}.$$

The simple theoretical scheme based on simple shear is a special case of a self-similar solution of the HPT process. Please note that simple shear can only be homogeneous along the height of the specimen. If this is not the case, then $\left(\partial\sigma'_{\varphi z}/\partial z\right) \neq 0$ and Equation 31 would imply that $\sigma'_{r\varphi} \neq 0$ (to satisfy the equilibrium Equation 31), consequently, for any shear in the plane φz there is always some shear in the plane φr.

We note that all the arguments in this section are formally valid not only when $\omega = \text{const}$, but also when this parameter is a function of the radius. It can then be represented in the form $\omega(r) = k(r)\omega$. One can interpret $\omega(r)$ as an angular velocity of the metal on the surface plane of the anvil. If k is equal to 1 there is no slippage. If k is smaller than 1 the possibility of slippage is taken into account. Hence, k can be called "slippage coefficient". Thus, all conclusions about the self-similarity of the HPT process made above are valid when the slippage coefficient is constant or a given function of r only.

We can conclude this section with the following interesting observation. It has been shown in [22] that the power-law hardening is originating from the self-similarity of the microstructure, while it has been shown in the present work that the self-similarity of HPT at the macro-level requires power-law hardening, Thus, there is a relationship between self-similarities at different scales in HPT: Self-similarity at the micro-level is a physical cause of self-similarity at the macro-level.

Results of numerical simulations

In subsection 2 of the section "Model" it has been shown that if the hardening law of the material has a power-law form, the HPT process must evolve in a self-similar fashion, and its parameters must have a power dependence on the torsion angle of the anvil (satisfying the scaling law). For the velocity field and the strain-rate field, the exponent is 0 in this case (the right hand sides of Equation 36 and Equation 37 do not depend on β). For shear strain and for von Mises strain, the exponent is 1 (see Equation 38). Finally, for shear stress and torque, the exponent is equal to the exponent of the hardening law (see Equation 39 and Equation 40).

The second-order differential Equation 32 cannot be solved analytically. Therefore, numerical simulations are needed to identify self-similar solutions. In this section, we illustrate this conclusion by finding a numerical solution to a concrete HPT problem using the finite element method. Moreover, we will use numerical modeling to show that whenever a given hardening curve has an interval of power dependence, the process will enter a self-similar regime. The regime persists for some time (for an interval of rotation) and then disappears.

All calculations were done using the DEFORM software employing a 2D axisymmetric torsion model [23]. The number of initial meshes for the workpiece was 10,000, which was sufficient to explore the local deformation behavior. There was no need to update the mesh because it remained undistorted during the simulation. The process is described in Figure 1. The geometric parameters were $H = 3$ mm and $R = 10$ mm. All calculations were done assuming the rigid plastic flow model

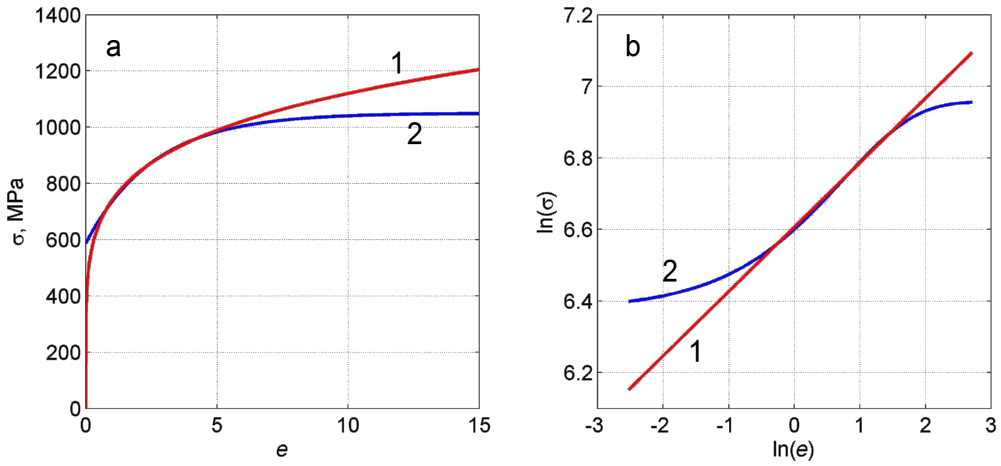


Figure 2: Strain hardening curves used in the numerical simulations. (a): Curve 2 is the experimentally measured stress–strain curve [24] and curve 1 is a fit by the power function σ [MPa] = $740e^{0.18}$. (b): log–log Plot of (a) showing that curve 1 is a good approximation of curve 2 in some interval.

with strain hardening curves displayed in Figure 2. Curve 1 is experimentally measured [24] for compacted iron powder. Curve 2 is a power function σ [MPa] = $740e^{0.18}$, providing a good fit to Curve 1 in the interval between 0.5 to 5.0, see also in the log–log plot (Figure 2b).

We considered two values for the friction coefficient m on the side surface of the bottom anvil: $m = 0.25$ and $m = 0$. The first case simulates a high-friction case while the second corresponds to low friction on the side surface. A description of our numerical simulation conditions are given in Table 1. The results of the simulations are displayed in Figures 3–5.

Analysis of the simulation results obtained by power-law hardening (cases a and b)

These cases revealed self-similar regimes for HPT, in complete accord with the results of the analysis presented in subsection 2 of section "Model". Indeed, as can be seen in Figure 3a,b, the strain-rate field does not change as the torsion angle increases. This implies that the strain depends linearly on β, at any point of the specimen. This linear dependence is illustrated in Figure 4a,b for five characteristic points shown in Figure 1. The plots in Figure 5 show that the logarithm of the torque depends linearly on the logarithm of the β. This means that the torque is a power function of β. The exponent in both (a) and (b) is the respective exponent of the hardening law: $n = 0.18$.

The numerical calculations are in accordance with the analysis of subsection 2 of section "Model": Self-similarity is caused precisely by a power law form of the hardening curve, while friction at the side surface of the specimen affects only the dependence of the stress–strain state on the spatial coordinates. If there is no friction (regime a), the stress–strain state is uniform along the height of the specimen.

Analysis of the results of the numerical simulations using a hardening curve with an interval of power-law dependence (cases c and d)

In the case of low friction ($m = 0$), the strain-rate field is constant in some interval of β (Figure 3c). The plot of ln M as a function of ln β coincides with the straight line in the same interval (see Figure 5c). The exponent in this straight line is the respective exponent in the hardening law, namely $n = 0.18$. Thus, HPT has a self-similar behavior within this interval of β. If the friction coefficient is large ($m = 0.25$), the interval of self-similarity is practically nonexistent (see Figure 3c, Figure 4c and Figure 5c).

Based on the simulation results, we can conclude that when the hardening law has a power law interval, self-similar regimes can emerge in HPT in some ranges of β when side-wall friction

Table 1: Conditions of the numerical simulations.

simulation condition	a	b	c	d
hardening curve	power law (curve 1)	power law (curve 1)	no power law (curve 2)	no power law (curve 2)
friction, m	0	0.25	0	0.25

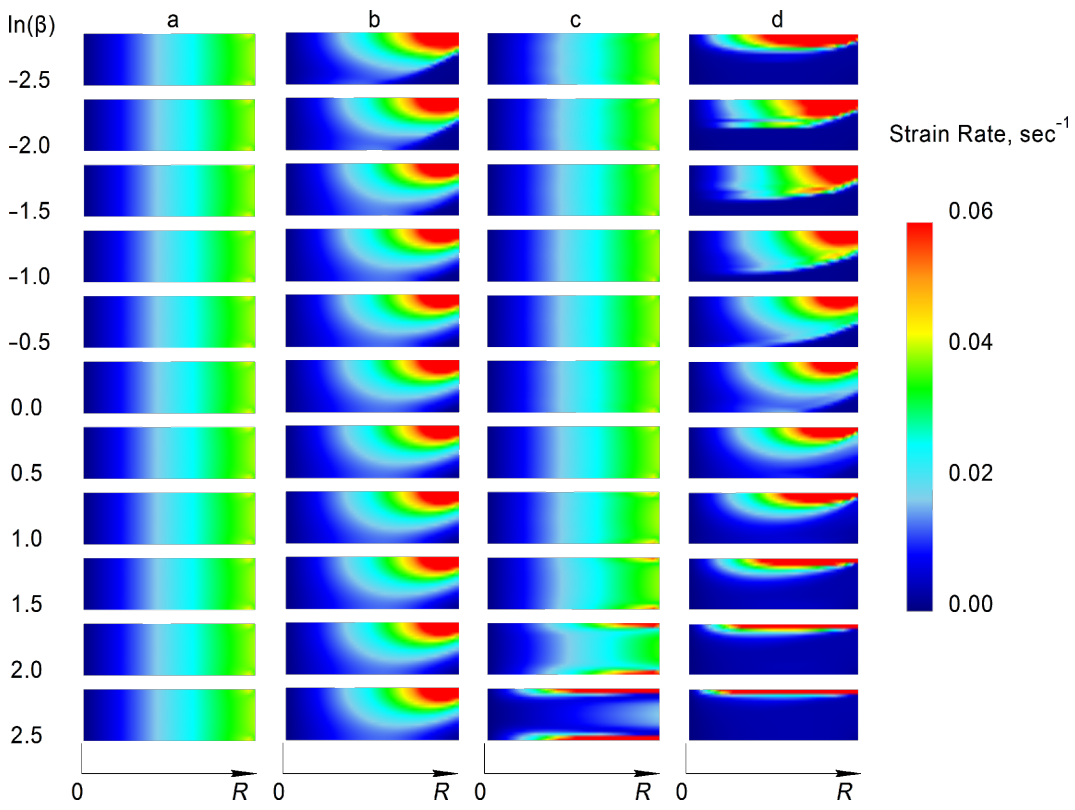


Figure 3: Maps of the von Mises strain rate in the (*r*,*z*) plane for different rotation angles β. An index above each figure corresponds to the index of the respective case in Table 1.

is small. This intermediate self-similarity guarantees a simple mathematical description of the process in the corresponding β range. Outside this range, the plasticity problem has to be solved for each value of β, since the simple power-law function dependencies are not valid outside the interval. In particular, in order to calculate the shear strain, we cannot use the linear dependencies of Equation 1 and Equation 2, which, according to Figure 4c,d, give results that are substantially different from the results obtained numerically. In the absence of self-similarity, the strain value depends on the hardening curve.

Discussion

We have shown in subsection 2 of the section "Model" that the uniform simple shear state along the height of the specimen is a solution of the HPT problem in the case of ideally plastic material when there is no friction on the cylindrical surface of the anvil. On the other hand, according to Figure 3c the saturation in hardening in HPT (see curve 2 in Figure 2) leads to a localization of the deformation in two thin layers near the plain surfaces of the anvils. One can verify by direct substitution that a velocity field in the form of two thin layers of simple shear separated by a cylindrical rigid zone is also a solution of the HPT problem for a perfectly plastic body when $m = 0$. This is a known problem of non-uniqueness of solutions of the problem of the ideal rigid plastic body [25]. A well-known method for the regularization of this problem is introducing viscosity [25] that allows for the allocation of only one velocity field. In the case of large deformation of metals under HPT, such regularization has a physical justification. It is due to the fact that the flow stress of metallic materials in a sub-microcrystalline state significantly depends on the strain rate, even at room temperature. For this reason, there is need in the future to find self-similar regimes of HPT in the frame of a viscoplastic model.

A natural question arises: What do these results imply for the practice of HPT processing? This paper shows that, under certain conditions, HPT evolves in a self-similar way, admitting a simple mathematical description. This means that for some range of torsion angles (henceforth, scaling range), the HPT parameters are proportional to $(\beta/\beta_0)^q$, where β_0 is an arbitrary angle that belongs to the scaling range (e.g., its median), $q = 0$ for velocity and strain rate, $q = 1$ for shear strain and for von Mises strain, $q = n$ for shear stress and torque (where n is the exponent of the power-law function approximating the hardening curve in the given interval).

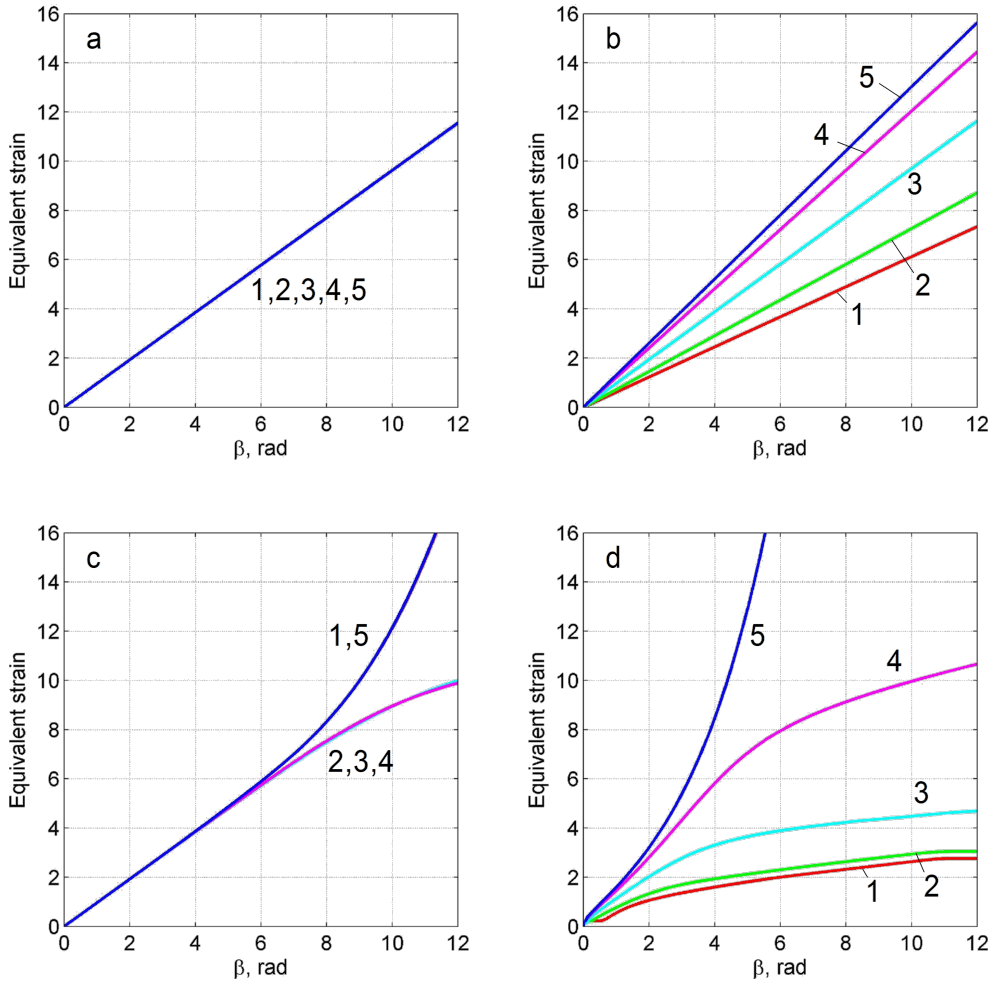


Figure 4: Dependence of the von Mises strain on β in points 1–5 shown in Figure 1. The indices a, b, c and d correspond to the simulation conditions shown in Table 1.

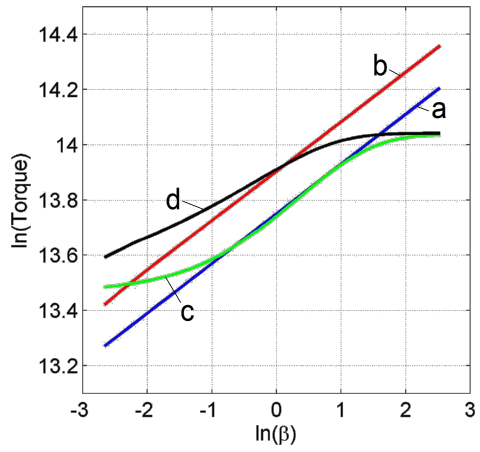


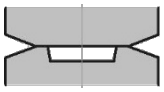
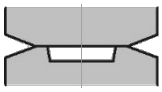
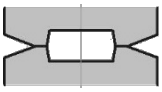
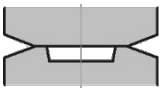
Figure 5: Dependence of torque on β in log–log coordinates. Each curve is indexed with the index of the respective conditions given in Table 1.

To apply this result to HPT in practice, let us formulate the following scaling hypothesis: If, experimentally, there is a range of torsion angles where the torque is a power function of the angle, then the process is self-similar in this range. We give a concrete example illustrating the application of this hypothesis.

We have performed HPT experiments with different materials. We used anvils of different types together with different sample sizes. The experimental conditions are presented in Table 2. Figure 6 shows a log–log plot of the dependence of the torque on β, for different alloys.

In all plots in Figure 6, there are clear linear intervals testifying that at some stage of the process, the dependence of the moment on β has a power form. Table 3 gives scaling ranges of beta and their respective exponents.

Table 2: The conditions of the HPT experiments.

	1	2	3	4	5
material	Ti Grade 1	Cu8Ag	Steel C45	Al10Mg	77Ni23Cu
anvil type					
specimen size	Ø10 × 0.2 mm	Ø10 × 0.2 mm	Ø8 × 0.4 mm	Ø10 × 0.2 mm	Ø12 × 0.15 mm
pressure, GPa	7	4.5	6	5	7
rotation, rpm	1	1	1	1	1
temperature, °C	20	20	380	20	20

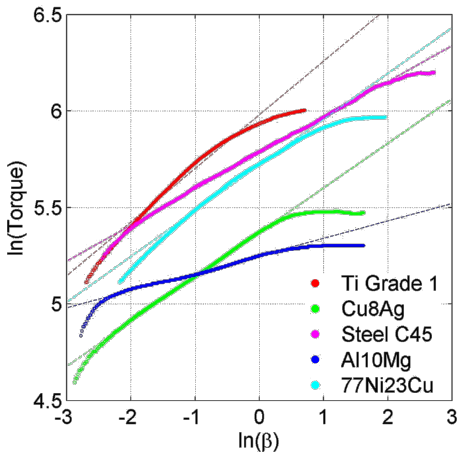


Figure 6: Log–log plot of the dependence of the torque on β, obtained from experimental data.

In the scaling ranges in Table 2, the slope n of the tangent line is equal to the exponent of the hardening curve, while the shear strain in any point of the specimen is given by the formula:

$$\gamma = \frac{\beta}{\beta_0}\Phi_0(r,z). \qquad (41)$$

Here $\Phi(r,z)$ is the shear strain distribution in the specimen when $\beta = \beta_0$.

Conclusion

This paper shows that HPT admits a simple mathematical description when the deformed material hardens according to a power function. In this case, the process is self-similar, and all its parameters have a power form dependence on the torsion angle β of the anvil. In particular, the shear strain in any point of the specimen is a linear function of the torsion angle β.

When the hardening curve has an interval that is well approximated by a power function, HPT can become self-similar in the corresponding range of β. According to the scaling hypothesis formulated in the Discussion section, this range corresponds to the interval where the plot of ln M as a function of ln β can be well approximated by a straight line.

To conclude, any simple scaling expressions for HPT parameters in terms of β are valid only in the scaling ranges. Outside the scaling ranges, we still have to solve a plasticity problem to determine the HPT parameters for each β value. In particular, one cannot use Equation 1 and Equation 2 to compute shear strain in this case.

In [22] the scaling nature of the power-law interval of the hardening curve was established based on the self-similarity of the microstructure. Therefore, self-similarity at the micro-level is a physical reason of self-similarity at the macro-level.

Table 3: Scaling ranges and their respective exponents.

		Ti Grade 1	Cu8Ag	Steel C45	Al10Mg	77Ni23Cu
n		0.278	0.231	0.186	0.09	0.273
self-similarity starts	rad	0.18	0.09	0.15	0.10	0.30
	turns	0.028	0.015	0.024	0.016	0.048
self-similarity stops	rad	0.72	1.34	8.00	1.65	1.60
	turns	0.11	0.21	1.27	0.26	0.25

References

1. Gleiter, H. *Acta Mater.* **2000,** *48,* 1–29. doi:10.1016/S1359-6454(99)00285-2
2. Zhilyaev, A. P.; Langdon, T. G. *Prog. Mater. Sci.* **2008,** *53,* 893–979. doi:10.1016/j.pmatsci.2008.03.002
3. Valiev, R. Z.; Estrin, Y.; Horita, Z.; Langdon, T. G.; Zehetbauer, M. J.; Zhu, Y. *JOM* **2016,** *68,* 1216–1226. doi:10.1007/s11837-016-1820-6
4. Feng, B.; Levitas, V. I. *J. Appl. Phys.* **2013,** *114,* 213514. doi:10.1063/1.4840875
5. Feng, B.; Levitas, V. I. *J. Appl. Phys.* **2016,** *119,* 015902. doi:10.1063/1.4939488
6. Levitas, V. I. *Phys. Rev. B* **2004,** *70,* 184118. doi:10.1103/PhysRevB.70.184118
7. Edalati, K.; Horita, Z.; Langdon, T. G. *Scr. Mater.* **2009,** *60,* 9–12. doi:10.1016/j.scriptamat.2008.08.042
8. Kim, H. S. *J. Mater. Process. Technol.* **2001,** *113,* 617–621. doi:10.1016/S0924-0136(01)00709-9
9. Yoon, S. C.; Horita, Z.; Kim, H. S. *J. Mater. Process. Technol.* **2008,** *201,* 32–36. doi:10.1016/j.jmatprotec.2007.11.204
10. Pereira, P. H. R.; Figueiredo, R. B.; Cetlin, P. R.; Langdon, T. G. *Mater. Sci. Eng., A* **2015,** *631,* 201–208. doi:10.1016/j.msea.2015.02.052
11. Figueiredo, R. B.; Aguilar, M. T. P.; Cetlin, P. R.; Langdon, T. G. *J. Mater. Sci.* **2012,** *47,* 7807–7814. doi:10.1007/s10853-012-6506-z
12. Levitas, V. I.; Zarechnyy, O. M. *High Pressure Res.* **2010,** *30,* 653–669. doi:10.1080/08957959.2010.534990
13. Lee, D. J.; Yoon, E. Y.; Park, L. J.; Kim, H. S. *Scr. Mater.* **2012,** *67,* 384–387. doi:10.1016/j.scriptamat.2012.05.024
14. Cao, Y.; Kawasaki, M.; Wang, Y. B.; Alhajeri, S. N.; Liao, X. Z.; Zheng, W. L.; Ringer, S. P.; Zhu, Y. T.; Langdon, T. G. *J. Mater. Sci.* **2010,** *45,* 4545–4553. doi:10.1007/s10853-010-4485-5
15. Barenblatt, G. I. *Scaling, Selfsimilarity, and Intermediate Asymptotics;* Cambridge Texts in Applied Mathematics, Vol. 14; Cambridge University Press: Cambridge, United Kingdom, 1996. doi:10.1017/CBO9781107050242
16. Taylor, G. *Proc. R. Soc. London, Ser. A* **1950,** *201,* 175–186. doi:10.1098/rspa.1950.0050
17. Hughes, D. A.; Liu, Q.; Chrzan, D. C.; Hansen, N. *Acta Mater.* **1997,** *45,* 105–112. doi:10.1016/S1359-6454(96)00153-X
18. Hill, R. *The mathematical theory of plasticity;* Oxford University Press: Oxford, United Kingdom, 1998.
19. Crank, J. *The mathematics of diffusion;* Oxford University Press: Oxford, United Kingdom, 1975.
20. Levitas, V. I. *Large Deformation of Materials with Complex Rheological Properties at Normal and High Pressure;* Nova Science Publishers, Inc.: New York, NY, U.S.A., 1996.
21. Pippan, R.; Scheriau, S.; Taylor, A.; Hafok, M.; Hohenwarter, A.; Bachmaier, A. *Annu. Rev. Mater. Res.* **2010,** *40,* 319–343. doi:10.1146/annurev-matsci-070909-104445
22. Beygelzimer, Y.; Toth, L. S.; Jonas, J. J. *Adv. Eng. Mater.* **2015,** *17,* 1783–1791. doi:10.1002/adem.201500097
23. Scientific Forming Technologies Corporation. DEFORM v11.0 Documentation. http://www.deform.com/ (accessed June 14, 2016).
24. Zhao, Y.; Massion, R.; Grosdidier, T.; Toth, L. S. *Adv. Eng. Mater.* **2015,** *17,* 1748–1753. doi:10.1002/adem.201500012
25. Mosolov, P. P.; Myasnikov, V. P. *Mechanics of rigid plastic bodies;* M.-Nauka, 1981. In Russian.

License and Terms

This is an Open Access article under the terms of the Creative Commons Attribution License (http://creativecommons.org/licenses/by/4.0), which permits unrestricted use, distribution, and reproduction in any medium, provided the original work is properly cited.

The license is subject to the *Beilstein Journal of Nanotechnology* terms and conditions: (http://www.beilstein-journals.org/bjnano)

The definitive version of this article is the electronic one which can be found at: doi:10.3762/bjnano.7.117

BEILSTEIN JOURNAL OF NANOTECHNOLOGY

Microwave synthesis of high-quality and uniform 4 nm $ZnFe_2O_4$ nanocrystals for application in energy storage and nanomagnetics

Christian Suchomski‡[1], Ben Breitung‡[2], Ralf Witte[3], Michael Knapp[4], Sondes Bauer[5], Tilo Baumbach[5], Christian Reitz*[3] and Torsten Brezesinski*[2,3]

Full Research Paper

Open Access

Address:
[1]Institute of Physical Chemistry, Justus-Liebig-University Giessen, Heinrich-Buff-Ring 17, 35392 Giessen, Germany, [2]Battery and Electrochemistry Laboratory, Institute of Nanotechnology, Karlsruhe Institute of Technology, Hermann-von-Helmholtz-Platz 1, 76344 Eggenstein-Leopoldshafen, Germany, [3]Institute of Nanotechnology, Karlsruhe Institute of Technology, Hermann-von-Helmholtz-Platz 1, 76344 Eggenstein-Leopoldshafen, Germany, [4]Institute for Applied Materials, Karlsruhe Institute of Technology, Hermann-von-Helmholtz Platz 1, 76344 Eggenstein-Leopoldshafen, Germany and [5]Institute for Photon Science and Synchrotron Radiation, Karlsruhe Institute of Technology, Hermann-von-Helmholtz-Platz 1, 76344 Eggenstein-Leopoldshafen, Germany

Email:
Christian Reitz* - christian.reitz@kit.edu; Torsten Brezesinski* - torsten.brezesinski@kit.edu

* Corresponding author ‡ Equal contributors

Keywords:
1-phenylethanol route; lithium-ion battery; nanomagnetism; nanoparticles; nonaqueous sol–gel synthesis; zinc ferrite

Beilstein J. Nanotechnol. **2016,** *7,* 1350–1360.
doi:10.3762/bjnano.7.126

Received: 22 June 2016
Accepted: 07 September 2016
Published: 27 September 2016

This article is part of the Thematic Series "Advances in nanomaterials II".

Guest Editor: M. Ruben

© 2016 Suchomski et al.; licensee Beilstein-Institut.
License and terms: see end of document.

Abstract

Magnetic nanocrystals with a narrow size distribution hold promise for many applications in different areas ranging from biomedicine to electronics and energy storage. Herein, the microwave-assisted sol–gel synthesis and thorough characterization of size-monodisperse zinc ferrite nanoparticles of spherical shape is reported. X-ray diffraction, ^{57}Fe Mössbauer spectroscopy and X-ray photoelectron spectroscopy all show that the material is both chemically and phase-pure and adopts a partially inverted spinel structure with Fe^{3+} ions residing on tetrahedral and octahedral sites according to $(Zn_{0.32}Fe_{0.68})^{tet}[Zn_{0.68}Fe_{1.32}]^{oct}O_{4\pm\delta}$. Electron microscopy and direct-current magnetometry confirm the size uniformity of the nanocrystals, while frequency-dependent alternating-current magnetic susceptibility measurements indicate the presence of a superspin glass state with a freezing temperature of about 22 K. Furthermore, as demonstrated by galvanostatic charge–discharge tests and ex situ X-ray absorption near edge structure spectroscopy, the as-prepared zinc ferrite nanocrystals can be used as a high-capacity anode material for Li-ion batteries, showing little capacity fade – after activation – over hundreds of cycles. Overall, in addition to the good material characteristics, it is remarkable that the microwave-based synthetic route is simple, easily reproducible and scalable.

Introduction

Spinel ferrites of the general formula MFe_2O_4 constitute a well-known class of materials with unique physical and chemical properties and they hold promise for use in various fields of nanotechnology [1,2]. One of those properties is magnetism. In recent years, it has been shown that particularly size-monodisperse nanoparticles provide an attractive platform for future magnetic data storage and theranostics (that is, imaging and therapy in biomedicine). The challenges and prospects in using Fe-based nanoparticles for such applications have been described in excellent papers elsewhere and will therefore not be discussed here [3-8]. The magnetic properties of spinel ferrites are known to be strongly dependent upon their size [9-11]. Part of the reason for this is that, for example, significant spin disorder occurs when the particle size is reduced to the nanometer level. Nevertheless, the cation site occupancy also plays a central role in the magnetism (exchange interactions) and usually exhibits a variety among different synthesis methods. Overall, this means that the magnetic properties can be tailored to some extent by means of the preparation conditions.

Furthermore, spinel ferrites have been shown to be capable of reacting electrochemically with Li to form Li_2O and reduced metal phases [12-14]. However, bulk forms of these materials have not proven to be of interest for battery applications because of sluggish conversion reaction kinetics and fast capacity decay on cycling. Since small-size particles can better accommodate the strain from the Li insertion, nanocrystallinity seems to be playing the key role to achieving "good" charge storage characteristics or, in other words, high performance.

Various synthetic methods to produce single-phase spinel ferrite nanoparticles have been reported in the literature, including hydrothermal, mechanochemical and sol–gel routes (to name but a few) [15-19], and in particular solution-phase approaches seem promising with respect to exercising control over size and shape [20,21]. As an example, the preparation of uniform 4–8 nm diameter MFe_2O_4 (M = Fe, Co, Mn, Ni) nanoparticles has been achieved by microwave-assisted nonaqueous sol–gel synthesis using benzyl alcohol as a high-boiling solvent [22,23]. Inspired by this work, we show here that high-quality and size-monodisperse zinc ferrite (referred to as ZFO in the following) nanocrystals can be produced via facile microwave synthesis by the use of *rac*-1-phenylethanol. 1-Phenylethanol exhibits excellent solvent properties – especially for anhydrous zinc acetate – and therefore ensures that both salt precursors are completely dissolved, so that the formation of impurity phases, such as Fe_3O_4, can be avoided.

Experimental

Synthesis

In a typical synthesis, anhydrous zinc acetate (91.7 mg, 99.99%, Sigma-Aldrich) was dissolved by sonication in dry *rac*-1-phenylethanol (15 mL, 98%, Sigma-Aldrich). Then, iron(III) acetylacetonate (353.2 mg, 99.9%, Sigma-Aldrich) was added, followed by sonication for 5 min. The resulting dark red solution was transferred to a borosilicate vial (30 mL), sealed with a screw cap and heated at 200 °C under microwave irradiation for 25 min. The stirring rate was set to 300 rpm. After quenching with compressed cold air, the ZFO nanoparticles were precipitated by addition of n-pentane and collected by centrifugation, followed by washing twice with a solution of acetone and ethanol. Finally, the obtained brown powder was allowed to dry at room temperature.

Microwave syntheses were performed using both Monowave 300 and Masterwave BTR reactors (f = 2.45 GHz, Anton Paar Germany GmbH) equipped with either one or two 850 W magnetrons. The temperature was monitored with a ruby thermometer (fiber-optic probe) placed inside the reaction vial (Monowave 300) and with an IR sensor (Pt100) mounted at the bottom of the Masterwave BTR cavity. Pressure sensing was accomplished by a hydraulic sensor.

Electrode processing

ZFO nanoparticle electrodes were prepared by casting a water slurry containing 79 wt % ZFO, 11 wt % Super C65 carbon black additive (Timcal) and 10 wt % Selvol 425 poly(vinyl alcohol) (Sekisui) onto Cu foil (Gould Electronics), followed by drying in vacuum at 80 °C for 12 h. The areal loading was 2.4 mg_{ZFO}/cm^2 on average. Coin-type cells with 600 µm-thick Li metal foil (Rockwood Lithium Inc.) and glass microfiber film separator (Whatman, GF/D grade) were assembled inside an argon-filled glovebox (MBraun) with $[O_2]$ and $[H_2O]$ < 1 ppm. The electrolyte was 1 M $LiPF_6$ in fluoroethylene carbonate and ethyl methyl carbonate (1:1 weight ratio). The cycling performance was evaluated at rates ranging from C/10 to C/2 (1C = 1000.5 mA/g_{ZFO}).

Characterization

Powder X-ray diffraction patterns were recorded on a STOE diffractometer with a Mo $K\alpha_1$ radiation source, focusing Ge 111 monochromator and a Dectris Mythen strip detector. Rietveld refinement was performed by use of the FullProf software. X-ray photoelectron spectroscopy data were obtained on a VersaProbe PHI 5000 Scanning ESCA Microprobe from Physical Electronics with an Al Kα radiation source and a hemispherical electron energy analyzer. The C 1s signal from adventitious hydrocarbon at 284.8 eV was used as the energy reference

to correct for charging. Mössbauer spectroscopy was performed in transmission geometry using a constant acceleration spectrometer with a ^{57}Co radiation source embedded in a Rh matrix. The center shifts are quoted relative to α-Fe foil at room temperature. The spectra were analyzed using the WinNORMOS software [24]. Transmission electron microscopy was performed on a Tecnai G2-F20ST microscope (FEI) operated at 200 keV. The bright-field images were analyzed using the iTEM software. Thermogravimetric analysis was performed on a Netzsch STA 409 PC. The thermobalance was coupled to a Balzers QMG 421 quadrupole mass spectrometer. The ionization energy was 70 eV. Gas chromatography-mass spectrometry was performed on an Agilent 6890 gas chromatograph equipped with an Agilent 5973 MSD. Diffuse reflectance ultraviolet–visible spectra were collected on a Lambda 750 UV–vis–NIR spectrophotometer (PerkinElmer) equipped with a Praying Mantis diffuse reflectance accessory. An MPMS XL-5 superconducting quantum interference device magnetometer (Quantum Design) was used for magnetic susceptibility measurements in the field range from +45 kOe (+4.5 T) to −45 kOe (−4.5 T). Electrochemical measurements were performed in a BINDER cooled incubator using a MACCOR Series 4000 cycler (Tulsa). 2D imaging of chemical phase transformations at the nanoscale by full-field transmission X-ray microscopy using a Carl Zeiss TXM and the corresponding data treatment steps are described elsewhere [25]. To determine the oxidation state of Fe, several different Fe-based compounds were measured and used as the references. The fitting of X-ray absorption near edge structure spectra is based on a least-squares linear combination of reference spectra and was carried out by use of TXM-XANES Wizard after normalization [26]. The quality of fits was assessed by the misfit factor, *R*.

Results and Discussion

Highly crystalline ZFO nanoparticles were prepared by microwave-assisted nonaqueous sol–gel synthesis using anhydrous zinc acetate and iron(III) acetylacetonate as the precursors and *rac*-1-phenylethanol as a solvent. Details on the formation mechanism from gas chromatography-mass spectrometry (GC-MS) are given in Supporting Information File 1, Figure S1–S4 and Table S1.

The size and shape of the ZFO nanoparticles was investigated by means of transmission electron microscopy (TEM). The low-magnification bright-field TEM image in Figure 1a shows that they are spherical in shape with a narrow size distribution around 4 nm. Both high-resolution TEM (HRTEM, Figure 1b) and selected-area electron diffraction (SAED, Figure 1c) demonstrate the high crystallinity of the ZFO nanoparticles. In addition, SAED indicates that the sol–gel derived material is single-phase and adopts a cubic structure. Figure 1d presents the size distribution obtained by particle counting from TEM images. These data can be fitted by a log-normal distribution with a mean of 3.3 nm and standard deviation of 0.2 nm.

The microstructure of the as-prepared ZFO nanoparticles was analyzed in more detail by powder X-ray diffraction (XRD). The XRD pattern in Figure 2 corroborates the SAED results, showing only reflections characteristic of spinel-type franklinite with $Fd\bar{3}m$ space group (ICDD-JCPDS card no. 22-1012) [27]. A fit applying a modified Thompson–Cox–Hastings pseudo-Voigt profile function revealed lattice parameters of $a = b = c = 8.4141(7)$ Å and a crystallite size of 4(1) nm – in line with the size distribution from particle counting. The quality of the refinement (NIST Si 640c was used as the instrument line-broadening standard) was assessed by the magnitude of the weighted profile *R*-factor ($R_{wp} = 8.0\%$) and the goodness-of-fit parameter ($\chi^2 = 0.463$). The fact that the observed and calculated XRD patterns match with each other well and the latter values are low implies that the fit can be considered good.

As mentioned in the introduction, ZFO belongs to the spinel ferrite family of the general formula AB_2O_4. The inversion parameter, λ, typically serves as a measure of the cation distribu-

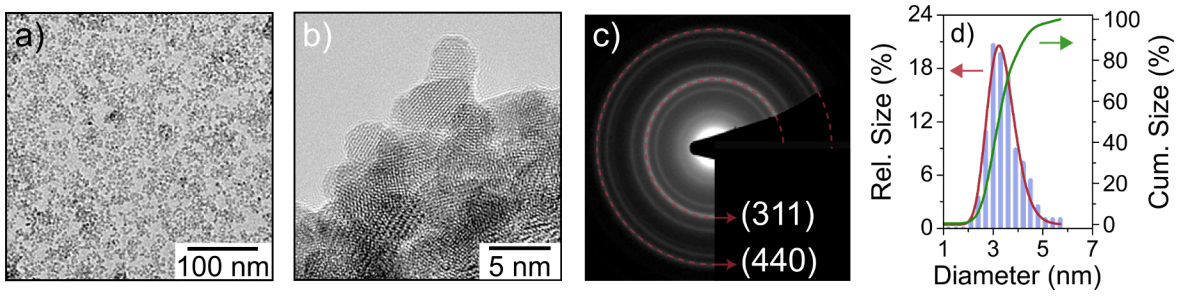


Figure 1: Electron microscopy of as-prepared ZFO nanoparticles. (a) Bright-field TEM image. (b) HRTEM image and (c) SAED pattern demonstrating the crystallinity. Note that only the most intense diffraction rings are indexed in (c). (d) Relative and cumulative particle size distributions. The red line is a log-normal fit to the data.

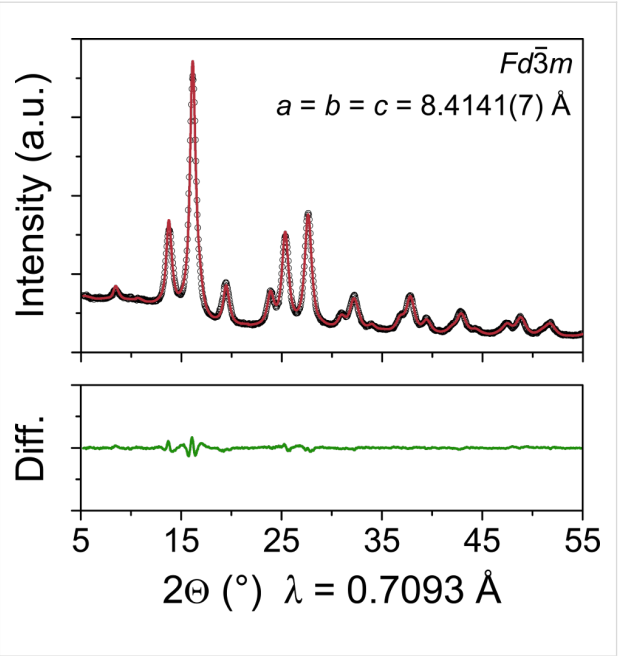


Figure 2: Observed (open circles) and calculated (red line) XRD patterns of as-prepared ZFO nanoparticles. The difference profile of the fit is shown in green.

tion according to $(A_{1-\lambda}B_{\lambda})^{tet}[A_{\lambda}B_{2-\lambda}]^{oct}O_4$. Bulk ZFO has been shown to exhibit virtually no inversion ($\lambda \approx 0$) and thus is considered a normal spinel [28,29]. In this structure, the A cations occupy the tetrahedral 8a sites (Wyckoff notation), while the B cations reside on two equivalent octahedral 16d sites. In contrast, the octahedral coordination sites are randomly occupied in a 1:1 ratio by the A and B cations and the tetrahedral sites are only occupied by the B cations in inverse spinels ($\lambda = 1$). In both cases, the O^{2-} ions form a cubic close-packed structure and reside on 32e sites. However, nanoscale spinel ferrites prepared by wet chemical methods are known to often have a partially inverted structure [30-32]. Therefore, the cation site occupancy in the ZFO nanoparticles employed in this work was expected to differ from that of bulk material.

The distribution of Fe among the tetrahedral and octahedral sites was studied by X-ray photoelectron spectroscopy (XPS) and Mössbauer spectroscopy. Figure 3a–c presents detailed XPS spectra of the Fe 2p, O 1s and C 1s core level regions. The Fe 2p spectrum shows a single doublet with strong satellite peaks around 8 eV higher in binding energy than the main peaks. This result is characteristic of Fe in the Fe(III) state [33,34]. The apparent asymmetry of the Fe 2p peaks suggests that the inversion parameter must be greater than zero. The main peaks at binding energies of (724.59 ± 0.05) eV and (710.65 ± 0.05) eV for the $2p_{1/2}$ and $2p_{3/2}$ orbital lines, respectively, correspond to octahedral Fe^{3+} ions and the minor peaks at (727.12 ± 0.05) eV and (713.05 ± 0.05) eV to tetrahedral Fe^{3+} ions [35-37]. The inversion parameter was determined to be 0.68 by comparing the areas under the peaks. Accordingly, the formula can be expressed as $(Zn_{0.32}Fe_{0.68})^{tet}[Zn_{0.68}Fe_{1.32}]^{oct}O_{4\pm\delta}$. The deconvolution of the O 1s spectrum identified three different oxygen bonding states. The main peak at (529.60 ± 0.05) eV corresponds to lattice oxygen and the minor peaks at higher binding energies of (531.11 ± 0.05) eV and (532.07 ± 0.05) eV can be assigned to hydroxyl oxygen/oxygen from C–O and C=O functionalities, respectively, with the latter originating from surface ligands. The C 1s spectrum can also be fitted into three peaks at (284.56 ± 0.05) eV, (286.06 ± 0.05) eV and (288.49 ± 0.05) eV. We ascribe the main peak centered at 284.6 eV to sp^3-hybridized carbon (C–C); the minor peaks at higher binding energies arise from organic compounds containing C–O and C=O bonds, respectively. The fact that the as-prepared nanoparticles are not "naked" was also confirmed by thermogravimetric analysis-mass spectrometry (TGA-MS). The TGA-MS data of vacuum-dried material in Supporting Information File 1,

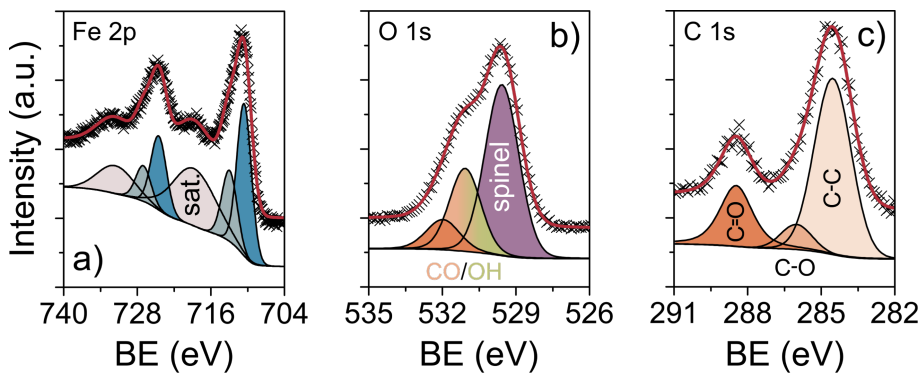


Figure 3: XPS spectra of the (a) Fe 2p, (b) O 1s and (c) C 1s core levels of as-prepared ZFO nanoparticles. The peaks in gray, blue, violet and orange/green correspond to tetragonal Fe^{3+}, octahedral Fe^{3+}, lattice oxygen as well as hydroxyl oxygen and different organic compounds containing carbon–oxygen functionalities. The red lines are the sum of the peak fits.

Figure S5 indicate a mass loss of 13% in the temperature range between 150 °C and 400 °C due to release of water and combustion of acetate and acetylacetonate ligands.

To verify the XPS results, ^{57}Fe Mössbauer spectroscopy was performed on the ZFO nanoparticles. A representative spectrum measured at 5 K is provided in Figure 4. It reveals a sextet pattern because of the presence of magnetic ordering. This is in accordance with both the magnetometry data below and temperature-dependent Mössbauer spectra shown in Supporting Information File 1, Figure S6. The low-temperature data can be fitted reasonably well with three sub-spectra, in line with findings by Chinnasamy et al. on nanoscale ZFO prepared by ball-milling [10]. They identified two octahedral B-site components (oct-1, oct-2) due to different local environments of the Fe^{3+} ions and one tetrahedral A-site component (tet) using Mössbauer spectroscopy with and without an external magnetic field. Table 1 summarizes the fitted parameters, which agree with the ratio of tetrahedral to octahedral Fe in the partially inverted spinel structure from XPS. In addition, Figure 4 confirms that all Fe ions are in the Fe(III) state. This is also corroborated by the fact that the formation of acetophenone can be ruled out on the basis of the GC-MS data (Supporting Information File 1, Figure S1). The latter compound is found in the microwave synthesis of Fe_3O_4 nanoparticles under identical conditions due to partial oxidation of 1-phenylethanol (data not shown), which is accompanied by the reduction of Fe^{3+} to Fe^{2+}.

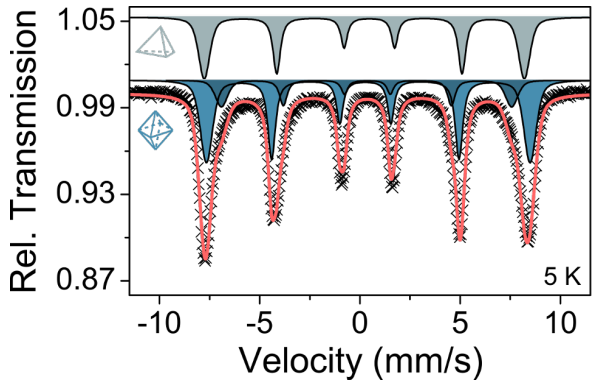


Figure 4: Low-temperature Mössbauer data of as-prepared ZFO nanoparticles. The gray spectrum represents Fe^{3+} on tetrahedral sites, while the blue spectra correspond to Fe^{3+} residing on octahedral sites. The red line is the sum of the different sub-spectra.

Table 1: Summary of fitted Mössbauer parameters.[a]

Site	CS (mm/s)	QS (mm/s)	B_{Hf} (T)	Area ratio
oct-1	0.45(1)	0.16(1)	50.0(5)	0.45(2)
oct-2	0.46(1)	−0.04(1)	45.0(1)	0.23(1)
tet	0.45(1)	−0.26(1)	49.6(1)	0.32(2)

[a]CS: center shift relative to α-Fe at 298 K, QS: quadrupole splitting, B_{Hf}: magnetic hyperfine splitting.

The magnetic properties were thoroughly investigated by both direct-current (DC) and alternating-current (AC) superconducting quantum interference device (SQUID) magnetometry. Zero-field-cooled (ZFC) and field-cooled (FC) curves obtained on the as-prepared ZFO nanoparticles at an applied field of 10 mT are shown in Figure 5. As seen, the magnetic moment continuously increases until a maximum, T_{max}, is reached at about 22 K. The fact that this maximum is rather sharp supports the size uniformity of the particles with a similar magnetic anisotropy. Upon further cooling, the FC curve diverges from the ZFC curve and the material exhibits ferrimagnetic behavior.

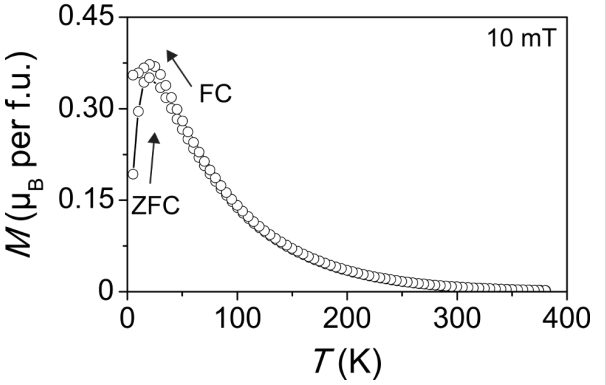


Figure 5: Direct-current SQUID magnetometry of as-prepared ZFO nanoparticles. ZFC/FC curves measured with $\mu_0 H_{DC}$ = 10 mT.

To determine whether T_{max} can be associated with either a freezing temperature, T_f, for spin glasses or a blocking temperature, T_B, for superparamagnetic particles, frequency-dependent AC magnetic susceptibility measurements were carried out. We note that single-domain particle ensembles, in which interparticle interactions are non-negligible, are referred to as superspin glasses in the following [38,39]. The amplitude of the AC field was set to $\mu_0 H_{AC}$ = 0.35 mT and the driving frequency, ν, was varied from 1 Hz to 500 Hz. Figure 6a,b shows the in-phase, χ', and out-of-phase, χ'', parts of the complex susceptibility (with $\chi_{AC} = \chi' - i\chi''$) in units of μ_B per formula unit (f.u.). In the plot of χ' vs T, T_{max} shifts to higher temperatures but lower magnetization values with increasing frequency. In contrast, the χ''(T) curve shows an increase in susceptibility with increasing frequency. Unfortunately, such frequency and temperature dependencies are usually found for both (super)spin glasses and superparamagnets. Therefore, the relative variation of T_{max} (defined as the peak temperature in the χ'(T) curve) per frequency decade was analyzed in more detail. First, the data were

fitted according to $p = \Delta T_{max}/[T_{max} \times \Delta\log(\nu)]$, where p is the frequency sensitivity. From the fit (Figure 6c), we obtained $p = 0.044$, which is in the range observed for canonical spin glasses [35,39,40]. The frequency dependence of the peak temperature can also be described by a critical power law according to $\nu = \nu_0 \times [(T_{max} - T_0)/T_0]^{z\upsilon}$ with $\tau_0 = 1/2\pi\nu_0$ and $T_r = (T_{max} - T_0)/T_0$, where τ_0 is the microscopic spin relaxation time, T_r is the reduced temperature and $z\upsilon$ is the dynamical exponent [39,41]. The best fit (Figure 6d) was obtained with $\tau_0 = 1.43 \times 10^{-8}$ s, $T_0 = 21.7$ K and $z\upsilon = 5.9$. Both the value of τ_0 and $z\upsilon$ falls within the range expected for canonical spin glasses [42]. Lastly, the data were fitted according to the Néel–Brown equation ($\nu = \nu_0 \times \exp[KV/k_BT_{max}]$) for ideal non-interacting superparamagnetic particle ensembles, where K is the effective uniaxial magnetic anisotropy, V is the particle volume and k_B is the Boltzmann's constant [43]. As shown in Supporting Information File 1, Figure S7, the frequency dependence of the peak temperature does not follow Néel–Brown model, which is supported by the finding that the Néel–Arrhenius relation gave an unphysically large value of E_a/k_B (1365 K). This has also been observed for other materials with (super)spin glass behavior and thus confirms the conclusion of spin glass freezing rather than superparamagnetic blocking [44,45]. For slightly interacting nanoparticle ensembles, the frequency dependence should follow the empirical Vogel–Fulcher law ($\nu = \nu_0 \times \exp[-E_a/k_B(T_{max} - T_0)]$ with $-E_a = KV$), where T_0 is the interparticle interaction strength parameter and E_a is the activation energy [46,47]. From the best fit to the data (Figure 6e), we obtained $\tau_0 = 1.21 \times 10^{-8}$ s, $T_0 = 18.8$ K and $E_a/k_B = 70.2$ K. These values are in good agreement with those reported in the literature and those obtained from the power law plot in Figure 6d [38,48]. Overall, the DC and AC magnetization data reveal the signatures of a superspin glass state with a freezing temperature $T_f \approx 22$ K.

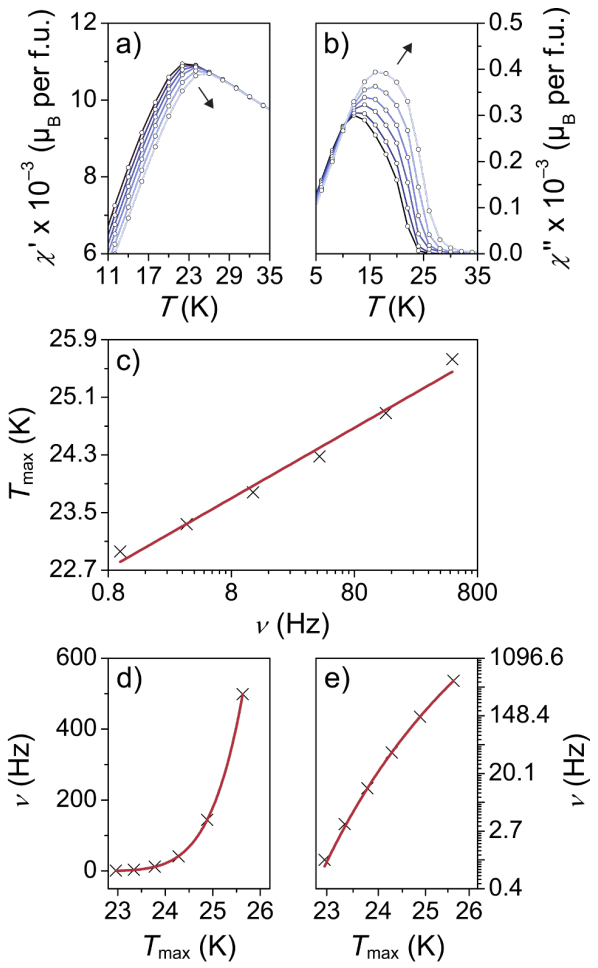


Figure 6: Alternating-current SQUID magnetometry of as-prepared ZFO nanoparticles with $\mu_0 H_{AC} = 0.35$ mT. (a) In-phase and (b) out-of-phase parts of the magnetic susceptibility. (c–e) Frequency dependence of the peak temperature in the $\chi'(T)$ curve. The red lines are fits to the data according to $p = \Delta T_{max}/[T_{max} \times \Delta\log(\nu)]$ in (c), $\nu = \nu_0 \times [(T_{max} - T_0)/T_0]^{z\upsilon}$ in (d) and $\nu = \nu_0 \times \exp[-E_a/k_B(T_{max} - T_0)]$ in (e).

Figure 7a–c shows results from field-dependent SQUID magnetometry. The $M(H)$ curve measured at 5 K (Figure 7a,b) indicates ferrimagnetic behavior with a coercive field $H_C \approx 12$ mT. As evident, the magnetization is not completely saturated. Similar observations have been made for other nanocrystalline solids and are often associated with spin canting, spin freezing and so forth. Although the origin of these effects is largely unclear, they are typically attributed to magnetic frustration, surface disorder and/or finite size effects [49,50]. However, the theoretical saturation magnetization (3.2 μ_B per f.u.) based on the inversion parameter from XPS agrees with the experimental data. The nonlinearity of the room temperature $M(H)$ curve in Figure 7c can be interpreted as arising from the presence of superspin glass clusters – well above their freezing temperature – in a paramagnetic environment. These data can be fitted using a simple Langevin model ($L(x)$ with additional paramagnetic susceptibility term) of the form $M = M_0L(x) + kH$ with $L(x) = \coth(x) - 1/x$ and $x = \mu H/(k_BT)$, where M_0 is the magnetization of the superspin glass part, k is the paramagnetic susceptibility, μ is the magnetic moment per cluster, k_B is the Boltzmann's constant and T is the temperature. The best fit was obtained with M_0, k and μ values equal to 0.84 μ_B/f.u., 7.8×10^{-2} emu/(T × f.u.) and 1090 μ_B, respectively. Using these data and assuming a spherical cluster shape (with eight f.u. per unit cell), the cluster size was estimated to be 3.7 nm in diameter, which is in excellent agreement with the crystallite size determined by Rietveld refinement.

In a nutshell, the results from electron microscopy, XRD, XPS, ^{57}Fe Mössbauer spectroscopy as well as DC and AC magnetometry are all consistent and confirm the quality of the

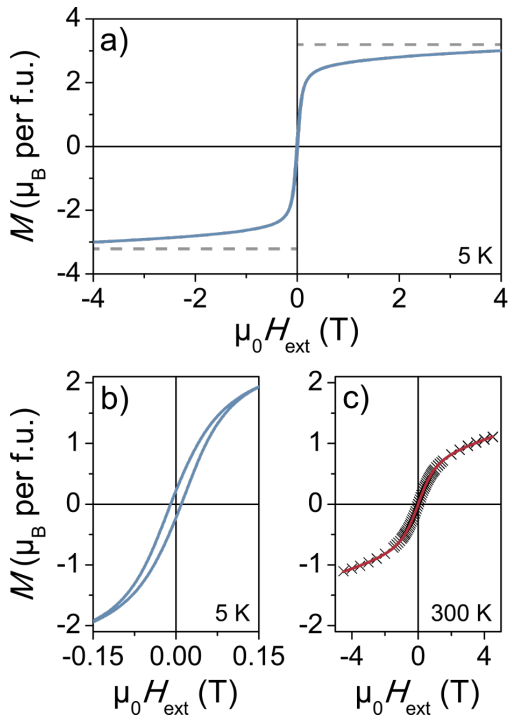


Figure 7: Field-dependent SQUID magnetometry of as-prepared ZFO nanoparticles at (a,b) 5 K and (c) 300 K. The dashed lines in (a) indicate the theoretical saturation magnetization. The red line in (c) is the best Langevin model fit to the data.

partially inverted ZFO nanoparticles. This is also supported by the analysis of the optical properties. The Tauc plots shown in Supporting Information File 1, Figure S8 indicate an indirect band gap transition at about 650 nm (≈1.9 eV), which is in accordance with literature values and further corroborated by density functional theory calculations [51,52].

As mentioned above, spinel ferrites can, in principle, be used as negative electrode materials in rechargeable Li-ion batteries. However, they have been shown to undergo conversion at low potential and these electrochemical reactions with Li are accompanied by significant volume changes (mechanical strain), which may result in pulverization of the active material (formation of reactive surfaces) and poor cycling performance. In addition, there is usually a large hysteresis between charge and discharge, which adversely affects the energy efficiency. And this is why ZFO and other spinel ferrites are not used in commercial secondary batteries, despite high theoretical specific capacities. Nevertheless, because nanomaterials are known to better resist stresses, it was worthwhile testing the 4 nm diameter ZFO nanocrystals in Li half-cells.

The cycling performance of electrodes having a ZFO content of 79 wt % and areal loading of 2.4 mg_{ZFO}/cm^2 in the potential range from 0.01 to 3.0 V with respect to Li^+/Li was evaluated at different C-rates through galvanostatic charge/discharge measurements. Top view SEM images (Supporting Information File 1, Figure S9) obtained on the ZFO nanoparticle electrodes prior to cycling indicate that they are porous and there are no major structural defects and inhomogeneities, such as cracks on the micrometer level. Figure 8a shows representative charge/discharge profiles of the 1st, 2nd, 5th and 10th cycle. We note that the first two (formation) cycles were performed at C/20 before increasing the C-rate. The specific capacity in the initial cycle was always in the range of (1270 ± 20) mAh/g_{ZFO}. The fact that this value exceeds the theoretical specific capacity of ZFO (q_{th} = 1000.5 mAh/g_{ZFO}) indicates that irreversible reactions occurred upon lithiation, including decomposition of surface ligands and formation of a solid electrolyte interface (SEI) on the nanoparticles. However, this relatively large capacity loss (≈30%) was limited to the initial cycle.

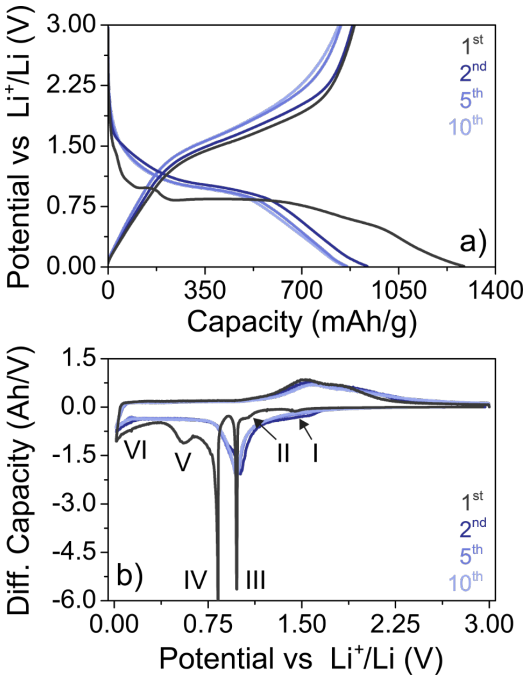


Figure 8: (a) Charge/discharge profiles and (b) corresponding differential capacity curves of ZFO nanoparticle electrodes in Li half-cells. The first two cycles were performed at C/20 and then the rate was increased to C/10 for the subsequent cycles. The Roman numbers in (b) indicate different electrochemical reactions in the initial cycle.

The electrochemical reaction of ZFO with Li can be expressed by $ZnFe_2O_4 + 9Li \rightarrow LiZn + 2Fe + 4Li_2O$. Bresser et al. recently investigated the first cycle lithiation of ZFO nanoparticles by means of in situ XRD and correlated the result with data from charge/discharge measurements [53]. They showed that different reactions (indicated by Roman numbers in the first cycle differential capacity plot in Figure 8b) occur depending

upon the potential, which is consistent with findings of others [54-56]. According to their study, the weak peak (I) at around 1.45 V can be assigned to the reversible insertion of ≈0.4 Li per f.u., while the shoulder peak (II) in the potential range from 1.2 to 1.0 V corresponds to the formation of $Li_{0.9}ZnFe_2O_4$. The sharp peak (III) at 0.98 V (first plateau in Figure 8a) indicates the phase transformation from spinel to rock-salt-type Zn_xFe_yO due to decomposition of $Li_xZnFe_2O_4$ (with $x \approx 1.5$). However, we note that the underlying mechanism is not fully understood yet. The strong peak (IV) at 0.83 V can be attributed to the main conversion reaction (second plateau in Figure 8a), which results in the formation of Zn(0), Fe(0) and Li_2O. The broad peak (V) at 0.55 V has not been observed before and likely arises due to some irreversible reactions associated with the ZFO nanoparticles. The sloping behavior of the curve (VI) below 0.4 V is characteristic of the alloying of Zn with Li [57]. In the subsequent cycles at a rate of C/10, only broad peaks centered at 0.97 V (cathodic) as well as 1.54 V and 1.85 V (anodic) were observed, which agrees with previous studies and the apparent amorphization of the material during the initial cycle [14,53,55].

After the first two cycles at C/20 (Figure 9a), the ZFO nanoparticle electrodes exhibited specific capacities of about 890 mAh/g_{ZFO}, 870 mAh/g_{ZFO} and 770 mAh/g_{ZFO} at C/10, C/5 and C/2, respectively. Regardless of C-rate, they showed some kind of activation with a minimum in specific capacity between cycle number 50 and 80. Such behavior has been observed before for ZFO and other conversion-type anode materials [53,55,58]. The capacity degradation in the subsequent cycles – after the specific capacity had leveled off – was quite small (e.g., 0.017% per cycle at C/10). For the C/2 rate, even an increase in specific capacity by 20 mAh/g_{ZFO} was observed between the 50th and 500th cycle. After 500 cycles, the cell at C/10 rate was still capable of delivering an areal capacity of 1.5 mAh/cm^2. These results were achieved with a non-optimized electrode structure, thereby indicating that high-quality ZFO nanocrystals may, in fact, hold promise for battery applications. We also note that dendrite growth, which was visible in some of the cells, apparently did not strongly affect the cyclability. Figure 9b shows the Coulombic efficiency of the cell cycled at C/5. As evident, the Coulombic efficiency stabilized quickly above 97% after four cycles and then increased steadily up to 99.8% by cycle number 300. This is notable in particular for conversion-type materials in Li half-cells. However, irrespective of the stable cycling performance and high specific capacities, there are still issues, such as relatively large capacity loss in the initial cycle and discontinuous capacity fading, that prevent such materials from becoming a commercial reality.

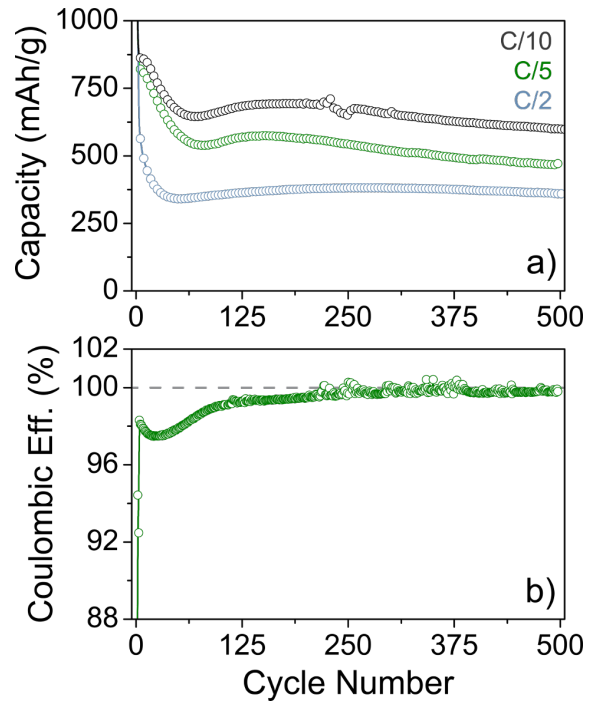


Figure 9: (a) Long-term cycling performance of ZFO nanoparticle electrodes in Li half-cells at C/10 (black), C/5 (green) and C/2 (blue). (b) Coulombic efficiency of the cell cycled at C/5. The dashed line in (b) indicates 100% efficiency. After about 220 cycles, signs of dendrite growth are visible in the curve.

To gain further insight into both the electrochemical reactions of ZFO with Li and the oxidation state of Fe, combined full-field transmission X-ray microscopy (TXM) and X-ray absorption near edge structure (XANES) spectroscopy was conducted on "pristine" and pre-cycled nanoparticle electrodes at the NANO beamline at the ANKA Synchrotron Radiation Facility and the preliminary data are shown in Figure 10 [25]. For these measurements, Li half-cells were disassembled inside an argon-filled glovebox and the obtained electrodes sealed using Kapton tape to maintain airtight conditions. Since XANES imaging is unaffected by the polymer binder, carbon additive, electrolyte and separator residues, the electrodes were used as is, thus ensuring minimal effects from cell disassembly. In the present work, two electrodes of the same batch but at different lithiation states were investigated. The "pristine" electrode was kept at about 3.0 V with respect to Li^+/Li and the other was lithiated until a potential of 0.85 V was reached, which is within the main plateau. FeO (wüstite), Fe_3O_4 (magnetite) and α-Fe_2O_3 (hematite) were used as the reference materials for Fe(II) in cubic and cubic/spinel and Fe(III) in trigonal/hexagonal configuration, respectively. Furthermore, the partially inverted ZFO nanoparticles themselves and α-Fe were used as the reference materials to quantify the amount of spinel-type Fe(III) and for Fe(0), respectively. Figure 10a shows the integrated XANES

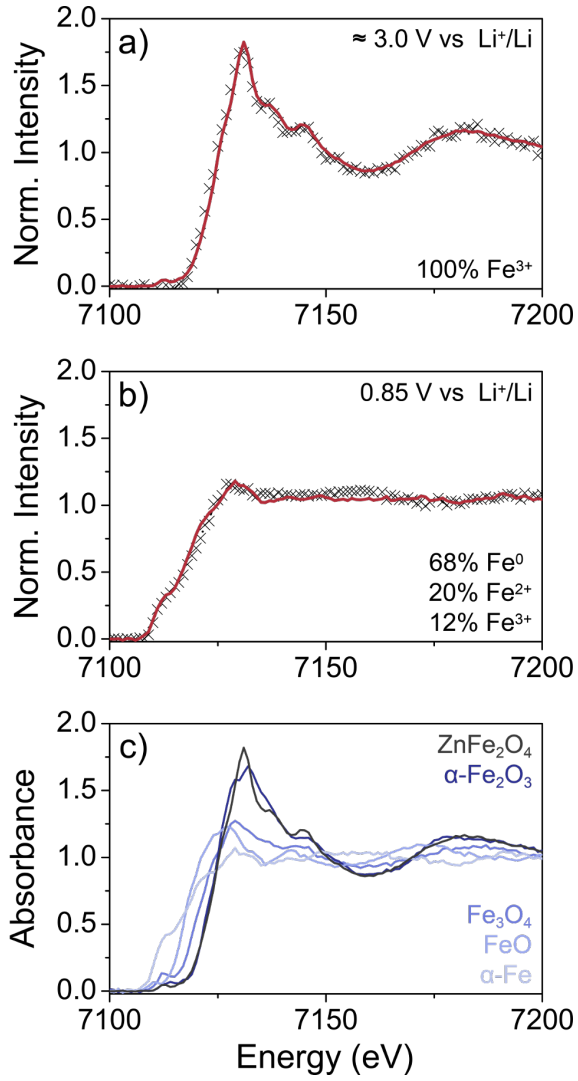


Figure 10: XANES spectra of ZFO nanoparticle electrodes (a) before cycling and (b) in a lithiated state and corresponding least-squares linear combination fits (red lines). (c) XANES reference spectra used for fitting.

spectrum obtained on the "pristine" electrode and the corresponding least-squares linear combination fit. As expected, the fit matches well with the reference material (R = 0.0024, χ^2 = 0.0022), thereby indicating a ZFO content of virtually 100%. The XANES data for the pre-cycled electrode are presented in Figure 10b, where the changes in the integrated spectrum are clearly visible. The fit (R = 0.0021, χ^2 = 0.0017) revealed 12% ZFO, 68% Fe(0) and 20% Fe(II) in cubic configuration. Collectively, these data are in agreement with the conversion of rock-salt-type Zn_xFe_yO to Fe(0), Zn(0) and Li_2O in this potential range. However, further measurements are needed to unambiguously identify the apparently amorphous Fe-based charge/discharge products.

Conclusion

In summary, we have shown that zinc ferrite particles of spherical shape and uniform size around 4 nm in diameter can be prepared by facile microwave synthesis using *rac*-1-phenylethanol as a high-boiling solvent. As evidenced by electron microscopy, X-ray diffraction, X-ray photoelectron spectroscopy and ^{57}Fe Mössbauer spectroscopy, the sol–gel derived material is chemically well-defined and adopts a partially inverted spinel structure. The magnetization results confirm the size monodispersity of the zinc ferrite nanocrystals with low-temperature superspin glass behavior. Furthermore, we have demonstrated that they can be used as a high-capacity conversion-type anode material, showing good long-term cycling performance in Li half-cells. On the basis of the results presented herein, we conclude that the particles are of good quality and thus hold promise for application in various fields of nanotechnology.

Supporting Information

Supporting Information File 1

GC-MS, TGA-MS, Mössbauer spectra, alternating-current magnetometry and Tauc plots of as-prepared ZFO nanoparticles; SEM images of ZFO nanoparticle electrodes.
[http://www.beilstein-journals.org/bjnano/content/supplementary/2190-4286-7-126-S1.pdf]

Acknowledgements

We thank Dr. Leichtweiss, Dr. Schneider and Dr. Marschall for assistance with the XPS, TEM and UV–vis measurements, respectively. We acknowledge the Synchrotron Light Source ANKA for provision of instruments at their beamlines and we would like to thank Dr. Bauer for assistance in using beamline NANO. C.S. and T.B. acknowledge financial support within the SIGNO project (03SHWB073) by the German Federal Ministry for Economic Affairs and Energy (BMWi) and by the German Academic Exchange Service (DAAD), respectively.

References

1. O'Neill, H. S. C.; Navrotsky, A. *Am. Mineral.* **1983,** *68,* 181–194.
2. Hasany, S. F.; Abdurahman, N. H.; Sunarti, A. R.; Jose, R. *Curr. Nanosci.* **2013,** *9,* 561–575. doi:10.2174/15734137113099990085
3. Lu, A.-H.; Salabas, E. L.; Schüth, F. *Angew. Chem., Int. Ed.* **2007,** *46,* 1222–1244. doi:10.1002/anie.200602866
4. Thanh, N. T. K.; Green, L. A. W. *Nano Today* **2010,** *5,* 213–230. doi:10.1016/j.nantod.2010.05.003
5. Ho, D.; Sun, X.; Sun, S. *Acc. Chem. Res.* **2011,** *44,* 875–882. doi:10.1021/ar200090c
6. Priyadharsini, P.; Pradeep, A.; Rao, P. S.; Chandrasekaran, G. *Mater. Chem. Phys.* **2009,** *116,* 207–213. doi:10.1016/j.matchemphys.2009.03.011

7. Lee, J.-G.; Park, J. Y.; Kim, C. S. *J. Mater. Sci.* **1998,** *33,* 3965–3968. doi:10.1023/A:1004696729673
8. Dai, Q.; Berman, D.; Virwani, K.; Frommer, J.; Jubert, P.-O.; Lam, M.; Topuria, T.; Imaino, W.; Nelson, A. *Nano Lett.* **2010,** *10,* 3216–3221. doi:10.1021/nl1022749
9. Sato, T.; Haneda, K.; Seki, M.; Iijima, T. *Appl. Phys. A* **1990,** *50,* 13–16. doi:10.1007/BF00323947
10. Chinnasamy, C. N.; Narayanasamy, A.; Ponpandian, N.; Chattopadhyay, K.; Guérault, H.; Greneche, J.-M. *J. Phys.: Condens. Matter* **2000,** *12,* 7795. doi:10.1088/0953-8984/12/35/314
11. Chinnasamy, C. N.; Narayanasamy, A.; Ponpandian, N.; Joseyphus, R. J.; Chattopadhyay, K.; Shinoda, K.; Jeyadevan, B.; Tohji, K.; Nakatsuka, K.; Greneche, J.-M. *J. Appl. Phys.* **2001,** *90,* 527. doi:10.1063/1.1377297
12. Cabana, J.; Monconduit, L.; Larcher, D.; Palacín, M. R. *Adv. Mater.* **2010,** *22,* E170–E192. doi:10.1002/adma.201000717
13. Lavela, P.; Tirado, J. L. *J. Power Sources* **2007,** *172,* 379–387. doi:10.1016/j.jpowsour.2007.07.055
14. Chu, Y.-Q.; Fu, Z.-W.; Qin, Q.-Z. *Electrochim. Acta* **2004,** *49,* 4915–4921. doi:10.1016/j.electacta.2004.06.012
15. Haetge, J.; Suchomski, C.; Brezesinski, T. *Inorg. Chem.* **2010,** *49,* 11619–11626. doi:10.1021/ic102052r
16. Šepelák, V.; Bergmann, I.; Feldhoff, A.; Heitjans, P.; Krumeich, F.; Menzel, D.; Litterst, F. J.; Campbell, S. J.; Becker, K. D. *J. Phys. Chem. C* **2007,** *111,* 5026–5033. doi:10.1021/jp067620s
17. Lefelshtel, N.; Nadiv, S.; Lin, I. J.; Zimmels, Y. *Powder Technol.* **1978,** *20,* 211–217. doi:10.1016/0032-5910(78)80051-5
18. Masthoff, I.-C.; Gutsche, A.; Nirschl, H.; Garnweitner, G. *CrystEngComm* **2015,** *17,* 2464–2470. doi:10.1039/C4CE02068E
19. Jeong, U.; Teng, X.; Wang, Y.; Yang, H.; Xia, Y. *Adv. Mater.* **2007,** *19,* 33–60. doi:10.1002/adma.200600674
20. Park, J.; Joo, J.; Kwon, S. G.; Jang, Y.; Hyeon, T. *Angew. Chem., Int. Ed.* **2007,** *46,* 4630–4660. doi:10.1002/anie.200603148
21. Jun, Y.-w.; Choi, J.-s.; Cheon, J. *Angew. Chem., Int. Ed.* **2006,** *45,* 3414–3439. doi:10.1002/anie.200503821
22. Bilecka, I.; Kubli, M.; Amstad, E.; Niederberger, M. *J. Sol-Gel Sci. Technol.* **2011,** *57,* 313–322. doi:10.1007/s10971-010-2165-1
23. Kubli, M.; Luo, L.; Bilecka, I.; Niederberger, M. *Chimia* **2010,** *64,* 170–172. doi:10.2533/chimia.2010.170
24. Brand, R. A. *WinNormos-for-Igor Users Manual 2.0l*; 2006.
25. Bauer, S.; de Biasi, L.; Glatthaar, S.; Toukam, L.; Geßwein, H.; Baumbach, T. *Phys. Chem. Chem. Phys.* **2015,** *17,* 16388–16397. doi:10.1039/C5CP02075A
26. Liu, Y.; Meirer, F.; Williams, P. A.; Wang, J.; Andrews, J. C.; Pianetta, P. *J. Synchrotron Radiat.* **2012,** *19,* 281–287. doi:10.1107/S0909049511049144
27. O'Neill, H. S. C. *Eur. J. Mineral.* **1992,** *4,* 571–580. doi:10.1127/ejm/4/3/0571
28. Verwey, E. J. W.; Heilmann, E. L. *J. Chem. Phys.* **1947,** *15,* 174–180. doi:10.1063/1.1746464
29. Schäfer, W.; Kockelmann, W. A.; Kirfel, A.; Potzel, W.; Burghart, F. J.; Kalvius, G. M.; Martin, A.; Kaczmarek, W. A.; Campbell, S. J. *Mater. Sci. Forum* **2000,** *321–324,* 802–807. doi:10.4028/www.scientific.net/MSF.321-324.802
30. Hofmann, M.; Campbell, S. J.; Ehrhardt, H.; Feyerherm, R. *J. Mater. Sci.* **2004,** *39,* 5057–5065. doi:10.1023/B:JMSC.0000039185.80910.59
31. Hamdeh, H. H.; Ho, J. C.; Oliver, S. A.; Willey, R. J.; Oliveri, G.; Busca, G. *J. Appl. Phys.* **1997,** *81,* 1851–1857. doi:10.1063/1.364068
32. Reitz, C.; Suchomski, C.; Haetge, J.; Leichtweiss, T.; Jagličić, Z.; Djerdj, I.; Brezesinski, T. *Chem. Commun.* **2012,** *48,* 4471–4473. doi:10.1039/c2cc31006f
33. Yamashita, T.; Hayes, P. *Appl. Surf. Sci.* **2008,** *254,* 2441–2449. doi:10.1016/j.apsusc.2007.09.063
34. Grosvenor, A. P.; Kobe, B. A.; Biesinger, M. C.; McIntyre, N. S. *Surf. Interface Anal.* **2004,** *36,* 1564–1574. doi:10.1002/sia.1984
35. Reitz, C.; Suchomski, C.; Chakravadhanula, V. S. K.; Djerdj, I.; Jagličić, Z.; Brezesinski, T. *Inorg. Chem.* **2013,** *52,* 3744–3754. doi:10.1021/ic302283q
36. Šepelák, V.; Becker, K. D. *Mater. Sci. Eng., A* **2004,** *375–377,* 861–864. doi:10.1016/j.msea.2003.10.178
37. Druska, P.; Steinike, U.; Šepelák, V. *J. Solid State Chem.* **1999,** *146,* 13–21. doi:10.1006/jssc.1998.8284
38. Suzuki, M.; Fullem, S. I.; Suzuki, I. S.; Wang, L.; Zhong, C.-J. *Phys. Rev. B* **2009,** *79,* 024418. doi:10.1103/PhysRevB.79.024418
39. Bedanta, S.; Kleemann, W. *J. Phys. D: Appl. Phys.* **2009,** *42,* 013001. doi:10.1088/0022-3727/42/1/013001
40. Chinnasamy, C. N.; Narayanasamy, A.; Ponpandian, N.; Chattopadhyay, K.; Shinoda, K.; Jeyadevan, B.; Tohji, K.; Nakatsuka, K.; Furubayashi, T.; Nakatani, I. *Phys. Rev. B* **2001,** *63,* 184108. doi:10.1103/PhysRevB.63.184108
41. Cador, O.; Grasset, F.; Haneda, H.; Etourneau, J. *J. Magn. Magn. Mater.* **2004,** *268,* 232–236. doi:10.1016/S0304-8853(03)00504-3
42. Binder, K.; Young, A. P. *Rev. Mod. Phys.* **1986,** *58,* 801–976. doi:10.1103/RevModPhys.58.801
43. Neel, L. *Ann. Geophys. (C. N. R. S.)* **1949,** *5,* 99–136.
44. Goldfarb, R. B.; Patton, C. E. *Phys. Rev. B* **1981,** *24,* 1360–1373. doi:10.1103/PhysRevB.24.1360
45. Nadeem, K.; Krenn, H.; Traussnig, T.; Würschum, R.; Szabó, D. V.; Letofsky-Papst, I. *J. Appl. Phys.* **2012,** *111,* 113911. doi:10.1063/1.4724348
46. Tackett, R. J.; Parsons, J. G.; Machado, B. I.; Gaytan, S. M.; Murr, L. E.; Botez, C. E. *Nanotechnology* **2010,** *21,* 365703. doi:10.1088/0957-4484/21/36/365703
47. Shtrikman, S.; Wohlfarth, E. P. *Phys. Lett. A* **1981,** *85,* 467–470. doi:10.1016/0375-9601(81)90441-2
48. Ying, Y.; Eom, T. W.; Lee, Y. P.; Ling, L. S.; Mathe, V. L. *J. Appl. Phys.* **2010,** *108,* 023911. doi:10.1063/1.3457223
49. Nunes, W. C.; Folly, W. S. D.; Sinnecker, J. P.; Novak, M. A. *Phys. Rev. B* **2004,** *70,* 014419. doi:10.1103/PhysRevB.70.014419
50. Knobel, M.; Nunes, W. C.; Socolovsky, L. M.; De Biasi, E.; Vargas, J. M.; Denardin, J. C. *J. Nanosci. Nanotechnol.* **2008,** *8,* 2836–2857. doi:10.1166/jnn.2008.017
51. Gao, D.; Shi, Z.; Xu, Y.; Zhang, J.; Yang, G.; Zhang, J.; Wang, X.; Xue, D. *Nanoscale Res. Lett.* **2010,** *5,* 1289–1294. doi:10.1007/s11671-010-9640-z
52. Cheng, C. *Phys. Rev. B* **2008,** *78,* 132403. doi:10.1103/PhysRevB.78.132403
53. Bresser, D.; Paillard, E.; Kloepsch, R.; Krueger, S.; Fiedler, M.; Schmitz, R.; Baither, D.; Winter, M.; Passerini, S. *Adv. Energy Mater.* **2013,** *3,* 513–523. doi:10.1002/aenm.201200735
54. Ding, Y.; Yang, Y.; Shao, H. *Electrochim. Acta* **2011,** *56,* 9433–9438. doi:10.1016/j.electacta.2011.08.031
55. Won, J. M.; Choi, S. H.; Hong, Y. J.; Ko, Y. N.; Kang, Y. C. *Sci. Rep.* **2014,** *4,* No. 5857. doi:10.1038/srep05857

56. Guo, X.; Lu, X.; Fang, X.; Mao, Y.; Wang, Z.; Chen, L.; Xu, X.; Yang, H.; Liu, Y. *Electrochem. Commun.* **2010,** *12,* 847–850. doi:10.1016/j.elecom.2010.04.003
57. Wang, J.; King, P.; Huggins, R. A. *Solid State Ionics* **1986,** *20,* 185–189. doi:10.1016/0167-2738(86)90212-2
58. Ren, S.; Prakash, R.; Wang, D.; Chakravadhanula, V. S. K.; Fichtner, M. *ChemSusChem* **2012,** *5,* 1397–1400. doi:10.1002/cssc.201200139

License and Terms

This is an Open Access article under the terms of the Creative Commons Attribution License (http://creativecommons.org/licenses/by/4.0), which permits unrestricted use, distribution, and reproduction in any medium, provided the original work is properly cited.

The license is subject to the *Beilstein Journal of Nanotechnology* terms and conditions: (http://www.beilstein-journals.org/bjnano)

The definitive version of this article is the electronic one which can be found at: doi:10.3762/bjnano.7.126

BEILSTEIN JOURNAL OF NANOTECHNOLOGY

Deformation-driven catalysis of nanocrystallization in amorphous Al alloys

Rainer J. Hebert*[1], John H. Perepezko[2], Harald Rösner[3] and Gerhard Wilde[3]

Letter

Open Access

Address:
[1]Department of Materials Science and Engineering, University of Connecticut, Storrs, 97 N Eagleville Rd., Storrs, CT 06269, USA, [2]Department of Materials Science and Engineering, University of Wisconsin-Madison, 1509 University Avenue, Madison, Wisconsin, 53706, USA and [3]Institut für Materialphysik, Universität Münster, Wilhelm-Klemm Str. 10, 48149 Münster, Germany

Email:
Rainer J. Hebert* - rainer.hebert@uconn.edu

* Corresponding author

Keywords:
amorphous alloy; annealing; cold-rolling; nanocrystal; shear-band

Beilstein J. Nanotechnol. **2016,** *7,* 1428–1433.
doi:10.3762/bjnano.7.134

Received: 15 June 2016
Accepted: 16 September 2016
Published: 11 October 2016

This article is part of the Thematic Series "Advances in nanomaterials II".

Guest Editor: H. Hahn

© 2016 Hebert et al.; licensee Beilstein-Institut.
License and terms: see end of document.

Abstract

Nanocrystals develop in amorphous alloys usually during annealing treatments with growth- or nucleation-controlled mechanisms. An alternative processing route is intense deformation and nanocrystals have been shown to develop in shear bands during the deformation process. Some controversy surrounded the idea of adiabatic heating in shear bands during their genesis, but specific experiments have revealed that the formation of nanocrystals in shear bands has to be related to localized deformation rather than thermal effects. A much less debated issue has been the spatial distribution of deformation in the amorphous alloys during intense deformation. The current work examines the hypothesis that intense deformation affects the regions outside shear bands and even promotes nanocrystal formation in those regions upon annealing. Melt-spun amorphous $Al_{88}Y_7Fe_5$ alloy was intensely cold rolled. Microcalorimeter measurements at 60 °C indicated a slight but observable growth of nanocrystals in shear bands over the annealing time of 10 days. When the cold-rolled samples were annealed at 210 °C for one hour, transmission electron images did not show any nanocrystals for as-spun ribbons, but nanocrystals developed outside shear bands for the cold rolled samples. X-ray analysis indicated an increase in intensity of the Al peaks following the 210 °C annealing while the as-spun sample remained “X-ray amorphous”. These experimental observations strongly suggest that cold rolling affects regions (i.e., spatial heterogeneities) outside shear bands and stimulates the formation of nanocrystals during annealing treatments at temperatures well below the crystallization temperature of undeformed ribbons.

Findings

Crystallization reactions in metallic glasses have been extensively studied due to the beneficial effect of nanocrystal dispersions on mechanical [1-4] and magnetic properties [5-8], but also as experimental case studies for nucleation and growth theories [9-11]. The devitrification of metallic glasses is commonly considered as a thermally activated process, but some

glassy alloys crystallize during intense deformation at temperatures well below the glass transition temperature. Examples of deformation-induced crystallization reactions include Fe-based amorphous alloys [12-16], amorphous Ni–P alloy [17], bulk amorphous Zr and Cu–Zr alloys, and amorphous Al alloys [18-22]. The deformation techniques used so far include bending [23], ball milling [14-16,24], cold rolling [12,25-32], high-pressure torsion straining [18,33], nanoindentation [34], and uniaxial compression [35]. The results of intense deformation have demonstrated nanocrystals with number densities of up to 10^{22} m^{-3} and average sizes of less than 10 nm, but the origin of the deformation-driven nanocrystallization remains an area of active research. Intense deformation in metallic glasses occurs in shear bands at stress levels of more than about 30% of the shear modulus and at temperatures of below approximately $0.7 \cdot T_g$ [36]. If intense deformation can induce nanocrystals in some amorphous alloys and the intense deformation occurs within shear bands, a key question then is how the nanocrystal formation is related to the shear bands. Literature results clearly point toward the formation of nanocrystals within shear bands [37] and the shear band crystallization can be motivated with enhanced mobility within the shear bands [37] and the localization of atomic motion within shear bands [38]. Comparatively little is known, however, about the effect of intense deformation on the amorphous phase surrounding the shear bands. The common conception is that the amorphous matrix remains unchanged during deformation [3]. On the other hand, Gupta concluded based on Mössbauer spectroscopy of an Fe-based amorphous alloy after cold rolling that the deformation-induced atomic rearrangements exist throughout the entire sample and not only in shear bands [39]. This letter yields further evidence that intense deformation does indeed affect the regions between shear bands and even promotes crystallization in non-shear band regions.

Melt-spun amorphous $Al_{88}Y_7Fe_5$ alloy was annealed in a TAM microcalorimeter (TA Instruments) at 60 °C, i.e., about 200 K below the glass-transition temperature [40]. The isothermal microcalorimeter trace of the as-spun ribbon shown in Figure 1 demonstrates that during the annealing time of 10 days the heat flux reaches a plateau with fluctuations on the order of approximately 7 nW/g. The trace for the as-spun ribbon represents the instrument baseline. If the same amorphous $Al_{88}Y_7Fe_5$ alloy is cold-rolled at room temperature to $\varepsilon_{true} = -3$ at a strain rate of 0.1 s^{-1}, the same microcalorimeter measurement reveals a clear exothermic heat release as also shown in Figure 1. The total heat release (hatched area in Figure 1) amounts to about 2 J/g. The dark-field (DF) TEM analysis of both samples, the cold-rolled sample and the cold-rolled sample after annealing in the microcalorimeter, shows clear evidence of nanocrystals in shear bands of both samples (Figure 2). The TEM images shown in this work were obtained from samples prepared by grinding, polishing, and electrolytic thinning with dilute perchloric acid. The nanocrystals in the partially devitrified $Al_{88}Y_7Fe_5$ alloy have been identified as Al nanocrystals [40]. The size distribution analysis of the Al nanocrystals inside the shear bands of the rolled sample before and after the annealing, which is depicted in Figure 3 reveals a small but definite shift in the size distribution after the annealing. The size of the nanocrystals could be determined with an uncertainty of approximately 1 nm. The error bars in Figure 3 show that despite the measurement uncertainty, a trend of nanocrystal growth behavior is evident. The size measurement for the size distribution in Figure 3 refers to the longest projected diameter.

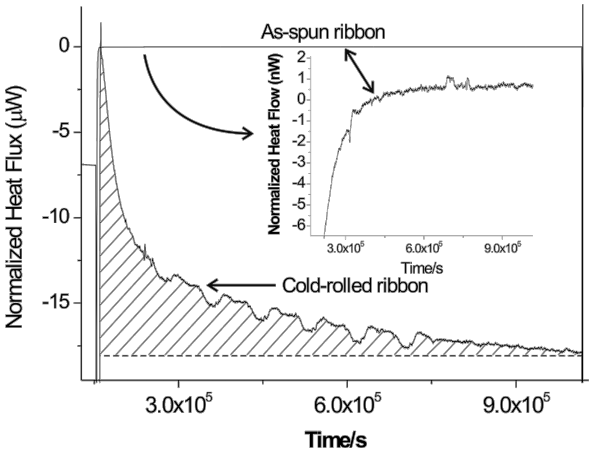


Figure 1: Isothermal microcalorimeter trace at 60 °C for as-spun and cold-rolled ribbons. The inset shows the trace of the as-spun ribbon at a scale of nanowatts.

The difference between the as-spun and the cold-rolled samples after annealing at 60 °C seems at first glance to be limited to the formation of shear bands and nanocrystals inside the shear bands of the deformed sample. Possible atomic rearrangements resulting from the intense deformation outside shear bands are difficult to detect with electron microscopy. But if it is hypothesized that the deformation locally rearranges atoms to promote the formation of nanocrystals, then an adequate probe for the hypothesis should be additional annealing treatments. If the intensely deformed samples are annealed at temperatures much below the crystallization onset temperature of the as-spun material, deformation outside of shear bands might trigger the formation of nanocrystals during the annealing treatment. The continuous heating differential scanning calorimetry (DSC) trace of a cold-rolled $Al_{88}Y_7Fe_5$ ribbon that is depicted in Figure 4 shows that the onset temperature for the primary crystallization reaction is approximately 175 °C for the cold-rolled sample. By comparison, the undeformed amorphous $Al_{88}Y_7Fe_5$ alloy

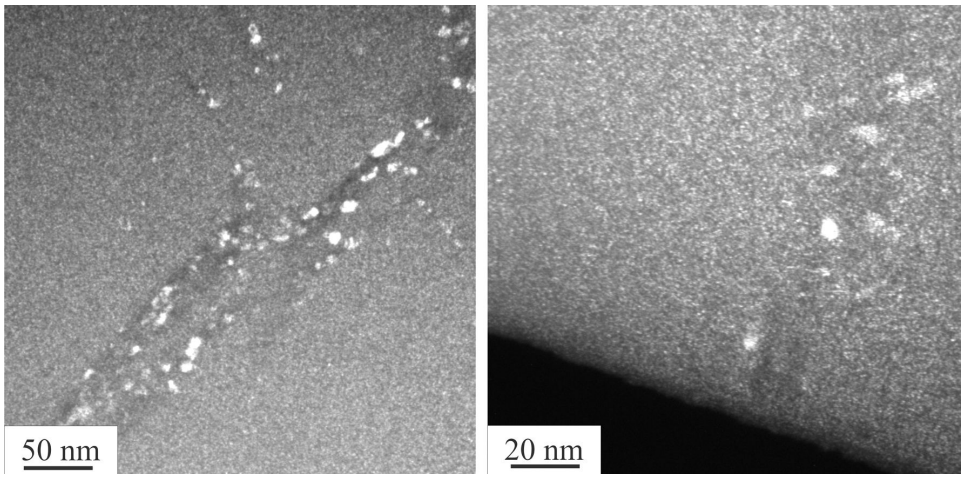


Figure 2: Dark field TEM analysis of cold-rolled (left) and cold-rolled and annealed samples. The sample was annealed at 60 °C for 10 days (right).

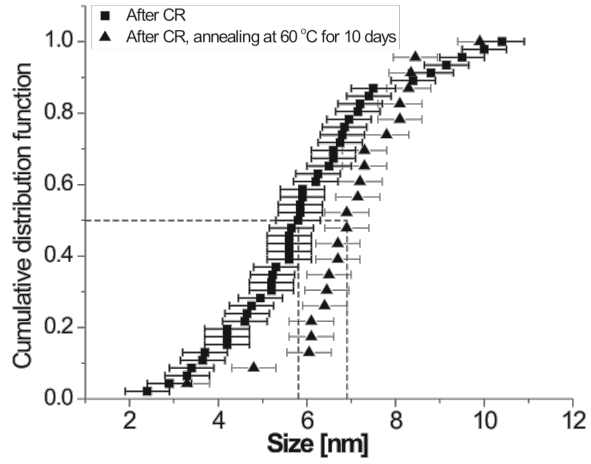


Figure 3: The cumulative size distribution for Al nanocrystals inside shear bands. Square markers represent measurements on samples that were only cold-rolled. Triangular markers represent samples that were cold-rolled and annealed at 60 °C for 10 days.

reveals a primary crystallization onset temperature of approximately 260 °C. Cold-rolled $Al_{88}Y_7Fe_5$ ribbons were annealed at 210 °C for 10 min and were subsequently analyzed with X-ray diffraction (XRD) and with transmission electron microscopy. The comparison between the different XRD curves depicted in Figure 5 shows an increase in the intensity of the Al peaks after annealing of the cold-rolled sample. An as-spun sample, on the other hand, remained X-ray amorphous after annealing for 10 min at 225 °C. The dark-field TEM image in Figure 6 shows that nanocrystals have developed homogeneously throughout the deformed sample rather than in localized regions. Shear bands are not detected in the dark-field TEM images after the annealing. With shear band distances of the order of micrometers [41] and good contrast between shear bands and matrix in Al-based amorphous alloys [42], it can therefore be concluded that the nanocrystals in Figure 6 that are observed after the annealing at 210 °C developed in the matrix and not in shear bands.

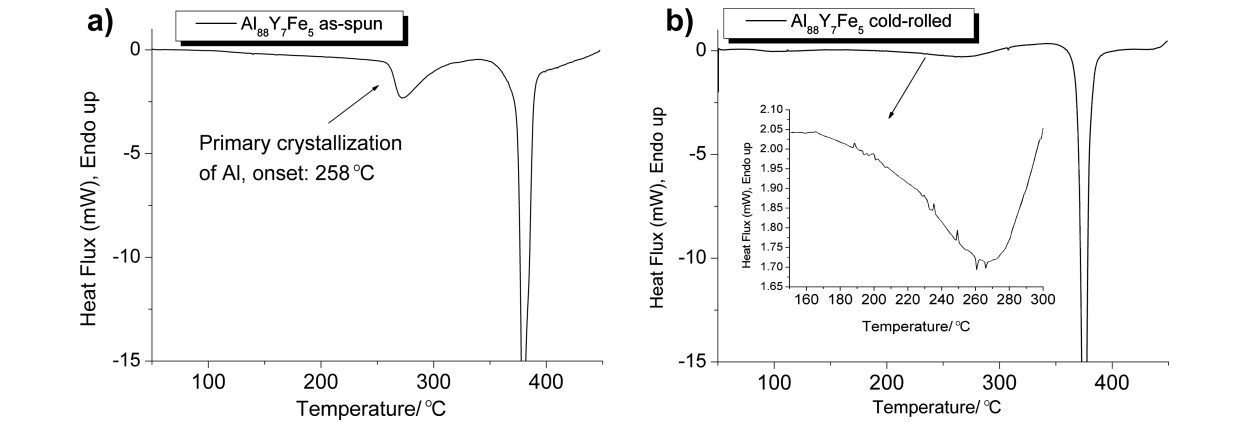


Figure 4: (a) DSC trace for an as-spun $Al_{88}Y_7Fe_5$ ribbon sample. (b) DSC trace for the cold-rolled $Al_{88}Y_7Fe_5$ ribbon sample. The inset shows the primary crystallization range after cold rolling. The heating rate was 20 K/min for both measurements.

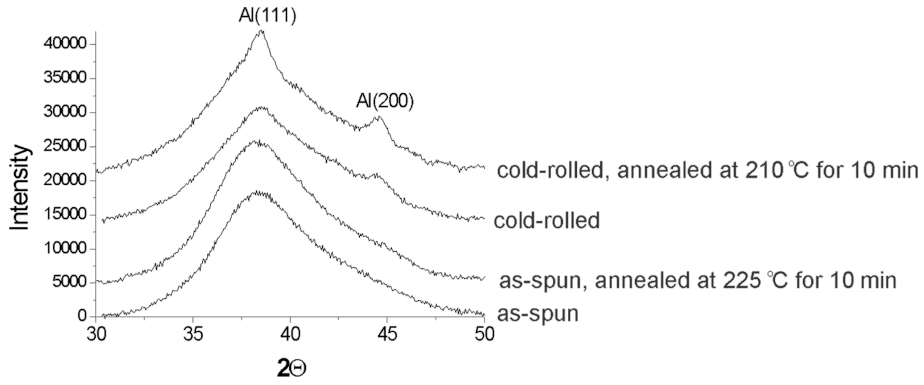


Figure 5: XRD results showing an increase in intensity of the Al peaks after annealing of a cold-rolled sample.

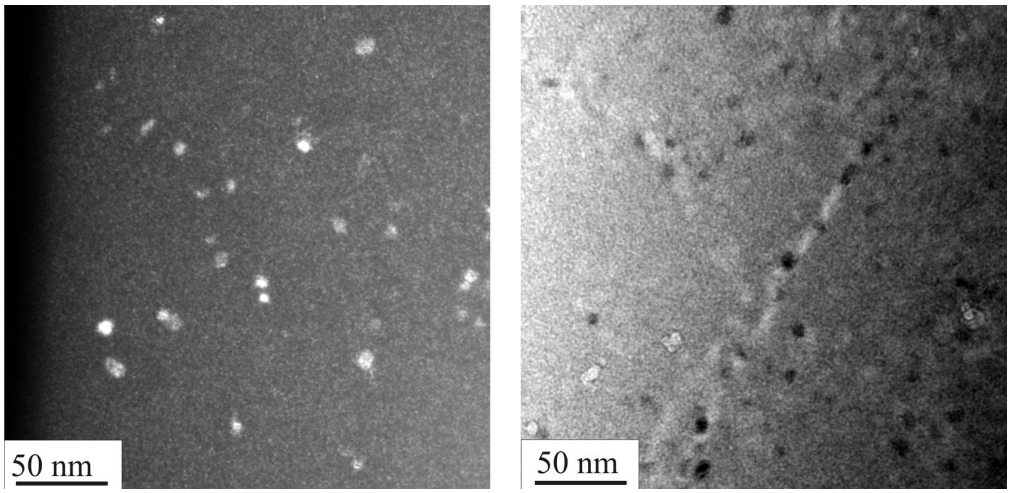


Figure 6: DF TEM (left) and BF TEM (right) after 210 °C anneal of cold-rolled sample.

The combination of HRTEM, DF-TEM, XRD, and DSC results provides strong evidence that cold-rolling does promote crystallization outside shear bands at annealing temperatures that are insufficient to induce crystallization for undeformed samples. This cold-rolling enabled crystallization upon annealing in regions outside shear bands could be perceived of as a result of heating due to the temperature spikes in the shear bands. The localized heating in the shear band would spread into the adjacent matrix and promote crystallization. The question of adiabatic heating in shear bands during deformation has been discussed in the literature quite extensively. Evidence was provided for temperature spikes with shear band formation [43], but models were also developed that demonstrated stick–slip of shear bands and "cold" temperatures in the shear bands [44]. The findings on temperature behavior in shear bands of metallic glasses over the last years were summarized by Greer, Cheng, and Ma [45]. One of the major findings of recent years was that heating occurs as a result of shear-banding but not as a reason for the formation of shear bands. It was also found that the heating in shear bands is not truly adiabatic, but extends beyond the regions that can be identified as shear bands in images after deformation [45]. Additional evidence in the current work for a limited temperature rise at shear bands comes from the TEM images of deformed samples: The regions adjacent to the shear bands are just amorphous without any evidence for a gradual transition from a nanocrystal-populated zone toward an amorphous zone that would be expected if the shear bands were heat sources. If shear band heating cannot account for the observed annealing response of cold-rolled $Al_{88}Y_7Fe_5$ ribbons, a plausible conclusion is that regions outside shear bands are affected by the cold rolling and induce atomic rearrangements that promote nanocrystal formation during subsequent annealing. This conclusion resonates with earlier literature results. Inoue and coworkers, for example, explained the changes in superconducting properties of their $Nb_{50}Zr_{35}Si_{15}$ metallic glass after cold rolling with deformation-induced structural rearrange-

ments that occurred not only in shear bands, but also in the region between the shear bands [46]. Argon [47] and Steif [48] demonstrated that shear localization was preceded by homogeneous plastic flow. Cahn and co-workers concluded based on density changes that plastic deformation of a metallic glass leads to a distribution of free volume intermediate between a complete localization and a completely uniform distribution [49]. More recent work by Stolpe and coworkers demonstrated that based on measured shear band densities and exothermic heat releases during heating, free volume changes must have occurred throughout the metallic glass during cold rolling and not only within shear bands [50]. Recent measurements of time-dependent tracer diffusion along shear bands that showed a non-monotonic behavior with an initial increase of the diffusivity upon relaxation moreover suggest that regions in the matrix adjacent to the shear bands are affected by the deformation [51]. It is also in line with measurements of internal friction in a bulk metallic glass, where early irreversible events upon cyclic straining have been observed at strain levels lower than 0.001. In that study, it was also shown that straining the glassy material at room temperature led to a significant shift of the crystallization onset temperature, even though the crystallization occurred several tens degrees above the glass transition [52]. These results support the current results and highlight the importance of local irreversible re-configurations concerning the early stages of yielding of metallic glasses, but also stress their importance concerning the onset of crystal formation. The genesis of nanocrystals during intense deformation raises intriguing questions, for example, about the impact of deformation on quenched-in spatial heterogeneities and the indirect impact on thermally induced mechanisms such as nucleation and growth during annealing as well as concerning their possible coupling in an externally applied stress field.

Acknowledgements

It is a pleasure for us to honor Professor Herbert Gleiter on his 75th birthday. We are most grateful for his keen insight, novel ideas, great enthusiasm, wise counsel, warm and pleasant personality and encouragement. JHP is privileged to have his friendship over the past four decades.

The support of ONR (N99914-16-1-2401) and the Alexander von Humboldt Stiftung for JHP and the DFG for GW is gratefully acknowledged.

References

1. Inoue, A.; Ohtera, K.; Tsai, A.-P.; Masumoto, T. *Jpn. J. Appl. Phys., Part 2* **1988,** *27,* 479–482. doi:10.1143/JJAP.27.L479
2. Masumoto, T.; Maddin, R. *Mater. Sci. Eng.* **1975,** *19,* 1–24. doi:10.1016/0025-5416(75)90002-6
3. Schuh, C. A.; Hufnagel, T. C.; Ramamurty, U. *Acta Mater.* **2007,** *55,* 4067–4109. doi:10.1016/j.actamat.2007.01.052
4. Yeong-Hwan, K.; Inoue, A.; Masumoto, T. *Mater. Trans., JIM* **1991,** *32,* 599–608.
5. Hasegawa, R. *Mater. Sci. Eng., A* **2004,** *375–377,* 90–97. doi:10.1016/j.msea.2003.10.258
6. Heil, T. M.; Wahl, K. J.; Lewis, A. C.; Mattison, J. D.; Willard, M. A. *Appl. Phys. Lett.* **2007,** *90,* 212508. doi:10.1063/1.2742598
7. McHenry, M. E.; Willard, M. A.; Laughlin, D. E. *Prog. Mater. Sci.* **1999,** *44,* 291–433. doi:10.1016/S0079-6425(99)00002-X
8. Willard, M. A.; Harris, V. G. *JOM* **2002,** *54,* 44–46. doi:10.1007/BF02822620
9. Kelton, K. F. *Philos. Mag. Lett.* **1998,** *77,* 337–343. doi:10.1080/095008398178318
10. Perepezko, J. H.; Hebert, R. J.; Tong, W. S. *Intermetallics* **2002,** *10,* 1079–1088. doi:10.1016/S0966-9795(02)00144-9
11. Drehman, A. J.; Greer, A. L. *Acta Metall.* **1984,** *32,* 323–332. doi:10.1016/0001-6160(84)90105-6
12. Noskova, N. I.; Vil'danova, N. F.; Tagirov, R. I.; Potapov, A. P.; Glazer, A. A. *Phys. Met. Metallogr.* **1989,** *67,* 136–143.
13. Pak, H.-R.; Chu, J.; Deangelis, R. J.; Okazaki, K. *Mater. Sci. Eng., A* **1989,** *118,* 147–153. doi:10.1016/0921-5093(89)90067-1
14. Schulz, R.; Trudeau, M. L.; Dussault, D.; Van Neste, A. *Colloq. Phys.* **1990,** *51,* 259–264. doi:10.1051/jphyscol:1990431
15. Xu, J.; Atzmon, M. *Appl. Phys. Lett.* **1998,** *73,* 1805–1807. doi:10.1063/1.122288
16. Fan, G. J.; Song, X. P.; Quan, M. X.; Hu, Z. Q. *Nanostruct. Mater.* **1995,** *5,* 433–440. doi:10.1016/0965-9773(95)00255-D
17. Ogura, A.; Tarumi, R.; Shimojo, M.; Takashima, K.; Higo, Y. *Appl. Phys. Lett.* **2001,** *79,* 1042–1044. doi:10.1063/1.1395526
18. Boucharat, N.; Hebert, R.; Rösner, H.; Valiev, R.; Wilde, G. *Scr. Mater.* **2005,** *53,* 823–828. doi:10.1016/j.scriptamat.2005.06.004
19. Perepezko, J. H.; Hebert, R. J. *JOM* **2002,** *54,* 34. doi:10.1007/BF02822618
20. Jiang, W. H.; Pinkerton, F. E.; Atzmon, M. *J. Mater. Res.* **2005,** *20,* 696–702. doi:10.1557/JMR.2005.0090
21. Perepezko, J. H.; Imhoff, S. D.; Hebert, R. J. *J. Alloys Compd.* **2010,** *495,* 360–364. doi:10.1016/j.jallcom.2009.10.051
22. Chen, H.; He, Y.; Shiflet, G. J.; Poon, S. J. *Nature* **1994,** *367,* 541–543. doi:10.1038/367541a0
23. Ogura, A.; Sato, M.; Tarumi, R.; Shimojo, M.; Takashima, K.; Higo, Y. *MRS Online Proc. Libr.* **2001,** *634,* B1. doi:10.1557/PROC-634-B1.10.1
24. He, Y.; Shiflet, G. J.; Poon, S. J. *Acta Metall. Mater.* **1995,** *43,* 83–91. doi:10.1016/0956-7151(95)90264-3
25. Koike, J.; Parkin, D. M.; Nastasi, M. *J. Mater. Res.* **1990,** *5,* 1414–1418. doi:10.1557/JMR.1990.1414
26. Hebert, R. J.; Perepezko, J. H. *Mater. Sci. Eng., A* **2004,** *375–377,* 728–732. doi:10.1016/j.msea.2003.10.059
27. Takahara, Y.; Matsuda, H. *Trans. Jpn. Inst. Met.* **1987,** *28,* 535–541. doi:10.2320/matertrans1960.28.535
28. Louzguine-Luzgin, D. V.; Inoue, A. *J. Non-Cryst. Solids* **2006,** *352,* 3903–3909. doi:10.1016/j.jnoncrysol.2006.06.022
29. Nakayama, H.; Tsuchiya, K.; Liu, Z.-G.; Umemoto, M.; Morii, K.; Shimizu, T. *Mater. Trans.* **2001,** *42,* 1987–1993. doi:10.2320/matertrans.42.1987
30. Cao, Q. P.; Li, J. F.; Zhou, Y. H.; Horsewell, A.; Jiang, J. Z. *Acta Mater.* **2006,** *54,* 4373–4383. doi:10.1016/j.actamat.2006.05.030
31. Jin, H. J.; Zhou, F.; Wang, L. B.; Lu, K. *Scr. Mater.* **2001,** *44,* 1083–1087. doi:10.1016/S1359-6462(01)00656-X

32. Gupta, A.; Lal, S.; Verma, R. P. *J. Appl. Phys.* **1984,** *56,* 3485–3489. doi:10.1063/1.333900
33. Révész, Á.; Hóbor, S.; Szabó, P. J.; Zhilyaev, A. P.; Kovács, Zs. *Mater. Sci. Eng., A* **2007,** *460–461,* 459–463. doi:10.1016/j.msea.2007.01.081
34. Kim, J.-J.; Choi, Y.; Suresh, S.; Argon, A. S. *Science* **2002,** *295,* 654–657. doi:10.1126/science.1067453
35. Lee, S.-W.; Huh, M.-Y.; Chae, S.-W.; Lee, J.-C. *Scr. Mater.* **2006,** *54,* 1439–1444. doi:10.1016/j.scriptamat.2006.01.002
36. Spaepen, F. *Acta Metall.* **1977,** *25,* 407–415. doi:10.1016/0001-6160(77)90232-2
37. Wilde, G.; Rösner, H. *Appl. Phys. Lett.* **2011,** *98,* 251904. doi:10.1063/1.3602315
38. Bokeloh, J.; Divinski, S. V.; Reglitz, G.; Wilde, G. *Phys. Rev. Lett.* **2011,** *107,* 235503. doi:10.1103/PhysRevLett.107.235503
39. Kane, S. N.; Gupta, A.; Varga, L. K. *J. Magn. Magn. Mater.* **2003,** *254–255,* 501–503. doi:10.1016/S0304-8853(02)00851-X
40. Allen, D. R.; Foley, J. C.; Perepezko, J. H. *Acta Mater.* **1998,** *46,* 431–440. doi:10.1016/S1359-6454(97)00279-6
41. Liu, J. W.; Cao, Q. P.; Chen, L. Y.; Wang, X. D.; Jiang, J. Z. *Acta Mater.* **2010,** *58,* 4827–4840. doi:10.1016/j.actamat.2010.05.018
42. Schmidt, V.; Rösner, H.; Peterlechner, M.; Wilde, G.; Voyles, P. M. *Phys. Rev. Lett.* **2015,** *115,* 035501. doi:10.1103/PhysRevLett.115.035501
43. Lewandowski, J. J.; Greer, A. L. *Nat. Mater.* **2006,** *5,* 15–18. doi:10.1038/nmat1536
44. Cheng, Y. Q.; Han, Z.; Li, Y.; Ma, E. *Phys. Rev. B* **2009,** *B80,* 134115–134118. doi:10.1103/PhysRevB.80.134115
45. Greer, A. L.; Cheng, Y. Q.; Ma, E. *Mater. Sci. Eng., R* **2013,** *74,* 71–132. doi:10.1016/j.mser.2013.04.001
46. Inoue, A.; Okamoto, S.; Masumoto, T.; Chen, H. S. *Scr. Metall.* **1982,** *16,* 1393–1396. doi:10.1016/0036-9748(82)90434-3
47. Argon, A. S. *Acta Metall.* **1979,** *27,* 47–58. doi:10.1016/0001-6160(79)90055-5
48. Steif, P. S.; Spaepen, F.; Hutchinson, J. W. *Acta Metall.* **1982,** *30,* 447–455. doi:10.1016/0001-6160(82)90225-5
49. Cahn, R. W.; Pratten, N. A.; Scott, M. G.; Sinning, H. R.; Leonardsson, L. *Mater. Res. Soc. Symp. Proc.* **1984,** *28,* 241–252. doi:10.1557/PROC-28-241
50. Stolpe, M.; Kruzic, J. J.; Busch, R. *Acta Mater.* **2013,** *64,* 231–240. doi:10.1016/j.actamat.2013.10.035
51. Binkowski, I.; Shrivastav, G. P.; Horbach, J.; Divinski, S. V.; Wilde, G. *Acta Mater.* **2016,** *109,* 330–340. doi:10.1016/j.actamat.2016.02.061
52. Mitrofanov, Yu. P.; Peterlechner, M.; Binkowski, I.; Zadorozhnyy, M. Yu.; Golovin, I. S.; Divinski, S. V.; Wilde, G. *Acta Mater.* **2015,** *90,* 318–329. doi:10.1016/j.actamat.2015.03.001

License and Terms

This is an Open Access article under the terms of the Creative Commons Attribution License (http://creativecommons.org/licenses/by/4.0), which permits unrestricted use, distribution, and reproduction in any medium, provided the original work is properly cited.

The license is subject to the *Beilstein Journal of Nanotechnology* terms and conditions: (http://www.beilstein-journals.org/bjnano)

The definitive version of this article is the electronic one which can be found at: doi:10.3762/bjnano.7.134

BEILSTEIN JOURNAL OF NANOTECHNOLOGY

The effect of dry shear aligning of nanotube thin films on the photovoltaic performance of carbon nanotube–silicon solar cells

Benedikt W. Stolz[1,2], Daniel D. Tune[1,3] and Benjamin S. Flavel[*1]

Full Research Paper

Open Access

Address:
[1]Institute of Nanotechnology, Karlsruhe Institute of Technology, 76021 Karlsruhe, Germany, [2]Department of Physics, Karlsruhe Institute of Technology, 76131 Karlsruhe, Germany and [3]Centre for Nanoscale Science and Technology, The Flinders University of South Australia, Adelaide 5042, Australia

Email:
Benjamin S. Flavel[*] - benjamin.flavel@kit.edu

* Corresponding author

Keywords:
absorbance; carbon nanotubes; current-voltage; dry shear aligning; order parameter

Beilstein J. Nanotechnol. **2016,** *7,* 1486–1491.
doi:10.3762/bjnano.7.141

Received: 15 June 2016
Accepted: 07 October 2016
Published: 20 October 2016

This article is part of the Thematic Series "Advances in nanomaterials II".

Guest Editor: H. Hahn

© 2016 Stolz et al.; licensee Beilstein-Institut.
License and terms: see end of document.

Abstract

Recent results in the field of carbon nanotube–silicon solar cells have suggested that the best performance is obtained when the nanotube film provides good coverage of the silicon surface and when the nanotubes in the film are aligned parallel to the surface. The recently developed process of dry shear aligning – in which shear force is applied to the surface of carbon nanotube thin films in the dry state, has been shown to yield nanotube films that are very flat and in which the surface nanotubes are very well aligned in the direction of shear. It is thus reasonable to expect that nanotube films subjected to dry shear aligning should outperform otherwise identical films formed by other processes. In this work, the fabrication and characterisation of carbon nanotube–silicon solar cells using such films is reported, and the photovoltaic performance of devices produced with and without dry shear aligning is compared.

Introduction

During the last decade or so, the potential benefits of using carbon nanotubes in solar cells has been explored from both a fundamental theory point of view [1,2], as well as experimentally in a host of different device architectures, including as additives in dye solar cells [3,4], organic photovoltaics [5,6], and perovskites [7,8] and as the active light absorbing component in conjunction with acceptors such as fullerenes [9-12]. Carbon nanotube–silicon heterojunctions can also function as solar cells [13,14] and over the last few years of development the power conversion efficiency (PCE) of these devices has been steadily increasing [15-22], with the most recent high efficiency record by Wang et al. now standing at ≈17% [23]. The understanding of precisely how these junctions operate is still incomplete and although progress in this respect is ongoing [24-41], there are

still many questions unanswered. What has been established is that, as one should expect, the quality of the junction plays a large role in overall performance. Since the underlying silicon base is usually a high-grade monocrystalline material, junction quality is dominated by aspects relating to the nanotube thin film. An important factor in many devices is the degree of coverage of the films on the silicon surface, itself dependent on the films' porosity. Jung et al. [17], Li et al. [28] and Tune et al. [42] have shown that alignment of the nanotubes by solution shearing (as known as slide casting, liquid film shearing, shear force casting) from solutions of either the nanotubes dissolved natively in chlorosulphonic acid (Jung, Li), or the nanotubes dissolved as polyelectrolyte salts in polar, aprotic solvent (Tune) yields higher performing devices than their randomly oriented counterparts, and explained these observations with reference to the better surface coverage provided by such films.

Recently, the process of dry shear aligning (DSA), wherein a randomly oriented thin film of nanotubes is flattened and aligned by application of shear force in the dry state, was reported to yield similar films as those obtained by solution shearing. It was further suggested that perhaps such films may yield similar improvements in carbon nanotube–silicon solar cell performance [43]. To address this question, we report herein the results of a direct comparison between two sets of solar cells fabricated with either, a) nanotube films produced by common vacuum filtration from aqueous suspension or, b) identical films (from the same filtration membrane) that have been subjected to DSA before deposition onto the silicon surface.

Results and Discussion

SEM images (Figure 1) reveals clear differences between the nanotube films as captured on the filtration membranes, and the same films after DSA. As well as the obvious alignment of the nanotubes in the direction of shear, the porosity of the film has also been reduced due to better packing of the nanotubes in their aligned configuration. The films are now also visibly flatter, with atomic force microscopy showing two orders of magnitude reductions in surface roughness (from ≈140 nm to only 3–4 nm) [43], which should lead to the desired improvements in interfacial contact between the nanotube film and the silicon substrate.

The optical properties of the nanotube films (Figure 2a) show the typical features of large diameter, arc discharge SWCNTs with a broad S_{11} region around 1900 nm, corresponding to a di-

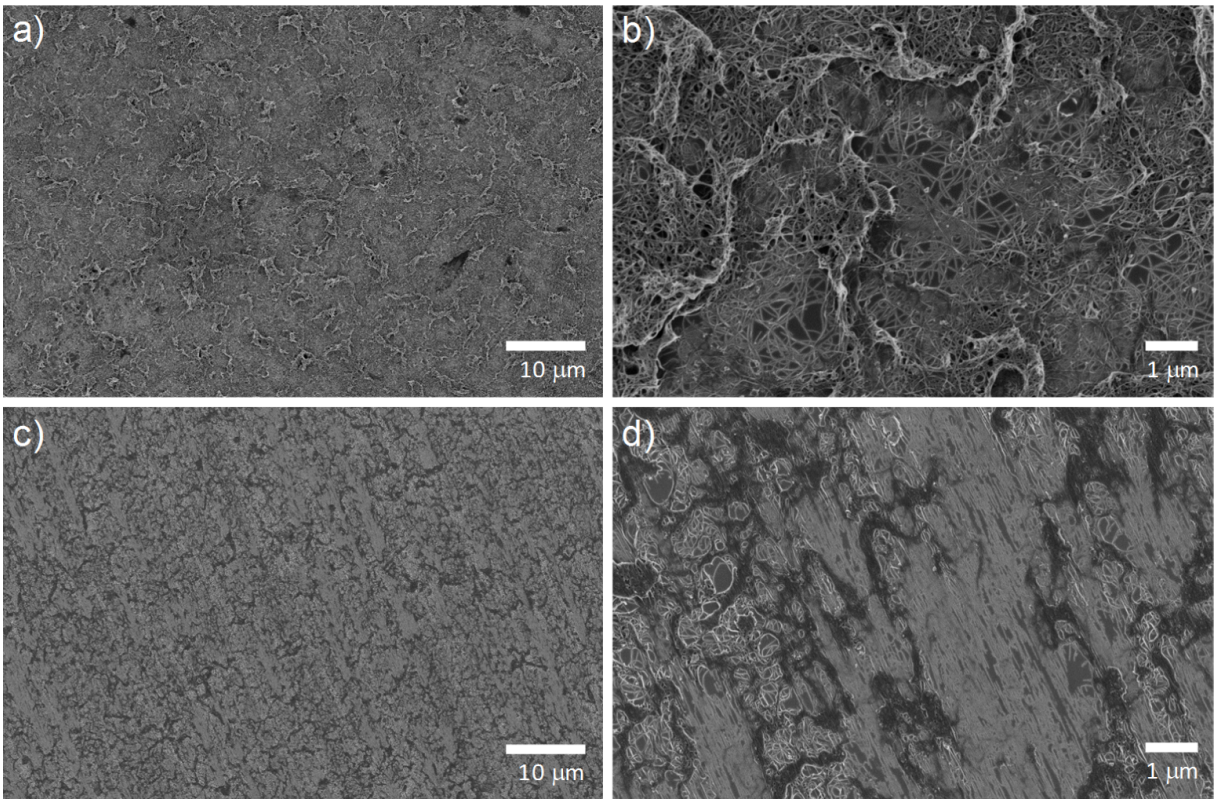


Figure 1: Effect of dry shear aligning (DSA) on film morphology. a) and b) show SEM images of thin films produced by vacuum filtration, before DSA, whereas c) and d) show the same films after DSA.

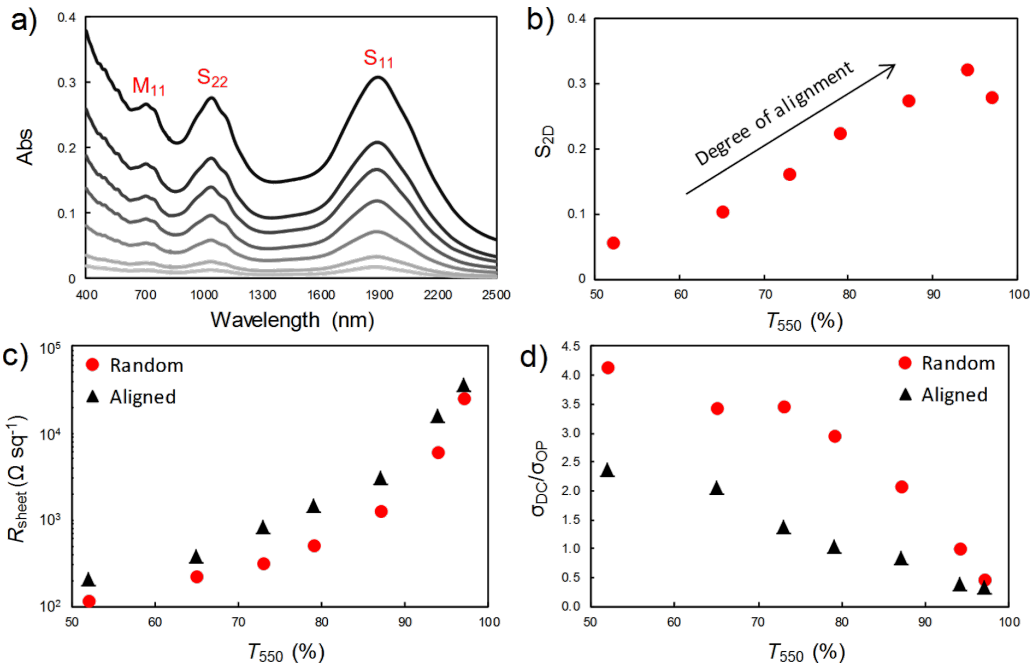


Figure 2: a) Optical spectra of the various thicknesses of a SWCNT film, b) variation of the degree of alignment with film thickness, c) variation of sheet resistance with film thickness for random and aligned SWCNT films and, d) variation in the ratio of DC electrical to optical conductivity with film thickness for random and aligned SWCNT films.

ameter distribution centred about 1.4 nm. The features on either side of the main peak are better resolved in the similarly shaped S_{22} region and indicate that there are many (n,m) species in the distribution, with the M_{11} region also displaying several components. The data is presented in Figure 2a on the familiar absorbance scale but a simple conversion yields the T_{550} value commonly used in the quantification of transparent films' performance. The isotropic absorbance spectra were unchanged by DSA however, Figure 2b shows the variation in the degree of alignment of the nanotubes in the films after DSA, where the 2D order parameter is calculated from polarised optical transmittance measurements as in Equation 1 [44] and reveals that the degree of alignment increases as the film thickness decreases. This has been explained previously by considering that DSA affects mostly the nanotubes on the surface of the film, leaving the nanotubes in the 'bulk' of the film relatively unaffected. As the thickness decreases, the ratio of surface nanotubes to the bulk increases and the surface nanotubes thus contribute more to the overall absorbance of the film.

$$S_{2D} = \frac{\log(T_{//}) - \log(T_{\perp})}{\log(T_{//}) + 2\log(T_{\perp})} \quad (1)$$

The sheet resistance of the films varies with thickness as shown in Figure 2c. Taking into account the log resistance scale, there are two main regions below and above T_{550} = 85–90%, corresponding to the transition between the two dominant conduction mechanisms of variable range hopping through denser films and percolation through sparse films. The measurements were taken with a linear four-point probe using a DC bias, however no anisotropy in the resistance was observed with rotation of the probe. The sheet resistance, R_{sheet}, of the films was marginally increased after DSA, which is made clearer when considering the DC electrical to optical conductivity ratio, σ_{OP}/σ_{DC} (Figure 2d), calculated as per Equation 2 [45], which takes into account the sheet resistance and the (isotropic) transmittance and where μ_0 and ε_0 have their usual meaning.

$$T_{550} = \left(1 + \frac{1}{R_{sheet}} \cdot \sqrt{\frac{\mu_0}{\varepsilon_0}} \cdot \frac{\sigma_{OP}}{\sigma_{DC}}\right)^{-2} \quad (2)$$

The as-prepared films and those aligned by DSA were deposited on silicon substrates patterned with electrodes, and the photovoltaic performance was measured, with the results summarised in Figure 3 (and with the full *J*–*V* curves shown in Supporting Information File 1, Figure S1). Whilst the DSA devices exhibited a slightly higher open circuit voltage (V_{oc}) for films of around T_{550} = 70–80%, the short circuit current density (J_{sc}) was lower for all film thicknesses, especially the thicker films, and the fill factor (FF) was also increasingly poorer tending towards thicker films. The overall result in terms of PCE is that the DSA devices performed relatively the same as

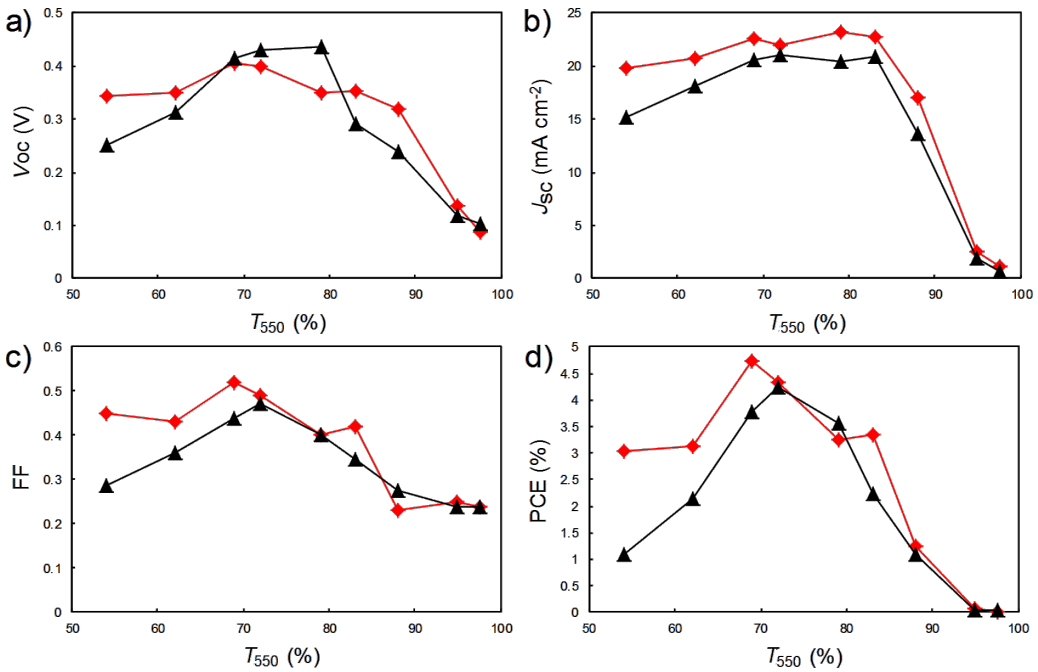


Figure 3: The variation of solar cell parameters with nanotube film thickness for films both before (red diamonds) and after (black triangles) DSA, a) open circuit voltage, b) short circuit current density, c) fill factor and, d) power conversion efficiency.

the devices with as-prepared films for $T_{550} \geq 70\%$, but performed increasing worse for the thicker films, with the DSA devices of $T_{550} = 54\%$ generating only a third of their as-prepared film counterparts.

The reasons for the poorer performance are not immediately obvious. Although there is a clear difference in the sheet resistance, and thus DC electrical to optical conductivity ratio, it does not appear to be large enough to account for the observed difference in performance. Indeed, the two trends are somewhat different; the relative difference in sheet resistance is lowest at the two ends of the transmittance range, and is greatest in the middle of the range, whereas the relative difference in the solar cell performance (as seen most clearly in the short circuit current density, Figure 3b) is at a minimum for the thinnest films and maximum for the thickest films. It was observed that the upper side of the nanotube films on the filtration membranes became visibly more reflective after DSA and although the films were deposited with the reflective side down, it was thought that perhaps this could change the reflectance of the silicon surface differently to when an as-prepared film was deposited. However, reflectance measurements taken of the completed devices not only showed that this was not the case, but that the devices with the DSA films were, on average, 5–10% less reflective than those with the as-prepared films, across all wavelengths. Thus, when mounted on silicon, a higher photon current is penetrating through the films than the transmittance measurements suggest, which should result in a higher short circuit current density for all film thicknesses – the opposite of what is observed for the thicker films. Another possibility is that the quality of the interface between the nanotubes and silicon is inferior after DSA, though that is the opposite of what was intended. However, the diode ideality factors extracted from the dark current characteristics were similar for both the as-prepared and DSA film devices (around 1.5–2), and showed no clear trend in either case. In short, the origin of the observed performance reduction for devices fabricated with thick nanotube films that have been flattened and aligned by DSA remains undetermined, despite the fact that previous results have suggested an improvement in performance.

Conclusion

In conclusion, a comparison was made between carbon nanotube–silicon solar cells made with either as-prepared, vacuum filtration nanotube films or the same films after flattening and aligning of the nanotubes on the contacting surface of the films using the newly developed technique of dry shear aligning. Whilst the DSA process produced films that were two orders of magnitude flatter and exhibited a 2D order parameter of up to 0.3, both of which have been previously observed to improve the photovoltaic performance of carbon nanotube–silicon junctions, in this case this was accompanied instead by a reduction in the sheet resistance and thus DC electrical to optical conductivity ratio of the films. In terms of the performance of solar

cells made with the DSA films, the net result for thin films (T_{550} > 70%) was that there was no overall change compared to the devices with as-prepared nanotube films. However, there was a significant decrease in performance for films thicker than T_{550} = 70%, with the devices using the thickest DSA films (T_{550} = 54%) producing only a third of the photovoltaic output of the devices made with as-prepared films of the same transmittance.

Experimental

Single walled carbon nanotubes (P2-SWNT, Carbon Solutions) were added to aqueous TritonX-100 (1% v/v, Sigma-Aldrich) at 0.1 mg mL^{-1} then bath sonicated (1 h). After centrifugation (20 000*g*, 20 min), the nanotube films were captured from the supernatant by vacuum filtration onto mixed cellulose ester (MCE) membranes (0.45 µm, HAWP, Merck Millipore) and rinsed thoroughly with copious DI water as per Wu et al. [46] and Hu et al. [47]. For the DSA preparation, a cylindrical Teflon stir bar (8 × 30 mm) was used as the aligner. The membranes were placed on a flat glass surface (nanotube side up) and held in place while the stir bar was very firmly (≈60 N) sheared across the film surface (2–3 mm s^{-1}) such that approximately half of the film was thus aligned and the other half remained in the as-prepared state. The nanotube films changed in appearance from matt grey/black to become visibly smoother and more reflective, with the direction of shear faintly discernible to the eye. Small circular regions (0.08 cm^2) of each film were then taken from both the aligned and as-prepared parts of the membranes and used in devices. The films were deposited by placing them, nanotube side down, on the solar cells such that they completely covered the active area; they were then wet with a drop of water, compressed with Teflon and baked in air (110 °C, 15 min). To remove the MCE from the films, the cooled substrates were placed in an acetone (EMSURE, Merck) bath for 30 min then transferred to two fresh acetone baths for a further 30 min each.

Carbon nanotube–silicon solar cells were fabricated as described previously [36]. Briefly, Cr/Au front electrodes were patterned onto phosphorous doped n-type silicon substrates (SSP, 525 µm thick, 1–5 Ω cm, <100>, with a 100 nm thermal oxide) by photolithography and defined circular active areas (0.08 cm^2) in which the SiO_2 was removed by buffered oxide etch. The films were deposited as described above and the cells were completed with GaIn eutectic back electrodes and mounted on steel support plates. Before testing, all cells were treated sequentially with 2% HF, $SOCl_2$ and 2% HF again. This treatment sequence removes the thin oxide from the silicon surface as well as p-doping the nanotubes and dramatically increasing the conductivity of the nanotube films. Current–voltage data was taken from cells in the dark and under 100 mW cm^{-2} AM1.5G illumination (Class 2A, with irradiance measured by a silicon reference cell with NIST-traceable calibration).

Supporting Information

Supporting Information File 1

Additional experimental information.
[http://www.beilstein-journals.org/bjnano/content/supplementary/2190-4286-7-141-S1.pdf]

Acknowledgements

B. Stolz thanks the Carbon Nanotube Solar Cells and Sensors group at the Institute of Nanotechnology, Karslruhe Institute of Technology for hosting the research project. B. Flavel gratefully acknowledges support from the Deutsche Forschungsgemeinschafts (DFG) Emmy Noether Programm under grant numbers FL 834/1-1 and FL 834/2-1.

References

1. Tune, D. D.; Shapter, J. G. *Energy Environ. Sci.* **2013,** *6,* 2572. doi:10.1039/c3ee41731j
2. Bierman, D. M.; Lenert, A.; Chan, W. R.; Bhatia, B.; Celanović, I.; Soljačić, M.; Wang, E. N. *Nat. Energy* **2016,** *1,* No. 16068. doi:10.1038/nenergy.2016.68
3. Macdonald, T. J.; Tune, D. D.; Dewi, M. R.; Gibson, C. T.; Shapter, J. G.; Nann, T. *ChemSusChem* **2015,** *8,* 3396. doi:10.1002/cssc.201500945
4. Batmunkh, M.; Biggs, M. J.; Shapter, J. G. *Small* **2015,** *11,* 2963. doi:10.1002/smll.201403155
5. Shastry, T. A.; Hartnett, P. E.; Wasielewski, M. R.; Marks, T. J.; Hersam, M. C. *ACS Energy Lett.* **2016,** *1,* 548–555. doi:10.1021/acsenergylett.6b00291
6. Salim, T.; Lee, H.-W.; Wong, L. H.; Oh, J. H.; Bao, Z.; Lam, Y. M. *Adv. Funct. Mater.* **2016,** *26,* 51. doi:10.1002/adfm.201503256
7. Schulz, P.; Dowgiallo, A.-M.; Yang, M.; Zhu, K.; Blackburn, J. L.; Berry, J. J. *J. Phys. Chem. Lett.* **2016,** *7,* 418. doi:10.1021/acs.jpclett.5b02721
8. Aitola, K.; Sveinbjörnsson, K.; Correa-Baena, J.-P.; Kaskela, A.; Abate, A.; Tian, Y.; Johansson, E. M. J.; Grätzel, M.; Kauppinen, E. I.; Hagfeldt, A.; Boschloo, G. *Energy Environ. Sci.* **2016,** *9,* 461. doi:10.1039/C5EE03394B
9. Gong, M.; Shastry, T. A.; Xie, Y.; Bernardi, M.; Jasion, D.; Luck, K. A.; Marks, T. J.; Grossman, J. C.; Ren, S.; Hersam, M. C. *Nano Lett.* **2014,** *14,* 5308. doi:10.1021/nl5027452
10. Pfohl, M.; Glaser, K.; Ludwig, J.; Tune, D. D.; Dehm, S.; Kayser, C.; Colsmann, A.; Krupke, R.; Flavel, B. S. *Adv. Energy Mater.* **2016,** *6,* No. 1501345. doi:10.1002/aenm.201501345
11. Ihly, R.; Mistry, K. S.; Ferguson, A. J.; Clikeman, T. T.; Larson, B. W.; Reid, O.; Boltalina, O. V.; Strauss, S. H.; Rumbles, G.; Blackburn, J. L. *Nat. Chem.* **2016,** *8,* 603. doi:10.1038/nchem.2496
12. Pfohl, M.; Glaser, K.; Graf, A.; Mertens, A.; Tune, D. D.; Puerckhauer, T.; Alam, A.; Wei, L.; Chen, Y.; Zaumseil, J.; Colsmann, A.; Krupke, R.; Flavel, B. S. *Adv. Energy Mater.* **2016,** *6,* No. 1600890. doi:10.1002/aenm.201600890

13. Wei, J.; Jia, Y.; Shu, Q.; Gu, Z.; Wang, K.; Zhuang, D.; Zhang, G.; Wang, Z.; Luo, J.; Cao, A.; Wu, D. *Nano Lett.* **2007,** *7,* 2317. doi:10.1021/nl070961c
14. Tune, D. D.; Flavel, B. S.; Krupke, R.; Shapter, J. G. *Adv. Energy Mater.* **2012,** *2,* 1043. doi:10.1002/aenm.201200249
15. Jia, Y.; Li, P.; Wei, J.; Cao, A.; Wang, K.; Li, C.; Zhuang, D.; Zhu, H.; Wu, D. *Mater. Res. Bull.* **2010,** *45,* 1401. doi:10.1016/j.materresbull.2010.06.045
16. Jia, Y.; Li, P.; Gui, X.; Wei, J.; Wang, K.; Zhu, H.; Wu, D.; Zhang, L.; Cao, A.; Xu, Y. *Appl. Phys. Lett.* **2011,** *98,* No. 133115. doi:10.1063/1.3573829
17. Jung, Y.; Li, X.; Rajan, N. K.; Taylor, A. D.; Reed, M. A. *Nano Lett.* **2012,** *13,* 95. doi:10.1021/nl3035652
18. Shi, E.; Zhang, L.; Li, Z.; Li, P.; Shang, Y.; Jia, Y.; Wei, J.; Wang, K.; Zhu, H.; Wu, D.; Zhang, S.; Cao, A. *Sci. Rep.* **2012,** *2,* No. 884. doi:10.1038/srep00884
19. Cui, K.; Chiba, T.; Omiya, S.; Thurakitseree, T.; Zhao, P.; Fujii, S.; Kataura, H.; Einarsson, E.; Chiashi, S.; Maruyama, S. *J. Phys. Chem. Lett.* **2013,** *4,* 2571. doi:10.1021/jz401242a
20. Tune, D. D.; Flavel, B. S.; Quinton, J. S.; Ellis, A. V.; Shapter, J. G. *ChemSusChem* **2013,** *6,* 320. doi:10.1002/cssc.201200600
21. Cui, K.; Anisimov, A. S.; Chiba, T.; Fujii, S.; Kataura, H.; Nasibulin, A. G.; Chiashi, S.; Kauppinen, E. I.; Maruyama, S. *J. Mater. Chem. A* **2014,** *2,* 11311. doi:10.1039/C4TA01353K
22. Yu, L.; Tune, D. D.; Shearer, C. J.; Shapter, J. G. *Sol. Energy* **2015,** *118,* 592. doi:10.1016/j.solener.2015.06.014
23. Wang, F.; Kozawa, D.; Miyauchi, Y.; Hiraoka, K.; Mouri, S.; Ohno, Y.; Matsuda, K. *Nat. Commun.* **2015,** *6,* No. 6305. doi:10.1038/ncomms7305
24. Wadhwa, P.; Liu, B.; McCarthy, M. A.; Wu, Z.; Rinzler, A. G. *Nano Lett.* **2010,** *10,* 5001. doi:10.1021/nl103128a
25. Jia, Y.; Cao, A.; Bai, X.; Li, Z.; Zhang, L.; Guo, N.; Wei, J.; Wang, K.; Zhu, H.; Wu, D.; Ajayan, P. M. *Nano Lett.* **2011,** *11,* 1901. doi:10.1021/nl2002632
26. Wadhwa, P.; Seol, G.; Petterson, M. K.; Guo, J.; Rinzler, A. G. *Nano Lett.* **2011,** *11,* 2419. doi:10.1021/nl200811z
27. Jia, Y.; Cao, A.; Kang, F.; Li, P.; Gui, X.; Zhang, L.; Shi, E.; Wei, J.; Wang, K.; Zhu, H.; Wu, D. *Phys. Chem. Chem. Phys.* **2012,** *14,* 8391. doi:10.1039/c2cp23639g
28. Li, X.; Jung, Y.; Sakimoto, K.; Goh, T.-H.; Reed, M. A.; Taylor, A. D. *Energy Environ. Sci.* **2013,** *6,* 879–887. doi:10.1039/c2ee23716d
29. Pintossi, C.; Salvinelli, G.; Drera, G.; Pagliara, S.; Sangaletti, L.; Del Gobbo, S.; Morbidoni, M.; Scarselli, M.; De Crescenzi, M.; Castrucci, P. *J. Phys. Chem. C* **2013,** *117,* 18688. doi:10.1021/jp404820k
30. Tune, D. D.; Shapter, J. G. *Nanomaterials* **2013,** *3,* 655. doi:10.3390/nano3040655
31. Tune, D. D.; Hennrich, F.; Dehm, S.; Klein, M. F. G.; Glaser, K.; Colsmann, A.; Shapter, J. G.; Lemmer, U.; Kappes, M. M.; Krupke, R.; Flavel, B. S. *Adv. Energy Mater.* **2013,** *3,* 1091. doi:10.1002/aenm.201200949
32. Wang, F.; Kozawa, D.; Miyauchi, Y.; Hiraoka, K.; Mouri, S.; Matsuda, K. *Appl. Phys. Express* **2013,** *6,* No. 102301. doi:10.7567/APEX.6.102301
33. Li, X.; Guard, L. M.; Jiang, J.; Sakimoto, K.; Huang, J.-S.; Wu, J.; Li, J.; Yu, L.; Pokhrel, R.; Brudvig, G. W.; Ismail-Beigi, S.; Hazari, N.; Taylor, A. D. *Nano Lett.* **2014,** *14,* 3388. doi:10.1021/nl500894h
34. Li, X.; Jung, Y.; Huang, J.-S.; Goh, T.; Taylor, A. D. *Adv. Energy Mater.* **2014,** *4,* No. 1400186. doi:10.1002/aenm.201400186
35. Ponzoni, S.; Galimberti, G.; Sangaletti, L.; Castrucci, P.; Del Gobbo, S.; Morbidoni, M.; Scarselli, M.; Pagliara, S. *J. Phys. Chem. C* **2014,** *118,* 24110. doi:10.1021/jp506684b
36. Tune, D. D.; Blanch, A. J.; Krupke, R.; Flavel, B. S.; Shapter, J. G. *Phys. Status Solidi A* **2014,** *211,* 1479. doi:10.1002/pssa.201431043
37. Harris, J. M.; Semler, M. R.; May, S.; Fagan, J. A.; Hobbie, E. K. *J. Phys. Chem. C* **2015,** *119,* 10295. doi:10.1021/acs.jpcc.5b02626
38. Pintossi, C.; Pagliara, S.; Drera, G.; De Nicola, F.; Castrucci, P.; De Crescenzi, M.; Crivellari, M.; Boscardin, M.; Sangaletti, L. *ACS Appl. Mater. Interfaces* **2015,** *7,* 9436. doi:10.1021/am508973b
39. Saini, V.; Bourdo, S. E.; Abdulrazzaq, O.; Dervishi, E.; Kannarpady, G. K.; Biris, A. S. *RSC Adv.* **2015,** *5,* 621. doi:10.1039/C4RA10735G
40. Grace, T.; Yu, L.; Gibson, C.; Tune, D.; Alturaif, H.; Al Othman, Z.; Shapter, J. *Nanomaterials* **2016,** *6,* 52. doi:10.3390/nano6030052
41. Harris, J. M.; Headrick, R. J.; Semler, M. R.; Fagan, J. A.; Pasquali, M.; Hobbie, E. K. *Nanoscale* **2016,** *8,* 7969. doi:10.1039/C5NR08703A
42. Tune, D. D.; Blanch, A. J.; Shearer, C. J.; Moore, K. E.; Pfohl, M.; Shapter, J. G.; Flavel, B. S. *ACS Appl. Mater. Interfaces* **2015,** *7,* 25857. doi:10.1021/acsami.5b08212
43. Tune, D. D.; Stolz, B. W.; Pfohl, M.; Flavel, B. S. *Nanoscale* **2016,** *8,* 3232. doi:10.1039/C5NR08784H
44. White, D. L.; Taylor, G. N. *J. Appl. Phys.* **1974,** *45,* 4718. doi:10.1063/1.1663124
45. Hecht, D. S.; Heintz, A. M.; Lee, R.; Hu, L.; Moore, B.; Cucksey, C.; Risser, S. *Nanotechnology* **2011,** *22,* 169501. doi:10.1088/0957-4484/22/16/169501
46. Wu, Z.; Chen, Z.; Du, X.; Logan, J. M.; Sippel, J.; Nikolou, M.; Kamaras, K.; Reynolds, J. R.; Tanner, D. B.; Hebard, A. F.; Rinzler, A. G. *Science* **2004,** *305,* 1273. doi:10.1126/science.1101243
47. Hu, L.; Hecht, D. S.; Grüner, G. *Nano Lett.* **2004,** *4,* 2513. doi:10.1021/nl048435y

License and Terms

This is an Open Access article under the terms of the Creative Commons Attribution License (http://creativecommons.org/licenses/by/4.0), which permits unrestricted use, distribution, and reproduction in any medium, provided the original work is properly cited.

The license is subject to the *Beilstein Journal of Nanotechnology* terms and conditions: (http://www.beilstein-journals.org/bjnano)

The definitive version of this article is the electronic one which can be found at: doi:10.3762/bjnano.7.141

BEILSTEIN JOURNAL OF NANOTECHNOLOGY

Effect of triple junctions on deformation twinning in a nanostructured Cu–Zn alloy: A statistical study using transmission Kikuchi diffraction

Silu Liu[1,2], Xiaolong Ma[2], Lingzhen Li[1], Liwen Zhang[2], Patrick W. Trimby[3], Xiaozhou Liao[4], Yusheng Li[1], Yonghao Zhao[*1] and Yuntian Zhu[*1,2]

Full Research Paper

Open Access

Address:
[1]Nano Structural Materials Center, School of Materials Science and Engineering, Nanjing University of Science and Technology, Nanjing, Jiangsu 210094, China, [2]Department of Materials Science and Engineering, North Carolina State University, Raleigh, North Carolina 27695, USA, [3]Australian Centre for Microscopy and Microanalysis, The University of Sydney, Sydney, NSW 2006, Australia and [4]School of Aerospace, Mechanical and Mechatronic Engineering, The University of Sydney, Sydney, NSW 2006, Australia

Email:
Yonghao Zhao[*] - yhzhao@njust.edu.cn; Yuntian Zhu[*] - ytzhu@ncsu.edu

* Corresponding author

Keywords:
nanocrystalline materials; transmission Kikuchi diffraction; triple junctions; twins

Beilstein J. Nanotechnol. **2016,** *7,* 1501–1506.
doi:10.3762/bjnano.7.143

Received: 22 July 2016
Accepted: 04 October 2016
Published: 24 October 2016

This article is part of the Thematic Series "Advances in nanomaterials II".

Guest Editor: H. Hahn

© 2016 Liu et al.; licensee Beilstein-Institut.
License and terms: see end of document.

Abstract

Scanning electron microscopy transmission Kikuchi diffraction is able to identify twins in nanocrystalline material, regardless of their crystallographic orientation. In this study, it was employed to characterize deformation twins in Cu/10 wt % Zn processed by high-pressure torsion. It was found that in 83% of grains containing twins, at least one twin intersects with a triple junction. This suggests that triple junctions could have promoted the nucleation of deformation twins. It should be cautioned that this technique might be unable to detect extremely small nanoscale twins thinner than its step size.

Introduction

The Hall–Petch relationship has inspired materials scientists to refine grains to increase the strength of materials since the early 1950s [1-3]. However, research in this area has met the paradox of strength and ductility tradeoff, especially when materials are refined to ultrafine-grained or nanostructured range [4-8]. They are usually either strong or ductile, but rarely both at the same time. Deformation twinning is one of a few mechanisms that can simultaneously improve both strength and ductility [5,6,9-11]. Consequently, deformation twinning in nanostructured metals has received extensive attention in recent years [10].

Among all of the twinning mechanisms in nanocrystalline materials, partial mission from grain boundaries has been found as the primary mechanism from both simulations [12,13] and experiments [14,15]. However, it still remains unclear whether such emissions from grain boundaries have any preference for sites with specific character such as triple junctions. This problem is of significant importance to both the scientific understanding and practical design of nanostructured materials. Previously, triple junctions have been reported to play a critical role in other deformation mechanisms in nanostructured materials, like grain rotation [16] and grain boundary sliding [17]. Additionally, earlier studies revealed that triple junctions were energetically more active than grain boundaries [18] and they were able to emit and absorb free volumes upon deformation, which promotes partial emission [12]. Therefore, one may reasonably hypothesize that triple junctions may promote deformation twinning in nanocrystalline materials. Up to now, there has been no solid experimental study to verify this issue largely due to technical difficulties.

So far, high-resolution transmission electron microscopy (HRTEM) has achieved great success in revealing the atomic-level details of deformation/growth twins, including formation mechanisms [14,19-22], interactions with dislocations [11,23-26] and macroscopic strain [10,25,27], due to its extraordinary spatial resolution. However, reliable statistical analysis based on extensive data still seems a grand challenge for HRTEM studies on twinning [28,29]. It is time consuming and sometimes impractical to examine twins in a massive number of grains, as each grain needs tilting into a specific zone axis under HRTEM to observe the twin. For example, to observe a twin in a face-centered cubic (fcc) grain, observation along the <110> zone axis on the coherent twin plane is typically needed [29]. In other words, the electron beam needs to be parallel to a close-packed orientation and the twin boundary needs to be edge-on. It is tedious to rotate the sample to various orientations to look for twins in each grain. In addition, the limited sample tilting range makes it impossible to observe all twins in a grain. Therefore, HRTEM substantially underestimates the number of twins in a nanostructured sample. Furthermore, HRTEM also has the same difficulty in characterizing other interfaces like grain boundaries and triple junctions. This is especially problematic when studying the relationship between twins and triple junctions from a statistical view and when the sample has a significant texture.

In the last few years, an innovative microscopy technique has been developed using a conventional electron backscatter diffraction (EBSD) system in a scanning electron microscope (SEM) to collect transmission Kikuchi diffraction (TKD) patterns from sub-10-nm domains in an electron transparent sample [28,30,31]. Like conventional EBSD, TKD can measure grain size, morphology, phase distribution and crystalline lattice orientation. However, the biggest advantage of TKD compared with EBSD is its improvement in spatial resolution, which has been shown to be in the range of 2–10 nm for a variety of materials [30]. Therefore, this technique enables researchers to characterize, with relative ease, truly nanostructured materials. Although strongly dependent on materials and deformation state, the resolution of TKD can complement TEM to provide useful information in characterizing nanostructured materials.

Another great advantage of TKD is that various interfaces, including grain boundaries and twin boundaries, can be identified without the requirement of them being edge-on. Therefore, no tedious sample tilting is required, and all twins can be identified irrespective of their orientation. Furthermore, TKD and subsequent data processing are time/labor-saving and relatively easy due to fast indexing rates and a high level of automation [28,31]. This is in sharp contrast with HRTEM for which the analyses are time consuming and difficult to perform. In addition, comprehensive microstructural information is collected simultaneously from samples analyzed by TKD. This eliminates any subjective judgment of the researcher. Therefore, TKD can achieve the desired balance between spatial resolution, angular accuracy and a high level of automation to give objective results. With these advantages, TKD is ideal for performing statistical analyses on deformation twinning and triple junctions in nanostructured materials.

Experimental

A 1 mm thick sheet of commercial Cu/10 wt % Zn was first homogenized at 700 °C for 3 h, cooled down to room temperature, and then punched into 10 mm diameter disks for high pressure torsion (HPT) processing. The HPT processing was conducted at room temperature for ten revolutions with an imposed pressure of 1 GPa at a speed of 1.5 rpm. All electron-transparent TKD foils were mechanically ground and punched from the outer region of the as-deformed disks, where the greatest degree of grain refinement was achieved. Samples were subsequently electropolished by means of double-jet electropolishing using an electrolyte of 1:1:2 $H_3PO_4/C_2H_5OH/H_2O$. TKD characterization was conducted in a Zeiss Auriga SEM operating with a 30 kV accelerating voltage. The measurement step size was set to 6 nm for the microscopic observation, taken into consideration the heavily deformed state and other factors. All misindexed points and unindexed pixels in the data sets were screened out prior to analyzing twins. Nearly 1500 grains, ranging in size from 30 to 200 nm, were characterized to enable a statistical analysis of the twinning. TEM observations were performed in a JEOL-2010F microscope under 200 kV as a control group.

Results and Discussion

In this work, we investigated deformation twinning in a nanostructured Cu–Zn alloy using TKD. Two kinds of twinning phenomena were statistically studied using large TKD data sets: 1) their connections with triple junctions, and 2) the effect of grain size on deformation twinning.

Figure 1 shows a typical TEM image of the HPT Cu–Zn alloy, revealing equiaxed ultrafine and nanocrystalline grains. Most grain boundaries are not well defined and the interiors of most grains are "messy", especially in large grains. Those are typical microstructures in highly deformed samples with a high density of entangled dislocations produced by severe plastic deformation [32]. The inset shows a corresponding diffraction pattern. The presence of smeared and ring-like diffraction patterns implies lots of nanoscale grains and their low-angle misorientations. This result is consistent with previous reports of copper alloys processed by high-strain torsion [33,34].

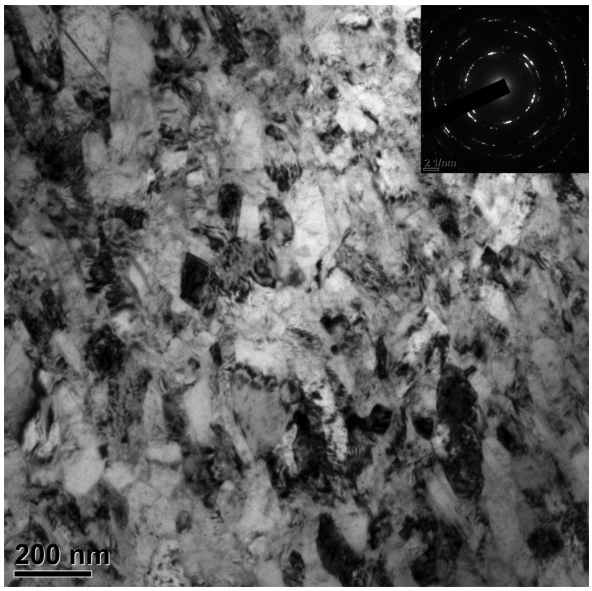


Figure 1: A typical bright-field TEM image of the HPT Cu–Zn alloy showing severe deformation and grain refinement. Inset is a corresponding selected area diffraction pattern.

Figure 2a presents a typical TKD orientation map of the HPT-processed Cu–Zn alloy. The orientation map is coded by the inverse pole figure coloring scheme as demonstrated in the inset, in which grains with {001}, {101}, {111} planes parallel to the sample disk surface are indicated by red, green and blue, respectively. The black, silver and red boundary lines correspond to high-angle grain boundaries (>15°), low-angle grain boundaries (2–15°), and Σ3 twin boundaries, respectively. The black points are unindexed points in the orientation map. As shown, the overview of grain size and morphology agrees well with the TEM observation. Severe deformation has induced grain refinement down to the nanoscale. Equiaxed nanoscale grains were found dotted around ultrafine-grains. The grains highlighted by A, B and C have a specific twin feature, which will be discussed in detail in the following section. As in B and C, numerous twins are observed to intersect with triple junctions in the orientation maps. Most grains have significant internal orientation change due to the intragranular deformation that occurred during HPT, as indicated by the abundance of low-angle boundaries and a change in color within grains. The pole figures presented in Figure 2b reveal that there is only a weak texture. These details are consistent with the deformation features observed under TEM.

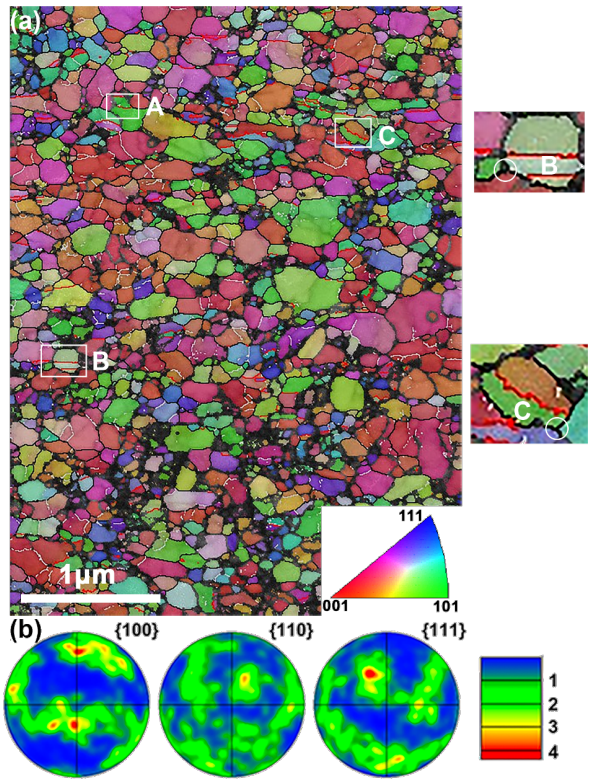


Figure 2: (a) A typical TKD orientation map of the HPT Cu–Zn alloy. The inverse pole figure coloring scheme in the inset is utilized to code the orientation map, in which grains with {001}, {101}, and {111} planes parallel to the sample surface are indicated by red, green and blue, respectively. The black, silver and red boundary lines represent high-angle grain boundaries (>15°), low-angle grain boundaries (2–15°), and Σ3 twin boundaries, respectively. Grains highlighted with white squares and labeled with A, B and C present three typical twin structures that correspond to those shown in Figure 3a–c, respectively. In B and C, twins intersect with triple junctions (highlighted by circles), which is a common phenomenon in all orientation maps. (b) Pole figures of the area presented in (a). Only a weak texture is observed here.

Figure 3a–c shows TEM images of three typical types of twins. They corresponds to the three most common twin morphologies observed in TKD orientation maps, as indicated by A, B

and C in Figure 2a. These three twins are categorized based on their thicknesses relative to the TKD step size. Generally, for the software to display a twin boundary, it needs to measure the orientation difference across the boundary. But when the twin is extremely small and thinner than one step size (6 nm), it cannot be detected by TKD in our study. Therefore, when the twin domain thickness is around or slightly larger than the step size, as in the case of Figure 3a, TKD is able to detect the twin, but unable to resolve the twin domain. This whole twin appears as one single Σ3 red line in the TKD orientation map and bounded by two separate matrices with the same orientation, as shown in frame A in Figure 2a. Second, when the twin thickness is much larger than the TKD step size (Figure 3b), two Σ3 red lines bounding the twin can be clearly observed, as shown in frame B of Figure 2a. The third case is shown in Figure 3c: when the twinning propagates to the grain boundary and the twin domain thereby becomes large enough to cover part of a grain, only one coherent twin boundary appears in the grain. In this case, a red Σ3 twin boundary line splits the grain with two different orientations, as shown in frame C in Figure 2a.

The statistical information on the relationship of triple junctions and twins is listed in Table 1, which shows results from 300 twinned grains. “Yes” and “No” in the table denote whether a twin intersects with a triple junction. It has been reported that the area nearby a triple junction would emit or absorb free volumes to promote the emission of partial dislocations [12] and then emitted partial dislocations would induce the growth of stacking faults or twins [14,15]. Therefore, a twin meeting the triple junction could be nucleated from the triple junction. The statistics in Table 1 reveals that 248 out of 300 twinned grains (83%) have at least a twin connected with a triple junction. Two grain size subsets, 30–100 nm and 100–200 nm, are selected to make a comparison in order to avoid possible grain size effect on twin–triple junction connections. Each subset has 110 and 190 counted grains, respectively. It is shown that the fractions of twin–triple junction connections are almost the same for the full grain size range, suggesting that there is no discernible grain size effect on twin–triple junction connections. This relatively high percentage of twin–triple junction connections also implies that triple junctions could be playing a significant role in the nucleation of deformation twins. This is the first time such statistical data is reported.

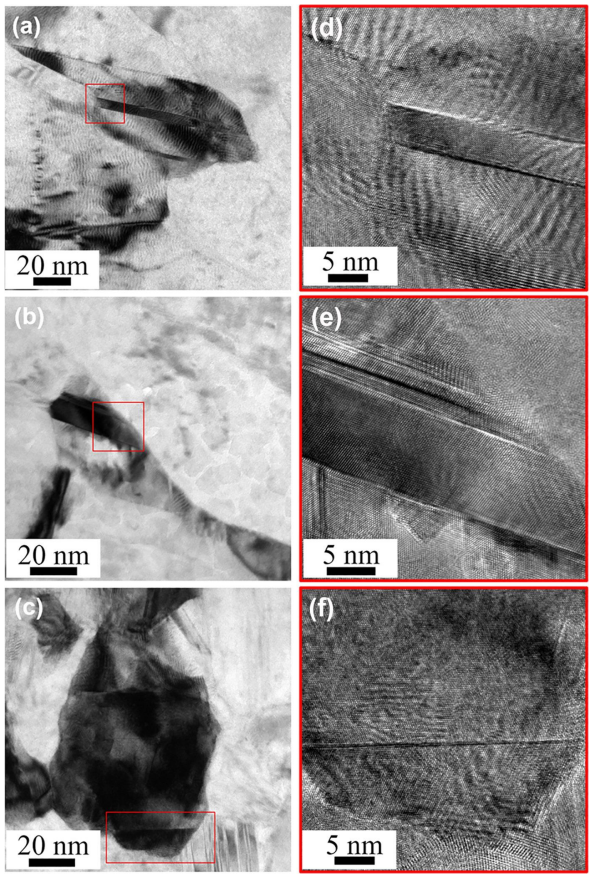


Figure 3: Typical TEM images of the three most common twin morphologies highlighted in Figure 2a: (a) twin thickness is around or slightly larger than the TKD step size; (b) twin thickness is much larger than step size; (c) twin thickness is much larger than step size and there is only one coherent twin boundary in the grain interior; (d), (e) and (f) are enlarged features under HRTEM from (a), (b) and (c), respectively.

A well-known deformation mechanism in nanocrystalline fcc metals is partial emission from grain boundaries, resulting in stacking faults and twins. This has been firstly observed through

Table 1: Statistical data of triple junction related twinning. Yes and No in this table denote whether a twin (boundary or domain) is connected to a triple junction.

Grain size range (nm)	Twinned grain (counts)	No		Yes	
		Count	Fraction (%)	Count	Fraction (%)
30–200	300	52	≈17	248	≈83
30–100	110	19	≈17	91	≈83
100–200	190	33	≈17	157	≈83

simulation [12,13] and then verified by TEM characterization [14,15]. It has also been demonstrated that triple junctions were energetically more favorable [18,35], and therefore were more effective in promoting partial emissions than grain boundaries. It was found that high densities of triple junctions in nanostructured materials could promote twin nucleation [36]. Although some twins connecting with triple junctions might have not been nucleated at the triple junctions, the statistical results obtained from this investigation suggest that triple junctions might have promoted the nucleation of deformation twins.

Although TKD can only perform post-mortem characterization of nanostructure at this stage, it has the advantage of resolving grain boundaries, triple junctions and twin boundaries without them being edge-on. This makes it more suitable than HRTEM for studying triple junction/twinning relationships. Based on the statistical data, it is reasonable to state that triple junctions in nanostructured metals could play a significant role in the nucleation of deformation twins.

Figure 4a shows the grain size distribution and the size distribution of twinned grains in the grain size range from 30 to 200 nm. When analyzing the TKD data, we recorded the information of twinned grains and their sizes. It must be noted that our TKD data volume here is ten times that reported in TEM studies [22,34], and therefore provides more reliable statistics. The average grain size is ≈80 nm. Based on Figure 4a, the fraction of grains that are twinned in each size range is shown in Figure 4b. It clearly reveals an inverse grain size effect, in which the fraction of twinned grains decreases with decreasing grain size [10,22]. However, the optimum grain size for twinning in our observation is not the same as that observed under HRTEM [34]. This discrepancy could be caused by the fact that TKD does not have sufficient resolution to observe very thin twins, that is, twins with a thickness close to or smaller than the 6 nm step size. Smaller grains may contain a large fraction of such small twins, which may have significantly biased the data in Figure 4.

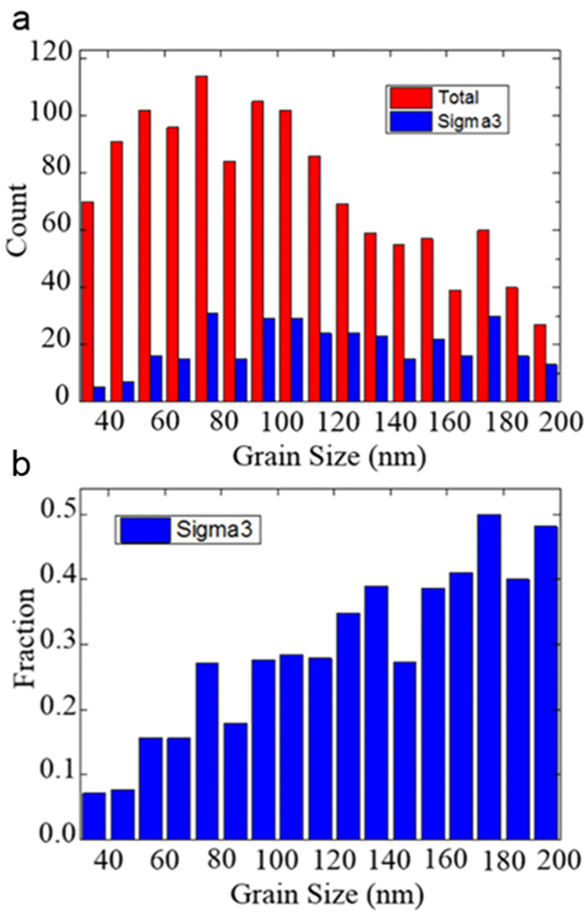


Figure 4: (a) Grain size distribution and the size distribution of twinned grains indicated by red and blue histogram, respectively. (b) Histogram showing the fraction of grains that are twinned in each size range.

Conclusion

Compared with HRTEM, TKD has the advantage of easily collecting a large data set for statistical analysis of deformation twinning. In addition, it has the advantage of being able to characterize defect structures, such as grain boundaries, triple junctions and twins, without requiring them to be edge-on and in the <110> zone axis. This makes it possible to detect twins in all orientations. Statistical TKD data reveals that triple junctions could promote nucleation of deformation twins in a nanostructured Cu–Zn alloy. TKD has limitations in detecting thin twins and therefore becomes unreliable when the grain size is thinner than its step size.

Acknowledgements

This work is supported by Jiangsu Key Laboratory of Advanced Micro & Nano Materials and Technology, Nanjing University of Science and Technology. Y.T. Zhu acknowledges support from the U. S. Army Research Office (W911NF-12-1-0009), the U. S. National Science Foundation (DMT-1104667) as well as the National Natural Science Foundation of China (No. 11172187). Y.S. Li acknowledges support from the National Natural Science Foundation of China (Grant No. 51301092).

References

1. Zhilyaev, A. P.; Langdon, T. G. *Prog. Mater. Sci.* **2008,** *53,* 893–979. doi:10.1016/j.pmatsci.2008.03.002
2. Valiev, R. Z.; Langdon, T. G. *Prog. Mater. Sci.* **2006,** *51,* 881–981. doi:10.1016/j.pmatsci.2006.02.003
3. Saito, Y.; Utsunomiya, H.; Tsuji, N.; Sakai, T. *Acta Mater.* **1999,** *47,* 579–583. doi:10.1016/S1359-6454(98)00365-6
4. Zhu, Y. T.; Liao, X. *Nat. Mater.* **2004,** *3,* 351–352. doi:10.1038/nmat1141

5. Zhao, Y.-H.; Bingert, J. F.; Liao, X.-Z.; Cui, B.-Z.; Han, K.; Sergueeva, A. V.; Mukherjee, A. K.; Valiev, R. Z.; Langdon, T. G.; Zhu, Y. T. *Adv. Mater.* **2006,** *18,* 2949–2953. doi:10.1002/adma.200601472
6. Zhu, T.; Li, J.; Samanta, A.; Kim, H. G.; Suresh, S. *Proc. Natl. Acad. Sci. U. S. A.* **2007,** *104,* 3031–3036. doi:10.1073/pnas.0611097104
7. Ma, X. L.; Huang, C. X.; Xu, W. Z.; Zhou, H.; Wu, X. L.; Zhu, Y. T. *Scr. Mater.* **2015,** *103,* 57–60. doi:10.1016/j.scriptamat.2015.03.006
8. Huang, C. X.; Hu, W. P.; Wang, Q. Y.; Wang, C.; Yang, G.; Zhu, Y. T. *Mater. Res. Lett.* **2015,** *3,* 88–94. doi:10.1080/21663831.2014.968680
9. Lu, L.; Chen, X.; Huang, X.; Lu, K. *Science* **2009,** *323,* 607–610. doi:10.1126/science.1167641
10. Zhu, Y. T.; Liao, X. Z.; Wu, X. L. *Prog. Mater. Sci.* **2012,** *57,* 1–62. doi:10.1016/j.pmatsci.2011.05.001
11. Zhu, Y. T.; Liao, X. Z.; Wu, X. L.; Narayan, J. *J. Mater. Sci.* **2013,** *48,* 4467–4475. doi:10.1007/s10853-013-7140-0
12. Van Swygenhoven, H.; Derlet, P. M.; Hasnaoui, A. *Phys. Rev. B* **2002,** *66,* No. 024101. doi:10.1103/PhysRevB.66.024101
13. Van Swygenhoven, H. *Science* **2002,** *296,* 66–67. doi:10.1126/science.1071040
14. Liao, X. Z.; Zhou, F.; Lavernia, E. J.; Srinivasan, S. G.; Baskes, M. I.; He, D. W.; Zhu, Y. T. *Appl. Phys. Lett.* **2003,** *83,* 632. doi:10.1063/1.1594836
15. Zhu, Y. T.; Wu, X. L.; Liao, X. Z.; Narayan, J.; Mathaudhu, S. N.; Kecskés, L. J. *Appl. Phys. Lett.* **2009,** *95,* No. 031909. doi:10.1063/1.3187539
16. Gutkin, M. Yu.; Ovid'ko, I. A.; Skiba, N. V. *Acta Mater.* **2003,** *51,* 4059–4071. doi:10.1016/S1359-6454(03)00226-X
17. Kumar, K. S.; Suresh, S.; Chisholm, M. F.; Horton, J. A.; Wang, P. *Acta Mater.* **2003,** *51,* 387–405. doi:10.1016/S1359-6454(02)00421-4
18. Palumbo, G.; Aust, K. T. *Mater. Sci. Eng., A* **1989,** *113,* 139–147. doi:10.1016/0921-5093(89)90300-6
19. Wu, X.-L.; Zhu, Y. T.; Ma, E. *Appl. Phys. Lett.* **2006,** *88,* No. 121905. doi:10.1063/1.2186968
20. Wu, F.; Zhu, Y. T.; Narayan, J. *Mater. Res. Lett.* **2014,** *2,* 63–69. doi:10.1080/21663831.2013.862874
21. Wu, X. L.; Liao, X. Z.; Srinivasan, S. G.; Zhou, F.; Lavernia, E. J.; Valiev, R. Z.; Zhu, Y. T. *Phys. Rev. Lett.* **2008,** *100,* No. 095701. doi:10.1103/PhysRevLett.100.095701
22. Wu, X. L.; Zhu, Y. T. *Phys. Rev. Lett.* **2008,** *101,* No. 025503. doi:10.1103/PhysRevLett.101.025503
23. Cao, Y.; Wang, Y. B.; An, X. H.; Liao, X. Z.; Kawasaki, M.; Ringer, S. P.; Langdon, T. G.; Zhu, Y. T. *Scr. Mater.* **2015,** *100,* 98–101. doi:10.1016/j.scriptamat.2015.01.001
24. Wang, Y. B.; Sui, M. L. *Appl. Phys. Lett.* **2009,** *94,* No. 021909. doi:10.1063/1.3072801
25. Zhu, Y. T.; Wu, X. L.; Liao, X. Z.; Narayan, J.; Kecskés, L. J.; Mathaudhu, S. N. *Acta Mater.* **2011,** *59,* 812–821. doi:10.1016/j.actamat.2010.10.028
26. Ni, S.; Wang, Y. B.; Liao, X. Z.; Li, H. Q.; Figueiredo, R. B.; Ringer, S. P.; Langdon, T. G.; Zhu, Y. T. *Phys. Rev. B* **2011,** *84,* No. 235401. doi:10.1103/PhysRevB.84.235401
27. Ma, X. L.; Zhou, H.; Narayan, J.; Zhu, Y. T. *Scr. Mater.* **2015,** *109,* 89–93. doi:10.1016/j.scriptamat.2015.07.027
28. Trimby, P. W.; Cao, Y.; Chen, Z.; Han, S.; Hemker, K. J.; Lian, J.; Liao, X.; Rottmann, P.; Samudrala, S.; Sun, J.; Wang, J. T.; Wheeler, J.; Cairney, J. M. *Acta Mater.* **2014,** *62,* 69–80. doi:10.1016/j.actamat.2013.09.026
29. Wu, X. L.; Qi, Y.; Zhu, Y. T. *Appl. Phys. Lett.* **2007,** *90,* No. 221911. doi:10.1063/1.2745250
30. Keller, R. R.; Geiss, R. H. *J. Microsc.* **2012,** *245,* 245–251. doi:10.1111/j.1365-2818.2011.03566.x
31. Trimby, P. W. *Ultramicroscopy* **2012,** *120,* 16–24. doi:10.1016/j.ultramic.2012.06.004
32. Huang, J. Y.; Zhu, Y. T.; Jiang, H.; Lowe, T. C. *Acta Mater.* **2001,** *49,* 1497–1505. doi:10.1016/S1359-6454(01)00069-6
33. Hebesberger, T.; Stüwe, H. P.; Vorhauer, A.; Wetscher, F.; Pippan, R. *Acta Mater.* **2005,** *53,* 393–402. doi:10.1016/j.actamat.2004.09.043
34. Ma, X. L.; Xu, W. Z.; Zhou, H.; Moering, J. A.; Narayan, J.; Zhu, Y. T. *Philos. Mag.* **2015,** *95,* 301–310. doi:10.1080/14786435.2014.1000418
35. Lin, B.; Jin, Y.; Hefferan, C. M.; Li, S. F.; Lind, J.; Suter, R. M.; Bernacki, M.; Bozzolo, N.; Rollett, A. D.; Rohrer, G. S. *Acta Mater.* **2015,** *99,* 63–68. doi:10.1016/j.actamat.2015.07.041
36. Miura, H.; Sakai, T.; Hamaji, H.; Jonas, J. J. *Scr. Mater.* **2004,** *50,* 65–69. doi:10.1016/j.scriptamat.2003.09.035

License and Terms

This is an Open Access article under the terms of the Creative Commons Attribution License (http://creativecommons.org/licenses/by/4.0), which permits unrestricted use, distribution, and reproduction in any medium, provided the original work is properly cited.

The license is subject to the *Beilstein Journal of Nanotechnology* terms and conditions: (http://www.beilstein-journals.org/bjnano)

The definitive version of this article is the electronic one which can be found at: doi:10.3762/bjnano.7.143

BEILSTEIN JOURNAL OF NANOTECHNOLOGY

Influence of hydrothermal synthesis parameters on the properties of hydroxyapatite nanoparticles

Sylwia Kuśnieruk*§, Jacek Wojnarowicz, Agnieszka Chodara, Tadeusz Chudoba, Stanislaw Gierlotka and Witold Lojkowski

Full Research Paper

Open Access

Address:
Laboratory of Nanostructures, Institute of High Pressure Physics (UNIPRESS), Polish Academy of Sciences, Sokolowska Street 29/37, 01-142 Warsaw, Poland

Email:
Sylwia Kuśnieruk* - s.kusnieruk@poczta.fm

* Corresponding author
§ Tel.: (+48) 22 876 04 34

Keywords:
hydroxyapatite; microwave hydrothermal synthesis; nanoparticle size control; physical properties of HAp NPs; room temperature synthesis

Beilstein J. Nanotechnol. **2016,** *7,* 1586–1601.
doi:10.3762/bjnano.7.153

Received: 18 April 2016
Accepted: 13 October 2016
Published: 04 November 2016

This article is part of the Thematic Series "Advances in nanomaterials II".

Guest Editor: H. Hahn

© 2016 Kuśnieruk et al.; licensee Beilstein-Institut.
License and terms: see end of document.

Abstract

Hydroxyapatite (HAp) nanoparticles of tunable diameter were obtained by the precipitation method at room temperature and by microwave hydrothermal synthesis (MHS). The following parameters of the obtained nanostructured HAp were determined: pycnometric density, specific surface area, phase purity, lattice parameters, particle size, particle size distribution, water content, and structure. HAp nanoparticle morphology and structure were determined using scanning electron microscopy (SEM) and transmission electron microscopy (TEM). X-ray diffraction measurements confirmed crystalline HAp was synthesized, which was pure in terms of phase. It was shown that by changing the synthesis parameters, the diameter of HAp nanoparticles could be controlled. The average diameter of the HAp nanoparticles was determined by Scherrer's equation via the Nanopowder XRD Processor Demo web application, which interprets the results of specific surface area and TEM measurements using the dark-field technique. The obtained nanoparticles with average particle diameter ranging from 8–39 nm were characterized by having homogeneous morphology with a needle shape and a narrow particle size distribution. Strong similarities were found when comparing the properties of some types of nanostructured hydroxyapatite with natural occurring apatite found in animal bones and teeth.

Introduction

Hydroxyapatite (HAp) is a naturally occurring mineral (a form of calcium apatite), which is also an inorganic component of bones, with approximately 8 wt % water, 22 wt % protein and 70 wt % mineral. HAp is a form of calcium phosphate with the chemical formula $Ca_{10}(PO_4)_6(OH)_2$ and a hexagonal crystalline structure. Bones contain about 65 wt % hydroxyapatite, a needle-shaped compound with a width of 5–20 nm and length of 60 nm, which is responsible for rigidity and strength [1,2].

The wide range of potential applications of nanostructured HAp have drawn much attention among researchers, industry and investors. Hydroxyapatite is characterized by its biocompatibility and osteoconductivity. The material has been commonly and successfully used in regenerative medicine and in drug delivery systems [3,4]. Nanostructured hydroxyapatite particles can be applied as building blocks for damaged enamel in caries therapy [5]. Various studies demonstrate that owing to its high surface energy, nanoscale HAp can enhance its mechanical features, enabling a quicker implant surface turnover [6]. Hydroxyapatite materials are used as substitute bones, antiwrinkle creams, and sun creams. They are used in the production of toothpaste formulations and to speed up wound healing. There are patches and ointments using the unique properties of HAp that were developed by scientists in Poland [7]. Hydroxyapatite has also received great interest in the regeneration of animal bone loss.

It has been proved that HAp nanoparticles (nano-HAp) are better positioned to serve as an apatite substitute of bone in biomedical applications than micrometer-sized hydroxyapatite (micro-HAp) [8]. The impact of nano-HAp particles with different morphology on highly malignant melanoma cells was analyzed. The obtained results showed that proliferation of such malignant cells was inhibited more efficiently by the occurrence of the nanoscale effect than by HAp particle morphology [9]. Another study analyzed the effects of different sized nano-HAp – ranging from 20 to 80 nm – on the proliferation of bone-related cells (bone marrow mesenchyme stem cells and osteosarcoma cells) [10]. The cell culture experiment confirmed that in comparison to conventional HAp, cytophilicity of the nanophase mineral improved with nano-HAp. In addition, an increased viability and spread of stem cells was observed for nano-HAP, in particular for the smallest 20 nm particles. In the same vein, the smallest 20 nm particles turned out to be the best inhibitor of growth of osteosarcoma cells, yet all nano-HAp retarded the growth process. Another study also reported the antitumor action of nano-HAp [11].

It is believed that nano-HAp demonstrates desirable cell multiplication in order to optimize biological functionality, a property which is highly dependent on particle size [8]. The above mentioned findings play an important role in the comprehension of nano-HAp biological activity and cytophilicity during biomineralization.

Its ability to circulate in blood and its capacity to deliver a payload to cells and tissues makes nano-HAp a strong candidate to enhance the current effectiveness of disease diagnosis, which was already proved by applying nanoparticles to bioimaging and therapy [3,12].

HAp-based compounds and substances can also play a significant role in waste management and catalyst production [13,14] because of HAp's high sorption activity to numerous ions including several heavy metals and radionuclides [15]. A model compound reflecting bone mineral phase is a nonstoichiometric hydroxyapatite with a molar ratio different than 1.67. Nevertheless, regarding biological apatite, the main substituent is carbonate, which normally occurs at 5 to 8 wt % in bone mineral. Moreover, calcium deficiency is always observed in biological apatites along with a relatively low degree of crystallinity – with diameter on the order of 0.2 μm and smaller [16-18].

In the hydroxyapatite structure, PO_4^{3-} anions can be substituted to a certain extent by carbonate groups, whereas calcium ions can be substituted by magnesium (≈0.7 wt %), sodium (≈0.9 wt %), potassium (0.03 wt %) chlorine (0.13 wt %), fluorine (0.03 wt %) and a few trace elements: Sr, Pb, Zn, Cu, and Fe. The occurrence of the aforementioned elements affects the activity of bone-cell-related enzymes. The introduction of Mg^{2+} and CO_3^{2-} ions causes a decrease in the size of crystals and an increase in solubility. The high reactivity of bone apatite is a result of low crystallinity. The reactivity is reflected in bone resorption processes. The amount of elements substituted depends on the conditions under which that structure is formed. Their occurrence also influences stoichiometry, crystallinity, and thermal and chemical stability of a compound [19]. In line with the increase in calcium deficiency, the number of crystalline structure defects, caused by calcium ion vacancies, increases, diminishing material stability, and as a result, enhancing its solubility [20,21].

A range of various methods have been developed in order to produce HAp powder, among others, combustion preparation [22], and numerous wet chemistry techniques, such as direct precipitation from aqueous solutions, electrochemical deposition [23], sol–gel processes [24] and hydrothermal synthesis [25-27] (Table 1).

In the majority of cases, the synthesized powder is a stoichiometric hydroxyapatite, and oftentimes contains additional phases and substances such as by-products or unreacted substrates [25,32]. Apart from all aforementioned methods, the hydrothermal technique seems to have many advantages [33]. Microwave hydrothermal synthesis (MHS) is a development of the hydrothermal technique [34]. MHS can be defined as a microwave-assisted process in a closed reaction vessel, inducing decomposition or a chemical reaction(s) between the precursor(s) in the presence of a water solvent at a temperature higher than the water boiling point. The technique was developed early on in order to synthesize HAp and was well received because it is easy to use, cost efficient and environmentally friendly [35].

Table 1: Summary of methods of obtaining HAp.

Ref.	Starting materials	Synthesis and process methods[a]	Particle shape/size	End products
[25]	$(Ca(NO_3)_2{\cdot}4H_2O)$, $(NH_4)_2HPO_4$	ppt + 48/72 h in 200 °C + ultrasonic bath washing + drying	median length 100–600 nm, median width 20–40 nm	monetite $CaHPO_4$ after drying
[28]	$(Ca(NO_3)_2){\cdot}4H_2O$, H_3PO_4, NH_4OH	ppt + MW + washing + calcination (500 °C)	nano-rods *L* = 37 nm, *D* = 8 nm	NH_4NO_3 before washing
[29]	$(Ca(NO_3)_2){\cdot}4H_2O$, $(NH_4)_2HPO_4$	ppt + centrifugation (6000 rpm for 10 min) + washing + freeze drying + calcination (550 °C/5 h)	rod-like crystals *L* = 40 nm, *D* = 15 nm	NH_4NO_3 before washing
[30]	$Ca(OH)_2$ calcinate to form CaO (improves the reactivity of lime), H_3PO_4	ppt (20 °C) + 24 h ripening + washing +calcination (900 °C)	300 nm	no impurities because of washing
[31]	$CaCl_2$, KOH, KH_2PO_4	ppt (70 °C) 1 h + reflux time (1 week) + filtration + washing + drying	length of the crystals 200–400 nm; SSA 70 m^2/g	Cl^- before washing, K^+ could substitute calcium ions into the HAp crystal lattice
[32]	$CaSO_4{\cdot}0.15H_2O$, $(NH_4)_2HPO_4$	ppt (25 °C) + 21 days in 25 °C + washing + drying	crystal size of 1 to 8 μm	$(NH_4)_2SO_4$, H_2SO_4 before washing, brushite after drying

[a]ppt, precipation; MW, microwave.

In a previous study [26,27], we reported microwave-driven hydrothermal synthesis of nano-HAp, with average particle size ranging from 6 to 30 nm, which varied with synthesis time. Further, it was found that the Ca/P ratio of the NPs was synthesis-time dependent. The purpose of this study was to further develop the previously reported synthesis methods in order to: further extend the range of particle sizes, scale up the synthesis process by six orders of magnitude of six types of nano-hydroxyapatite, and to demonstrate that a precise control of the average particle size and particle size distribution can be maintained and these parameters can still be precisely tuned.

Experimental

Materials

The HAp nanopowder was synthesized via a simple precipitation method (exactly in the acid/base neutralization process). The precursors for the synthesis were calcium hydroxide (10.3458 g) ($Ca(OH)_2$, pure, CHEMPUR, Poland) and orthophosphoric acid (5.7 mL) (H_3PO_4, 85 wt % solution, analytically pure, CHEMPUR, Poland). Deionized water was used for the synthesis (450 mL) (HLP 20UV, Hydrolab, Poland). The molar ratio of the starting materials used was Ca/P 1.67. Phosphoric acid was added dropwise to the water suspension of calcium hydroxide at a rate of 0.01 mL every 0.5 s (Titrator, SI Analytics, Titronic universal, TZ3260, Germany); hydroxyapatite was formed with the following reaction scheme:

$$10\,Ca(OH)_2 + 6\,H_3PO_4 \rightarrow Ca_{10}(PO_4)_6(OH)_2(\downarrow) + 18\,H_2O. \quad (1)$$

The hydroxyapatite precipitate was intensively stirred using a mechanical stirrer at room temperature. The suspension of Type 1 hydroxyapatite was obtained after 30 min of additional stirring. In order to obtain Type 2–Type 6 hydroxyapatite materials, the reaction water suspension was transferred into a capped Teflon® vessel and heated using microwave radiation in the MSS2 reactor (ITeE-PIB, IHPP PAS, Ertec Poland [36]) as shown in Figure 1.

The parameters of the reactor are as follows: $p <= 6$ MPa, $T <= 260$ °C, $V = 470$ mL, $P = 3$ kW. Hydroxyapatite (Type 2–Type 6) was obtained by microwave hydrothermal synthesis (MHS). The MSS2 reactor (Figure 1) permits rapid, uniform heating and synthesis under high purity conditions in a closed vessel with precise control of the reaction time (Table 2).

The synthesis was carried out in the MSS2 reactor at a constant power during the process, over the duration times of 55, 90, 600 and 1200 s, depending on the type of the synthesized powder (Type 2–Type 6) at varied pressures (Table 2).

The only by-product of hydroxyapatite synthesis is water, which enables the washing of synthesis products to be skipped. The as-obtained precipitate was dried in a lyophilizing cabinet (Lyovac GT-2, SRK Systemtechnik GmbH, Germany), attached with a vacuum pump by Leybold Trivac. The drying parameters depended on the amount and type of powder batch.

Methods

X-ray diffraction (XRD). XRD patterns of nano-HAp powders were collected on an X'Pert PRO, PANalytical diffractometer equipped with a copper anode (Cu $K\alpha_1$) and an ultra-fast PIXcel^{1D} detector [37]. The analysis was performed at room

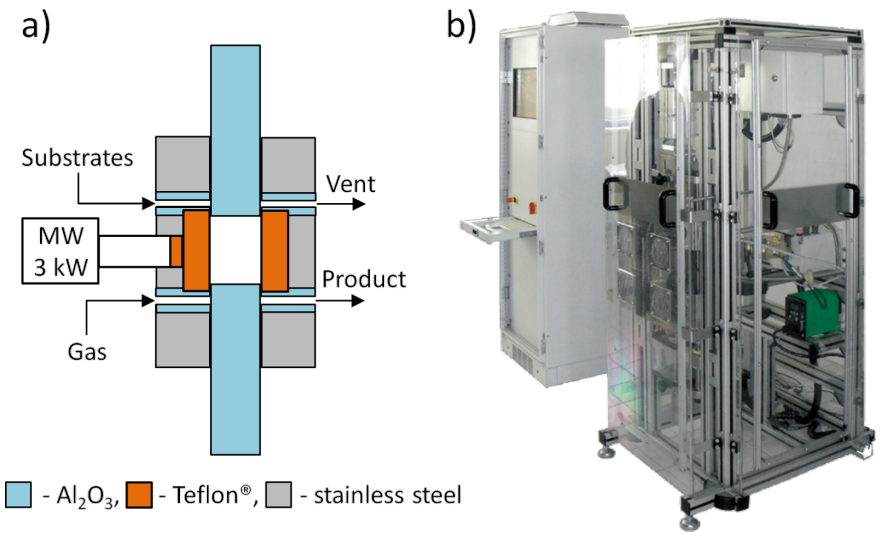


Figure 1: The MSS2 reactor [36]: a) general draft of the MSS2 reactor; b) view of the prototype; c) principle of operation of the load and unload system.

Table 2: Synthesis parameters.

Sample	Synthesis parameters of the MSS2 reactor			
	Time (s)	Pressure (Bar)	Temperature (°C)	Power (kW)
HAp Type 1	obtained without using the reactor			
HAp Type 2	55	≈1	115	3
HAp Type 3	90	3	140	3
HAp Type 4	600	3	140	3
HAp Type 5	600	10	190	3
HAp Type 6	1200	20	220	3

temperature in the range 2θ = 10–100° with a step of 0.03°. The average diameter of nano-HAp crystallites (d_{hkl}) was calculated on the basis of the Scherrer's equation [38].

Density measurements. The density of two nano-HAp types were measured using a helium pycnometer (AccuPyc II 1340, Micromeritics) at 24 ± 2 °C, according to ISO 12154:2014.

Specific surface area (SSA). SSA of the nanopowders was measured by analysis of the BET isotherm method using a Gemini 2360 instrument by Micromeritics according to ISO 9277:2010. Before the density and SSA measurements were carried out, the powders were dried at 150 °C for 2 h in a constant flow of helium (FlowPrep 060 desorption station by Micromeritics). The average diameter of the particles (d_{BET}) was calculated on the basis of SSA and density (see Equation 2); assuming that all HAp particles were spherical and identical.

$$d_{BET}\left[\text{nm}\right] = \frac{6000}{\text{SSA}\left[\frac{\text{m}^2}{\text{g}}\right]\cdot\rho\left[\frac{\text{g}}{\text{cm}^3}\right]}, \quad (2)$$

where d_{BET} is the average particle diameter calculated using the SSA value, SSA is the specific surface area calculated using the BET isotherm, and ρ is the material density.

TG-DSC. TG-DSC analysis was carried out using an STA 449 F1 Jupiter by Netzsch. The analysis was performed with a heating rate of 5 °C/min; the top temperature was 1350 °C. The measurement was performed under a constant flow of helium at 60 mL/min.

SEM and TEM. The morphology of the nanopowder samples was examined using SEM (Ultra Plus; Carl Zeiss Meditec AG, Jena, Germany) and transmission electron microscopy (TEM)

(JEM2000EX; JEOL, Tokyo, Japan). The TEM, high-resolution TEM, and selected area electron diffraction tests were conducted at 200 kV. The samples for the TEM observations were prepared by dropping the methanol particle dispersion, created by an ultrasonic technique, on a carbon film supported on a 300-mesh copper grid. Additionally, TEM tests were used to determine the nanoparticle size distribution. The particle size histograms were obtained by examining an area of a sample containing about 250 nanoparticles. The nanoparticle shape was nearly to spherical. The obtained histograms were fitted to either normal or log-normal distributions (X-squared test and Pearson's coefficient) [26].

Chemical composition of the powders. The experimentally measured ion content in the powders may not be identical to that in the solutions. The chemical composition analysis of powders was examined by inductively coupled plasma optical emission spectrometry (ICP-OES) with induction in argon plasma (Thermo Scientific, iCAP 6000 series, United Kingdom). The samples analyzed using ICP-OES were prepared as follows: 5 mg of powder was weighed in a 110 mL Teflon® vessel and 15 mL of deionized water (HLP 20UV, Hydrolab, Poland) was added. Then, 6 mL of HNO_3 was added and the solution was subjected to one microwave heating cycle in the microwave reactor (Magnum II, Ertec, Poland). After cooling, the sample volume was replenished to 50 mL with deionized water [39].

Crystallite size distribution. A Nanopowder XRD Processor Demo was used for the analysis of the XRD peak profile by using an analytical formula for polydispersive powders [40]. This technique provides four parameters: average particle size, error of average particle size, dispersion of size and error of dispersion of size. Hence, a full particle size distribution curve and an estimation of "thickness" of this curve (error bars) are obtained. For calculating the crystallite diameter and size distribution, the Nanopowder XRD Processor Demo web application employs equations derived for spherical crystallites. The website http://www.science24.com/xrd provides an on-line tool where diffraction files can be directly dropped. The files are processed on a server to extract particle size distribution for XRD peaks. Unlike standard fitting, the tool does not act in the reciprocal space at but solves all sets of equations in a few auxiliary spaces simultaneously. This allows an analysis of XRD data with heavily convoluted reciprocal space peaks [41].

Results and Discussion

The precise control of particle size and particle size distribution is one of the main challenges faced by nanoparticle technology [42]. An increased scale up of hydroxyapatite production was achieved as a result of increasing the initial volume of reagents and using a new reactor, MSS2, as described previously. The precursor, and at the same time HAp Type 1, was synthesized, obtaining ≈500 mL of suspension. This was dried in a lyophilizing cabinet and ≈14 g (95% efficiency) was obtained from a single synthesis. In previous work [26,27] the precursor was prepared from 75 mL of the suspension (where HAp was not obtained at room temperature). 350 mL of the suspension (≈11 g of HAp) was fed to the MSS2 reactor (maximum permitted feedstock volume in MSS2 reactor's reaction chamber), in comparison with previous work [26,27], where a different microwave reactor was used (Ertec Magnum-II) and only 70 mL of the suspension (≈2 g of HAp) could be synthesized at one time. When using the MSS2 reactor, up to 150 g of HAp could be synthesized over one day (10 working hours), while in the case when using the Ertec Magnum-II reactor, up to 20 g could be produced [26,27].

An XRD analysis of all obtained HAp powders was carried out. The results confirmed that Type 1–Type 6 HAp powders were pure crystalline products (Figure 2).

Based on the diffraction patterns, the gradual growth of the crystallites (nanoparticles) from Type 1 to Type 6 was observed. The presence of other crystalline phases or any amorphous components was not observed. In addition, the XRD method was used to test a beef bone, a rabbit bone, a horse bone, a turkey bone, a pork bone and a duck bone (Figure 3).

Additionally, the XRD results of a cod bone, a human tooth with enamel and a tooth root were summarized. Pastilles with a diameter of 12 mm, obtained by pressing pulverized bones under a pressure of 10 MPa, were used for the EDX measurement. The above mentioned natural samples were used as a comparison and reference to natural apatite. The crystal structures of the tested samples of bones and the tooth without enamel are almost identical. The diffraction pattern of HAp Type 1 nanopowder coincides with the result of HAp NPs for the tooth without enamel. It is also very similar to bone hydroxyapatite NPs. The publication by Martin et al. [43] contains XRD results of human bone. When juxtaposing the XRD results of human bone and of a HAp Type 1 sample, it can be found that they look identical. The HAp particles obtained and described in this paper display peaks with hexagonal crystalline structure and P63/m space group, which was confirmed by TEM results. The presence of no other crystalline phase than hydroxyapatite was detected. The peaks characteristic of hydroxyapatite were observed at angles of 26° and 30–34° [44]. These results for HAp Type 1 confirm that the obtained hydroxyapatite is pure and homogeneous. For HAp Type 1 and natural apatites juxtaposed in this paper and juxtaposed with the results for human bone [43], the peaks are located in the same

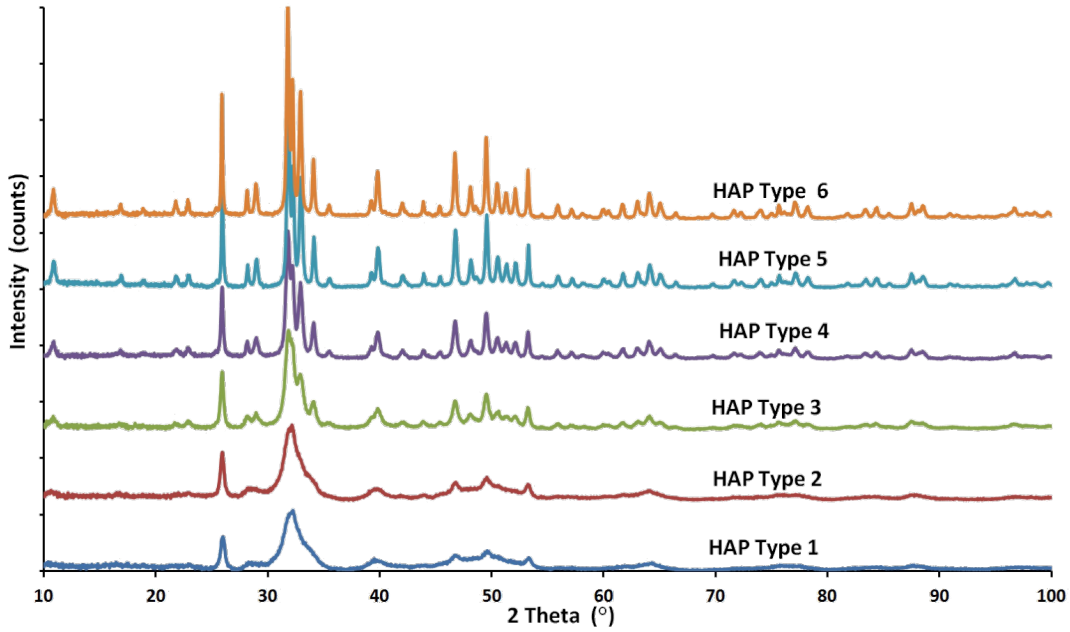


Figure 2: XRD patterns of HAp powders.

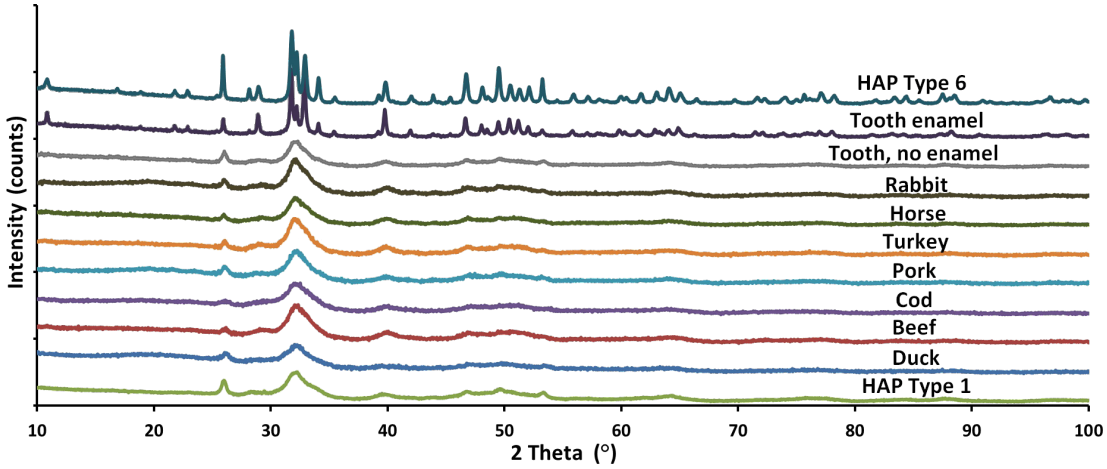


Figure 3: XRD patterns of a duck bone, a beef bone, a pork bone, a turkey bone, a horse bone, a rabbit bone, a cod bone and a tooth with and without enamel, as well as HAp Type 1 and Type 6 nanopowders.

places in diffraction patterns and are broadened at the same peak proportions. The peak broadening for HAp Type 1 and natural HAp of animal bones and human bone displays the same crystalline morphology, which means that synthetic HAp Type 1 is characterized by the identical morphology to human HAp [43], and identical to HAp occurring in animal bones (Figure 3). On this basis it can be stated that HAp Type 1 is a synthetic equivalent of natural bone. HAp Type 6 is characterized by a larger nanoparticle size, which is visible through a narrower width of the peaks in the diffraction pattern. The crystalline structure of HAp Type 6 is very similar to the crystalline structure of tooth enamel.

Type 1–Type 6 hydroxyapatite indicates high nonstoichiometry (Table 3): the Ca/P molar ratio is 1.61 ± 0.03, where synthesized hydroxyapatites are apatites with calcium deficiency (Ca-def). The molar ratio of the obtained hydroxyapatites is very similar to the Ca/P molar ratio present in natural bone (1.65), or enamel (1.62) [5,45]. The Ca/P molar ratio does not depend on the synthesis parameters.

Table 3: The Ca/P ratio determined by ICP-OES measurements.

Sample	Ca/P
HAp Type 1	1.64 ± 0.02
HAp Type 2	1.61 ± 0.02
HAp Type 3	1.61 ± 0.02
HAp Type 4	1.59 ± 0.01
HAp Type 5	1.61 ± 0.02
HAp Type 6	1.60 ± 0.03

The papers by Smolen et al. [26,27] are very interesting publications, describing that the Ca/P molar ratio for the obtained HAp powders depended on the duration and temperature of the synthesis reaction carried out in an Ertec Magnum II microwave reactor. They adopted a constant molar ratio of reagents of Ca/P 1.67 for all syntheses. In order to prepare the reaction suspension, H_3PO_4 was added dropwise to the water suspension of $Ca(OH)_2$ at a speed of 0.01 mL every 3 s, while intensely stirring the suspension at room temperature. The authors did not obtain HAp NPs at room temperature. They treated the suspension obtained at room temperature solely as the precursor for microwave hydrothermal synthesis of HAp NPs. After the completed syntheses they flushed the obtained suspensions with ethanol and water and subsequently dried in a laboratory drying cabinet [26,27].

The synthesis described herein reports a similar technology for obtaining HAp NPs. We used the same reagents (H_3PO_4, $Ca(OH)_2$) and we adopted the same constant molar ratio of the reagents being Ca/P 1.67. However, our method differs in several very important aspects from the afore mentioned paper. Namely, we added H_3PO_4 dropwise to the $Ca(OH)_2$ suspension at a six times greater speed (0.01 mL every 0.5 s). We did not flush the obtained suspensions but only dried them in the lyophilizing cabinet. At room temperature we always obtained fully crystalline HAp Type 1. In order to obtain HAp Type 2–6, we used a MSS2 microwave reactor, where HAp Type 1 suspension was used as the precursor. During our experiment, we did not observe any impact of synthesis duration and temperature on the Ca/P molar ratio of HAp powders. In order to confirm this, it was decided to synthesize a powder with a different starting Ca/P molar ratio and determine the parameters of the obtained powder. The hydroxyapatite precursor was prepared with calcium deficiency, with the molar ratio Ca/P 1.57. The synthesis procedure was the same as described in the section Materials. The results of ICP-OES tests revealed that powders (Type 1–Type 6) characterized by high nonstoichiometry were obtained with calcium deficiency, as was assumed. The molar ratio of the synthesized hydroxyapatite types was Ca/P 1.52 ± 0.01. The achieved results clearly show the manner in which stoichiometry was controlled. The stoichiometry was controlled by modifying the precursor at the initial synthesis stage (see the section Materials). Contrary to the previous results, the Ca/P ratio was not a function of the synthesis parameters [26,27].

We believe that the major reasons for differences between our method and the method presented by Smolen et al. [26,27] in terms of controlling the Ca/P molar ratio of HAp NPs are as follows: the use a different type of precursor, a different manner of flushing, and a different manner of drying.

The density of the HAp Type 1–Type 6 nanopowders was 2.86 to 3.03 g/cm^3 (Table 4). Literature data show that the density of hydroxyapatite nanopowders is 3.05 g/cm^3 [45]. For Type 1–Type 3 powders, the density values were lower by 4–6%. Such a difference results from the nano-size of the particles of the obtained nanopowder. In the case of nanomaterials, a decrease in density is observed in comparison with micropowders, because the material surface layer is not as closely packed as the whole volume of particles [46] (with the observed appropriately small surface in relation to the higher density value), or the presence of small quantities of the amorphous phase. The specific surface area ranged from 51 to 258 m^2/g (Table 4), where the average particle diameter calculated based on the SSA was 8 to 39 nm (Table 5).

Table 4: Density and specific surface area (SSA) of synthesized hydroxyapatite powders.

Sample	SSA a_s ± σ (m^2/g)	Density ρ_s ± σ (g/cm^3)
HAp Type 1	258 ± 1	2.86 ± 0.02
HAp Type 2	211 ± 1	2.92 ± 0.02
HAp Type 3	149 ± 1	2.95 ± 0.01
HAp Type 4	85 ± 1	3.00 ± 0.01
HAp Type 5	61 ± 1	3.03 ± 0.01
HAp Type 6	51 ± 1	3.04 ± 0.01

Based on an analysis of the XRD diffraction patterns, a distribution of crystallite sizes was determined for HAp NPs (Figure 4).

Depending on the synthesis time and applied pressure, the HAp nanomaterial density gradually increased and the SSA considerably decreased – the data are presented in Table 4. For Type 6 hydroxyapatite, a SSA of 51 m^2/g and a density of 3.04 g/cm^3 were found. The average particle diameter was calculated based on SSA and density results. For Type 1 hydroxyapatite, the average particle diameter was 8 nm, while for Type 6 it was 39 nm. For Type 3, a decrease in SSA to 149 m^2/g was observed. The density increased by 0.09 g/cm^3 to 2.95 g/cm^3; the

Table 5: Comparison of particle diameter for the various HAp nanopowders, calculated by four different methods.

Sample	Average particle diameter from SSA/BET $d \pm \sigma$ (nm)	Average crystallite size from the Scherrer's equation		Average particle diameter from TEM $x_c \pm \sigma$ (nm)	Average crystallite size from Nanopowder XRD Processor Demo $d \pm \sigma$ (nm)
		Length (nm)	Width (nm)		
HAp Type 1	8.1 ± 0.1	19 ± 9	6 ± 2	6.5	9.6 ± 7
HAp Type 2	9.7 ± 0.1	24 ± 9	7 ± 0.5	7.3 ± 0.3	11.4 ± 6.4
HAp Type 3	13.7 ± 0.1	28 ± 12	14 ± 6	11.7 ± 0.3	15.7 ± 9.8
HAp Type 4	23.5 ± 0.3	38 ± 17	23 ± 6	18.4 ± 0.6	24.4 ± 16.9
HAp Type 5	32.5 ± 0.4	50 ± 20	30 ± 9	26.9 ± 0.6	38.4 ± 28.1
HAp Type 6	38.7 ± 0.6	60 ± 20	33 ± 9	34.8 ± 0.9	63.7 ± 45

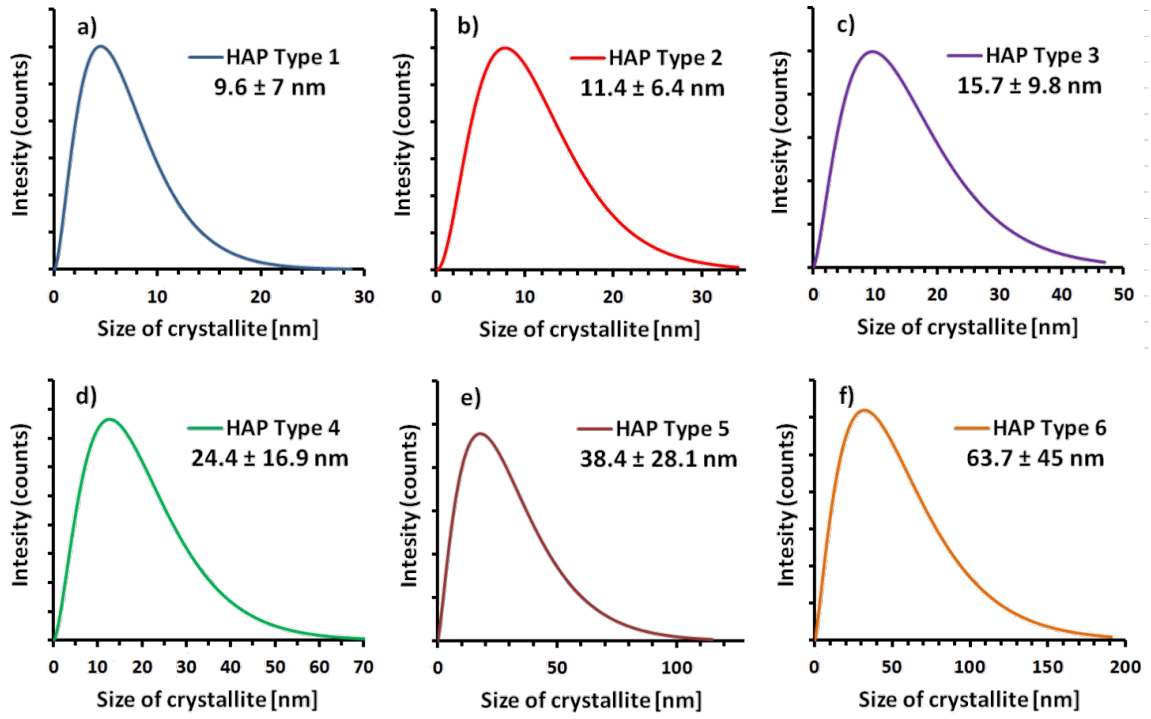


Figure 4: Crystallite size distribution, obtained using Nanopowder XRD Processor Demo [48]: a) HAp Type 1; b) HAp Type 2; c) HAp Type 3; d) HAp Type 4; e) HAp Type 5; f) HAp Type 6.

average particle size was 14 nm. Due to the longer synthesis time and accordingly higher temperature in the reactor, the SSA was reduced to 85 m^2/g for Type 4, to 61 m^2/g for Type 5, and to 51 m^2/g for Type 6. Therefore, the density was found to be 3.00 g/cm^3 (Type 4), while the particle diameter increased to 24 nm. For Type 6, the average diameter of the obtained particles was 39 nm and the density was 3.04 g/cm^3, which was nearly equal to the literature value for hydroxyapatite [47].

The material was characterized by an average particle diameter between 10 and 64 nm from data obtained using Nanopowder XRD Processor Demo (Table 5). The calculations of the average crystallite size (XRD) coincide with an accuracy of 2–25 nm with average particle diameters calculated based on the SSA, which confirms that the nanopowder is monocrystalline and does not form aggregates. However, a change in the nanoparticle diameter is directly proportional to the density and inversely proportional to the SSA.

Hydroxyapatite is the primary component of bones and teeth [5]. The crystallite (particle) size of natural apatites present in bones (Table 6), calculated based on XRD using Scherrer's equation, revealed a strong similarity to the results of synthetic Type 1 and Type 2 hydroxyapatites (Table 5).

Table 6: Comparison of crystallite sizes in bones as examples of natural apatite, calculated using XRD and Scherrer's equation.

Examples of natural apatite	Average crystallite size from Scherrer's equation	
	Length (nm)	Width (nm)
Duck bone	17 ± 2	7 ± 1
Beef bone	21 ± 5	6 ± 1
Cod bone	19 ± 2	5 ± 1
Pork bone	16 ± 6	6 ± 1
Turkey bone	20 ± 7	6 ± 3
Horse bone	20 ± 2	8 ± 1
Rabbit bone	20 ± 3	6 ± 2
Tooth, no enamel	21 ± 4	8 ± 2
Tooth, with enamel	48 ± 30	40 ± 22

Thus, the hydroxyapatite that was synthesized displayed a structural similarity to bones and teeth. The width and length of crystallites in bones and teeth without enamel are comparable, where the values fall within the distribution range. Bones contain a considerable quantity of carbonate ions (5–8%). Apatite present in bones contains very few hydroxyl groups. Among the examples of natural apatites given, only the apatite present in tooth enamel contains less carbonates and a higher concentration of hydroxyl ions [49]. In her work, Sharon Kehoe [50] draws attention to the importance of atmospheric environment. She states that when chemical precipitating process occurs, adsorption of atmospheric CO_2 can follow in a way that the carbonate anion in the form of CO_3^{2-} can become imbedded into the crystalline lattice of HAp. This could give rise to the appearance of microscale stresses and deformations in the crystal lattice of the stoichiometric HAp [51]. Crystallographic changes in the structure of biological apatites are caused by carbonate substitutions in the apatite crystalline lattice [52]. Carbonate substitutions in the hydroxyapatite lattice are unstable and depend on synthesis temperature. Table 7 summarizes the results of the lattice parameters of synthesized HAp.

Table 7: Results of the lattice parameters determined by the XRD analysis for synthesized hydroxyapatite.

Sample	Lattice parameter *a* (Å)	Lattice parameter *c* (Å)	*a*/*c*
HAp Type 1	9.436 ± 0.003	6.874 ± 0.002	1.373
HAp Type 2	9.431 ± 0.002	6.878 ± 0.001	1.371
HAp Type 3	9.421 ± 0.001	6.878 ± 0.001	1.370
HAp Type 4	9.421 ± 0.001	6.878 ± 0.001	1.370
HAp Type 5	9.421 ± 0.001	6.877 ± 0.001	1.370
HAp Type 6	9.420 ± 0.001	6.877 ± 0.001	1.370

The highest value of the *a* lattice parameter was found for Type 1 HAp. Type 1 hydroxyapatite was obtained by a precipitation method at room temperature, where the quantity of CO_2 dissolved in water is the greatest (increase in *a* direction), and lower when HAp was synthesized using the reactor (i.e., Type 2–Type 6, increased reaction temperature). An advantage of the product synthesized at room temperature is the greater carbonate content, which better correlates to the natural apatite present in bones.

Changes in the *a*/*c* ratio would translate into corresponding changes in the lattice parameters. Hence, lowering the *a*/*c* ratio would mean a reduction in the *a* lattice parameter and a simultaneous increase in the *c* lattice parameter, making it more beneficial than an increased *a*/*c* ratio, which efficiently reduces the crystallinity response [50]. The increased *a*/*c* ratio (an increase in *a* and a decrease in *c*) contributes to reduced crystallinity and the presence of a foreign phase, β-TCP [53].

When comparing the various methods of converting the XRD results, Scherrer's equation and the Nanopowder XRD Processor Demo (Tab. 5) showed similar results that fell within the standard deviation of methods. The results of the XRD method calculated using Scherrer's equation coincide with an accuracy of ≈5% with the results of the method based on SSA and density results. The average particle diameter of HAp samples obtained from TEM measurements (Table 5) is inconsistent with the results found by the other methods. These differences may be caused by the small quantity of the tested sample in comparison with the diffraction method, as well as sample image overlapping and particle shape.

Hydroxyapatite nanoparticles are not spherical; they occur in the form of lamellas, which generates an error and discrepancies between the methods. When comparing the four methods used for determining the particle/crystallite size, the use of Scherrer's equation yielded most accurate results [54]. It was the only method which could provide two dimensions (length and width) of the crystallites, based on which we inferred also the shape of the obtained particles (needles/lamellas). The same particle shape was independently confirmed by TEM measurements of HAp powders (see Figures 6–11 that follow), which confirms that Scherrer's equation is capable of determining the shape of the particles. All the other methods of the Nanopowder XRD Processor Demo web application, converting the SSA results and TEM measurements using the dark field technique, provided the dimension (diameter) of particles/crystallites using the equations derived for spherical particles/crystallites. The adopted assumption is a significant simplification for the purpose of making calculations easier, which however introduces the systematic error in the results indicated in Table 5.

However, the results of particle/crystallite size generated by all the mentioned methods constitute excellent data for controlling the quality and repeatability of HAp powders we obtain. Morphology was also evaluated by SEM and TEM techniques. Figure 5 presents SEM images of Type 1–Type 6 HAp nanoparticles.

The analysis of six hydroxyapatite types using SEM indicated that homogeneous powders of nanoscale particles were formed (Figure 5). It was observed that the morphology of the nanopowder changed from homogeneous, elongated particles (Type 1 and Type 2) to spherical particles (Type 3, 4, 5 and 6). This depended on the adopted synthesis parameters resulting from recrystallization. Crystallinity is the quantity of the crystalline phase in comparison with the content of the amorphous phase present in a material. HAp crystallization occurs in accordance with the Ostwald's rule, so it usually forms from recrystallization of such precursor phases as octacalcium phosphate (OCP), dicalcium phosphate dihydrate (DCPD) and amorphous calcium phosphate (ACP) [55]. HAp crystallization during the synthesis ensues in accordance with the mechanism of crystallization from a solution. During the growth process, particles may grow on the surface of sediment or precipitate in all directions. Their growth may be expected to increase with the synthesis time until the crystallization process equilibrium has been achieved [55].

During the synthesis in the MSS2 reactor, HAp particles are dissolved and undergo recrystallization. Sharon Kehoe [50] noticed that when dealing with such a process, the smaller particles dissolve completely for the benefit of larger particles that continue to grow. As a result, the total number of particles decreases in line with the increase in their sizes, similar to the granularity of their area [50]. Both phenomena, the increase and decrease of roughness, result from the tendency to reduce the matter surface energy by a reduction of the SSA [31] (Table 4).

HAp morphology varies depending on the executed process parameters. The synthesis temperature growth (Type 3, 4, 5 and 6) leads to more regular, spherical HAp particles (Figure 5). Numerous reports have proved that synthesis at a low temperature leads to HAp crystals with needle morphology [31], which is confirmed by the SEM and TEM results of Type 1 HAp nanopowder. According to the literature review by Kehoe [50], many researchers who run synthesis at low temperatures obtained particles that were slightly thinner and longer, and more irregular, having less distinct borders. Additionally, these particles demonstrated a greater inclination to agglomerate [56]. It was also shown that the higher the crystallinity of the powder, the more regular the shape of the particle. This finding came from the observation that transition from irregular to regular morphologies, along with rise of the reaction temperature, coincided with the increase of the HAp particle crystallinity [50].

The TEM analysis indicated that each of the obtained hydroxyapatite types was a hydroxyapatite with P63/m space group, displaying a hexagonal structure with parameters a = 9.424 Å, c = 6.879 Å [57]. Variable synthesis parameters, such as time, temperature (pressure), or synthesis without the use of a reactor, were found to exert no visible impact on the phase composition

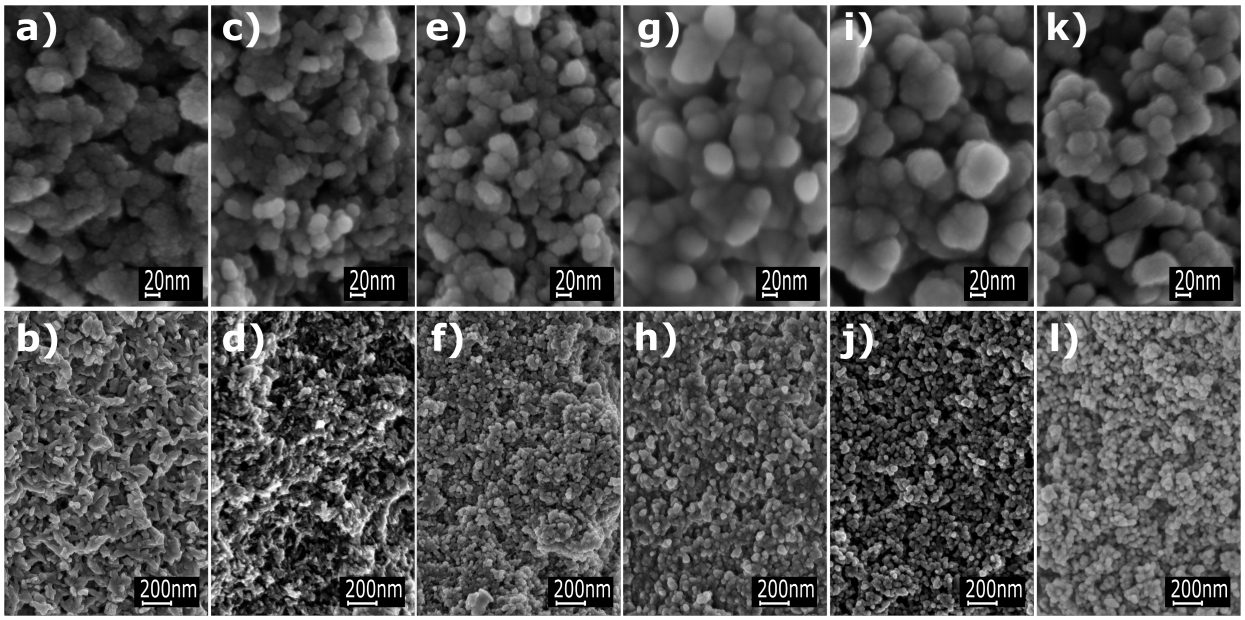


Figure 5: SEM micrographs of HAp powders: (a, b) Type 1; (c, d) Type 2; (e, f) Type 3; (g, h) Type 4; (i, j) Type 5; (k, l) Type 6.

and on the crystalline lattice parameters (Table 7). In all cases, obtaining hexagonal hydroxyapatite without the presence of foreign phases was observed.

A microscope image of Type 1 HAp (Figure 6), taken with the bright field technique, shows elongated structures with similar diameters of ≈6.5 nm (ranging from 4 to 9 nm), but with outliers ranging from more than ten to several hundred nanometers.

It was impossible to determine the length distribution of these structures precisely due to their agglomeration (Figure 6). The average nanoparticle size for Type 2 HAp was 7.3 nm (Figure 7).

An analysis of the histogram reveals that the sample contained a considerable fraction of similar sized particles, ranging from 5 to 10 nm. Crystallites did not display considerable differences in size and shape, but rather elongated, rice grain-shaped nanoparticles prevailed. The average particle size for Type 3 HAp was 11.7 nm. The sample contained a considerable fraction ranging from 5 to 20 nm. Type 3 HAp particles were of a similar size but quite diverse shape (Figure 8).

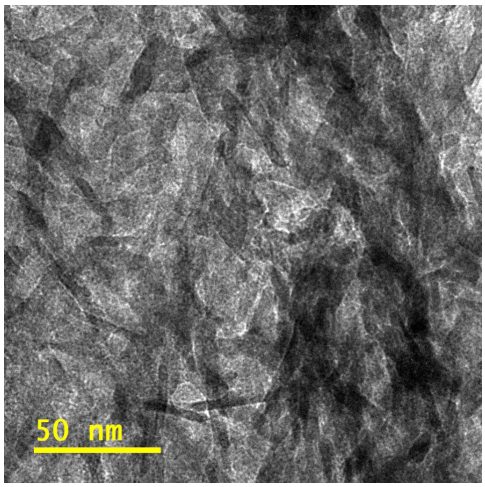


Figure 6: The bright field TEM image of Type 1 HAp.

The average particle size for Type 4 HAp was 18.4 nm. The sample displayed a considerable diversity in average nanoparticle size in relation to samples of Type 1, 2 and 3 HAp. HAp crystallites for this type differed in shape and size as can be seen in Figure 9.

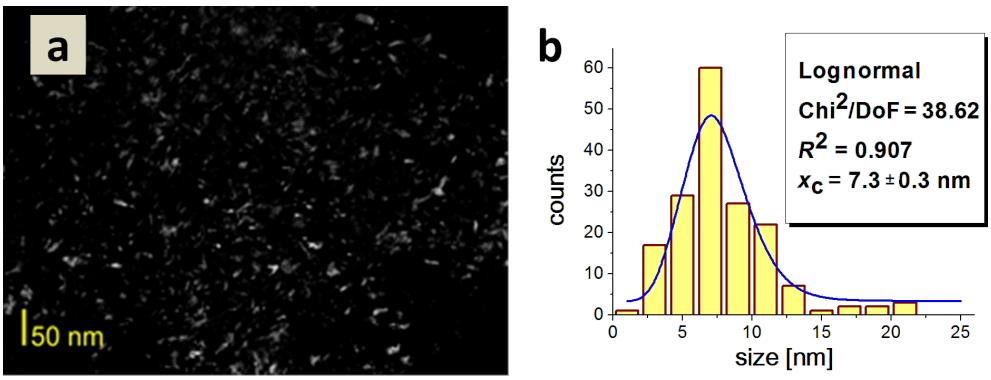


Figure 7: a) A dark field TEM image of Type 2 HAp; b) a histogram of the particle size distribution.

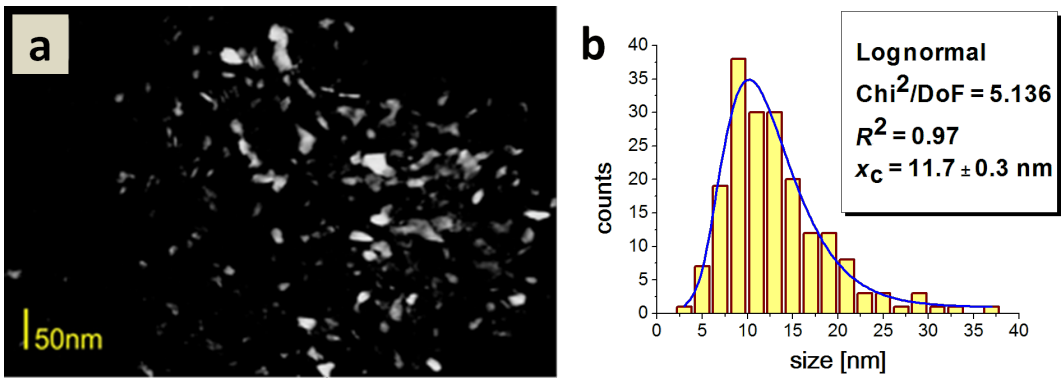


Figure 8: a) A dark field TEM image of Type 3 HAp; b) a histogram of the particle size distribution.

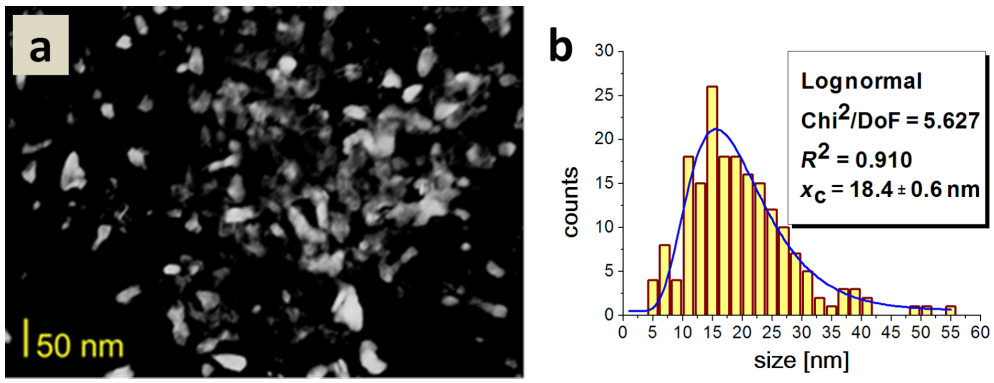


Figure 9: a) A dark field TEM image of Type 4 HAp; b) a histogram of the particle size distribution.

The average particle size for Type 5 HAp was 26.9 nm. The crystallites did not display significant differences in shape (Figure 10).

The average particle size for Type 6 HAp was 35 nm. Similarly, in this case, the particles did not display significant differences in shape, but they differed in size as shown in Figure 11.

The size distribution was found to be broader as compared with our previous publications [26,27]; this results primarily from an increased volume of the reaction mixture (6-fold increase in reagent volume). The volume of the reaction feedstock (350 mL, 3 kW) in the MSS2 reactor is considerably greater than that possible for the Ertec Magnum II reactor (70 mL, 0.6 kW). The increase in production scale (volume) contributes

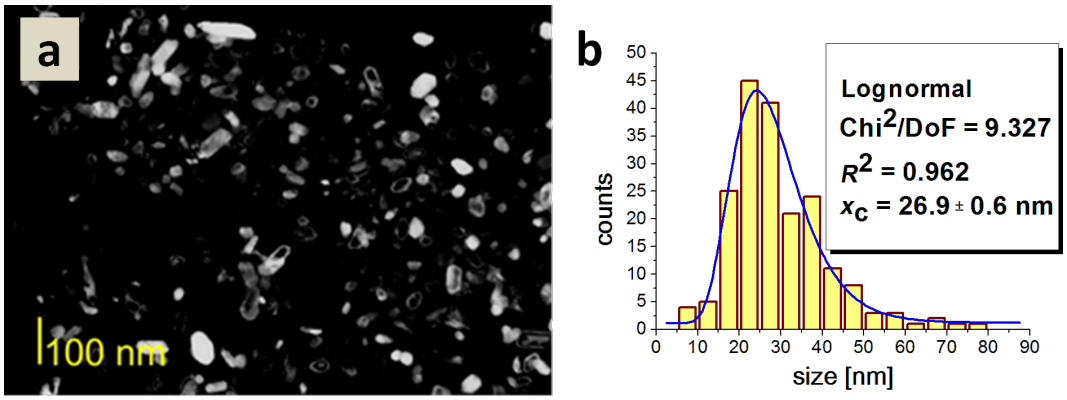


Figure 10: a) A dark field TEM image of Type 5 HAp; b) a histogram of the particle size distribution.

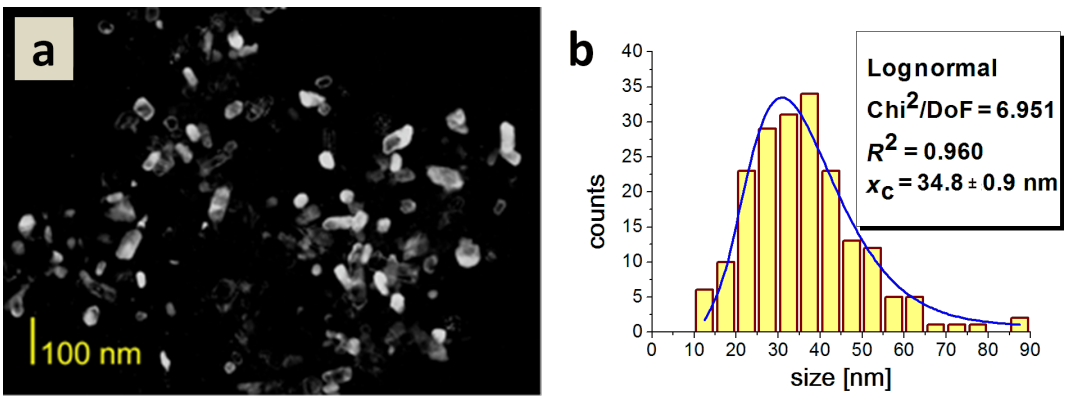


Figure 11: a) A dark field TEM image of Type 6 HAp; b) a histogram of the particle size distribution.

to decreased homogeneity of the obtained materials despite the use of microwave heating. It is common knowledge that scale-up in nanomaterial production is very problematic [58]. This is mainly due to the nonuniform heating of precursors. Despite the fact that we employ the microwave heating method [35,38,59], i.e., the most efficient and quickest method of supplying energy to reagents, an increase in the size distribution of the obtained particles in line with an increase in the volume of the reaction feedstock is noticeable. This results from restricted microwave penetration into the reaction chamber interior containing the water reaction suspension (to ≈2.5 cm). Another significant factor is the problem related to the stirring of the heated reagents during the microwave reaction, which determines the homogeneity of the obtained products. Precursor stirring during the synthesis in the MSS2 reactor is spontaneous and results from the temperature gradient in the reaction chamber. Stirring, phosphoric acid addition speed, pH of the synthesized suspension, precursor suspension stirring, and heating speed are some of the important factors taken into account when increasing the production scale of HAp nanoparticles.

As confirmed by the obtained results, fully crystalline HAp Type 1 was obtained without the use of the reactor at room temperature. The described reaction of obtaining HAp Type 1 is a reaction of the neutralization of $Ca(OH)_2$ base with H_3PO_4 acid, where water is the sole byproduct. This is an exothermic process, the where the emitted energy is sufficient for the occurrence of the crystalline hydroxyapatite synthesis reaction. This is unique because according to Sharon Kehoe [50], ACP accompanied by small quantities of HAp was the main phase obtained from the synthesis at room temperature, whereas the quantity of HAp grew as the synthesis temperature increased [55]. The properties of the obtained primary product (HAp) are affected by the substrates used (Table 1) and the speed of adding (batching) acid to the calcium hydroxide suspension. Other works [60] have defined the optimum conditions for the synthesis of pure, monocrystalline HAp. According to the authors [60], the speed of adding the phosphoric acid solution should be moderate (below 100 mL/min), while the reaction temperature should be kept lower than 60 °C. Only then will the reaction ensue at 100% and the SSA of the obtained HAp will be ≈75 m^2/g. If the speed of adding the phosphoric acid is very high, the pH value in the reaction environment considerably decreases. In this case, H_3PO_4 is not completely dissociated. An insufficient amount of phosphate ions bring about damage to the structure of HAp and the appearance of an undesirable phase, $Ca(OH)_2$ [50]. In this paper, the adding speed was 1.2 mL/min, and the product obtained at room temperature was fully crystalline and characterized by a SSA as large as 258 m^2/g. According to the authors of [55], the primary synthesis product at room temperature was ACP, and they obtained HAp only at 90 °C. This can be explained by the fact that the quantity of one of the reagents was greater than the quantity needed for producing HAp or that the speed of batching the reagents was greater than the speed of reaction of obtaining HAp at a given temperature. This resulting supersaturation of the suspension with calcium and phosphate ions was the primary reason for the formation of ACP [61].

The thermogravimetric analysis (TGA) results (Table 8) provided information about total water content. The surface water and structural water can be distinguished. While heating, the water adsorbed on the surface evaporates up to 200 °C, then the structural water is evaporated subsequently in the temperature range 200–600 °C [62]. Even if this simplification is imprecise, it is sufficient to indicate trends in apatite hydration. Therefore, the total water content in our samples decreases in the following order: Type 1 HAp > Type 2 HAp > Type 3 HAp > Type 4 HAp > Type 5 HAp > Type 6 HAp (Figure 12).

Thermogravimetric tests reveal that the greatest quantity of water adsorbed on the particle surface was measured in the case of Type 1 and 2 HAp nanopowder, which is probably connected with the highly developed SSA. HAp is a hygroscopic material and hence the primary component adsorbed on the surface is water. The remaining analyzed powders are characterized by a lower SSA value, so the quantity of adsorbed water is accordingly lower. Powders 1 and 2 are also characterized by the

Table 8: Analysis of the quantity of water adsorbed on the surface and present in the structure of the tested hydroxyapatites.

Sample	SSA, a_s (m^2/g)	Weight loss 25–200 °C (absorbed water), (%)	Weight loss above 200 °C (lattice water), (%)	Total weight loss up to 1350 °C, (%)
HAp Type 1	258	5.85	4.83	10.68
HAp Type 2	211	4.91	5.08	9.99
HAp Type 3	149	2.93	3.88	6.81
HAp Type 4	85	1.40	3.13	4.53
HAp Type 5	61	0.84	2.48	3.32
HAp Type 6	51	0.46	2.22	2.68

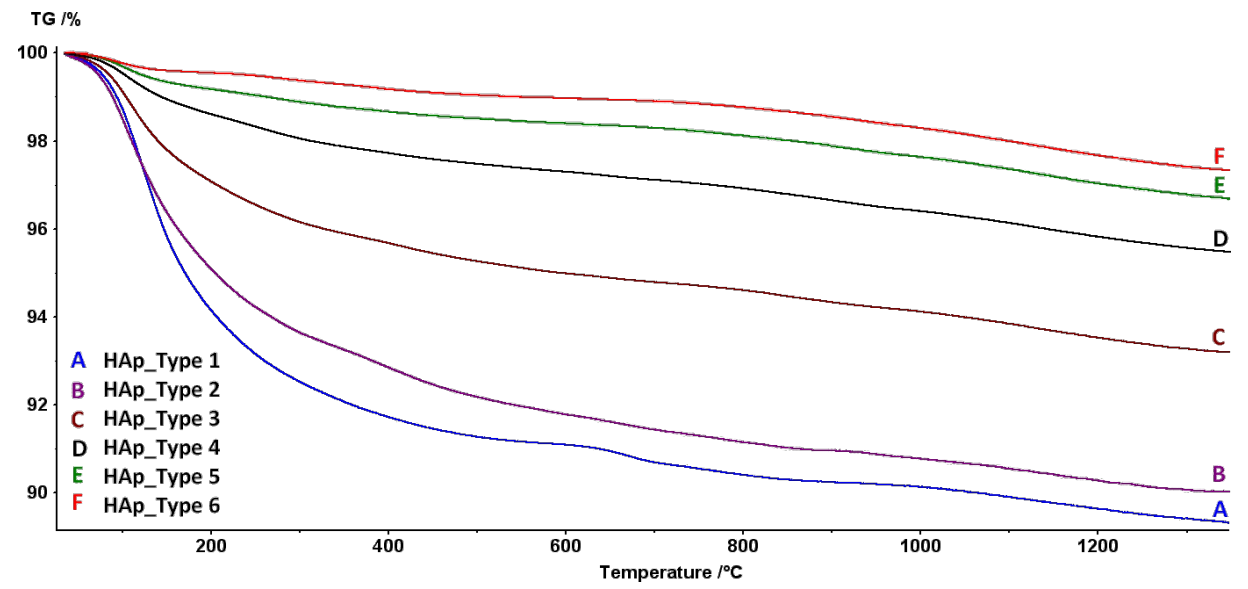


Figure 12: Results of thermogravimetric analysis for Type 1–Type 6 HAp nanopowder heated in helium atmosphere from room temperature to 1350 °C at 5 °C/min.

highest content of structural water, i.e., built in the crystalline lattice (200–600 °C).

Conclusion

A synthesis method was developed allowing for HAp nanoparticles to be produced with controlled size ranging from 8 to 39 nm. The synthesis was carried out using two methods: precipitation method with the precursor $Ca(OH)_2$ + H_3PO_4, where the single by-product was water and microwave hydrothermal synthesis, where the Type 1 HAp suspension was used as the precursor and heated in the MSS2 microwave reactor. The test proved that fully crystalline, clear nonstoichiometric, nanoscale HAp can be obtained without the use of the MSS2 reactor, which was a novelty.

The average HAp size was controlled by synthesis conditions such as time, temperature, and pressure. Crystalline HAp with hexagonal structure with pure phase was obtained. The HAp nanoparticles were characterized by a homogeneous morphology with needle or spherical/elliptical shape and a significant specific surface area. The morphology and density of the nanoparticles was found to depend on their size. The reaction time was short and the process was carried out entirely in water. MSS2 technology uses high power density, microwave radiation and enables a nanoscale, fully crystalline structure to be produced for all types of hydroxyapatite. The MSS2 reactor permits the control of the parameters of the obtained hydroxyapatite nanopowder, for example, the surface area in the range 51–258 m^2/g, and density of 2.86–3.04 g/cm^3. The developed precipitation and MHS methods enabled homogeneous HAp nanoparticles to be obtained with controlled and narrow particle size distribution. However, when increasing the production scale, the size distribution of HAp NPs was increased. An advantage of the developed precipitation synthesis and MSH methods is the low cost of the whole process and the purity of the obtained materials. The XRD results confirmed that Type 1 and Type 2 hydroxyapatite is a synthetic equivalent of natural apatite. A considerable content of structural water and water adsorbed in nanoscale HAp of diameter less than 20 nm, reaching 10 wt %, was found.

The unique design of the MSS2 rector permits precise synthesis time control with an accuracy of 1 s. One of the MSS2 reactor's operation features is the emptying the reactor chamber immediately after the heating has ended, which leads to rapid cool down and freezing of the reaction, whereby highest purity preserved. With the MSS2 reactor, it is possible to obtain intermediates of any reaction at any time during the microwave synthesis without post-reaction reheating effects. Microwave irradiation is a highly efficient heating method for transferring energy into the reaction chamber and provides more uniform heating with a rapid temperature rise in comparison with conventional heat transfer methods. MHS is generally much simpler, cleaner, faster, very energy efficient and more economical than conventional methods. This low-energy technology is also environmentally friendly.

The technology is ready to be employed in production conditions, while powder parameters can be adjusted to the consumer needs. The method of nanoparticle size control developed

herein can be used for optimizing the HAp properties in specific applications.

Acknowledgements

The tests presented in this paper were conducted at the Institute of High Pressure Physics, Polish Academy of Sciences (PAS). The authors are grateful to the M-Era.Net project GoIMPLANT: Tough, Strong and Resorbable Orthopaedic Implants (2013-2016) for the financial support. The research was carried out using the equipment funded by the CePT project, financed by the European Regional Development Fund within the Operational Program "Innovative Economy" (2007-2013). The authors would like also to thank R. Mukhovskyi and J. Mizeracki from the Institute of High Pressure Physics, PAS and K. Sobczak from the Institute of Physics PAS. We are deeply grateful to P. Wiecińska from the Faculty of Chemistry of Warsaw University of Technology for helping with measurements.

References

1. Alobeedallah, H.; Ellis, J. L.; Rohanizadeh, R.; Coster, H.; Dehghani, F. *Trends Biomater. Artif. Organs* **2011,** *25,* 12–19.
2. Ferraz, M. P.; Monteiro, F. J.; Manuel, C. M. *J. Appl. Biomater. Biomech.* **2004,** *2,* 74–80.
3. Uskoković, V.; Uskoković, D. P. *J. Biomed. Mater. Res., Part B* **2010,** *96B,* 152–191. doi:10.1002/jbm.b.31746
4. Krajewski, A.; Ravaglioli, A.; Roncari, E.; Pinsco, P.; Montanari, L. *J. Mater. Sci.: Mater. Med.* **2000,** *11,* 763–772. doi:10.1023/A:1008988127294
5. Orlovskii, V. P.; Komlev, V. S.; Barinov, S. M. *Inorg. Mater.* **2002,** *38,* 973–984. doi:10.1023/A:1020585800572
6. Bigi, A.; Fini, M.; Bracci, B.; Boanini, E.; Torricelli, P.; Giavaresi, G.; Aldini Nicolo, N.; Facchini, A.; Sbaiz, F.; Giardino, R. *Biomaterials* **2008,** *29,* 1730–1736. doi:10.1016/j.biomaterials.2007.12.011
7. Polish ointments and patches for every wound. http://scienceinpoland.pap.pl/en/news/news,400106,polish-ointments-and-patches-for-every-wound.html (accessed March 21, 2016).
8. Zhou, H.; Lee, J. *Acta Biomater.* **2011,** *7,* 2769–2781. doi:10.1016/j.actbio.2011.03.019
9. Li, B.; Guo, B.; Fan, H.; Zhang, X. *Appl. Surf. Sci.* **2008,** *255,* 357–360. doi:10.1016/j.apsusc.2008.06.114
10. Cai, Y.; Liu, Y.; Yan, W.; Hu, Q.; Tao, J.; Zhang, M.; Shi, Z.; Tang, R. *J. Mater. Chem.* **2007,** *17,* 3780–3787. doi:10.1039/b705129h
11. Chu, S.-H.; Feng, D.-F.; Ma, Y.-B.; Li, Z.-Q. *Int. J. Nanomed.* **2012,** *7,* 3659–3666. doi:10.2147/IJN.S33584
12. Loo, S. C. J.; Moore, T.; Banik, B.; Alexis, F. *Curr. Pharm. Biotechnol.* **2010,** *11,* 333–342. doi:10.2174/138920110791233343
13. Ma, Q. Y.; Traina, S. J.; Logan, T. J.; Ryan, J. A. *Environ. Sci. Technol.* **1993,** *27,* 1803–1810. doi:10.1021/es00046a007
14. Mizuno, N. *Modern Heterogeneous Oxidation Catalysis: Design, Reactions and Characterization;* Wiley-VCH: Weinheim, Germany, 2009. doi:10.1002/9783527627547
15. Elliott, J. C. *Stud. Inorg. Chem.* **1994,** *18,* 1–389. doi:10.1016/B978-0-444-81582-8.50006-7
16. Choi, D.; Kumta, P. M. *J. Am. Ceram. Soc.* **2006,** *89,* 444–449. doi:10.1111/j.1551-2916.2005.00738.x
17. Aoki, H. *Science and medical applications of hydroxyapatite;* Takayama Press: Tokyo, 1991.
18. de Groot, K. *Bioceramics of calcium phosphate;* CRC Press: Boca Raton, FL, 1983.
19. Sobczak, A.; Kowalski, Z. *Czas. Tech. - Politech. Krakow.* **2007,** *104,* 150–156.
20. Ginebra, M.-P.; Fernández, E.; Driessens, F. C. M. *J. Am. Ceram. Soc.* **1999,** *82,* 2808–2812. doi:10.1111/j.1151-2916.1999.tb02160.x
21. Meyer, J. L.; Fowler, B. O. *Inorg. Chem.* **1982,** *21,* 3029–3035. doi:10.1021/ic00138a021
22. Tas, A. C. *J. Eur. Ceram. Soc.* **2000,** *20,* 2389–2394. doi:10.1016/S0955-2219(00)00129-1
23. Huang, L.-Y.; Xu, K.-W.; Lu, J. *J. Mater. Sci.: Mater. Med.* **2000,** *11,* 667–673. doi:10.1023/A:1008934522363
24. Kuriakose, T. A.; Kalkura, S. N.; Palanichamy, M.; Arivuoli, D.; Dierks, K.; Bocelli, G.; Betzel, C. *J. Cryst. Growth* **2004,** *263,* 517–523. doi:10.1016/j.jcrysgro.2003.11.057
25. Earl, J. S.; Wood, D. J.; Milne, S. J. *J. Phys.: Conf. Ser.* **2006,** *26,* 268–271. doi:10.1088/1742-6596/26/1/064
26. Smolén, D.; Chudoba, T.; Gierlotka, S.; Kedzierska, A.; Łojkowski, W.; Sobczak, K.; Święszkowski, W.; Kurzydłowski, K. J. *J. Nanomater.* **2012,** 841971. doi:10.1155/2012/841971
27. Smolen, D.; Chudoba, T.; Malka, I.; Kedzierska, A.; Lojkowski, W.; Swieszkowski, W.; Kurzydlowski, K. J.; Kolodziejczyk-Mierzynska, M.; Lewandowska-Szumiel, M. *Int. J. Nanomed.* **2013,** *8,* 653–668. doi:10.2147/IJN.S39299
28. Radha, G.; Balakumar, S.; Venkatesan, B.; Vellaichamy, E. *Mat. Sci. Eng. C* **2015,** *50,* 143–150. doi:10.1016/j.msec.2015.01.054
29. Liang, T.; Qian, J.; Yuan, Y.; Liu, C. *J. Mater. Sci.* **2013,** *48,* 5334–5341. doi:10.1007/s10853-013-7328-3
30. Bernard, L.; Freche, M.; Lacout, J. L.; Biscans, B. *Powder Technol.* **1999,** *103,* 19–25. doi:10.1016/S0032-5910(99)00009-1
31. Koutsopoulos, S. *J. Biomed. Mater. Res., Part A* **2002,** *62,* 600–612. doi:10.1002/jbm.10280
32. Bingöl, O. R.; Durucan, C. *Am. J. Biomed. Sci.* **2012,** *4,* 50–59. doi:10.5099/aj120100050
33. Yoshimura, M.; Byrappa, K. *J. Mater. Sci.* **2008,** *43,* 2085–2103. doi:10.1007/s10853-007-1853-x
34. Zhu, Y.-J.; Chen, F. *Chem. Rev.* **2014,** *114,* 6462–6555. doi:10.1021/cr400366s
35. Lojkowski, W.; Leonelli, C.; Chudoba, T.; Wojnarowicz, J.; Majcher, A.; Mazurkiewicz, A. *Inorganics* **2014,** *2,* 606–619. doi:10.3390/inorganics2040606
36. Majcher, A.; Wiejak, J.; Przybylski, J.; Chudoba, T.; Wojnarowicz, J. *Int. J. Chem. React. Eng.* **2013,** *11,* 361–368. doi:10.1515/ijcre-2012-0009
37. Clearfield, A.; Reibenspies, J.; Bhuvanesh, N. *Principles and Applications of Powder Diffraction;* Wiley-Blackwell, 2008. doi:10.1002/9781444305487
38. Wojnarowicz, J.; Opalinska, A.; Chudoba, T.; Gierlotka, S.; Mukhovskyi, R.; Pietrzykowska, E.; Sobczak, K.; Lojkowski, W. *J. Nanomater.* **2016,** *2016,* 2789871. doi:10.1155/2016/2789871
39. Wojnarowicz, J.; Kusnieruk, S.; Chudoba, T.; Gierlotka, S.; Lojkowski, W.; Knoff, W.; Lukasiewicz, I. M.; Witkowski, S. B.; Wolska, A.; Klepka, T. M.; Story, T.; Godlewski, M. *Beilstein J. Nanotechnol.* **2015,** *6,* 1957–1969. doi:10.3762/bjnano.6.200
40. Pielaszek, R. *J. Alloys Compd.* **2004,** *382,* 128–132. doi:10.1016/j.jallcom.2004.05.040

41. Wojnarowicz, J.; Mukhovskyi, R.; Pietrzykowska, E.; Kusnieruk, S.; Mizeracki, J.; Lojkowski, W. *Beilstein J. Nanotechnol.* **2016,** *7,* 721–732. doi:10.3762/bjnano.7.64
42. Bowen, P. *J. Dispersion Sci. Technol.* **2002,** *23,* 631–662. doi:10.1081/DIS-120015368
43. Adam, M.; Ganz, C.; Xu, W.; Sarajian, H.-R.; Goetz, W.; Gerber, T. *Int. J. Nanomed.* **2014,** *9,* 975–984. doi:10.2147/IJN.S48416
44. Guo, X.; Yan, H.; Zhao, S.; Zhang, L.; Li, Y.; Liang, X. *Adv. Powder Technol.* **2013,** *24,* 1034–1038. doi:10.1016/j.apt.2013.03.002
45. Brown, P. W.; Constantz, B. *Hydroxyaptite and Related Materials;* CRC Press Inc., 1994.
46. Chang, J.; Johnson, E. *Philos. Mag.* **2005,** *85,* 3617–3627. doi:10.1080/14786430500228663
47. Clark, D. E.; Sutton, W. H. *Annu. Rev. Mater. Sci.* **1996,** *26,* 299–331. doi:10.1146/annurev.ms.26.080196.001503
48. Nanopowder XRD Processor Demo. http://science24.com/xrd/ (accessed March 21, 2016).
49. Tõnsuaadu, K.; Gross, K. A.; Plūduma, L.; Veiderma, M. *J. Therm. Anal. Calorim.* **2012,** *110,* 647–659. doi:10.1007/s10973-011-1877-y
50. Kehoe, S. Optimisation of hydroxyapatite (HAp) for orthopaedic application via the chemical precipitation technique. Ph.D. Thesis, Dublin City University, U.K., 2008.
51. LeGeros, R. Z.; Singer, I.; Ophaug, R.; Quirolgico, G. *Osteoporosis;* Wiley and Sons: New York, 1982.
52. Nelson, D. G. A.; McLean, J. D.; Sanders, J. V. *J. Ultrastruct. Res.* **1983,** *84,* 1–15. doi:10.1016/S0022-5320(83)90081-3
53. Hench, L. L.; Wilson, J. An Introduction to Bioceramics. In *Advanced Series in Ceramics;* McLaren, M.; Niesz, D. E., Eds.; World Scientific Publishing Co.: Singapore, 1998; Vol. 1. doi:10.1142/9789814317351_0001
54. Uvarov, V.; Popov, I. *Mater. Charact.* **2013,** *85,* 111–123. doi:10.1016/j.matchar.2013.09.002
55. Seckler, M. M.; Danese, M.; Derenzo, S.; Valarelli, J. V.; Giulietti, M.; Rodríguez-Clemente, R. *Mater. Res. (Sao Carlos, Braz.)* **1999,** *2,* 59–62. doi:10.1590/S1516-14391999000200003
56. Pang, Y. X.; Bao, X. *J. Eur. Ceram. Soc.* **2003,** *23,* 1697–1704. doi:10.1016/S0955-2219(02)00413-2
57. Sudarsanan, K.; Young, R. A. *Acta Crystallogr., Sect. B* **1969,** *25,* 1534–1543. doi:10.1107/S0567740869004298
58. Charitidis, C. A.; Georgiou, P.; Koklioti, M. A.; Trompeta, A.-F.; Markakis, V. *Manuf. Rev.* **2014,** *1,* 11. doi:10.1051/mfreview/2014009
59. Schanche, J.-S. *Mol. Diversity* **2003,** *7,* 291–298. doi:10.1023/B:MODI.0000006866.38392.f7
60. Bouyer, E.; Gitzhofer, F.; Boulos, M. I. *J. Mater. Sci.: Mater. Med.* **2000,** *11,* 523–531. doi:10.1023/A:1008918110156
61. McDowell, H.; Gregory, T. M.; Brown, W. E. *J. Res. Natl. Bur. Stand., Sect. A* **1977,** *81A,* 273–281. doi:10.6028/jres.081A.017
62. Levingstone, T. J. *Ceramics for Medical Applications;* Dublin City University, 2008.

License and Terms

This is an Open Access article under the terms of the Creative Commons Attribution License (http://creativecommons.org/licenses/by/4.0), which permits unrestricted use, distribution, and reproduction in any medium, provided the original work is properly cited.

The license is subject to the *Beilstein Journal of Nanotechnology* terms and conditions: (http://www.beilstein-journals.org/bjnano)

The definitive version of this article is the electronic one which can be found at: doi:10.3762/bjnano.7.153

BEILSTEIN JOURNAL OF NANOTECHNOLOGY

A new approach to grain boundary engineering for nanocrystalline materials

Shigeaki Kobayashi*[1], Sadahiro Tsurekawa[2] and Tadao Watanabe[3]

Review

Open Access

Address:
[1]Division of Mechanical Engineering, Department of Innovative Engineering, Faculty of Engineering, Ashikaga Institute of Technology, Omae 268-1, Ashikaga, Tochigi 326-8558, Japan, [2]Department of Materials Science and Engineering, Graduate School of Science and Technology, Kumamoto University, Kumamoto 860-8555, Japan, and [3]Key Laboratory for Anisotropy and Texture of Materials, Northeastern University, Shenyang 110004, China, Formerly, Tohoku University, Sendai, Japan

Email:
Shigeaki Kobayashi* - skoba@ashitech.ac.jp; Tadao Watanabe - tywata@fk9.so-net.ne.jp

* Corresponding author

Keywords:
electrical resistivity control; fractal analysis; grain boundary engineering (GBE); intergranular fracture control; nanocrystalline materials

Beilstein J. Nanotechnol. **2016,** *7,* 1829–1849.
doi:10.3762/bjnano.7.176

Received: 14 June 2016
Accepted: 28 October 2016
Published: 25 November 2016

This article is part of the Thematic Series "Advances in nanomaterials II".

Guest Editor: H. Hahn

© 2016 Kobayashi et al.; licensee Beilstein-Institut.
License and terms: see end of document.

Abstract

A new approach to grain boundary engineering (GBE) for high performance nanocrystalline materials, especially those produced by electrodeposition and sputtering, is discussed on the basis of some important findings from recently available results on GBE for nanocrystalline materials. In order to optimize their utility, the beneficial effects of grain boundary microstructures have been seriously considered according to the almost established approach to GBE. This approach has been increasingly recognized for the development of high performance nanocrystalline materials with an extremely high density of grain boundaries and triple junctions. The effectiveness of precisely controlled grain boundary microstructures (quantitatively characterized by the grain boundary character distribution (GBCD) and grain boundary connectivity associated with triple junctions) has been revealed for recent achievements in the enhancement of grain boundary strengthening, hardness, and the control of segregation-induced intergranular brittleness and intergranular fatigue fracture in electrodeposited nickel and nickel alloys with initial submicrometer-grained structure. A new approach to GBE based on fractal analysis of grain boundary connectivity is proposed to produce high performance nanocrystalline or submicrometer-grained materials with desirable mechanical properties such as enhanced fracture resistance. Finally, the potential power of GBE is demonstrated for high performance functional materials like gold thin films through precise control of electrical resistance based on the fractal analysis of the grain boundary microstructure.

Review

Introduction

Nanocrystalline metals and alloys have been receiving increased interest from many researchers because of their unique mechanical [1-20] and functional [21-23] properties, since Birringer, Herr and Gleiter first reported on the processing of nanocrystalline materials and the important characterization of their unique properties in 1986 [1]. Nanocrystalline or nanostructured crystalline materials have opened a new horizon toward the generation of enhanced strength beyond the expectation from the Hall–Petch relationship for conventional polycrystalline structural materials with ordinary grain structure, and conventional grain size range. It is evident that the much higher strength of nanocrystalline materials compared to ordinary polycrystals originates from the extensive interaction between grain boundaries and dislocations. On the other hand, poor ductility and severe brittleness of nanocrystalline materials have been generally observed and still remain unsolved, even beyond our control based on the current discipline of materials science and engineering (MSE).

The unique bulk properties of existing nanocrystalline materials are known to be ascribed to the presence of extremely high density grain boundaries and triple junctions. This is often associated with the nonequilibrium deformation of microstructures introduced by severe plastic deformation (SPD) with less thermal stability, excess structural defects and chemical composition by segregation to grain boundaries and interfaces [12,15,24-29]. Since the concept of grain boundary design and control was first proposed by Watanabe [30], an increasing number of researchers have been involved in the development of high performance polycrystalline materials, including nanocrystalline or nanostructured materials. Engineering applications were successfully achieved first by Aust, Palumbo, Erb and their coworkers [31,32] and then by the authors of this work [33-35]. The nonequilibrium structure, structural defect and chemical composition by segregation as well as grain boundary character as the importance of grain boundary segregation have already been discussed for polycrystalline materials [30,36]. Watanabe et al. [25] have reviewed the recent achievements in GBE by magnetic field application for powerful control of abnormal grain growth and intergranular brittleness due to segregation of detrimental elements in nanocrystalline and ordinary polycrystalline materials [24,25]. More recently, Raabe et al. [27,28] proposed grain boundary segregation engineering for improvement of material properties, such as the stabilization of grains in nanocrystalline steel by carbon and solute element segregation. Kalidindi et al. [29] have suggested that the stability of the nanocrystalline structure is improved by preferential segregation of solute atoms to grain boundaries because their excess free energy can be reduced. Therefore, it is very likely that the grain boundary microstructure characterized by appropriate microstructural parameters (e.g., grain boundary character distribution (GBCD) [30], grain boundary connectivity [30] and triple junction character distribution (TJCD)) may dominantly affect and control the bulk mechanical, physicochemical, electro-magnetic and other grain-boundary-related properties in nanocrystalline materials, as well as ordinary polycrystalline materials.

Accordingly, it is reasonable to consider that the GBE approach that the authors of this work have been deeply involved so far should become of increasing importance in the development of high performance and multifunctional nanocrystalline materials. In recent years, the control of brittle fracture [37,38], creep deformation [39-41], fatigue fracture [42-45], corrosion [46-49] and stress corrosion cracking [40,41,50,51] have been successfully achieved by applying the concept of GBE based on the control of GBCD and grain boundary connectivity in polycrystalline engineering materials. GBE has been extensively achieved by the incorporation of a high fraction of $\Sigma 3^n$ boundaries by annealing in low-stacking fault energy FCC metals and alloys. However, it should be noted that the utility of GBE for control of brittleness was already demonstrated for BCC materials with high-stacking fault energy, such as in the very early work of the present author on Fe–6.5 mass % Si alloy with excellent soft magnetic properties but severe brittleness. Ductile, high performance Fe–6.5 mass % Si ribbon material was successfully produced by precise control of grain boundary microstructure associated with the evolution of a sharp <110> texture in the 1980s [52], soon after the first report on nanocrystalline materials.

A number of excellent review papers have been published on nanocrystalline materials produced by different processing methods up to now. The importance of the dominant occurrence of the extremely high density of grain boundaries (in single- phase materials) and interphase boundaries (in multiphase materials such as steels and composite alloys) is generally well understood with respect to the generation of the unique bulk properties of nanocrystalline materials. It is suggested that the dominant effects of grain boundaries on bulk properties of nanocrystalline structural or functional materials should be examined in relation to the applied processing methods, because the details of generation mechanisms of grain boundaries are strongly affected by processing routes and conditions [53,54]. As for those bulk ultrafine-grained (UFG) materials produced by severe plastic deformation (SPD) (e.g., equal-channel angular pressing (ECAP) and high-pressure torsion (HPT) initiated by Valiev and Langdon [55,56]), and also by other quite

different methods such as crystallization from amorphous solids [57], extensive work has been performed on the mechanical properties of bulk UFG and nanostructured materials and excellent reviews have been written. Among those previous reviews [19,20,55-61], the most recent review by Pineau et al. [20] may help the reader to understand the past, present and future prospect of this research area, especially on fracture and fatigue of nanostructured metallic materials.

On the other hand, in the present article, a new approach to GBE is introduced for enhanced strength and brittle fracture control in structural and functional nanocrystalline materials produced by electrodeposition and sputtering. This was first applied by Gleiter and coworkers during the very early stage development of nanocrystalline materials [1,2] and was later practically applied by Palumbo, Erb and Aust for the development of high performance structural engineering materials [3,62,63]. For this objective, first, we will discuss the effect of grain boundary microstructures, characterized by the grain boundary character and triple junction character, on the bulk mechanical properties such as hardness and on control of segregation-induced intergranular brittleness and fatigue fracture. Then we will introduce a new approach to GBE based on fractal analysis of grain boundary microstructure for development of nanocrystalline materials with high performance and desirable mechanical properties. Finally, our most recent work on GBE for the control of electrical resistivity in gold thin films is introduced as an example of a possible challenge toward GBE for high performance functional materials.

Effect of grain boundary microstructure on hardness in electrodeposited nanocrystalline materials

Effect of grain boundary density on hardness

As mentioned in the Introduction, nanocrystalline materials show considerably high strength and hardness, due to the presence of the extremely high density of grain boundaries and triple junctions, as well as other defects. Figure 1 shows the relationship between the Vickers hardness and the average grain size for pure nickel (Ni) and nickel–phosphorus (Ni–P) alloy specimens produced by electrodeposition and subsequent annealing. The data obtained from our recent investigation are shown together with those for pure Ni [62,64] and Ni–1.2 mass % P alloy [3] reported by other researchers. The state of the supersaturated solid solution in as-electrodeposited Ni–4.4 mass % P alloy specimens was confirmed, although the Ni–P phase diagram [65] indicates that the solubility limit of phosphorus into nickel matrix is 0.17 mass %. Accordingly, the Ni_3P phase may precipitate in the Ni–4.4 mass % P alloy specimens during annealing. As shown in Figure 1a, the hardness drastically increased in the Ni and Ni–P alloy specimens with an average grain size of less than 10^3 nm (1 μm), while the hardness gently increased in the specimen with conventional grain size. It has been reported that the density of grain boundaries and triple junctions also drastically increased in the materials with average grain size less than 1 μm [66]. Therefore, it is suggested that an increase of grain boundary density was essential for a considerably high strength and hardness in nanocrystalline and submicrometer-grained materials.

The Hall–Petch relationship between the hardness and the average grain size fails when the average grain size is much smaller than 30 nm, as shown in Figure 1b. It has been suggested that the dominant deformation mechanism in nanocrystalline materials with an extremely high density of grain boundaries is different in polycrystalline materials with conventional grain structure. Grain boundary sliding, grain boundary diffusion-controlled creep, and the contribution of triple line diffusion have been proposed as possible mechanisms of deformation in nanocrystalline materials [67].

It should be noted that the P composition strongly affects the hardness of nanocrystalline Ni. In as-electrodeposited Ni–4.4 mass % P alloy specimens, P atoms mostly segregate at grain boundaries, because of the low solubility limit (0.17 mass %) of P atoms in the Ni matrix and of a very high density of grain boundaries and triple junctions. Although the average grain size in as-electrodeposited pure Ni and Ni–4.4 mass % P alloy specimens is almost the same, the hardness of the as-electrodeposited Ni–4.4 mass % P alloy specimen increased by 40% compared to the as-electrodeposited pure Ni specimen. The grain boundary segregation of P atoms may result in the observed excess hardening of nanocrystalline Ni due to the enhancement of grain boundary hardening [68]. Moreover, the precipitation of the Ni_3P phase affects the hardening of the Ni–P alloy. The positive Hall–Petch slope behavior between the hardness and average grain size was observed. The Ni/Ni_3P alloy specimens prepared by annealing of electrodeposited Ni–4.4 mass % P solid solution show that the hardness of the Ni/Ni_3P alloy more strongly depends on the grain size than in Ni specimens.

Structure-dependent grain boundary hardening and effects of GBCD and triple junction character distribution on the hardness

It has been revealed that the hardness locally increases around grain boundaries against the grain interior, depending on the grain boundary character [69-74] and the degree of grain boundary segregation [69,75-77]. The present authors have reported that the hardening ratio for neighboring grain interiors of specific types of grain boundaries can change and tend to be

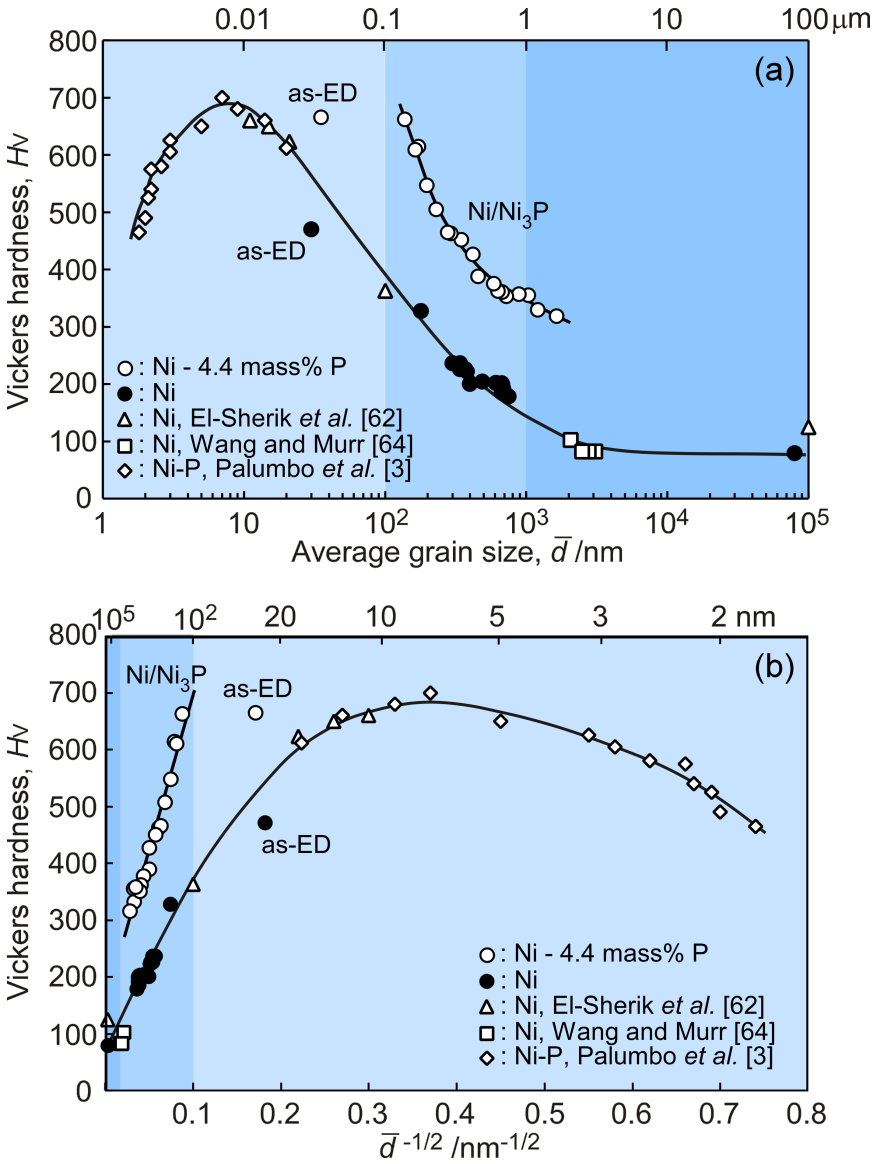


Figure 1: (a) The Vickers hardness as a function of the average grain size in electrodeposited and subsequently annealed Ni and Ni–P alloys. (b) The Hall–Petch plot of grain size dependence of the Vickers hardness.

lower at low-angle boundary and low-Σ CSL boundaries than at random boundaries in polycrystalline molybdenum. The generated dislocations can transfer or pass across low-angle boundaries more easily than random boundaries composed of more complicated tilt and twist components at room temperature [72]. It is evident that the grain boundary character can strongly affect the hardness at individual grain boundaries in bicrystals and polycrystalline materials.

Figure 2 shows the relationship between the Vickers hardness and the fraction of low-Σ CSL boundaries including low-angle (Σ1) boundaries in submicrometer-grained Ni specimens with the average grain size of 680 nm. These specimens were prepared by annealing at different temperatures from the electrodeposited nanocrystalline Ni specimens. The Vickers hardness decreased with increasing fraction of low-Σ CSL (Σ1–Σ29) boundaries for the studied specimens with almost the same average grain size. The hardness obviously decreased from 34 to 39%, with a slight change (5%) of the fraction of low-Σ CSL boundaries. Thus, it is evident that the GBCD-dependent hardness becomes more remarkable in nanocrystalline and submicrometer-grained materials in comparison with conventional polycrystalline materials.

Here, it should be noted that the specimens with the same fraction of low-Σ CSL boundaries of 34%, designated by A and B,

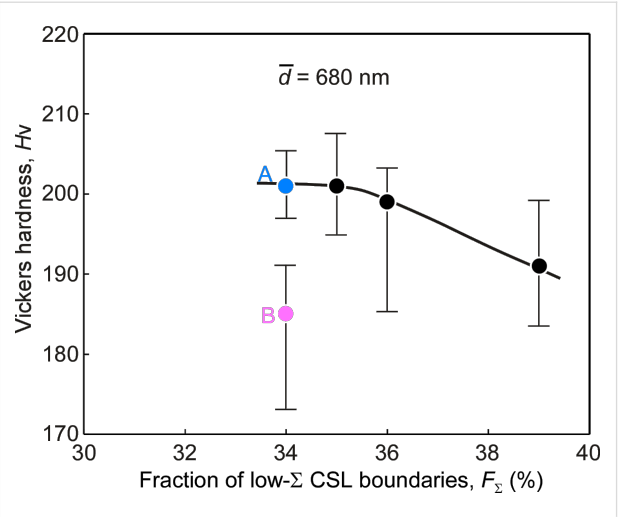


Figure 2: Relationship between the Vickers hardness and the fraction of low-Σ CSL boundaries for the submicrometer-grained Ni specimens with an average grain size of 680 nm.

showed quite different values of hardness, by almost 10%. The observed difference of the hardness may originate from other factors associated with grain boundary microstructure, that is, the triple point character. In order to clarify this, we further examined the grain boundary microstructure in the studied specimens. In principle, triple junctions are simply classified into four different types in terms of the connectivity of two different types of grain boundaries, i.e., random type and special low-Σ CSL boundaries, as discussed in [78] and [72,74]: (1) R0 type with no random boundaries, (2) R1 type with 1 random and 2 low-Σ CSL boundaries (including low-angle boundaries), (3) R2 type with 2 random and 1 low-Σ CSL boundaries, and (4) R3 type with 3 random boundaries.

Figure 3 shows the relationship between the Vickers hardness and the total fraction of specific types (R0 and R1) of the triple junctions observed in the same specimens corresponding to the specimens indicated in Figure 2. It was found that the hardness of the studied specimens clearly decreased with increasing total fraction of R0 and R1 type triple junctions with less random boundaries, and that the triple junctions with the higher connectivity of low-Σ CSL boundaries showed the lower triple junction hardening, as expected from the previous similar work for ordinary polycrystals [72]. Therefore, it is suggested that the triple junction character distribution (TJCD) also strongly affects the hardness of submicrometer-grained nickel specimens as well as GBCD. This is probably because the interaction of crystal dislocations with grain boundaries was found to strongly depend on the boundary character, leading to the passage of them across the boundaries, as discussed in detail in [79]. Accordingly, it is reasonable to understand that the TJCD plays an important role in the mechanical properties of nanocrystalline and submicrometer-grained materials with a very high density of triple junctions together with grain boundaries. However, a more precise understanding and control of grain boundary microstructures are necessary for further improvement of their mechanical properties and the generation of new functions in nanocrystalline materials with desirable bulk properties in future.

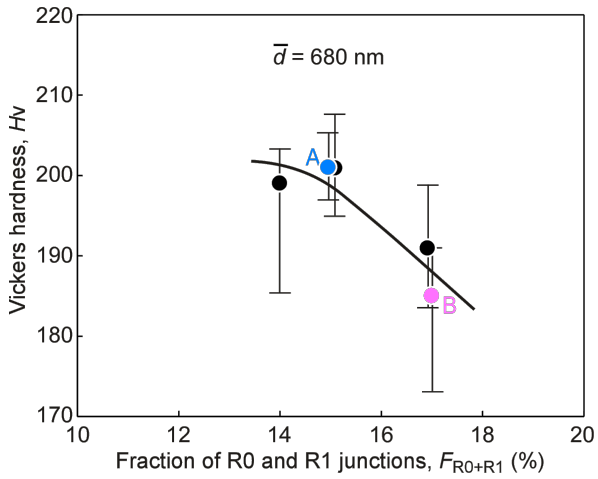


Figure 3: Relationship between the Vickers hardness and the fraction of R0 and R1 type triple junctions composed of less random boundaries in the submicrometer-grained Ni specimens.

GBE for control of segregation-induced embrittlement in nanocrystalline and submicrometer-grained Ni

Segregation-induced intergranular embrittlement is a serious problem that degrades the performance reliability of various types of structural materials. In nanocrystalline and submicrometer-grained materials possessing a very high density of grain boundaries and triple junctions, the detrimental effect of intergranular segregation seems to be more serious in comparison with conventional polycrystalline materials with the ordinary grain size ranging from the micrometer to the millimeter level. The amount of segregating impurity atoms at grain boundaries is well known to strongly depend on the grain boundary character and structure [69,80-84]. Bouchet and Priester [82,83] have found that the intergranular segregation of sulfur in Ni occurred preferentially at high-energy general random boundaries, but is very difficult or small at low-energy special boundaries. They suggested that the grain boundary plane orientation or low boundary planar atomic density can affect the amount of segregation even at such special CSL boundaries as Σ3, depending on either the coherent or incoherent part. As is clear from the general finding of structure-dependent grain boundary segregation, the segregation-induced intergranular embrittle-

ment should become more serious in nanocrystalline materials and needs to be effectively controlled through GBE.

Now let us look at the results on the GBCD-dependent fracture process in submicrometer-grained materials. Figure 4 shows SEM micrographs of the propagation path of cracks produced by Vickers indentation tests at a load of 1.96 N for the sulfur-doped submicrometer-grained Ni specimens with different grain boundary microstructures [85]. Type A and Type B specimens had different fractions of low-Σ CSL boundaries (including low-angle boundaries) of 49 and 40%, but almost the same average grain size of 300 and 340 nm, respectively. It was found that the crack length from the tip of indentation in the Type A specimen with a higher fraction of low-Σ CSL boundaries (F_Σ = 49%) was shorter than in the Type B specimen with a lower fraction of low-Σ CSL boundaries (F_Σ = 40%). The fracture toughness K_{IC} measured by indentation fracture (IF) method for the Type A and the Type B specimens were 2.5 MPa $m^{1/2}$ and 1.1 MPa $m^{1/2}$, respectively. Evidently, the fracture toughness of the Type A specimen with a higher fraction of low-Σ CSL boundaries is more than twice higher when the fraction of low-Σ CSL boundaries was increased by about 10%. This was because the crack that preferentially propagated along weak random boundaries with preferential S-segregation in the Ni–S alloy specimen, as shown in Figure 4d. The fraction and the connectivity of fracture-resistant low-Σ CSL boundaries, or crack-leading weak random boundaries are key parameters in controlling the typical percolation-dependent intergranular brittle fracture mode, or combined mode of mixture of intergranular and transgranular fracture. This finally leads to the characteristic bulk fracture properties in submicrometer-grained Ni. The more precise control of the occur-

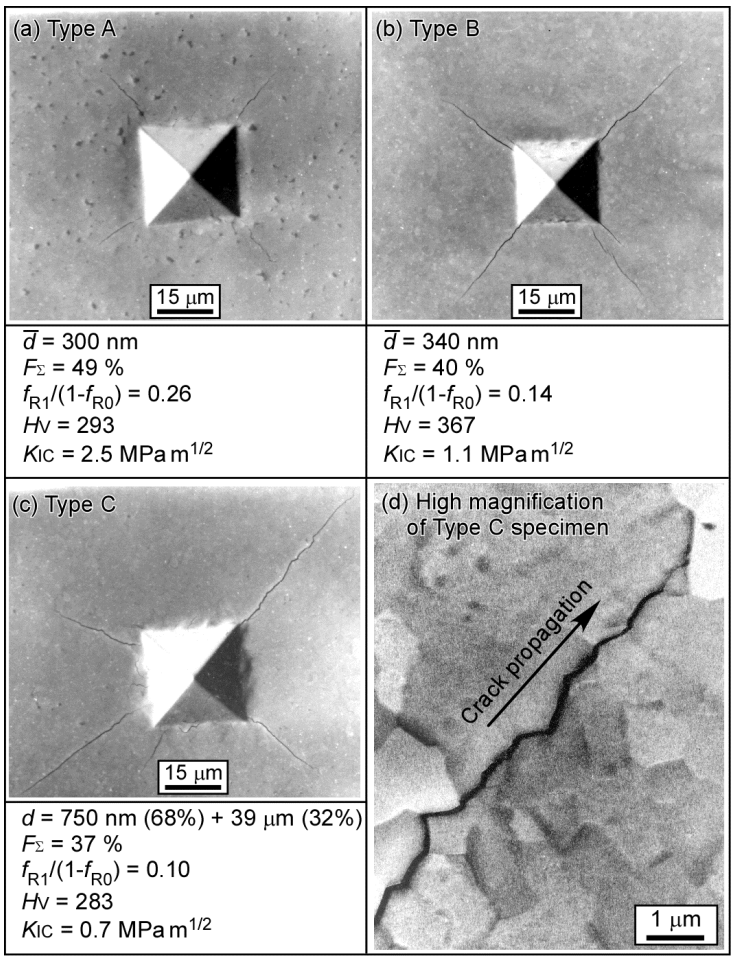


Figure 4: SEM micrographs of cracks introduced by indentation tests in the sulfur-doped fine-grained Ni specimens with different grain boundary microstructures. Type A and Type B specimens have similar average grain size, but different fractions of low-Σ CSL boundaries of 49 and 40%, respectively (a,b). Type B and Type C specimens have similar GBCD, but different grain sizes of 340 nm and 750 nm and 39 μm, respectively (b,c). The SEM micrograph of the crack path in the Type C specimen exhibiting coarse grains (d) [85]. Figure reprinted with permission from [85], copyright 2010 Elsevier Ltd.

rence of segregation-susceptive grain boundaries (high-energy random boundaries) by GBE based on the percolation-dependent fracture must be necessary for the control of segregation-induced intergranular embrittlement.

Along this line, the fraction of percolation-resistant triple junctions, $f_{R1}/(1-f_{R0})$, was evaluated, following Kumar et al. [86], as shown in Figure 4. The values of $f_{R1}/(1-f_{R0})$ were 0.26 and 0.14 for the Type A and the Type B specimens, respectively. Accordingly, the crack propagation in the Type A specimen was probably inhibited by the combined effects originating from the high fractions of low-Σ CSL boundaries and percolation-resistant triple junctions. As a result, the fracture toughness drastically increased for the Type A specimen. The Vickers hardness of the Type A specimen (H_V = 293) is lower than that of the Type B specimen (H_V = 367), because the degree of grain boundary hardening at low-Σ CSL boundaries is lower than that at random boundaries, as discussed in the previous section. This suggests that there exists some plasticity during the dislocation-boundary interaction.

It is worth noting that the crack length in the Type C specimen with duplex grain structure with different grain sizes of 750 nm and 39 μm was longer than that in the Type B specimen, despite having almost the same fraction of low-Σ CSL boundaries in the Type C and Type B specimens. The fracture toughness K_{IC} was 1.1 MPa $m^{1/2}$ and 0.7 MPa $m^{1/2}$, for the Type B and the Type C specimens, respectively. The fraction of percolation-resistant triple junctions, $f_{R1}/(1-f_{R0})$ was 0.14 and 0.10, in the Type B and the Type C specimens, respectively. Therefore, the crack propagation can be prevented more effectively in the Type B specimen. On the other hand, a crack nucleated at a random boundary of coarse grain can readily propagate further at longer, random boundaries until it reaches the percolation-resistant triple junction in the Type C specimen composed of a mixture of coarse and fine grains. These findings confirm that segregation-induced embrittlement in polycrystalline materials can be well controlled by optimizing the grain boundary microstructure, especially by GBCD, the grain boundary connectivity, and the heterogeneity of the grain size distribution. This is true even when local in nature, as revealed by our recent work on sulfur-doped polycrystalline Ni [87].

Effects of grain boundary microstructure on fatigue deformation and fracture in nanocrystalline Ni–P alloy

In recent years, it has been revealed that grain boundaries play important and different roles in fatigue crack nucleation [88-97] and propagation [44,45,98,99] in polycrystalline materials, depending on the grain boundary character and structure. The present authors have confirmed that intergranular fatigue cracks preferentially nucleate along random boundaries in polycrystalline aluminum, while they do not nucleate along low-angle boundaries [97]. The low-Σ CSL boundaries show the higher resistance to fatigue cracking than the random boundaries [97], although the preferential nucleation at coherent twin boundaries, namely {111}/Σ3 CSL boundaries, were previously reported for face-centered cubic (FCC) materials such as copper [90,91].

In the case of nanocrystalline and submicrometer-grained materials, it has been suggested that the roles of grain boundaries in fatigue deformation and fracture become more important due to the instability of grain boundary microstructure [100-106]. However, unfortunately, the effect of the instability of grain boundary microstructure on fatigue deformation and fracture in nanocrystalline materials has not been fully studied and understood yet, despite extensive previous works on the fatigue property in nanocrystalline materials [107-110]. It is difficult to fully understand the characteristics and dominant mechanisms of fatigue deformation and fracture in nanocrystalline materials without fundamental knowledge of microstructural change, especially grain boundary microstructure during cyclic deformation, resulting in the instability of grain boundary microstructure characterized by several key parameters, mentioned already.

Figure 5a shows the *S–N* curve which indicates the relationship between the stress amplitude and number of cycles to fracture in electrodeposited nanocrystalline Ni–2.0 mass % P alloy specimens with the initial average grain size of 45 nm [110]. The fatigue limit data are shown in Figure 5a together with those taken from the literature for electrodeposited nanocrystalline Ni with the average grain size of 20 nm [107], for ultrafine-grained nickel with the average grain size of 300 nm [107] and for electrodeposited microcrystalline nickel with conventional grain size [111]. The fatigue limit of about 360 MPa estimated for the Ni–P alloy specimens was two times higher than that of the microcrystalline nickel with conventional grain size. This estimated value of fatigue limit was close to the data reported for ultrafine-grained Ni specimens, and lower than for nanocrystalline Ni with the average grain size of 20 nm.

Figure 5b shows the *S–N* curve indicating the relationship between the stress amplitude normalized by the ultimate tensile strength (fatigue ratio, σ_a/UTS) and number of cycles to fracture (N_f). It was found that the fatigue limit for Ni–2.0 mass % P alloy specimens was about 23% of their ultimate tensile strength of 1550 MPa. The fatigue ratio of the fatigue limit of conventional polycrystalline Ni ranged between 0.35 and 0.50 [112]. Thus, it was found that the enhanced ratio of the fatigue limit was limited to a lower degree in nanocrystalline

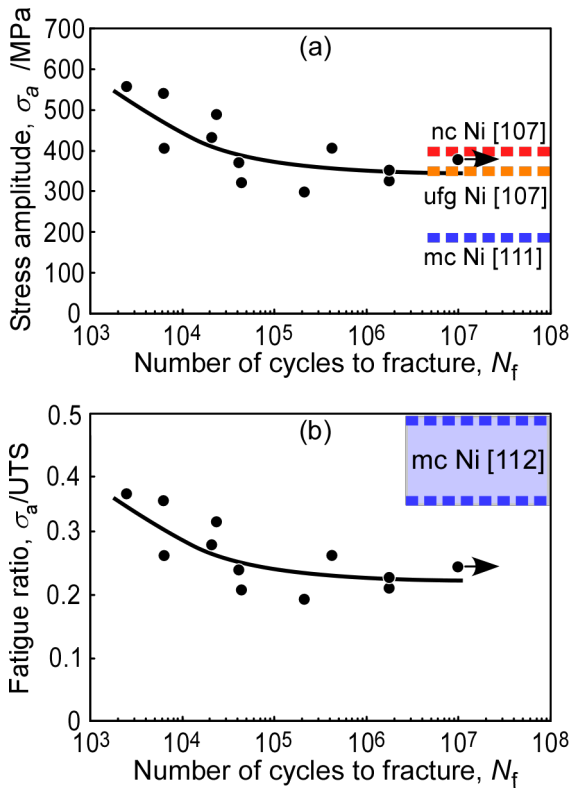


Figure 5: *S–N* curves of nanocrystalline Ni–2.0 mass % P alloy specimens: (a) stress amplitude versus logarithm of number of cycles to fracture [110] and (b) stress amplitude normalized by ultimate tensile strength (fatigue ratio) versus logarithm of number of cycles to fracture. Figure reprinted with permission from [110], copyright 2009 Elsevier Ltd.

Ni–2.0 mass % P alloy. This finding is very interesting and deserves to be explored in a more detailed investigation.

Quite recently, the present authors have found from more detailed SEM/electron backscattered diffraction (EBSD)/orientation imaging microscopy (OIM) observations during fatigue deformation that the low fatigue ratio for the fatigue limit in nanocrystalline Ni–2.0 mass % P alloy resulted from the instability of the grain boundary microstructure [113]. Figure 6a,b shows the OIM micrographs with the inverse pole figures inserted at the bottom corner for the prefatigued specimen and for the postfatigued specimens of Ni–2.0 mass % P alloy [113]. The grain and grain boundary microstructure drastically changed from those of initially nanocrystalline grain structure in the prefatigued specimen (Figure 6a) to the fine-grained structure with submicrometer average grain size during high cycle fatigue test, although the sharpness of the {001} texture hardly changed among the pre- and postfatigued specimens. It should be noted that the trace of grain boundaries exhibits an interesting characteristic feature that grain boundaries are migrated and aligned at about 45° against the stress axis. This results in the evolution of a "diamond-shaped" grain structure, which was observed in conventional polycrystalline materials during cyclic deformation at high temperatures [114-117]. The grain growth by high-cycle fatigue may result from a rapid migration of low-angle boundaries involving some dislocation mechanisms and enhanced by segregated P atoms at finally resultant random boundaries along shear bands. The operating mechanism will be explained later in some detail.

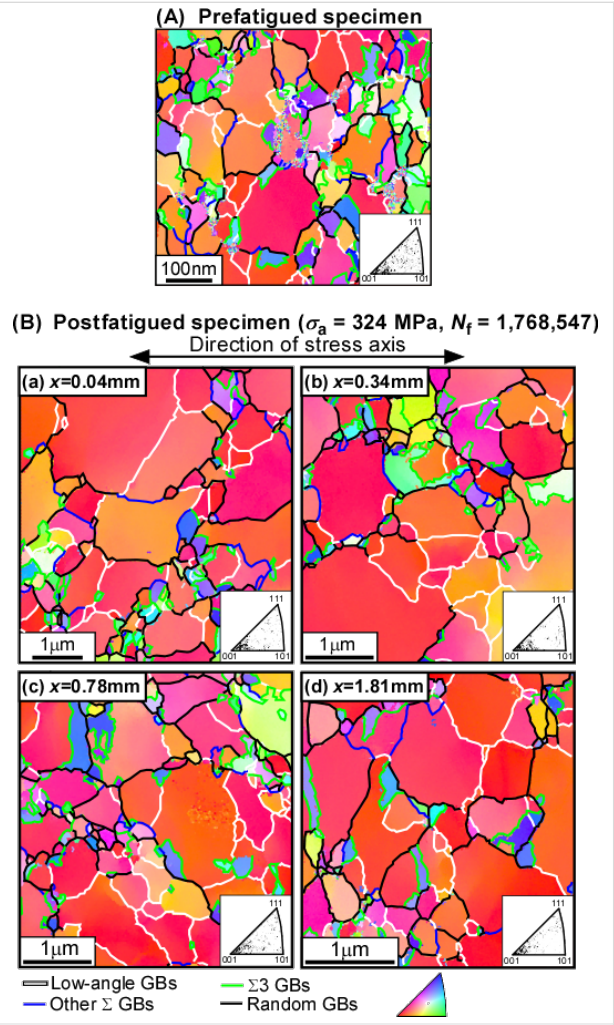


Figure 6: OIM micrographs with inverse pole figures (IPF) of grain orientation distribution for (A) prefatigued and (B) postfatigued Ni–2.0 mass % P alloy specimens [113]. Published by Elsevier Ltd. Figure reprinted with permission from [113], copyright 2015 Elsevier Ltd.

Figure 7 shows the misorientation angle distributions of grain boundaries before and after fatigue deformation involving the cyclic stress-induced grain growth [113]. The misorientation angle distribution for a random polycrystal, theoretically predicted by Mackenzie, is shown by the dotted curve in this figure [118]. A certain fraction of low-angle boundaries with a misorientation angle lower than 3° in the prefatigued specimen

(Figure 7a) transformed into the grain boundaries having the misorientation angles 3° < θ < 25° in the postfatigued specimen (Figure 7b). A higher fraction of Σ3 CSL boundaries hardly changed during fatigue. The cyclic stress-induced grain growth, accompanying the transformation of low-angle boundaries into the boundaries with higher misorientation angle, is associated with the evolution of a "diamond-shaped" grain structure along initially formed shear bands. This resulted in intergranular fatigue fracture due to grain boundary sliding, as can be seen from the fracture surface of fatigue fractured nanocrystalline Ni–2.0 mass % P alloy specimens (Figure 8). It is surprising to see that, as indicated in Figure 7b, there was no large difference of the misorientation angle distribution as a function of the distance from the position of the main crack in the postfatigued specimen. This suggests that more homogeneous fatigue deformation is assisted by dynamic grain growth.

Figure 9 shows the schematic illustrations of the possible mechanism of intergranular fatigue fracture assisted by the cyclic stress-induced grain growth and the grain boundary configuration forming the "diamond-shaped" grain structure. The details of the proposed mechanism of grain growth-assisted fatigue intergranular fracture can be obtained from the original article [113].

The formation of a large width of striations and large size of dimples was often observed in the fracture surface of fatigued nanocrystalline metals and alloys [102,110,113,119] in relation

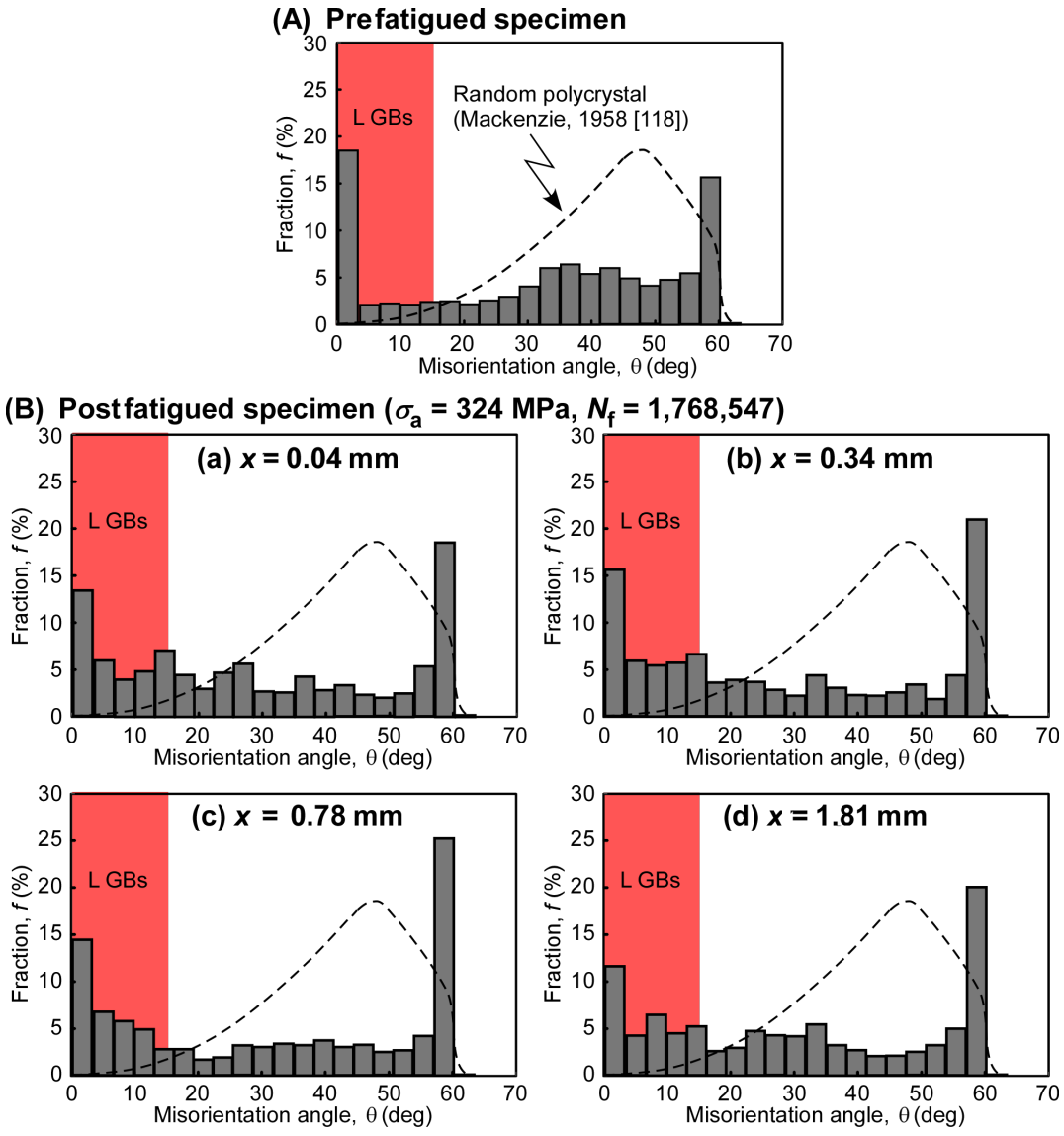


Figure 7: Misorientation angle distributions for (a) prefatigued and (b) postfatigued Ni–2.0 mass % P alloy specimens, where *x* indicates the position from the fracture surface [113]. Figure reprinted with permission from [113], copyright 2015 Elsevier Ltd.

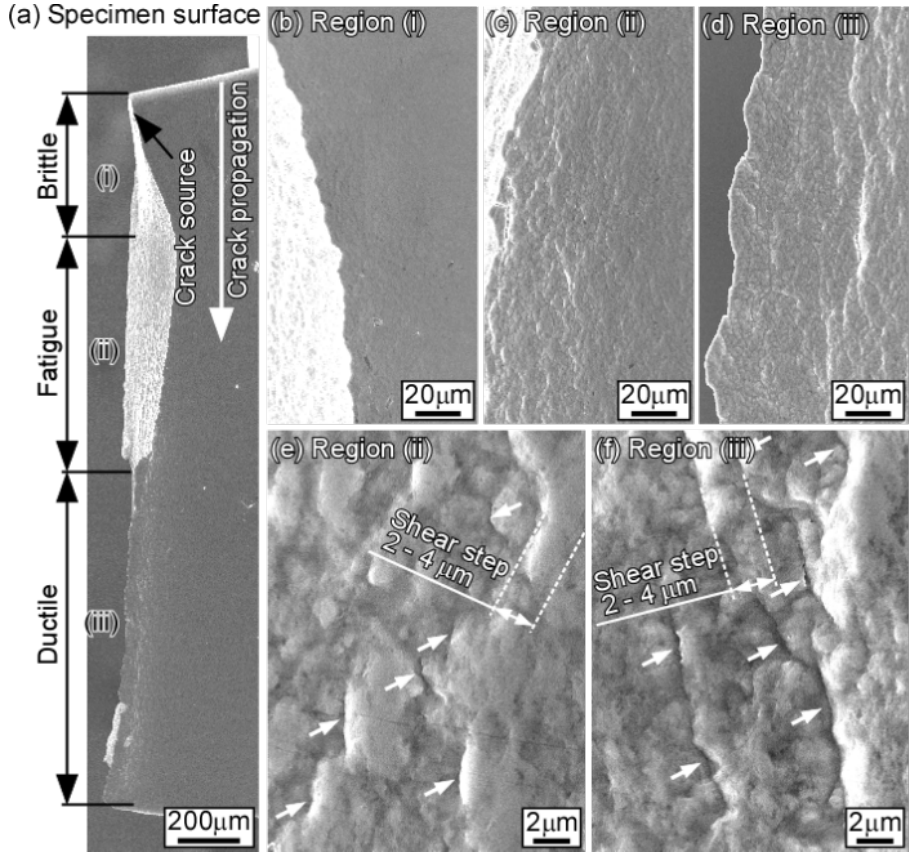


Figure 8: Specimen surface of electrodeposited nanocrystalline Ni–2.0 mass % P alloy specimen after high-cycle fatigue test: (a) low-magnification image of the whole fracture surface; (b–d) are medium-magnification images and (e–f) are high-magnification images of areas corresponding to the regions (i), (ii) and (iii), respectively [113]. Figure reprinted with permission from [113], copyright 2015 Elsevier Ltd.

to the presence of the {001} grain clusters. The {001} grain clusters interconnected by low-angle boundaries (indicated by white lines in Figure 6b) were probably deformed by shear stress as in the case of a single crystal, because the persistent slip bands (PSBs) can continuously transfer across the low-angle boundaries [97].

The fatigue cracks preferentially nucleated along random boundaries whose boundary plane may almost correspond to the direction of shear band. They nucleate at the deformation ledge produced at sliding random boundaries by the interaction with PSBs or triple junctions of high connectivity of random boundaries, as discussed in detail by Watanabe [120]. In fatigue fracture of nanocrystalline Ni, Kumar et al. [121] also reported the formation mechanism of deformation ledge, although the stress-induced grain growth and arrangement of random boundaries toward 45° to the stress axis was not observed in their nanocrystalline Ni specimens. Our recent observations strongly suggested the important roles of gran boundary microstructure in fatigue property and fracture behavior in nanocrystalline materials.

A new approach to GBE based on fractal analysis of grain boundary microstructures in nanocrystalline materials

This section concerns the bulk mechanical properties of nanocrystalline materials, especially focusing on the intrinsic and extrinsic brittleness of grain boundaries in different environments. For this purpose, a new approach to GBE based on the fractal analysis of grain boundary microstructures is needed. This must take into account the structure-dependent intrinsic grain boundary properties in order to produce polycrystalline and nanocrystalline materials with high performance and desirable bulk properties. The effectiveness of individual grain boundaries is required to be quantitatively evaluated based on the fundamental data obtained from systematic works by using orientation-controlled bicrystals of metallic, intermetallic, semiconductor and ceramic materials. In order to evaluate the effects of the grain boundary microstructures on bulk properties of polycrystals, we need to reveal the characteristic features of grain boundary microstructures produced by applying various kinds of materials processing in 2D (thin films) or 3D bulky conventional polycrystalline materials.

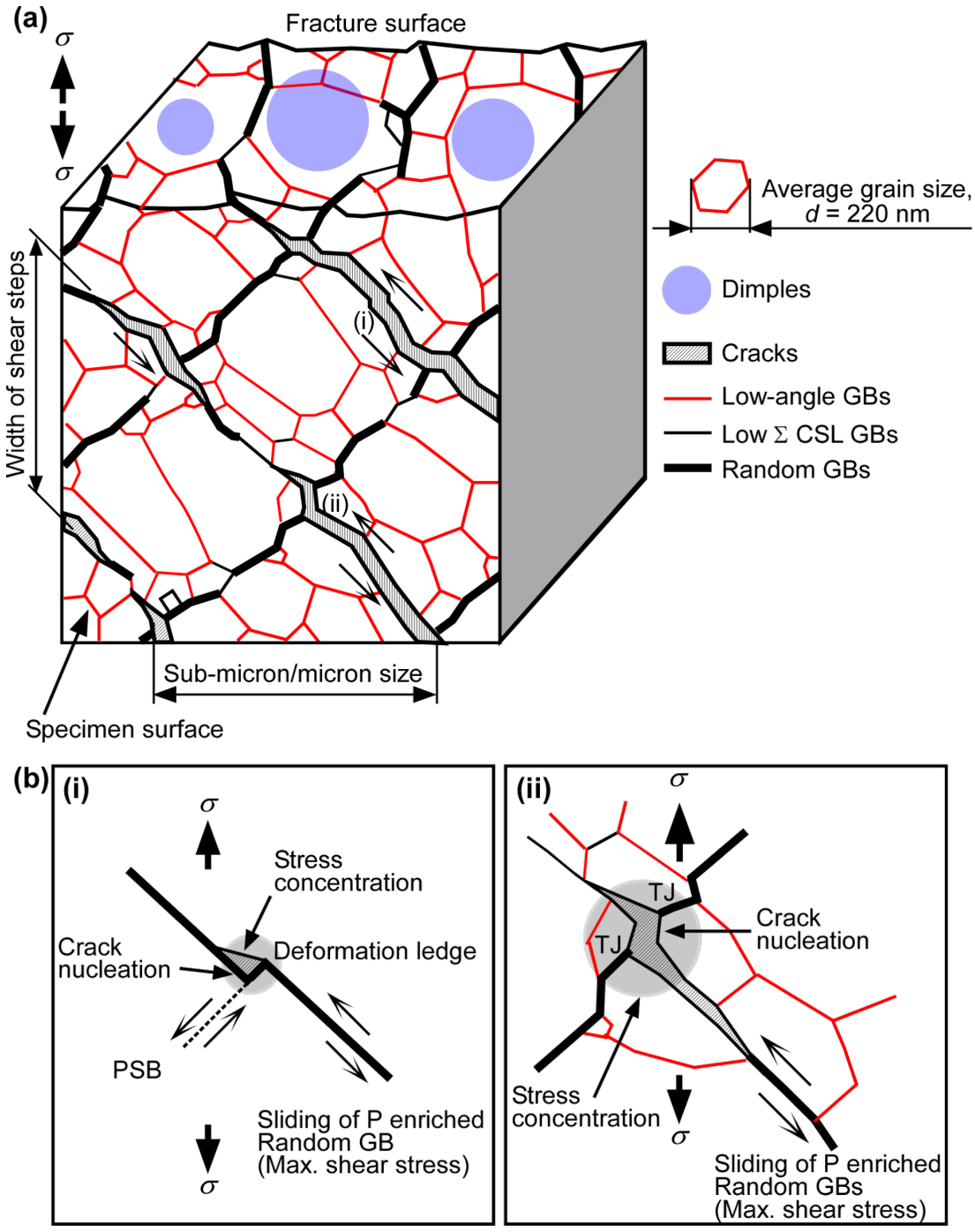


Figure 9: (a) Schematic illustration of the mechanism of intergranular fatigue fracture at random boundaries and the formation of morphological features of the specimen surface and fracture surface associated with propagation of intergranular fatigue cracks in the nanocrystalline Ni–2.0 mass % P alloy specimen during high-cycle fatigue. (b) Possible mechanism of fatigue crack nucleation at random boundaries by (i) the formation of deformation ledge and (ii) the stress concentration of the triple junctions composed of random boundaries [113]. Figure reprinted with permission from [113], copyright 2015 Elsevier Ltd.

Here we take two examples of a new approach to GBE based on fractal analysis of grain boundary microstructures in nanocrystalline materials. One is GBE for control of segregation-induced intergranular brittle fracture, the other is GBE for improvement of corrosion resistance in existing stainless steels, as a typical engineering metallic material with enhanced corro-

sion resistance. This kind of GBE has been originally attempted by us quite recently and provided us important clues to future development of GBE. First, let us explain the basic method of fractal analysis of grain boundary microstructures in polycrystalline materials. Here, we briefly mention the basis of the fractal analysis of grain boundary microstructure in a real polycrystalline specimen [87,122].

In our investigations, the fractal analysis was carried out by the box-counting method for the random boundary network containing the maximum connectivity of random boundaries (maximum random boundary connectivity, MRBC) in the grain boundary map obtained from SEM/EBSD analysis on the specimen surface [87]. Figure 10a,b shows an example of the set of grain boundary map and the corresponding fractal trace of MRBC determined for a SUS316L austenitic stainless steel specimens [122]. The whole observed area is covered by the square box net with a given unit size, η.

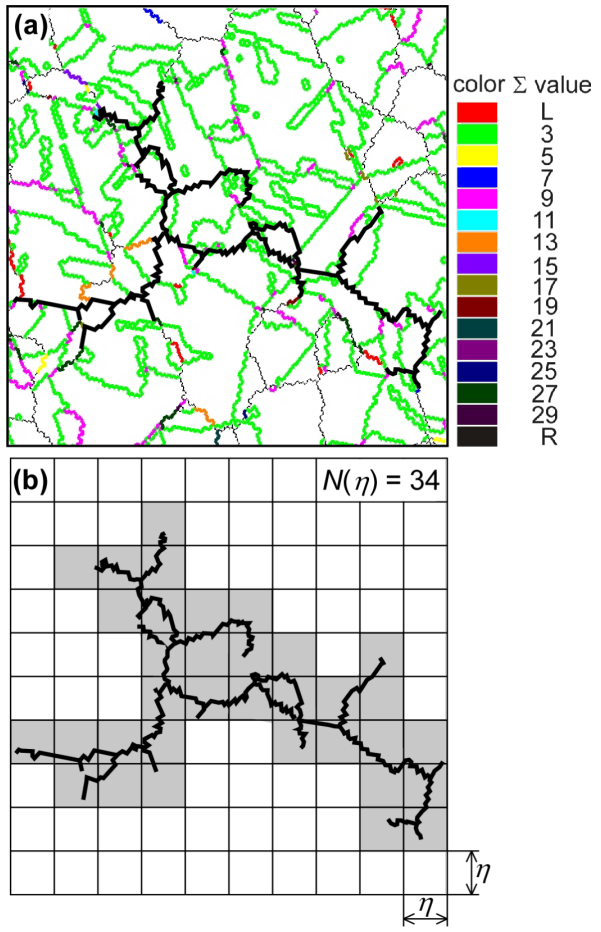


Figure 10: (a) Definition of the fractal dimension of the maximum random boundary connectivity (MRBC) and (b) demonstration of fractal analysis of MRBC by the box counting method [122]. Figure reprinted with permission from [122], copyright 2016 Elsevier Ltd.

Figure 11 shows the double-logarithm plots of the number of boxes $N(\eta)$ for complete coverage of the MRBC and the box size η for the SUS316L specimens produced by thermomechanical processing in the different process conditions [122]. The value of $N(\eta)$ was found to be a linear function of η. These results from different specimens indicate that the MRBC for different grain boundary microstructures in SUS316L steel specimens is of fractal nature. The fractal dimensions D_R evaluated by the slope of the log $N(\eta)$ versus log η were found to change systematically from 1.07 to 1.67 for the studied SUS316L steel specimens. Namely, the fractal dimensions show a reasonable correlation with the total length of random boundary network, as seen from Figure 12. The longer percolation path composed of intergranular corrosion susceptive, random boundaries is characterized by the higher fractal dimension of MRBC. This finding has provided us with experimental evidence that the fractal dimension for MRBC, D_R is useful as a tool for quantitative evaluation of the random boundary connectivity controlling the intergranular corrosion susceptibility in polycrystalline materials.

Figure 13 shows the relationship between the fractal dimension for MRBC, D_R and the fraction of random boundaries, F_R, or low-Σ CSL boundaries, F_Σ [122]. The coefficients of variation of the grain size distributions, $\sigma / \bar{d}$ are indicated together with the data points in the figure. The value of D_R tends to decrease monotonically with decreasing value of F_R or with increasing value of F_Σ. The larger value of $\sigma / \bar{d}$ tends to generate the larger value of D_R, even if the value of F_R or F_Σ would be kept similar, suggesting the path of percolation is more irregularly bent depending on the connectivity of random weak boundaries. The fractal dimension for MRBC, D_R may include the effect of a spread of the grain size distribution together with the effect of GBCD.

From the result shown in Figure 13, the value of D_R was estimated at about 1.10, by extrapolating the fitting curve to the experimental data up to the threshold value of F_Σ (65%) for the percolation-resistant low-Σ boundaries, or F_R (35%) for the percolation-assisting random boundaries. In the case of the SUS316L specimen hiving low F_R and low D_R, the curve runs into the shaded area in Figure 13. This suggests the intrinsically high corrosion resistance associated with GB microstructure. This is because of an interruption of the corrosion path along the random boundary network by the arrangement of corrosion-resistant low-Σ boundaries.

Figure 14 shows the SEM micrographs taken from the specimen surface and the vertical cross section for the two corroded SUS316L specimens with ordinary grain sizes and different values of the fractal dimension of MRBC, D_R [122]. Type A

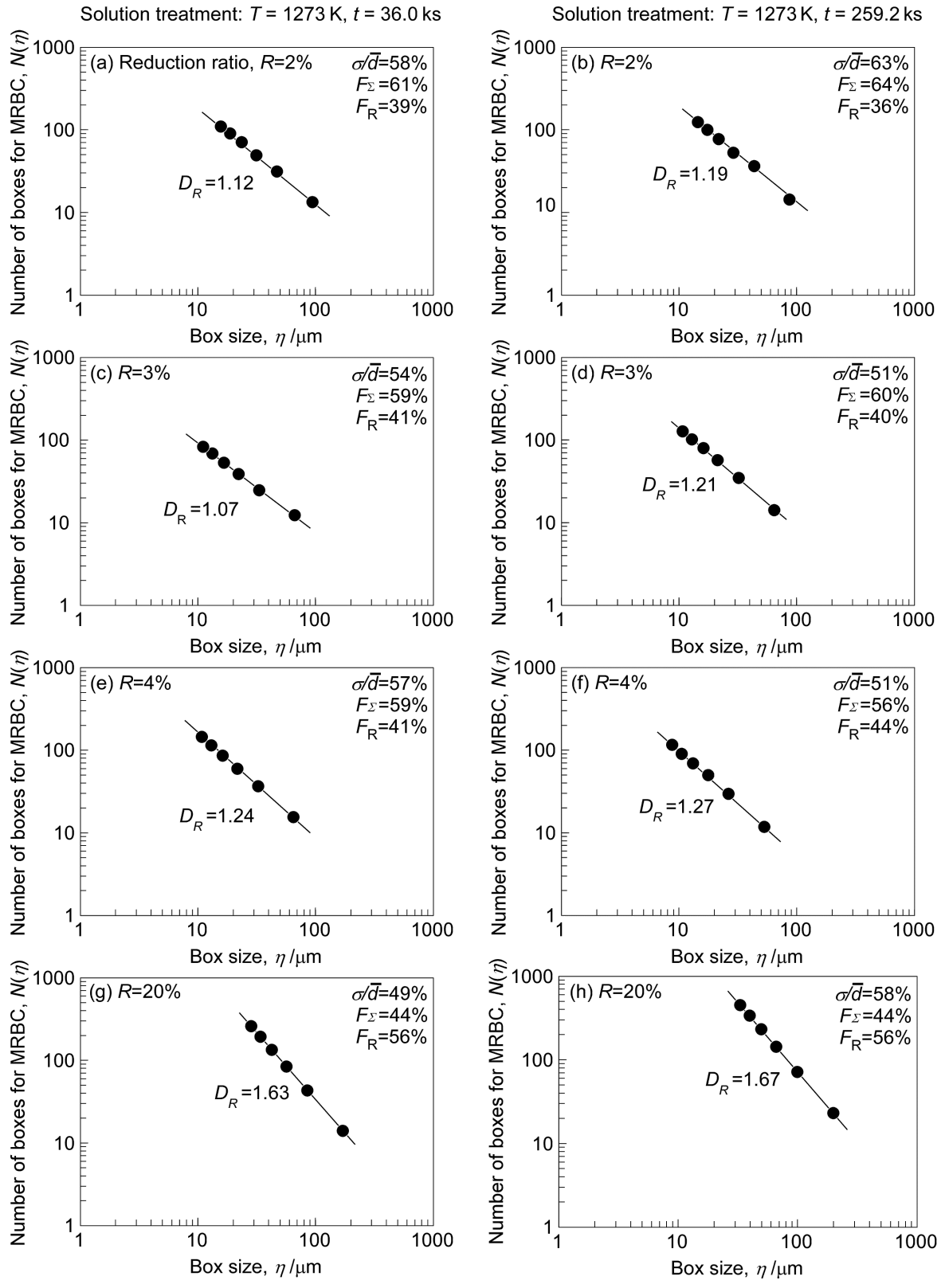


Figure 11: Relationship between the number of boxes $N(\eta)$ for complete coverage of the maximum random boundary connectivity and the box size η for the SUS316L specimens subjected to different thermomechanical processing conditions of (a–h) [122]. Figure reprinted with permission from [122], copyright 2016 Elsevier Ltd.

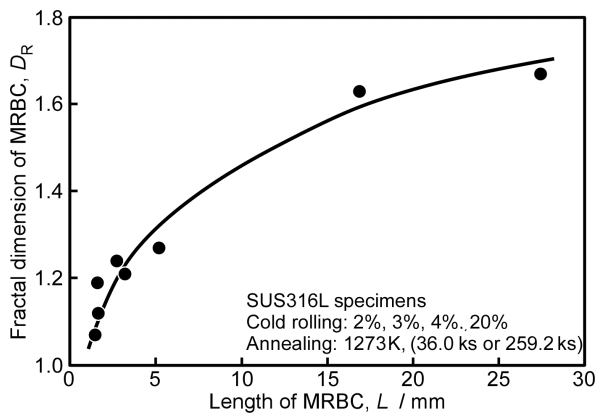


Figure 12: Relationship between the fractal dimension of MRBC and the length of MRBC.

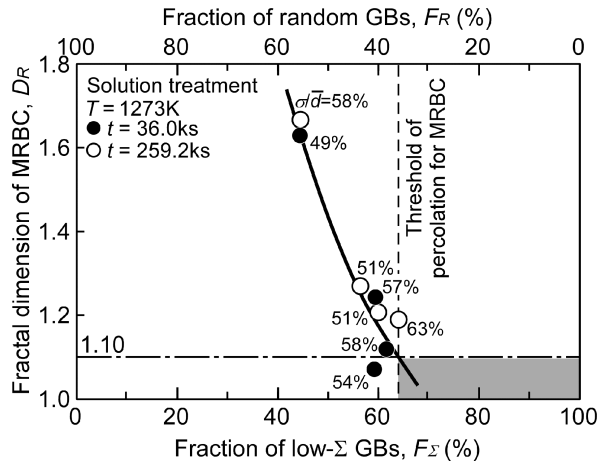


Figure 13: Relationship between the fractal dimension of the MRBC and the fraction of low-Σ boundaries F_Σ or random boundaries F_R for SUS316L specimens [122]. Figure reprinted with permission from [122], copyright 2016 Elsevier Ltd.

specimen had an average grain size of 41 μm, a fraction of low-Σ CSL boundaries of F_Σ = 64%, or of random boundaries F_R = 36%, and the fractal dimension of MRBC, D_R = 1.19. On the other hand, Type B specimen had the smaller average grain size of 17 μm, and the lower fraction of low Σ CSL boundaries of 44% (random boundaries of 56%) and the higher fractal dimension of MRBC of 1.63, in comparison with the Type A specimen.

From SEM observations of the surface of Type A specimen, it is evident that intergranular corrosion was inhibited by Σ3 CSL boundaries, but dominantly proceeded at random boundaries, as indicated by black arrows in Figure 14a. As a result, Type A specimen showed the higher resistance to intergranular corrosion, while Type B specimen was more heavily corroded

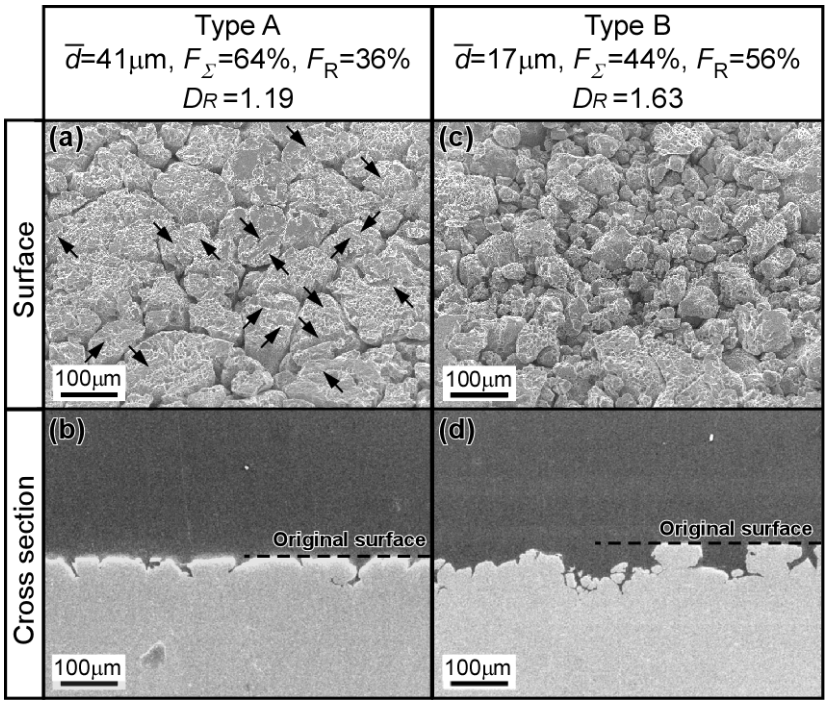


Figure 14: SEM micrographs of the surface (a,c) and the cross section (b,d) for the corroded specimens with different levels of the fractal dimension of MRBC. The black arrows show the position of annealing twin boundaries, namely {111}/Σ3 boundaries [122]. Figure reprinted with permission from [122], copyright 2016 Elsevier Ltd.

because of the occurrence of a much higher fraction of random boundaries (F_R = 56%), resulting in the falling off of a number of grains and heavier roughening of the specimen surface, as seen from Figure 14c,d. These observations strongly suggest that the fractal dimension D_R can be a measure to predict the percolation potential for intergranular corrosion together with GBCD in SUS316L stainless steel.

In the case of nanocrystalline materials with grain size less than 100 nm, namely, the much higher density of grain boundaries, the more precise control of the grain boundary connectivity is required for controlling the percolation-dominating grain boundary phenomena. In view of this, a new approach to GBE based on the fractal analysis is expected to work for control of intrinsic or extrinsic intergranular brittleness caused by a dominant contribution of the network of percolation susceptive random boundaries. In particular, the MRBC first introduced by the present authors [87] is very likely applicable to solve the pending problem of poor ductility and intergranular brittleness, and further to confer desirable bulk mechanical properties to nanocrystalline materials through GBE.

Figure 15 shows a schematic diagram illustrating our current knowledge of GBE through the incorporation of optimum grain boundary microstructure for desirable bulk properties controlled by the percolation-dominating intergranular phenomena in nanocrystalline materials. The illustrated grain boundary maps were drawn based on observed grain boundary maps to demonstrate real grain boundary microstructures with a sharp texture, in real nanocrystalline materials, such as electrodeposited Ni alloys and sputtered gold thin films mentioned later.

As a brief summary of our findings, first, Type A specimen may exhibit a low resistance to percolation-related intergranular degradation phenomena. This is because the fraction of low Σ CSL boundaries is lower than the percolation threshold value of MRBC and the high coefficient of variation of grain size distribution $\sigma / \bar{d}$, namely, the wide spread of grain size distribution. Second, since Type B specimen has the fractal dimension of MRBC being of the middle level of percolation resistance because of the fraction of low Σ CSL boundaries higher than the value of percolation threshold of MRBC and the high $\sigma / \bar{d}$. Third, Type C specimen, which has a high fraction of low-Σ CSL boundaries (more than the value of percolation threshold of MRBC and low $\sigma / \bar{d}$, may bring about the highest percolation resistance, due to a low fractal dimension of MRBC.

Electrical resistivity manipulated by GBE in nanocrystalline gold thin films

The improvement of electrical conductivity or precise control of electrical resistivity is required for the development of high performance electrical and magnetic materials for modern electronic devices such as MEMS and NEMS. It has been revealed that the electrical resistivity of individual grain boundaries

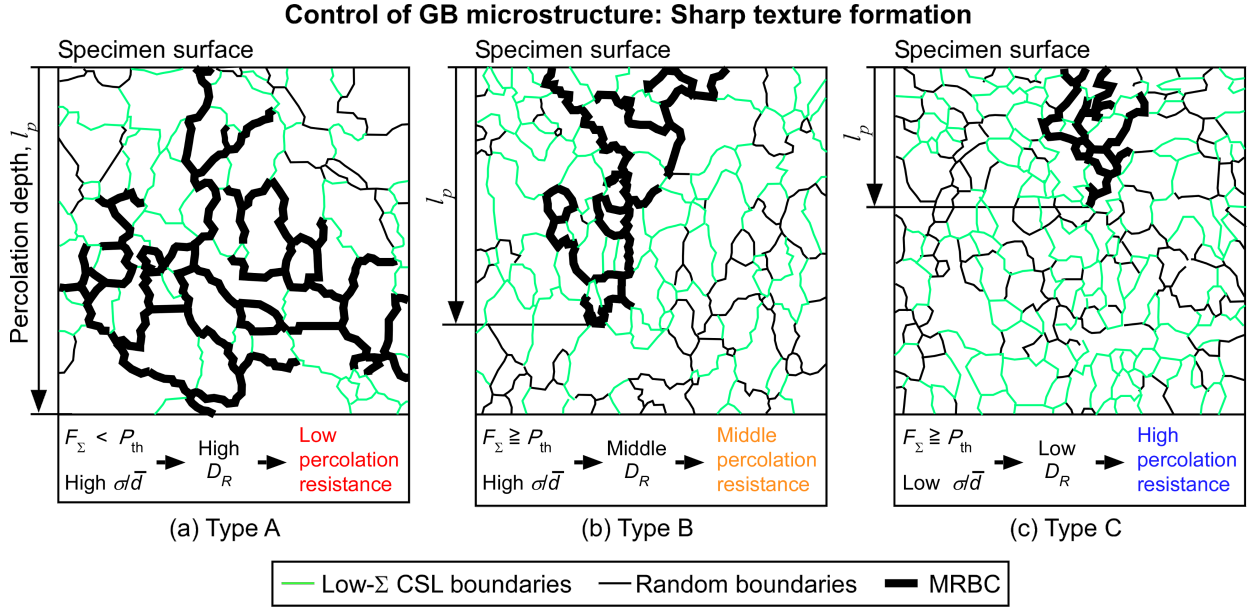


Figure 15: Schematic illustration showing the bulk mesoscopic propensity to percolation-related phenomena in the nanocrystalline materials with different grain boundary microstructures: (a) Type A with the highest value of D_R, (b) Type B with the middle value of D_R and (c) Type C with the lowest value of D_R. The process of grain boundary microstructure control is associated with the formation of a sharp texture, as observed in the electrodeposited nanocrystalline Ni and sputtered gold thin film specimens.

strongly depends on the grain boundary character and structure from fundamental studies with orientation-controlled bicrystalline or coarse-grained metallic (Al) [123,124], semiconductor (Si) [125,126], and ceramic materials (ZnO) [127]. Nakamichi and Kino [124] have found from their systematic studies that low-energy/low-Σ CSL boundaries exhibit lower electrical resistivity than that of high-energy/random boundaries. Recent observations of electrical properties in silicon have revealed the dominant effects of the character of boundaries, their crystallographic plane, triple junctions and dopants. Accordingly, we expect that GBE based on the control of grain boundary microstructure must be useful for future improvement of electrical conductivity in polycrystalline materials, especially nanocrystalline materials which can be produced by advanced processing methods like various types of deposition methods and used in shape of tiny parts for microelectronic devices.

In thin film materials, the application of surface energy-driven grain growth is very useful and powerful for controlling the grain boundary microstructure. When a sharp texture is introduced in thin films with help of orientation-dependent surface free energy (namely by applying the surface energy-driven grain growth during annealing), specific low-Σ CSL boundaries can be preferentially introduced, depending on the type and the sharpness of texture [52,128-132]. In the case of gold thin films, the high fraction of low-Σ CSL boundaries predicted for the <111> rotation axis, such as Σ3, Σ7, Σ13, Σ19 and Σ21 boundaries preferentially occurred in relation to development of the sharp {111} texture, as observed in real polycrystalline materials [133-136].

Figure 16 shows OIM micrographs and corresponding grain boundary maps for as-sputtered gold thin film specimen on Pyrex glass substrates and specimens annealed in Ar at 873 K for three different times (3.6, 10.8 and 18.0 ks). The three specimens subjected to different annealing times were designated as Type A, Type B and Type C specimens, respectively. The sharpness of the {111} texture was increased in these specimens by surface energy-driven grain growth during annealing. The Type A specimen had the smallest average grain size of 91 nm and the highest total fraction of low-angle (17%) and low-Σ CSL boundaries (49%), especially including CSL boundaries with Σ values predicted for <111> rotation axis (46%). The Type B specimen had an average grain size of 110 nm and has the high fraction of low-angle (17%) and low-Σ CSL boundaries (45%) similar to the Type A specimen. The Type C specimen had an average grain size (113 nm) similar to the Type B specimen, but the lowest total fraction of low-angle (20%) and low-Σ CSL boundaries (30%).

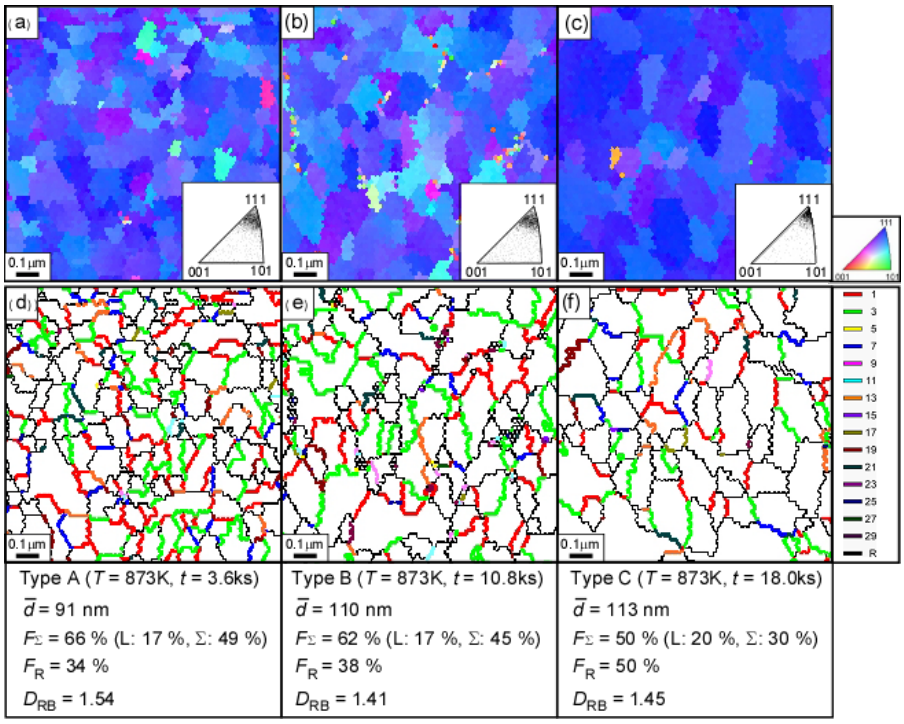


Figure 16: (a–c) OIM micrographs with inverse pole figures (IPF) of grain orientation distribution and (d–f) grain boundary microstructure for the gold thin film specimens sputtered on Pyrex grass substrates and subsequently annealed in Ar at 873 K for 3.6 ks (a,d), 10.8 ks (b,e) and 18.0 ks (c,f), respectively.

Figure 17 shows the results of the quantitative evaluation of GBCD obtained from the three differently processed gold thin film specimens, i.e., Type A, Type B and Type C. These specimens had a high fraction (17–20%) of low-angle boundaries, together with a high fraction low-Σ CSL boundaries with such specific Σ-values as Σ3, Σ7, Σ13, Σ19 and Σ21, predicted for the sharp <111> texture. Of particular interest is that Σ3, Σ13, Σ19 and Σ21 boundaries occurred with a much higher fraction than theoretical values of GBCD for the sharp {111} texture with deviation angle less than 3°. Moreover, a high fraction of Σ9 CSL boundaries also occurred in these specimens than in random polycrystals, although the predicated value for Σ9 is not available in the reported literature. This is probably because these specific low-Σ CSL boundaries with Σ3, Σ13, Σ19 and Σ21 belong to the group of CSL boundaries with the lowest grain boundary energy, and Σ9 CSL boundary belongs to the group of medium boundary energy in FCC materials [134,137].

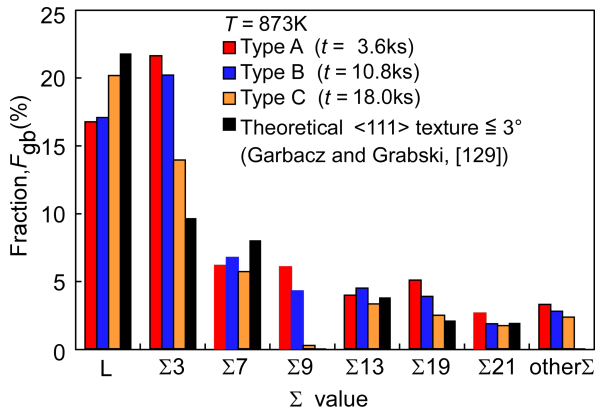


Figure 17: Change in grain boundary character distribution in the sputtered gold thin film specimens after annealing in Ar at 873 K for 3.6, 10.8 and 18.0 ks.

In our new approach to GBE based on fractal analysis, we performed the fractal analysis for the grain boundary microstructures in the three different types of gold thin film specimens. One of the results obtained from our fractal analysis of GB microstructure in Type B specimen is shown in Figure 18, which indicates the result from the surface over a quite large area (≈3 × 3 μm), as being easily recognizable from the box size (50 nm) of the fractal analysis applied in this work. It is evident how interconnected random boundaries extend by depending on the grain boundary microstructures in individual studied gold thin film specimens, i.e., the heterogeneity of grain size distribution, GBCD, and grain boundary connectivity, or triple junction character distribution. To our knowledge, no literature is available which has reported such detailed information about grain boundary microstructure based on fractal analysis for real nanocrystalline materials, such as gold thin film in this work.

From the image of the connectivity of random boundaries indicated by connected black lines in Figure 18, we can intuitively recognize and get such useful image of the grain boundary microstructure and quantitative evaluation of characteristic features from the combined analysis based on OIM and fractal analysis. This is yet to be achieved by computer simulation for understanding of grain boundary microstructure and bulk properties of polycrystalline and nanocrystalline materials.

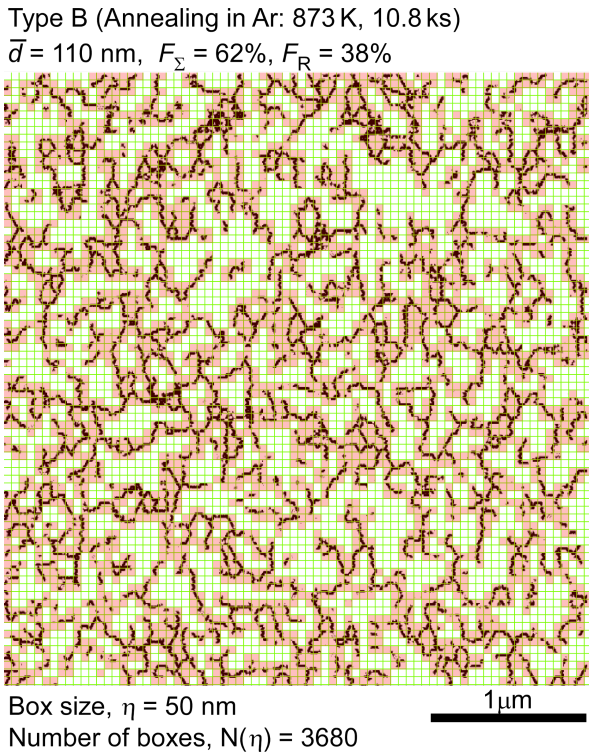


Figure 18: Example of the fractal analysis by box counting method for spatial distribution of random boundaries in gold thin film specimen (Type B).

Lastly, in order to give the reader a flavor of our new challenge of GBE for nanocrystalline materials introduced so far, let us just mention the most recent result on the effect of grain boundary microstructure on the electrical resistivity for the three types of gold thin film specimens with different grain boundary microstructure, already mentioned.

Figure 19 shows the experimental results on the electrical resistivity ρ as a function of the fractal dimension, associated with the spatial distribution of random boundaries as the primary scattering center of electrons in a polycrystal. Again it is evident that the electrical resistivity tends to increase systematically with increasing fractal dimension of random boundary connectivity. This result is first reported in this article to demonstrate the usefulness of our new approach to GBE for

nanocrystalline functional materials. Here, a gold thin film as the most probable candidate as the highest performance electrical conductive material for advanced electronic devices.

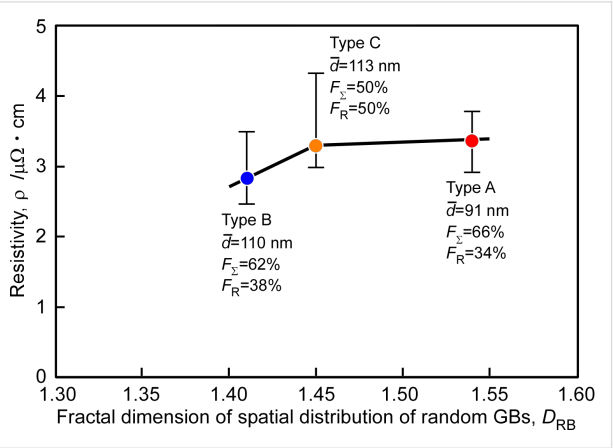


Figure 19: Relationship between the electrical resistivity and fractal dimension of spatial distribution of random boundaries in gold thin film specimens.

Continuing the discussion about the results in Figure 19, the Type B specimen with a larger average grain size, namely due to a lower grain boundary density, showed lower electrical resistivity than the Type A specimen. It is feasible that the electrical resistivity in the latter with a higher grain boundary density became higher than that in the former even if a similar fraction of low-Σ CSL boundaries was kept in both specimens. The observation of the enhanced electrical resistivity in nanocrystalline materials was in good agreement with the previous works by Aus et al. [22]. Moreover, the electrical resistivity in the Type B specimen was lower than that in the Type C specimen. This result may provide some evidence that the electrical resistivity becomes lower in the specimen with a higher fraction of low-Σ CSL boundaries under the condition of similar GB density. It is natural that low-angle boundaries with a larger misorientation angle must have a higher value of the electrical resistivity owing to increase of the volume of dislocation core scattering at these grain boundaries. This is because the space of lattice dislocations becomes finer, decreasing with increasing misorientation angle [124]. We may conclude that a new approach to GBE based on the fractal analysis of GB microstructure is useful for precise control and improvement of electrical properties in nanocrystalline gold thin films. A historical background and a recent situation of GBE were introduced in the recent review by Watanabe [134].

Conclusion

In this Review we have introduced our recent challenge, a new approach to grain boundary engineering (GBE) based on fractal analysis for grain boundary microstructures. This new approach has been undertaken quite recently for GBE in structural and functional polycrystalline materials, especially electrodeposited and sputtered nanocrystalline materials with an extremely high density of grain boundaries. It is shown that a more precise and quantitative evaluation of the effects of grain boundary microstructures are required for nanocrystalline materials than for ordinary polycrystalline materials. This is found by using the grain boundary character distribution (GBCD) and the grain boundary connectivity through SEM/EBSD/OIM analysis. It is well demonstrated that our new approach to GBE based on fractal analysis is very useful for the precise control of grain boundary microstructure-dependent bulk properties. This is especially helpful for mediating poor ductility and brittleness, which are long pending problems to be urgently solved in nanocrystalline materials. Our recent challenge of GBE based on fractural analysis for functional materials is also introduced. A solution was proposed for the future development of high performance functional materials, such as high performance electrical conductive materials, like gold thin films produced by the new approach of GBE.

Acknowledgements

The present work was financially supported by Japan Society for the Promotion of Science (JSPS) KAKENHI Grant Number 23560845, 26420709 and 16H06366. One of the authors (T.W.) gratefully appreciates the long term collaboration as Visiting Professor with Prof. Zuo Liang (now, the president of Taiyuan UST) and Prof. Zhao Xiang at Northeastern University in Shenyang, through the 111 project.

References

1. Birringer, R.; Herr, U.; Gleiter, H. *Trans. Jpn. Inst. Met.* **1986,** *27,* 43–52.
2. Gleiter, H. *Prog. Mater. Sci.* **1989,** *33,* 223–315. doi:10.1016/0079-6425(89)90001-7
3. Palumbo, G.; Erb, U.; Aust, K. T. *Scr. Metall. Mater.* **1990,** *24,* 2347–2350. doi:10.1016/0956-716X(90)90091-T
4. Nieman, G. W.; Weertman, J. R.; Siegel, R. W. In *Microcomposites and Nanophase Materials;* Ghosh, A. K.; Von Aken, D. C.; Was, G. S., Eds.; The Minerals, Metals & Materials Society (TMS): PA, USA, 1991; pp 15–25.
5. Gleiter, H. *Nanostruct. Mater.* **1992,** *1,* 1–19. doi:10.1016/0965-9773(92)90045-Y
6. Erb, U.; El-Sherik, A. M.; Palumbo, G.; Aust, K. T. *Nanostruct. Mater.* **1993,** *2,* 383–390. doi:10.1016/0965-9773(93)90180-J
7. Gertsman, V. Y.; Hoffmann, M.; Gleiter, H.; Birringer, R. *Acta Metall. Mater.* **1994,** *42,* 3539–3544. doi:10.1016/0956-7151(94)90486-3
8. Sanders, P. G.; Youngdahl, C. J.; Weertman, J. R. *Mater. Sci. Eng., A* **1997,** *234–236,* 77–82. doi:10.1016/S0921-5093(97)00185-8
9. Suryanarayanan Iyer, R.; Frey, C. A.; Sastry, S. M. L.; Waller, B. E.; Buhro, W. E. *Mater. Sci. Eng., A* **1999,** *264,* 210–214. doi:10.1016/S0921-5093(98)01027-2

10. Morris-Muñoz, M. A.; Dodge, A.; Morris, D. G. *Nanostruct. Mater.* **1999,** *11,* 873–885. doi:10.1016/S0965-9773(99)00385-2
11. Gleiter, H. *Acta Mater.* **2000,** *48,* 1–29. doi:10.1016/S1359-6454(99)00285-2
12. Torre, F. D.; Van Swygenhoven, H.; Victoria, M. *Acta Mater.* **2002,** *50,* 3957–3970. doi:10.1016/S1359-6454(02)00198-2
13. Kobayashi, S.; Kashikura, Y. *Mater. Sci. Eng., A* **2003,** *358,* 76–83. doi:10.1016/S0921-5093(03)00285-5
14. Koch, C. C. *Scr. Mater.* **2003,** *49,* 657–662. doi:10.1016/S1359-6462(03)00394-4
15. Valiev, R. Z.; Sergueeva, A. V.; Mukherjee, A. K. *Scr. Mater.* **2003,** *49,* 669–674. doi:10.1016/S1359-6462(03)00395-6
16. Kumar, K. S.; Van Swygenhoven, H.; Suresh, S. *Acta Mater.* **2003,** *51,* 5743–5774. doi:10.1016/j.actamat.2003.08.032
17. Dao, M.; Lu, L.; Asaro, R. J.; De Hosson, J. T. M.; Ma, E. *Acta Mater.* **2007,** *55,* 4041–4065. doi:10.1016/j.actamat.2007.01.038
18. Rupert, T. J.; Trelewicz, J. R.; Schuh, C. A. *J. Mater. Res.* **2012,** *27,* 1285–1294. doi:10.1557/jmr.2012.55
19. Tschopp, M. A.; Murdoch, H. A.; Kecskes, L. J.; Darling, K. A. *JOM* **2014,** *66,* 1000–1019. doi:10.1007/s11837-014-0978-z
20. Pineau, A.; Benzerga, A. A.; Pardoen, T. *Acta Mater.* **2016,** *107,* 508–544. doi:10.1016/j.actamat.2015.07.049
21. Aus, M. J.; Szpunar, B.; El-Sherik, A. M.; Erb, U.; Palumbo, G.; Aust, K. T. *Scr. Metall. Mater.* **1992,** *27,* 1639–1643. doi:10.1016/0956-716X(92)90158-B
22. Aus, M. J.; Szpunar, B.; Erb, U.; Palumbo, G.; Aust, K. T. *Mater. Res. Soc. Symp. Proc.* **1993,** *318,* 39–44. doi:10.1557/PROC-318-39
23. Aus, M. J.; Szpunar, B.; Erb, U.; El-Sherik, A. M.; Palumbo, G.; Aust, K. T. *J. Appl. Phys.* **1994,** *75,* 3632–3634. doi:10.1063/1.356076
24. Watanabe, T.; Tsurekawa, S.; Zhao, X.; Zuo, L. *Scr. Mater.* **2006,** *54,* 969–975. doi:10.1016/j.scriptamat.2005.11.036
25. Watanabe, T.; Tsurekawa, S.; Zhao, X.; Zuo, L.; Esling, C. *J. Mater. Sci.* **2006,** *41,* 7747–7759. doi:10.1007/s10853-006-0740-1
26. Valiev, R. Z.; Murashkin, M. Yu.; Kilmametov, A.; Straumal, B.; Chinh, N. Q.; Langdon, T. G. *J. Mater. Sci.* **2010,** *45,* 4718–4724. doi:10.1007/s10853-010-4588-z
27. Raabe, D.; Herbig, M.; Sandlöbes, S.; Li, Y.; Tytko, D.; Kuzmina, M.; Ponge, D.; Choi, P.-P. *Curr. Opin. Solid State Mater. Sci.* **2014,** *18,* 253–261. doi:10.1016/j.cossms.2014.06.002
28. Kuzmina, M.; Ponge, D.; Raabe, D. *Acta Mater.* **2015,** *86,* 182–192. doi:10.1016/j.actamat.2014.12.021
29. Kalidindi, A. R.; Chookajorn, T.; Schuh, C. A. *JOM* **2015,** *67,* 2834–2843. doi:10.1007/s11837-015-1636-9
30. Watanabe, T. *Res Mech.* **1984,** *11,* 47–84.
31. Aust, K. T.; Palumbo, G. Interface Control in Materials. In *Proceedings of International Symposium on Advanced Masterials;* Wilkinson, D. S., Ed.; Pergamon Press, 1989; pp 215–226. doi:10.1016/B978-0-08-036090-4.50028-8
32. Erb, U.; Palumbo, G., Eds. *Proceedings of Karl T. Aust International Symposium on Grain Boundary Engineering, 5th Canadian Materials Science Conference,* June 22–25, 1993; Canadian Institute of Mining, Metallurgy and Petroleum: Ontario, Canada, 1993.
33. Watanabe, T. A. Prospect of Grain Boundary Design and Control for Structural Materials. In *Proceedings of D. McLean Symposium on Structural Materials: Engineering Application Through Sceintific Insight;* Hondros, E. D.; McLean, M., Eds.; The Instiute of Materials, 1996; pp 43–57.
34. Watanabe, T.; Tsurekawa, S. *Acta Mater.* **1999,** *47,* 4171–4185. doi:10.1016/S1359-6454(99)00275-X
35. Watanabe, T. *Ann. Chim. (Cachan, Fr.)* **2002,** *27* (Suppl. 1), S327–S344.
36. Lejček, P. *Springer Ser. Mater. Sci.* **2010,** 173–201. doi:10.1007/978-3-642-12505-8_7
37. Tsurekawa, S.; Watanabe, T. *Mater. Res. Soc. Symp. Proc.* **2000,** *586,* 237–242. doi:10.1557/PROC-586-237
38. Bechtle, S.; Kumar, M.; Somerday, B. P.; Launey, M. E.; Ritchie, R. O. *Acta Mater.* **2009,** *57,* 4148–4157. doi:10.1016/j.actamat.2009.05.012
39. Was, G. S.; Thaveeprungsriporn, V.; Crawford, D. C. *JOM* **1998,** *50,* 44–49. doi:10.1007/s11837-998-0249-y
40. Was, G. S.; Alexandreanu, B.; Andresen, P.; Kumar, M. *Mater. Res. Soc. Symp. Proc.* **2004,** *819,* 87–100. doi:10.1557/PROC-819-N2.1
41. Alexandreanu, B.; Was, G. S. *Scr. Mater.* **2006,** *54,* 1047–1052. doi:10.1016/j.scriptamat.2005.11.051
42. Gao, Y.; Ritchie, R. O.; Kumar, M.; Nalla, R. K. *Metall. Mater. Trans. A* **2005,** *36,* 3325–3333. doi:10.1007/s11661-005-0007-5
43. Gao, Y.; Stölken, J. S.; Kumar, M.; Ritchie, R. O. *Acta Mater.* **2007,** *55,* 3155–3167. doi:10.1016/j.actamat.2007.01.033
44. Kobayashi, S.; Hirata, M.; Tsurekawa, S.; Watanabe, T. *Procedia Eng.* **2011,** *10,* 112–117. doi:10.1016/j.proeng.2011.04.021
45. Kobayashi, S.; Nakamura, M.; Tsurekawa, S.; Watanabe, T. *J. Mater. Sci.* **2011,** *46,* 4254–4260. doi:10.1007/s10853-010-5238-1
46. Lin, P.; Palumbo, G.; Erb, U.; Aust, K. T. *Scr. Metall. Mater.* **1995,** *33,* 1387–1392. doi:10.1016/0956-716X(95)00420-Z
47. Shimada, M.; Kokawa, H.; Wang, Z. J.; Sato, Y. S.; Karibe, I. *Acta Mater.* **2002,** *50,* 2331–2341. doi:10.1016/S1359-6454(02)00064-2
48. Tsurekawa, S.; Nakamichi, S.; Watanabe, T. *Acta Mater.* **2006,** *54,* 3617–3626. doi:10.1016/j.actamat.2006.03.048
49. Michiuchi, M.; Kokawa, H.; Wang, Z. J.; Sato, Y. S.; Sakai, K. *Acta Mater.* **2006,** *54,* 5179–5184. doi:10.1016/j.actamat.2006.06.030
50. Palumbo, G.; King, P. J.; Aust, K. T.; Erb, U.; Lichtenberger, P. C. *Scr. Metall. Mater.* **1991,** *25,* 1775–1780. doi:10.1016/0956-716X(91)90303-I
51. West, E. A.; Was, G. S. *J. Nucl. Mater.* **2009,** *392,* 264–271. doi:10.1016/j.jnucmat.2009.03.008
52. Watanabe, T.; Fujii, H.; Oikawa, H.; Arai, K. I. *Acta Metall.* **1989,** *37,* 941–952. doi:10.1016/0001-6160(89)90021-7
53. Terhune, S. D.; Swisher, D. L.; Oh-Ishi, K.; Horita, Z.; Langdon, T. G.; McNelley, T. R. *Metall. Mater. Trans. A* **2002,** *33,* 2173–2184. doi:10.1007/s11661-002-0049-x
54. Bober, D. B.; Khalajhedayati, A.; Kumar, M.; Rupert, T. J. *Metall. Mater. Trans. A* **2016,** *47,* 1389–1403. doi:10.1007/s11661-015-3274-9
55. Valiev, R. Z.; Islamgaliev, R. K.; Alexandrov, I. V. *Prog. Mater. Sci.* **2000,** *45,* 103–189. doi:10.1016/S0079-6425(99)00007-9
56. Valiev, R. Z.; Langdon, T. G. *Prog. Mater. Sci.* **2006,** *51,* 881–981. doi:10.1016/j.pmatsci.2006.02.003
57. Lu, K. *Mater. Sci. Eng., R* **1996,** *16,* 161–221. doi:10.1016/0927-796X(95)00187-5
58. Valiev, R. A.; Estrin, Y.; Horita, Z.; Langdon, T. G.; Zehetbauer, M. J.; Zhu, Y. T. *JOM* **2006,** *58,* 33–39. doi:10.1007/s11837-006-0213-7
59. Estrin, Y.; Vinogradov, A. *Acta Mater.* **2013,** *61,* 782–817. doi:10.1016/j.actamat.2012.10.038
60. Kumar, P.; Kawasaki, M.; Langdon, T. G. *J. Mater. Sci.* **2016,** *51,* 7–18. doi:10.1007/s10853-015-9143-5
61. Valiev, R. A.; Estrin, Y.; Horita, Z.; Langdon, T. G.; Zehetbauer, M. J.; Zhu, Y. T. *JOM* **2016,** *68,* 1216–1226. doi:10.1007/s11837-016-1820-6

62. El-Sherik, A. M.; Erb, U.; Palumbo, G.; Aust, K. T. *Scr. Metall. Mater.* **1992,** *27,* 1185–1188. doi:10.1016/0956-716X(92)90596-7
63. Klement, U.; Erb, U.; El-Sherik, A. M.; Aust, K. T. *Mater. Sci. Eng., A* **1995,** *203,* 177–186. doi:10.1016/0921-5093(95)09864-X
64. Wang, S.-L.; Murr, L. E. *Metallography* **1980,** *13,* 203–224. doi:10.1016/0026-0800(80)90001-4
65. Massalski, T. B.; Murray, J. L. In *Binary Alloy Phase Diagrams;* Bennett, L. H.; Baker, H., Eds.; ASM International: Materials Park: OH, 1986; pp 1739 ff.
66. Volpp, T.; Göring, E.; Kuschke, W.-M.; Arzt, E. *Nanostruct. Mater.* **1997,** *8,* 855–865. doi:10.1016/S0965-9773(98)00019-1
67. Chokshi, A. H.; Rosen, A.; Karch, J.; Gleiter, H. *Scr. Metall.* **1989,** *23,* 1679–1684. doi:10.1016/0036-9748(89)90342-6
68. Aust, K. T. Mechanical Effects of Grain Boundaries. In *Surface and Interface II: Physical and Mechanical Properties;* Burke, J. J.; Reed, N. L.; Weiss, V., Eds.; Springer US: Syracuse, NY, 1968; pp 235–275. doi:10.1007/978-1-4757-0178-4_8
69. Watanabe, T.; Kitamura, S.; Karashima, S. *Acta Metall.* **1980,** *28,* 455–463. doi:10.1016/0001-6160(80)90135-2
70. Chou, Y. T.; Cai, B. C.; Romig, A. D., Jr.; Lin, L. S. *Philos. Mag. A* **1983,** *47,* 363–368. doi:10.1080/01418618308245232
71. Schweitzer, E.; Göken, M. *Z. Metallkd.* **2004,** *95,* 492–498. doi:10.3139/146.017976
72. Kobayashi, S.; Tsurekawa, S.; Watanabe, T. *Acta Mater.* **2005,** *53,* 1051–1057. doi:10.1016/j.actamat.2004.11.002
73. Soer, W. A.; Aifantis, K. E.; De Hosson, J. T. M. *Acta Mater.* **2005,** *53,* 4665–4676. doi:10.1016/j.actamat.2005.07.001
74. Kobayashi, S.; Tsurekawa, S.; Watanabe, T. *Philos. Mag.* **2006,** *86,* 5419–5429. doi:10.1080/14786430600672711
75. Westbrook, J. H.; Aust, K. T. *Acta Metall.* **1963,** *11,* 1151–1163. doi:10.1016/0001-6160(63)90042-7
76. Aust, K. T.; Hanneman, R. E.; Niessen, P.; Westbrook, J. H. *Acta Metall.* **1968,** *16,* 291–302. doi:10.1016/0001-6160(68)90014-X
77. Braunovic, M.; Haworth, C. W. *J. Mater. Sci.* **1974,** *9,* 809–820. doi:10.1007/BF00761801
78. Fortier, P.; Miller, W. A.; Aust, K. T. *Acta Mater.* **1997,** *45,* 3459–3467. doi:10.1016/S1359-6454(97)00004-9
79. Dingley, D. J.; Pond, R. C. *Acta Metall.* **1979,** *27,* 667–682. doi:10.1016/0001-6160(79)90018-X
80. Balluffi, R. W. Grain Boundary Structure and Segregation. In *Interfacial Segregation;* Johnson, W. C.; Blakely, J. M., Eds.; ASM: OH, USA, 1979; pp 193–237.
81. Lejček, P.; Hofmann, S. *Crit. Rev. Solid State Mater. Sci.* **1995,** *20,* 1–85. doi:10.1080/10408439508243544
82. Bouchet, D.; Priester, L. *Scr. Metall.* **1986,** *20,* 961–966. doi:10.1016/0036-9748(86)90417-5
83. Bouchet, D.; Priester, L. *Scr. Metall.* **1987,** *21,* 475–478. doi:10.1016/0036-9748(87)90184-0
84. Juhas, M. C.; Priester, L. *Mater. Res. Soc. Symp. Proc.* **1991,** *229,* 319–324. doi:10.1557/PROC-229-319
85. Kobayashi, S.; Tsurekawa, S.; Watanabe, T.; Palumbo, G. *Scr. Mater.* **2010,** *62,* 294–297. doi:10.1016/j.scriptamat.2009.11.022
86. Kumar, M.; King, W. E.; Schwartz, A. J. *Acta Mater.* **2000,** *48,* 2081–2091. doi:10.1016/S1359-6454(00)00045-8
87. Kobayashi, S.; Maruyama, T.; Tsurekawa, S.; Watanabe, T. *Acta Mater.* **2012,** *60,* 6200–6212. doi:10.1016/j.actamat.2012.07.065
88. Kim, W. H.; Laird, C. *Acta Metall.* **1978,** *26,* 789–799. doi:10.1016/0001-6160(78)90029-9
89. Lim, L. C. *Acta Metall.* **1987,** *35,* 1653–1662. doi:10.1016/0001-6160(87)90113-1
90. Neumann, P.; Tönnessen, A. Cyclic deformation and crack initiation. In *Proc. of the Third International Conference on Fatigue and Fatigue Thresholds (Fatigue '87),* Charlottesville, Virginia, June 28–July 3, 1987; Ritchie, R. O.; Starke, E. A., Jr., Eds.; Virginia, 1987; pp 3–22.
91. Heinz, A.; Neumann, P. *Acta Metall. Mater.* **1990,** *38,* 1933–1940. doi:10.1016/0956-7151(90)90305-Z
92. Liu, W.; Bayerlein, M.; Mughrabi, H.; Day, A.; Quested, P. N. *Acta Metall. Mater.* **1992,** *40,* 1763–1771. doi:10.1016/0956-7151(92)90119-Y
93. Zhang, Z. F.; Wang, Z. G. *Mater. Sci. Eng., A* **2000,** *284,* 285–291. doi:10.1016/S0921-5093(00)00796-6
94. Zhang, Z. F.; Wang, Z. G. *Philos. Mag. Lett.* **2000,** *80,* 483–488. doi:10.1080/09500830050057189
95. Qu, S.; Zhang, P.; Wu, S. D.; Zang, Q. S.; Zhang, Z. F. *Scr. Mater.* **2008,** *59,* 1131–1134. doi:10.1016/j.scriptamat.2008.07.037
96. Zhang, Z. F.; Wang, Z. G. *Prog. Mater. Sci.* **2008,** *53,* 1025–1099. doi:10.1016/j.pmatsci.2008.06.001
97. Kobayashi, S.; Inomata, T.; Kobayashi, H.; Tsurekawa, S.; Watanabe, T. *J. Mater. Sci.* **2008,** *43,* 3792–3799. doi:10.1007/s10853-007-2236-z
98. Vinogradov, A.; Hashimoto, S.; Miura, S. *Scr. Metall. Mater.* **1995,** *32,* 427–431. doi:10.1016/S0956-716X(99)80077-6
99. Kaneko, Y.; Kitagawa, K.; Hashimoto, S. *Interface Sci.* **1999,** *7,* 147–158. doi:10.1023/A:1008787703423
100. Suzuki, M.; Takahashi, H. *Z. Metallkd.* **1966,** *57,* 484–487.
101. Witney, A. B.; Sanders, P. G.; Weertman, J. R.; Eastman, J. A. *Scr. Metall. Mater.* **1995,** *33,* 2025–2030. doi:10.1016/0956-716X(95)00441-W
102. Yang, Y.; Imasogie, B.; Fan, G. J.; Liaw, P. K.; Soboyejo, W. O. *Metall. Mater. Trans. A* **2008,** *39,* 1145–1156. doi:10.1007/s11661-008-9487-4
103. Meirom, R. A.; Alsem, D. H.; Romasco, A. L.; Clark, T.; Polcawich, R. G.; Pulskamp, J. S.; Dubey, M.; Ritchie, R. O.; Muhlstein, C. L. *Acta Mater.* **2011,** *59,* 1141–1149. doi:10.1016/j.actamat.2010.10.047
104. Padilla, H. A., II; Boyce, B. L. *Exp. Mech.* **2010,** *50,* 5–23. doi:10.1007/s11340-009-9301-2
105. Boyce, B. L.; Padilla, H. A., II. *Metall. Mater. Trans. A* **2011,** *42,* 1793–1804. doi:10.1007/s11661-011-0708-x
106. An, X. H.; Wu, S. D.; Wang, Z. G.; Zhang, Z. F. *Acta Mater.* **2014,** *74,* 200–214. doi:10.1016/j.actamat.2014.04.053
107. Hanlon, T.; Kwon, Y.-N.; Suresh, S. *Scr. Mater.* **2003,** *49,* 675–680. doi:10.1016/S1359-6462(03)00393-2
108. Hanlon, T.; Tabachnikova, E. D.; Suresh, S. *Int. J. Fatigue* **2005,** *27,* 1147–1158. doi:10.1016/j.ijfatigue.2005.06.035
109. Cavaliere, P. *Int. J. Fatigue* **2009,** *31,* 1476–1489. doi:10.1016/j.ijfatigue.2009.05.004
110. Kobayashi, S.; Kamata, A.; Watanabe, T. *Scr. Mater.* **2009,** *61,* 1032–1035. doi:10.1016/j.scriptamat.2009.08.021
111. Aktaa, J.; Reszat, J. T.; Walter, M.; Bade, K.; Hemker, K. J. *Scr. Mater.* **2005,** *52,* 1217–1221. doi:10.1016/j.scriptamat.2005.03.004
112. Stephens, R. I.; Fatemi, A.; Stephens, R. R.; Fuchs, H. O. *Metal Fatigue in Engineering;* John Wiley & Sons, Inc.: NY, USA, 2001.
113. Kobayashi, S.; Kamata, A.; Watanabe, T. *Acta Mater.* **2015,** *91,* 70–82. doi:10.1016/j.actamat.2015.03.028
114. Westwood, H. J.; Taplin, D. M. R. *Metall. Trans.* **1972,** *3,* 1959–1965. doi:10.1007/BF02642585
115. Singh, V.; Rao, P. R.; Cocks, G. J.; Taplin, D. M. R. *J. Mater. Sci.* **1977,** *12,* 373–383. doi:10.1007/BF00566281

116. Yavari, P.; Langdon, T. G. *J. Mater. Sci.* **1983,** *18,* 3219–3229. doi:10.1007/BF00544146
117. Chen, S.; Gottstein, G. *Acta Metall.* **1988,** *36,* 3093–3101. doi:10.1016/0001-6160(88)90046-6
118. Mackenzie, J. K. *Biometrika* **1958,** *45,* 229–240. doi:10.1093/biomet/45.1-2.229
119. Cheng, S.; Stoica, A. D.; Wang, X.-L.; Wang, G. Y.; Choo, H.; Liaw, P. K. *Scr. Mater.* **2007,** *57,* 217–220. doi:10.1016/j.scriptamat.2007.04.013
120. Watanabe, T. *Metall. Trans. A* **1983,** *14,* 531–545. doi:10.1007/BF02643771
121. Kumar, K. S.; Suresh, S.; Chisholm, M. F.; Horton, J. A.; Wang, P. *Acta Mater.* **2003,** *51,* 387–405. doi:10.1016/S1359-6454(02)00421-4
122. Kobayashi, S.; Kobayashi, R.; Watanabe, T. *Acta Mater.* **2016,** *102,* 397–405. doi:10.1016/j.actamat.2015.08.075
123. Lormand, G. J. *J. Phys. (Paris)* **1982,** *43,* 283–291.
124. Nakamichi, I.; Kino, T. *Proc. 4th JIM Int. Symp. on Grain Boundary Structure and Related Phenomena, Supplement to Trans. Jpn. Inst. Met.;* 1986; Vol. 27, pp 1013–1020.
125. Tsurekawa, S.; Kido, K.; Watanabe, T. *Philos. Mag. Lett.* **2005,** *85,* 41–49. doi:10.1080/09500830500153859
126. Tsurekawa, S.; Takahashi, H.; Nishibe, Y.; Watanabe, T. *Philos. Mag.* **2013,** *93,* 1413–1424. doi:10.1080/14786435.2012.753482
127. Sato, Y.; Oba, F.; Yodogawa, H.; Yamamoto, T.; Ikuhara, Y. *J. Appl. Phys.* **2004,** *95,* 1258–1264. doi:10.1063/1.1636816
128. Watanabe, T.; Arai, K.-I.; Yoshimi, K.; Oikawa, H. *Philos. Mag. Lett.* **1989,** *59,* 47–52. doi:10.1080/09500838908214776
129. Garbacz, A.; Grabski, M. W. *Scr. Metall.* **1989,** *23,* 1369–1374. doi:10.1016/0036-9748(89)90061-6
130. Gerzman, V. Yu.; Zhilyaev, A. P.; Pschenichnyuk, A. I.; Variev, R. Z. *Acta Metall. Mater.* **1992,** *40,* 1433–1441. doi:10.1016/0956-7151(92)90445-K
131. Garbacz, A.; Grabski, M. W. *Acta Metall. Mater.* **1993,** *41,* 475–483. doi:10.1016/0956-7151(93)90076-5
132. Zuo, L.; Watanabe, T.; Esling, C. *Z. Metallkd.* **1994,** *85,* 554–558.
133. Watanabe, T. *Textures Microstruct.* **1993,** *20,* 195–216. doi:10.1155/TSM.20.195
134. Watanabe, T. *J. Mater. Sci.* **2011,** *46,* 4095–4115. doi:10.1007/s10853-011-5393-z
135. Kobayashi, S.; Fukasawa, R.; Watanabe, T. *Mater. Sci. Forum* **2012,** *706–709,* 2880–2885. doi:10.4028/www.scientific.net/MSF.706-709.2880
136. Kobayashi, S.; Takagi, H.; Watanabe, T. *Philos. Mag.* **2013,** *93,* 1425–1442. doi:10.1080/14786435.2012.756991
137. Yamaura, S.; Igarashi, Y.; Tsurekawa, S.; Watanabe, T. *Acta Mater.* **1999,** *47,* 1163–1174. doi:10.1016/S1359-6454(99)00007-5

License and Terms

This is an Open Access article under the terms of the Creative Commons Attribution License (http://creativecommons.org/licenses/by/4.0), which permits unrestricted use, distribution, and reproduction in any medium, provided the original work is properly cited.

The license is subject to the *Beilstein Journal of Nanotechnology* terms and conditions: (http://www.beilstein-journals.org/bjnano)

The definitive version of this article is the electronic one which can be found at:
doi:10.3762/bjnano.7.176

BEILSTEIN JOURNAL OF NANOTECHNOLOGY

Ferromagnetic behaviour of ZnO: the role of grain boundaries

Boris B. Straumal[*1,2,3,4], Svetlana G. Protasova[2,3], Andrei A. Mazilkin[1,2], Eberhard Goering[3], Gisela Schütz[3], Petr B. Straumal[4,5] and Brigitte Baretzky[1]

Review

Open Access

Address:
[1]Karlsruher Institut für Technologie, Institut für Nanotechnologie, Hermann-von-Helmholtz-Platz 1, 76344 Eggenstein-Leopoldshafen, Germany, [2]Institute of Solid State Physics, Russian Academy of Sciences, Ac. Ossipyan str. 2, 142432 Chernogolovka, Russia, [3]Max-Planck-Institut für Intelligente Systeme, Heisenbergstrasse 3, 70569 Stuttgart, Germany, [4]National University for Research and Technology "MISiS", Leninsky prospect 4, 119991 Moscow, Russia and [5]Institute of Metallurgy and Materials Science, Russian Academy of Sciences, Leninsky prospect 49, 117991 Moscow, Russia

Email:
Boris B. Straumal[*] - straumal@mf.mpg.de

* Corresponding author

Keywords:
ferromagnetism; grain boundaries; zinc(II) oxide (ZnO)

Beilstein J. Nanotechnol. **2016,** *7,* 1936–1947.
doi:10.3762/bjnano.7.185

Received: 24 August 2016
Accepted: 09 November 2016
Published: 07 December 2016

This article is part of the Thematic Series "Advances in nanomaterials II" and is dedicated to Professor Herbert Gleiter, a significant contributor to modern knowledge of structure, physics and chemistry of grain boundaries, on the occasion of his 75th anniversary.

Guest Editor: H. Hahn

© 2016 Straumal et al.; licensee Beilstein-Institut.
License and terms: see end of document.

Abstract

The possibility to attain ferromagnetic properties in transparent semiconductor oxides such as ZnO is very promising for future spintronic applications. We demonstrate in this review that ferromagnetism is not an intrinsic property of the ZnO crystalline lattice but is that of ZnO/ZnO grain boundaries. If a ZnO polycrystal contains enough grain boundaries, it can transform into the ferromagnetic state even without doping with "magnetic atoms" such as Mn, Co, Fe or Ni. However, such doping facilitates the appearance of ferromagnetism in ZnO. It increases the saturation magnetisation and decreases the critical amount of grain boundaries needed for FM. A drastic increase of the total solubility of dopants in ZnO with decreasing grain size has been also observed. It is explained by the multilayer grain boundary segregation.

Review

Introduction

In 2000 the seminal work of Tomasz Dietl et al. appeared [1]. In this work it was predicted theoretically that many semiconductor oxides can become ferromagnetic (FM) if one dopes them with "magnetic" atoms such as iron, manganese and cobalt. Other theoreticians published in that time similar works [2]. It has been predicted that the Curie temperature of such diluted doped magnetic semiconductor oxides can be quite high, even above room temperature. Especially promising was zinc oxide. According to Dietl, ZnO should possess the highest Curie temperature [1].

Of course, such a prediction could not be ignored by experimentalists in the field of semiconductors, because the possibility to make a transparent broadband semiconductor, such as ZnO, ferromagnetic is very promising for future spintronic applications. The ferromagnetism (FM) opens a way to change the optical and/or electrical properties of such a material by applying an external (permanent or alternating) magnetic field. And vice versa, by applying an external (permanent or alternating) electric field one could influence the magnetic behaviour of such a material. Especially attractive is that zinc oxide is cheap. It is widely used for various applications from sunblock creams to varistors for power electronics [3,4]. The various technologies of deposition of pure and doped ZnO films, sintering of ZnO ceramics and growth of single crystals, are well known and well elaborated. It seemed that nothing could prevent the success of the synthesis of ferromagnetic ZnO doped by iron, manganese, cobalt, or other "magnetic" atoms. Indeed first successes came soon. Ferromagnetic ZnO films were synthesised by pulsed laser deposition (PLD), or magnetron sputtering [5-9]. However, the first disappointments also appeared immediately. Namely, single crystals, ceramics sintered from coarse-grained powders and single-crystalline films deposited by molecular beam epitaxy (MBE) were never ferromagnetic. Other synthesis technologies such as wet-chemistry methods or chemical vapour deposition (CVD) sometimes yielded ferromagnetic ZnO and sometimes they did not.

It was of course a challenge for solid-state physics and materials science to explain such strange behaviour and to develop the methods to predict (at least qualitatively) where and when the ferromagnetism appears in zinc oxide. We supposed that ferromagnetic behaviour of pure and doped ZnO is controlled by grain boundaries (GBs) and appears only if the grain boundary network (the "ferromagnetic foam") is dense enough [7]. Our first results concerning the role of grain boundaries in the ferromagnetic behaviour of pure ZnO and ZnO doped by Mn and Co as well as concerning the dependence of the solubility of Mn and Co in ZnO on the grain size were published in two reviews [10,11] summarizing the essential findings obtained at that time. Later, the hypothesis about the role of GB in ferromagnetic behaviour was supported by our new results on ZnO doped with nickel and iron [6,9,12] as well as by measurements with low-energy muon spin relaxation combined with molecular dynamics modeling and density functional theory calculations [13]. These new results constitute the additional contribution of the current review. It aims to give the comprehensive and updated view on the GB contribution to the ferromagnetic behaviour of ZnO as well as on the multilayer GB adsorption drastically increasing the overall dopant solubility in ZnO. This review is also a modest tribute to the 75th anniversary of Professor Herbert Gleiter who contributed so much to the development of our knowledge of structure, physics and chemistry of grain boundaries.

Critical grain size for the ferromagnetic behaviour of ZnO

First of all we analysed the whole corpus of published data on ferromagnetic behaviour of zinc oxide and developed our own method for the synthesis of pure and doped nanocrystalline ZnO films. The obtained data are summarized in Figure 1 for pure ZnO and ZnO doped with manganese, cobalt, iron and nickel [6-9]. The full list of used references can be found in [6-9]. In each of the five parts of Figure 1 the temperature is plotted along the vertical axis. It is either the synthesis temperature or the temperature of last annealing of the oxides. The grain boundary specific area s_{GB} is given in the horizontal axis. s_{GB} is the area of GBs in a unit volume. We added an experimental point to the diagrams in Figure 1 if it was possible to estimate from the published experimental work (a) the grain size, (b) the grain shape – equiaxial, elongated or flattened – and (c) porosity of sample, i.e., the portion of grain boundaries and free surfaces. When possible, we tried also to take into account the so-called grain boundary character [14]. In other words we tried to include the high-angle grain boundaries and to exclude the low-angle ones [15]. It is easy to calculate s_{GB} if the grains are equiaxial (circles in Figure 1).

The optimal space-filling grain shape for such polycrystals with a minimal surface area is the tetrakaidecahedron, a polyhedron with 14 faces. Thus, the GB-area-to-volume ratio is $s_{GB} = 1.65/D$, where D is the mean grain size [16]. If the grains were elongated or flattened, the aspect ratio was taken in the account, and s_{GB} was modified accordingly (triangles in Figure 1). The equation for s_{GB} from [16] is true if a sample is dense and does not contain any pores. In case of porous samples (like for example for partially sintered powders or nanowires, diamonds and downward triangles in Figure 1) the value of s_{GB} was multiplied by the porosity factor $p < 1$. In the upper horizontal axis the values of grain size are given as recalculated from s_{GB} supposing that the sample is dense and the grains are equiaxial. Squares correspond to the single crystalline samples. They do not contain any GBs, therefore, we put them in the diagram at grain size of 10^{-1} m. Filled symbols in Figure 1 show the data where the ZnO samples were ferromagnetic. Open symbols correspond to the samples for which no FM behaviour has been observed.

Large filled circles show our own experimental data obtained using ZnO films synthesized using the original "liquid ceramics" method. This is a kind of so-called wet-chemistry methods for the synthesis of nanograined oxide films. The precursor was zinc(II) butanoate dissolved in an organic solvent. It

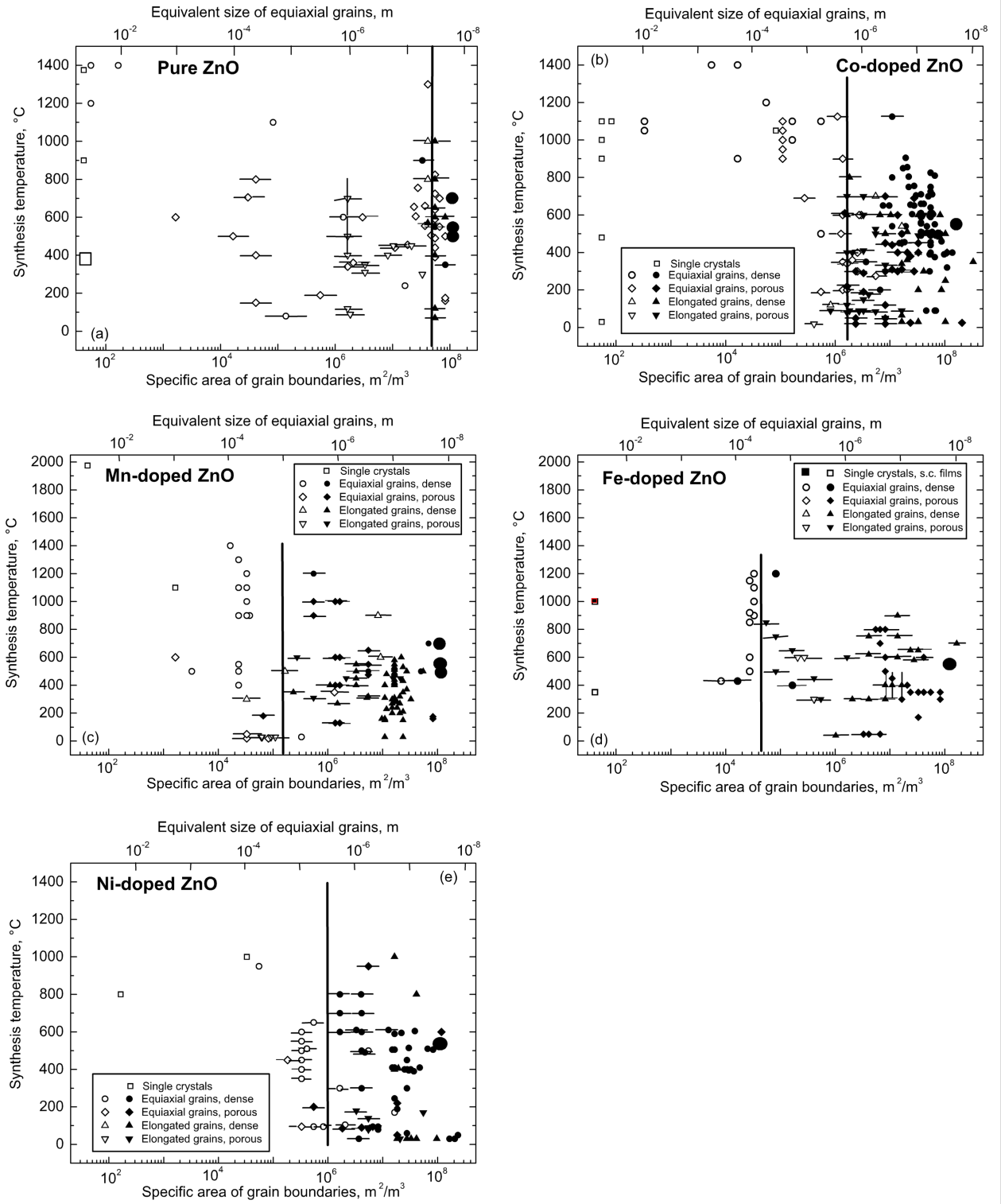


Figure 1: Ferromagnetic (full symbols) and paramagnetic or diamagnetic properties (open symbols) of (a) pure zinc oxide [7] and ZnO doped with (b) cobalt [8], (c) manganese [7], (d) iron [9] and (e) nickel [6] versus the specific area of grain boundaries s_{GB} (ratio of the area of the boundaries to the volume) at various synthesis temperatures T. In the upper horizontal axis the values of grain size are given as recalculated from s_{GB} supposing that the sample is dense and grains are equiaxial. Vertical lines mark the threshold values of s_{th} dividing FM (right) and non-FM behaviour of ZnO. Large symbols correspond to the experimental data obtained in the works [6-9]. Figure was replotted basing on the plots reproduced with permission from [6-9], copyright Institute of Problems of Mechanical Engineering, Russian Academy of Sciences (PME RAS, "Advanced Study Center" Co. Ltd), American Physical Society and Taylor & Francis.

was used for the preparation of pure zinc oxide. Similar solutions of Mn, Co, Ni and Fe butanoates of were also prepared. The Zn precursor was mixed, respectively, with Mn, Co, Ni or Fe butanoates in appropriate proportions (in order to obtain doped ZnO with dopant contents from 0.1 to 50 atom %). The mixture of liquid precursors was deposited on a substrate (aluminium polycrystalline foil or sapphire single crystalline plate). Then the deposited liquid mixture was dried at 150 °C. After drying the pyrolysis took place in argon or in air at temperatures between 500 and 600 °C. The resulted pure and doped ZnO films of thicknesses between 50 and 200 nm (measured by electron-probe X-ray microanalysis and transmission electron microscopy) were dense (i.e., pore free) and contained equiaxial grains with sizes of about 20 nm (Figure 2). The films were transparent and slightly greenish.

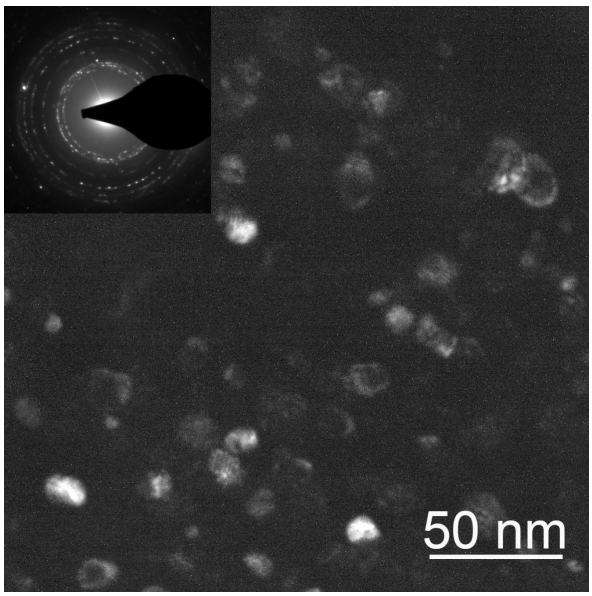


Figure 2: Dark-field TEM micrograph of a thin zinc oxide nanocrystalline film obtained using the liquid-ceramics method.

The composition of the films was controlled by atomic absorption spectroscopy in a Perkin-Elmer spectrometer and by electron-probe X-ray microanalysis with a Tescan Vega TS5130 MM scanning electron microscope (SEM) equipped by energy dispersive X-ray spectrometer (Oxford Instruments). TEM studies were performed using JEM-4000FX microscope at an accelerating voltage of 400 kV. X-ray diffraction (XRD) was studied using a Siemens diffractometer with a graphite monochromator and a gas flow detector using Fe Kα radiation. The grain size in pure and doped ZnO was measured by TEM and additionally by XRD. It was calculated from the angular dependence of the line broadening [17]. The magnetic properties were measured using a SQUID interferometer (Quantum Design MPMS-7 and MPMS-XL) in the external magnetic field applied parallel to the sample plane. The diamagnetic signal from a sample holder and a substrate was accurately subtracted from the magnetization curves.

In Figure 3 the magnetization curves are plotted for pure ZnO and ZnO-doped with 0.1 and 10 atom % Mn [7]. All three curves demonstrated typical ferromagnetic behaviour with saturation (the saturation magnetization J_s is, respectively, 1×10^{-3} μB/f.u. = 0.06 emu/g, 2×10^{-3} μB/f.u. = 0.16 emu/g, and 0.8×10^{-3} μB/f.u. = 0.04 emu/g) and hysteresis with a coercive force H_c of about 0.01–0.02 T (see insets in Figure 4). All three samples have grain sizes well below the barrier value (Figure 2) leading to the FM behaviour. J_s increases linearly with the increasing thickness of the ZnO film (Figure 4). The temperature dependence of J_s permits to estimate the Curie temperature T_C. At room temperature the saturation magnetization of pure zinc oxide films was only 40% lower than J_s measured at 40 K [7]. It means that T_C of our films is much higher than the room temperature. The main feature of all five plots in Figure 1 is that ZnO becomes ferromagnetic only if s_{GB} exceeds a certain critical value s_{th}. In other words, FM properties appear if the grains are small enough. Moreover, one needs grain boundaries. If the ZnO powders are fine- or even nanograined, but not sintered (i.e., $p << 1$), they have few GBs. Then they are not ferromagnetic and, as a result, appear in the left part of a diagram.

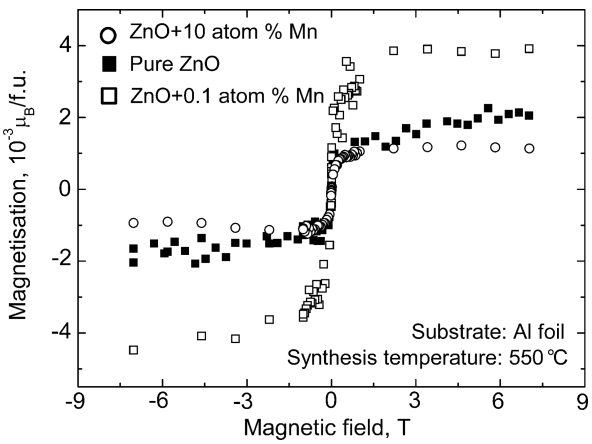


Figure 3: Magnetization J_s (in units of 10^{-3} μB/f.u.) as a function of the applied external magnetic field for pure zinc oxide films and zinc oxide films doped with 0.1 and 10 atom % Mn at room temperature. Reproduced with permission from [7], copyright 2009 American Physical Society.

From Figure 1 follow two important contradictions with the seminal prediction of T. Dietl [1]: (1) bulk ZnO, even doped with “magnetic” atoms, is not ferromagnetic; (2) even undoped

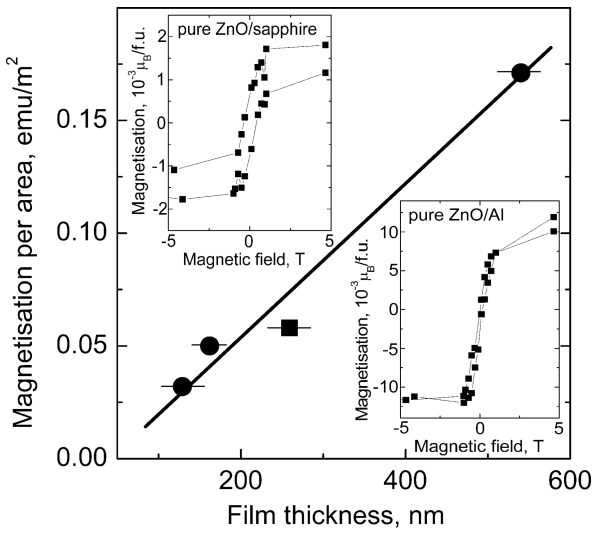


Figure 4: Dependence of magnetization per area unit (calibrated in emu/m^2) on the film thickness (circles are pure zinc oxide, square is for ZnO doped by 10 atom % Mn) measured at room temperature. Insets show magnetic hysteresis for pure ZnO deposited on the sapphire single crystal (left) and on the aluminium polycrystal (right). Reproduced with permission from [7], copyright 2009 American Physical Society.

pure ZnO can become ferromagnetic if it contains enough grain boundaries. Indeed, pure ZnO possesses ferromagnetic properties at $s_{GB} > s_{th} = 5.3 \times 10^7$ m^2/m^3 [7], in other words at grain sizes below 20 nm (Figure 1a). However, the addition of manganese, cobalt, iron and nickel positively influences the FM of ZnO polycrystals. Such additions decrease the amount of GBs needed for FM behaviour. This fact somehow coincides with the prediction of Dietl et al. [1]. For example, in a number of works where s_{GB} fell between s_{th} for pure and manganese-doped ZnO, paramagnetic properties were observed in pure zinc oxide and ferromagnetic properties in manganese-doped samples [18,19]. As a result, s_{th} increases with doping starting from pure ZnO. The following s_{th} values for different dopants have been observed: pure ZnO $s_{th} = 5.3 \times 10^7$ m^2/m^3 [7], cobalt-doped ZnO, $s_{th} = 1.5 \times 10^6$ m^2/m^3 [8], manganese-doped ZnO, $s_{th} = 2.4 \times 10^5$ m^2/m^3 [7], nickel-doped ZnO, is $s_{th} = 1.0 \times 10^6$ m^2/m^3 [6] and iron-doped ZnO, $s_{th} = 5 \times 10^4$ m^2/m^3 [9]. Thus, iron most actively promotes the FM behaviour of zinc oxide. ZnO polycrystals doped with Fe become ferromagnetic already at an effective grain size of about 40 μm.

Direct evidence of grain boundary influence on the ferromagnetic behaviour of ZnO

Figure 1 shows the correlation between grain size (or specific density s_{GB} of grain boundaries in the volume unit) and the presence or absence of ferromagnetic behaviour in ZnO. These plots are based on the data collected from hundreds independent investigations and show that FM appears only above a certain critical value s_{th} of the GB specific density s_{GB}. This is impressive evidence that GBs are the key to FM in ZnO. However, this evidence is indirect. Can we find the method that would be able to give us the direct and unambiguous evidence that ferromagnetic properties in ZnO derives from GBs?

Such direct evidence can be obtained from the local-probe method of low-energy muon spin relaxation (LE-μSR) [13]. This method is based on the idea to implant spin-polarized low-energy positive muons into ZnO. Due to their positive charge, the low-energy muons are trapped in the interstitial lattice sites. The motion of the muon spin is due to the magnetic field experienced by the muon. Therefore, low-energy muons act as highly sensitive probes of magnetic fields originating from magnetic moments in their close proximity and can provide information on the local environment of the muonin a very similar way to other magnetic resonance techniques. More details on the μSR method can be found in [20,21].

Low-energy muon spin relaxation measurements were carried out at the μE4 Low-Energy Muon (LEM) beamline at the Swiss Muon Source (SμS), Paul Scherrer Institute, Switzerland [22,23]. During these measurements the positive muons were implanted into the films. The positive muons were 100% spin polarized. The spin polarization was parallel to the sample surface. The measurements were done in zero field at different temperatures of −223, −103, and 23 °C. Different sample implantation depths were also used (10 to 75 nm). No dependence on temperature or penetration depth was observed. Therefore, the μSR spectra were obtained by averaging the data obtained at different temperatures and different sample penetration depths in order to improve the signal to noise ratio.

Three different samples were investigated with different values of s_{GB}. One sample was single crystalline (purchased from the Mateck Company, Germany) and contained, therefore, no GBs. The second sample (coarse-grained or CG) had a grain size of 65 nm and $s_{GB} = 2.65 \cdot 10^7$ m^2/m^3. The third sample (fine grained or FG) had small grains with a size of 31 nm and $s_{GB} = 5.32 \cdot 10^7$ m^2/m^3. These s_{GB} values are, respectively, slightly below and above the threshold value $s_{th} = 5.3 \times 10^7$ m^2/m^3 for pure ZnO (Figure 1a and [7]). The magnetic measurements supported the choice of three specimens. Namely, the single crystal showed only a negligibly small saturation magnetization of 2×10^{-4} emu/cm^3 [13]. The CG sample was weakly ferromagnetic with $J_s = 1.25$ emu/cm^3 [13]. The FG sample with the smallest grains had the highest saturation magnetization of $J_s = 8.3 \cdot$emu/cm^3. The J_s values measured at 50 K and RT were very similar (like in [7]). This fact is an important indicator for true ferromagnetism in ZnO and a high Curie temperature T_C [13].

When using LE-μSR the spin relaxation of muons in zero field (ZF-μSR) is measured. It shows the dephasing of muons and permits to determine the corresponding decay in the muon asymmetry spectrum [24]. As a result the decay in the muon asymmetry spectrum can be obtained. Such decay is due to the presence of an internal magnetic field distribution. In Figure 5 one can see three such time-dependent spectra of μSR asymmetry for the three studied samples with different GB specific density. In Figure 5 we plotted the normalized asymmetry. The experimental points have broad scatter and were fitted using the program Musrfit [25]. A measure for the fraction of magnetic volume in a sample is given by the relaxing amplitude of the asymmetry. The strongest relaxation is observed for the ZnO films with smallest grains (lower curve, open squares). It corresponds to a total magnetic volume fraction of about 35%. The lowest relaxation is observed for the ZnO single crystal (upper curve, open circles).The non-magnetic single crystal has no significant magnetic volume fraction at all. In the middle lies the curve for coarse-grained ZnO (filled squares). The magnetic volume fraction for this ZnO film was about 15%. Using the local-probe method of low-energy muon spin relaxation measurements we obtained the expected direct evidence that ferromagnetic behaviour of ZnO is due to the atoms located in ZnO grain boundaries and not in the bulk [13].

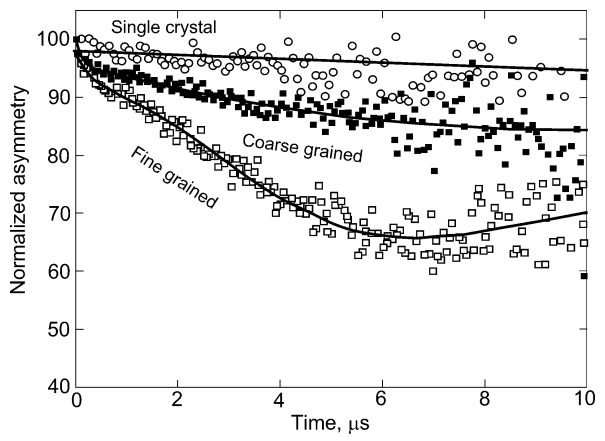


Figure 5: Averaged zero-field μSR spectra for the single crystal (top curve, open circles), the coarse grained (middle curve, filled squares), and the fine grained (bottom curve, open squares) ZnO samples. Replotted with permission from [13], copyright 2015 Nature Publishing Group.

The LE-μSR measurements were supported by theoretical studies [13]. Using molecular dynamics the simulations of 4800 atoms in a periodic box were performed for two grain boundaries. They permitted to simulate the atomic disorder in the grain boundary region. The simulation periodic box was first equilibrated at 300 K and constant pressure of 10^5 Pa for 0.5 ns, then heated to 2700 K and equilibrated for 1 ns. Then it was cooled to 300 K and equilibrated for 1 ns. The atomic configurations in GBs obtained by the molecular dynamics formed the basis for the further density functional theory calculations. For the cluster with about 200 atoms in an effective electrostatic field formed by the rest of the simulated system the electronic structure was determined. The calculation show that for single-crystalline ZnO the energy difference between highest occupied molecular orbital (HOMO) and lowest unoccupied molecular orbital (LUMO) is quite high and reaches about 4 eV. However, this difference for the sample containing the disordered GB area diminishes almost to zero. Moreover, energy of the lowest magnetic triplet state for GB is only 0.2 eV higher than the closed shell ground state. Both these results permit us to conclude that unpaired electrons can exist in GBs and atomic configurations may exist where such electrons are coupled ferromagnetically [13].

Influence of dopant concentration on the ferromagnetic behaviour of ZnO

In Figure 1b–e the data on presence or absence of ferromagnetic behaviour are given in dependence on the grain size for pure ZnO and ZnO doped with different atoms. However, they are given without taking in account how much manganese, cobalt, iron and nickel is in ZnO. How does the concentration of these elements influence the magnetisation of ZnO? We tried to answer this question using doped ZnO films synthesised using the liquid ceramics technology. Figure 6 shows the concentration dependences of the saturation magnetisation J_s for such ZnO films doped with manganese [26], cobalt [8], or iron [9].

In all three cases the J_s value strongly increases (about 4 to 20 times) when small fractions (0.02–0.12 atom %) of Co, Mn or Fe are added to pure ZnO. Around 0.5 atom % of Co, Mn or Fe the saturation magnetization reaches maximum and then decreases again down to the value close to that of pure ZnO or even less. Thus, the addition of small amount of "magnetic atoms" indeed makes ZnO "more ferromanetic" as predicted by Dietl et al. [1]. However, above a dopant concentration of 5–10 atom % the behaviour of J_s is different for Co, Mn and Fe. In the case of cobalt (Figure 6a), the $J_s(c)$ curve has only one maximum, and J_s remains low up to the solubility limit of Co in ZnO (shown by the vertical dotted line at 32 atom % Co). In the case of iron (Figure 6c), J_s increases again above solubility limit of Fe in ZnO (shown by the vertical dotted line at 18 atom % Fe) and the $J_s(c)$ curve has two maxima. In the case of manganese (Figure 6b), J_s strongly increases again above 5 atom % Mn, reaches a maximum close to the solubility limit of Mn in ZnO (shown by the vertical dotted line at 26 atom % Mn) and decreases for the second time down to the value for pure ZnO or less above the solubility limit of Mn in ZnO. Thus, the $J_s(c)$ curve has two maxima and two minima.

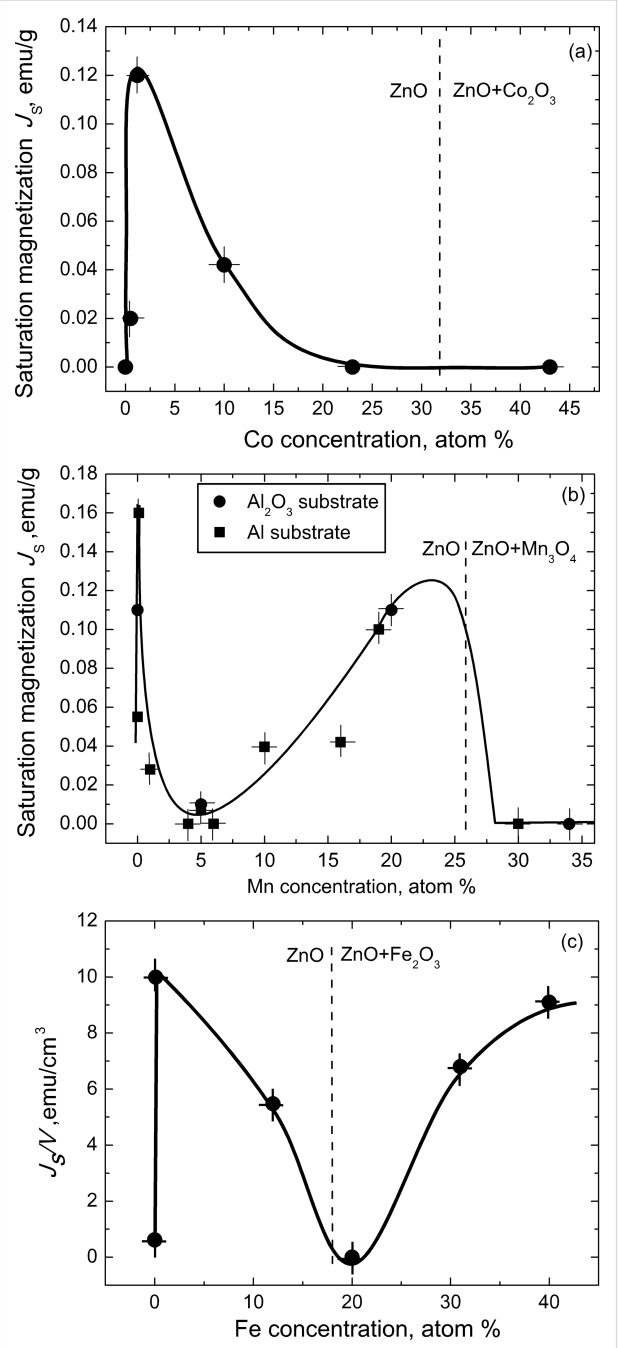


Figure 6: Saturation magnetization of doped zinc oxide films versus the concentration of (a) cobalt [8], (b) manganese [26], and (c) iron [9]. Figure was replotted based on the figures from [8,9,26] with permission, copyright Taylor & Francis and AIP Publishing.

How we can explain the different number of maxima and minima in Figure 6? Remember that manganese can possess three different oxidation states in ZnO, namely Mn^{2+}, Mn^{3+}, and Mn^{4+} [27-32]. Iron can be present in ZnO in the form of Fe^{2+} and Fe^{3+} ions [33-36]. It is known that the dependence of the fraction of manganese or iron ions with various valences on the manganese or iron concentration, respectively, is complicated [27-36]. Cobalt is mainly present as Co^{2+}. It looks that the more possible oxidation states has the dopant, the more complex is the shape of $J_s(c)$ curve. It is clear that if we substitute a Zn^{2+} ion with a Co^{2+}, Fe^{2+} or Mn^{2+} ion, the amount of oxygen ions O^{2-} remains the same in the structure of ZnO. If the dopant has a higher valence than Zn^{2+}, the amount of oxygen ions O^{2-} should decrease to preserve the neutral charge of doped ZnO. However, if the concentration of oxygen changes, the whole structure of the nanograined zinc oxide should change, like for example the structure and properties of titanium oxide changes by the addition of dopants with different valence [37].

We compared in [8,9,26] the shape of our concentration dependencies with those observed in other published works, i.e., in samples synthesised by other methods. In the majority of cases the concentration dependencies are also non-monotonous, but depend on the topology of the GB network. Most similar to the plots shown in Figure 6 are the $J_s(c)$ curves obtained from poreless films with equiaxial grains. If the grains are elongated or flattened, the shape of the $J_s(c)$ curves is different. Most different look the $J_s(c)$ curves obtained in measurements with ZnO samples built of dense polycrystalline spheres loosely sintered [8,9,26].

Increase of dopant solubility with decreasing grain size: role of grain boundaries

The vertical dotted lines in Figure 6 show the concentrations where the solubility limit c_s of Fe, Mn or Co in ZnO is reached. Above c_s a second phase appears in the system, and the peaks of Fe, Mn or Co oxide become visible in the XRD patterns together with wurtzite peaks of ZnO (Figure 7). However, why are these solubilities so high and exceed 30 atom %, for example, in the case of cobalt? Bates et al. [38] determined the temperature dependencies of the solubilities c_s of several elements (including Fe, Mn and Co) in a volume of zinc oxide. Those c_s values do not exceed few percent, even at high temperatures. In several micro- and nanograined materials the overall solubility exceeds the c_s value [39-44].

Already in 1957, McLean [45] proposed the idea that grain boundary segregation of a second component can change the overall solubility of this second component. If we add a second component B into lattice of a matrix A, the lattice parameter of A would change (like the increase of the lattice parameter of ZnO after adding cobalt atoms, Figure 7a [46]). If the bulk solubility limit c_{sb} is reached, a second phase will appear in addition to the first one, and the lattice parameter stops to change and remains constant with a further increase of the concentration of B. However, the atoms of the second component that are segregated in GBs cannot build the lattice of a second phase. As a result, the second phase would appear not at c_{sb} but later, at

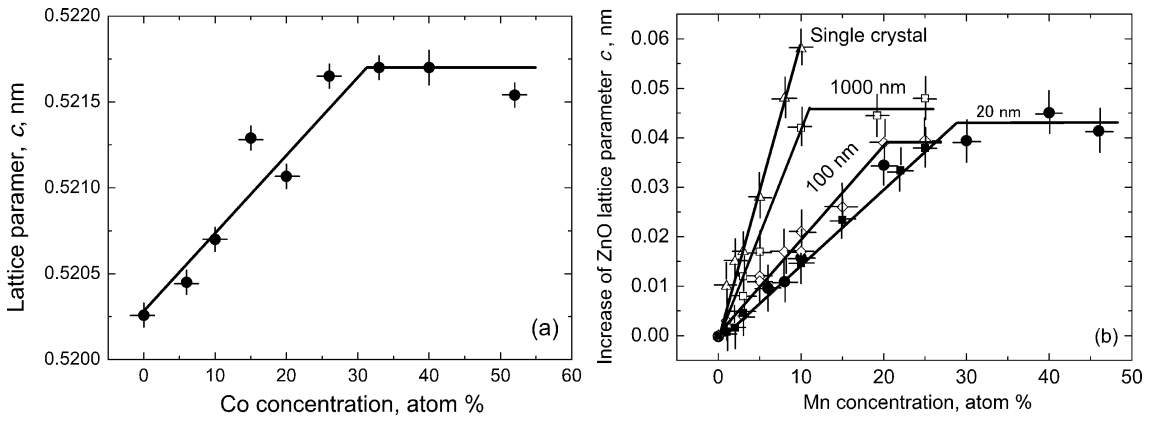


Figure 7: (a) Lattice parameter *c* in Co-doped ZnO films deposited using the liquid ceramics method versus the cobalt concentration [47]. (b) Period of a ZnO wurtzite lattice versus the manganese concentration for different grain size [46]. Figure was replotted basing on the figures is reproduced with permission from [46,47], copyright 2008 Elsevier Ltd. (panel a) and copyright 2009 AIP Publishing (panel b).

higher concentrations of B. This is well visible in Figure 7b where the dependence of ZnO lattice parameter is shown for different grain sizes and Mn contents [26,47]. The steepest curve is for the single crystal. The c_{sb} value for Mn in ZnO lattice is only about 7 atom % Mn. In this case Mn atoms only substitute Zn atoms at the wurtzite lattice sites. If we have GBs in the sample, each new Mn atom has a choice, where to substitute Zn, in the crystalline wurtzite lattice or in a GB. Thus, the curve for a grain size of 1000 nm is less steep and c_s is reached at 10 atom % Mn. With decreasing grain size and increasing specific GB area s_{GB} the solubility c_s limit increases further. Thus, c_s = 20 atom % Mn for a grain size of 100 nm and c_s = 28 atom % Mn for a grain size of 20 nm (Figure 7b). We see how drastically the solubility of Co and Mn increases with decreasing grain size and increasing specific GB area s_{GB}.

The full dependencies of the lattice parameters on the dopant concentration are measured rather seldom [26,47]. However, the hundreds of papers on the ferromagnetic behaviour of ZnO give us an extremely rich source for analysing how the dopant solubility depends on the grain size. It is because when searching for ferromagnetic ZnO, the experimentalists had to be sure that the ferromagnetic signal comes from a doped wurtzite ZnO and not from a (possibly ferromagnetic) second phase. Therefore, data on the presence or absence of a second phase are usually present in such publications. Quite frequently the grain size is also given (in other case it is possible to estimate the grain size from TEM micrographs or the width of XRD peaks). The temperature *T* of synthesis or the last thermal treatment can also be determined from the publications (such as for the construction of Figure 1).

If we separate the data points for different grain sizes into different plots, $c_s(T)$ curves can be drawn for each grain size interval. Such plots for nickel-doped zinc oxide are shown in Figure 8a–d [6] and for iron-doped zinc oxide in Figure 8e,f [12]. Similar solubility lines for different values of grain size are shown in Figure 9 for manganese-doped [16] and cobalt-doped [47] ZnO polycrystals. In Figure 9 the experimental points are omitted for simplicity, and only the solubility limit lines are displayed. The full plots with all points and respective list of references can be found in [46,47]. It is well visible how drastically the solubility increases with decreasing grain size. Namely, ZnO polycrystals with grain sizes of 20 nm and below can dilute dozens of atomic per cent of "magnetic atoms" without any sign of peaks of a second phase in the XRD patterns. The loosely sintered (nano)powders contain less GBs, the main defects are free surfaces. In such samples the overall solubility also increases, but now so drastically as in poreless polycrystals [46,47].

Can the monolayer grain boundary or surface segregation ensure such a high increase of solubility? We estimated the thickness of the segregation layer for polycrystals with grain boundaries and with free surfaces [46,47]. It appeared that the GB contains more than 10 monolayers of Mn or Co [46,47]. Moreover, the GB input in the total Mn or Co concentration increases with decreasing grain size. The free surfaces are also enriched by "magnetic atoms", but the thickness of enriched surface layers is only half to about a third of that in GBs. Can we observe these layers directly, using TEM?

Figure 10 shows the bright-field HREM micrographs for two zinc oxide films doped with 10 (Figure 10a) and 15 atom % Mn (Figure 10b) [48]. In both micrographs the ZnO nanograins are visible. They have a lattice with wurtzite structure (see the inset A with Fourier transform from crystalline area). Between crystalline ZnO nanograins the amorphous intercrystalline layers

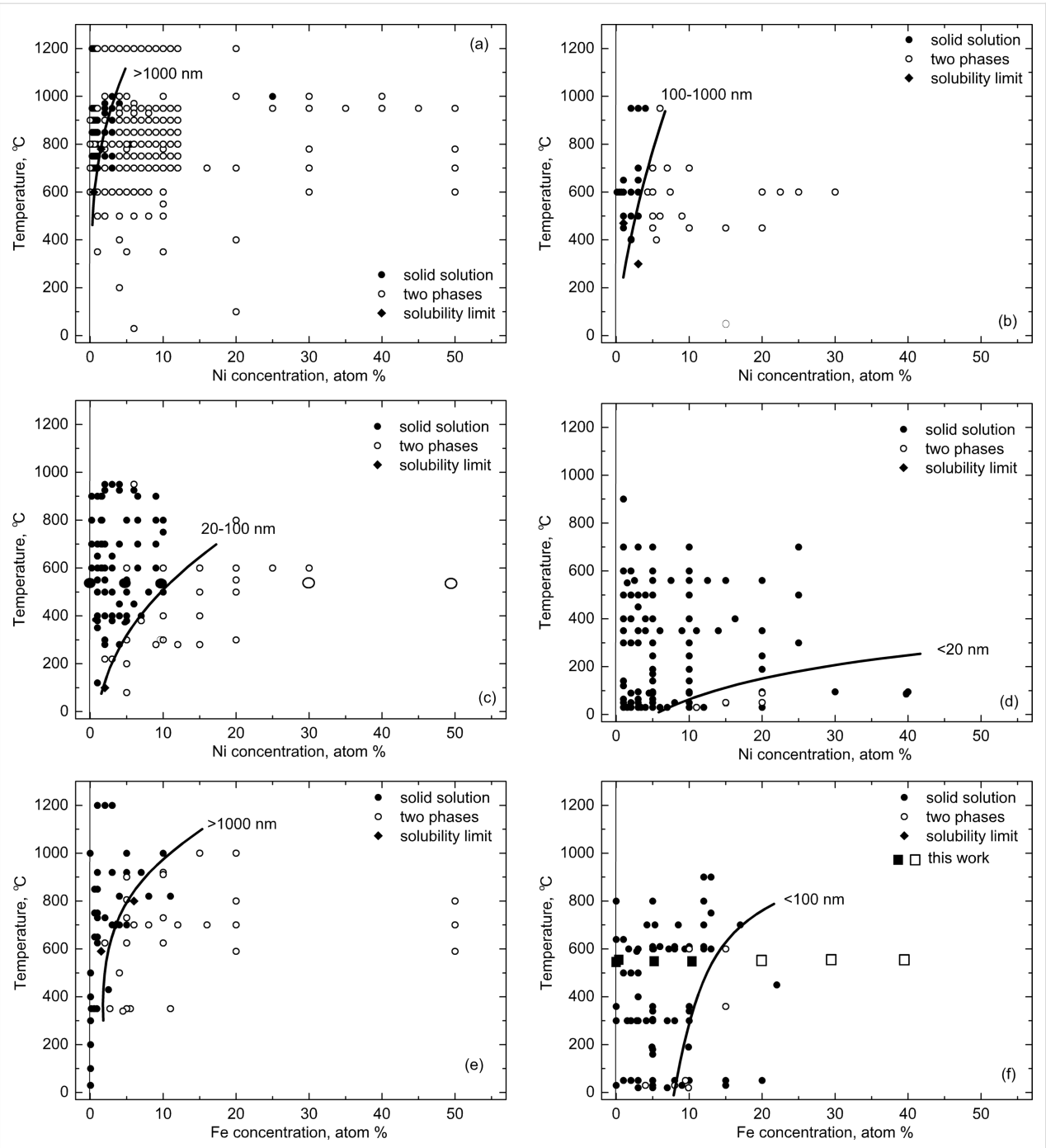


Figure 8: (a–d) Solubility limit of nickel in zinc oxide polycrystals with grain sizes (a) larger than 1000, (b) between 1000 and 100 nm, (c) between 20 and 100 nm, and (d) smaller than 20 nm [6]. (e,f) Solubility limit of iron in zinc oxide polycrystals with grain sizes (e) larger than 1000 and (f) smaller than 100 nm [12]. The filled and open symbols correspond to one- and two-phase samples, respectively. Diamonds mark the solubility limit. Replotted based on figures reproduced with permission from [6,12], copyright 2015 Institute of Problems of Mechanical Engineering, Russian Academy of Sciences (PME RAS, "Advanced Study Center" Co. Ltd, panels a–d) and copyright 2014 Springer Science+Business Media New York (panels e,f).

can be seen. The inset B shows the Fourier transform from such an amorphous intergranular area. It is easy to see that the amount of amorphous phase in ZnO/ZnO GBs increases with increasing manganese content. Thus, in the alloy with 10 atom % Mn the amorphous layers are visible between crystalline ZnO nanograins. In the alloy with 15 atom % Mn the crystalline ZnO nanograins are completely surrounded by amorphous layers. Such thick GB layers, indeed, correspond to the estimations made in [46,47]. However, one can find such synthesis conditions for nanograined ZnO for which, even in the

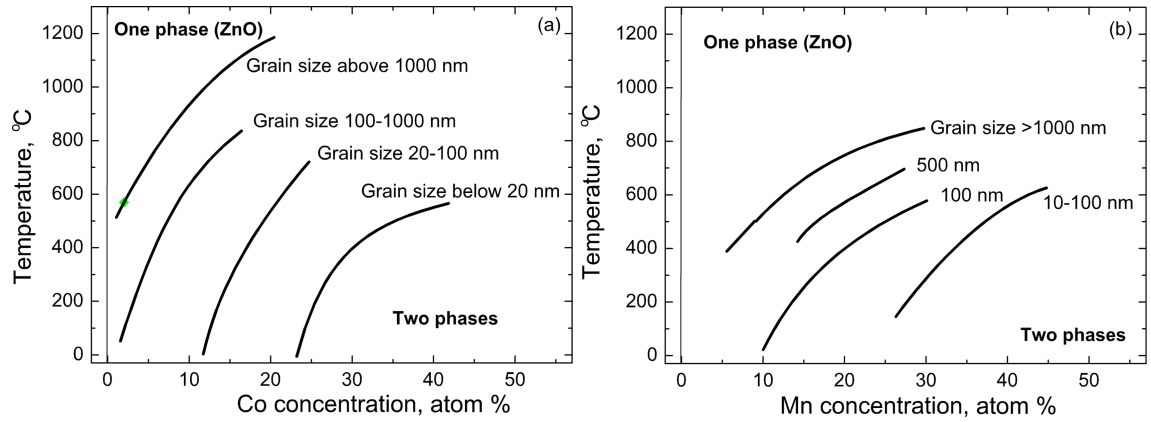


Figure 9: Solubility limit of (a) cobalt [47] and (b) manganese [46] in zinc oxide polycrystals with various grain sizes. Replotted based on figures reproduced with permission from [46,47], copyright 2008, 2009 Elsevier Ltd.

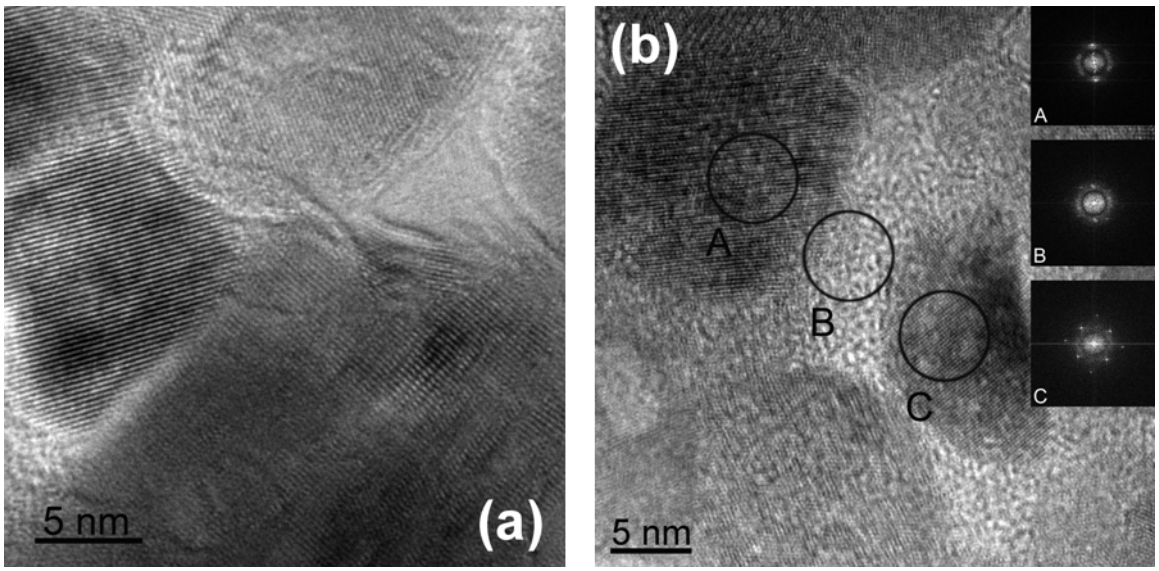


Figure 10: Bright-field HREM micrographs [48] for zinc oxide films doped with (a) 10 atom % Mn and (b) 15 atom % Mn. The insets show the Fourier transforms for amorphous and crystalline areas marked by letters A, B, C. Reproduced with permission from from [48], copyright 2010 Science+Business Media New York for Pleiades Publishing Inc.

case of very small grains below the threshold value (Figure 1), the sample will not have ferromagnetic properties [45,46]. The magnetic properties depend critically on the texture of films and the structure of amorphous GB layers [49,50]. Thus, the condition $s_{GB} > s_{th}$ is necessary but not sufficient for ferromagnetism of undoped ZnO. One needs also a certain texture and structure of amorphous intercrystallite layers.

The morphology and mutual arrangement of amorphous intergranular layers and nanocrystals recalls the structures appearing in case of grain boundary wetting [51,52]. In particular, the approaches developed for the description of so-called GB complexions or intergranular films (IGFs) can be very effective in the future for the explanation and prediction of GB phenomena leading to the ferromagnetic behaviour in the nanograined semiconducting oxides [53-64]. The amorphous intergranular layers appear also in nanograined alloys obtained by the severe plastic deformation [65,66].

Conclusion

In summary, we observed that, contrary to the prediction of Dietl et al. [1], the doping of bulk ZnO with Mn, Co, Fe or Ni does not make it ferromagnetic. On the other hand, nanograined ZnO becomes ferromagnetic even without doping. The presence of grain boundaries is the essential and necessary condition for the FM behavior of pure ZnO. The specific area of GBs

s_{GB} has to exceed a certain critical or threshold value s_{th}. However, the presence of grain boundaries with $s_{GB} > s_{th}$ is not a sufficient condition for ferromagnetism of undoped ZnO. A certain texture and structure of amorphous intercrystalline layers is necessary. Nevertheless, the key role of GBs in the ferromagnetic behaviour of ZnO is proven by LE-μSR. Modelling with molecular dynamics combined with density functional theory calculations permitted to find ferromagnetically coupled electron states in ZnO GBs.

The doping of ZnO with Mn, Co, Fe or Ni, indeed, facilitates the transition into a ferromagnetic state and decreases the respective threshold values s_{th}. Also, the addition of few tenths of atom percent of Mn, Co, Fe or Ni drastically increases the saturation magnetization J_s. J_s changes non-monotonously with further increase of the dopant content c. The number of minima and maxima of the $J_s(c)$ curves correlates with number of valence states of dopants. Most probably, it is due to the change of oxygen content in GBs driven by the condition of electrical neutrality. The drastic increase of the total solubility of dopants in ZnO with decreasing grain size has been also observed. It is explained by the multilayer GB segregation.

Acknowledgements

Authors thank the Russian Foundation for Basic Research (grants 15-03-04220, 15-53-06008 and 15-33-70051), Deutsche Forschungsgemeinschaft, Ministry of Education and Science of the Russian Federation (Increase Competitiveness Program of NUST«MISiS» and project 14.B25.31.0018 from ISSP RAS), programme ‘‘New Materials’’ of Russian Academy of Sciences for financial support.

References

1. Dietl, T.; Ohno, H.; Matsukura, F.; Cibert, J.; Ferrand, D. *Science* **2000,** *287,* 1019–1022. doi:10.1126/science.287.5455.1019
2. Sato, K.; Katayama-Yoshida, H. *Semicond. Sci. Technol.* **2002,** *17,* 367–376. doi:10.1088/0268-1242/17/4/309
3. Gupta, T. K. *J. Am. Ceram. Soc.* **1990,** *73,* 1817–1840. doi:10.1111/j.1151-2916.1990.tb05232.x
4. Onreabroy, W.; Sirikulrat, N.; Brown, A. P.; Hammond, C.; Milne, S. J. *Solid State Ionics* **2006,** *177,* 411–420. doi:10.1016/j.ssi.2005.10.032
5. Dietl, T. *Nat. Mater.* **2010,** *9,* 965–974. doi:10.1038/NMAT2898
6. Straumal, B. B.; Mazilkin, A. A.; Protasova, S. G.; Stakhanova, S. V.; Straumal, P. B.; Bulatov, M. F.; Schütz, G.; Tietze, T.; Goering, E.; Baretzky, B. *Rev. Adv. Mater. Sci.* **2015,** *41,* 61–71.
7. Straumal, B. B.; Mazilkin, A. A.; Protasova, S. G.; Myatiev, A. A.; Straumal, P. B.; Schütz, G.; van Aken, P. A.; Goering, E.; Baretzky, B. *Phys. Rev. B* **2009,** *79,* 205206. doi:10.1103/PhysRevB.79.205206
8. Straumal, B. B.; Mazilkin, A. A.; Protasova, S. G.; Straumal, P. B.; Myatiev, A. A.; Schütz, G.; Goering, E.; Tietze, T.; Baretzky, B. *Philos. Mag.* **2013,** *93,* 1371–1383. doi:10.1080/14786435.2012.736693
9. Straumal, B. B.; Protasova, S. G.; Mazilkin, A. A.; Straumal, P. B.; Schütz, G.; Tietze, T.; Goering, E.; Baretzky, B. *Beilstein J. Nanotechnol.* **2013,** *4,* 361–369. doi:10.3762/bjnano.4.42
10. Straumal, B. B.; Mazilkin, A. A.; Protasova, S. G.; Straumal, P. B.; Myatiev, A. A.; Schütz, G.; Goering, E.; Baretzky, B. *Phys. Met. Metallogr.* **2012,** *113,* 1244–1256. doi:10.1134/S0031918X12130030
11. Straumal, B. B.; Protasova, S. G.; Mazilkin, A. A.; Schütz, G.; Goering, E.; Baretzky, B.; Straumal, P. B. *JETP Lett.* **2013,** *97,* 367–377. doi:10.1134/S0021364013060143
12. Protasova, S. G.; Straumal, B. B.; Mazilkin, A. A.; Stakhanova, S. V.; Straumal, P. B.; Baretzky, B. *J. Mater. Sci.* **2014,** *49,* 4490–4498. doi:10.1007/s10853-014-8146-y
13. Tietze, T.; Audehm, P.; Chen, Y.-C.; Schütz, G.; Straumal, B. B.; Protasova, S. G.; Mazilkin, A. A.; Straumal, P. B.; Prokscha, T.; Luetkens, H.; Salman, Z.; Suter, A.; Baretzky, B.; Fink, K.; Wenzel, W.; Danilov, D.; Goering, E. *Sci. Rep.* **2015,** *5,* 8871. doi:10.1038/srep08871
14. Watanabe, T. *Mater. Sci. Forum* **1997,** *243–245,* 21–30. doi:10.4028/www.scientific.net/msf.243-245.21
15. Gleiter, H.; Chalmers, B. *High-Angle Grain Boundaries;* Pergamon Press: Oxford, New York, Toronto, Sydney, Braunschweig, 1972.
16. Hosford, W. F. *Materials Science: An Intermediate Text;* Cambridge Univ. Press: Cambridge, UK, 2006. doi:10.1017/CBO9780511618345
17. Lábár, J. L. *Microsc. Microanal.* **2008,** *14,* 287–295. doi:10.1017/S1431927608080380
18. Wang, D. F.; Park, S. Y.; Lee, H. W.; Lee, Y. S.; Lam, V. D.; Lee, Y. P. *Phys. Status Solidi A* **2007,** *204,* 4029–4032. doi:10.1002/pssa.200777334
19. Gopalakrishnan, N.; Elanchezhiyan, J.; Bhuvana, K. P.; Balasubramanian, T. *Scr. Mater.* **2008,** *58,* 930–933. doi:10.1016/j.scriptamat.2008.01.020
20. Yaouanc, A.; Dalmas de Réotier, P. *Muon Spin Rotation, Relaxation and Resonance;* Oxford Science Publications: Oxford, UK, 2011.
21. Dalmas de Réotier, P.; Yaouanc, A. *J. Phys.: Condens. Matter* **1997,** *9,* 9113–9166. doi:10.1088/0953-8984/9/43/002
22. Morenzoni, E.; Prokscha, T.; Suter, A.; Luetkens, H.; Khasanov, R. *J. Phys.: Condens. Matter* **2004,** *16,* S4583. doi:10.1088/0953-8984/16/40/010
23. Prokscha, T.; Morenzoni, E.; Deiters, K.; Foroughi, F.; George, D.; Kobler, R.; Suter, A.; Vrankovic, V. *Nucl. Instrum. Methods Phys. Res., Sect. A* **2008,** *595,* 317–331. doi:10.1016/j.nima.2008.07.081
24. Blundell, S. J. *Contemp. Phys.* **1999,** *40,* 175–192. doi:10.1080/001075199181521
25. Suter, A.; Wojek, B. M. *Phys. Procedia* **2012,** *30,* 69–73. doi:10.1016/j.phpro.2012.04.042
26. Straumal, B. B.; Protasova, S. G.; Mazilkin, A. A.; Myatiev, A. A.; Straumal, P. B.; Schütz, G.; Goering, E.; Baretzky, B. *J. Appl. Phys.* **2010,** *108,* 073923. doi:10.1063/1.3486044
27. Cong, C. J.; Zhang, K. L. *Phys. Status Solidi A* **2006,** *243,* 2764–2771. doi:10.1002/pssb.200642258
28. Thakur, P.; Chae, K. H.; Kim, J.-Y.; Subramanian, M.; Jayavel, R.; Asokan, K. *Appl. Phys. Lett.* **2007,** *91,* 162503. doi:10.1063/1.2794764
29. Abbamonte, P.; Venema, L.; Rusydi, A.; Sawatzky, G. A.; Logvenov, G.; Bozovic, I. *Science* **2002,** *297,* 581–584. doi:10.1126/science.1070903

30. Pellegrin, E.; Nücker, N.; Fink, J.; Molodtsov, S. L.; Gutiérrez, A.; Navas, E.; Strebel, O.; Hu, Z.; Domke, M.; Kaindl, G.; Uchida, S.; Nakamura, Y.; Markl, J.; Klauda, M.; Saemann-Ischenko, G.; Krol, A.; Peng, J. L.; Greene, R. L. *Phys. Rev. B* **1993,** *47,* 3354–3367. doi:10.1103/PhysRevB.47.3354
31. Asokan, K.; Jan, J. C.; Rao, K. V. R.; Chiou, J. W.; Tsai, H. M.; Mookerjee, S.; Pong, W. F.; Tsai, M.-H.; Kumar, R.; Husain, S.; Srivastava, J. P. *J. Phys.: Condens. Matter* **2004,** *16,* 3791–3799. doi:10.1088/0953-8984/16/21/027
32. Guo, J.-H.; Gupta, A.; Sharma, P.; Rao, K. V.; Marcus, M. A.; Dong, C. L.; Guillen, J. M. O.; Butorin, S. M.; Mattesini, M.; Glans, P. A.; Smith, K. E.; Chang, C.; Ahuja, R. *J. Phys.: Condens. Matter* **2007,** *19,* 172202. doi:10.1088/0953-8984/19/17/172202
33. Liu, H.; Yang, J.; Zhang, Y.; Yang, L.; Wei, M.; Ding, X. *J. Phys.: Condens. Matter* **2009,** *21,* 145803. doi:10.1088/0953-8984/21/14/145803
34. Wu, P.; Saraf, G.; Lu, Y.; Hill, D. H.; Gateau, R.; Wielunski, L.; Bartynski, R. A.; Arena, D. A.; Dvorak, J.; Moodenbaugh, A.; Siegrist, T.; Raley, J. A.; Yeo, Y. K. *Appl. Phys. Lett.* **2006,** *89,* 012508. doi:10.1063/1.2213519
35. Lin, Y.; Jiang, D.; Lin, F.; Shi, W. Z.; Ma, X. M. *J. Alloys Compd.* **2007,** *436,* 30–33. doi:10.1016/j.jallcom.2006.07.011
36. Karmakar, D.; Mandal, S. K.; Kadam, R. M.; Paulose, P. L.; Rajarajan, A. K.; Nath, T. K.; Das, A. K.; Dasgupta, I.; Das, G. P. *Phys. Rev. B* **2007,** *75,* 144404. doi:10.1103/PhysRevB.75.144404
37. Yermakov, A. Ye.; Uimin, M. A.; Mysik, A. A.; Vykhodets, V. B.; Kurennykh, T. E.; Sokolov, V. I.; Gaviko, V. S.; Schegoleva, N. N.; Gruzdev, N. B. *J. Magn. Magn. Mater.* **2007,** *310,* 2102–2104. doi:10.1016/j.jmmm.2006.10.780
38. Bates, C. H.; White, W. B.; Roy, R. *J. Inorg. Nucl. Chem.* **1966,** *28,* 397–405. doi:10.1016/0022-1902(66)80318-4
39. Trudeau, M. L.; Huot, J. Y.; Schulz, R. *Appl. Phys. Lett.* **1991,** *58,* 2764–2766. doi:10.1063/1.104779
40. Suzuki, K.; Makino, A.; Inoue, A.; Masumoto, T. *J. Appl. Phys.* **1991,** *70,* 6232–6237. doi:10.1063/1.350006
41. Heera, V.; Madhusoodanan, K. N.; Skorupa, W.; Dubois, C.; Romanus, H. *J. Appl. Phys.* **2006,** *99,* 123716. doi:10.1063/1.2208299
42. Straumal, B. B.; Dobatkin, S. V.; Rodin, A. O.; Protasova, S. G.; Mazilkin, A. A.; Goll, D.; Baretzky, B. *Adv. Eng. Mater.* **2011,** *13,* 463–469. doi:10.1002/adem.201000312
43. Lemier, C.; Weissmüller, J. *Acta Mater.* **2007,** *55,* 1241–1254. doi:10.1016/j.actamat.2006.09.030
44. Rizea, A.; Chirlesan, D.; Petot, C.; Petot-Ervas, G. *Solid State Ionics* **2002,** *146,* 341–353. doi:10.1016/S0167-2738(01)01024-4
45. McLean, D. *Grain Boundaries in Metals;* Clarendon Press: Oxford, 1957.
46. Straumal, B. B.; Mazilkin, A. A.; Protasova, S. G.; Myatiev, A. A.; Straumal, P. B.; Baretzky, B. *Acta Mater.* **2008,** *56,* 6246–6256. doi:10.1016/j.actamat.2008.08.032
47. Straumal, B.; Baretzky, B.; Mazilkin, A.; Protasova, S.; Myatiev, A.; Straumal, P. B. *J. Eur. Ceram. Soc.* **2009,** *29,* 1963–1970. doi:10.1016/j.jeurceramsoc.2009.01.005
48. Straumal, B. B.; Myatiev, A. A.; Straumal, P. B.; Mazilkin, A. A.; Protasova, S. G.; Goering, E.; Baretzky, B. *JETP Lett.* **2010,** *92,* 396–400. doi:10.1134/S0021364010180074
49. Straumal, B. B.; Mazilkin, A. A.; Protasova, S. G.; Myatiev, A. A.; Straumal, P. B.; Goering, E.; Baretzky, B. *Phys. Status Solidi B* **2011,** *248,* 1581–1586. doi:10.1002/pssb.201001182
50. Straumal, B. B.; Mazilkin, A. A.; Protasova, S. G.; Myatiev, A. A.; Straumal, P. B.; Goering, E.; Baretzky, B. *Thin Solid Films* **2011,** *520,* 1192–1194. doi:10.1016/j.tsf.2011.04.154
51. Straumal, B. B.; Baretzky, B.; Kogtenkova, O. A.; Straumal, A. B.; Sidorenko, A. S. *J. Mater. Sci.* **2010,** *45,* 2057–2061. doi:10.1007/s10853-009-4014-6
52. Straumal, B. B.; Gust, W.; Watanabe, T. *Mater. Sci. Forum* **1999,** *294–296,* 411–414. doi:10.4028/www.scientific.net/MSF.294-296.411
53. Clarke, D. R. *J. Am. Ceram. Soc.* **1987,** *70,* 15–22. doi:10.1111/j.1151-2916.1987.tb04846.x
54. Cantwell, P. R.; Ming, T.; Dillon, S. J.; Luo, J.; Rohrer, G. S.; Harmer, M. P. *Acta Mater.* **2014,** *62,* 1–48. doi:10.1016/j.actamat.2013.07.037
55. Kaplan, W. D.; Chatain, D.; Wynblatt, P.; Carter, W. C. *J. Mater. Sci.* **2013,** *48,* 5681–5717. doi:10.1007/s10853-013-7462-y
56. Bueno, P. R.; Varela, J. A.; Longo, E. *J. Eur. Ceram. Soc.* **2008,** *28,* 505–529. doi:10.1016/j.jeurceramsoc.2007.06.011
57. Luo, J.; Chiang, Y.-M.; Cannon, R. M. *Langmuir* **2005,** *21,* 7358–7365. doi:10.1021/la0505420
58. Luo, J.; Tang, M.; Cannon, R. M.; Carter, W. C.; Chiang, Y.-M. *Mater. Sci. Eng., A* **2006,** *422,* 19–28. doi:10.1016/j.msea.2006.01.001
59. Luo, J. *Crit. Rev. Solid State Mater. Sci.* **2007,** *32,* 67–109. doi:10.1080/10408430701364388
60. Luo, J.; Chiang, Y.-M. *Annu. Rev. Mater. Res.* **2008,** *38,* 227–249. doi:10.1146/annurev.matsci.38.060407.132431
61. Subramaniam, A.; Koch, C. T.; Cannon, R. M.; Rühle, M. *Mater. Sci. Eng., A* **2006,** *422,* 3–18. doi:10.1016/j.msea.2006.01.004
62. MacLaren, I. *Ultramicroscopy* **2004,** *99,* 103–113. doi:10.1016/j.ultramic.2003.10.002
63. Dillon, S. J.; Tang, M.; Craig Carter, W.; Harmer, M. P. *Acta Mater.* **2007,** *55,* 6208–6218. doi:10.1016/j.actamat.2007.07.029
64. Luo, J.; Cheng, H.; Asl, K. M.; Kiely, C. J.; Harmer, M. P. *Science* **2011,** *333,* 1730–1733. doi:10.1126/science.1208774
65. Straumal, B. B.; Mazilkin, A. A.; Baretzky, B. *Curr. Opin. Solid State Mater. Sci.* **2016,** *20,* 247–256. doi:10.1016/j.cossms.2016.05.006
66. Straumal, B. B.; Sauvage, X.; Baretzky, B.; Mazilkin, A. A.; Valiev, R. Z. *Scr. Mater.* **2014,** *70,* 59–62. doi:10.1016/j.scriptamat.2013.09.019

License and Terms

This is an Open Access article under the terms of the Creative Commons Attribution License (http://creativecommons.org/licenses/by/4.0), which permits unrestricted use, distribution, and reproduction in any medium, provided the original work is properly cited.

The license is subject to the *Beilstein Journal of Nanotechnology* terms and conditions: (http://www.beilstein-journals.org/bjnano)

The definitive version of this article is the electronic one which can be found at: doi:10.3762/bjnano.7.185

BEILSTEIN JOURNAL OF NANOTECHNOLOGY

Annealing-induced recovery of indents in thin Au(Fe) bilayer films

Anna Kosinova[1], Ruth Schwaiger[2], Leonid Klinger[1] and Eugen Rabkin[*1]

Full Research Paper

Open Access

Address:
[1]Department of Materials Science and Engineering, Technion – Israel Institute of Technology, 32000 Haifa, Israel and [2]Karlsruhe Institute of Technology, Institute for Applied Materials, PO Box 3640, 76021 Karlsruhe, Germany

Email:
Eugen Rabkin[*] - erabkin@technion.ac.il

* Corresponding author

Keywords:
annealing; diffusion; dislocation loops; nanoindenation; thin films

Beilstein J. Nanotechnol. **2016,** *7,* 2088–2099.
doi:10.3762/bjnano.7.199

Received: 13 June 2016
Accepted: 20 December 2016
Published: 28 December 2016

This article is part of the Thematic Series "Advances in nanomaterials II".

Guest Editor: H. Hahn

© 2016 Kosinova et al.; licensee Beilstein-Institut.
License and terms: see end of document.

Abstract

We employed depth-sensing nanoindentation to produce ordered arrays of indents on the surface of 50 nm-thick Au(Fe) films deposited on sapphire substrates. The maximum depth of the indents was approximately one-half of the film thickness. The indented films were annealed at a temperature of 700 °C in a forming gas atmosphere. While the onset of solid-state dewetting was observed in the unperturbed regions of the film, no holes to the substrate were observed in the indented regions. Instead, the film annealing resulted in the formation of hillocks at the indent locations, followed by their dissipation and the formation of shallow depressions nearby after subsequent annealing treatments. This annealing-induced evolution of nanoindents was interpreted in terms of annihilation of dislocation loops generated during indentation, accompanied by the formation of nanopores at the grain boundaries and their subsequent dissolution. The application of the processes uncovered in this work show great potential for the patterning of thin films.

Introduction

The intentional introduction of defects into bulk metallic material by plastic deformation followed by heat treatments, i.e., thermo-mechanical treatment, is a technological cornerstone of human civilization and has been used for millennia to design microstructures and properties of materials. Yet, applying this approach to thin metal films is problematic because the traditional methods of high-strain deformation, such as rolling or forging, are not applicable. Nanoindentation is widely used for characterizing the mechanical properties of nano- and micro-scale specimens. It can also be employed to produce defects of controlled shape and size, and to introduce high plastic strain in thin films. Here, we present the results of a study investigating the recovery of indentation-induced defects in Au(Fe) bilayer films. The motivation for our work is two-fold: (i) to explore the concept of thermo-mechanical treatment of thin films by combining localized plastic strain introduced by nanoindentation with subsequent annealing, and (ii) to understand the effect of nanoindentation-induced localized plastic deformation on the

thermal stability and solid-state dewetting of thin films. In what follows, we will give a short overview of what is known about the recovery of indents in thin metal films at elevated temperatures and about solid-state dewetting of thin metal films.

To the best of our knowledge, very few publications report studies of the thermo-mechanical processing of thin metal films by combining nanoindentation and annealing. Lee et al. [1,2] investigated the microstructural changes and phase transformations induced by nanoindentation and annealing in Ni [1] and Ag thin films [2] on Si substrates. They revealed that the distortion of the crystalline structure induced by indentation enhances the diffusivity of metal atoms and prompts the formation of nickel and silver silicide phases. Similar enhancement of diffusivity and the formation of a eutectic phase were observed in the indented region of a Au thin film on Si (with a Cr interlayer) [3]. Also, the material pileup around the indents in the as-deposited film fully recovered and disappeared after annealing in the temperature range of 250–450 °C [3]. It should be noted that in all three works [1-3] the maximum indentation depth was larger than the metal film thickness, which resulted in significant modification of the Si substrate. Still, the microscopic mechanisms responsible for redistribution of matter in the indented region and the microstructural changes caused by annealing remained poorly understood.

Annealing-induced shape recovery of indents produced by nanoindentation is well-documented for thin nickel–titanium films; yet, in this case the recovery is related to diffusionless martensite–austenite transformation [4]. Thermally activated strain recovery has been reported for thin Al and Au films [5]. It has been suggested that plastic deformation recovery is restricted to small grain sizes and driven by inhomogeneous residual internal stresses. The above short overview shows that the understanding of the processes occurring in deformed thin metal films upon annealing is quite poor compared to the great wealth of data on recovery and recrystallization of deformed bulk metals [6].

The introduction of defects into thin metal films can significantly affect their thermal and mechanical stability. For example, solid-state dewetting of thin metal films is a well-known phenomenon, which results in temperature-induced morphology changes, exposure of the substrate, and transformation of a film into an array of individual particles. This process is driven by the reduction of the total surface and interfacial energy of the system. Since a wide range of applications of thin metal films in the microelectronics requires featureless and defect-free surfaces, the knowledge of the effect of localized plastic strain on dewetting is of high practical importance. Surface and interface defects, such as grooves at grain boundaries and triple junctions [7,8], voids at the interface between the film and the substrate [9], and localized impurities on the substrate or on the film surface can serve as nucleation sites for the onset of solid-state dewetting upon heating. Localized plastic deformation by indents on the film surface is expected to play a two-fold role in dewetting. On the one hand, the indents could serve as additional nucleation sites for the holes and, thus, accelerate the dewetting process. On the other hand, they could add fast diffusion paths in the near-surface region and, thus, accelerate the healing processes in the material controlled by capillary forces [10,11] or the interaction of defects [12]. The healing capability of defects was recently demonstrated for Au [13] and Fe [14] nanoparticles. It was shown that the controlled injection of dislocations into single-crystalline faceted metal nanoparticles results in their much faster equilibration, i.e., achieving the equilibrium crystal shape, during subsequent annealing as compared to their defect-free counterparts [13,14].

Recently, Amram and Rabkin [15] studied the role of Fe underlayers in the growth of quasi-single-crystalline heteroepitaxial Au thin films on sapphire. The Au layer deposited on Fe exhibited a high degree of in-plane ordering with a large grain size. In the Au(Fe)-sapphire system, the thin Fe underlayer reduces the lattice mismatch between Au and sapphire and increases the adhesion energy, which lowers the concentration of structural defects in the film and improves its thermal stability. The Au layer exhibited a strong [111] out-of-plane texture and two twinning-related in-plane orientations related by a 60° rotation around the surface normal. The Fe underlayer exhibited a strong [110] out-of-plane texture with three in-plane orientations. The morphological stability and initial stages of dewetting of quasi-single-crystalline Au(Fe) thin films has been described in detail in [16]. Thus, this system represents a convenient model object for the studies of the effect of indentation-induced surface defects on the film behavior at elevated temperatures. This is because these films exhibit only one type of grain boundaries ($\Sigma 3$ twin boundary, where Σ is a reciprocal density of coincident sites) and are intrinsically stable against dewetting. The interdiffusion coefficients in the Au(Fe) system have been determined by Iijima and Yamazaki [17]. At the temperature of 700 °C employed in the present study, the full intermixing of a 50 nm thick bilayer takes less than 1 s, and, therefore, in what follows we will refer to the Au(Fe) bilayers as a single-phase face-centered cubic dilute solid solution of Fe in Au, or Au(Fe) thin films.

The goals of the present work were to determine the thermal stability of Au(Fe) films containing indentation-induced surface defects, and to establish the mechanisms of indent recovery. The latter goal should be considered in a wider framework of thermo-mechanical processing of thin metal films. The

localized defects in the film were introduced by load-controlled nanoindentation. We employed atomic force microscopy (AFM) for studying the surface morphology evolution upon annealing; special attention was paid to the healing processes in the indented area and the dewetting process in the unperturbed film.

Results

The microstructure of the ultrathin (5–20 nm) Au(Fe) films has been described in detail in [15]. It was shown that the deposition of a Au film on a thin Fe underlayer resulted in a high-quality quasi-single-crystalline Au films with large grains having diameters of several micrometers. In the case of the thicker films studied in the present work (the total thickness is 50 nm), the average grain size was comparable to the film thickness (Figure 1a). Triple junctions are clearly observed between the majority of grains, which is typical of a polycrystalline film. The presence of triple junctions in the film is related to the deviations from the ideal Σ3 misorientation between the grains, as also confirmed by an angular spread of the {111} reflections in the X-ray diffraction (XRD) pole figure shown in Figure 1b. Indeed, thin films with the perfect <111> texture, in which all grain boundaries are of the exact <111>Σ3 type, so-called mazed bicrystalline films [18,19], exhibit a special type of microstructure without triple junctions. The electron backscatter diffraction data obtained on the as-deposited film (not shown here) confirmed that only the near-<111>Σ3 tilt grain boundaries, and low-angle grain boundaries were present in the film.

The atomic force microscopy (AFM) image of the Au(Fe) film surface (Figure 2) was taken four months after the film deposition. Hillocks with a height up to 25 nm were present on the film surface, which could be the result of slow stress relaxation in the as-deposited Au(Fe) bilayers at room temperature. After the first annealing for 10 min, the hillocks disappeared.

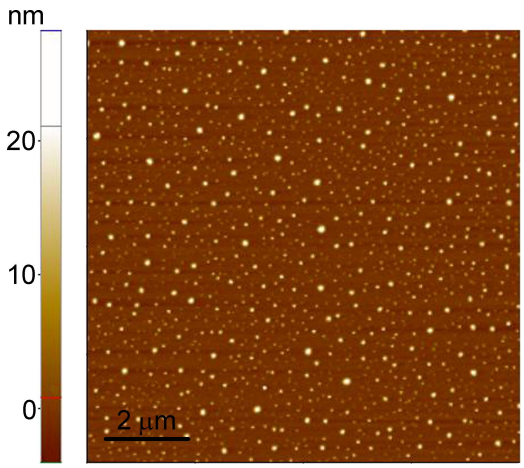


Figure 2: AFM micrograph of the surface of the as-deposited Au(Fe) film, four months after deposition.

AFM line profiles were used to determine the indent depth before and after annealing. The average depths of the as-produced indents were 18 and 25 nm for the maximum indentation loads of 0.1 and 0.2 mN, respectively, which is less than half the film thickness. Since a three-sided pyramidal, Berkovich tip was used for the indentation, the initial indent shape was triangular (Figure 3a). Setting the level of the unperturbed film to zero, we calculated the amount of piled-up (positive) and displaced (negative) material by integrating all negative and positive pixels in the indented region. The volumes of piled-up and displaced material were approximately balanced.

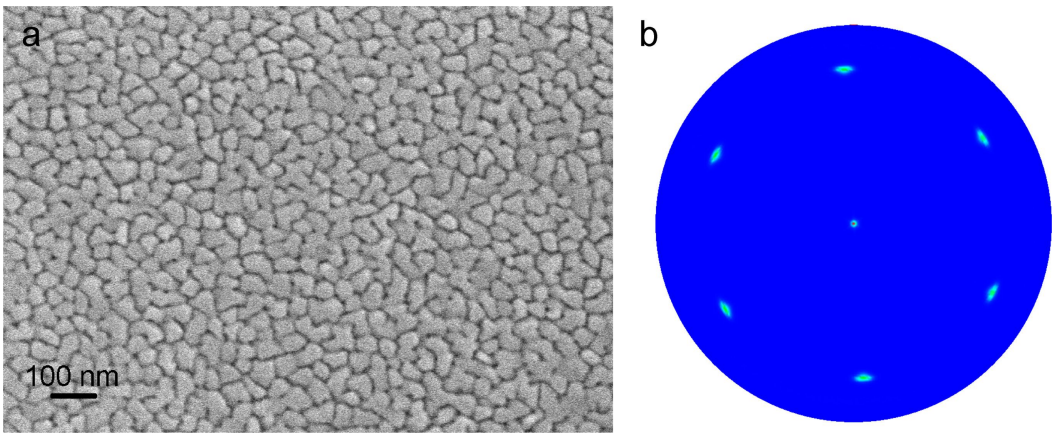


Figure 1: The microstructure of the as-deposited Au(Fe) film. (a) High-resolution scanning electron microscopy (SEM) micrograph of the Au(Fe) film, which contains grains of 40 to 50 nm in diameter; (b) XRD pole figure of the Au {111} reflections from the as-deposited Au(Fe) film. Two orientation variants are distinguishable, rotated by 60° with respect to each other around the [111] surface normal.

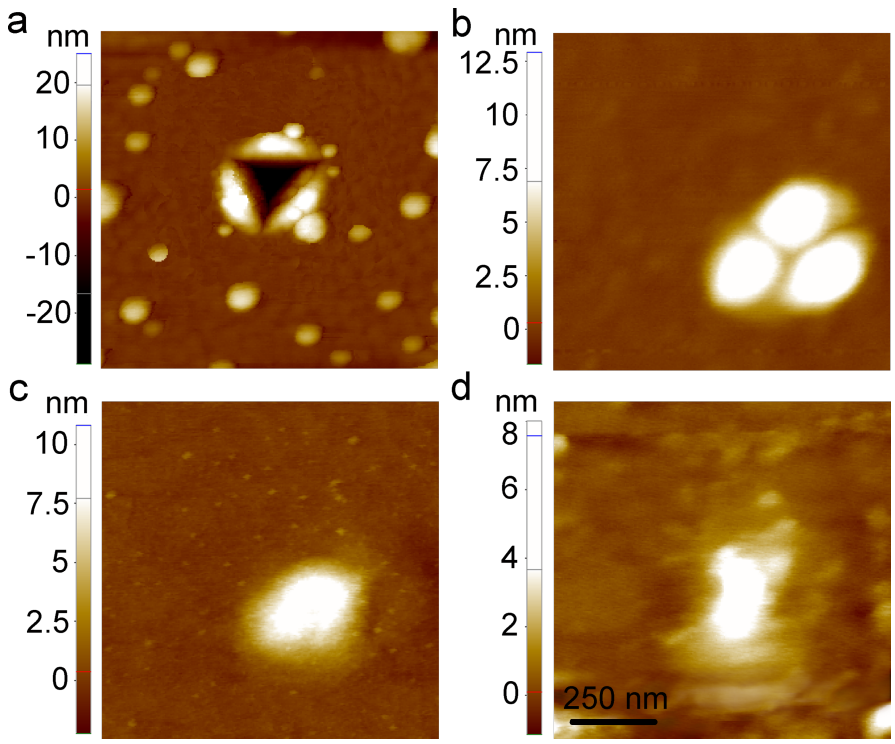


Figure 3: AFM topography images of one and the same imprint produced at P = 0.2 mN (a) after indentation, after annealing for (b) 10 min, (c) 20 min, (d) 290 min. Cumulative annealing times are given.

Thermally induced morphology evolution of the indents produced at the maximum load of P = 0.2 mN is shown in Figure 3 for one and the same indent, and in Figure 4 for random locations within the indented area. Upon heating, the healing process of the indents was thermally initiated. After annealing for 10 min, the piled-up material transformed into three-lobe hillocks (Figure 3b and Figure 4b), which resulted in a decrease of the maximum indent depth and in the lateral expansion of the indent. After the next heat treatment, the three lobes tend to merge into a single hillock (Figure 3c and Figure 4c). Annealing for 30 min results in the formation of near-hillock surface depressions accompanied by a slight reduction of the hillock height (Figure 4d). The depressions were observed near approximately 40% of all hillocks, which may have been caused by a local variation of the kinetic parameters or microstructure inhomogeneities. Interestingly, during subsequent annealing treatments, the hillocks with and without a nearby depression behaved differently. The height of the hillocks without a nearby depression stabilized at a value of 6–8 nm after the hillocks had been fully formed, and did not change upon subsequent anneals. The hillock-depression couples did change their morphology, with the depression becoming deeper consuming the nearby hillock. The latter process resulted in a shallow cavity adjacent to the disappearing hillock (Figure 4e and Figure 4f). Figure 5 shows the typical morphology of an indent transformed into a hillock-depression couple after prolonged annealing (290 min). The depth of the depression is about 5 nm, while the hillock height is reduced to 3 nm. It is worth noting that the depression has an elongated shape with gently sloping edges and a root exhibiting an abrupt change of the surface slope (Figure 5c). This fact testifies to a significant contribution of grain boundaries to the depression formation. Indeed, an abrupt change of the surface slope is an essential attribute of the grain boundary groove, indicating a balance of surface and grain boundary energies at the triple line [7,20]. Our EBSD observations have demonstrated that significant grain growth and texture sharpening had occurred in the film upon annealing, so that either a single grain boundary or no grain boundary at all were present in the immediate vicinity of the indents. We believe that the depressions were formed only in the cases when a grain boundary was available near the hillock.

The indents produced at P = 0.1 mN behaved in a similar manner. For these smaller indents, the formation of a single hillock followed by the appearance of a depression occurred slightly faster than in the case of indents produced at P = 0.2 mN. After annealing for 10 min, most of the indents were transformed into single hillocks, while some indents had a

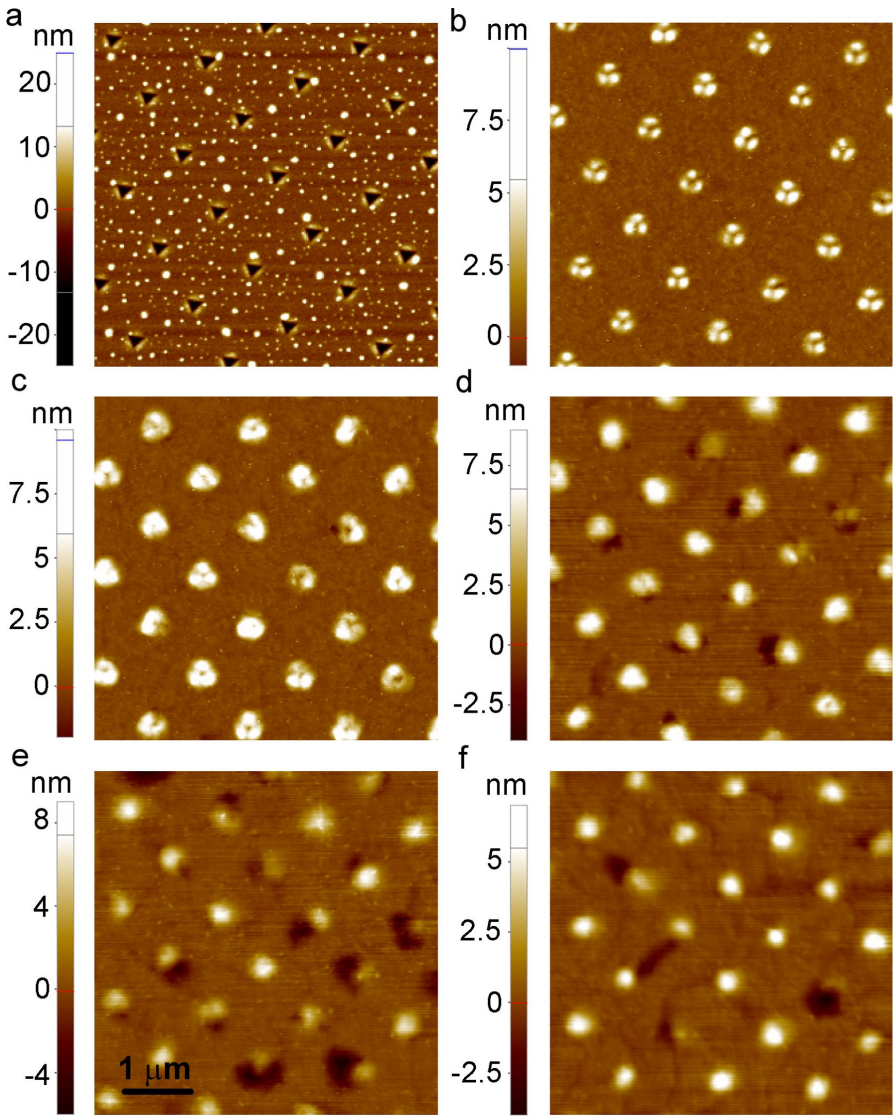


Figure 4: AFM topography images of nanoimprints produced at P = 0.2 mN (a) after indentation, after annealing for (b) 10 min, (c) 20 min, (d) 30 min, (e) 110 min, (f) 290 min. Cumulative annealing times are given.

slightly distinguishable three-lobe shape. The depth of the shallow depressions did not exceed 5 nm after the last heat treatment.

We also examined the film morphology far from the indented area. The onset of dewetting was observed right after the first annealing. The holes were randomly distributed and exhibited hexagonal symmetry. All holes nucleated at once, i.e., no new nucleation events were observed during subsequent anneals, and their density was about 5×10^8 m^{-2}. A typical hole formed during solid-state dewetting of the film is shown in Figure 6. The hexagonal shape of the holes tends to transform into a triangular one over time, as it was observed for a Au(Fe) film with lower thickness [16]. This fact is attributed to the faster surface diffusion along the disappearing facets. In contrast to the holes observed in [16], the holes observed in this study did not exhibit elevated rims. Yet, most of the holes were surrounded by a ring of small bumps. The volume of the material in the bumps is much smaller compared to the material removed from the hole. Hillocks as observed in the as-deposited film were not observed. This raises a question about the relocation of material consumed by the hole. It is reasonable to assume that the material is redistributed along the film–substrate interface, similar to what has been observed in Ni thin films with the mazed bicrystal microstructure [21]. This type of dewetting greatly differs from the classical one, implying the accumulation of the material in the rims of the holes [22]. The central feature inside the hole indicates its nucleation site. Such features were observed in many studies of the solid-state dewetting, yet the mechanism of their formation is still unknown [22].

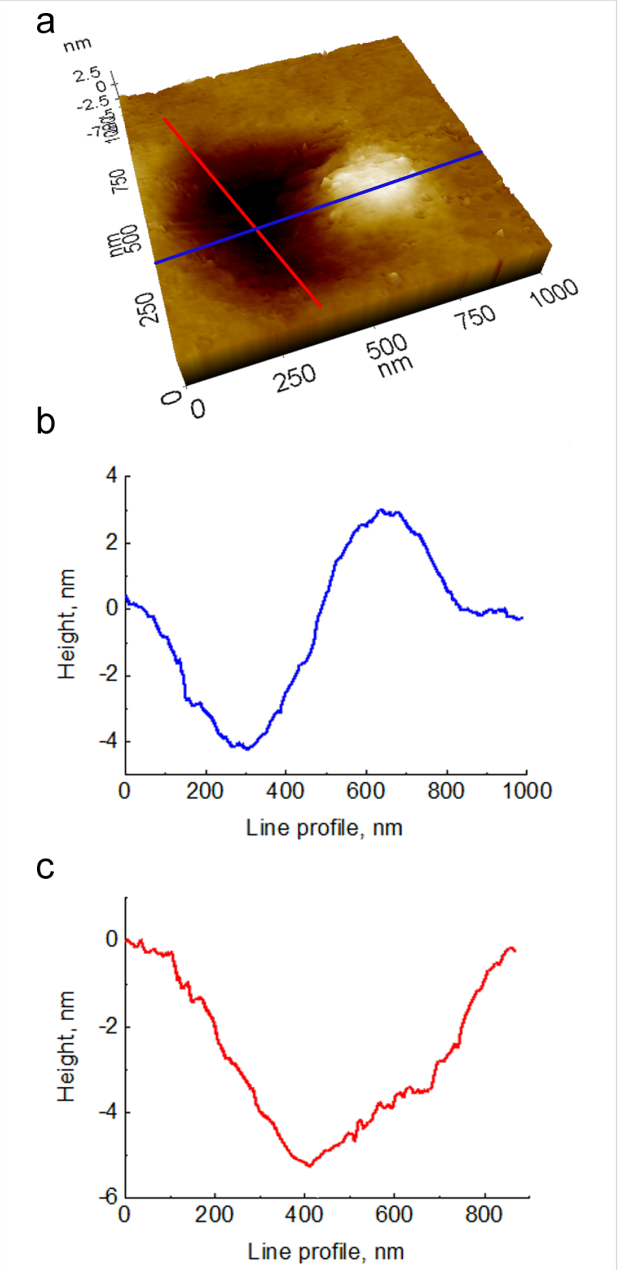


Figure 5: A three-dimensional AFM image of the indent after annealing for (a) 290 min and AFM profiles taken along the (b) blue and (c) red lines.

Discussion

In this study, we found that thermal treatment results in recovery of indents produced at the applied loads of 0.1 and 0.2 mN, with depths reaching up to half of the film thickness. It is interesting that no holes nucleated in the indented regions, whereas the dewetting process had started in the pristine, unperturbed regions of the film. This means that shallow indents, which do not reach the substrate, do not promote dewetting. The healing process does not lead to an entirely flat metal surface, but results in a hillock-depression morphology instead. The apparent stability of these hillock-depression couples can be explained by their low surface curvature, and, hence, low driving force for surface diffusion, which controls the flattening process [11]. Yet, the intermittent stage of relaxation, in which the hillock is formed at the site of the indent, is very counterintuitive and apparently defies the condition of mass conservation. In what follows, we will discuss the possible mechanisms of indent→hillock→depression transformations. This chain of relaxation processes is a result of a complex, synergetic interplay of different types of defects, including dislocation loops, grain boundaries, and pores, and diffusion paths, such as the surface, grain boundaries, and the film–substrate interface, which were either present in the as-deposited film or produced during indentation.

Let us first demonstrate that surface diffusion alone cannot explain the transformation of a volume-conserving surface indent into a hillock. Such a transformation could occur because Mullins' solution of the governing equation describing surface diffusion-controlled morphology evolution of a surface with a singular perturbation exhibits secondary and higher-order extrema in the surface profile [7]. Thus, the indents of certain morphologies can evolve into a central hillock surrounded by a shallow, but wide depression. We considered a conical, axisymmetrical indent with volume-conserving pileups and area function corresponding to a Berkovich indenter tip (see Appendix for details). We employed a small-slope approximation [7] and calculated the evolution of the topography of the indented region by a surface diffusion mechanism (Figure 7). For short annealing times, the bottom of the indent and the tops of the pileups undergo fast smoothing, while the walls of the indent remain almost straight. For long annealing times, the topography evolves into a minor central depression surrounded by a slightly elevated ring. At this stage, the evolution of the surface slows down drastically because of the decrease in surface curvature. Thus, these simulations demonstrate that surface diffusion alone cannot lead to the transformation of an indent into a hillock.

It is important to note that the pre-existing hillocks on the film surface (Figure 2) do not play any significant role in annealing-induced evolution of the film topography. We performed several control indentation-annealing experiments with the as-deposited Au(Fe) film free of surface hillocks. This film exhibited the same phenomenon of indent recovery accompanied by the formation of characteristic hillock-depression couples.

We believe that prismatic dislocation loops produced during indentation are responsible for the upward relaxation of the indent. We will assume that intensive plastic flow of the materi-

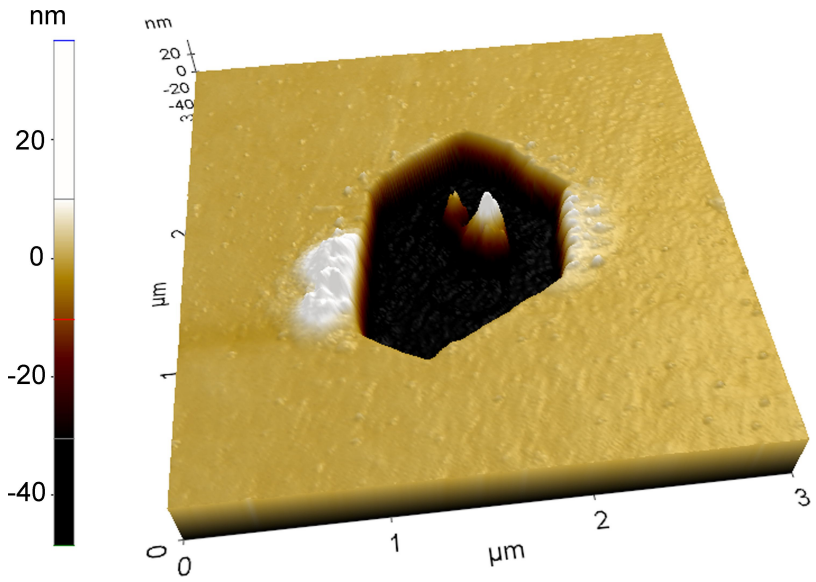


Figure 6: Three-dimensional AFM image of the hole in the Au(Fe) film far from the indented regions after annealing for 20 min.

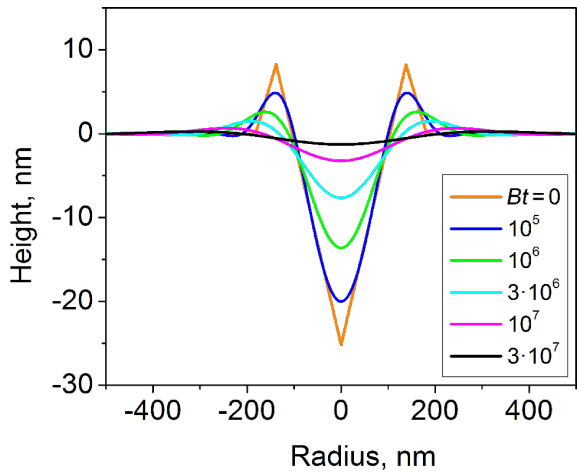


Figure 7: The simulated surface topography of the indent evolving by a surface diffusion mechanism, for different annealing times. *B* and *t* are the Mullins coefficient and the annealing time, respectively (see Appendix).

al around and underneath the indenter during indentation results both in the formation of material pileups, and of dislocation loops partly compensating for the displaced material in the indent (see Figure 8a). Some hints about the geometry of the plastic flow during a nanoindentation test consistent with the schematic model presented in Figure 8 can be obtained from the nanoindentation experiments on metallic multilayers [23]. Also, the nature of prismatic dislocation loops in the indented region has been recently discussed by Gagel et al. [24]. In Figure 8, we present the schematic drawings of the film topography after different annealing times (based on experimentally measured topography profiles averaged for several indents), together with the schematic presentation of the corresponding changes of the material microstructure. Upon annealing, the dislocation loops will tend to annihilate, both under the action of their own line tension and the residual stresses in the indented region. These residual stresses arise due to strong adhesion between the film and the substrate as well as the plastic strain associated with the indentation. The annihilation of the dislocation loops, which proceeds by a dislocation climb mechanism, leads to the elevation of the middle part of the indent and the formation of a hillock, with the surface diffusion causing the edges to smoothen and the affected surface region to widen (Figure 8b). Since the annihilation of dislocation loops is non-conservative, it generates a flux of excess vacancies. The vacancies can reach the film-substrate interface and the nearby grain boundary, which both can serve as vacancy sinks. The annihilation of vacancies at the film-substrate interface leads to the slight decrease of the film thickness [21], whereas annihilation of vacancies at the grain boundaries helps to relax compressive stresses in the film formed during heating due to the mismatch of thermal expansion coefficients between the film and the substrate. The rim-less shape of the dewetting holes observed far from the indented region (see Figure 6) confirms that the film-substrate interface is indeed a potent sink and source of vacancies; the vacancies that originated at the interface are consumed by the expanding hole. Some fraction of the vacancy flux generated by annihilating dislocation loops may lead to the nucleation of a pore, with the triple line where the grain boundary emerges at the film–substrate interface being a preferable site for this nucleation (see Figure 8b). Such pores were observed in our studies of the large indents, which reached to the substrate, in

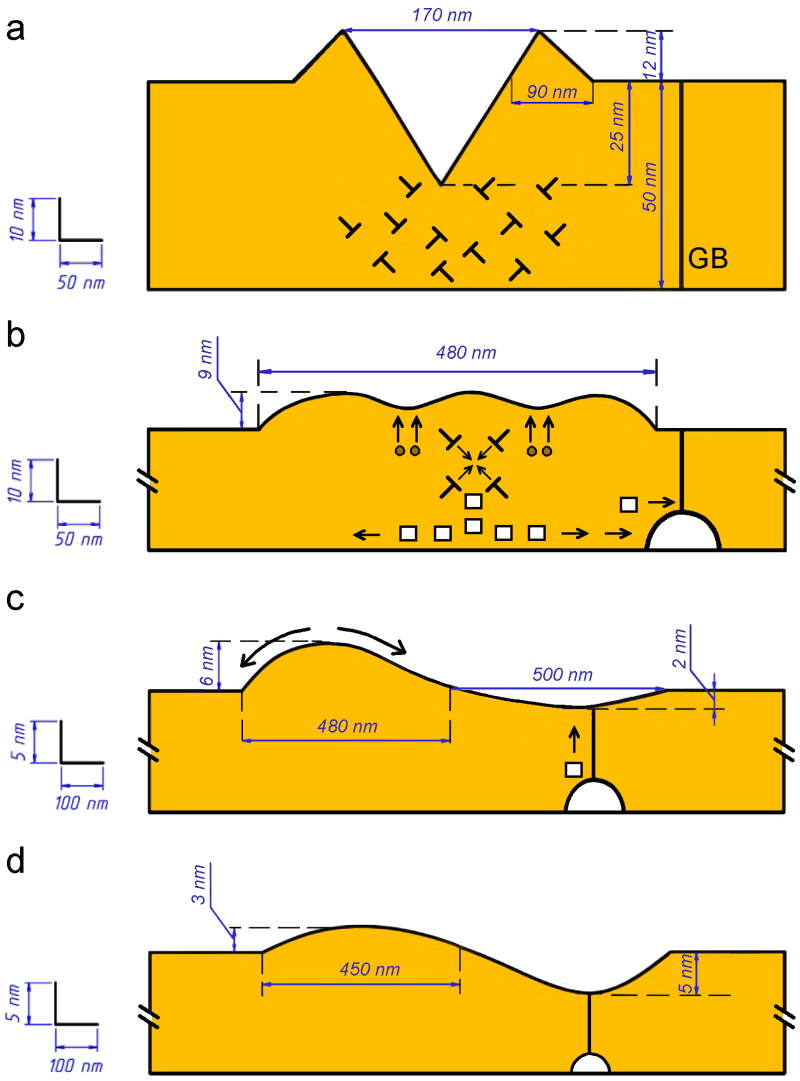


Figure 8: Schematic illustration of indent evolution with increasing annealing time: (a) before annealing, (b) 20 min, (c) 50 min, (d) 290 min. Various topography features are shown in-scale (as indicated by the scale bars on the left hand side of the figure), and their dimensions were obtained by averaging of AFM topography data for several indents. It should be noted that the arrangement of the dislocations shown does not represent the crystallography of the sample, but rather symbolizes the high dislocation density accounting for mass conservation and that is typical of indentation. The envisioned process should occur for all crystal orientations.

the same thin film, see Figure 9 [25], where the pores at the film–substrate interface with a diameter of 10–20 nm can be clearly seen. In the present case of low-load indents, the pores were probably too small to be detected with the aid of the employed sample preparation method. Once the pore is formed, it begins to drain the film material from the triple line at the film surface, leading to the formation of a near-hillock surface depression, see Figure 8c and Figure 8d. In the meantime, the hillock continues to dissipate by surface diffusion. Part of the material rejected by the shrinking hillock arrives at the grain boundary and contributes to the dissipation of the pore. At the end, the film should return to its original, planar state, slightly disturbed by the grain boundary grooves. According to this scenario, an apparent violation of mass conservation in Figure 8b and Figure 8c is compensated for by the grain boundary pore, by a slight decrease of the local film thickness, and by the relaxation of the compressive stresses in the film. It should be noted that a similar apparent violation of the mass conservation condition was observed during nanoindentation studies of thin Ni films, and it was also attributed to the formation of subsurface interface and grain boundary pores or cracks [26]. A simple, mass-conservation based estimate of the dislocation density, ρ, which is required to produce the hillock with typical dimensions shown in Figure 8b yielded $\rho \approx 10^{16}$ m^{-2}, which is

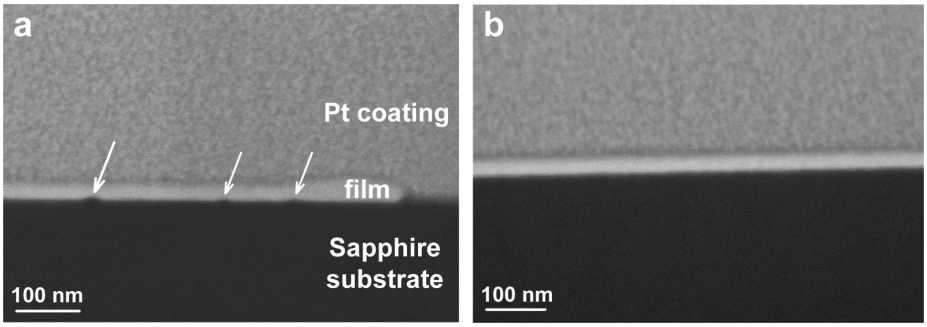


Figure 9: (a) Cross-sectional SEM image from the region indented at a high load (P = 1 mN), and (b) of the unperturbed region of the film. The images were taken under the tilt angle of 35°. One can see the indent that reached to the substrate (on the right side of the image (a), where the Pt coating covers the substrate directly) and the pores at the film–substrate interface (indicated by arrows). The annealing time was 10 min.

close to the maximum dislocation density in heavily deformed metals [27].

According to the proposed qualitative model, the annealing-induced evolution of indented metal is correlated to the following changes of the material microstructure in the indented region: (i) indentation-induced plastic flow and formation of prismatic dislocation loops, (ii) annihilation of the loops, formation of the hillock, and generation of excess vacancies and the grain boundary pore, (iii) dissipation of the hillock and the grain boundary pore by surface and grain boundary diffusion mechanisms. This morphology transformation is controlled by irreversible processes, such as dislocations climb, surface diffusion, and grain boundary diffusion. It is interesting that reversible formation/annihilation of hillocks at the indented sites upon heating/cooling was demonstrated in bulk and thin film samples of shape memory NiTi alloy [28]. This was achieved by planarizing the as-produced indents by mechanical polishing. The mechanism of the hillock formation upon heating is in that case related to the martensite–austenite phase transformation, which is affected by residual stress and very different from the irreversible mechanisms discussed in the present study.

Conclusion

From the results of the present study, the following conclusions can be drawn:

1. Thin polycrystalline Au(Fe) films on basal-plane oriented sapphire substrates were produced by electron beam deposition. The films exhibited a strong [111] texture and all grain boundaries were either of the near-Σ3<111> tilt, or of the low-angle type.
2. The shallow indents reaching up to one half of the film thickness, produced by depth-sensing nanoindentation did not affect the thermal stability of the film against the solid-state dewetting.
3. Upon heat treatments at a temperature of 700 °C in a forming gas atmosphere, the indents evolve into hillocks, in some cases followed by the formation of a near-hillock surface depression. For the long annealing times, the depression becomes deeper, while the hillock is dissipated.
4. We demonstrated quantitatively that the hillock formation at the indented site cannot be explained by surface diffusion alone. We proposed a qualitative scenario in which the hillock formation is related to the climb-controlled annihilation of prismatic dislocation loops formed during nanoindentation. The annihilation generates excess vacancies, which condense in the pore at the triple line between the grain boundary and the film-substrate interface. Later, the pore absorbs the material from the film surface by grain boundary diffusion, leading to the development of the near-hillock depression.

The phenomenon observed in this work can be employed for the design of surface topography of thin metal films. While patterning with the aid of nanoindentation imprints is quite obvious, we demonstrated that a thermo-mechanical treatment of the film, i.e., nanoindentation followed by annealing, can result in the formation of ordered arrays of hillocks. While the parameters of the naturally formed hillocks can hardly be controlled, the size, spacing, and arrangement of the hillocks produced by the suggested thermo-mechanical treatment can be fine-tuned by nanoindentation parameters, such as load and indent spacing, and annealing duration and temperature.

Experimental

Au(Fe) thin films (48 nm thick Au film on a 2 nm thick Fe underlayer) were deposited on c-plane sapphire (α-Al_2O_3) substrates at room temperature using electron beam deposition. The deposition took place in a VST e-beam evaporator with a base pressure of 5×10^{-7} Torr (6.7×10^{-7} mbar). Deposition rates were 0.2–0.3 Å·s^{-1} for Fe and 0.7 Å·s^{-1} for Au.

After the deposition, the films were patterned by square arrays of nanoimprints using a G200 DCM II nanoindenter (Agilent/Keysight Technologies) equipped with the Express Test and NanoVision options. Five big indents were used as markers in order to identify the locations of the different arrays with an optical microscope. For load-controlled nanoindentation tests, a three-sided diamond pyramidal Berkovich tip of approximately 20 nm radius of curvature at the apex was used. The arrays of nanoimprints (array size 100 × 100 μm) were produced on the film surface at applied loads of 0.1 and 0.2 mN, and contained 100 × 100 nanoimprints, so that the distance between the imprints was 1 μm. For both loading conditions, the penetration depth was significantly lower than the film thickness.

The indented samples were annealed in a quartz tube resistance furnace under forming gas flow (Ar + 10% H_2, 99.999% pure) at a temperature of 700 °C for the consecutive time intervals of 10, 10, 10, 20, 60 and 180 min. The samples were placed in a quartz boat and introduced to the hot zone of the furnace by a mechanical manipulator. The heating time of the boat containing the sample from room temperature to 700 °C was 3 min, followed by an isothermal annealing for the required time. Quenching was achieved by rapid withdrawal of the boat with the sample from the hot zone.

After each treatment, the samples were characterized by atomic force microscopy (AFM; Park Systems XE-70) in intermittent-contact mode, using NSG30 Si probes supplied by NT-MDT with an average nominal value of resonant frequency of 270 kHz, and an average nominal radius of curvature at the apex of <25 nm.

The microstructure of the films was characterized by high-resolution scanning electron microscopy (HRSEM; Zeiss Ultra Plus), and by X-ray diffraction (XRD; Rigaku SmartLab) using Cu Kα radiation in a parallel beam configuration. HRSEM micrographs were taken using a secondary electron detector, at an acceleration voltage of 3 kV. Pole figures were measured using slit collimation. Precise alignment of the samples was performed using rocking curves (ω scans) on the Au (111) reflection. Cross-section samples were prepared in a dual-beam focused ion beam microscope (FIB; FEI Strata 400-S).

Appendix

Topography evolution of an axisymmetrical indent by surface diffusion (small slope approximation)

To check whether surface diffusion alone can lead to indent transformation into a hillock, we simulated topography evolution of an axisymmetrical conical indent in a small-slope approximation.

The axial surface is described by the topography profile $Y = Y(r,t)$, where r is the distance from the central axis and t is the annealing time. We assume that $\partial Y/\partial r << 1$, so that the small-slope approximation can be used. The chemical potential of atoms on the surface, μ, is proportional to a local curvature of the surface $\mu = \Omega\gamma\kappa$, where the curvature, κ, is given by

$$\kappa = -\frac{\partial^2 Y}{\partial r^2} - \frac{1}{r}\frac{\partial Y}{\partial r} \tag{1}$$

and Ω, γ are the atomic volume and the surface energy, respectively. The diffusion flux, j, is proportional to the gradient of the chemical potential

$$j = -\frac{D_s \nu_s}{kT}\frac{\partial \mu}{\partial r} = -\frac{D_s \nu_s \Omega \gamma}{kT}\frac{\partial \kappa}{\partial r} \tag{2}$$

The accumulation of atoms on the surface is proportional to the divergence of the diffusion flux. Thus,

$$\frac{\partial Y}{\partial t} = -\Omega\frac{1}{r}\frac{\partial (rj)}{\partial r} = B\left[\frac{\partial^2 \kappa}{\partial r^2} + \frac{1}{r}\frac{\partial \kappa}{\partial r}\right] \tag{3}$$

where

$$B = \frac{D_s \nu_s \Omega^2 \gamma}{kT}$$

is the Mullins coefficient. D_s and ν_s are the surface self-diffusion coefficient and the number of mobile atoms per unit area of the surface, respectively, and kT has its usual thermodynamic meaning. Equation 1–3 represent full analogs of Mullins equations for a cylindrical surface.

Numerical scheme

For the numerical solution of Equation 1–3, we introduce the circles $r_n = n\Delta$ and $Y_n = Y(r_n)$, $0 \le n \le N$. We will approximate the shape of the surface between the circles r_n by a cone. The chemical potential of atoms on the surface for $r = r_n$ is determined as

$$\mu_n = \Omega\frac{\delta E}{\delta Y_n} / \frac{\delta V}{\delta Y_n},$$

$$\text{where } \frac{\delta E}{\delta Y_n} \text{ and } \frac{\delta V}{\delta Y_n}$$

are the variations of the surface energy and the cone volume, respectively, with the displacement of the y-coordinate of the nth circle. Direct calculation yields the following expressions:

$$\frac{\delta V}{\delta Y_n}=\frac{\pi}{3}(r_{n+1}-r_{n-1})(r_n+r_{n+1}+r_{n-1})=2\pi\Delta^2 n,\quad 0<n<N \tag{4}$$

$$\frac{\delta V}{\delta Y_0}=\frac{\pi}{3}\Delta^2,\quad \frac{\delta V}{\delta Y_N}=\frac{\pi}{3}\Delta^2(3N-1) \tag{5}$$

$$\frac{\delta E}{\delta Y_n}=\pi\gamma\left[(2n-1)(Y_n-Y_{n-1})+(2n+1)(Y_n-Y_{n+1})\right],\quad 0<n<N \tag{6}$$

$$\frac{\delta E}{\delta Y_0}=2\pi\gamma(Y_0-Y_1),\quad \frac{\delta E}{\delta Y_N}=\pi\gamma(2N-1)(Y_N-Y_{N-1}) \tag{7}$$

Combining the Equations 4–7 yields $\mu_n=\Omega\gamma\kappa_n$, where

$$\kappa_n=\frac{2Y_n-(1-1/2n)Y_{n-1}-(1+1/2n)Y_{n+1}}{\Delta^2},\quad 0<n<N \tag{8}$$

$$\kappa_0=\frac{6(Y_0-Y_1)}{\Delta^2},\quad \kappa_N=\frac{(2N-1)(Y_N-Y_{N-1})}{\Delta^2(N-1/3)} \tag{9}$$

The total atomic flux between the circles n and $n+1$ is

$$\begin{aligned}J_{n\to n+1}&=\pi(r_n+r_{n+1})\frac{D_s\nu_s}{kT}\frac{\mu_n-\mu_{n+1}}{\Delta}\\&=\pi\frac{D_s\nu_s\Omega\gamma}{kT}(2n+1)(\kappa_n-\kappa_{n+1})\end{aligned} \tag{10}$$

Final kinetic equations follow from the condition of mass balance:

$$\frac{dY_n}{dt}=\Omega(J_{n-1\to n}-J_{n\to n+1})/\frac{\delta V}{\delta Y_n},\quad 0<n<N \tag{11}$$

$$\frac{dY_0}{dt}=-\Omega J_{0\to 1}/\frac{\delta V}{\delta Y_0},\quad \frac{dY_N}{dt}=\Omega J_{N-1\to N}/\frac{\delta V}{\delta Y_N} \tag{12}$$

Substituting Equations 4, 5 and 10 in Equations 11, 12 yields:

$$\frac{dY_n}{dt}=B\frac{(2n-1)(\kappa_{n-1}-\kappa_n)-(2n+1)(\kappa_n-\kappa_{n+1})}{2\Delta^2 n},\quad 0<n<N \tag{13}$$

$$\frac{dY_0}{dt}=B\frac{3(\kappa_1-\kappa_0)}{\Delta^2},\quad \frac{dY_N}{dt}=B\frac{2N-1}{3N-1}\frac{3(\kappa_{N-1}-\kappa_N)}{\Delta^2} \tag{14}$$

The set of the ordinary differential equations (Equations 8, 9 and Equations 13, 14) was solved employing the standard Euler method with the parameter $Bdt/\Delta^4<0.05$. The results of the simulations are shown in Figure 7.

Acknowledgements

A.K. wishes to thank the Technion for the post-doctoral fellowship. Helpful discussions with Prof. O. Kraft are heartily appreciated. This work was supported by the Israel Science Foundation (Grant No 1628/15), and in part by the Russell Berry Nanotechnology Institute. The assistance of Dr. D. Amram and Mr. O. Kovalenko is heartily acknowledged.

References

1. Lee, W.-S.; Chen, T.-H.; Lin, C.-F.; Chen, J.-M. *Appl. Phys. A* **2010,** *100,* 1089–1096. doi:10.1007/s00339-010-5706-0
2. Lee, W.-S.; Chen, T.-H.; Lin, C.-F.; Wu, C.-L. *Mater. Trans.* **2011,** *52,* 1868–1875. doi:10.2320/matertrans.M2011160
3. Lee, W.-S.; Fong, F.-J. *Mater. Sci. Eng., A* **2008,** *475,* 319–326. doi:10.1016/j.msea.2007.04.083
4. Shaw, G. A.; Stone, D. S.; Johnson, A. D.; Ellis, A. B.; Crone, W. C. *Appl. Phys. Lett.* **2003,** *83,* 257–259. doi:10.1063/1.1591235
5. Rajagopalan, J.; Han, J. H.; Taher, M.; Saif, A. *Science* **2007,** *315,* 1831–1834. doi:10.1126/science.1137580
6. Humphreys, F. J.; Hatherly, M. *Recrystallization and related annealing phenomena,* 2nd ed.; Elsevier: Amsterdam, Netherlands, 2004.
7. Mullins, W. W. *J. Appl. Phys.* **1957,** *28,* 333–339. doi:10.1063/1.1722742
8. Génin, F. Y.; Mullins, W. W.; Wynblatt, P. *Acta Metall. Mater.* **1992,** *40,* 3239–3248. doi:10.1016/0956-7151(92)90037-F
9. Shaffir, E.; Riess, I.; Kaplan, W. D. *Acta Mater.* **2009,** *57,* 248–256. doi:10.1016/j.actamat.2008.09.004
10. Packard, C. E.; Schroers, J.; Schuh, C. A. *Scr. Mater.* **2009,** *60,* 1145–1148. doi:10.1016/j.scriptamat.2009.02.056
11. Mullins, W. W. *J. Appl. Phys.* **1959,** *30,* 77–83. doi:10.1063/1.1734979
12. Xu, G. Q.; Demkowicz, M. J. *Phys. Rev. Lett.* **2013,** *111,* 145501. doi:10.1103/PhysRevLett.111.145501
13. Kovalenko, O.; Rabkin, E. *Scr. Mater.* **2015,** *107,* 149–152. doi:10.1016/j.scriptamat.2015.06.007
14. Kovalenko, O.; Chikli, F. O.; Rabkin, E. *Scr. Mater.* **2016,** *123,* 109–112. doi:10.1016/j.scriptamat.2016.06.006
15. Amram, D.; Rabkin, E. *Acta Mater.* **2013,** *61,* 4113–4126. doi:10.1016/j.actamat.2013.03.038
16. Amram, D.; Klinger, L.; Rabkin, E. *Acta Mater.* **2012,** *60,* 3047–3056. doi:10.1016/j.actamat.2012.02.009
17. Iijima, Y.; Yamazaki, Y. *Defect Diffus. Forum* **2005,** *237–240,* 62–73. doi:10.4028/www.scientific.net/DDF.237-240.62
18. Radetic, T.; Ophus, C.; Omsted, D. L.; Asta, M.; Dahmen, U. *Acta Mater.* **2012,** *60,* 7051–7063. doi:10.1016/j.actamat.2012.09.012
19. Dehm, G.; Inkson, B. J.; Wagner, T. *Acta Mater.* **2002,** *50,* 5021–5032. doi:10.1016/S1359-6454(02)00347-6
20. Rabkin, E.; Amouyal, Y.; Klinger, L. *Acta Mater.* **2004,** *52,* 4953–4959. doi:10.1016/j.actamat.2004.06.027
21. Amram, D.; Klinger, L.; Gazit, N.; Gluska, H.; Rabkin, E. *Acta Mater.* **2014,** *69,* 386–396. doi:10.1016/j.actamat.2014.02.008
22. Thompson, C. V. *Annu. Rev. Mater. Res.* **2012,** *42,* 399–434. doi:10.1146/annurev-matsci-070511-155048
23. Zhang, G. P.; Liu, Y.; Wang, W.; Tan, J. *Appl. Phys. Lett.* **2006,** *88,* 013105. doi:10.1063/1.2159581

24. Gagel, J.; Weygand, D.; Gumbsch, P. *Acta Mater.* **2016,** *111,* 399–406. doi:10.1016/j.actamat.2016.04.002
25. Kosinova, A.; Schwaiger, R.; Kraft, O.; Rabkin, E. to be submitted to *Acta Materialia*.
26. Rabkin, E.; Deuschle, J. K.; Baretzky, B. *Acta Mater.* **2010,** *58,* 1589–1598. doi:10.1016/j.actamat.2009.11.002
27. Callister, W. D.; Rethwisch, D. G. *Fundamentals of Materials Science and Engineering: an Integrated Approach,* 4th ed.; John Wiley and Sons: New York, NY, U.S.A., 2012; p 264.
28. Zhang, Y.; Cheng, Y.-T.; Grummon, D. S. *Appl. Phys. Lett.* **2006,** *89,* 041912. doi:10.1063/1.2222173

License and Terms

This is an Open Access article under the terms of the Creative Commons Attribution License (http://creativecommons.org/licenses/by/4.0), which permits unrestricted use, distribution, and reproduction in any medium, provided the original work is properly cited.

The license is subject to the *Beilstein Journal of Nanotechnology* terms and conditions: (http://www.beilstein-journals.org/bjnano)

The definitive version of this article is the electronic one which can be found at: doi:10.3762/bjnano.7.199

BEILSTEIN JOURNAL OF NANOTECHNOLOGY

Sub-nanosecond light-pulse generation with waveguide-coupled carbon nanotube transducers

Felix Pyatkov[*,‡1,2], Svetlana Khasminskaya[‡1], Vadim Kovalyuk[1,3], Frank Hennrich[1], Manfred M. Kappes[1,4], Gregory N. Goltsman[3,5], Wolfram H. P. Pernice[6] and Ralph Krupke[1,2]

Full Research Paper

Open Access

Address:
[1]Institute of Nanotechnology, Karlsruhe Institute of Technology, Karlsruhe 76021, Germany, [2]Department of Materials and Earth Sciences, Technische Universität Darmstadt, Darmstadt 64287, Germany, [3]Department of Physics, Moscow State Pedagogical University, Moscow 119992, Russia, [4]Institute of Physical Chemistry, Karlsruhe Institute of Technology, Karlsruhe 76021, Germany, [5]National Research University Higher School of Economics, Moscow 101000, Russia and [6]Institute of Physics, University of Münster, Münster 48149, Germany

Email:
Felix Pyatkov[*] - feliks.pyatkov@kit.edu

* Corresponding author ‡ Equal contributors

Keywords:
carbon nanotubes; infrared; integrated optics devices; nanomaterials

Beilstein J. Nanotechnol. **2017,** *8,* 38–44.
doi:10.3762/bjnano.8.5

Received: 15 August 2016
Accepted: 20 December 2016
Published: 05 January 2017

This article is part of the Thematic Series "Advances in nanomaterials II".

Guest Editor: H. Hahn

© 2017 Pyatkov et al.; licensee Beilstein-Institut.
License and terms: see end of document.

Abstract

Carbon nanotubes (CNTs) have recently been integrated into optical waveguides and operated as electrically-driven light emitters under constant electrical bias. Such devices are of interest for the conversion of fast electrical signals into optical ones within a nanophotonic circuit. Here, we demonstrate that waveguide-integrated single-walled CNTs are promising high-speed transducers for light-pulse generation in the gigahertz range. Using a scalable fabrication approach we realize hybrid CNT-based nanophotonic devices, which generate optical pulse trains in the range from 200 kHz to 2 GHz with decay times below 80 ps. Our results illustrate the potential of CNTs for hybrid optoelectronic systems and nanoscale on-chip light sources.

Introduction

Efficient transducers that allow converting electrical signals into optical ones and vice versa are essential ingredients for emerging applications in on-chip optoelectronic circuits. In particular, nanoscale transducers that can be seamlessly integrated into optical waveguide structures are needed to enable on-chip data communication in devices with small footprint. In this context carbon nanotubes (CNTs) have been identified as promising active components [1,2]. As a first step towards CNT-based optoelectronic photonic devices, light generation in waveguide-like electrodes [3] and optical waveguides [4-6] via electrically driven CNTs has been demonstrated. Very recently electroluminescent CNTs integrated into photonic circuits

emerged as sources of non-classical light [7]. Besides electrical drive, optically stimulated light emission from CNTs coupled into waveguides [8] and to cavities [9] has been achieved. It was demonstrated, that the wavelength and the line shape of a CNT emission can be tailored by the photonic environment [6,10]. Beyond continuous wave generation of light, an important aspect that needs to be addressed is the question of how fast a waveguide-coupled CNT transducer can respond to an electrical signal. Indeed, time-dependent incandescence from a CNT film in free-space has been measured [11] and modulation of CNT emission with decay times below 250 ps has been shown [6]. The intrinsic characteristic timescale for CNT incandescence is expected to be of the order of 10 ps, estimated from the heat capacitance of the CNTs and the thermal coupling to the dielectric substrate and metallic leads [11]. Hence, CNT-based transducers operating at 100 GHz seem to be possible.

In this work, we investigated the dynamic response and coupling efficiency of waveguide-coupled CNT transducers to electrical signals and analyze the optical pulses propagating in the waveguide.

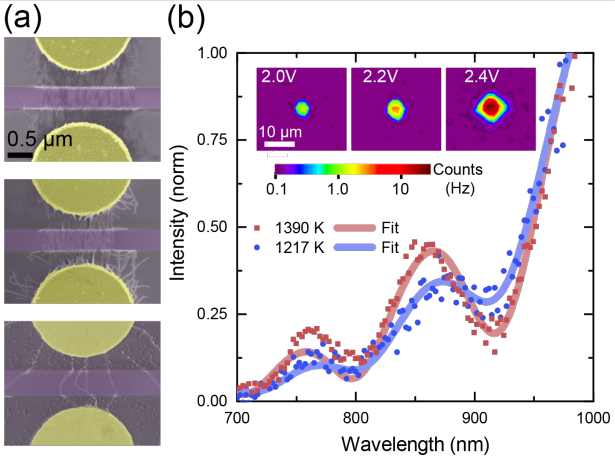


Figure 1: (a) Waveguide-integrated CNT transducers. False-colored scanning electron image of the waveguides (purple), horizontally aligned between metallic contacts (yellow). The CNTs can be seen as thin vertical lines between the electrodes crossing the waveguides. The density of CNTs varies from ca. 100 μm^{-1} to ca. 10 μm^{-1} to ca. 3 μm^{-1} (SEM images from the top to the bottom). (b) Emission spectra from a waveguide-integrated CNT transducer, driven with 200 ns electrical pulses at 200 kHz repetition rate for 2.5 V_{DC} + 2 V_{pulse} (blue circles) and 2.5 V_{DC} + 3 V_{pulse} (red squares). The full lines are fits to a black-body radiation curve modulated by a substrate-induced interference. The thermal emitter temperature from the fit is 1217 K (1390 K). Inset: spatially resolved light emission from a CNT emitter driven with 100 ns electrical pulses at 200 kHz rate for V_{pulse} = 2.0, 2.2, 2.4 V.

Results and Discussion

Fabrication of waveguide-integrated CNT emitters

Our waveguide-coupled CNT (WG-CNT) transducers consist of three components: a rib waveguide, metallic contacts next to the waveguide, and metallic single-walled carbon nanotubes (SWCNTs) placed on top of the waveguide, bridging the contacts (Figure 1a). We use the design and fabrication approach for our samples that has been described in detail elsewhere [4]. Both electrodes and waveguides were defined using several steps of electron beam lithography on top of $Si_3N_4/SiO_2/Si$ substrate. Au/Cr contacts were produced by physical vapor deposition, and 600 nm wide, half-etched Si_3N_4-waveguides were formed with reactive ion etching. A typical sample contains tens of contact pairs and CNTs that were placed in between using dielectrophoresis (DEP) [12,13]. DEP allows for site-selective placement of CNTs onto electrodes with their long axis aligned perpendicular to the waveguide [4]. We used gel-filtrated metallic CNTs obtained from HiPco material [14]. The deposition density has been varied in the range of 1–100 CNTs per 1 µm waveguide length. After DEP the samples were baked for 1.5 h at 150 °C in ambient air in an oven to improve the contact adhesion. Several waveguide coupled CNT devices are shown in Figure 1a.

By connecting the driving electrodes of the CNT to a modulated voltage source, the nanoscale emitter can be driven into incandescence. We employ a pulse generator (Agilent 8131A for long pulses and Agilent 8133A for short electrical pulses) in combination with a Keithley 6430 source-meter for additional DC-biasing via a bias tee (ZFBT-6GHz, Mini-Circuits) to apply a time-varying voltage to the driving electrodes. Light emission from WG-CNT transducers was characterized with both a free-space setup and a fiber-coupled system. The free-space setup allows for the spatial and spectral analysis of light emitted from a transducer along the surface normal. The fiber-coupled system is dedicated to analyzing short light pulses, emitted by the transducer, and propagating within the waveguide.

Light emission from waveguide-coupled CNTs under pulsed excitation

For analysis with the free-space setup, the transducers were placed in a lighttight system comprising of a Zeiss AxioTech Vario microscope, directly attached to an Acton SpectraPro 2360 spectrometer. The latter consists of a switchable mirror and grating, and is equipped with a PIXIS 256E CCD camera (Princeton Instruments) [15]. The spectrum of the light, emitted at the position of the CNT, is shown in Figure 1b, while the spatial distribution of the emission is presented in the inset. The signal intensity increases towards longer wavelengths with a superimposed intensity modulation. This behavior is characteristic for an incandescent emitter on a layered substrate that leads to interference fringes in the spectral profile, as observed for light emitting CNTs [4] and graphene [16]. The emitter temperature was extracted by fitting the data to a Planck spectrum

$$I_{\text{therm}}(\lambda,T) \propto \left(\lambda^5\left(e^{hc/\lambda k_B T}-1\right)\right)^{-1},$$

modulated by the substrate-induced interference [3]. Depending on the density of the CNTs as well as the biasing conditions, the temperature of the emitter lies within the range of 1000 to 1500 K, and increases with the pulse amplitude. The temperature of the CNT in the pulsed regime is similar to temperatures reached under DC-biasing [4,17].

For a comprehensive characterization of the emitter response to a modulated electrical signal, we varied the pulse amplitude V_{pulse}, the pulse width w, pulse period T, and thereby the duty cycle $D = w/T$. We measured the total intensity of the incandescent CNT emitters, I_E, for each parameter set. Emission is observed above a device-dependent threshold V_{th} of about 1.5 V, which is independent of w and D over a broad frequency range, as shown in Figure 2a for contacts with similar CNT-density. The maximum RF amplitude of the pulse generator was not always sufficiently high to record light emission. Therefore a device-specific DC offset $V_{\text{DC}} \leq V_{\text{th}}$ was applied to raise the emission count rate slightly below the dark count rate of the system without RF contribution (Figure 2a, green and yellow symbols).

The emission was remarkably stable over hours. As expected, the absolute intensity depends on the duty cycle. Therefore, to consolidate all data sets into one graph, we have plotted in Figure 2a the normalized intensity $I_{\text{norm}} = I_E/D$ for pulses with 10 to 1000 ns width and duty cycles ranging from 0.002 to 0.2. As a general trend we observe that I_{norm} increases with $V = V_{\text{pulse}} + V_{\text{DC}}$ by four orders of magnitude. Moreover, by plotting I_{norm} on a logarithmic scale against the inverse voltage V^{-1}, the data collapses onto a straight line. This establishes the dependence $I_{\text{norm}} \propto e^{\text{const}/V}$. For further understanding it is important to realize that the emission has been recorded in the high-bias regime where the current through the CNT reaches saturation, and the dissipated power and, hence, the temperature increases linearly with voltage [18-20]. As a result $I_{\text{norm}} \propto e^{\text{const}/V}$ can be converted into $I_{\text{norm}} \propto e^{-E/kT}$, similar to previous measurements with metallic CNTs [17]. To rationalize this dependence we have modeled the temperature-dependent spectral distribution $I_{\text{spectral,mod}}(\lambda,T)$ as the product of the Planck spectrum $I_{\text{therm}}(\lambda,T)$ and the spectral sensitivity of the detector $S(\lambda)$ and plotted the result in the inset of Figure 2b. For simplicity, we have approximated the sensitivity of our detector by a Gaussian spectral profile centered at 830 nm and a FWHM of about 250 nm. From these spectra we calculated the wavelength-integrated, temperature-dependent intensity of the collected light $I_{\text{integrated,mod}}(T)$ presented in Figure 2b (red symbols). Since the limited detection range of the CCD camera allows for the detection of broadband CNT-emitted light only for $hc/\lambda >> kT$, the temperature dependence of $I_{\text{integrated,mod}}(T)$ can be described using Wien's approximation of Planck's law.

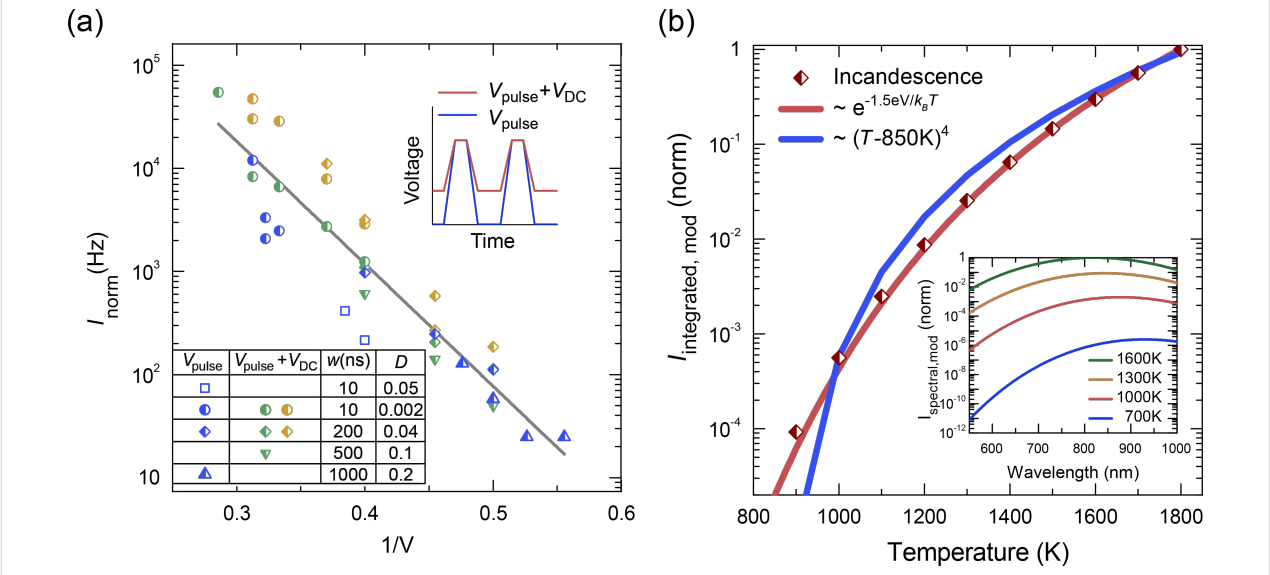


Figure 2: (a) Normalized total intensity I_{norm} versus $1/V$ under variation of electrical pulse width, w, and duty cycle, D. The full line is a fit to the data. Data acquired with an additional offset voltage V_{DC} = 1.5 V is labeled with green and yellow symbols, data acquired without offset is shown as blue symbols. The inset schematically illustrates two biasing schemes. All measurements refer to light propagating along the surface normal collected with the free-space setup. (b) Simulation of the temperature-dependent total intensity of the incandescent light collected with a CCD camera $I_{\text{integrated,mod}}(T)$ (red symbols), compared with exponential (red line) and power law (blue line) fits. Inset: Simulated spectra $I_{\text{spectral,mod}}(\lambda,T)$ of incandescent light sources emitting at the indicated temperatures. The shape of the spectra deviates from the Planck curve $I_{\text{therm}}(\lambda,T)$ because of the spectral sensitivity of the detector $S(\lambda)$.

The best fit to the modelled data is the function $I_{\text{norm}} \propto e^{-E/kT}$ with the energy E = 1.5 eV (830 nm) corresponding to the maximum spectral sensitivity of our detector. Alternatively, the often considered power-law fit was tested, which requires assuming a temperature offset T_0. However even the closest fit with T_0 = 850 K does not match the data well and can be used only as an approximation for higher temperatures.

Before discussing the generation of short light pulses in waveguides we would like to comment on the efficiency of the coupling of evanescent light from the CNT emitter into the waveguide. To determine the coupling efficiency we compare the emission recorded above the emitter I_E with the emission recorded above the Bragg grating coupler I_C. The grating coupler serves to couple out light from the waveguide into free space. A spatially resolved emission measured on a device with a short waveguide is shown in Figure 3a.

The coupling efficiency of pulsed CNT emitters can then be calculated by $\eta \geq 2I_C/(I_E + 2I_C)$. Since we cannot account for loss of light due to interaction with the substrate or emission under shallow angle, we are actually considering an apparent coupling efficiency. The data measured with three devices in the broad intensity range provide an average value of $\eta \approx 0.48$ (Figure 3b). The value of η varies in the range between 45% and 55% independent of the emission intensity and pulse width, as shown in Figure 3c. It is also comparable to previous results with DC-biased WG-CNTs [4] and exceeds the calculated values for electroluminescent CNT emitters on a SOI-waveguide by a factor of 1.5 to 2 [21].

Optical pulses from waveguide-coupled CNTs

Finally we discuss light-pulse propagation in the waveguide studied with a fiber-coupled system. In contrast to the free-space setup, the fiber-coupled setup provides no spectral resolution, but allows us to resolve pulses with sub-nanosecond resolution in the time domain.

The operation principle is shown in Figure 4a. The CNTs were driven with electrical pulses applied with a pulse generator to the source and drain contacts via an RF-probe (Cascade Microtech). Waveguided light pulses were partly coupled out via Bragg grating couplers, designed with a central wavelength 750 ± 20 nm for guiding light into an optical fiber. Optical pulses were measured with either a single-photon avalanche detector (τ-SPAD-100, PicoQuant) or a superconducting nanowire single-photon detector [22] (SNSPD or SSPD, SCONTEL). The photon arrival times were accumulated into a histogram with 4 ps bin size using a time-correlated single-photon counting (TCSPC) unit [23] (Picoharp 300, PicoQuant), triggered by the time-synchronized pulse generator. This allows for the measurement of time-resolved, low-intensity signals and an estimation of the emission decay. The light collection effi-

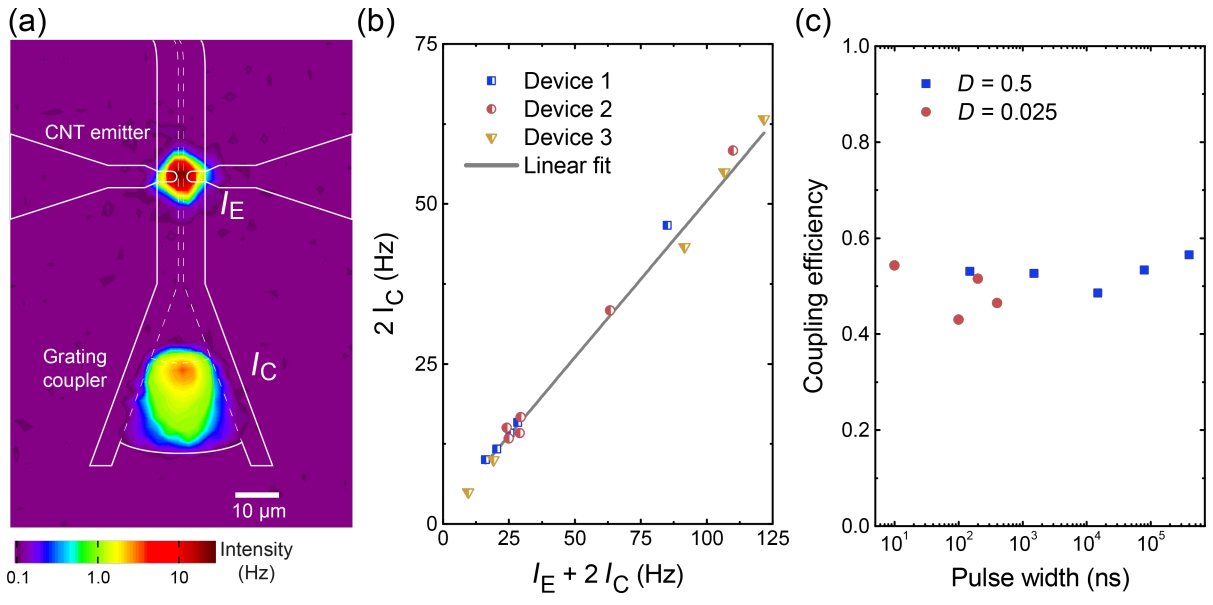


Figure 3: (a) Spatially resolved light emission showing intensity at the position of the CNT emitter and the grating coupler. The device geometry is indicated with white lines. The dashed lines mark the waveguide. (b) Integrated intensity recorded at the grating couplers $2I_C$ over the sum of intensities measured at the CNT emitter and grating couplers $I_E + 2I_C$. The data were collected for three devices (blue, red and yellow symbols) in the free-space setup. A linear fit to the data provides an average coupling efficiency $\eta \approx 0.48$. (c) Coupling efficiency for pulsed emitters with duty cycles of 0.5 (blue symbols) and 0.025 (red symbols).

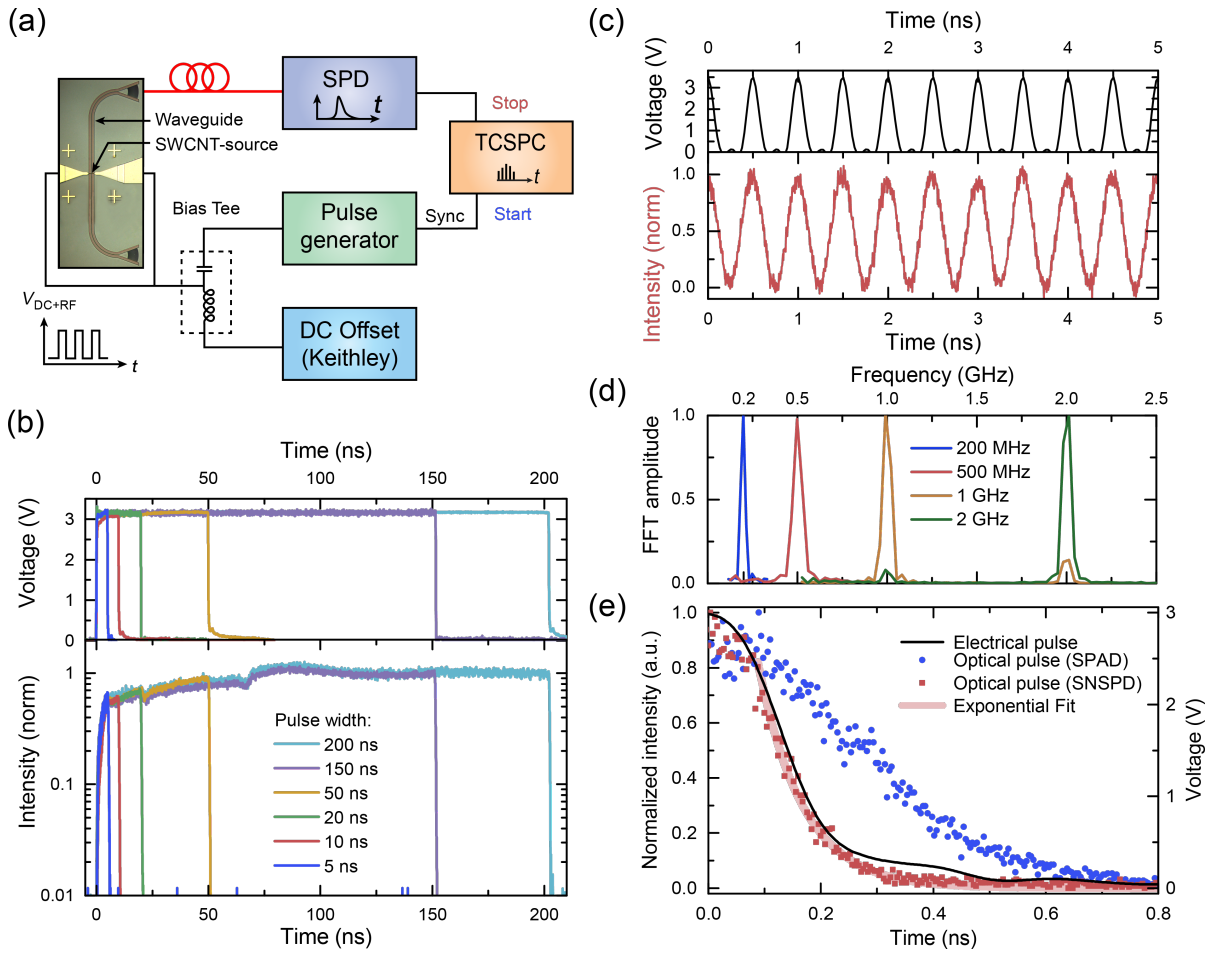


Figure 4: (a) WG-CNT transducer characterized by the fiber-coupled setup. (b) Comparison of electrical pulses with TCSPC-histograms of optical pulses, measured at a grating coupler. (c) Sequence of electrical pulses (150 ps width, 2 GHz, 10 V_{DC} and 3.3 V_{pulse}) as well as emission pulses. (d) Normalized fast Fourier transform (FFT) spectra of modulated CNTs, emitting at frequencies of 0.2, 0.5, 1 and 2 GHz. (e) The decay of the CNT-emission following the trailing edge of an electrical pulse (black line) was measured with the slow SPAD (blue symbols) and fast SNSPD (red symbols) along with fitted exponential decay curve (decay time τ = 79 ps). The broadening of the electrical signal along with a small bump at 0.4 ns occurs because of impedance mismatch.

ciency of the fiber-coupled system is several orders of magnitude lower than that of the free-space setup. This is due to the limited bandwidth of the grating coupler (ca. 50 nm) and the lower numerical aperture of the fiber (NA = 0.14) compared to the microscope objective (NA = 0.42). To partially compensate the lower detection efficiency, we operated the devices at higher voltages under vacuum conditions (10^{-5} to 10^{-7} mbar). The integration time was typically set to 1–30 minutes for maximizing the signal to noise ratio. The acquired histogram was averaged over many cycles. The count rate under RF pulses was typically 1 kHz to 1 MHz.

Figure 4b shows the time-resolved optical emission versus the electrical signal amplitude applied with the pulse generator. The optical signal of the WG-CNT transducers follows the electrical signal for a pulse width ranging from 5 to 200 ns, albeit deviations are clearly visible. The dips at the relative times of 25 and 75 ns, after the electrical bias was switched on, might originate from the impedance mismatch between the pulse generator output and the RF probe along with on-chip electrical wiring. Upon switching the electrical signal on and off, we observe a fast initial response on a sub-nanosecond timescale, followed by an additional slower response on the scale of 10–100 ns. A similar behavior has been observed with electrically biased SWCNT films and was attributed to fast heating of SWCNTs and slow heating of the substrate [11]. We believe that this interpretation holds also for the response of our WG-CNT transducers. However, for shorter pulses the slow heating does not set in before the end of the pulse, as shown in Figure 4c. The data demonstrates a sequence of 150 ps wide pulses at 2 GHz repetition rate, which constitutes the fastest modulation for CNT transducers so far. The Fourier transfor-

mations of TSCPC histograms demonstrate the modulation of photon emission measured with different devices at 200 MHz, 500 MHz, 1 GHz and 2 GHz (Figure 4d). Higher repetition rates are limited by the setup.

In theory, the characteristic timescale of a thermal emitter τ_{therm} solely depends on the mass density ρ_{CNT}, the specific heat capacitance c_{CNT}, and thermal conductance g between the CNTs and the substrate, as pointed out previously [11,19]: $\tau_{therm} = \rho_{CNT} \cdot c_{CNT}/g$. For our CNTs with a diameter of 0.8–1.2 nm at 1000–1500 K, ρ_{CNT} varies between $0.7 \cdot 10^{-15}$ and $1.8 \cdot 10^{-15}$ kg/m, g is in the range of 0.1–0.3 W/K·m [19] and c_{CNT} = 2500–3900 Ws/kg·K [24]. c_{CNT} and consequently τ_{therm} increases with CNT diameter and with temperature. The calculated τ_{therm} for the parameter range given above is 5–70 ps, making CNTs an ultra-fast thermal light source.

Indeed by using an ultra-fast single-photon detector, we were able to prove that our WG-CNT transducers have a characteristic time scale for signal conversion of about 80 ps. Figure 4e shows measurements using single-photon detectors with different time resolutions given by the timing jitter of the detectors (350 ps for τ-SPAD and 40 ps for SNSPD for a wavelength range of 700–900 nm).

Upon switching off the electrical signal, the emission intensity decays exponentially. Experimentally, τ_{therm} extracted from a time-domain histogram (Figure 4e, measured with SNSPD) is somewhat larger than the theoretically expected value, which could be due to the decay time of electrical pulses $\tau_{pulse} \approx 80$ ps, as measured on chip (Figure 4e, black line). Moreover, the cumulative timing jitter of detector, pulse generator and connectors lead to additional broadening of the light pulse and thus increase of the measured decay time. Due to these instrumental restrictions, we are not able to determine the upper limit of the switching rate for the presented waveguide-coupled CNT-based light emitter. However, even the demonstrated rates are exceptionally high for an integrated thermal emitter on chip. Both dense films as well as single CNTs emerge as reproducible, stable light sources in the gigahertz range within our experimental resolution.

Funding

R.K. and F.P. acknowledge funding by the Volkswagen Foundation. W.P. acknowledges support by the Deutsche Forschungsgemeinschaft (DFG) grants PE 1832/1-1 & PE 1832/2-1 and the Helmholtz Association through grant HIRG-0005. W.P. also acknowledges support by the DFG and the State of Baden-Württemberg through the DFG-Center for Functional Nanostructures (CFN). F.H., M.M.K.and R.K. acknowledge support by Helmholtz Association through program Science and Technology of Nanosystems (STN) and by the Karlsruhe Nano Micro Facility (KNMF). V.K. and G.G. acknowledge financial support by Russian Foundation for Basic Research (RFBR) grant No. 15-02-07787 and State Contract No.14.B25.31.0007.

Acknowledgements

We thank "Superconducting nanotechnology" (SCONTEL) for providing SNSPDs as well as Dr. S. Lebedkin for comments that greatly improved the manuscript. We also gratefully thank S. Diewald and S. Kühn for the help with device fabrication.

References

1. Misewich, J. A.; Martel, R.; Avouris, P.; Tsang, J. C.; Heinze, S.; Tersoff, J. *Science* **2003,** *300,* 783–786. doi:10.1126/science.1081294
2. Avouris, P.; Freitag, M.; Perebeinos, V. *Nat. Photonics* **2008,** *2,* 341–350. doi:10.1038/nphoton.2008.94
3. Rai, P.; Hartmann, N.; Berthelot, J.; Arocas, J.; Colas Des Francs, G.; Hartschuh, A.; Bouhelier, A. *Phys. Rev. Lett.* **2013,** *111,* 026804. doi:10.1103/PhysRevLett.111.026804
4. Khasminskaya, S.; Pyatkov, F.; Flavel, B. S.; Pernice, W. H.; Krupke, R. *Adv. Mater.* **2014,** *26,* 3465–3472. doi:10.1002/adma.201305634
5. Fechner, R. G.; Pyatkov, F.; Khasminskaya, S.; Flavel, B. S.; Krupke, R.; Pernice, W. H. P. *Opt. Express* **2016,** *24,* 966. doi:10.1364/OE.24.000966
6. Pyatkov, F.; Fütterling, V.; Khasminskaya, S.; Flavel, B. S.; Henrich, F.; Kappes, M. M.; Krupke, R.; Pernice, W. H. P. *Nat. Photonics* **2016,** *10,* 420–427. doi:10.1038/nphoton.2016.70
7. Khasminskaya, S.; Pyatkov, F.; Słowik, K.; Ferrari, S.; Kahl, O.; Kovalyuk, V.; Rath, P.; Vetter, A.; Hennrich, F.; Kappes, M. M.; Gol'tsman, G.; Korneev, A.; Rockstuhl, C.; Krupke, R.; Pernice, W. H. P. *Nat. Photonics* **2016,** *10,* 727–733. doi:10.1038/nphoton.2016.178
8. Gaufrès, E.; Izard, N.; Noury, A.; Le Roux, X.; Rasigade, G.; Beck, A.; Vivien, L.; Roux, X. L. *ACS Nano* **2012,** *6,* 3813–3819. doi:10.1021/nn204924n
9. Watahiki, R.; Shimada, T.; Zhao, P.; Chiashi, S.; Iwamoto, S.; Arakawa, Y.; Maruyama, S.; Kato, Y. K. *Appl. Phys. Lett.* **2012,** *101,* 141124. doi:10.1063/1.4757876
10. Miura, R.; Imamura, S.; Ohta, R.; Ishii, A.; Liu, X.; Shimada, T.; Iwamoto, S.; Arakawa, Y.; Kato, Y. K. *Nat. Commun.* **2014,** *5,* 5580. doi:10.1038/ncomms6580
11. Mori, T.; Yamauchi, Y.; Honda, S.; Maki, H. *Nano Lett.* **2014,** *14,* 3277–3283. doi:10.1021/nl500693x
12. Vijayaraghavan, A.; Blatt, S.; Weissenberger, D.; Oron-Carl, M.; Hennrich, F.; Gerthsen, D.; Hahn, H.; Krupke, R. *Nano Lett.* **2007,** *7,* 1556–1560. doi:10.1021/nl0703727
13. Vijayaraghavan, A.; Hennrich, F.; Stürzl, N.; Engel, M.; Ganzhorn, M.; Oron-Carl, M.; Marquardt, C. W.; Dehm, S.; Lebedkin, S.; Kappes, M. M.; Krupke, R. *ACS Nano* **2010,** *4,* 2748–2754. doi:10.1021/nn100337t
14. Moshammer, K.; Hennrich, F.; Kappes, M. M. *Nano Res.* **2009,** *2,* 599–606. doi:10.1007/s12274-009-9057-0
15. Marquardt, C. W.; Grunder, S.; Błaszczyk, A.; Dehm, S.; Hennrich, F.; Löhneysen, H.; Mayor, M.; Krupke, R. *Nat. Nanotechnol.* **2010,** *5,* 863–867. doi:10.1038/nnano.2010.230

16. Kim, Y. D.; Kim, H.; Cho, Y.; Ryoo, J. H.; Park, C.-H.; Kim, P.; Kim, Y. S.; Lee, S.; Li, Y.; Park, S.-N.; Yoo, Y. S.; Yoon, D.; Dorgan, V. E.; Pop, E.; Heinz, T. F.; Hone, J.; Chun, S.-H.; Cheong, H.; Lee, S. W.; Bae, M.-H.; Park, Y. D. *Nat. Nanotechnol.* **2015,** *10,* 676–681. doi:10.1038/nnano.2015.118
17. Mann, D.; Kato, Y. K.; Kinkhabwala, A.; Pop, E.; Cao, J.; Wang, X.; Zhang, L.; Wang, Q.; Guo, J.; Dai, H. *Nat. Nanotechnol.* **2007,** *2,* 33–38. doi:10.1038/nnano.2006.169
18. Yao, Z.; Kane, C. L.; Dekker, C. *Phys. Rev. Lett.* **2000,** *84,* 2941–2944. doi:10.1103/PhysRevLett.84.2941
19. Pop, E.; Mann, D. A.; Goodson, K. E.; Dai, H. *J. Appl. Phys.* **2007,** *101,* 093710. doi:10.1063/1.2717855
20. Marquardt, C. W.; Dehm, S.; Vijayaraghavan, A.; Blatt, S.; Hennrich, F.; Krupke, R. *Nano Lett.* **2008,** *8,* 2767–2772. doi:10.1021/nl801288d
21. Ma, Z.; Liang, S.; Liu, Y.; Wang, F.; Wang, S.; Peng, L.-M. *Appl. Phys. Lett.* **2016,** *108,* 63114. doi:10.1063/1.4941813
22. Gol'tsman, G. N.; Okunev, O.; Chulkova, G.; Lipatov, A.; Semenov, A.; Smirnov, K.; Voronov, B.; Dzardanov, A.; Williams, C.; Sobolewski, R. *Appl. Phys. Lett.* **2001,** *79,* 705–707. doi:10.1063/1.1388868
23. Kapusta, P.; Wahl, M.; Erdmann, R., Eds. *Advanced Photon Counting;* Springer Series on Fluorescence, Vol. 15; Springer: Berlin, Germany, 2015. doi:10.1007/978-3-319-15636-1
24. Hepplestone, S. P.; Ciavarella, A. M.; Janke, C.; Srivastava, G. P. *Surf. Sci.* **2006,** *600,* 3633–3636. doi:10.1016/j.susc.2005.12.070

License and Terms

This is an Open Access article under the terms of the Creative Commons Attribution License (http://creativecommons.org/licenses/by/4.0), which permits unrestricted use, distribution, and reproduction in any medium, provided the original work is properly cited.

The license is subject to the *Beilstein Journal of Nanotechnology* terms and conditions: (http://www.beilstein-journals.org/bjnano)

The definitive version of this article is the electronic one which can be found at: doi:10.3762/bjnano.8.5

BEILSTEIN JOURNAL OF NANOTECHNOLOGY

Selective photodissociation of tailored molecular tags as a tool for quantum optics

Ugur Sezer[1], Philipp Geyer[1], Moritz Kriegleder[1], Maxime Debiossac[1], Armin Shayeghi[1], Markus Arndt[1], Lukas Felix[2] and Marcel Mayor[*2,3,4]

Full Research Paper

Open Access

Address:
[1]Faculty of Physics, VCQ, University of Vienna, Boltzmanngasse 5, A-1090 Vienna, Austria, [2]Department of Chemistry, University of Basel, St. Johannsring 19, CH-4056 Basel, Switzerland, [3]Institute of Nanotechnology (INT), Karlsruhe Institute of Technology (KIT), Hermann-von-Helmholtz-Platz 1, D-76344 Eggenstein-Leopoldshafen, Germany and [4]Lehn Institute of Functional Materials (LIFM), Sun Yat-Sen University (SYSU), Xingang Rd. W., Guangzhou, China

Email:
Marcel Mayor* - marcel.mayor@unibas.ch

* Corresponding author

Keywords:
molecular quantum optics; photodepletion; photodissociation; synthetic photo-tags

Beilstein J. Nanotechnol. **2017,** *8,* 325–333.
doi:10.3762/bjnano.8.35

Received: 18 September 2016
Accepted: 17 January 2017
Published: 02 February 2017

This article is part of the Thematic Series "Advances in nanomaterials II".

Guest Editor: H. Hahn

© 2017 Sezer et al.; licensee Beilstein-Institut.
License and terms: see end of document.

Abstract

Recent progress in synthetic chemistry and molecular quantum optics has enabled demonstrations of the quantum mechanical wave–particle duality for complex particles, with masses exceeding 10 kDa. Future experiments with even larger objects will require new optical preparation and manipulation methods that shall profit from the possibility to cleave a well-defined molecular tag from a larger parent molecule. Here we present the design and synthesis of two model compounds as well as evidence for the photoinduced beam depletion in high vacuum in one case.

Introduction

Chemistry builds on the fact that the electronic structure, dynamics and properties of molecules are determined or influenced by quantum effects. However, it has only recently been experimentally verified that also the translational motion of an entire complex molecule has to be described by a quantum wave function under appropriate circumstances [1,2].

Since the de Broglie wave nature of atoms has already become a central element in sensitive matter-wave interferometers with applications in geodesy, navigation and fundamental science [3], it is now natural to ask how complex an object may be while still displaying quantum delocalization over macroscopic times and length scales [4,5]. Matter-waves can then become tools for chemistry too, for instance in novel measurements of molecular properties [6-8].

First experiments with complex molecules realized the idea of Young's double slit experiment and demonstrated diffraction of

fullerenes [1] and functionalized phthalocyanines [9] at nanomechanical gratings. Later studies used variants of Talbot–Lau interferometry to demonstrate the quantum wave nature of more than a dozen of different molecules and clusters [10-16], up to tailored porphyrin derivatives as massive as 10 kDa [17]. In these experiments, every single molecule contained 810 atoms and yet it still needed to be described by a quantum wave function with a de Broglie wavelength of 300–500 fm. The molecular coherence spanned several hundred nanometers for several milliseconds [17].

We are now looking for new techniques which shall enable new molecular matter-wave experiments. We are in particular interested in identifying an optical depletion mechanism for molecular beams, since this will enable the realization of absorptive optical gratings. Standing waves of light can imprint a spatially periodic structure onto molecular beams – very similar to nanomechanical material gratings – if they are capable of depleting the molecular beam in the antinodes of the optical grating. In previous studies, this goal has been achieved by exposing molecules to a vacuum ultra-violet (VUV) light emitted by a laser of 157.6 nm wavelength [18,19]. The light field can ionize or dissociate the incident clusters of molecules in the anti-nodes of the optical gratings [13,18,20].

These previous attempts proved successful but were not yet generally scalable to covalently bound organic molecules. In particular, large biomolecules – which are interesting candidates for quantum-interference experiments and gas-phase metrology [7] – often neither ionize nor dissociate upon absorption of a single photon, not even at 7.9 eV photon energy [21].

Here we address this challenge and study tailored tags that are optimized to respond to light of lower photon energy with cleavage at a deterministic location. Click chemistry shall then allow attaching them to a wide class of analyte molecules and thus solve the problem.

Results

Design of the model compounds

A large number of photocleavable groups can be found in the literature [22]. Here, we have chosen a 2-(phenoxymethyl)-1-nitrobenzene motive as photocleavable linker, because of its photoinduced cleavage sequence, sketched in Figure 1. It requires only the intramolecular exchange of electrons and atoms but no solvent molecule in this cleaving mechanism. Our hypothesis is that this independence increases the cleavage probability also for molecules in high vacuum – even though the solvent may still support the process by stabilizing certain intermediates. The photocleavable label was further decorated with an ethynyl group in 5-position as a functional group that enables various coupling procedures and which can link the functional subunit to the structure of interest (e.g., R^1 in Figure 1). We also add CF_3 groups to the phenol subunit which shall be released upon photocleavage in order to increase the molecular weight while keeping the molecular polarizability low. Former experiments have shown that the perfluoroalkyl-functionalization of complex molecules can reduce the intermolecular adhesion, facilitate the volatilization and thus also facilitate the formation of a molecular beam [23,24]. It is also important to tailor the mass of the ejected fragment because one may later use the momentum transfer in this process to remove both fragments from an initially tightly collimated molecular beam.

The photoresponse of the nitrobenzyl group has been studied in great detail in solution [22,25] and the sequence resulting in the separation of both subunits is summarized in Figure 1. After excitation with UV-light from its equilibrium form to the singlet state $\mathbf{S_1}$, the molecule decays to the triplet state $\mathbf{T_1}$ which can undergo a hydrogen transfer to yield the *E*-aci-nitro form. The latter decays over the cyclic isoxazol form to a 2-nitrosobenzaldehyde and a phenol subunit (red in Figure 1). Even though the reaction sequence is well understood in solution, it remains an open question if a similar cleavage occurs and which decay channels are accessible when the photoactive molecule is isolated in high vacuum at 300 K or more. For that to happen, a number of complex reactions and atomic position changes need to be allowed. They may change in the absence of solvent molecules which provide both a polarizable environment, possibly stabilizing dipole moments of transition states, and a thermal bath for energy and momentum exchange.

For our proof-of-principle investigation we assembled the model compound **1**, which consists of a central benzene core and three of the photocleavable subunits. The symmetric arrangement of three subunits was meant to lower the resonant absorption energy and to enhance the effective cross section for photoabsorption and cleavage.

The synthesis of the target structure **1** is displayed in Scheme 1. Reduction of the commercially available 4-bromo-2-nitrobenzaldehyde with sodium borohydride gave the benzyl alcohol **2**, which was obtained in quantitative yield after column chromatography (CC) as colourless solid. Applying Mitsunobu reaction conditions, the benzyl ether **3** was obtained from **2** and 3,5-bis(trifluoromethyl)phenol. The reagents were dissolved in 0 °C cold tetrahydrofuran (THF) while diisopropyl azodicarboxylate (DIAD) was added dropwise. After stirring for 12 h in the dark, work-up followed by CC provided **3** in 96% yield as colourless solid. The bromine substituent of **3** was substituted by trimethylsilylacetylene using Sonogashira conditions. The aryl bromide **3** and trimethylsilylacetylene were dissolved in tri-

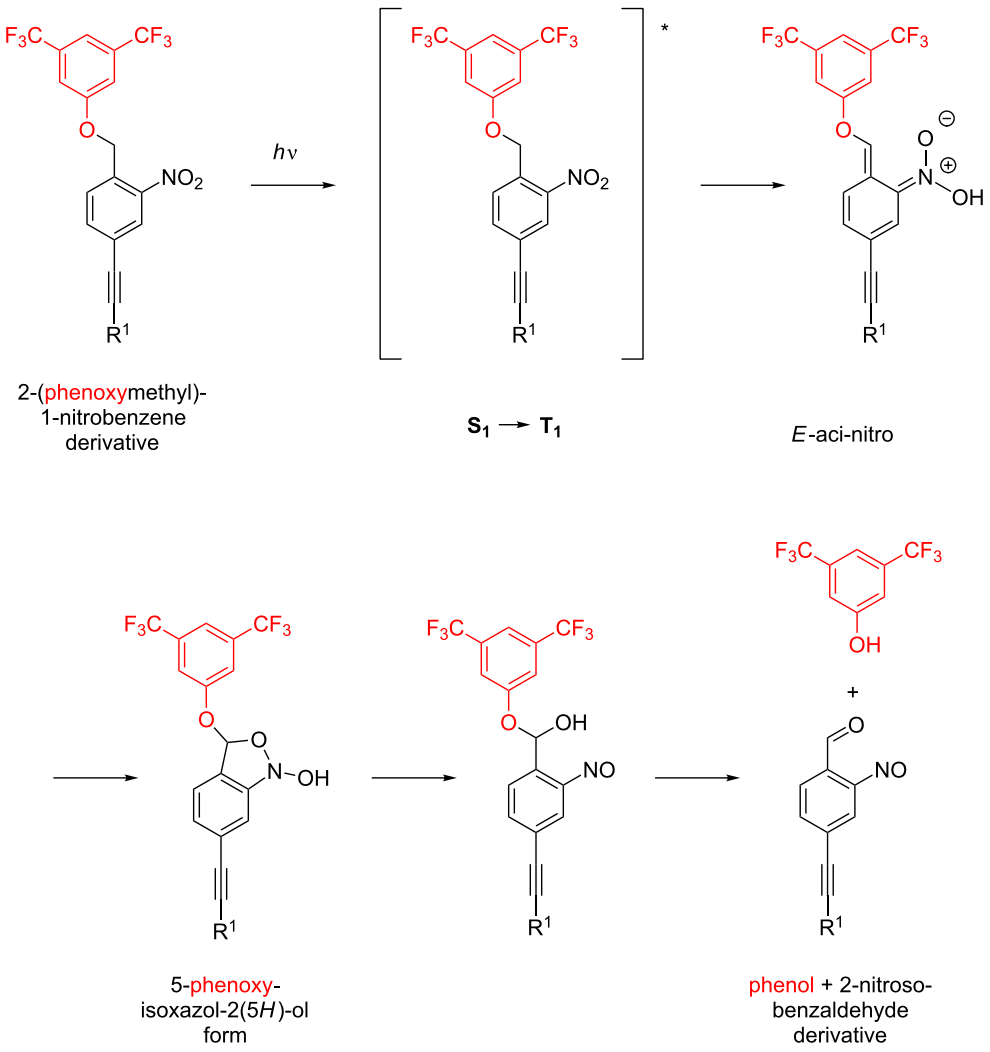


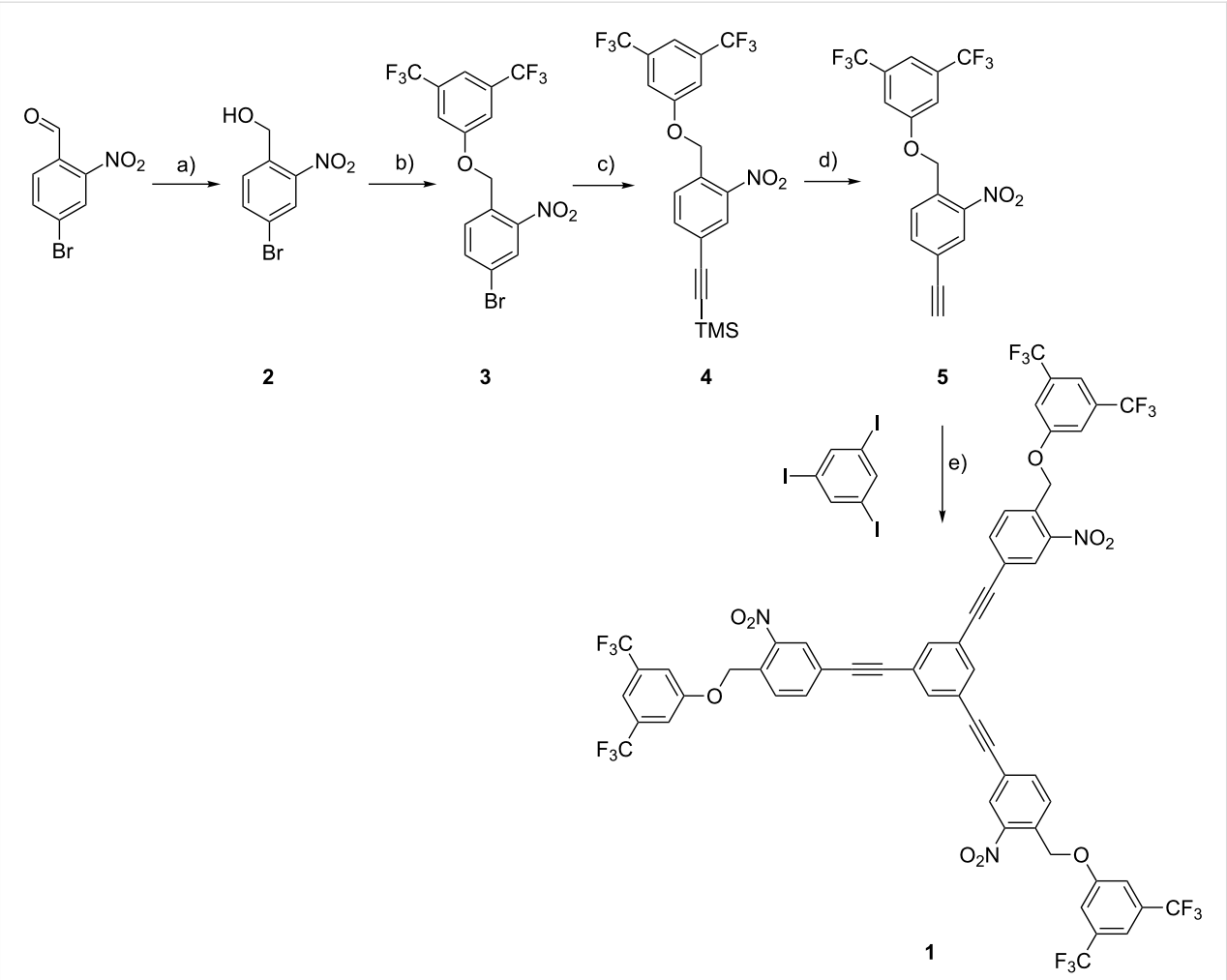
Figure 1: Sketch of the photocleavable 2-(phenoxymethyl)-1-nitrobenzene subunit and its intramolecular photon induced degradation sequence which leads to the release of the phenol subunit (red).

ethylamine (TEA) and $Pd(PPh_3)_4$ and CuI were added as catalysts, before the reaction mixture was refluxed for 12 h. Work-up by CC provided the TMS-ethynyl functionalized benzyl ether **4** in 99% yield as colourless solid. Treatment of **4** with tetrabutylammonium fluoride (TBAF) in a dichloromethane/THF mixture provided the free arylethynyl **5** in quantitative yield. The trimeric target compound **1** was also synthesized using Sonogashira coupling conditions. 1,3,5-Triiodobenzene together with 4.5 equiv of the arylethynyl **5** were dissolved in a THF/TEA (3:1) mixture, to which catalytic amounts (5 mol %) of $Pd(PPh_3)_4$ and CuI were added before the reaction mixture was warmed up to 50 °C for 12 h. Aqueous work-up and recrystallization of the crude reaction product from chloroform provided the target compound **1** in 80% yield as colourless solid.

All new compounds were fully characterized by ^{1}H, ^{19}F and ^{13}C NMR spectroscopy and high-resolution mass spectrometry (HRMS). Detailed experimental protocols together with analytical data are provided in Supporting Information File 1.

Photocleavage in solution

The photoinduced degradation of the target compound was first studied in solution. Initially, we planned to investigate the photocleavage of the target trimer **1** by NMR spectroscopy to be able to analyse the products of the photodegradation. Due to the poor solubility of the trimer **1**, these studies were made with the monomeric building block **4**, which allowed for suitable concentrations in dichloromethane-d_2 for the NMR experiment. In a qualitative degradation experiment, the NMR tube was



Scheme 1: Synthesis of the trimeric target structure **1**. Reagents and conditions: a) $NaBH_4$, THF, 30 min, rt, quant.; b) 3,5-bis(trifluoromethyl)phenol, DIAD, Ph_3P, THF, 12 h, rt, 96%; c) TMS-CC-H, $Pd(PPh_3)_4$, CuI, TEA, 90 °C, 12 h, 99%; d) TBAF (1 M in THF), CH_2Cl_2, rt, 30 min, quant.; e) 1,3,5-triiodobenzene, **5** (4.5 equiv), $Pd(PPh_3)_4$, CuI, THF/TEA (3:1), 12 h, 50 °C, 80%.

directly irradiated inside the NMR spectrometer with a glass fibre exposing the sample to the 355 nm light from an 8 W UV lamp, filtered by a monochromator with a spectral transmission band of 2 nm. As expected, the formation of the nitrosoaldehyde **6** and the 3,5-bis(trifluoromethyl)phenol (**7**) were observed during irradiation. Figure 2 displays the increase of the aldehyde proton (H_A) at 10.35 ppm with increasing duration of the light exposure.

The limited solubility of the trimer **1** prevented the investigation of its photodegradation by the same set-up. We therefore analysed its photoresponse using UV absorption spectroscopy.

Figure 3 displays the decay of the UV absorption of the trimer **1** in CH_2Cl_2 upon illumination by UV light at 254 nm and 365 nm respectively. The UV cuvette was exposed to a UV-lamp (8 W, 230 V, 50 Hz) at a constant distance of 1.5 cm. In order to avoid variations in concentrations, the solvent level in the cuvette was kept constant during the illumination experiment. An exponentially decaying molar extinction coefficient measured at the absorption maximum of 289 nm shows the photochemical activity of the compound. The initial extinction coefficient of $\varepsilon_{pc} \simeq 1.4 \times 10^5$ L·mol^{-1}·cm^{-1} corresponds to an absorption cross section of $\sigma_{pc} \simeq 5.7 \times 10^{-16}$ cm^2. The photodecay upon exposure to the more energetic 254 nm photons is about twice as fast compared to the 365 nm illumination.

In summary, the NMR measurements as well as the solution spectra display the expected photodegradation of these model compounds in solution. Their optical properties and photoreaction pathways may, however, vary in high vacuum, where the stabilization of the intermediates by surrounding solvent molecules is no longer possible and bathochromic line shifts and broadenings are common.

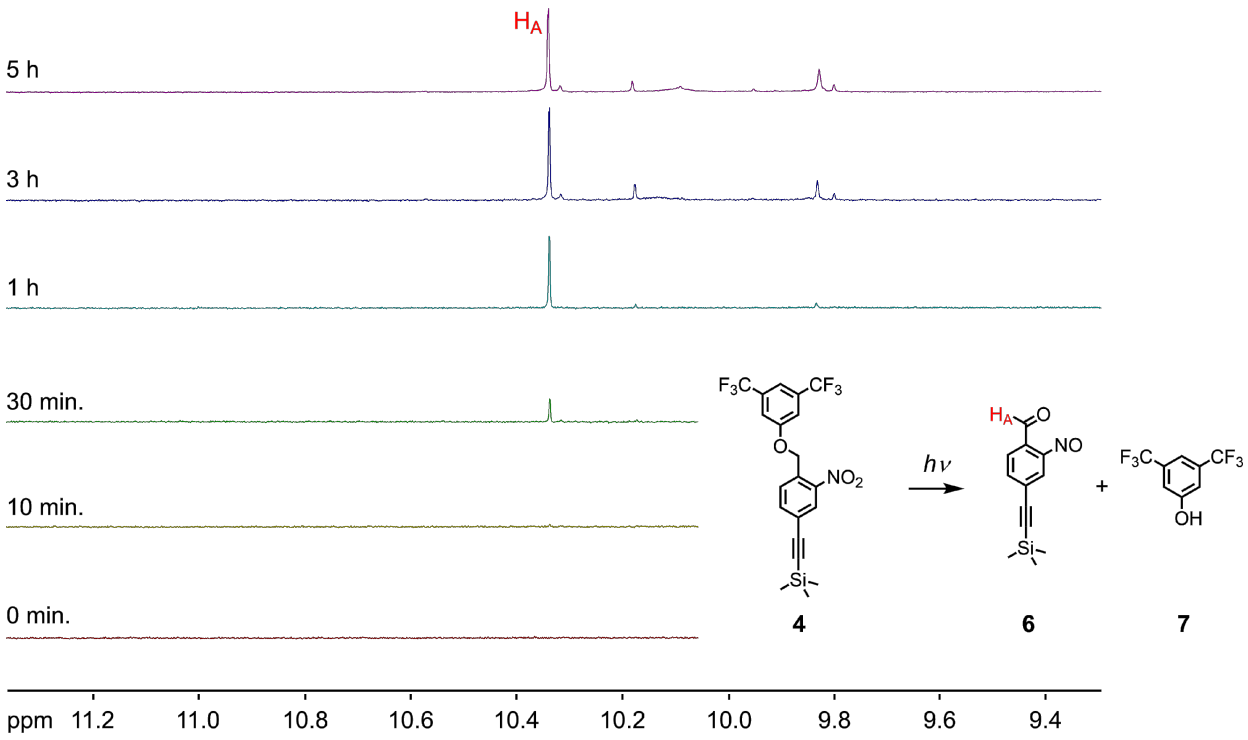


Figure 2: Qualitative photocleavage experiment of the monomer **4** irradiated at 355 nm inside the NMR spectrometer. The background displays the increase of the aldehyde signal of the 2-nitrosoaldehyde **6** with increasing light exposure.

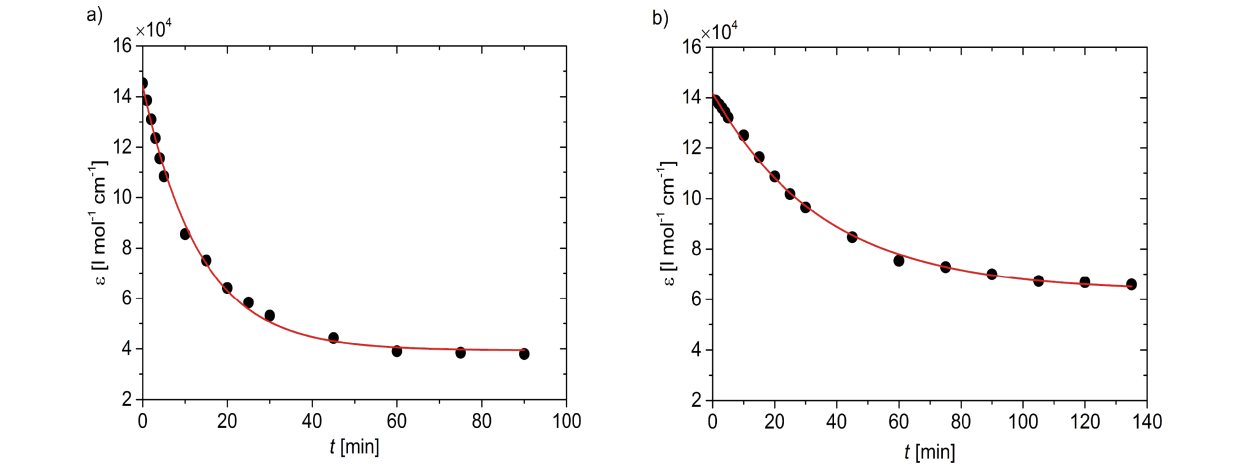


Figure 3: Continuous illumination of the trimer **1** in dichloromethane solution by UV light of 254 nm (a) and 365 nm (b). The exponential decay (red line) of the molar extinction coefficient illustrates the phototriggered dissociation of the parent structure.

Photoresponse of neutral model compounds in high vacuum

Experiments with neutral molecules were done in a molecular beam machine as sketched in Figure 4. In order to generate a pulsed beam of isolated neutral molecules we used nanosecond pulsed laser desorption into a supersonic neon seed gas jet [26]. The solid material was dissolved and spread on a glassy carbon wheel, from where it was desorbed by a 1064 nm laser pulse (10 ns duration, 38 mJ pulse energy, 10 Hz repetition rate, 3 mm beam waist). The laser pulse was synchronized with the opening of a pulsed Even–Lavie valve, 3 mm in front of the laser plume. Starting from a 30 bar stagnation pressure at room temperature, the neon gas cools down during the expansion and entrains the analyte molecules.

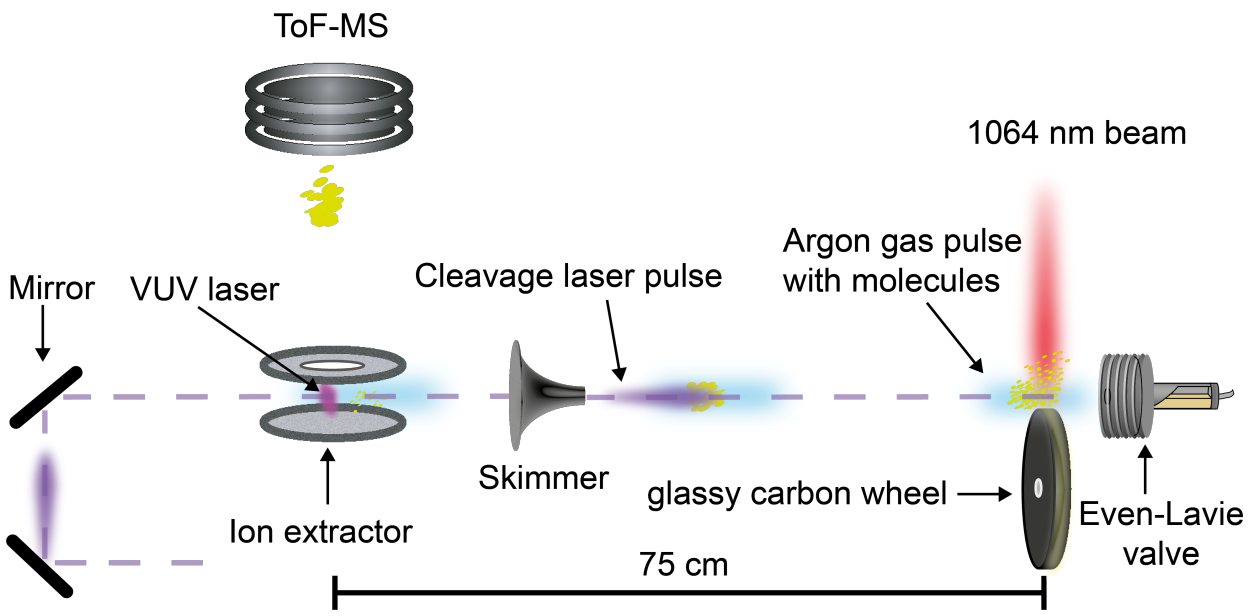


Figure 4: Molecular beam machine to study the photodepletion of the photoactive monomer in high vacuum. The pulsed infrared laser beam desorbs the molecules which are entrained by the adiabatically expanding neon gas jet. The neutral beam propagates for 75 cm in high vacuum before it is ionized by the pulsed radiation of a 157.6 nm F_2 laser and analysed in a time-of-flight mass spectrometer. On the way to the detector the molecular beam is exposed to a collinear UV laser beam at 266 nm.

The molecular beam propagates over 75 cm towards the extraction region of a time-of-flight mass spectrometer where it is crossed and ionized by the beam of a pulsed vacuum-ultraviolet fluorine (F_2) laser. The laser pulse has an energy of up to 1.1 mJ in 10 ns at a wavelength of 157.6 nm. The base pressure in the chamber was 6×10^{-7} mbar. The post-ionized particles were then extracted and the time-resolved ion signal was amplified and recorded by a fast digitizing oscilloscope. We verified that no ions were detected from the source in the absence of the VUV light.

In order to test for photoinduced dissociation in high vacuum, a 266 nm UV laser beam was aligned parallel and counter-propagating to the molecular beam. This UV beam was derived from a frequency quadrupled Nd–YAG laser with up to 5 mJ pulse energy, 7 ns pulse duration, and 10 Hz repetition rate (3.3(1) mm beam diameter).

In solution, the UV light led to strong cleavage of both the monomer **4** and the trimer **1** – with similar absorption cross sections at 254 nm and 366 nm – but faster decay at higher photon energy. Preliminary dissociation experiments at 355 nm did not reveal any major cleavage of the trimer **1** at the laser energies that were sufficient to cleave the monomer **4** at 266 nm. Because of this, the following experiments were performed exclusively on the monomer.

Photoresponse of the monomer **4**

When we shine 266 nm light onto the propagating beam of isolated monomers, we observe a depletion of the parent signal, as shown in Figure 5 (red line). Even in the absence of any UV light, one can see fragments which we attribute to the IR laser desorption (black line in Figure 5). The strongest beam depletion was observed when the 266 nm laser pulse arrived about 600 µs before the VUV ionizing laser pulse, i.e., shortly behind the beam source. Neutral fragments emerging from that process will experience a dissociative recoil that kicks them beyond the detector acceptance angle of 4 mrad.

In Figure 6, we plot the decay of the monomer ion signal as a function of the UV depletion pulse energy, with all other settings as for Figure 5. We deplete the beam by more than 50%. Using the exponential decay

$$I/I_0 = (1-\alpha) + \alpha \cdot \exp(-\sigma_{dep} \cdot \Phi),$$

we find the experimental beam overlap parameter $\alpha = 0.64(8)$ and an in-vacuum beam depletion cross section $\sigma_{dep} = 0.4(2)$ Å^2 $= 4(2) \times 10^{-17}$ cm^2 where Φ is the laser fluence, i.e., the photon number in a single pulse per laser beam area.

The depletion of the parent signal is attributed to photoactivated dissociation. To exclude the contribution of ionization, we

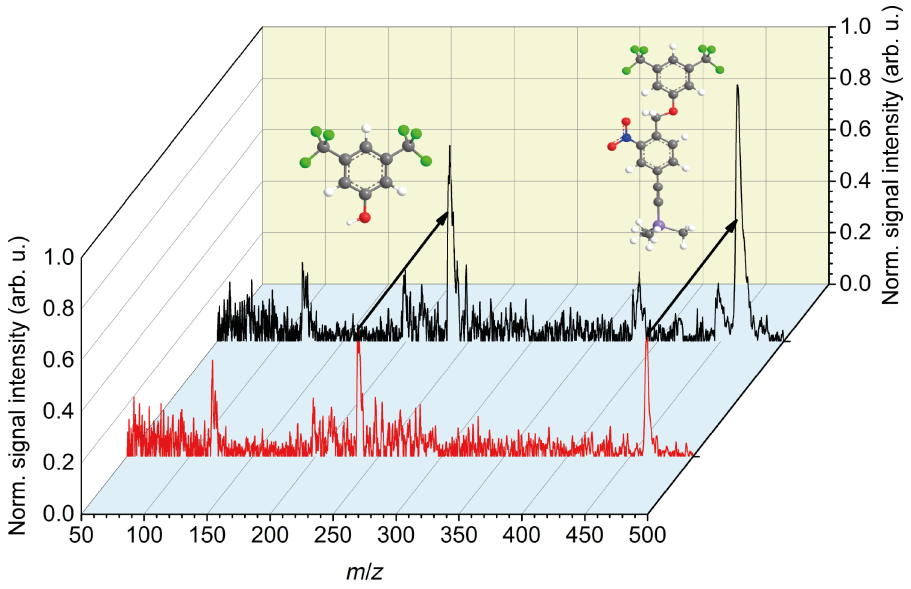


Figure 5: Photodepletion of the photocleavable nitrobenzyl derivative. When the dissociation laser pulse with an energy of 3.7(1) mJ in a beam diameter of 3.3(1) mm preceded the VUV ionization pulse by 600 µs, we observed beam depletion of the neutral parent molecule by a factor of four (red curve). The black spectrum represents the calibration curve without cleavage laser beam.

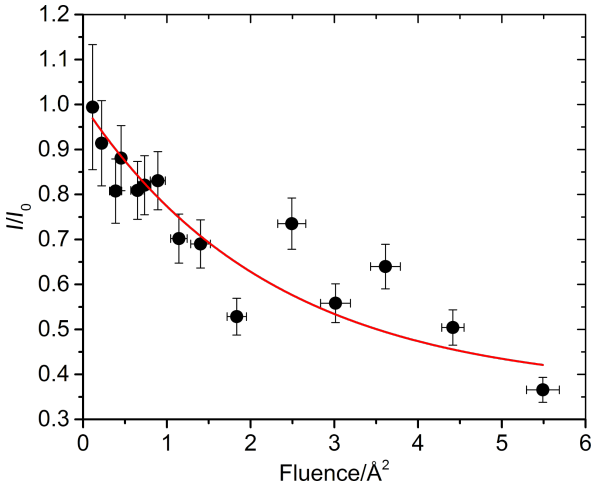


Figure 6: Depletion ratio, i.e., fraction of remaining parent molecules, versus laser fluence (photons per pulse and area). The continuous line is a fit to the data to derive the depletion cross section of the photoactive monomer.

have verified that the 266 nm light does not lead to any additional photoions when the UV laser pulse coincides with the ionizing VUV pulse. In this configuration it only enhances the parent signal, indicating absorption and heating of the monomer. We cannot exclude that the same thermal process leads to delayed fragmentation and subsequent beam depletion. However, the strong decay of the parent peak compared to its fragment is consistent with the picture that the fragment has no second remaining 'weak link'.

Discussion and Conclusion

A novel concept for the realization of optical gratings based on photocleavable subunits is presented. For that purpose, we have designed, synthesized and characterized a molecular tag based on a 2-(phenoxymethyl)-1-nitrobenzene motive comprising an ethynyl group enabling its modular attachment by covalent coupling chemistry. The covalent attachment has been demonstrated with the trimeric model compound **1** while the here presented preliminary gas-phase photocleavage experiments have been performed with the monomeric building block **4**, which displayed favourable photodissociation features compared to **1**. Interestingly we find that photoactivated molecular beam depletion is even possible in high vacuum and with a cross section high enough for accessible laser sources.

When isolated in high vacuum many details of the photochemistry are expected to change, opening interesting questions for future research with regard to the time-dependent reaction pathways in the gas-phase.

For future applications in molecule interferometry with complex biomolecules, it will be important that beam depletion is possible at a wavelength which is not absorbed by the untagged molecule. Otherwise the photon would be dissipated without triggering any action. Our labels are chosen such that they respond at 250–270 nm and 350–370 nm, i.e., at wavelengths longer than typical resonance lines in non-aromatic biomolecules. We expect photocleavage to become important for the realization of optical gratings and for the photoactivated change

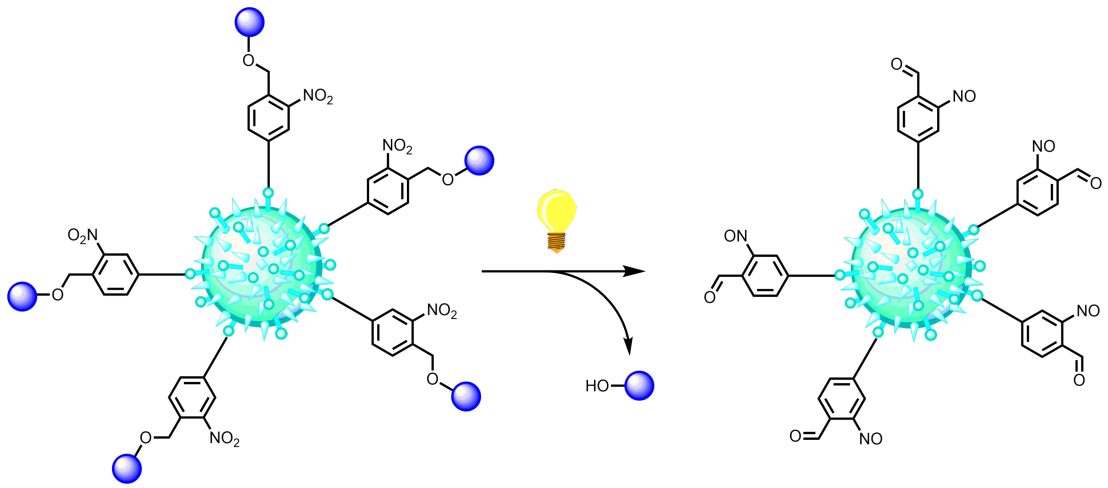


Figure 7: Bond-selective dissociation and photoinduced beam depletion shall enable novel absorptive optical gratings for complex nanobiological materials, which cannot be handled by established optical manipulation techniques based on photoionization. The idea is here illustrated for a nitrobenzyl tagged virus (artist's view).

of the charge state in mesoscopic objects. Both will be crucial for molecular quantum optics and future matter-wave experiments. An open future challenge will be to explore how well this method scales with the size of particles from individual monomer to trimers, chromophore-labelled biomolecules up to decorated viruses, as displayed as visionary sketch in Figure 7. Currently we are investigating the potential of the concept for biomolecules with tagged oligo- and poly-peptides.

Supporting Information

Here we describe the synthesis and characterisation of the chemical compounds and the photocleavable molecules used for this study.

Supporting Information File 1

Synthetic protocols.
[http://www.beilstein-journals.org/bjnano/content/supplementary/2190-4286-8-35-S1.pdf]

Dedication

This contribution is dedicated to Herbert Gleiter, a pioneer of nanotechnology with a joint passion in the foundations of physics and matter-waves.

Acknowledgements

We acknowledge financial support by the European Research Council in project 320694, the Austrian Science Funds FWF W1210-3, the Swiss National Science Foundation (200020_159730), and the Swiss Nanoscience Institute (P1403).

References

1. Arndt, M.; Nairz, O.; Voss-Andreae, J.; Keller, C.; van der Zouw, G.; Zeilinger, A. *Nature* **1999,** *401,* 680–682. doi:10.1038/44348
2. Juffmann, T. Surface based detection schemes for molecular matter-wave interferometry. Ph.D. Thesis, University of Vienna, Austria, 2012.
3. Tino, G.; Kasevich, M. *Atom Interferometry. Proceedings of the International School of Physics "Enrico Fermi";* IOS Press: Amsterdam, The Netherlands, 2014; Vol. 188.
4. Arndt, M.; Hornberger, K. *Nat. Phys.* **2014,** *10,* 271–277. doi:10.1038/nphys2863
5. Arndt, M.; Juffmann, T.; Vedral, V. *HFSP J.* **2009,** *3,* 386–400. doi:10.2976/1.3244985
6. Arndt, M.; Dörre, N.; Eibenberger, S.; Haslinger, P.; Rodewald, J.; Hornberger, K.; Nimmrichter, S.; Mayor, M. Matter-wave interferometry with composite quantum objects. In *Atom Interferometry, Proceedings of the International School of Physics "Enrico Fermi";* Tino, G. M.; Kasevich, M., Eds.; IOS Press: Amsterdam, The Netherlands, 2014; Vol. 188, pp 89–141. arXiv:1501.07770.
7. Arndt, M. *Phys. Today* **2014,** *67,* 30–36. doi:10.1063/PT.3.2381
8. Gerlich, S.; Gring, M.; Ulbricht, H.; Hornberger, K.; Tüxen, J.; Mayor, M.; Arndt, M. *Angew. Chem., Int. Ed.* **2008,** *47,* 6195–6198. doi:10.1002/anie.200801942
9. Juffmann, T.; Milic, A.; Müllneritsch, M.; Asenbaum, P.; Tsukernik, A.; Tüxen, J.; Mayor, M.; Cheshnovsky, O.; Arndt, M. *Nat. Nanotechnol.* **2012,** *7,* 297–300. doi:10.1038/nnano.2012.34
10. Gerlich, S.; Eibenberger, S.; Tomandl, M.; Nimmrichter, S.; Hornberger, K.; Fagan, P. J.; Tüxen, J.; Mayor, M.; Arndt, M. *Nat. Commun.* **2011,** *2,* 263. doi:10.1038/ncomms1263
11. Gerlich, S.; Hackermüller, L.; Hornberger, K.; Stibor, A.; Ulbricht, H.; Gring, M.; Goldfarb, F.; Savas, T.; Müri, M.; Mayor, M.; Arndt, M. *Nat. Phys.* **2007,** *3,* 711–715. doi:10.1038/nphys701
12. Hornberger, K.; Gerlich, S.; Haslinger, P.; Nimmrichter, S.; Arndt, M. *Rev. Mod. Phys.* **2012,** *84,* 157–173. doi:10.1103/RevModPhys.84.157

13. Haslinger, P.; Dörre, N.; Geyer, P.; Rodewald, J.; Nimmrichter, S.; Arndt, M. *Nat. Phys.* **2013,** *9,* 144–148. doi:10.1038/nphys2542
14. Brezger, B.; Arndt, M.; Zeilinger, A. *J. Opt. B: Quantum Semiclassical Opt.* **2003,** *5,* 82–89. doi:10.1088/1464-4266/5/2/362
15. Brezger, B.; Hackermüller, L.; Uttenthaler, S.; Petschinka, J.; Arndt, M.; Zeilinger, A. *Phys. Rev. Lett.* **2002,** *88,* 100404. doi:10.1103/PhysRevLett.88.100404
16. Hackermüller, L.; Uttenthaler, S.; Hornberger, K.; Reiger, E.; Brezger, B.; Zeilinger, A.; Arndt, M. *Phys. Rev. Lett.* **2003,** *91,* 090408. doi:10.1103/PhysRevLett.91.090408
17. Eibenberger, S.; Gerlich, S.; Arndt, M.; Mayor, M.; Tüxen, J. *Phys. Chem. Chem. Phys.* **2013,** *15,* 14696–14700. doi:10.1039/c3cp51500a
18. Reiger, E.; Hackermüller, L.; Berninger, M.; Arndt, M. *Opt. Commun.* **2006,** *264,* 326–332. doi:10.1016/j.optcom.2006.02.060
19. Haslinger, P. A universal matter-wave interferometer with optical gratings. Ph.D. Thesis, University of Vienna, Austria, 2013.
20. Dörre, N.; Rodewald, J.; Geyer, P.; von Issendorff, B.; Haslinger, P.; Arndt, M. *Phys. Rev. Lett.* **2014,** *113,* 233001. doi:10.1103/PhysRevLett.113.233001
21. Schlag, E. W.; Grotemeyer, J.; Levine, R. D. *Chem. Phys. Lett.* **1992,** *190,* 521–527. doi:10.1016/0009-2614(92)85185-D
22. Klán, P.; Šolomek, T.; Bochet, C. G.; Blanc, A.; Givens, R.; Rubina, M.; Popik, V.; Kostikov, A.; Wirz, J. *Chem. Rev.* **2013,** *113,* 119–191. doi:10.1021/cr300177k
23. Sezer, U.; Schmid, P.; Felix, L.; Mayor, M.; Arndt, M. *J. Mass Spectrom.* **2015,** *50,* 235–239. doi:10.1002/jms.3526
24. Sezer, U.; Wörner, L.; Horak, J.; Felix, L.; Tüxen, J.; Götz, C.; Vaziri, A.; Mayor, M.; Arndt, M. *Anal. Chem.* **2015,** *87,* 5614–5619. doi:10.1021/acs.analchem.5b00601
25. Il'ichev, Y. V.; Wirz, J. *J. Phys. Chem. A* **2000,** *104,* 7856–7870. doi:10.1021/jp000261v
26. Geyer, P.; Sezer, U.; Rodewald, J.; Mairhofer, L.; Dörre, N.; Haslinger, P.; Eibenberger, S.; Brand, C.; Arndt, M. *Phys. Scr.* **2016,** *91,* 063007. doi:10.1088/0031-8949/91/6/063007

License and Terms

This is an Open Access article under the terms of the Creative Commons Attribution License (http://creativecommons.org/licenses/by/4.0), which permits unrestricted use, distribution, and reproduction in any medium, provided the original work is properly cited.

The license is subject to the *Beilstein Journal of Nanotechnology* terms and conditions: (http://www.beilstein-journals.org/bjnano)

The definitive version of this article is the electronic one which can be found at: doi:10.3762/bjnano.8.35

BEILSTEIN JOURNAL OF NANOTECHNOLOGY

Copper atomic-scale transistors

Fangqing Xie*[1], Maryna N. Kavalenka[2], Moritz Röger[2], Daniel Albrecht[1], Hendrik Hölscher[2], Jürgen Leuthold[3] and Thomas Schimmel*[1,4]

Full Research Paper

Open Access

Address:
[1]Institute of Applied Physics, Karlsruhe Institute of Technology, Campus South, 76128 Karlsruhe, Germany, [2]Institute of Microstructure Technology, Karlsruhe Institute of Technology, Campus North, 76021 Karlsruhe, Germany, [3]Institute of Electromagnetic Fields, ETH Zurich, 8092 Zurich, Switzerland and [4]Institute of Nanotechnology, Karlsruhe Institute of Technology, Campus North, 76021 Karlsruhe, Germany

Email:
Fangqing Xie* - fangqing.xie@kit.edu; Thomas Schimmel* - thomas.schimmel@kit.edu

* Corresponding author

Keywords:
electrochemistry; encapsulation; metallic atomic-scale transistor; nanotechnology; photolithography

Beilstein J. Nanotechnol. **2017,** *8,* 530–538.
doi:10.3762/bjnano.8.57

Received: 15 November 2016
Accepted: 07 February 2017
Published: 01 March 2017

This article is part of the Thematic Series "Advances in nanomaterials II".

Guest Editor: H. Hahn

© 2017 Xie et al.; licensee Beilstein-Institut.
License and terms: see end of document.

Abstract

We investigated copper as a working material for metallic atomic-scale transistors and confirmed that copper atomic-scale transistors can be fabricated and operated electrochemically in a copper electrolyte ($CuSO_4 + H_2SO_4$) in bi-distilled water under ambient conditions with three microelectrodes (source, drain and gate). The electrochemical switching-on potential of the atomic-scale transistor is below 350 mV, and the switching-off potential is between 0 and −170 mV. The switching-on current is above 1 μA, which is compatible with semiconductor transistor devices. Both sign and amplitude of the voltage applied across the source and drain electrodes (U_{bias}) influence the switching rate of the transistor and the copper deposition on the electrodes, and correspondingly shift the electrochemical operation potential. The copper atomic-scale transistors can be switched using a function generator without a computer-controlled feedback switching mechanism. The copper atomic-scale transistors, with only one or two atoms at the narrowest constriction, were realized to switch between 0 and $1G_0$ ($G_0 = 2e^2/h$; with e being the electron charge, and h being Planck's constant) or $2G_0$ by the function generator. The switching rate can reach up to 10 Hz. The copper atomic-scale transistor demonstrates volatile/non-volatile dual functionalities. Such an optimal merging of the logic with memory may open a perspective for processor-in-memory and logic-in-memory architectures, using copper as an alternative working material besides silver for fully metallic atomic-scale transistors.

Introduction

Enormous research efforts worldwide are aimed at finding new solutions and technologies to manufacturing electronic components "beyond the silicon age". Resistive switching is one of the most promising alternative concepts. Resistive nanoelectronic devices are operated under one of the following switching mechanisms: electrostatic/electronic, electrochemical metalliza-

tion, valence-change memory, thermochemical memory or phase change [1-5]. Resistive devices are a non-volatile and have been systematically investigated as two-terminal memristive devices with fast switching rate, high endurance, and long retention [6-8]. While two-terminal devices are able to constitute a completely new type of logic circuits as demonstrated by crossbar circuits [9], three-terminal devices can potentially be applied as logic operation devices that can fully utilize semiconductor circuit technology. Switching mechanisms such as valence-change memory effect, thermochemical memory effect, and electrochemical metallization effect have been previously exploited for three-terminal devices in solids [10-17]. But the performance of the solid resistive-switching three-terminal devices has to be improved in terms of switching rate, endurance and retention.

This work focuses on developing a three-terminal resistive device that utilizes the electrochemical metallization effect in an aqueous electrolyte to reduce mechanical stress during cycling. Silver atomic-scale transistors that operate in an aqueous nitric electrolyte at voltages in the millivolt range were previously demonstrated [18-22]. Here, we report our progress in the development of an atomic-scale transistor with a copper quantum point contact as switching block. The fabrication and electron-transport properties of metallic point contacts have been investigated both experimentally and theoretically [23-41]. The copper atomic-scale point contacts have been fabricated as mechanically controllable break junctions (MCBJ) [42-45], by using scanning probe microscopy (SPM) with a conductive tip [46,47], or electrochemical techniques [24-26,48,49]. Copper is an interconnection material in ultra-large scale integrated (ULSI) circuits, and its use as a working material for fully metallic atomic-scale transistors makes these devices adaptable for integration into advanced integrated circuits. The copper atomic-scale transistor is fabricated using standard photolithography and subsequent electrochemical deposition of the copper point-contact between two microfabricated gold electrodes (source and drain), and a thin copper film on a gate electrode. Its electrochemical operation parameters are explored systematically.

Results and Discussion

The fabrication of copper atomic-scale transistor consists of three steps. First, a silicon chip with three microfabricated electrodes – source, drain and gate – and a microchannel for on-chip electrolyte delivery are fabricated using standard photolithography (Figure 1a, Method 1 described in the Experimental section). The electrodes consist of Cr/Au films with a thickness of 3 nm/40 nm deposited on a silicon wafer covered with a thermal oxide layer (300 nm) using e-beam evaporation. The gap between the source and the drain is 2 μm, and the distance from the gate to the source is approximately 147 μm. The electrolyte channel developed in an SU-8 photoresist film is 8 μm wide and 2 μm high, as shown in Figure 1a.

In the second step, a copper film is electrochemically deposited on source and drain with a copper wire (99.9%, metal basis, diameter of 0.5 mm) as a counter electrode. During the deposition of the copper film source and drain become thicker and wider. Consequently, the gap between the two electrodes becomes narrower until, finally, a copper point contact is formed in the gap. The deposition continues for additional 20 min to stabilize the point contact. Simultaneously, a copper film is deposited on the gate electrode by grounding the gate electrode. After the stabilizing procedure, the gate electrode is disconnected from the ground and electrically suspended in the electrolyte in order to prevent copper dissolution from the gate during the following training procedure.

The third step is the training and switching procedure, which is similar to the one previously described for the silver atomic-

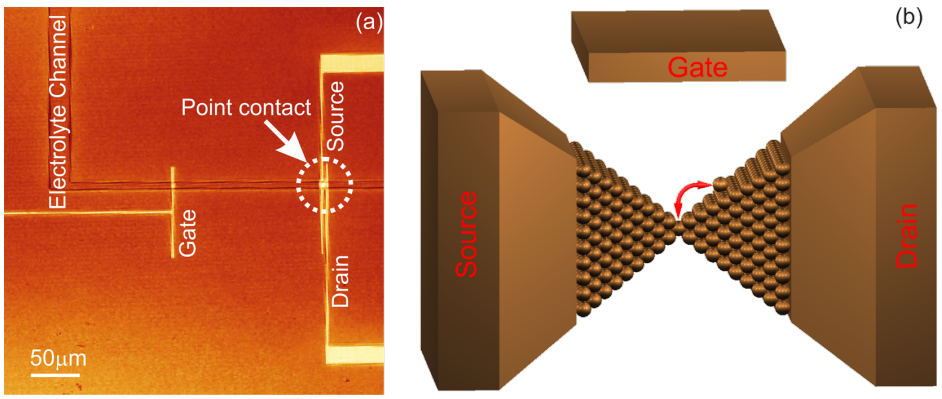


Figure 1: Copper atomic-scale transistor. (a) Confocal optical microscopy image of the microelectrodes, electrolyte channel and the copper point contact (indicated with a dotted circle), which was deposited between the source and the drain. (b) Schematic diagram of an atomic-scale transistor.

scale transistors [21]. When the copper atomic-scale transistor can switch reproducibly, the copper wire as the counter electrode is disconnected electrically and taken out of the copper electrolyte. The gate electrode is reconnected as an electrochemical counter electrode. By changing the potential on the gate in a bipolar manner, the as-fabricated copper atomic-scale point contact is alternately dissolved and formed, resulting in resistive switching between the source and the drain. The sign and the magnitude of the voltage (U_{bias}) applied across these two electrodes directly influence the growth of the quantum point contact. Because the electrochemical current is less than 1 nA in our experiment, the use of a reference electrode is not necessary. The conductance between the source and drain electrodes is measured with a current-to-voltage converter, in which the drain is virtually grounded via an operation amplifier. A bias voltage (U_{bias}) is applied on the source electrode. Electrochemical deposition/dissolution is realized by changing the potential on the counter electrode. At the beginning of the experiment the electrochemical potential is set to 350 mV. A confocal optical microscopy image of the copper transistor is shown in Figure 1a. A schematic diagram of an atomic-scale transistor is illustrated in Figure 1b.

To achieve conductance switching of copper atomic-scale transistors, the potential applied to the gate was controlled by a program developed in "NI LabVIEW" and the conductance was recorded simultaneously with the same program. The electrochemical potential was set using a feedback mechanism, in which the measured conductance was compared with a preset value of quantum conductance of the copper atomic-scale transistor. A transistor conductance switching between 0 and $1G_0$ (quantum conductance $G_0 = 2e^2/h$; with e being the electron charge, and h being Planck's constant), and 0 and $5G_0$ results from the change of potential applied to the gate electrode (Figure 2). To operate the transistor, the chip is covered with a glass slide and sealed in the electrochemical cell. The electrolyte channel delivers the electrolyte from a reservoir to gate, source and drain. The electrolyte consists of copper sulfate, $CuSO_4$ (5 mM), and sulfuric acid, H_2SO_4 (0.1 M), in bi-distilled water. The voltage applied between the source and drain electrodes is −12.9 mV in this case. With such a low applied voltage resistive switching is realized. The electrochemical potentials during operation are 220 mV (on) and −40 mV (off) for the switching between 0 and $1G_0$, and 72 mV (on) and −48 mV (off) for the switching between 0 and $5G_0$. The conductance switching between 0 and $1G_0$ demonstrates that only single copper atom is connecting source and drain.

To further investigate the performance of copper as a material for metallic atomic-scale transistors, copper atomic-scale transistors switching between 0 and arbitrary integer multiples of G_0 were fabricated in which well-controlled, stable and long switching sequences could be achieved. Examples of the switching of copper atomic-scale transistors (0–$10G_0$, 0–$11G_0$, 0–$12G_0$, and 0–$13G_0$) are shown in Figure 3 with eight switching cycles presented for each case for better comparison.

In order to observe fabrication and operation of the transistor in situ, and to test the operation of copper atomic-scale transistors in small volumes of electrolyte necessary for on-chip integration, chips with a circular window for containing the electrolyte were designed and fabricated with another standard lithography method using direct laser writing and reactive ion etching techniques (Method 2 described in the Experimental section). The window with a diameter of 3 mm and height of 0.05 mm was fabricated in the SU-8 photoresist. In order to observe fabrication and operation of the copper transistor in situ, a ceramic microscope objective was contacted with a drop of copper elec-

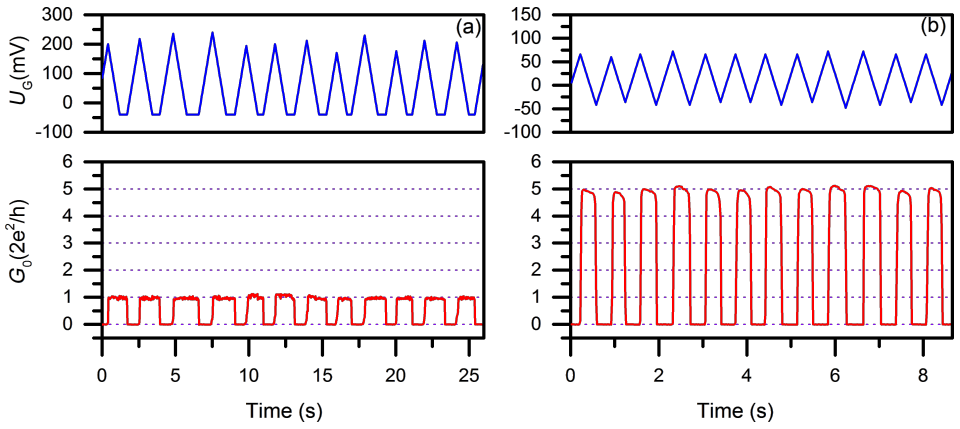


Figure 2: The performance of copper atomic-scale transistors. (a) 0–$1G_0$ quantum conductance switching at 0.5 Hz. (b) 0–$5G_0$ quantum conductance switching at 1.5 Hz.

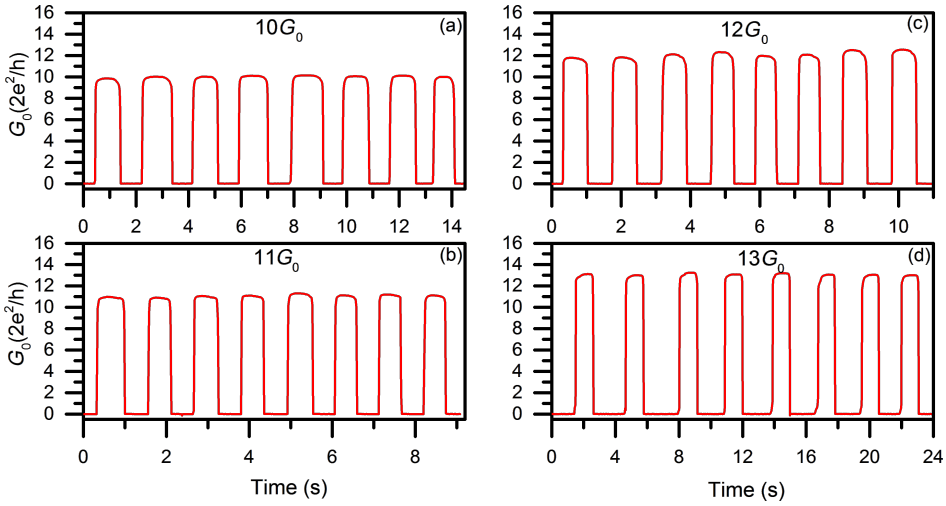


Figure 3: Controlled bistable quantum conductance switching of copper atomic-scale transistors. (a) 0–10G_0 switching at 0.57 Hz, U_G: −40 mV/210 mV (off/on). (b) 0–11G_0 switching at 0.73 Hz, U_G: −60 mV/120 mV. (c) 0–12G_0 switching at 0.89 Hz, U_G: −80 mV/140 mV. (d) 0–13G_0 switching at 0.33 Hz, U_G: −80 mV/240 mV.

trolyte ($CuSO_4$ (4 mM) + H_2SO_4 (0.1 M)), and a copper wire serving as a counter electrode was partially immersed in the electrolyte. Electrochemical deposition/dissolution processes on the microelectrodes were observed in situ with a confocal microscope (Leica DMRXE, Germany). Images taken before the electrochemical deposition of copper, after the deposition, and during the operation of the copper atomic-scale transistor are shown in Figure 4. After initial copper deposition, the electrolyte on the chip was replaced with $CuSO_4$ (10 mM) + H_2SO_4 (0.1 M), and a glass slide was placed on the top of the chip to encapsulate the electrolyte in the circular window. A higher concentration of $CuSO_4$ was used for fabricating the point contact in the encapsulation. The insulating SU-8 layer is stable in the strong acidic electrolyte in which the devices are operated.

With the feedback mechanism the conductance switching is well controlled between "open" and "quantum conductance" (as displayed in Figure 2 and Figure 3), but the duration of each switching cycle varies. Moreover, the maximum/minimum potential values applied on the gate change from one cycle to another with a limit ramping rate of 300 mV/s. In order to get closer to real applications, the control of the device via a feedback mechanism was replaced with an external signal control. We demonstrate that the copper atomic-scale transistor can be operated with a signal from a function generator. The operation of the transistor driven with a function generator instead of the custom-developed software is demonstrated in Figure 5. The driving signal (rectangular wave) was applied by the function generator to the gate and switched the current between source and drain. Next, the current was converted to a voltage (U_{out}) using the current–voltage converter circuit consisting of the copper point-contact, a resistor (R) and an operational amplifier (Analog Devices, OP07) (Figure 5a). The wide supply and input voltage ranges of the operational amplifier are ±15 V and ±14 V, respectively. The output signal U_{out} and the rectangular waveform generated with the function generator were simulta-

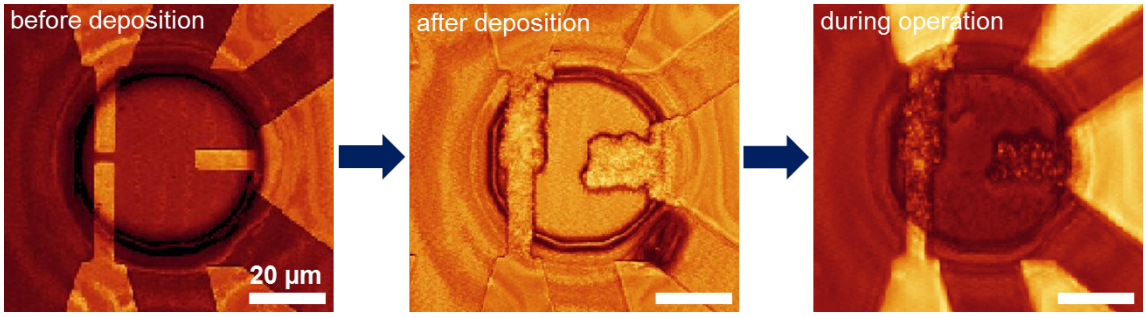


Figure 4: Observation of fabrication and operation of the copper atomic-scale transistor. Confocal microscopy images taken before electrochemical copper deposition, after deposition, and during transistor operation are shown (from left to right).

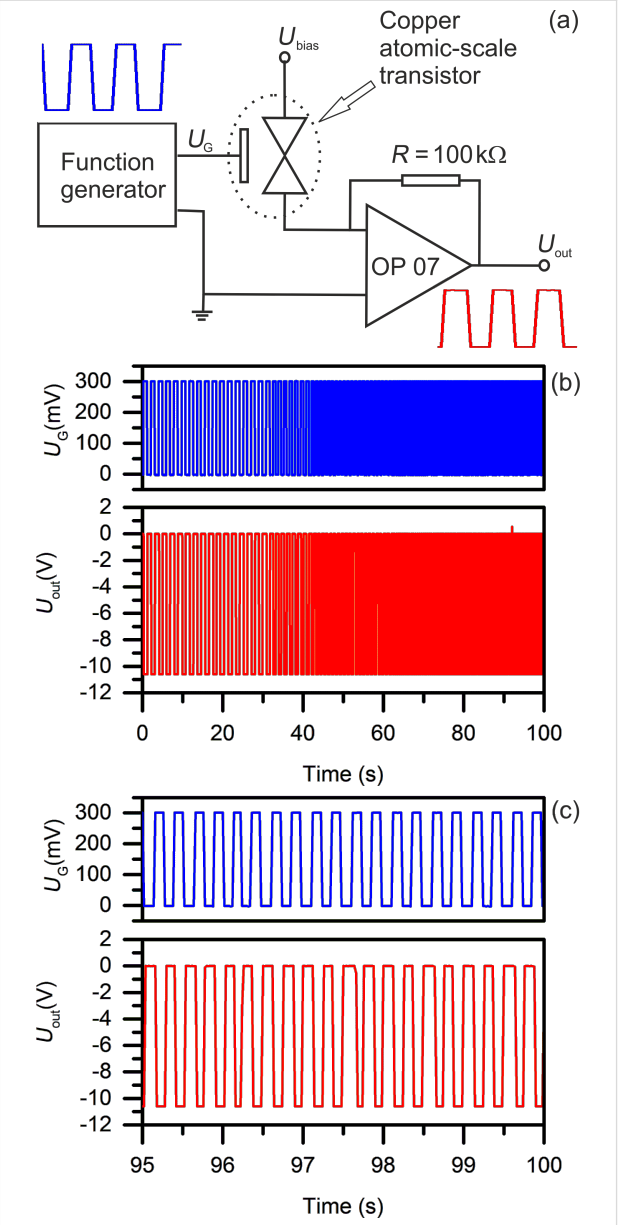


Figure 5: The operation of a copper atomic-scale transistor driven by a function generator. (a) Schematic diagram of the function-generator-driven copper atomic-scale transistor connected to a current-to-voltage converter circuit. (b) Rectangular wave signal from the function generator (blue) switched between 0 and 300 mV with frequencies from 0.5 Hz to 4 Hz. The output U_{out} (red), following the signal from the function generator, is driven between 0 and −10.6 V. (c) Zoom-in on the switching sequence from 95 to 100 s.

neously recorded using an A/D card (NI PCI-6221) with a custom-developed program. The maximum output of the A/D card is −10.6/10.6 V and the absolute read signal U_{out} is truncated by the A/D card when it exceeds 10.6 V. With U_{bias} = 120 mV), R = 100 kΩ, and U_{out} = −10.6 V, the quantum conductance of the copper point contact is calculated to be 11.4G_0. Therefore, any quantum conductance higher than 11.4G_0 is converted to −10.6 V with the setup illustrated in Figure 5a. The rectangular wave signal of the function generator switched between 0 and 300 mV with the frequency changing consecutively from 0.5 Hz to 4 Hz is shown in Figure 5b. The output signal U_{out} was driven between 0 and −10.6 V in the same manner. A zoom-in graph of the switching sequence between 95 and 100 s is shown in Figure 5c. The slope of the graph is an artifact due to the software sample rate (50 samples/s). All waveforms from the function generator as well as U_{out} are rectangular, as observed with an oscilloscope.

The magnitude of the bias voltage applied across source and has an important influence on the transistor switching rate. The switching rate obtained by setting U_{bias} at −12.9 mV is approximately 1 Hz. The sign and magnitude of U_{bias} change the electrochemical deposition behavior and shift the operation parameters of the electrochemical potential applied to the gate correspondingly. By setting U_{bias} at ca. 120 mV the switching rate can reach up to 10 Hz. With higher U_{bias} the copper atomic-scale transistor can be driven independently with the function generator instead of a computer.

Using the electronic circuit described in Figure 5a, the quantum conductance of the atomic-scale transistor is measured with U_{bias} is set at 129 mV. Two switching sequences of quantum conductance between 0–1G_0 and 0–2G_0 are shown in Figure 6.

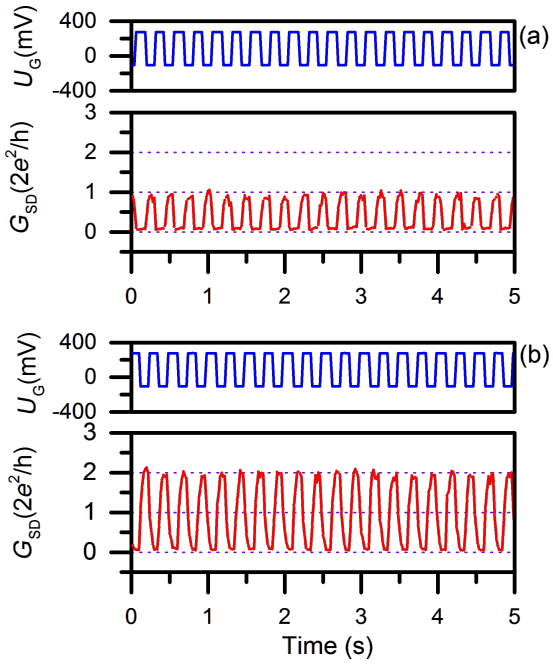


Figure 6: Demonstration of bistable quantum conductance switching of the copper atomic-scale transistor driven with a function generator. The bistable quantum conductance switching (red) between 0–1G_0 (a) and 0–2G_0 (b) follow the controlling rectangular wave (blue) at 4 Hz between −105 mV (off) and 275 mV (on) given by the function generator.

Copper electrolyte additives influence the morphology of the deposited copper film and, therefore, the switching behavior of the copper atomic-scale transistor. The copper electrolyte was prepared according to the recipe recommended by the supplier (Rohm and Haas, USA). The prepared electrolyte was diluted with bi-distilled water to 1:10 for better control over the electrochemical deposition/dissolution process during the fabrication of the copper atomic-scale transistor. The confocal microscopy image shown in Figure 7a was taken during the initial point-contact formation between source and drain. By comparing Figure 7a with Figure 4a we conclude, that the additives strongly influence the morphology of the deposited copper film and result in lower roughness. The sample used in this experiment was manually insulated with a polymer film. The switching sequence of the copper atomic-scale transistor driven by the function generator is displayed in Figure 7b with U_{bias} = 65 mV. As shown in Figure 7b, the rectangular wave signal switching between −170 and 350 mV at 10 Hz resulted in a rectangular U_{out} switching between 0 and −10.6 V.

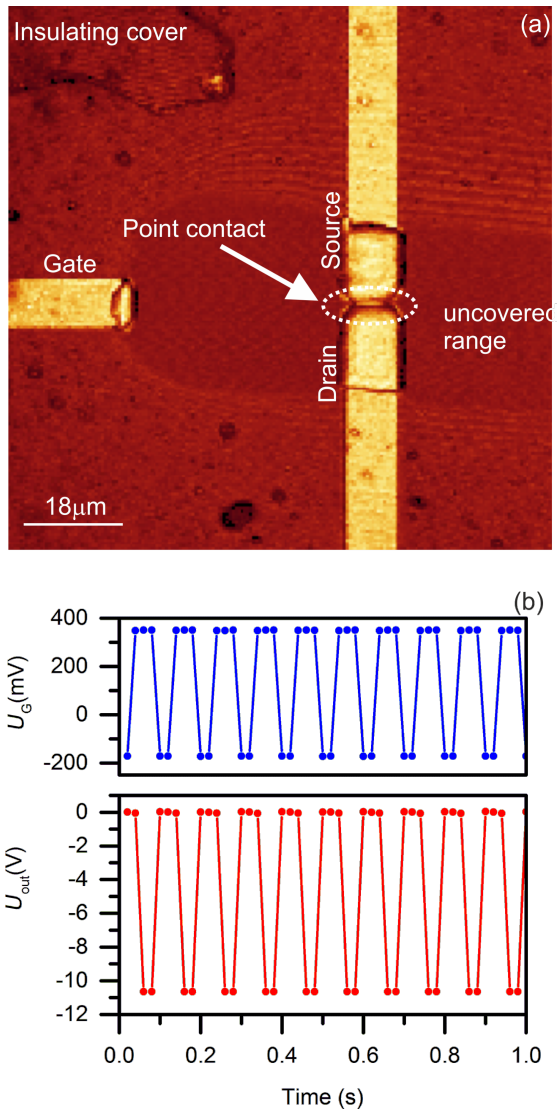


Figure 7: Influence of the copper electrolyte additives on the morphology of deposited copper film. (a) Confocal optical microscopy image of the copper atomic-scale transistor taken in situ. (b) The switching performance of the transistor implemented with a rectangular wave signal from a function generator applied to the gate at 10 Hz is plotted in the upper graph (blue). The output signal U_{out} is in the lower graph (red). The sampling rate of the recording software is 50 samples/s. The solid circles are the measured data and the lines are guides to the eye.

In this work, the switching block of the copper atomic-scale transistor is a copper point contact. The dimension of its functional unit is comparable with a molecular electronic device. Within the molecular electronic functional building blocks, it is generally found that the electronic coupling between molecules and electrodes has a profound influence on the properties of the molecular devices [50-57]. Therefore, it is difficult to achieve the mass production of molecular electronic devices with identical configurations of their building blocks. Because of the difficult interface coupling between the molecular functional block and the two metallic electrodes, the whole resistance in the device is in the range of megaohms. The operation current of molecular electronics is in the range of nanoamperes, and the low operation current leads to a low signal-to-noise ratio. The interface-coupling problem between the functional block and the electrodes does not exist in the copper atomic-scale transistor, because the material of the electrodes and the building blocks is the same. The “switching on” current of a copper atomic-scale transistors is in the range of microamperes, which is compatible with modern semiconductor devices [58]. Moreover, the operational potentials of the copper atomic-scale transistor are in the range between −170 mV and 350 mV, which is in the magnitude range of the operation voltages (ca. 0.5 V) of the three most promising approaches, namely multigate transistors, tunnel field-effect transistors, and germanium nanodevices [59-62]. The dynamic power dissipation of the CMOS devices is proportional to the square of drain supply voltage (V_{DD}) [58]. The copper atomic-scale transistors can be operated electrochemically with gate voltages less than 350 mV. This makes copper atomic-scale transistor a good alternative candidate for the development of electronic circuits with low power consumption.

Conclusion

A copper atomic-scale transistor was fabricated on microelectrode chips in an electrolyte of copper sulfate and sulfuric acid in bi-distilled water. The operational potentials of the copper atomic-scale transistor are compatible with the operation voltages (ca. 0.5 V) of multigate transistors, tunnel field-effect transistors, and germanium nanodevices [59-62]. There is no interface coupling problem, which is common of molecular elec-

tronic devices, in the copper atomic-scale transistor, because the material of the electrodes and the functional building block based on a copper point-contact is metallic. The switching-on current of copper atomic-scale transistors is in the range of microamperes, which is compatible with modern semiconductor devices. The copper atomic-scale transistor can be encapsulated and operated in small electrolyte volume (3.5 μL). We demonstrate that the copper atomic-scale transistors operate as an independent electronic device controlled by a function generator, including also atomic-scale transistors with only one or two atoms in the narrowest constrictions. The switching rate reaches up to 10 Hz. All metallic atomic-scale transistors demonstrate volatile/nonvolatile dual functionalities and could be configured to perform both logic and memory operations. This merging of logic with memory opens perspectives for processor-in-memory and logic-in-memory architectures based on metallic atomic-scale transistors.

Experimental

Fabrication of microelectrodes

Method 1: Two masks with patterns for microelectrodes and windows in the insulating layer were prepared with a direct laser writer (Heidelberg Instruments DWL 66). The microelectrodes covered with an SU-8 film on a silicon wafer with a thin thermally oxidized SiO_2 film (300 nm) were fabricated step by step as follows. A photoresist (AZ 5214E) was spin-coated on the wafer. With a mask aligner, the microelectrode pattern was transferred to the spin-coated photoresist. The photoresist film was developed in a developer (MIF 726). Cr/Au (3 nm/40 nm) films were evaporated with an e-beam evaporator (Lesker PVD75). The as-evaporated wafer was lifted in a photoresist remover in an ultrasonic bath. The wafer with the microelectrodes was spin-coated again with SU-8 to a thickness of 2 μm. The pattern with insulating windows was transferred to the spin-coated SU-8 film using the mask aligner. The wafer with the SU-8 film was developed in a developer (MicropositTM EC Solvent) and then baked at 210 °C for 1 h to solidify the SU-8 film.

Method 2: A photoresist (AZ 1505, 500 nm) was spin-coated on a thermally oxidized silicon wafer completely covered with evaporated Cr/Au (5 nm/60 nm) layer, and soft baked (95 °C, 2 min). The microelectrodes outline pattern was transferred into the photoresist film using direct laser writing (DWL 66, Heidelberg Instruments, Germany), and then developed. Reactive ion etching (RIE, Plasmalab100, Oxford Instruments, UK) was used to etch the Cr/Au film in the developed areas (120 W, 30 sccm Ar, 10 mTorr, 30 min) in order to isolate the microelectrodes from the surrounding Cr/Au film, and then the photoresist was stripped. To insulate the microelectrodes, an adhesion promoter (TI-Prime, MicroChemicals GmbH, Ulm, Germany) and SU-8 photoresist (3 μm) were spin-coated and soft baked (TI Prime: 120 °C, 2 min; SU-8: 95 °C, 5 min). The openings in the insulation layer were patterned using direct laser writing, and then developed after the post-exposure bake (PEB, 65 °C, 15 min). Next, the second SU-8 layer (50 μm) was spin-coated on the wafer, soft baked (95 °C, 20 min), exposed with direct laser writing, PEB (75 °C, 140 min) and developed. A circular window (d = 50 μm) above three microelectrodes and contact pad openings were patterned in the first insulating SU-8 layer (Figure 3). A larger circular window (d = 3 mm) (not shown in Figure 3) in the second SU-8 layer was used to contain the electrolyte for deposition and dissolution of the point contact.

Fabrication of copper atomic-scale transistors

The copper atomic-scale transistor fabrication and operation experiments were performed in a Nylon electrochemical cell and observed in situ under a Leica confocal microscope. At the initial stage, a copper wire was employed as a counter electrode for copper deposition on the three microelectrodes source, drain and gate. After the gap between the source and drain electrodes was closed with the deposited copper the deposition process continued for about 20 min to stabilize the contact. The copper point contacts were trained as atomic-scale switching units. After these stabilization and training processes, the gate electrode was utilized as the counter electrode in the electrochemical deposition/dissolution cycling. Main components in the copper electrolyte were copper sulfate and sulfuric acid in bi-distilled water. Copper Gleam HS-200A, Copper Gleam HS-200 B (Rohm Hass, USA) and hydrochloric acid were added as additives to deposit uniform flat copper films. The copper electrolyte was prepared according to the recipe recommended by the supplier (Rohm Hass, USA): copper sulfate ($CuSO_4 \cdot 5H_2O$), 100 g/L; sulfuric acid (96%), 200 g/L; chloride, 70 ppm (by adding hydrochloric acid); Copper Gleam HS-200A, 0.5 mL/L; Copper Gleam HS-200B, 10 mL/L.

Acknowledgements

This work was supported in part by the Funding Initiative of the VolkswagenStiftung: Integration of Molecular Components in Functional Macroscopic Systems, the Deutsche Forschungsgemeinschaft within the Center for Functional Nanostructures (CFN), project B1.6 and B5.1, and the Landesstiftung Baden-Württemberg within the Network of Excellence “Functional Nanostructures”. We are grateful to the Rohm and Haas Company for a donation of the copper electrolyte additives. This work was partly carried out with the support of the Karlsruhe Nano Micro Facility (KNMF, http://www.kit.edu/knmf), a Helmholtz Research Infrastructure at Karlsruhe Institute of Technology (KIT, http://www.kit.edu).

References

1. Hasegawa, T.; Terabe, K.; Tsuruoka, T.; Aono, M. *Adv. Mater.* **2012,** *24,* 252–267. doi:10.1002/adma.201102597
2. Lencer, D.; Salinga, M.; Wuttig, M. *Adv. Mater.* **2011,** *23,* 2030–2058. doi:10.1002/adma.201004255
3. Li, Y.; Long, S.; Liu, Y.; Hu, C.; Teng, J.; Liu, Q.; Lv, H.; Suñé, J.; Liu, M. *Nanoscale Res. Lett.* **2015,** *10,* 420. doi:10.1186/s11671-015-1118-6
4. Waser, R.; Dittmann, R.; Staikov, G.; Szot, K. *Adv. Mater.* **2009,** *21,* 2632–2663. doi:10.1002/adma.200900375
5. Yang, J. J.; Strukov, D. B.; Stewart, D. R. *Nat. Nanotechnol.* **2013,** *8,* 13–24. doi:10.1038/nnano.2012.240
6. Fackenthal, R.; Kitagawa, M.; Otsuka, W.; Prall, K.; Mills, D.; Tsutsui, K.; Javanifard, J.; Tedrow, K.; Tsushima, T.; Shibahara, Y.; Hush, G. A 16Gb ReRAM with 200MB/s write and 1GB/s read in 27nm technology. In *2014 IEEE International Solid-State Circuits Conference Digest of Technical Papers (ISSCC),* Feb 9–13, 2014; IEEE: Piscataway, NJ, U.S.A., 2014; pp 338–339. doi:10.1109/ISSCC.2014.6757460
7. Lee, M.-J.; Lee, C. B.; Lee, D.; Lee, S. R.; Chang, M.; Hur, J. H.; Kim, Y.-B.; Kim, C.-J.; Seo, D. H.; Seo, S.; Chung, U-I.; Yoo, I.-K.; Kim, K. *Nat. Mater.* **2011,** *10,* 625–630. doi:10.1038/nmat3070
8. Onofrio, N.; Guzman, D.; Strachan, A. *Nat. Mater.* **2015,** *14,* 440–446. doi:10.1038/nmat4221
9. Heath, J. R.; Kuekes, P. J.; Snider, G. S.; Williams, R. S. *Science* **1998,** *280,* 1716–1721. doi:10.1126/science.280.5370.1716
10. Hasegawa, T.; Itoh, Y.; Tanaka, H.; Hino, T.; Tsuruoka, T.; Terabe, K.; Miyazaki, H.; Tsukagoshi, K.; Ogawa, T.; Yamaguchi, S.; Aono, M. *Appl. Phys. Express* **2011,** *4,* 015204. doi:10.1143/APEX.4.015204
11. Kawaura, H.; Sakamoto, T.; Banno, N.; Kaeriyama, S.; Mizuno, M.; Terabe, K.; Hasegawa, T.; Aono, M. *Electron. Commun. Jpn.* **2011,** *94,* 55–61. doi:10.1002/ecj.10214
12. Sakamoto, T.; Banno, N.; Iguchi, N.; Kawaura, H.; Kaeriyama, S.; Mizuno, M.; Terabe, K.; Hasegawa, T.; Aono, M. Three terminal solid-electrolyte nanometer switch. In *IEEE International Electron Devices Meeting 2005,* IEEE: Piscataway, NJ, U.S.A., 2005; pp 475–478. doi:10.1109/iedm.2005.1609383
13. Sakamoto, T.; Iguchi, N.; Aono, M. *Appl. Phys. Lett.* **2010,** *96,* 252104. doi:10.1063/1.3457861
14. Tada, M.; Okamoto, K.; Banno, N.; Sakamoto, T.; Hada, H. *IEEE Trans. Electron Devices* **2014,** *61,* 505–510. doi:10.1109/TED.2013.2296036
15. Ungureanu, M.; Llopis, R.; Casanova, F.; Hueso, L. E. *Appl. Phys. Lett.* **2014,** *104,* 013503. doi:10.1063/1.4861430
16. Wang, Q.; Itoh, Y.; Hasegawa, T.; Tsuruoka, T.; Yamaguchi, S.; Watanabe, S.; Hiramoto, T.; Aono, M. *Appl. Phys. Lett.* **2013,** *102,* 233508. doi:10.1063/1.4811122
17. Xia, Q.; Pickett, M. D.; Yang, J. J.; Li, X.; Wu, W.; Medeiros-Ribeiro, G.; Williams, R. S. *Adv. Funct. Mater.* **2011,** *21,* 2660–2665. doi:10.1002/adfm.201100180
18. Obermair, C.; Xie, F.-Q.; Schimmel, T. *Europhys. News* **2010,** *41,* 25–28. doi:10.1051/epn/2010403
19. Xie, F.-Q.; Maul, R.; Augenstein, A.; Obermair, C.; Starikov, E. B.; Schön, G.; Schimmel, T.; Wenzel, W. *Nano Lett.* **2008,** *8,* 4493–4497. doi:10.1021/nl802438c
20. Xie, F.; Maul, R.; Obermair, C.; Wenzel, W.; Schön, G.; Schimmel, T. *Adv. Mater.* **2010,** *22,* 2033–2036. doi:10.1002/adma.200902953
21. Xie, F.-Q.; Nittler, L.; Obermair, C.; Schimmel, T. *Phys. Rev. Lett.* **2004,** *93,* 128303. doi:10.1103/PhysRevLett.93.128303
22. Xie, F.-Q.; Obermair, C.; Schimmel, T. *Solid State Commun.* **2004,** *132,* 437–442. doi:10.1016/j.ssc.2004.08.024
23. Agraït, N.; Yeyati, A. L.; van Ruitenbeek, J. M. *Phys. Rep.* **2003,** *377,* 81–279. doi:10.1016/S0370-1573(02)00633-6
24. Li, C. Z.; Bogozi, A.; Huang, W.; Tao, N. J. *Nanotechnology* **1999,** *10,* 221–223. doi:10.1088/0957-4484/10/2/320
25. Li, C. Z.; He, H. X.; Tao, N. J. *Appl. Phys. Lett.* **2000,** *77,* 3995–3997. doi:10.1063/1.1332406
26. Li, C. Z.; Tao, N. J. *Appl. Phys. Lett.* **1998,** *72,* 894–896. doi:10.1063/1.120928
27. Lin, X.; Dasgupta, A.; Xie, F.; Schimmel, T.; Evers, F.; Gross, A. *Electrochim. Acta* **2014,** *140,* 505–510. doi:10.1016/j.electacta.2014.05.160
28. Maul, R.; Xie, F.-Q.; Obermair, C.; Schön, G.; Schimmel, T.; Wenzel, W. *Appl. Phys. Lett.* **2012,** *100,* 203511. doi:10.1063/1.4719207
29. Mizukami, Y.-s.; Kurokawa, S.; Sakai, A. *Jpn. J. Appl. Phys.* **2010,** *49,* 095203. doi:10.1143/JJAP.49.095203
30. Morpurgo, A. F.; Marcus, C. M.; Robinson, D. B. *Appl. Phys. Lett.* **1999,** *74,* 2084–2086. doi:10.1063/1.123765
31. Pauly, F.; Dreher, M.; Viljas, J. K.; Häfner, M.; Cuevas, J. C.; Nielaba, P. *Phys. Rev. B* **2006,** *74,* 235106. doi:10.1103/PhysRevB.74.235106
32. Scheer, E.; Agraït, N.; Cuevas, J. C.; Yeyati, A. L.; Ludoph, B.; Martín-Rodero, A.; Bollinger, G. R.; van Ruitenbeek, J. M.; Urbina, C. *Nature* **1998,** *394,* 154–157. doi:10.1038/28112
33. Schnäbele, P.; Korytár, R.; Bagrets, A.; Roman, T.; Schimmel, T.; Groß, A.; Evers, F. *J. Phys. Chem. C* **2014,** *118,* 28252–28257. doi:10.1021/jp5093898
34. Shi, P.; Bohn, P. W. *ACS Nano* **2010,** *4,* 2946–2954. doi:10.1021/nn1003716
35. Tada, M.; Okamoto, K.; Sakamoto, T.; Miyamura, M.; Banno, N.; Hada, H. *IEEE Trans. Electron Devices* **2011,** *58,* 4398–4406. doi:10.1109/TED.2011.2169070
36. Valov, I.; Kozicki, M. N. *J. Phys. D: Appl. Phys.* **2013,** *46,* 074005. doi:10.1088/0022-3727/46/7/074005
37. Xie, F. Q.; Hüser, F.; Pauly, F.; Obermair, C.; Schön, G.; Schimmel, T. *Phys. Rev. B* **2010,** *82,* 075417. doi:10.1103/PhysRevB.82.075417
38. Xie, F. Q.; Maul, R.; Brendelberger, S.; Obermair, C.; Starikov, E. B.; Wenzel, W.; Schön, G.; Schimmel, T. *Appl. Phys. Lett.* **2008,** *93,* 043103. doi:10.1063/1.2955521
39. Zhang, Y.-h.; Wahl, P.; Kern, K. *Nano Lett.* **2011,** *11,* 3838–3843. doi:10.1021/nl201912u
40. Gleiter, H.; Schimmel, T.; Hahn, H. *Nano Today* **2014,** *9,* 17–68. doi:10.1016/j.nantod.2014.02.008
41. Lee, Y. J.; Brandbyge, M.; Puska, M. J.; Taylor, J.; Stokbro, K.; Nieminen, R. M. *Phys. Rev. B* **2004,** *69,* 125409. doi:10.1103/PhysRevB.69.125409
42. Krans, J. M.; Muller, C. J.; Yanson, I. K.; Govaert, T. C. M.; Hesper, R.; van Ruitenbeek, J. M. *Phys. Rev. B* **1993,** *48,* 14721–14724. doi:10.1103/PhysRevB.48.14721
43. Krans, J. M.; van Ruitenbeek, J. M.; Fisun, V. V.; Yanson, I. K.; de Jongh, L. J. *Nature* **1995,** *375,* 767–769. doi:10.1038/375767a0
44. Ludoph, B.; van Ruitenbeek, J. M. *Phys. Rev. B* **2000,** *61,* 2273–2285. doi:10.1103/PhysRevB.61.2273
45. Muller, C. J.; Krans, J. M.; Todorov, T. N.; Reed, M. A. *Phys. Rev. B* **1996,** *53,* 1022–1025. doi:10.1103/PhysRevB.53.1022
46. Such, B.; Glatzel, T.; Kawai, S.; Meyer, E.; Turanský, R.; Brndiar, J.; Štich, I. *Nanotechnology* **2012,** *23,* 045705. doi:10.1088/0957-4484/23/4/045705

47. Ternes, M.; González, C.; Lutz, C. P.; Hapala, P.; Giessibl, F. J.; Jelínek, P.; Heinrich, A. J. *Phys. Rev. Lett.* **2011,** *106,* 016802. doi:10.1103/PhysRevLett.106.016802
48. Li, J. Z.; Kanzaki, T.; Murakoshi, K.; Nakato, Y. *Appl. Phys. Lett.* **2002,** *81,* 123–125. doi:10.1063/1.1491015
49. Shu, C.; Li, C. Z.; He, H. X.; Bogozi, A.; Bunch, J. S.; Tao, N. J. *Phys. Rev. Lett.* **2000,** *84,* 5196–5199. doi:10.1103/PhysRevLett.84.5196
50. Aradhya, S. V.; Venkataraman, L. *Nat. Nanotechnol.* **2013,** *8,* 399–410. doi:10.1038/nnano.2013.91
51. Cui, X. D.; Primak, A.; Zarate, X.; Tomfohr, J.; Sankey, O. F.; Moore, A. L.; Moore, T. A.; Gust, D.; Harris, G.; Lindsay, S. M. *Science* **2001,** *294,* 571–574. doi:10.1126/science.1064354
52. Heurich, J.; Cuevas, J. C.; Wenzel, W.; Schön, G. *Phys. Rev. Lett.* **2002,** *88,* 256803. doi:10.1103/PhysRevLett.88.256803
53. Joachim, C.; Gimzewski, J. K.; Aviram, A. *Nature* **2000,** *408,* 541–548. doi:10.1038/35046000
54. Liang, W.; Shores, M. P.; Bockrath, M.; Long, J. R.; Park, H. *Nature* **2002,** *417,* 725–729. doi:10.1038/nature00790
55. Nitzan, A.; Ratner, M. A. *Science* **2003,** *300,* 1384–1389. doi:10.1126/science.1081572
56. Reed, M. A.; Zhou, C.; Muller, C. J.; Burgin, T. P.; Tour, J. M. *Science* **1997,** *278,* 252–254. doi:10.1126/science.278.5336.252
57. van der Molen, S. J.; Liljeroth, P. *J. Phys.: Condens. Matter* **2010,** *22,* 133001. doi:10.1088/0953-8984/22/13/133001
58. Chang, L.; Frank, D. J.; Montoye, R. K.; Koester, S. J.; Ji, B. L.; Coteus, P. W.; Dennard, R. H.; Haensch, W. *Proc. IEEE* **2010,** *98,* 215–236. doi:10.1109/JPROC.2009.2035451
59. Bernstein, K.; Cavin, R. K., III; Porod, W.; Seabaugh, A.; Welser, J. *Proc. IEEE* **2010,** *98,* 2169–2184. doi:10.1109/JPROC.2010.2066530
60. Ferain, I.; Colinge, C. A.; Colinge, J.-P. *Nature* **2011,** *479,* 310–316. doi:10.1038/nature10676
61. Ionescu, A. M.; Riel, H. *Nature* **2011,** *479,* 329–337. doi:10.1038/nature10679
62. Pillarisetty, R. *Nature* **2011,** *479,* 324–328. doi:10.1038/nature10678

License and Terms

This is an Open Access article under the terms of the Creative Commons Attribution License (http://creativecommons.org/licenses/by/4.0), which permits unrestricted use, distribution, and reproduction in any medium, provided the original work is properly cited.

The license is subject to the *Beilstein Journal of Nanotechnology* terms and conditions: (http://www.beilstein-journals.org/bjnano)

The definitive version of this article is the electronic one which can be found at: doi:10.3762/bjnano.8.57

BEILSTEIN JOURNAL OF NANOTECHNOLOGY

Diffusion and surface alloying of gradient nanostructured metals

Zhenbo Wang* and Ke Lu

Review

Open Access

Address:
Shenyang National Laboratory for Materials Science, Institute of Metal Research, Chinese Academy of Sciences, 72 Wenhua Road, Shenyang 110016, China

Email:
Zhenbo Wang* - zbwang@imr.ac.cn

* Corresponding author

Keywords:
diffusion; gradient nanostructures; grain boundary; interface; surface alloying

Beilstein J. Nanotechnol. **2017,** *8,* 547–560.
doi:10.3762/bjnano.8.59

Received: 01 November 2016
Accepted: 03 February 2017
Published: 03 March 2017

This article is part of the Thematic Series "Advances in nanomaterials II".

Guest Editor: H. Hahn

© 2017 Wang and Lu; licensee Beilstein-Institut.
License and terms: see end of document.

Abstract

Gradient nanostructures (GNSs) have been optimized in recent years for desired performance. The diffusion behavior in GNS metals is crucial for understanding the diffusion mechanism and relative characteristics of different interfaces that provide fundamental understanding for advancing the traditional surface alloying processes. In this paper, atomic diffusion, reactive diffusion, and surface alloying processes are reviewed for various metals with a preformed GNS surface layer. We emphasize the promoted atomic diffusion and reactive diffusion in the GNS surface layer that are related to a higher interfacial energy state with respect to those in relaxed coarse-grained samples. Accordingly, different surface alloying processes, such as nitriding and chromizing, have been modified significantly, and some diffusion-related properties have been enhanced. Finally, the perspectives on current research in this field are discussed.

Introduction

A gradient nanostructure is a unique architecture in which a layer of nanoscale-grained structure adheres to a ductile coarse-grained (CG) substrate of the same material; a transition layer with graded grain sizes is positioned between them. This architecture with a graded spatial variation of grain sizes offers a number of unique opportunities to enhance the properties of materials. It enables the delocalization of strains in the nano-grained structures, resulting in plastic deformation behavior fundamentally different from that of the free-standing homogeneous nano-grained and CG samples. For example, a considerable tensile ductility was achieved with the significantly enhanced strength in different metals with a gradient nanostructured (GNS) layer [1-3], distinct from the traditional trade-offs between strength and ductility in conventional metals and alloys. In addition, GNS materials exhibit significantly enhanced wear resistance and fatigue resistance compared with their nano-grained and CG counterparts [4-7].

Investigating the diffusion behavior of GNS materials is an important topic mostly due to the following reasons:

1. Numerous interfaces in the nanostructured layer make it possible to study interfacial diffusion and relative characteristics, such as interfacial structure, precipitation, phase transformation, plastic deformation, and chemical reaction, at lower temperatures. In comparison, it is difficult to obtain enough information on these aspects – particularly on the *C*-type diffusion regime as laid out in [8] – because of an insufficient number of interfaces in CG materials.
2. A graded variation of interface types may accompany the graded distribution of grain sizes in a GNS layer. Such a microstructure provides a unique sample to study the effects of grain size and interface type on diffusion properties.
3. Atomic diffusion is the essential factor in surface alloying processes (such as nitriding and chromizing), and diffusion studies in GNS materials provide insights for modifying traditional surface alloying processes of engineering metallic materials.

GNSs have been generated on various metals by methods with controlled surface plastic deformation [9-11]. In this paper, recent progress in the diffusion studies in GNS metals will be clarified to understand diffusion fundamentals and relationships between microstructure and diffusion in nanostructured materials, followed by some typical applications of GNS on advancing traditional surface alloying processes.

Review

Interfacial diffusion in GNS materials

In the 1980s, Gleiter et al. [12,13] successfully synthesized the first nanostructured metallic sample by means of inert gas condensation and consolidation (IGC). Since then, studies have been performed to reveal the diffusion behavior of nanostructured metals worldwide. However, the measured results were rather scattered and even controversial. For instance, markedly promoted diffusion coefficients with a lower activation enthalpy were measured in the nanostructured Cu synthesized by IGC [14-16]. And a comparable diffusivity with that of conventional grain boundaries (GBs) was revealed in a nanostructured γ-Fe–Ni alloy prepared by ball milling with subsequent sintering (BMS), while inter-agglomerate boundaries showed much faster diffusion rates (≈4 orders of magnitude higher) with a lower activation enthalpy than the GB diffusion [17]. Moreover, interfacial diffusion coefficients in an Fe_3Si nanocomposite produced by crystallization (CRY) from a melt-spun amorphous sample were revealed to be even lower in comparison with those in the CG sample [18].

Particular attention has been paid to the diffusion behavior in nanostructured or ultrafine grained (UFG) materials produced by using severe plastic deformation (SPD), mostly because of the bulk forms of nanostructures. Inconsistences also exist in the experimental results. For example, Würschum et al. [19] found that diffusivities in a SPD Pd sample are similar to those in conventional GBs. However, Kolobov et al. [20] detected an increment of 10^4–10^5 in GB diffusivities (with lower activation enthalpy) of Cu in a SPD Ni sample in comparison with those in a CG sample. The diffusion coefficients along some ultra-fast channels (together with some conventional GBs) in an UFG Cu–Zr alloy sample prepared via SPD were found to be $\approx 10^3$ times higher than those along GBs in a high-purity CG Cu sample [21]. In order to differentiate these ultra-fast diffusion channels from conventional GBs, the term "nonequilibrium" GBs was used. In this case, GBs might gather a large number of irregular (extrinsic) dislocation structures, so that extra free energy might be introduced in the interfaces, while misorientations across them remain stable [22,23]. The existence of nonequilibrium GBs after SPD processing has been supported by strain mapping results in a SPD Pd–Ag alloy, in which the GB thickness (with evident strain) is determined to be ≈1.5 nm and is markedly larger than the thickness of relaxed GBs (≈0.5 nm) [24]. In addition, the higher energy of nonequilibrium GBs as compared to conventional GBs has been demonstrated by the transformation of partial to complete GB wetting in Sn–Pb alloys during continuous strain by Straumal et al. [25]. However, this notion was confused by two works in the SPD Cu and Cu–Pb alloy [26,27], in which various defects such as vacancy agglomerations, nanometer- and micrometer-sized voids were observed. These defects might be linked and significantly accelerate atomic penetration in the materials. In addition, the concurrent influence from lattice diffusion might not be completely excluded from the mean diffusion flux in SPD metals, in which the grain sizes are usually in the submicrometer scale (>200 nm) and numerous dislocations exist in grains [28].

The microstructural observations revealed that the GNS layers on metals processed by surface mechanical attrition treatments (SMAT) are porosity-free, and the mean grain sizes are on the nanoscale (<100 nm) in the surface layers with a thickness of tens of micrometers, for example on pure Fe [29] and Cu [30]. In addition, a graded distribution of interfacial structure was obtained in the GNS surface layer of Cu [30], with interfaces sequentially dominated by twin boundaries (TBs), high-angle GBs (HAGBs), low-angle GBs (LAGBs) and dislocation walls with an increasing depth. These microstructures characteristics provided unique opportunities to study the relationship between the diffusion property and microstructure into the nanometer scale. The diffusion studies in these materials will be reviewed and compared with results from other nanostructured metals in this section.

Diffusion behavior in nanostructured surface layers

The diffusion properties of Cr in GNS Fe were measured within the temperature range of 300–380 °C on a SMAT Fe sample with a mean grain size of ≈10 nm in the top surface layer electroplated with a thin layer of Cr [31]. The apparent diffusivity of Cr in the GNS Fe is 7–9 orders of magnitude higher than that in the Fe lattice and 4–5 orders of magnitude higher than that along GBs of ferrite, as shown in Figure 1. In terms of the diffusion kinetics with Arrhenius dependence in the concerned temperature range, the pre-exponential factor and the activation enthalpy of Cr diffusion in the nanostructured Fe were calculated. It is seen that the pre-exponential factor of Cr diffusion in nanostructured Fe is much higher than that for conventional GB diffusion in α-Fe, and the diffusion activation enthalpy is slightly lower than that that of GB diffusion.

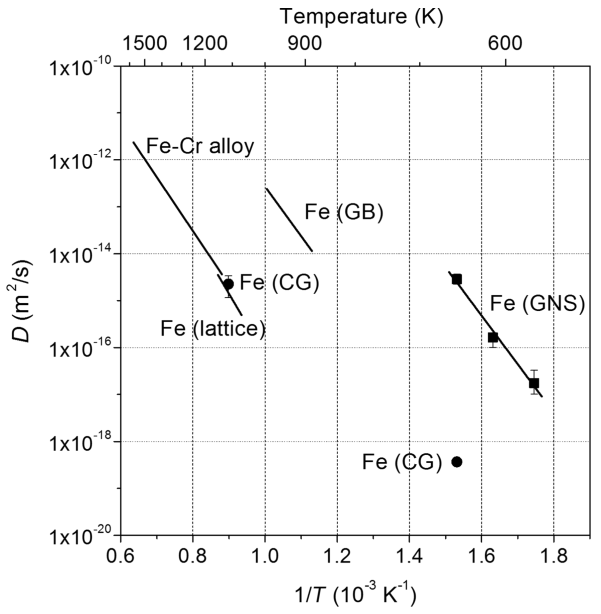


Figure 1: Temperature dependence of the diffusion coefficients of Cr in the GNS Fe produced by SMAT and in the CG Fe, in comparison with those for the α-Fe lattice diffusion, the α-Fe GB diffusion and the diffusion in Fe–Cr alloy. Figure reproduced with permission from [31], copyright 2003 Elsevier.

In addition, the Cr-diffusion depth values were determined in GNS low carbon steel samples chromized in a packed powder mixture of Cr–NH_4Cl–Al_2O_3, as shown in Figure 2 [32]. One can see that the diffusion depth into the as-SMAT sample was larger than that into the CG sample after the same chromizing treatment within the temperature range of 400–860 °C. The ratio of the value into the as-SMAT sample relative to the value into the CG sample decreased with elevating temperatures. A similar trend has also been observed in a GNS H13 steel sample, in which a significantly increased Cr-diffusion depth with respect to that in the CG sample was achieved at chromizing temperatures below 600 °C, and the depth even decreased with increasing temperatures above 600 °C [33]. Meanwhile, it was noticed that an isothermal preannealing might decrease the Cr-diffusion depth. For example, the pre-annealing at 400 °C decreased the Cr-diffusion depth values to ≈60% of the as-prepared GNS low carbon steel (also see Figure 2).

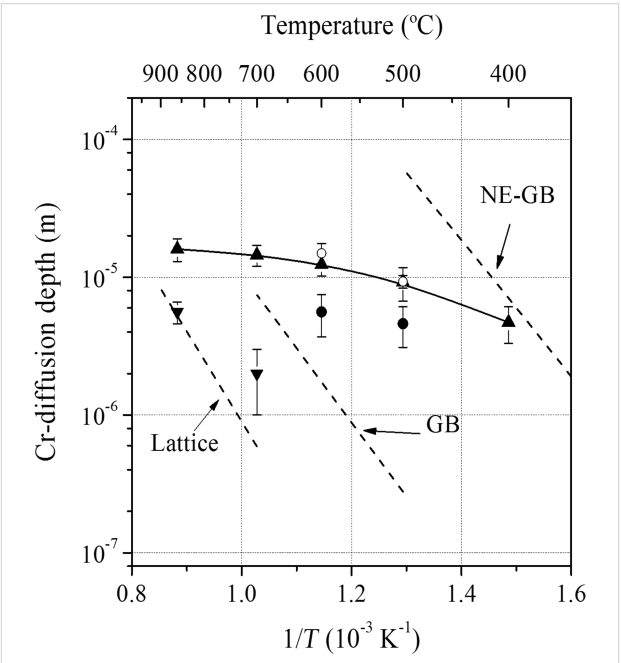


Figure 2: Variations of Cr-diffusion depth with temperature in different low carbon steel samples: as-SMAT (▲), CG (▼), SMAT with subsequent annealing at 300 °C (○) and 400 °C (●) for 180 min. In comparison, the calculation results in terms of the lattice diffusion [34], the conventional GB diffusion (GB) [35], and the diffusion in GNS Fe (NE-GB) [31] were also included. Figure reproduced with permission from [32], copyright 2005 Elsevier.

Since the surface Cr concentration is approximately constant during chromizing, the apparent diffusivity in the GNS surface layer (D_{GNS}) can be calculated from the measured Cr-diffusion depth (x) from

$$D_{GNS} = x^2 / \alpha t, \quad (1)$$

where α is a constant and t is the chromizing duration [36]. The results show that D_{GNS} is about 8.5×10^3 times higher than the diffusivity along GBs in the CG low carbon steel sample (D_{RGB}) at 400 °C, and the ratio of D_{GNS} to D_{RGB} decreases gradually with increasing temperature. While evident grain growth occurred in the nanostructured surface layer, the ratio of D_{GNS} to D_{RGB} is even less than 1. After the preannealing treatment at 400 °C, D_{GNS} decreases to ≈1/4 of that in the as-prepared sample.

Comparing the diffusion studies in GNS surface layers prepared by SMAT with the results in other nanostructured or UFG metals, as in Table 1, we may conclude:

1) The measured interfacial diffusivity is sensitive to the sample preparation method. Diffusivities in nanostructured samples produced by using SMAT or SPD reach a value of 10^3–10^5 times higher than those for GBs in CG samples. The diffusivity increment is typically within 10^2–10^4 in nanostructured metals produced via the IGC or BMS techniques. Additionally, the interfacial diffusivity in nanostructured samples produced via CRY is much lower than that along GBs in the CG form. Meanwhile, the interfacial diffusivities in nanostructured metals in the as-prepared states decrease significantly after preannealing treatments during which GBs may be relaxed, especially when evident grain growth has occurred.

2) The diffusion activation enthalpies in nanostructured metals are typically 0.5–0.9 of those along GBs in CG samples when no distinct relaxation or grain growth occurs. Additional-

Table 1: Diffusion studies in nanostructured metals prepared by different techniques.

Material (diffusant)	Grain size (nm)	Preparation method[a]	Diffusion temperature (°C)	D_{NS}/D_{RGB}[b]	Arrhenius parameters[c]		Ref.
					D^0_{NS}/D^0_{RGB}	Q_{NS}/Q_{RGB}	
Fe (Cr)	10–25	SMAT	300 340 380	2.0×10^4 9.4×10^3 1.2×10^4	7×10^2	0.9	[31]
Low-C-steel (Cr)	10–30	SMAT	400 500 600 700	8.5×10^3 2.1×10^2 7.9* 0.49*	NA	NA	[32]
Low-C-steel (Cr)	10–30	SMAT+PA	500 600	53 1.6*	NA	NA	[32]
H13-steel (Cr)	10−30	SMAT	550 600 650	17 11* 0.28*	NA	NA	[33]
Cu (Ni)	100	SMAT	130	1.1×10^4	NA	NA	[38]
Ni (Cu)	300	ECAP	125 175	1.1×10^5 1.0×10^4	4.4×10^{-11}	0.34	[20]
Pd (Fe)	80–150	SPD	98 200 300	3.0×10^3 11* 0.12*	NA	NA	[19]
Cu–Zr (Ni)	300	ECAP	151–280	0.7–1.4* $(0.2–1.3) \times 10^3$	0.2 2.3×10^3	0.93 s-GB 1.06 f-GB	[21]
Cu (Ni)	300	ECAP	151–201	0.5–1.5*	0.24	0.94	[39]
Ni (Ni)	300	ECAP	58–127 167–227	$(0.7–28) \times 10^5$ $(0.2–4.5) \times 10^3$	6.8×10^{-4}	0.52	[40]
Cu (Cu)	8	IGC	120	1.1×10^2	3×10^{-4}	0.59	[14,41]
Cu (Ag)	8	IGC	30–70 80–100	$\approx 2.3 \times 10^3$ $\approx 4.9 \times 10^2$	5.9×10^{-3} 1.8×10^2	0.53 0.86	[15]
Cu (Au)	10	IGC	100	1.85×10^4	NA	NA	[16]
Pd (Fe)	20	IGC	200 250	7* 0.7*	NA	NA	[19]
Cu (Zn)	120	DPD	85–100 115–190	11 0.05–3.5*	NA	NA	[42]
γ-FeNi (Ag)	100	BMS	411–547	≈1 $(0.34–3.7) \times 10^4$	≈1 2×10^{-3}	≈1 0.53 Al	[17]
Fe_3Si (Fe)	12	CRY	380–420	$\approx 4 \times 10^{-5}$	NA	1.12 a-IF	[18]

[a]Various preparation methods: SMAT+PA denotes SMAT with subsequent preannealing at 400 °C, when no evident grain growth occurs but microstrain decreases markedly [32]. Equal channel angular pressing (ECAP) is a representative SPD method. DPD denotes the dynamic plastic deformation technique. Other abbreviations are referred to in the main text. [b]Asterisked values indicate samples with remarkable grain growth during the concerned diffusion annealing. The thickness of GB (δ) was taken as 0.5 nm to calculate D_{RGB} when a triple product $s\delta D_{RGB}$ was reported. [c]Arrhenius parameters: D^0_{NS} and D^0_{RGB} denote the apparent pre-exponential factors for diffusion along interfaces in a nanostructured metal and the relaxed CG sample, respectively; Q_{NS} and Q_{RGB} denote the diffusion activation enthalpies along interfaces in the nanostructured metal and the relaxed CG sample, respectively; The superscripts s-GB and f-GB denote "slow GB" and "fast GB", respectively, in [21]; Al denotes agglomerate interfaces, along which the diffusivity (D_a) was derived from a relationship with the product (P_a) as $P_a = s_a \cdot \delta_a \cdot D_a/\lambda$ (referring to [17]); a-IF denotes amorphous interfaces in the nanocrystalline Fe_3Si prepared by CRY [18].

ly, no dependence on the preparation method or grain size is indicated.

3) The effect of grain size on diffusivity seems to be rather weak within the scale regime from 10 to 300 nm. Therefore, the contribution from triple junctions, of which the amount increases with decreased grain size and the diffusivity should be further enhanced due to the larger excess volume [31,37], might be insignificant within the present grain size scale.

This evidence suggests that GBs in the GNS layers are associated with a higher stored energy and/or with a higher density of defects compared to the GBs in conventional CG counterparts. According to the vacancy mechanism of GB diffusion [43,44], they may facilitate diffusion by decreasing the vacancy formation energy. For example, the existence of a large fraction of free volume in the GNS layer has been demonstrated by the high intensities of the short- and middle-lifetime components in the results of positron annihilation spectroscopy measurements of the surface layer of the SMAT Fe [45].

While GB defects (i.e., extrinsic GB dislocations) are difficult to be identified in GNS or SPD metals, it is argued that the GB diffusion might also be accelerated by GB thickening, resulting from either the GB prewetting (premelting) or the pseudo-partial GB wetting during sample preparation [46-49]. For example, a Zn-rich wetting layer of 2–10 nm in thickness has been formed along Al/Al GBs in UFG Al–Zn alloys after high pressure torsion at room temperature [47]. Dramatically enhanced GB diffusivities were observed in Cu–Bi and Fe–Si–Zn alloys with prewetted GBs [48,49]. Nevertheless, this notion might safely be excluded from the issues accelerating diffusion in the GNS layers, because no system (see Table 1) contains components which are inclined to form GB complexions connected with GB prewetting or pseudo-partial wetting [46,50].

Diffusion kinetics and free energy of different interfaces

As illustrated in Figure 3a, the grain size increases and interface structure is sequentially dominated by TBs (or TB-like interfaces), HAGBs, LAGBs and dislocation walls with increasing depth in the GNS surface layer on a SMAT pure Cu sample [30,38]. Similar to the accelerated diffusion of Cr observed in GNS Fe and steels, a remarkable penetration of Ni into the GNS surface layer of the SMAT Cu has been detected at temperatures below 150 °C [38,51,52]. The effective diffusivity in the top surface layer is ≈3 orders of magnitude higher than that along relaxed HAGBs in the annealed CG sample at 130 °C. Furthermore, it is noticed that the effective diffusivity in the subsurface layer is higher than that in the top surface layer, and increases with increasing depth up to 30–50 μm, as shown in Figure 3b. After the diffusivity reaches a maximum value of ≈4 orders of magnitude higher than that along the conventional HAGBs, it decreases with further increasing depth.

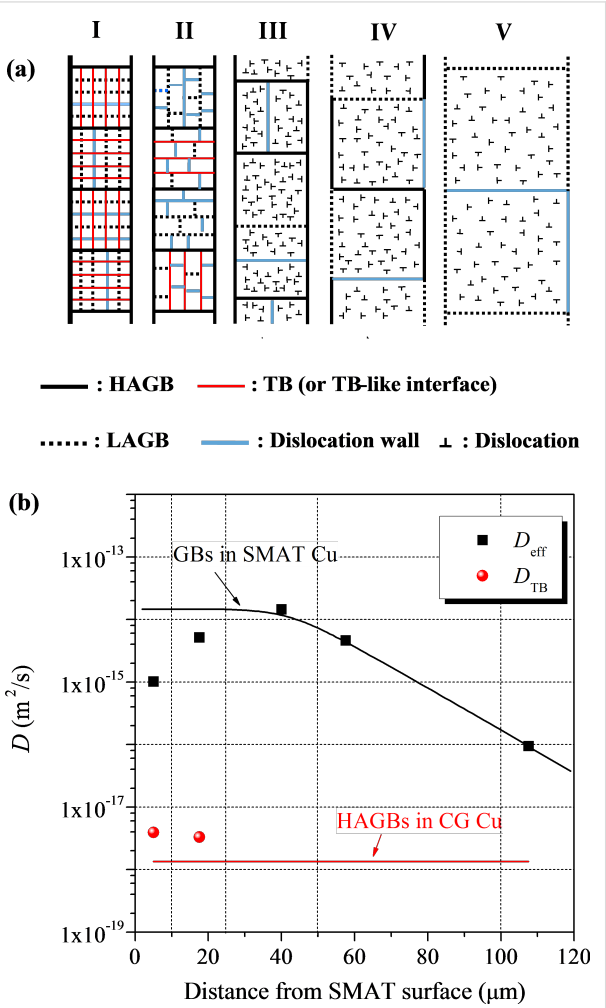


Figure 3: (a) A schematic illustration of the gradient microstructure of grain size and interface in the GNS surface layer of a SMAT Cu sample, and (b) variation in the effective diffusivity of ^{63}Ni in different regions at 130 °C. Figure adapted with permission from [38], copyright 2010 Elsevier.

Since the lattice diffusion distance is negligible at the concerned temperatures, diffusion in the GNS Cu proceeds in accordance to Harrison's *C*–type diffusion regime [8]. Therefore, the effective diffusivities are directly related to diffusion kinetics along interfaces. As shown in Figure 3b, diffusivities along different interfaces in the GNS surface layer are compared with the diffusivity along HAGBs in a high-purity CG Cu at 130 °C. It is noted that the diffusivities along HAGBs and TBs in the first 25 μm in thickness (i.e., regions I and II) were derived by using the so-called *C*–*B* diffusion mode developed by Divinski et al. [17] in hierarchic microstructures. In this case, the leakage of Ni tracer atoms from HAGBs into TBs (i.e., *B*-regime in the mode)

reduces the effective diffusivities in both regions. The diffusivities of HAGBs and TBs in the GNS Cu are about 1.41×10^{-14} and 3.65×10^{-18} $m^2 \cdot s^{-1}$, respectively.

Table 2 summarizes several works on diffusion along TBs in pure Cu. No comparison with diffusivity along coherent TBs can be made because no diffusion data was provided to the authors' knowledge. It is shown that the diffusivity along TBs in the SMAT Cu is even slightly higher than the extrapolated diffusivity along GBs in the relaxed CG sample, while those in the DPD and bicrystal samples [42,53] are much lower than the latter. This suggests a much higher diffusivity along TBs in the GNS sample than in other samples. Similar with the situations of GBs (referring to the section "Diffusion behavior in nanostructured surface layers"), the significantly enhanced diffusivity along TBs in the GNS Cu is also expected be induced by a higher stored energy and/or with a higher density of defects. The free energy of GBs varies with the misorientation angle and forms a sharp cusp only several degrees in deviation around the corresponding angle of the coherent TBs, i.e., 70.5° of twin/matrix with [110] symmetric tilt boundary in Cu [54]. In the GNS layer, various dislocations are accumulated at TBs, resulting in a significant increment of interface free energy with only a slight deviation from the ideal TB misorientations [42,54].

According to a semi-empirical approach developed by Borisov et al. [55], the interface excess free energy difference ($\Delta\gamma_B$), i.e., the difference between the excess free energy of interfaces in the GNS Cu and that of conventional GBs in a relaxed CG sample at a temperature (T), may be estimated from

$$\Delta\gamma_B = \frac{RT}{2a^2 N_A} \ln\left(\frac{D_B}{D_{RGB}}\right), \quad (2)$$

where a is the mean distance between atoms at the interface. N_A and R are the Avogadro's number and gas constant, respectively. D_B and D_{RGB} are the diffusivities of Ni along interfaces in the GNS Cu and along conventional GBs, respectively. By using the diffusion data for different interfaces in the GNS Cu, and D_{RGB} from [56], $\Delta\gamma_B$ values of different interfaces are derived. In comparison with γ_{RGB} (≈0.63 $J \cdot m^{-2}$ [57]), SMAT results in an increment up to 30% in the GB excess free energy in region III, and it decreases with an increasing depth (in regions IV and V). The TB excess free energy in the first 25 μm is comparable with γ_{RGB}.

Reactive diffusion behavior

Reactive diffusion is of great technological importance in the metallurgical industry and in electronic materials. While a reaction process at the interface between two (or more) primary phases usually involves the nucleation and the coarsening stages of the formed phase(s), the nucleation conditions at the interface play decisive roles on the subsequent reactive diffusion process [58].

In comparison with the reactive diffusion processes in CG samples, some previous studies demonstrated different characteristics in nanostructured materials. For instance, Charlot et al. [59] showed that the mechanical milling process applied before the self-propagating high-temperature syntheses (SHS) process markedly decreased the ignition temperature (≈100 °C) of the reaction in Fe and Al powder mixtures, and a nanostructured Fe–Al intermetallic compound was synthesized after the reaction. Meanwhile, more phases from a Ti–Al system were observed on a nanocrystalline Ti substrate with Al layer with respect to a microcrystalline substrate by Wiecinski et al. [60]. The intermetallic layer synthesized on the nanocrystalline Ti substrate was thicker and more homogeneous at 600 °C. Nevertheless, it was noted that grain size effects on reactive diffusion characteristics were still difficult to be understood in these works, mostly because the results were obtained in binary systems with a high heat release by intermetallic formation. SHS occurred at a high temperature and significantly elevated sample temperature after the reaction ignition in such systems [61,62].

In comparison, the enthalpy change and reaction temperature between Fe and Zn (or N) are relatively low, thus SHS will not occur and the nanostructures remain relatively stable during

Table 2: Diffusion data along TBs in different Cu samples.

Base material	Diffusant	Temperature (°C)	D_{TB}, P_{TB}[a] ($m^2 \cdot s^{-1}$, $m^3 \cdot s^{-1}$)	D_{RGB}, P_{RGB}[a] ($m^2 \cdot s^{-1}$, $m^3 \cdot s^{-1}$)	Ref.
SMAT Cu	Ni	130	3.65×10^{-18}	1.34×10^{-18}	[38]
DPD Cu	Zn	85 130	6.21×10^{-20} 8.61×10^{-19}	5.82×10^{-19} 2.19×10^{-17}	[42]
Σ3 ⟨011⟩ bicrystal Cu	Au	400 500	$(0.7–11) \times 10^{-23}$ $(0.4–5.8) \times 10^{-21}$	1.18×10^{-20} 9.6×10^{-19}	[53]

[a]Diffusivities were determined in the *C*-type regime in the SMAT and DPD samples. While the values were determined in the *B*-type regime in the bicrystal sample, a triple product *P* was given.

reactive diffusion. In this section, the reactive diffusion behavior of Zn and N into the GNS Fe prepared by SMAT [61,62] will be reviewed from both kinetic and thermodynamic aspects.

Promoted growth kinetics

The growth kinetics of the Fe–Zn compound layer (mostly ξ-$FeZn_{13}$ phase) was studied in the GNS Fe sample electroplated with a Zn layer at different temperatures from 280 to 340 °C [61]. It was found that the Fe–Zn compound layer formed on the GNS sample is much thicker than that on the CG sample under the same isothermal annealing treatment. According to the relationship between the measured thickness (l) of compound layers, diffusion temperature (T) and duration (t), the growth kinetics was determined from

$$\ln k^2 = \ln(k_0{}^2) - \frac{Q}{RT}, \tag{3}$$

where k is the growth constant derived from

$$l = k\sqrt{t}. \tag{4}$$

The pre-exponential factor k_0 is a constant related to atomic diffusion, and Q is the activation enthalpy for the growth of compound layer. As derived from Figure 4a, the activation enthalpy for the growth of the compound layer in the GNS sample is 108.0 ± 20.7 kJ·mol^{-1}, which is much lower than that in the CG sample (167.1 ± 10.1 kJ·mol^{-1}).

Significantly promoted growth kinetics has also been observed in the GNS Fe during gas nitriding at lower temperatures [62,63]. A continuous nitride surface layer (mostly ε-$Fe_{2-3}N$ and γ'-Fe_4N) of ≈10 μm in thickness was formed on the GNS sample after nitriding at 300 °C for 9 h. In comparison, there was no such nitride layer formed on the original CG sample after the same nitriding treatment.

The growth kinetics of the formed compound layer should be controlled by diffusion processes in both the substrates and the compound layer [61]. While the grain size of Fe in the nanostructured surface layer is much smaller than that in the CG matrix, grain sizes of the formed compounds in the GNS sample are still much smaller than those formed in the CG sample [61,62]. Therefore, diffusion of alloying elements in the GNS sample and in the compounds layer is evidently accelerated, and a smaller activation enthalpy is obtained than in the CG sample.

The promoted growth kinetics in GNS samples may also be understood in terms of the reaction kinetics of nucleation and growth. Because GBs usually act as preferable nucleation sites, the existence of a large number of GBs in the nanostructured substrate may result in a significant improvement in the reaction between alloying elements and substrate atoms. The nucleation rate, $\dot{G}(T)$, can be written as [64]:

$$\dot{G}(T) = \omega C_0 \exp\left(-\frac{Q}{RT}\right)\exp\left(-\frac{\Delta G^*}{RT}\right), \tag{5}$$

where ΔG^* is the critical Gibbs energy for nucleation, ω is a frequency factor, and C_0 is the number of atoms at contacting interfaces. While the value of the critical Gibbs energy for nu-

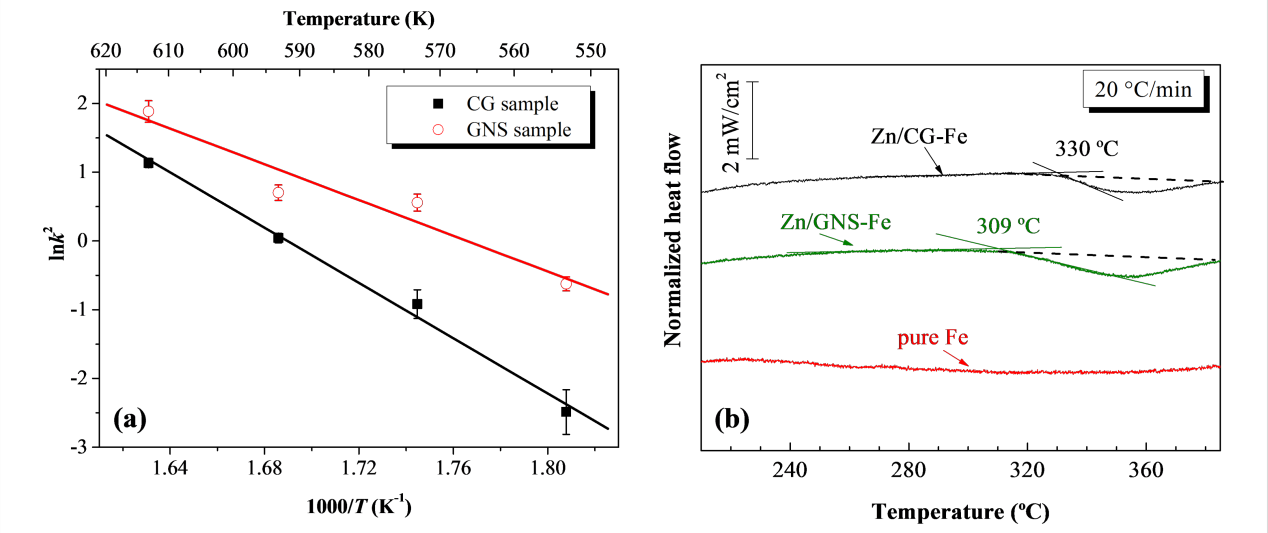


Figure 4: (a) The dependence of the growth constant k^2 on the reciprocal annealing temperature during reactive diffusion of Zn on the GNS and CG Fe samples, and (b) thermal analyses of the Zn/GNS-Fe and the Zn/CG-Fe couples at a heating rate of 20 °C·min^{-1}. Figure adapted with permission from [61], copyright 2012 Elsevier.

cleation at GBs is smaller than the value at other regions along the surface, the nucleation rate increases significantly with decreasing grain size in the nanostructured surface layer. The growth kinetics of the nuclei of formed compounds is expected to be significantly promoted by abundant GBs in the GNS layer at the earlier stage of reaction, mostly due to the accelerated diffusion rates of alloying elements along them [32,61].

It is also noted that homogenous reaction layers of FePt and FePt with ≈10 atom % Ag have been synthesized in Pt/Fe and Pt/Ag/Fe thin films, respectively, after annealing at temperatures when the bulk diffusion processes are still frozen [65]. The formation processes have been interpreted as a GB-diffusion-induced solid-state reaction in which the reaction interfaces migrate perpendicularly to the original GB plane, based on corresponding depth profiles of the element concentrations in both systems. This mechanism might also contribute to the promoted growth kinetics of a compound layer in GNS samples.

Stored energy and reaction thermodynamics

Thermal analysis (see Figure 4b) of the reaction between Zn and GNS Fe showed that an exothermic peak appears at about 309 °C, which is ≈21 °C lower than that in the Zn/CG–Fe couple. Mostly, the ξ-$FeZn_{13}$ phase formed after the exothermic peaks in both samples. In addition, the reaction enthalpy change is ≈58.6 mJ·cm^{-2} in the Zn/GNS–Fe couple, almost double that in the Zn/CG–Fe couple [61].

In addition to the promoted nucleation and growth kinetics related with numerous GBs, as discussed in the last section, the higher stored free energy might also contribute to the lower onset temperature and higher reaction enthalpy change of Fe–Zn reaction in the GNS sample. As we know, stored energy values in metallic systems processed by conventional cold working are typically within 0.01–0.2 kJ·mol^{-1}, and they may change either the kinetics or the path of a phase transition in solid-state with a typical free energy change of 0.5–3 kJ·mol^{-1} [66]. While the stored energy may be much higher because GBs are associated with a higher stored free energy in the GNS substrates produced by SMAT [38], an additional driving force will be provided for the formation of intermetallic compounds. For example, the stored energy value in the GNS Fe is estimated to be ≈2.07 kJ·mol^{-1} according to the value in a nanostructured Fe synthesized by ball milling [61,67]. In comparison, the standard Gibbs free energy change for the formation of $FeZn_{13}$ from elemental Fe and Zn atoms is about −2.50 kJ·mol^{-1} at 330 °C [68]. With the stored excess energy in the GNS layer, the Gibbs free energy change for this reaction becomes −4.57 kJ·mol^{-1}, so that the nucleation rate will be raised and the onset temperature may be decreased for the Fe–Zn reaction in the Zn/GNS–Fe couple [61].

The stored energy in the nanostructured surface layer also contributed to the promoted formation process of nitrides during nitriding GNS Fe at low temperatures [62]. The Gibbs free energy change for nitrides formation in the CG Fe at 500 °C is about −8.22 kJ·mol^{-1} for the γ' phase and −1.69 kJ·mol^{-1} for the ε phase. Both values might become positive and nitrides could not form at 300 °C. However, the free energy changes for the nitrides formation became negative with the stored excess energy in the nanostructured Fe phase, so that their formation became possible at the same temperature. The contributions of stored excess energy to the promoted nitriding kinetics have been confirmed by measurements on critical nitrogen potentials for the formation of ε phase. As shown in Figure 5, the ε-$Fe_{2-3}N$ phase formed at a lower temperature or with a smaller nitrogen potential in the GNS Fe sample in comparison with those in the CG sample [63,69].

Surface alloying of GNS materials

Inspired by the significantly promoted diffusion and chemical reaction kinetics in GNS layers, many works have been carried out on advancing surface alloying techniques of metals with a preformed nanostructured surface layer. The advantages are distinct, for example, improving surface properties such as wear and corrosion resistance with higher energy/time efficiency, reducing work-piece distortion and/or grain coarsening. In addition, GNS surface layers with promoted diffusion and chemical reaction were also produced to enhance formation of surface layers with modified microstructure and phase constitutions, in order to be made more protective and functional.

Surface alloying processes

Lower-temperature processes: Surface alloying processes, such as nitriding and aluminizing, have been achieved on various engineering metals with a GNS surface layer at temperatures much lower than the conventional processing temperatures, and properties such as resistance to wear and corrosion were significantly improved.

Gas nitriding of steel is conventionally carried out at temperatures above 500 °C over a long duration (60–80 h). A representative nitriding steel 38CrMoAl was submitted to SMAT followed by gas nitriding at 400 °C for 30 h [70]. As shown in Figure 6, a continuous compound layer containing mostly nanosized ε-$Fe_{2-3}N$ and γ'-Fe_4N phases followed by a diffusion zone was formed on the GNS sample, and the total thickness of the compound layer and the diffusion layer is more than 200 μm. In comparison, no continuous compound layer was formed on the CG sample after the same nitriding process, and only a diffusion zone with the thickness of ≈50 μm was observed. Thus, a much higher wear resistance was obtained due to the thicker nitride layer with increased hardness on the GNS sample.

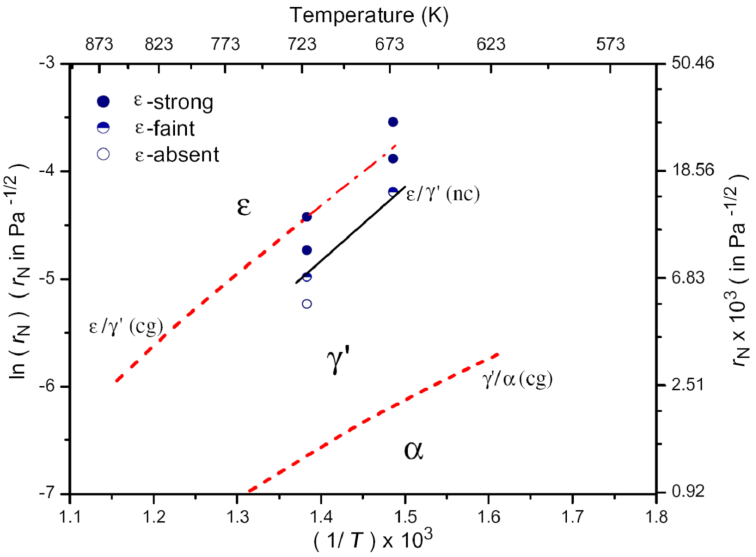


Figure 5: Correlation of temperature and nitrogen potential for the formation of ε-$Fe_{2-3}N$ phase in the GNS Fe (nc), in comparison with that for the CG Fe reported by Lehrer [69]. Figure reproduced with permission from [56], copyright 2007 Elsevier.

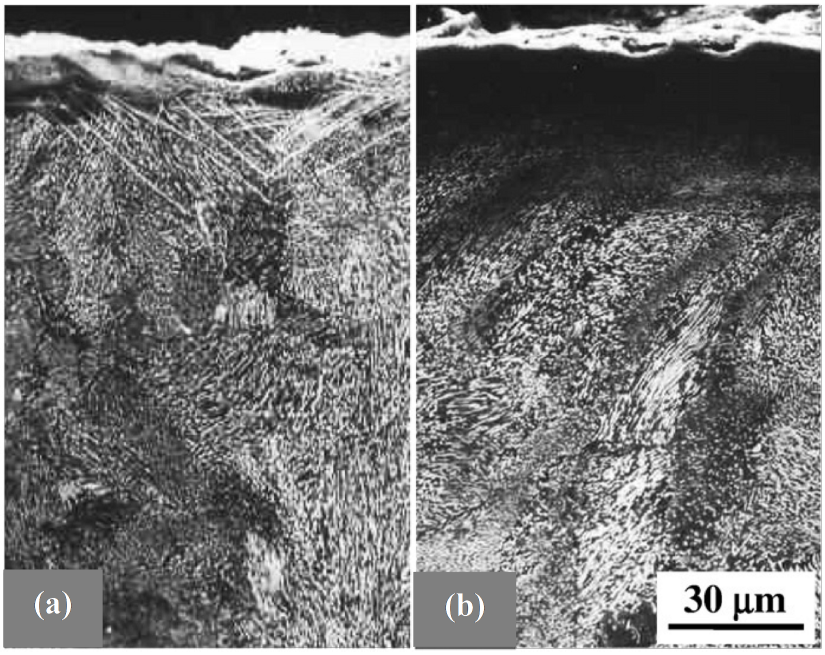


Figure 6: Cross-sectional observations of (a) the CG and (b) the GNS 38CrMoAl samples after gas nitriding at 400 °C for 30 h. Figure reproduced with permission from [70], copyright 2008 Elsevier.

Similarly, preformed GNS surface layers have also been used to successfully lower the boronizing temperature of tool steel [71-75], aluminizing temperature of Mg alloys [76] and ferritic steel [77,78], and nitriding temperature of plain carbon steel [79], stainless steel [80-82], Ti and Ti alloys [83-85], etc.

In addition, the simultaneous surface mechanical and alloying treatment has also been developed to promote the formation of alloyed or compound layers. By loading specimens, pack-aluminizing powder and alloy balls in a chamber, and then mechanically vibrating the chamber at an elevated temperature (≈600 °C), an aluminized coating consisting mostly of Fe_2Al_5 phase with some $FeAl_3$ and FeAl phases has been produced on low-carbon steel [86] and Fe-13Cr steel [87] by Zhan et al. While grain growth is effectively hindered in the simultaneous treatment, the alloyed/compound coating should be thicker than

that formed by SMAT with subsequent alloying treatment. Furthermore, the diffusive transport of species and phase transitions might be significantly promoted during SPD, which usually triggers the states equivalent to higher temperatures [88]. For example, Straumal et al. [89] demonstrated that high pressure torsion at room temperature produced a solid solution with a certain steady-state concentration equal to the solubility limit at an effective temperature of 680 °C in Cu–Ag alloys with different initial states. This will also contribute to the promoted surface alloying kinetics during simultaneous treatment, and might even result in the formation of metastable phases. However, deficiencies of such a treatment mainly come from technical difficulties in achieving simultaneous mechanical and alloying processes at elevated temperatures.

Duplex surface alloying processes: For surface alloying processes such as chromizing and aluminizing, temperatures as high as ≈1000 °C are conventionally required to achieved a satisfying (in terms of thickness and phase constitutions) alloyed/compound surface layer on steels. The formation kinetics of an alloyed layer might be significantly promoted by introducing a GNS surface layer. However, the formed alloyed layer was typically only on the micrometer scale in thickness at lower temperatures, even though a higher ratio was achieved by comparing the thickness of the alloyed layer on the GNS sample with that on the CG counterpart sample. A further increased processing temperature decreased the ratio or even reduce the thickness value due to the instability of nanostructures at higher temperatures, as mentioned previously. In addition, phase constitutions in compound layers formed at lower temperatures were sometimes different (sometimes not as satisfying) from conventional ones formed at higher temperatures. A duplex surface alloying processes, that is, a lower temperature (T_1) process followed by a higher temperature (T_2) process, have been developed to overcome these limitations [32,33,90]. The process at T_1 allowed an effective diffusion of alloying elements and compound formation along GBs, while the nanostructures were relatively stable. The following process at T_2 enhanced the growth (or phase transformation) kinetics of alloyed layers because the thermal stability in the surface layers was improved by the introduced alloying elements and/or compounds during the previous process.

The effects of both processes at T_1 and at T_2 on the formation of a chromized layer have been studied on a GNS H13 steel sample prepared by SMAT [33]. As shown in Figure 7, the thickness of the compound layer ($(Cr,Fe)_2N_{1-x}$ and $(Cr,Fe)_{23}C_6$ phases) increased gradually with increasing T_1 before reaching a maximum at ≈600 °C and then decreased with a further increase in T_1, when T_2 was fixed at 950 °C for 120 min. In comparison, the compound layer formed on the CG sample remained approximately a constant thickness with increasing T_1. When T_1 was fixed at 600 °C for 120 min, a much thicker compound surface layer was formed on the GNS sample than on the CG sample after the chromizing process at T_2 from 950 to 1050 °C. Subsequently, a duplex chromizing process at 600 °C followed by another at 1050 °C was employed to chromize the GNS sample. A chromized surface layer of ≈30 μm in thickness was formed, much thicker than that on the CG sample (≈10 μm) after the same chromizing process. And

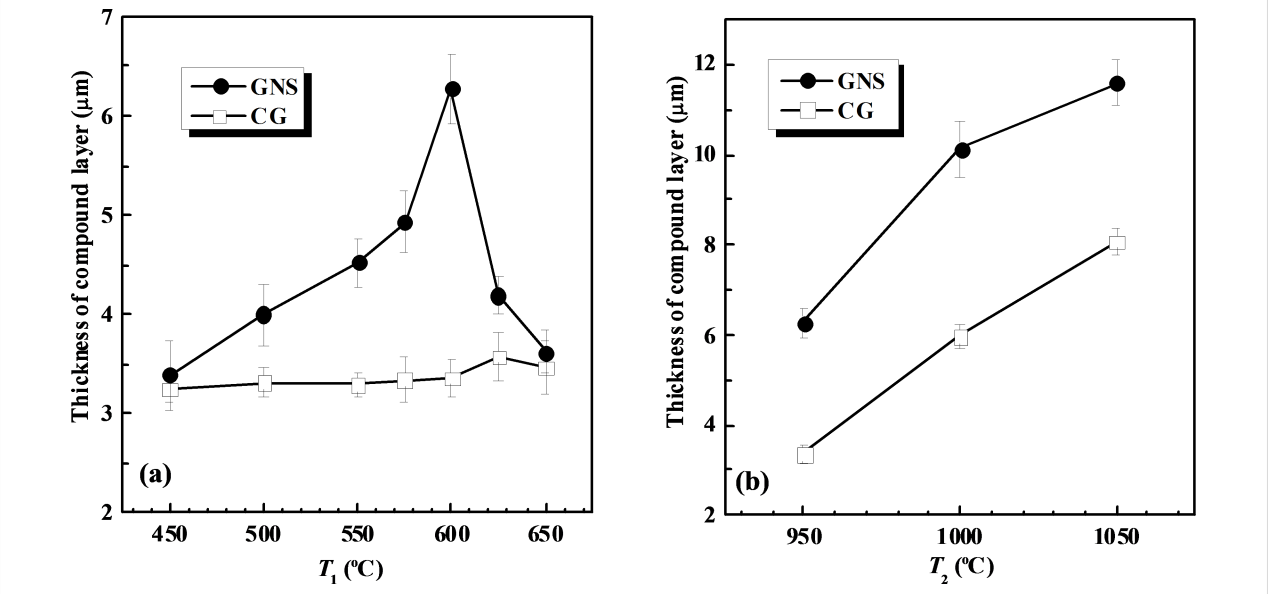


Figure 7: Effects of (a) T_1 (with T_2 = 950 °C for 120 min) and (b) T_2 (with T_1 = 600 °C for 120 min) on the compound layer thickness in the GNS and the CG H13 steel samples after duplex chromizing processes. Figure reproduced with permission from [33], copyright 2010 Elsevier.

the wear resistance of the GNS sample after the duplex chromizing was significantly enhanced due to the higher surface hardness, as well as the graded distribution of composition, structure, and hardness.

In addition, a duplex aluminizing process including a packed aluminization process at 560 °C and a subsequent diffusion annealing treatment at 720 °C was developed for the P92 ferritic–martensitic (F-M) steel with a preformed GNS surface layer [90]. A lower aluminum content aluminide (AlFe and α-(FeAl)) surface layer of ≈17 μm in thickness was produced on the F-M steel. Experiments showed that the oxidation resistance of the F-M steel in steam was significantly promoted at higher temperatures. In comparison with the brittle Al-rich aluminide (mostly Al_5Fe_2) surface layer formed on the CG sample after the same duplex process, the lower content Al aluminide layer formed on the GNS sample is more resistant to cracking and has better adhesion to the substrate [91].

Other diffusion-related processes

The coating/substrate interface is usually the most vulnerable part in a coated component due to the lower bonding strength between them. Some experiments showed that the bonding property of a coating on a substrate might be improved by preforming a GNS surface layer on the substrate. This was mostly due to the promoted atomic diffusion kinetics in the GNS layer, which strengthened the metallurgical bonding across the interface. For example, the interdiffusion distance between the elements of a cold-sprayed Zn–Al coating and a GNS interstitial-free steel substrate was significantly increased in the as-sprayed state, resulting in an increment of ≈30% in the bonding strength of the coating on the substrate [92]. In addition, a higher film cohesion strength and better wear resistance have been achieved on the 304 stainless steel with a preformed GNS surface layer after being sputter-deposited a DLC coating, in comparison with that of the DLC-coated CG sample [93].

A GNS surface layer has also been employed to facilitate the formation of nanoporous titania on the commercial pure Ti [94,95], which is used as an important material in human body implantation. After immersion in the H_2O_2 solution for 24 h at room temperature, crystallized titania with the nanoporous structure was synthesized on the GNS Ti plate, while only interfacial corrosion was observed on the CG sample. By studying the structure and surface morphology evolution of the GNS sample in the H_2O_2 solution, Wen et al. [95] revealed that the accelerated formation of nanoporous structure was mostly due to the higher chemical reactivity of the GNS Ti, which promoted the decomposition of H_2O_2 and the formation of amorphous titania. Furthermore, the formed titania showed an increased crystallinity and retained the nanoporous structure even after calcination at 600 °C [94]. These works indicated the possibility to improve the bioactivity of titanium bone implants and to accelerate osseointegration by introducing a preformed GNS surface layer [95].

Different from the phenomena that thicker alloyed layers commonly form on GNS materials, a much thinner oxide layer was observed on a GNS 9Cr2WVTa F-M steel, i.e., the oxidation resistance of the steel was improved by the preformed GNS surface layer [96]. As shown in Figure 8, a compact oxide layer with the thickness of ≈0.5 μm was formed on the GNS sample after oxidation at 600 °C for 510 h in air. In comparison, it was within 8–50 μm in thickness and with various cracks on the oxidized CG sample. Further comparisons of composition and phase distributions indicated that the oxide scale was enriched

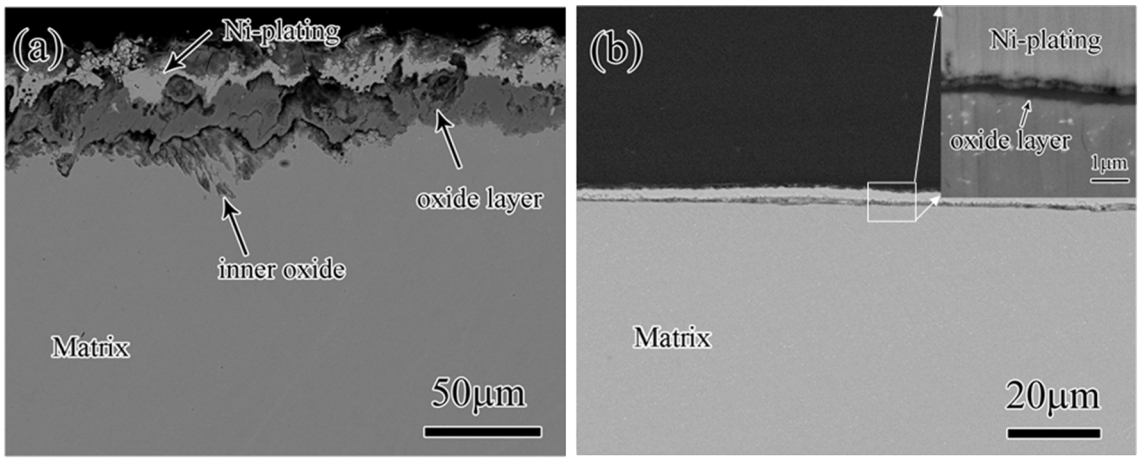


Figure 8: Typical cross-sectional morphologies of (a) the CG and (b) the GNS 9Cr2WVTa F-M steel samples oxidized at 600 °C for 510 h in air. Insert in (b) shows a magnified image of the boxed region. Figure reproduced with permission from [96], copyright 2016 Elsevier.

with Mn and contained a large amount of Mn_2O_3 phase on the GNS sample, while no Mn enrichment was observed and the oxide scale was mainly composed of $(Fe_{0.6}Cr_{0.4})_2O_3$ phase on the CG sample. Analysis confirmed that the markedly improved oxidation resistance of the GNS sample mostly resulted from the quicker formation of the Mn-enriched oxide scale. While the Mn oxide (i.e., Mn_2O_3) possessed the most negative free-energy among all possible oxides from 9Cr2WVTa steel, its formation was accelerated by the higher diffusivities in the GNS surface layer. In addition, the higher binding energy between Mn and vacancies, of which the concentration was much larger in the GNS sample than in the CG sample, also contributed to the quicker formation of Mn-enriched oxide scale [45,96,97].

Conclusion

Due to the importance of understanding the diffusion and surface alloying behavior of GNS metals, interfacial diffusion and reactive diffusion have been systematically studied on this kind of material and summarized in this review. It was confirmed that interfacial diffusivities in GNS layers are typically 3–5 orders of magnitude higher than those along GBs in CG counterparts. This was mainly associated with a higher energy state of GBs induced by the plastic deformation with high strain and strain rates. Meanwhile, the chemical diffusion and reaction kinetics have been promoted in GNS surface layers, in which numerous GBs accelerate atomic diffusion and increase the nucleation and growth rates of formed compounds. The extra stored free energy at GBs also thermodynamically facilitate the formation of compounds in GNS surface layers.

Benefitting from the promoted diffusion and reaction kinetics, different surface alloying treatments have been achieved at much lower temperatures on materials with a preformed GNS surface layer than those of the conventional treatments on CG samples, such as nitriding, boronizing, and aluminizing. In addition, some other diffusion-related properties, such as bonding strength of coating on substrate, bioactivity of Ti and Ti alloys, and oxidation resistance of F-M steels, have also been enhanced by GNS surface layers. By applying a duplex approach including a lower temperature step and a subsequent higher temperature step, chromizing and aluminizing treatments were further modified to obtain an alloyed (or compound) surface layer with larger thickness and better properties.

Studies of diffusion behavior might shed light on the structural characteristics and properties of internal interfaces in nanostructured materials. Novel microstructures such as LAGB-dominant interfaces and nanolaminates have been synthesized in GNS metals recently [98,99]. They showed unique performance, for example, ultrahigh hardness accompanied by superior thermal stability. Studying the diffusion kinetics and relative behavior in GNS layers with such novel microstructures is expected to help understand their unique features and provide insights on tailoring the microstructure for better performance.

Combined with surface alloying, a graded transition in composition and/or phase constitution is formed in a GNS surface layer. Besides the enhanced properties, novel and unique properties of such a material with graded distribution of microstructure, composition, and phase are expected to be further explored. For example, a synergic improvement in strength, ductility, and resistance to wear and corrosion might be expected, while the distribution of microstructure, composition, and phase can be controlled within broader ranges due to the promoted diffusion kinetics in the preformed GNS layers.

Acknowledgements

Financial support from the Ministry of Science and Technology projects of China (No. 2012CB932201), the National Natural Science Foundation of China (Nos. 51231006, 91226204), and Shenyang National Laboratory for Materials Science are acknowledged.

References

1. Fang, T. H.; Li, W. L.; Tao, N. R.; Lu, K. *Science* **2011,** *331,* 1587–1590. doi:10.1126/science.1200177
2. Wu, X.; Jiang, P.; Chen, L.; Yuan, F.; Zhu, Y. T. *Proc. Natl. Acad. Sci. U. S. A.* **2014,** *111,* 7197–7201. doi:10.1073/pnas.1324069111
3. Wei, Y.; Li, Y.; Zhu, L.; Liu, Y.; Lei, X.; Wang, G.; Wu, Y.; Mi, Z.; Liu, J.; Wang, H.; Gao, H. *Nat. Commun.* **2014,** *5,* 3580. doi:10.1038/ncomms4580
4. Han, Z.; Zhang, Y.; Lu, K. *J. Mater. Sci. Technol.* **2008,** *24,* 483–494.
5. Wang, Z. B.; Tao, N. R.; Li, S.; Wang, W.; Liu, G.; Lu, J.; Lu, K. *Mater. Sci. Eng., A* **2003,** *352,* 144–149. doi:10.1016/S0921-5093(02)00870-5
6. Yang, L.; Tao, N. R.; Lu, K.; Lu, L. *Scr. Mater.* **2013,** *68,* 801–804. doi:10.1016/j.scriptamat.2013.01.031
7. Huang, H. W.; Wang, Z. B.; Lu, J.; Lu, K. *Acta Mater.* **2015,** *87,* 150–160. doi:10.1016/j.actamat.2014.12.057
8. Harrison, L. G. *Trans. Faraday Soc.* **1961,** *57,* 1191–1199. doi:10.1039/tf9615701191
9. Lu, K.; Lu, J. *J. Mater. Sci. Technol.* **1999,** *15,* 193–197.
10. Lu, K.; Lu, J. *Mater. Sci. Eng., A* **2004,** *375–377,* 38–45. doi:10.1016/j.msea.2003.10.261
11. Lu, K. *Nat. Rev. Mater.* **2016,** *1,* 16019. doi:10.1038/natrevmats.2016.19
12. Gleiter, H. Materials with Ultrafine Grain Size. In *Proceedings of the 2nd Riso International Symposium on Metallurgy and Materials Science,* Roskilde, Denmark; Hansen, N., Ed.; 1981; pp 15–21.
13. Gleiter, H. *Prog. Mater. Sci.* **1989,** *33,* 223–315. doi:10.1016/0079-6425(89)90001-7
14. Horváth, J.; Birringer, R.; Gleiter, H. *Solid State Commun.* **1987,** *62,* 319–322. doi:10.1016/0038-1098(87)90989-6

15. Schumacher, S.; Birringer, R.; Strauss, R.; Gleiter, H. *Acta Metall.* **1989,** *37,* 2485–2488. doi:10.1016/0001-6160(89)90046-1
16. Höfler, H. J.; Averback, R. S.; Hahn, H.; Gleiter, H. *J. Appl. Phys.* **1993,** *74,* 3832–3839. doi:10.1063/1.354477
17. Divinski, S. V.; Hisker, F.; Kang, Y.-S.; Lee, J.-S.; Herzig, C. *Acta Mater.* **2004,** *52,* 631–645. doi:10.1016/j.actamat.2003.09.045
18. Würschum, R.; Farber, P.; Dittmar, R.; Scharwaechter, P.; Frank, W.; Schaefer, H.-E. *Phys. Rev. Lett.* **1997,** *79,* 4918–4921. doi:10.1103/PhysRevLett.79.4918
19. Würschum, R.; Reimann, K.; Gruss, S.; Kubler, A.; Scharwaechter, P.; Frank, W.; Kruse, O.; Carstanjen, H. D.; Schaefer, H. E. *Philos. Mag. B* **1997,** *76,* 407–417. doi:10.1080/01418639708241104
20. Kolobov, Yu. R.; Grabovetskaya, G. P.; Ivanov, M. B.; Zhilyaev, A. P.; Valiev, R. Z. *Scr. Mater.* **2001,** *44,* 873–878. doi:10.1016/S1359-6462(00)00699-0
21. Amouyal, Y.; Divinski, S. V.; Estrin, Y.; Rabkin, E. *Acta Mater.* **2007,** *55,* 5968–5979. doi:10.1016/j.actamat.2007.07.026
22. Nazarov, A. A.; Romanov, A. E.; Valiev, R. Z. *Scr. Mater.* **1996,** *34,* 729–734. doi:10.1016/1359-6462(95)00573-0
23. Valiev, R. Z.; Islamgaliev, R. K.; Alexandrov, I. V. *Prog. Mater. Sci.* **2000,** *45,* 103–189. doi:10.1016/S0079-6425(99)00007-9
24. Wilde, G.; Ribbe, J.; Reglitz, G.; Wegner, M.; Rösner, H.; Estrin, Y.; Zehetbauer, M.; Setman, D.; Divinski, S. *Adv. Eng. Mater.* **2010,** *12,* 758–764. doi:10.1002/adem.200900333
25. Straumal, B. B.; Kogtenkova, O. A.; Muktepavela, F.; Kolesnikova, K. I.; Bulatov, M. F.; Straumal, P. B.; Baretzky, B. *Mater. Lett.* **2015,** *159,* 432–435. doi:10.1016/j.matlet.2015.07.038
26. Ribbe, J.; Baither, D.; Schmitz, G.; Divinski, S. V. *Phys. Rev. Lett.* **2009,** *102,* 165501.
27. Divinski, S. V.; Ribbe, J.; Baither, D.; Schmitz, G.; Reglitz, G.; Rösner, H.; Sato, K.; Estrin, Y.; Wilde, G. *Acta Mater.* **2009,** *57,* 5706–5717. doi:10.1016/j.actamat.2009.07.066
28. Klinger, L.; Rabkin, E. *Acta Mater.* **1999,** *47,* 725–734. doi:10.1016/S1359-6454(98)00420-0
29. Tao, N. R.; Wang, Z. B.; Tong, W. P.; Sui, M. L.; Lu, J.; Lu, K. *Acta Mater.* **2002,** *50,* 4603–4616. doi:10.1016/S1359-6454(02)00310-5
30. Wang, K.; Tao, N. R.; Liu, G.; Lu, J.; Lu, K. *Acta Mater.* **2006,** *54,* 5281–5291. doi:10.1016/j.actamat.2006.07.013
31. Wang, Z. B.; Tao, N. R.; Tong, W. P.; Lu, J.; Lu, K. *Acta Mater.* **2003,** *51,* 4319–4329. doi:10.1016/S1359-6454(03)00260-X
32. Wang, Z. B.; Lu, J.; Lu, K. *Acta Mater.* **2005,** *53,* 2081–2089. doi:10.1016/j.actamat.2005.01.020
33. Lu, S. D.; Wang, Z. B.; Lu, K. *Mater. Sci. Eng., A* **2010,** *527,* 995–1002. doi:10.1016/j.msea.2009.10.030
34. Srikrishnan, V.; Ficalora, P. J. *Metall. Trans. A* **1975,** *6,* 2095–2102. doi:10.1007/BF03161836
35. Kaur, I.; Gust, W.; Kozma, L. *Handbook of Grain and Interphase Boundary Diffusion Data;* Ziegler Press: Stuttgart, Germany, 1989; Vol. 1 and 2. doi:10.1002/crat.2170251124
36. Callister, W. D. *Materials Science and Engineering: An Introduction,* 5th ed.; John Wiley & Sons: New York, NY, U.S.A., 2000.
37. Suryanarayana, C. *Int. Mater. Rev.* **1995,** *40,* 41–64. doi:10.1179/imr.1995.40.2.41
38. Wang, Z. B.; Lu, K.; Wilde, G.; Divinski, S. V. *Acta Mater.* **2010,** *58,* 2376–2386. doi:10.1016/j.actamat.2009.12.024
39. Amouyal, Y.; Divinski, S. V.; Klinger, L.; Rabkin, E. *Acta Mater.* **2008,** *56,* 5500–5513. doi:10.1016/j.actamat.2008.07.029
40. Divinski, S. V.; Reglitz, G.; Rösner, H.; Estrin, Y.; Wilde, G. *Acta Mater.* **2011,** *59,* 1974–1985. doi:10.1016/j.actamat.2010.11.063
41. Dickenscheid, W.; Birringer, R.; Gleiter, H.; Kanert, O.; Michel, B.; Günther, B. *Solid State Commun.* **1991,** *79,* 683–686. doi:10.1016/0038-1098(91)90613-Z
42. Wang, H. L.; Wang, Z. B.; Lu, K. *Acta Mater.* **2011,** *59,* 1818–1828. doi:10.1016/j.actamat.2010.11.048
43. Kaur, I.; Mishin, Y.; Gust, W. *Fundamentals of Grain and Interphase Boundary Diffusion;* John Wiley & Sons: Chichester, West Sussex, United Kingdom, 1995.
44. Mishin, Y. M. *Defect Diffus. Forum* **2001,** *194–199,* 1113–1125. doi:10.4028/www.scientific.net/DDF.194-199.1113
45. Wang, Z. B.; Tao, N. R.; Tong, W. P.; Lu, J.; Lu, K. *Defect Diffus. Forum* **2006,** *249,* 147–154. doi:10.4028/www.scientific.net/DDF.249.147
46. Straumal, B. B.; Mazilkin, A. A.; Baretzky, B. *Curr. Opin. Solid State Mater. Sci.* **2016,** *20,* 247–256. doi:10.1016/j.cossms.2016.05.006
47. Straumal, B. B.; Sauvage, X.; Baretzky, B.; Mazilkin, A. A.; Valiev, R. Z. *Scr. Mater.* **2014,** *70,* 59–62. doi:10.1016/j.scriptamat.2013.09.019
48. Divinski, S.; Lohmann, M.; Herzig, C.; Straumal, B.; Baretzky, B.; Gust, W. *Phys. Rev. B* **2005,** *71,* 8. doi:10.1103/PhysRevB.71.104104
49. Straumal, B. B.; Noskovich, O. I.; Semenov, V. N.; Shvindlerman, L. S.; Gust, W.; Predel, B. *Acta Metall. Mater.* **1992,** *40,* 795–801. doi:10.1016/0956-7151(92)90021-6
50. Cantwell, P. R.; Tang, M.; Dillon, S. J.; Luo, J.; Rohrer, G. S.; Harmer, M. P. *Acta Mater.* **2014,** *62,* 1–48. doi:10.1016/j.actamat.2013.07.037
51. Wang, Z. B.; Lu, K.; Wilde, G.; Divinski, S. V. *Scr. Mater.* **2011,** *64,* 1055–1058. doi:10.1016/j.scriptamat.2011.02.018
52. Wang, Z. B.; Lu, K.; Wilde, G.; Divinski, S. *Appl. Phys. Lett.* **2008,** *93,* 131904. doi:10.1063/1.2992628
53. Minkwitz, C.; Herzig, C.; Rabkin, E.; Gust, W. *Acta Mater.* **1999,** *47,* 1231–1239. doi:10.1016/S1359-6454(98)00429-7
54. Monzen, R.; Sumi, Y.; Kitagawa, K.; Mori, T. *Acta Metall. Mater.* **1990,** *38,* 2553–2560. doi:10.1016/0956-7151(90)90266-J
55. Borisov, V. T.; Golikov, V. M.; Scherbedinskiy, G. V. *Phys. Met. Metallogr.* **1964,** *17,* 10.
56. Divinski, S.; Ribbe, J.; Schmitz, G.; Herzig, C. *Acta Mater.* **2007,** *55,* 3337–3346. doi:10.1016/j.actamat.2007.01.032
57. Howe, J. M. *Interfaces in Materials;* Wiley: New York, NY, U.S.A., 1997.
58. Kidson, G. V. *J. Nucl. Mater.* **1961,** *3,* 21–29. doi:10.1016/0022-3115(61)90175-1
59. Charlot, F.; Gaffet, E.; Zeghmati, B.; Bernard, F.; Niepce, J. C. *Mater. Sci. Eng., A* **1999,** *262,* 279–288. doi:10.1016/S0921-5093(98)01017-X
60. Wiecinski, P.; Garbacz, H.; Murakami, H.; Kurzydlowski, K. J. *Phys. Status Solidi C* **2010,** *7,* 1395–1398. doi:10.1002/pssc.200983399
61. Wang, H. L.; Wang, Z. B.; Lu, K. *Acta Mater.* **2012,** *60,* 1762–1770. doi:10.1016/j.actamat.2011.12.016
62. Tong, W. P.; Tao, N. R.; Wang, Z. B.; Lu, J.; Lu, K. *Science* **2003,** *299,* 686–688. doi:10.1126/science.1080216
63. Tong, W. P.; Tao, N. R.; Wang, Z. B.; Zhang, H. W.; Lu, J.; Lu, K. *Scr. Mater.* **2004,** *50,* 647–650. doi:10.1016/j.scriptamat.2003.11.022
64. Porter, D.; Easterling, K. *Phase Transformation in Metals and Alloys,* 2nd ed.; Chapman & Hall: London, United Kingdom, 1992.
65. Katona, G. L.; Vladymyrskyi, I. A.; Makogon, I. M.; Sidorenko, S. I.; Kristaly, F.; Daróczi, L.; Csik, A.; Liebig, A.; Beddies, G.; Albrecht, M.; Beke, D. L. *Appl. Phys. A* **2014,** *115,* 203–211. doi:10.1007/s00339-013-7949-z

66. Embury, J. D.; Deschamps, A.; Brechet, Y. *Scr. Mater.* **2003,** *49,* 927–932. doi:10.1016/S1359-6462(03)00479-2
67. Fecht, H. J. Nanophase materials by mechanical attrition: synthesis and characterization. In *Nanophase materials: synthesis-properties-applications;* Hadjipanayis, G. C.; Siegel, R. W., Eds.; NATO ASI Series, Vol. 260; Kluwer: Amsterdam, Netherlands, 1994; pp 125–144. doi:10.1007/978-94-011-1076-1_18
68. Reumont, G.; Perrot, P.; Fiorani, J. M.; Hertz, J. *J. Phase Equilib.* **2000,** *21,* 371–378. doi:10.1361/105497100770339905
69. Lehrer, E. Z. *Elektrochem. Angew. Phys. Chem.* **1930,** *36,* 383–392.
70. Tong, W. P.; Han, Z.; Wang, L. M.; Lu, J.; Lu, K. *Surf. Coat. Technol.* **2008,** *202,* 4957–4963. doi:10.1016/j.surfcoat.2008.04.085
71. Yang, H. P.; Wu, X. C.; Min, Y. A.; Wu, T. R.; Gui, J. Z. *Surf. Coat. Technol.* **2013,** *228,* 229–233. doi:10.1016/j.surfcoat.2013.04.033
72. Balusamy, T.; Sankara Narayanan, T. S. N.; Ravichandran, K. *Surf. Coat. Technol.* **2012,** *213,* 221–228. doi:10.1016/j.surfcoat.2012.10.051
73. Balusamy, T.; Sankara Narayanan, T. S. N.; Ravichandran, K.; Park, I. S.; Lee, M. H. *Surf. Coat. Technol.* **2013,** *232,* 60–67. doi:10.1016/j.surfcoat.2013.04.053
74. Balusamy, T.; Sankara Narayanan, T. S. N.; Ravichandran, K.; Park, I. S.; Lee, M. H. *Vacuum* **2013,** *97,* 36–43. doi:10.1016/j.vacuum.2013.04.006
75. Yang, H.; Wu, X.; Yang, Z.; Pu, S.; Wang, H. *J. Alloys Compd.* **2014,** *590,* 388–395. doi:10.1016/j.jallcom.2013.12.151
76. Sun, H. Q.; Shi, Y. N.; Zhang, M.-X.; Lu, K. *Surf. Coat. Technol.* **2008,** *202,* 3947–3953. doi:10.1016/j.surfcoat.2008.02.010
77. Xiang, Z. D.; Datta, P. K. *Scr. Mater.* **2006,** *55,* 1151–1154. doi:10.1016/j.scriptamat.2006.08.016
78. Si, X.; Lu, B. N.; Wang, Z. B. *J. Mater. Sci. Technol.* **2009,** *25,* 433–436.
79. Gu, J. F.; Bei, D. H.; Pan, J. S.; Lu, J.; Lu, K. *Mater. Lett.* **2002,** *55,* 340–343. doi:10.1016/S0167-577X(02)00389-0
80. Balusamy, T.; Sankara Narayanan, T. S. N.; Ravichandran, K.; Park, I. S.; Lee, M. H. *Mater. Charact.* **2013,** *85,* 38–47. doi:10.1016/j.matchar.2013.08.009
81. Zhang, H. W.; Wang, L.; Hei, Z. K.; Liu, G.; Lu, J.; Lu, K. *Z. Metallkd.* **2003,** *94,* 1143–1147. doi:10.3139/146.031143
82. Lin, Y.; Lu, J.; Wang, L.; Xu, T.; Xue, Q. *Acta Mater.* **2006,** *54,* 5599–5605. doi:10.1016/j.actamat.2006.08.014
83. Farokhzadeh, K.; Qian, J.; Edrisy, A. *Mater. Sci. Eng., A* **2014,** *589,* 199–208. doi:10.1016/j.msea.2013.09.077
84. Ge, L.; Tian, N.; Lu, Z.; You, C. *Appl. Surf. Sci.* **2013,** *286,* 412–416. doi:10.1016/j.apsusc.2013.09.105
85. Sun, J.; Tong, W. P.; Zuo, L.; Wang, Z. B. *Mater. Des.* **2013,** *47,* 408–415. doi:10.1016/j.matdes.2012.11.029
86. Zhan, Z.; He, Y.; Wang, D.; Gao, W. *Intermetallics* **2006,** *14,* 75–81. doi:10.1016/j.intermet.2005.04.019
87. Zhan, Z.; He, Y.; Wang, D.; Gao, W. *Oxid. Met.* **2007,** *68,* 243–251. doi:10.1007/s11085-007-9073-y
88. Straumal, B.; Korneva, A.; Zięba, P. *Arch. Civil Mech. Eng.* **2014,** *14,* 242–249. doi:10.1016/j.acme.2013.07.002
89. Straumal, B. B.; Pontikis, V.; Kilmametov, A. R.; Mazilkin, A. A.; Dobatkin, S. V.; Baretzky, B. *Acta Mater.* **2017,** *122,* 60–71. doi:10.1016/j.actamat.2016.09.024
90. Guo, S.; Wang, Z. B.; Wang, L. M.; Lu, K. *Surf. Coat. Technol.* **2014,** *258,* 329–336. doi:10.1016/j.surfcoat.2014.09.005
91. Guo, S.; Wang, Z. B.; Lu, K. *J. Mater. Sci. Technol.* **2015,** *31,* 1268–1273. doi:10.1016/j.jmst.2015.09.015
92. Liang, Y. L.; Wang, Z. B.; Zhang, J.; Zhang, J. B.; Lu, K. *Appl. Surf. Sci.* **2016,** *385,* 341–348. doi:10.1016/j.apsusc.2016.05.142
93. Fu, T.; Zhou, Z. F.; Zhou, Y. M.; Zhu, X. D.; Zeng, Q. F.; Wang, C. P.; Li, K. Y.; Lu, J. *Surf. Coat. Technol.* **2012,** *207,* 555–564. doi:10.1016/j.surfcoat.2012.07.076
94. Wen, M.; Gu, J.-F.; Liu, G.; Wang, Z.-B.; Lu, J. *Surf. Coat. Technol.* **2007,** *201,* 6285–6289. doi:10.1016/j.surfcoat.2006.11.031
95. Wen, M.; Gu, J.-F.; Liu, G.; Wang, Z.-B.; Lu, J. *Appl. Surf. Sci.* **2008,** *254,* 2905–2910. doi:10.1016/j.apsusc.2007.10.035
96. Lu, Y. H.; Wang, Z. B.; Song, Y. Y.; Rong, L. J. *Corros. Sci.* **2016,** *102,* 301–309. doi:10.1016/j.corsci.2015.10.021
97. Konstantinović, M. J.; Bonny, G. *Acta Mater.* **2015,** *85,* 107–111. doi:10.1016/j.actamat.2014.11.026
98. Liu, X. C.; Zhang, H. W.; Lu, K. *Science* **2013,** *342,* 337–340. doi:10.1126/science.1242578
99. Liu, X. C.; Zhang, H. W.; Lu, K. *Scr. Mater.* **2015,** *95,* 54–57. doi:10.1016/j.scriptamat.2014.10.003

License and Terms

This is an Open Access article under the terms of the Creative Commons Attribution License (http://creativecommons.org/licenses/by/4.0), which permits unrestricted use, distribution, and reproduction in any medium, provided the original work is properly cited.

The license is subject to the *Beilstein Journal of Nanotechnology* terms and conditions: (http://www.beilstein-journals.org/bjnano)

The definitive version of this article is the electronic one which can be found at:
doi:10.3762/bjnano.8.59

BEILSTEIN JOURNAL OF NANOTECHNOLOGY

Computing the T-matrix of a scattering object with multiple plane wave illuminations

Martin Fruhnert*[1], Ivan Fernandez-Corbaton[2], Vassilios Yannopapas[3] and Carsten Rockstuhl[1,2]

Full Research Paper

Open Access

Address:
[1]Institute of Theoretical Solid State Physics, Karlsruhe Institute of Technology, Wolfgang-Gaede-Strasse 1, 76131 Karlsruhe, Germany, [2]Institute of Nanotechnology, Karlsruhe Institute of Technology, P.O. Box 3640, 76021 Karlsruhe, Germany and [3]Department of Physics, National Technical University of Athens, Heroon Polytechniou 9, 15780 Zografou, Greece

Email:
Martin Fruhnert* - martin.fruhnert@kit.edu

* Corresponding author

Keywords:
metamaterials; nanooptics; numerics; scattering; T-matrix

Beilstein J. Nanotechnol. **2017,** *8,* 614–626.
doi:10.3762/bjnano.8.66

Received: 18 October 2016
Accepted: 22 February 2017
Published: 14 March 2017

This article is part of the Thematic Series "Advances in nanomaterials II".

Guest Editor: H. Hahn

© 2017 Fruhnert et al.; licensee Beilstein-Institut.
License and terms: see end of document.

Abstract

Given an arbitrarily complicated object, it is often difficult to say immediately how it interacts with a specific illumination. Optically small objects, e.g., spheres, can often be modeled as electric dipoles, but which multipole moments are excited for larger particles possessing a much more complicated shape? The T-matrix answers this question, as it contains the entire information about how an object interacts with any electromagnetic illumination. Moreover, a multitude of interesting properties can be derived from the T-matrix such as the scattering cross section for a specific illumination and information about symmetries of the object. Here, we present a method to calculate the T-matrix of an arbitrary object numerically, solely by illuminating it with multiple plane waves and analyzing the scattered fields. Calculating these fields is readily done by widely available tools. The finite element method is particularly advantageous, because it is fast and efficient. We demonstrate the T-matrix calculation at four examples of relevant optical nanostructures currently at the focus of research interest. We show the advantages of the method to obtain useful information, which is hard to access when relying solely on full wave solvers.

Introduction

Recent advances in nanofabrication technology made the creation of large volumes of particles with complicated geometries possible [1-6]. The latter constitute the base for nanomaterials with advanced properties [7]. This also triggered the need for efficient computational tools to back up experimental findings with simulations that allow to understand the underlying principles that cause the properties of the respective nanomaterials [8-10]. With current possibilities it is fairly straightforward to calculate the scattered fields of an arbitrary object illuminated with a plane wave or more complicated illumination

scenarios. They all rely on the numerical solution of Maxwell's equations while considering a given distribution of material in space. Examples for such numerical routines are finite element solvers [11-13], finite-difference time-domain methods [14-16], discrete dipole approximation [17,18], or similar tools. This yields valuable information about the single structure. On the other hand, there are efficient methods to calculate the scattering of large clusters of spherical particles, for example the extended Mie theory [19,20]. This consideration of many particles is the prerequisite to study the emergence of properties if many of these particles are brought together to form artificial nanomaterials.

The principles of these two distinct approaches can be combined to the T-matrix method [21-23]. Using this method, the T-matrix, which contains the information about how an isolated object scatters the electromagnetic field, is calculated and subsequently used in a multiple-scattering algorithm, similar to the multi-Mie Method [20,24], to calculate the scattered fields of a large cluster of arbitrary particles.

There are several analytical and semi-analytical ways to calculate the T-matrix of simple particles with high symmetries [21,25-27]. Here, we present a method to calculate the T-matrix of an arbitrarily complex particle. Our approach only requires the object to be illuminated in a sequence of simulations with multiple plane waves. From these simulations the scattering coefficients and, ultimately, the T-matrix, are deduced from the scattered fields. These fields can be calculated with established methods, such as the finite element method but, in general, any other of the aforementioned methods can be considered as well. The resulting T-matrix is then independent of the form and direction of the external illumination. It only depends on the material and geometry of the object. The scattering coefficients that can then be calculated for any arbitrary illumination are vital for the calculation of all further quantities, such as the scattered fields and the scattering cross section for a specific illumination. The availability of the T-matrix simplifies particularly the analysis of quantities that require the evaluation of the same response of the object to a larger number of different illumination fields. A referential example therefore is the calculation of the force map for a complicated illumination in space exerted on the particle. There, the response of the same particle to the field at each spatial location of the illumination needs to be calculated. This can be a tedious task if every time a new full wave solution to Maxwell's equations is required. The situation is much more simplified if the T-matrix of the object is known. The coefficients can also be used to determine the strength of the individual multipole contributions to the scattering for example to check if the dipole approximation is applicable. This is particularly useful in the context of the homogenization, i.e., the assignment of effective material parameters to a medium. We emphasize the fact that when only the optical response of a given particle to a given illumination is needed, it does not make much sense to calculate the T-matrix first, as it requires the solution of multiple full-wave problems. However, whenever more complicated objects are of interest, or if the response of a given structure to many different illuminations is needed, as it is often required in the calculation of force and torque, it is expected that the computation of the T-matrix pays off. Furthermore, as we will point out when we investigate the example cases, the T-matrix itself is of scientific value, as it contains all the information available concerning how an object interacts with light.

In the following section we outline the multipole decomposition of the fields [28]. This is the theoretical basis for the T-matrix calculation. The numerical calculation of the T-matrix is demonstrated in the next section. Finally, we provide four numerical examples in the form of interesting but simple objects the T-matrix of which we calculate to demonstrate the usefulness of the method.

Multipole expansion of electromagnetic fields

We want do decompose the fields produced by scattering off of an illuminated object into contributions from different multipoles. We start by decomposing the total external fields surrounding the object into incident and scattered fields

$$\mathbf{E}_{\mathrm{ext}}(\mathbf{r},\omega)=\mathbf{E}_{\mathrm{inc}}(\mathbf{r},\omega)+\mathbf{E}_{\mathrm{sca}}(\mathbf{r},\omega). \tag{1}$$

Note that this is always possible for theoretical considerations, but experimentally a strict distinction is not possible. In the following we largely skip the space and frequency dependency of the fields for simplicity but these dependencies are always assumed.

Then, the fields are expanded into vector spherical harmonic functions

$$\mathbf{M}_{nm}^{(l)}=\gamma_{nm}z_n^{(l)}(kr)\nabla\times\left[\mathbf{r}P_n^m(\cos\theta)\mathrm{e}^{\mathrm{i}m\phi}\right], \tag{2}$$

$$\begin{aligned}\mathbf{N}_{nm}^{(l)}&=\frac{1}{k}\nabla\times\mathbf{M}_{nm}^{(l)}\\&=\gamma_{nm}\left[\frac{n(n+1)}{kr}z_n^{(l)}(kr)\frac{\mathbf{r}}{r}P_n^m(\cos\theta)\mathrm{e}^{\mathrm{i}m\phi}\right.\\&\left.+\frac{\mathrm{d}}{kr\,\mathrm{d}(kr)}\left(krz_n^{(l)}(kr)\right)r\nabla\left(P_n^m(\cos\theta)\mathrm{e}^{\mathrm{i}m\phi}\right)\right],\end{aligned} \tag{3}$$

with the normalization factor

$$\gamma_{nm} = \sqrt{\frac{(2n+1)(n-m)!}{4\pi n(n+1)(n+m)!}}. \tag{4}$$

Here, the index l represents the underlying function: $l = 1,2$ corresponds to spherical Bessel functions of first $z^{(1)} = j_n$ and second kind $z^{(2)} = y_n$, respectively, while $l = 3,4$ corresponds to Hankel functions of first and second kind $z^{(3,4)} = h_n^{(1,2)}$, respectively [29,30]. The incident field has to be finite in the center of the coordinate system. Thus, we have to take Bessel functions and the expansion reads as

$$\mathbf{E}_{\text{inc}} = \sum_{n=1}^{\infty}\sum_{m=-n}^{n}\left[p_{nm}\mathbf{N}_{nm}^{(1)} + q_{nm}\mathbf{M}_{nm}^{(1)}\right]. \tag{5}$$

The scattered field needs to satisfy the outgoing Sommerfeld radiation condition and is expanded with Hankel functions

$$\mathbf{E}_{\text{sca}} = \sum_{n=1}^{\infty}\sum_{m=-n}^{n}\left[a_{nm}\mathbf{N}_{nm}^{(3)} + b_{nm}\mathbf{M}_{nm}^{(3)}\right]. \tag{6}$$

Here, k is the wave number in the surrounding medium, which is characterized by the permittivity $\varepsilon(\omega)$ and the permeability $\mu(\omega)$. The complex expansion coefficients $a_{nm}(\omega)$ and $b_{nm}(\omega)$ are called scattering coefficients and the coefficients $p_{nm}(\omega)$ and $q_{nm}(\omega)$ are called incident coefficients. Together they contain all relevant information about the interaction of the particle with the given illumination. The physical meaning of the individual terms is also straightforward. For example in the expansion of the scattered field, the first term on the right hand side expresses the field scattered due to the induced electric multipole moments. The second term expresses the field scattered due to the induced magnetic multipole moments.

In order to be able to perform numerical calculations, we need to truncate the infinite sums in all expansions to a finite number N. This number is the multipole order that we take into account, $N = 1$ corresponding to dipoles, $N = 2$ to quadrupoles and so on. Thus, by choosing the maximum order we want to consider, we can strongly influence the computation time and final accuracy.

The scattering coefficients can be used to calculate the total scattering cross section of the system

$$C_{\text{sca}} = \eta\sum_{n=1}^{\infty}\sum_{m=-n}^{n}\left(|a_{nm}|^2 + |b_{nm}|^2\right). \tag{7}$$

Here, η is a scaling factor, depending on the illumination. For a plane wave we have $\eta = 1/(k^2|\mathbf{E}_0|^2)$, where $\mathbf{E}_0$ is the amplitude of the incident plane wave. In order to obtain more information, e.g., about a resonance, we can modify the equation to calculate the contributions of each multipolar order

$$C_{\text{sca}}^{(n')} = \eta\sum_{m=-n'}^{n'}|c_{n'm}|^2, \tag{8}$$

where n' is the multipolar index and c_{nm} stands for a_{nm} if we want to consider the electric part or b_{nm} if we consider the magnetic part, respectively. For example the electric and magnetic dipole contributions, which are usually the strongest contributions for electromagnetically small particles, read as

$$\begin{aligned} C_{\text{sca}}^{\text{el.dip.}} &= \eta\left(|a_{1-1}|^2 + |a_{10}|^2 + |a_{11}|^2\right) \\ C_{\text{sca}}^{\text{magn.dip.}} &= \eta\left(|b_{1-1}|^2 + |b_{10}|^2 + |b_{11}|^2\right). \end{aligned} \tag{9}$$

Thus, if we know the scattering coefficients of an object, we know exactly how the different multipoles contribute to the total scattering. That is particularly valuable if we want to design a specific multipole resonance of a nanoparticle or if we want to investigate a given resonance, e.g., from experimental measurements.

T-matrix calculation

In the previous section we showed the decomposition of the fields into scattering and incident coefficients. Now we introduce a link between them that represents the interaction of the object with the illumination: the T-matrix

$$\begin{pmatrix}\mathbf{a}\\ \mathbf{b}\end{pmatrix} = \mathbf{T}\cdot\begin{pmatrix}\mathbf{p}\\ \mathbf{q}\end{pmatrix}. \tag{10}$$

Here **a** and **b** are concatenated vectors that contain the scattering coefficients of the outgoing wave and **p** and **q** are concatenated vectors containing the coefficients of the incident field.

The T-matrix contains the entire near and far field information on how a specific object interacts with any illumination. It depends on the geometry and material composition of the structure in question. The T-matrix of a sphere is known analytically as the Mie coefficients. They form the T-matrix if they are ordered at the diagonal of the matrix. For arbitrary objects, however, the T-matrix is generally dense and is typically ordered in the following way

$$\mathbf{T}=\begin{pmatrix}\mathbf{T}_{\mathrm{ee}} & \mathbf{T}_{\mathrm{em}}\\ \mathbf{T}_{\mathrm{me}} & \mathbf{T}_{\mathrm{mm}}\end{pmatrix}, \tag{11}$$

where $\mathbf{T}_{\mathrm{ee}}$ describes coupling of electric incidence modes to electric scattered modes, $\mathbf{T}_{\mathrm{mm}}$ describes the magnetic coupling and the other parts correspond to mixing of electric and magnetic modes. These parts of the T-matrix can be ordered to show the coupling between the multipolar modes

$$\mathbf{T}_{\mathrm{ee}}=\begin{pmatrix}\mathbf{T}_{11}^{\mathrm{ee}} & \mathbf{T}_{12}^{\mathrm{ee}} & \cdots\\ \mathbf{T}_{21}^{\mathrm{ee}} & \mathbf{T}_{22}^{\mathrm{ee}} & \\ \vdots & & \ddots\end{pmatrix}. \tag{12}$$

Then **T**nn' is the part that represents the coupling of order n' to n. For a sphere, $\mathbf{T}_{11}$ would contain the first Mie coefficient a_1 on the diagonal, $\mathbf{T}_{22}$ the second and so on.

Please note that the vector spherical harmonic functions $\mathbf{N}_{nm}^{(l)}(\mathbf{r},\omega)$ and $\mathbf{M}_{nm}^{(l)}(\mathbf{r},\omega)$ in their presented form are normalized to the unit sphere. Therefore, also the T-matrix is normalized. In many cases it is crucial to use a normalized form of the T-matrix, e.g., when applying rotations [23,31] or for comparing the absolute value of different entries.

To perform simulations and to analyze a given object we need to calculate the T-matrix numerically. There are several established methods to calculate it, the first being the extended boundary condition method, originally introduced by Waterman [21,32,33]. Here, only homogeneous and isotropic particles can be considered and the method is quite time and resource consuming. A similar, more advanced possibility is the point matching method [34,35]. There, the coefficients of the incident, scattered and internal fields are related, but without the expensive surface integrations needed for the extended boundary condition method. Another established strategy to compute the T-matrix of an arbitrary object is to excite it with pure vector spherical harmonic functions to extract exactly one line of the T-matrix per illumination [22]. There, the fields are calculated with an integral equation solver. This method has the advantage that the incident field can be expressed in an exact way with a single incident coefficient. But the actual implementation of such an illumination with available tools is cumbersome. Similar methods have been proposed to retrieve the polarizability tensor of an object [36-39]. These techniques provide valuable information with comparatively little effort, but are restricted to dipolar objects.

Here, we propose a method that is easy to implement practically and, depending on the applied Maxwell solver, very efficient. We illuminate the particle with several different plane waves and extract the expansion coefficients by projecting the scattered fields onto vector spherical harmonic functions. To get the scattered field of the object for every plane wave, however, we need an additional tool that solves Maxwell's equations for an arbitrary particle under plane wave illumination. Such tools are widely available. We chose here the finite element solver JCMsuite [12] because it is especially fast for the simulation of several different illuminations of an object at the same frequency. But in general, any full-wave solver that provides the scattered fields of an object could be used.

The scattering coefficients can be obtained from the scattered fields by Equation 13 and similarly the incident coefficients by Equation 14.

The fields are evaluated at a virtual sphere of fixed radius R that completely encloses the object. Analytically, the chosen radius has no influence on the result. Yet, in numerical realizations the choice may effect the result due to the finite sampling. It is advisable to use a small R, to keep the computational domain small, without touching the actual object. Note that we need to take the full details of the scattered field into account.

Now we get a set of $\begin{pmatrix}\mathbf{p}\\ \mathbf{q}\end{pmatrix}^k$ and corresponding $\begin{pmatrix}\mathbf{a}\\ \mathbf{b}\end{pmatrix}^k$ for each illumination k. Then we can construct a system of equations to calculate the numerical T-matrix $\mathbf{T}_K$ from Equation 10

$$\begin{aligned}a_{nm}(\omega)&=\frac{\int_0^{2\pi}\int_0^{\pi}\mathbf{E}_{\mathrm{sca}}(|\mathbf{r}|=R,\omega)\left[\mathbf{N}_{nm}^{(3)}(|\mathbf{r}|=R,\omega)\right]^{*}\sin\theta\,\mathrm{d}\theta\mathrm{d}\phi}{\int_0^{2\pi}\int_0^{\pi}\left|\mathbf{N}_{nm}^{(3)}(|\mathbf{r}|=R,\omega)\right|^{2}\sin\theta\,\mathrm{d}\theta\mathrm{d}\phi}\\ b_{nm}(\omega)&=\frac{\int_0^{2\pi}\int_0^{\pi}\mathbf{E}_{\mathrm{sca}}(|\mathbf{r}|=R,\omega)\left[\mathbf{M}_{nm}^{(3)}(|\mathbf{r}|=R,\omega)\right]^{*}\sin\theta\,\mathrm{d}\theta\mathrm{d}\phi}{\int_0^{2\pi}\int_0^{\pi}\left|\mathbf{M}_{nm}^{(3)}(|\mathbf{r}|=R,\omega)\right|^{2}\sin\theta\,\mathrm{d}\theta\mathrm{d}\phi}\end{aligned} \tag{13}$$

$$p_{nm}(\omega)=\frac{\int_0^{2\pi}\int_0^{\pi}\mathbf{E}_{\mathrm{inc}}\left(|\mathbf{r}|=R,\omega\right)\left[\mathbf{N}_{nm}^{(1)}\left(|\mathbf{r}|=R,\omega\right)\right]^{*}\sin\theta\,\mathrm{d}\theta\mathrm{d}\phi}{\int_0^{2\pi}\int_0^{\pi}\left|\mathbf{N}_{nm}^{(1)}\left(|\mathbf{r}|=R,\omega\right)\right|^{2}\sin\theta\,\mathrm{d}\theta\mathrm{d}\phi}$$
$$q_{nm}(\omega)=\frac{\int_0^{2\pi}\int_0^{\pi}\mathbf{E}_{\mathrm{inc}}\left(|\mathbf{r}|=R,\omega\right)\left[\mathbf{M}_{nm}^{(1)}\left(|\mathbf{r}|=R,\omega\right)\right]^{*}\sin\theta\,\mathrm{d}\theta\mathrm{d}\phi}{\int_0^{2\pi}\int_0^{\pi}\left|\mathbf{M}_{nm}^{(1)}\left(|\mathbf{r}|=R,\omega\right)\right|^{2}\sin\theta\,\mathrm{d}\theta\mathrm{d}\phi} \quad (14)$$

$$\left(\begin{pmatrix}\mathbf{a}\\ \mathbf{b}\end{pmatrix}^{1}\begin{pmatrix}\mathbf{a}\\ \mathbf{b}\end{pmatrix}^{2}\cdots\begin{pmatrix}\mathbf{a}\\ \mathbf{b}\end{pmatrix}^{K}\right)=\mathbf{T}_K\cdot\left(\begin{pmatrix}\mathbf{p}\\ \mathbf{q}\end{pmatrix}^{1}\begin{pmatrix}\mathbf{p}\\ \mathbf{q}\end{pmatrix}^{2}\cdots\begin{pmatrix}\mathbf{p}\\ \mathbf{q}\end{pmatrix}^{K}\right), \quad (15)$$

which we invert to find the T-matrix. In order to get an invertible system, we need to calculate the response from K illuminations, where K is equal to or greater than the rank d of the T-matrix. This rank depends on the multipole order N we want to take into account

$$K\geq d=2N(N+2). \quad (16)$$

Using more illuminations is not strictly necessary, but will improve the accuracy of the result, as we will see in the following examples. The inversion of the rectangular matrix can then be done for example with QR decomposition [40]. Note that the resulting T-matrix is always a square matrix in our formalism.

Results and Discussion

Single sphere

As a first check to prove that the method delivers correct results, we investigate the most simple object: a single isolated sphere. We have the correct analytical solution for a single sphere available. The T-matrix has only the known Mie-coefficients on the diagonal and all other entries are zero.

Let us consider a single dielectric sphere with a radius of 100 nm and a relative permittivity of 16 in vacuum. The Mie-coefficients of this sphere for the first two orders are non-negligible at 600 THz. Such a high-permittivity sphere is nowadays at the focus of interest since it sustains a notable electric and magnetic dipole moment in the visible-light range.

To calculate the T-matrix numerically we illuminate the sphere with the appropriate number of plane waves K. The wave vectors are chosen, such that they are evenly distributed in all directions. They can be considered as normal vectors of the surface of an imaginary sphere. They are distributed with the same nearest neighbor distance, as is shown in Figure 1. The polarization of the electric field is then chosen randomly for each wave.

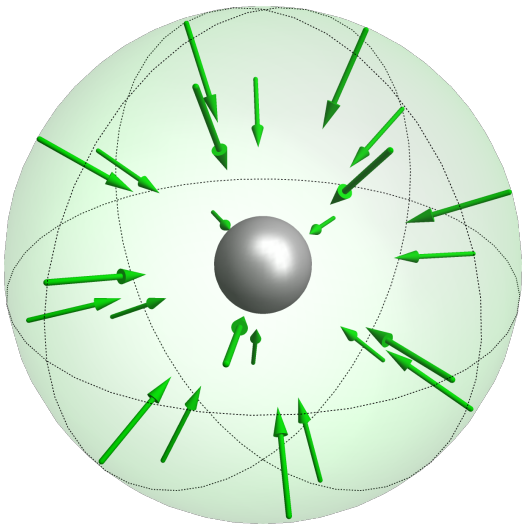


Figure 1: Single sphere with multiple plane wave illuminations, depicted with their wave vectors in green.

To check the convergence of our method we increase the number of illuminations used to calculate the T-matrix. We introduce

$$e(K)=\sqrt{\frac{\sum_i\left|\mathbf{T}_{\mathrm{Mie}}(i)-\mathbf{T}_K(i)\right|^2}{\sum_i\left|\mathbf{T}_{\mathrm{Mie}}(i)\right|^2+\left|\mathbf{T}_K(i)\right|^2}} \quad (17)$$

as a measure for the deviation of the T-matrix. Here, *(i)* represents an index that runs over all matrix components and $\mathbf{T}_{\mathrm{Mie}}$ the analytically known T-matrix. This quantity is visualized in Figure 2 in a double logarithmic plot.

We clearly see that the coefficients can be reproduced with sufficient precision. The deviation drops at first if we increase

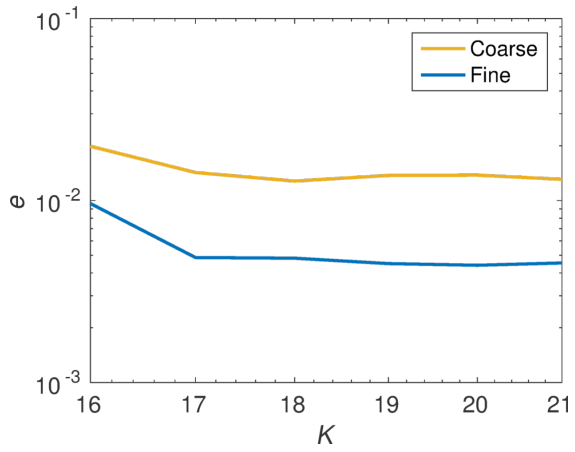


Figure 2: Convergence of the T-matrix calculation with the increase of the number of plane wave illuminations. The minimum number of illuminations to solve for all the unknown entries of the T-matrix for the multipole order $N = 2$ is 16. The error is shown for two different calculations, where the fine one has two times finer meshing.

the number of illuminations, then a plateau is reached. The remaining deviation can be explained by numerical errors introduced by the finite meshing of the sphere in the Maxwell solver as can be seen by considering a second calculation with a finer mesh.

Dimer

We now consider a slightly more complex object to further investigate the convergence of our method. The dimer, i.e., two coupled spheres, is a suitable example, because we can calculate the T-matrix semi-analytically as a reference. We get the T-matrix of the single spheres directly from the Mie coefficients and construct the total T-matrix by translating the coefficients with addition theorems [41]. Please note that this solution is not completely accurate, because we truncate the infinite sums at N. Additionally, we calculate the T-matrix from the illumination with plane waves with a finite element solver, according to Equaiton Equation 15 and compare the results.

The object we investigate consists of two strongly coupled silver spheres with radius $r = 30$ nm and a center-to-center distance of $d = 63$ nm embedded in glass with $\varepsilon = 2.25$ [42]. We take established experimental data for the dispersive permittivity of silver [43]. Such objects can be fabricated in large quantities by self assembly methods, e.g., by connecting commercially available metal nanospheres with a linker molecule [44].

We set $N = 2$, because the higher orders do not contribute notably. For general objects we can construct a condition to find the optimal multipole order. We perform the T-matrix calculation with increasing multipolar order and check the contribution of each order by summing the corresponding T-matrix entries

$$\sum_m |\mathbf{T}_{mn}(\omega)|^2.$$

If we reach an order that has only a negligible contribution compared to the dominant ones, we stop the procedure.

As depicted in Figure 3, the scattering cross sections obtained from the different T-matrix methods agree very well. We can clearly identify three different resonances: a broad electric dipole resonance at 680 THz, and two resonances with magnetic dipole and electric quadrupole contributions at 620 and 710 THz, respectively. While the broad resonance is connected to the eigenmode of the single sphere, the two sharper peaks can be explained by a hybridization caused by the coupling of the two spheres and coupling of higher order multipole modes, respectively [42]. Here the multipole contributions are calculated according to Equation 8.

We get additional insights by looking at the entries of the T-matrix in Figure 4 at a discrete frequency. The way the T-matrix is presented in that figure will be the same in all the following figures showing the T-matrix. Note that the entries are complex numbers and we always display the absolute values. At first we notice that the dominant entries are connected to the electric dipole $\mathbf{T}_{11}^{\mathrm{ee}}$ and, to a lesser extent, to the magnetic dipole $\mathbf{T}_{11}^{\mathrm{mm}}$ and electric quadrupole components $\mathbf{T}_{22}^{\mathrm{ee}}$. Additionally, we see the aforementioned cross coupling between magnetic dipole and electric quadrupole in the submatrix $\mathbf{T}_{12}^{\mathrm{me}}$ and all permutations. This cross coupling also became evident in the scattering cross section.

Now, we investigate the behavior when we increase the number of illuminations K in the T-matrix calculation. We consider the T-matrix with $N = 4$ at the frequency 600 THz, where several multipole orders contribute to the total scattering. As a reference, we take the calculation based on Mie coefficients. In Figure 5 we can observe the expected behavior of the error, the deviation goes down exponentially as we increase the number of plane wave illuminations. So the more complicated structure actually benefits from multiple additional illuminations. In Figure 6 we see the T-matrix entries of two different numbers of illuminations. We clearly see that the numerical noise, i.e., the parts of the matrix that should be zero, is going down significantly.

In conclusion, we can state that the presented method delivers correct results and that it is highly beneficial to use a few illuminations more than absolutely necessary.

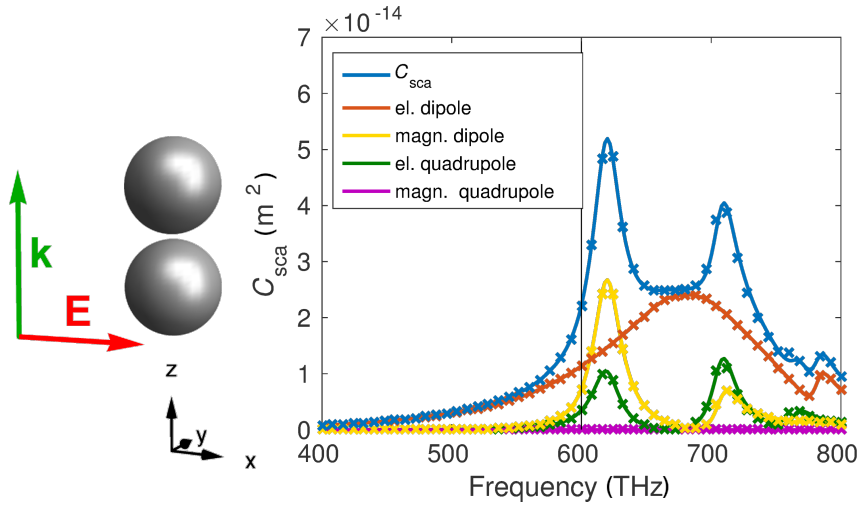


Figure 3: Total scattering cross section (blue) of the dimer and the contributions of different multipoles. The solid lines correspond to the semi-analytical calculation based on the Mie coefficients of the spheres and the crosses correspond to the calculation with the FEM solver. We observe an excellent visual agreement. The black vertical line shows the spectral position that is used for further calculations to show the T-matrix entries. 10 additional plane wave illuminations were used for the numerical T-matrix calculation. On the left side we display the geometry and illumination direction of the dimer setup. Note that this illumination is only relevant for this particular cross section calculation and the T-matrix is generally independent of the illumination.

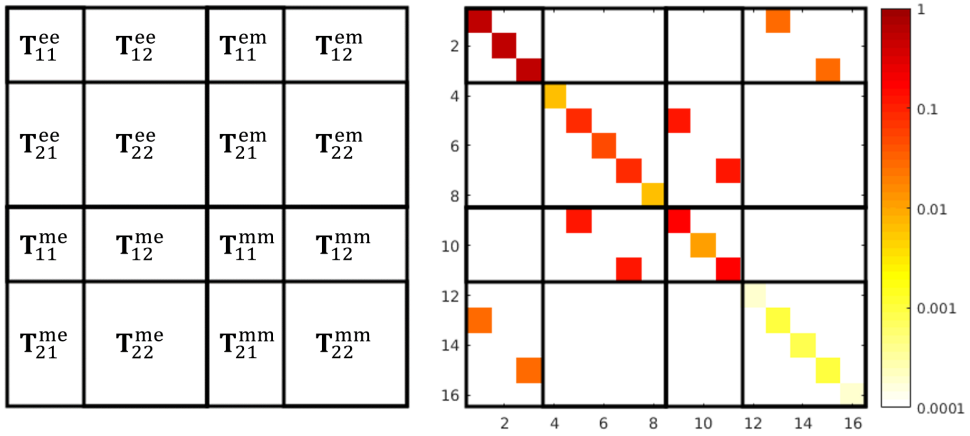


Figure 4: The left picture shows the general form of the T-matrix, as described in the previous section. For example $\mathbf{T}_{11}^{ee}(\omega)$ represents the electric dipole coupling. In the following we always present the T-matrix in this way. On the right hand side we see the absolute values of the T-matrix entries for the dimer on a logarithmic scale at 600 THz. This matrix was calculated semi-analytically with the Mie coefficients of the single spheres. The numbers on the axis count the rows and columns, respectively.

Sandwich particle

Another interesting and in a sense similar object is the sandwich particle. It consists of two metallic disks, usually separated by a dielectric spacer layer. This particle is preferably fabricated by top-down procedures, such as electron beam lithography [5,45].

The investigated object has a disk radius of 60 nm, a disk height of 30 nm and a gap thickness of 10 nm. The metal disks consist of gold [43] and the spacer is made of SiO_2 where we assumed a constant permittivity of $\varepsilon = 2.13$ and the surrounding is vacuum. Similarly to the dimer case, the two separated disks support a magnetic dipole resonance at 336 THz, as can be seen in Figure 7. Additionally, there is a strong and broad electric dipole resonance at 520 THz that is, again, attributed to the resonance of a single disk.

We can observe a magnetic resonance that is weaker than in the case of the dimer, but the big advantage is that the peak is well isolated from other resonances. Furthermore, we observe no higher multipole-order contributions at all in the investigated frequency region. This is particularly beneficial for homogenization, because we can apply the Clausius–Mosotti relation, which is only valid in dipole approximation. The different ge-

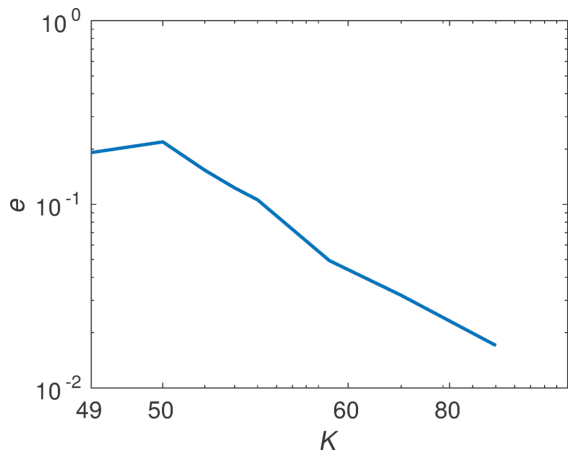


Figure 5: Convergence of the T-matrix calculation with the increase of the number of plane wave illuminations. The minimum number of illuminations necessary to solve for all the unknown entries of the T-matrix for the multipole order $N = 4$ is 48.

ometry makes it now possible to shift the electric and magnetic dipole resonances almost independently, because we have more parameters. The electric mode depends strongly on the radius of the disks, while the magnetic mode can be shifted by changing the thickness of the gold and spacer layers, respectively.

Again, we can get a deeper understanding of the response, by looking at the T-matrix. Figure 8 shows the entries of the matrix of the presented structure at the position of the magnetic resonance, 336 THz. We notice a strong similarity to the previous case of the dimer. This is because the object has almost exactly the same geometrical symmetries. However, we also see some notable differences. Firstly, the particle can be described in very good approximation as a dipole, because the parts corresponding to higher multipoles are negligible. Furthermore, the cross coupling between the magnetic dipole and the electric quadrupole is significantly lower than in the previous case. This is the cause of the well isolated magnetic resonance we saw in the scattering cross section in Figure 7 in contrast to the mixed magnetic dipole and electric quadrupole resonances of the dimer.

Additionally, we can deduce the preferential orientation of the induced multipoles from the pattern of the T-matrix. Let us investigate the electric dipolar part and call the entries

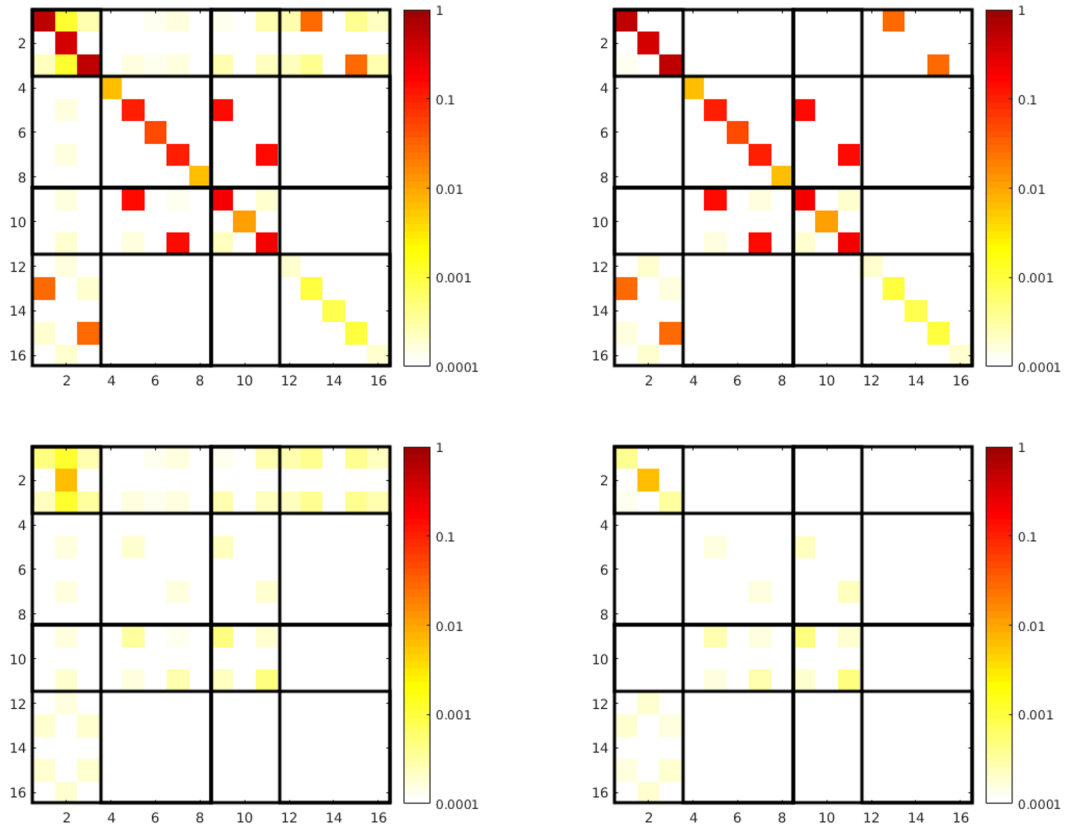


Figure 6: T-matrix entries of the dimer, calculated with the presented method at 600 THz. For the sake of clarity we show only the parts connected to the lowest two multipole contributions. On the left hand side we see the matrix with the minimum number of plane wave illuminations 48, on the right hand side with 50 extra illuminations. The bottom row shows the absolute difference to the semi-analytic solution $\left|\mathbf{T}_{\mathrm{Mie}} - \mathbf{T}_K\right|$.

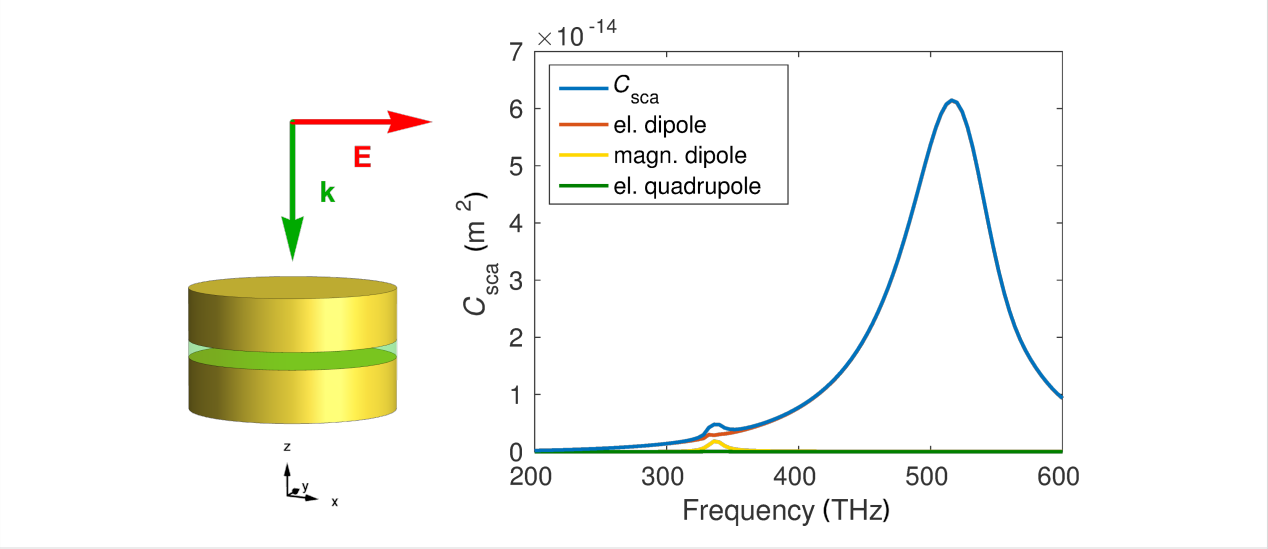


Figure 7: Total scattering cross section (blue) of the sandwich particle and the contributions of different multipole orders. We observe an electric and a magnetic dipole resonance. On the left side we display the geometry and illumination direction of the sandwich. Note that this illumination is only relevant for this particular cross section calculation and the T-matrix is generally independent of the illumination.

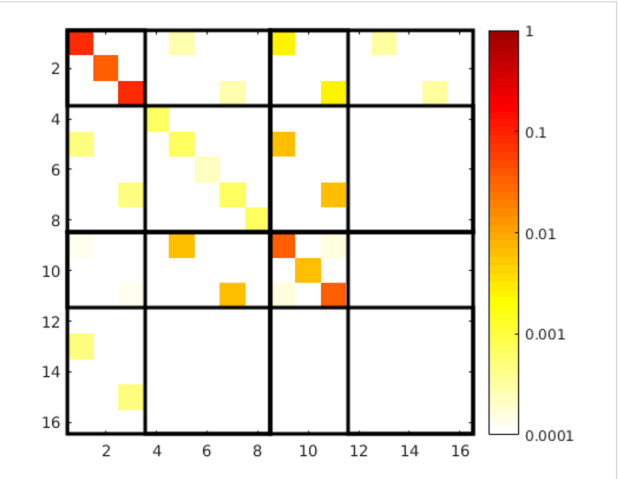


Figure 8: T-matrix entries of the sandwich particle, calculated with the presented method at 336 THz with 50 extra illuminations. See Figure 4 for a description of the submatrices.

$$\mathbf{T}_{11}^{\mathrm{ee}} = \begin{pmatrix} T_{-1-1}^{\mathrm{ee}} & T_{-10}^{\mathrm{ee}} & T_{-11}^{\mathrm{ee}} \\ T_{0-1}^{\mathrm{ee}} & T_{00}^{\mathrm{ee}} & T_{01}^{\mathrm{ee}} \\ T_{1-1}^{\mathrm{ee}} & T_{10}^{\mathrm{ee}} & T_{11}^{\mathrm{ee}} \end{pmatrix}. \tag{18}$$

Now $T_{\mathrm{ij}}^{\mathrm{ee}}$ connects the incident coefficient $p_{1\mathrm{j}}$ to the scattering coefficient $a_{1\mathrm{i}}$. The same is true for all the other parts of the T-matrix, with adjustments for the higher-order parts. The entry T_{00}^{ee} is special because it is connected to the z-axis. The z-axis is distinguished in the definition of the vector spherical harmonic functions. This means that if this entry has a large absolute value, the corresponding object will exhibit a strong electric dipole in z-direction, $p_{\mathrm{z}} \propto T_{00}^{\mathrm{ee}}$. Conversely the dipole moments in the x–y-plane are proportional to linear combinations of entries with ±1 indices. This also translates directly to the magnetic part of the T-matrix. Considering this, we investigate again Figure 8. We see that the electric dipole is almost isotropic. This becomes clear when we compare the T-matrix to that of a sphere, as stated above, we would get $T_{-1-1}^{\mathrm{ee}} = T_{00}^{\mathrm{ee}} = T_{11}^{\mathrm{ee}}$ in this completely isotropic case. The magnetic dipole, however, is much stronger in the x–y plane because of the geometry of the investigated object with the gap. The magnetic dipole moment is induced by antiparallel currents in the metal disks. Please note that these considerations are completely independent of the illumination, because we investigate the T-matrix directly.

Helix

Now we can utilize the biggest advantage of the proposed method, namely that we can calculate the T-matrix of an arbitrarily complex object. To showcase this we compute the T-matrix of a metal helix. In this case we can not make use of inherent symmetries of the object a priori and have no analytic solution available.

Calculating the T-matrix is particularly interesting for the present object, because numerous electromagnetic properties can be deduced from its entries, such as the duality conservation and electromagnetic chirality [46]. The helix was optimized to express a strong electromagnetic chirality at a specific frequency and, thus, shows a strong contrast in the scattering cross section for two opposite circular polarized incident fields. The major radius of the helix is 6.48 µm, the pitch is 8.52 µm,

the minor radius is 0.8 μm, and the helix is surrounded by vacuum. The operating frequency of the system, i.e., the position of the resonance is at 1.5 THz. As we see in Figure 9, there is a strong difference in the scattering cross section if we illuminate with right-handed or left-handed circularly polarized light.

For the following considerations it is beneficial to introduce shortly the concept of duality symmetry. In free space, Maxwell's equations are invariant under the transformation [47]

$$\mathbf{E}' = \cos\theta\mathbf{E} + Z\sin\theta\mathbf{H}\,,\quad \mathbf{H}' = \cos\theta\mathbf{H} - \frac{\sin\theta}{Z}\mathbf{E}\,, \tag{19}$$

where **E** is the electric field, **H** is the magnetic field, Z is the impedance and θ is an arbitrary constant angle. The symmetry that is corresponding to this transformation invariance is duality. Helicity is defined as the product of the total angular momentum **J** and the direction of the linear momentum of the wave **P**/|**P**|[48]

$$\Lambda = \frac{\mathbf{J}\cdot\mathbf{P}}{|\mathbf{P}|}. \tag{20}$$

It has the two eigenvalues 1 and −1, and the corresponding eigenstates [49]

$$\mathbf{G}_{\pm} = \frac{1}{\sqrt{2}}\left(\mathbf{E} \pm iZ\mathbf{H}\right). \tag{21}$$

For example, a circularly polarized plane wave is a state of pure helicity and it is preserved if duality symmetry applies.

We can see directly that the object is approximately dual at the resonance frequency of 1.5 THz, because the magnetic and electric dipole contributions are balanced and no higher multipole contributions arise [50]. This means that the interaction of the particle with the incident light does not change the helicity of the incident waves.

Looking at the T-matrix entries in Figure 10 we see, like in the previous cases, that the object can be described mainly by the dipole contributions. The interesting aspect here is that the electric and magnetic dipoles have almost the same strength and are both aligned along the z-axis at the same frequency. Furthermore the mixing of electric and magnetic dipole moments is also very strong. This means that an electric dipole is induced

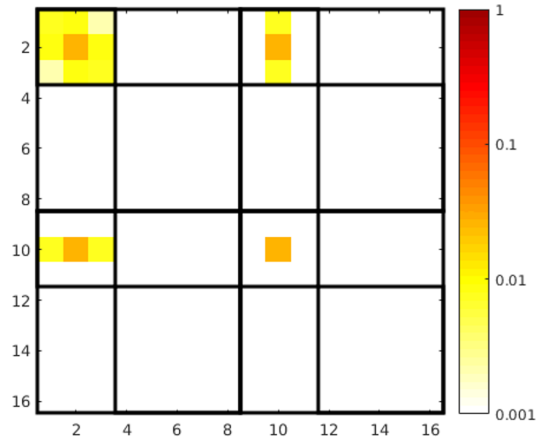


Figure 10: T-matrix entries of the right handed helix, calculated with the presented method at 1.5 THz with 10 extra illuminations. See Figure 4 for a description of the submatrices.

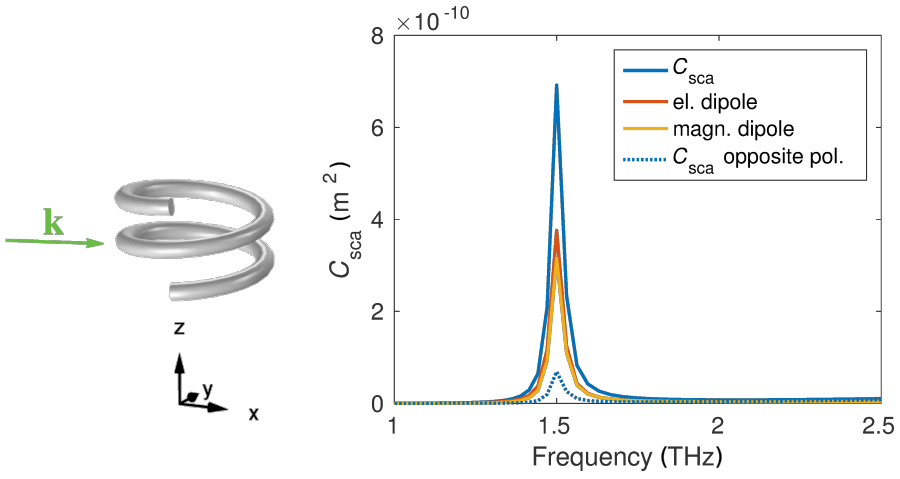


Figure 9: Right-handed metallic helix with two windings. Total scattering cross section for right-handed (solid) and left-handed (dotted) circular polarization. The electric and magnetic dipole contributions are approximately equal. On the left side we display the geometry and illumination direction of the helix.

by a magnetic dipole excitation and vice versa. All these properties lead to the approximate duality symmetry of the object.

As stated above, we can calculate measures for the duality breaking, electromagnetic chirality and the scattering cross section contrast for general plane wave illuminations from the T-matrix entries. This is done by transforming the T-matrix from its current form to the helicity basis

$$\begin{pmatrix} \mathbf{T}_{++}^{\text{helicity}} & \mathbf{T}_{+-}^{\text{helicity}} \\ \mathbf{T}_{-+}^{\text{helicity}} & \mathbf{T}_{--}^{\text{helicity}} \end{pmatrix} = \frac{1}{\sqrt{2}}\begin{pmatrix} 1 & 1 \\ 1 & -1 \end{pmatrix} \cdot \begin{pmatrix} \mathbf{T}_{\text{ee}} & \mathbf{T}_{\text{em}} \\ \mathbf{T}_{\text{me}} & \mathbf{T}_{\text{mm}} \end{pmatrix} \cdot \frac{1}{\sqrt{2}}\begin{pmatrix} 1 & 1 \\ 1 & -1 \end{pmatrix}. \quad (22)$$

The submatrices represent now the coupling of the helicity + and − states. In Figure 11 the entries of the transformed matrix are depicted for a left-handed and a right-handed helix. We can clearly distinguish the two cases, because each helix interacts mainly only with one helicity. The left handed helix interacts with helicity − ($\mathbf{T}_{--}^{\text{helicity}}$) states and the right handed interacts with helicity + ($\mathbf{T}_{++}^{\text{helicity}}$).

To further analyze the T-matrix of the object we can perform a singular value decomposition (svd) of the submatrices [46]. The values are ordered to get the vectors

$$\sigma_{+} = \left(\text{svd}\left[\mathbf{T}_{++}^{\text{helicity}}\right] \text{svd}\left[\mathbf{T}_{-+}^{\text{helicity}}\right]\right)$$

and

$$\sigma_{-} = \left(\text{svd}\left[\mathbf{T}_{+-}^{\text{helicity}}\right] \text{svd}\left[\mathbf{T}_{--}^{\text{helicity}}\right]\right)$$

from which we calculate the quantities that are related to helicity

$$\begin{aligned} \mathcal{D} &= \frac{\sum_i \left|\mathbf{T}_{+-}^{\text{helicity}}(i)\right|^2 + \left|\mathbf{T}_{-+}^{\text{helicity}}(i)\right|^2}{\sum_i \left|\mathbf{T}^{\text{helicity}}(i)\right|^2}, \\ C &= \sum_i \left(\sigma_{+}(i)\right)^2 + \left(\sigma_{-}(i)\right)^2, \\ \Delta &= \frac{1}{C}\sum_i \left(\sigma_{+}(i)\right)^2 - \left(\sigma_{-}(i)\right)^2, \\ \chi &= \sqrt{\frac{1}{C}\sum_i \left(\sigma_{+}(i) - \sigma_{-}(i)\right)^2}. \end{aligned} \quad (23)$$

Here, $\mathcal{D}$ is the duality breaking, C can be interpreted as the averaged total scattering cross section independent of a specific illumination, Δ is the cross section contrast for different circular polarizations, and χ is a measure for the electromagnetic chirality [46]. The values for the chosen helix are shown in Figure 12.

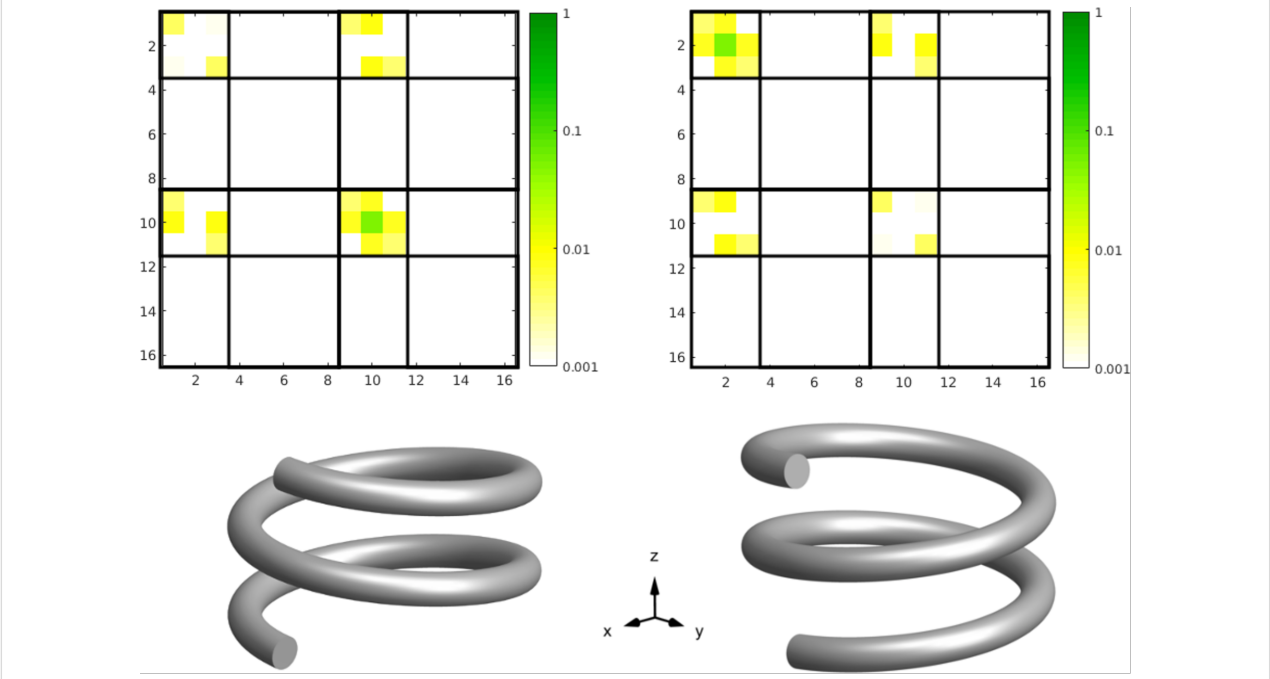


Figure 11: T-matrix entries in the helicity basis (obtained by Equation 22) of a left-handed and a right-handed helix. We clearly observe that each helix interacts primarily only with one helicity and that the mixing of different helicities is very low ($\mathbf{T}_{+-}^{h}$ and $\mathbf{T}_{-+}^{h}$). The T-matrices are ordered, in principle, in the same way as shown in Figure 4, but with helicity + and − states instead of e and m.

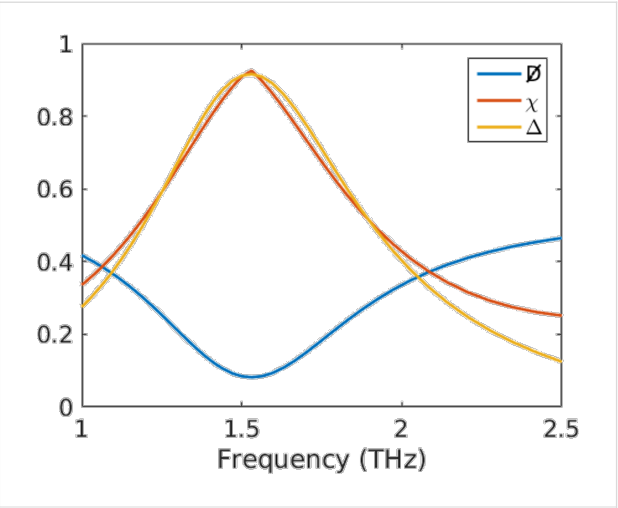


Figure 12: Duality breaking, electromagnetic chirality and cross section contrast of the left-handed helix.

We clearly see the anticipated minimum in the duality breaking. This means that the helix is approximately dual at the resonance frequency. Simultaneously the chirality reaches a maximum of 0.9, which means that the object responds differently to the two opposite polarizations of illuminating radiation. This is also evident from the strong cross section contrast.

The presented quantities, and possibly others, are only accessible because we calculated the T-matrix of the object. This information makes it also possible to optimize such objects numerically to achieve the desired behavior.

Conclusion

We demonstrated an algorithm to calculate the T-matrix of an arbitrary object. We showcased numerical examples by calculating the T-matrix of four objects. Especially the calculation of the silver helix demonstrates the strength of the approach. We investigated properties that are usually not available with established full wave solvers.

The T-matrix is calculated with the help of widely available and well established tools to calculate the scattered fields upon plane wave illumination. The T-matrix contains the electromagnetic scattering information independently of the illumination. By investigating the matrix, we get valuable information about the multipolar composition of the scattering cross section and electromagnetic chirality. This is extremely useful for understanding the nature of a given response.

Furthermore, the T-matrix can be used in an extended multiscattering formalism to calculate the response of a whole cluster of objects efficiently. This will speed up calculations by a considerable amount.

Acknowledgements

This work was supported by the German Science Foundation within project RO 3640/3-1. We also acknowledge partial financial support by the Deutsche Forschungsgemeinschaft through CRC 1173. We would like to thank JCMwave for providing us access to the FEM solver JCMsuite. M.F. also acknowledges the support by the Karlsruhe School of Optics & Photonics (KSOP).

References

1. Loudet, J.-C.; Barois, P.; Poulin, P. *Nature* **2000,** *407,* 611–613. doi:10.1038/35036539
2. Gantzounis, G.; Stefanou, N.; Yannopapas, V. *J. Phys.: Condens. Matter* **2005,** *17,* 1791. doi:10.1088/0953-8984/17/12/003
3. Frein, S.; Boudon, J.; Vonlanthen, M.; Scharf, T.; Barberá, J.; Süss-Fink, G.; Bürgi, T.; Deschenaux, R. *Helv. Chim. Acta* **2008,** *91,* 2321–2337. doi:10.1002/hlca.200890253
4. Wojcik, M.; Lewandowski, W.; Matraszek, J.; Mieczkowski, J.; Borysiuk, J.; Pociecha, D.; Gorecka, E. *Angew. Chem., Int. Ed.* **2009,** *48,* 5167–5169. doi:10.1002/anie.200901206
5. Lehr, D.; Dietrich, K.; Helgert, C.; Käsebier, T.; Fuchs, H.-J.; Tünnermann, A.; Kley, E.-B. *Opt. Lett.* **2012,** *37,* 157–159. doi:10.1364/OL.37.000157
6. Asadchy, V.; Albooyeh, M.; Tretyakov, S. *J. Opt. Soc. Am. B* **2016,** *33,* A16–A20. doi:10.1364/JOSAB.33.000A16
7. Alaee, R.; Albooyeh, M.; Rahimzadegan, A.; Mirmoosa, M. S.; Kivshar, Y. S.; Rockstuhl, C. *Phys. Rev. B* **2015,** *92,* 245130. doi:10.1103/PhysRevB.92.245130
8. Li, L. *J. Opt. Soc. Am. A* **1997,** *14,* 2758–2767. doi:10.1364/JOSAA.14.002758
9. Modinos, A.; Stefanou, N.; Yannopapas, V. *Opt. Express* **2001,** *8,* 197–202. doi:10.1364/OE.8.000197
10. Oskooi, A. F.; Roundy, D.; Ibanescu, M.; Bermel, P.; Joannopoulos, J. D.; Johnson, S. G. *Comput. Phys. Commun.* **2010,** *181,* 687–702. doi:10.1016/j.cpc.2009.11.008
11. Ippolito, S. J.; Kalantar-Zadeh, K.; Powell, D. A.; Wlodarski, W. A. 3-dimensional finite element approach for simulating acoustic wave propagation in layered SAW devices. In *Ultrasonics, 2003 IEEE Symposium on,* IEEE Publishing: Piscataway, NJ, U.S.A., 2003; pp 303–306.
12. Pomplun, J.; Burger, S.; Zschiedrich, L.; Schmidt, F. *Phys. Status Solidi B* **2007,** *244,* 3419–3434. doi:10.1002/pssb.200743192
13. Moreau, A.; Ciracì, C.; Mock, J. J.; Hill, R. T.; Wang, Q.; Wiley, B. J.; Chilkoti, A.; Smith, D. R. *Nature* **2012,** *492,* 86–89. doi:10.1038/nature11615
14. Yang, P.; Liou, K. N.; Mishchenko, M. I.; Gao, B.-C. *Appl. Opt.* **2000,** *39,* 3727–3737. doi:10.1364/AO.39.003727
15. Kuwata, H.; Tamaru, H.; Esumi, K.; Miyano, K. *Appl. Phys. Lett.* **2003,** *83,* 4625–4627. doi:10.1063/1.1630351
16. Nordlander, P.; Oubre, C.; Prodan, E.; Li, K.; Stockman, M. I. *Nano Lett.* **2004,** *4,* 899–903. doi:10.1021/nl049681c
17. Mackowski, D. W. *J. Opt. Soc. Am. A* **2002,** *19,* 881–893. doi:10.1364/JOSAA.19.000881

18. Draine, B. T. The discrete dipole approximation for light scattering by irregular targets. In *Light Scattering by Nonspherical Particles: Theory, Measurements, and Applications;* Mishchenko, M. I.; Hovenier, J. W.; Travis, L. D., Eds.; Academic Press: Cambridge, MA, U.S.A., 2000; p 131.
19. Xu, Y.-l. *Appl. Opt.* **1995,** *34,* 4573–4588. doi:10.1364/AO.34.004573
20. Mühlig, S.; Rockstuhl, C.; Pniewski, J.; Simovski, C. R.; Tretyakov, S. A.; Lederer, F. *Phys. Rev. B* **2010,** *81,* 075317. doi:10.1103/PhysRevB.81.075317
21. Waterman, P. C. *Proc. IEEE* **1965,** *53,* 805–812. doi:10.1109/PROC.1965.4058
22. Gimbutas, Z.; Greengard, L. *J. Comput. Phys.* **2013,** *232,* 22–32. doi:10.1016/j.jcp.2012.01.041
23. Fruhnert, M.; Monti, A.; Fernandez-Corbaton, I.; Alù, A.; Toscano, A.; Bilotti, F.; Rockstuhl, C. *Phys. Rev. B* **2016,** *93,* 245127. doi:10.1103/PhysRevB.93.245127
24. Auger, J.-C.; Stout, B. *J. Quant. Spectrosc. Radiat. Transfer* **2003,** *79–80,* 533–547. doi:10.1016/S0022-4073(02)00306-0
25. Mackowski, D. W.; Mishchenko, M. I. *J. Opt. Soc. Am. A* **1996,** *13,* 2266–2278. doi:10.1364/JOSAA.13.002266
26. Stefanou, N.; Yannopapas, V.; Modinos, A. *Comput. Phys. Commun.* **2000,** *132,* 189–196. doi:10.1016/S0010-4655(00)00131-4
27. Yannopapas, V.; Vanakaras, A. G. *Phys. Rev. B* **2011,** *84,* 085119. doi:10.1103/PhysRevB.84.085119
28. Bohren, C. F.; Huffman, D. R. *Absorption and scattering of light by small particles;* John Wiley & Sons: New York, NY, U.S.A., 2008.
29. Mie, G. *Ann. Phys.* **1908,** *330,* 377–445. doi:10.1002/andp.19083300302
30. Mischenko, M. I.; Travis, L. D.; Lacis, A. A. *Scattering, absorption, and emission of light by small particles;* Cambridge University Press: Cambridge, United Kingdom, 2002.
31. Mishchenko, M. I.; Travis, L. D.; Mackowski, D. W. *J. Quant. Spectrosc. Radiat. Transfer* **1996,** *55,* 535–575. doi:10.1016/0022-4073(96)00002-7
32. Tsang, L.; Kong, J.; Shin, R. *Theory of microwave remote sensing;* Wiley-Interscience: New York, NY, U.S.A., 1985.
33. Mishchenko, M. I.; Dlugach, J. M. *Planet. Space Sci.* **1993,** *41,* 173–181. doi:10.1016/0032-0633(93)90056-8
34. Nieminen, T. A.; Rubinsztein-Dunlop, H.; Heckenberg, N. R. *J. Quant. Spectrosc. Radiat. Transfer* **2003,** *79,* 1019–1029. doi:10.1016/S0022-4073(02)00336-9
35. Yannopapas, V. *J. Opt. Soc. Am. B* **2014,** *31,* 631–636. doi:10.1364/JOSAB.31.000631
36. Sersic, I.; Tuambilangana, C.; Kampfrath, T.; Koenderink, A. F. *Phys. Rev. B* **2011,** *83,* 245102. doi:10.1103/PhysRevB.83.245102
37. Asadchy, V. S.; Faniayeu, I. A.; Ra'di, Y.; Tretyakov, S. A. *Photonics Nanostruct. - Fundam. Appl.* **2014,** *12,* 298–304. doi:10.1016/j.photonics.2014.04.004
38. Liu, X.-X.; Zhao, Y.; Alù, A. *IEEE Trans. Antennas Propag.* **2016,** *64,* 2301–2310. doi:10.1109/TAP.2016.2546958
39. Yazdi, M.; Komjani, N. *J. Opt. Soc. Am. B* **2016,** *33,* 491–500. doi:10.1364/JOSAB.33.000491
40. Trefethen, L. N.; Bau, D., III. *Numerical linear algebra;* Siam, 1997.
41. Stein, S. *Q. Appl. Math.* **1961,** 15–24. doi:10.1090/qam/120407
42. Mühlig, S.; Menzel, C.; Rockstuhl, C.; Lederer, F. *Metamaterials* **2011,** *5,* 64–73. doi:10.1016/j.metmat.2011.03.003
43. Johnson, P. B.; Christy, R. W. *Phys. Rev. B* **1972,** *6,* 4370–4379. doi:10.1103/PhysRevB.6.4370
44. Fruhnert, M.; Kretschmer, F.; Geiss, R.; Perevyazko, I.; Cialla-May, D.; Steinert, M.; Janunts, N.; Sivun, D.; Hoeppener, S.; Hager, M. D.; Pertsch, T.; Schubert, U. S.; Rockstuhl, C. *J. Phys. Chem. C* **2015,** *119,* 17809–17817. doi:10.1021/acs.jpcc.5b04346
45. Hicks, E. M.; Zou, S.; Schatz, G. C.; Spears, K. G.; Van Duyne, R. P.; Gunnarsson, L.; Rindzevicius, T.; Kasemo, B.; Käll, M. *Nano Lett.* **2005,** *5,* 1065–1070. doi:10.1021/nl0505492
46. Fernandez-Corbaton, I.; Fruhnert, M.; Rockstuhl, C. *Phys. Rev. X* **2016,** *6,* 031013. doi:10.1103/PhysRevX.6.031013
47. Calkin, M. G. *Am. J. Phys.* **1965,** *33,* 958–960. doi:10.1119/1.1971089
48. Tung, W.-K. *Group theory in physics;* World Scientific Publishing Co Pte Ltd: Singapore, 1985.
49. Lipkin, D. M. *J. Math. Phys.* **1964,** *5,* 696–700. doi:10.1063/1.1704165
50. Fernandez-Corbaton, I.; Fruhnert, M.; Rockstuhl, C. *ACS Photonics* **2015,** *2,* 376–384. doi:10.1021/ph500419a

License and Terms

This is an Open Access article under the terms of the Creative Commons Attribution License (http://creativecommons.org/licenses/by/4.0), which permits unrestricted use, distribution, and reproduction in any medium, provided the original work is properly cited.

The license is subject to the *Beilstein Journal of Nanotechnology* terms and conditions: (http://www.beilstein-journals.org/bjnano)

The definitive version of this article is the electronic one which can be found at: doi:10.3762/bjnano.8.66

BEILSTEIN JOURNAL OF NANOTECHNOLOGY

Phospholipid arrays on porous polymer coatings generated by micro-contact spotting

Sylwia Sekula-Neuner*[1], Monica de Freitas[2], Lea-Marie Tröster[2], Tobias Jochum[2], Pavel A. Levkin[3,4], Michael Hirtz[1] and Harald Fuchs[1,5]

Full Research Paper

Open Access

Address:
[1]Institute of Nanotechnology (INT) and Karlsruhe Nano Micro Facility (KNMF) Karlsruhe Institute of Technology (KIT), 76344 Eggenstein-Leopoldshafen, Germany, [2]Institute for Photon Science and Synchrotron Radiation (IPS), Laboratory for Applications of Synchrotron Radiation (LAS), Karlsruhe Institute of Technology (KIT), 76344 Eggenstein-Leopoldshafen, Germany, [3]Institute of Toxicology and Genetics (ITG), Karlsruhe Institute of Technology (KIT), 76344 Eggenstein-Leopoldshafen, Germany, [4]Institute of Organic Chemistry, Karlsruhe Institute of Technology, 76021 Karlsruhe, Germany and [5]Physikalisches Institut and Center for Nanotechnology (CeNTech), Universität Münster, 48149 Münster, Germany

Email:
Sylwia Sekula-Neuner* - Sylwia.Sekula-Neuner@kit.edu

* Corresponding author

Keywords:
microcontact cantilever spotting; phospholipids; polymeric porous support; polymethacrylate

Beilstein J. Nanotechnol. **2017,** *8,* 715–722.
doi:10.3762/bjnano.8.75

Received: 18 November 2016
Accepted: 09 March 2017
Published: 27 March 2017

This article is part of the Thematic Series "Advances in nanomaterials II".

Guest Editor: M. Ruben

© 2017 Sekula-Neuner et al.; licensee Beilstein-Institut.
License and terms: see end of document.

Abstract

Nanoporous poly(2-hydroxyethyl methacrylate-*co*-ethylene dimethacrylate) (HEMA-EDMA) is used as a 3D mesh for spotting lipid arrays. Its porous structure is an ideal matrix for lipid ink to infiltrate, resulting in higher fluorescent signal intensity as compared to similar arrays on strictly 2D substrates like glass. The embedded lipid arrays show high stability against washing steps, while still being accessible for protein and antibody binding. To characterize binding to polymer-embedded lipids we have applied Streptavidin as well as biologically important biotinylated androgen receptor binding onto 1,2-dipalmitoyl-*sn*-glycero-3-phosphoethanolamine-*N*-(cap biotinyl) (Biotinyl Cap PE) and anti-DNP IgE recognition of 2,4-dinitrophenyl[1,2-dipalmitoyl-*sn*-glycero-3-phosphoethanolamine-*N*-[6-[(2,4-dinitrophenyl)amino]hexanoyl] (DNP)] antigen. This approach adds lipid arrays to the range of HEMA polymer applications and makes this solid substrate a very attractive platform for a variety of bio-applications.

Introduction

Starting with the creation of high density peptide microarrays in the 1990s [1] the development of arrays with DNA molecules and antibodies has produced a range of platforms for functional determination studies of molecules [2-4]. Nowadays, commercially available micro- and nanoarrays in a variety of design are readily available. Lipid arrays, however, are a comparably

novel platform and still not as well-developed. Studies using lipid micro-/nanoarrays are often hampered due to the lack of widely available technologies for lipid deposition [5] and the detection of lipid–protein interactions [6]. Increased biological importance of lipid arrays, demonstrated by the growing number of studies on autoimmune diseases such as multiple sclerosis [7,8], emphasizes the need for sustained progress in this field.

The work presented here demonstrates the potential of nanoporous poly(2-hydroxyethyl methacrylate-*co*-ethylene dimethacrylate) (HEMA-EDMA) as a novel advantageous substrate for lipid arrays. Porous HEMA support, with pore size distribution in the range of 150 nm , has already demonstrated advantages in pattern definition, spot homogeneity, and consistent spot dimensions for different dye sensors (phloxine B and bromophenol blue) spotted in ethanol based inks [9]. In the present approach, the pores of the HEMA-EDMA support act as a mesh that contains lipid ink in a confined space, providing high pattern definition, and presenting more binding sites than would be available on a flat substrate [10]. The main phospholipid component in our ink mixture is 1,2-dioleoyl-*sn*-glycero-3-phosphocholine (DOPC, $T_m = -16.5$ °C) which allowed for the control of ink fluidity under humidity controlled conditions [11,12]. Using quill-like pens (SPTs, short for surface patterning tool [13]) for lipid ink deposition permitted the reduction of the volume of phospholipids needed for array generation, as compared to other spotting techniques like ink jet printing, without decrease in the quality of the array or reduction of binding sites for analyte molecules. On the contrary, higher resolutions and smaller feature sizes are obtained with the SPTs in comparison with common ink jet procedures. We previously demonstrated the use of SPTs for the deposition of water-based click-chemistry inks [10,14,15] where CuAAC mediated covalent immobilization of ink molecules and embedment's within the polymer mesh makes the pattern highly stable in solution [10]. To determine if lipids deposited on nanoporous HEMA-EDMA polymer could be used to generate functional arrays we selected lipid–protein pairs applied in previous settings: Biotin-Cap-PE and streptavidin labeled with Cy3 dye (STV-Cy3) as a simple protein model; and DNP-cap-PE with anti-DNP IgE as a model for allergen/antibody recognition. These interactions are well-characterized for biomimetic lipid membranes on flat supports [16,17] and there, interactions occur without any special requirements, like pretreatment with co-activating molecules. For a more complex protein, the lipid/HEMA-EDMA substrate system was also characterized for the binding properties of biotinylated androgen receptor (AR^{biot}) [18] onto Biotin-cap-PE arrays in the presence of a hormone. We have chosen AR as a test protein because of its biological importance: the transcriptional activity of this steroid receptor is crucial not only for the normal development of the prostate in males, but it is also vital in the progression of prostate cancer [19]. AR contributes to breast cancer progression and development [20] and its mutation is involved in the progression of neurodegenerative diseases, such as the X-linked spinal and bulbar muscular atrophy [21]. In order to better understand and characterize the behavior and mechanism of action of this receptor new approaches are needed to facilitate studies with AR. Embedding AR in a lipid layer within HEMA-EDMA mesh might facilitate studies relying not only on fluorescence microscopy techniques but also on spectroscopy, to evaluate coactivators, co-chaperones [22] and even novel antiandrogens affinity to the receptor [6] and effects on the receptor's poly Q-extended mutations [23].

Results and Discussion

Microchannel cantilever spotting (μCS) with phospholipids

In order to establish best conditions for microchannel cantilever spotting (μCS) of phospholipids with the SPTs, we used simple phospholipid ink composed of DOPC [1,2-dioleoyl-*sn*-glycero-3-phosphocholine] doped with Rhodamine-PE [1,2-dioleoyl-*sn*-glycero-3-phosphoethanolamine-*N*-(lissamine rhodamine B sulfonyl) (ammonium salt)]. The ink was prepared by mixing DOPC and Rhodamine-PE to achieve 1 μM lipid content in chloroform with 1 mol % fluorescent dye admixture. The chloroform was evaporated and lipids were reconstituted with an ethanol and glycerol mixture in 7:3 v/v ratio. The ink was loaded onto a freshly oxygen plasma activated SPT and directly used for spotting. When varying the contact time between SPT and substrate (dwell time), different feature sizes can be obtained (Figure 1). The diameter of the spotted features varies from 6 +/− 0.3 μm to 4 +/− 0.2 μm for dwell times from 3 to 0.1 s. Interestingly, not only feature size, but also fluorescence intensity varies with dwell time (Figure 1b). This can be explained by the 3D nature of the features as they are actually embedded in the porous HEMA-EDMA substrate [10]. While on a flat glass substrate, features can only grow into 2D with dwell time, while in the present case features will also grow into the depth of the HEMA-EDMA film, resulting in brighter fluorescence as the ink below the feature surface also contributes to the signal.

Protein and antibody binding onto lipid arrays

The selective binding of proteins to the lipid arrays on HEMA polymer was first tested using fluorophore labelled streptavidin (STV-FITC) for the coupling with biotin headgroups. Biotin lipid arrays were prepared by admixing 4 mol % biotin lipid (1,2-dipalmitoyl-*sn*-glycero-3-phosphoethanolamine-*N*-(cap biotinyl)) into the DOPC carrier. It was shown previously [24], that this percentage admixture of biotin saturates the number of

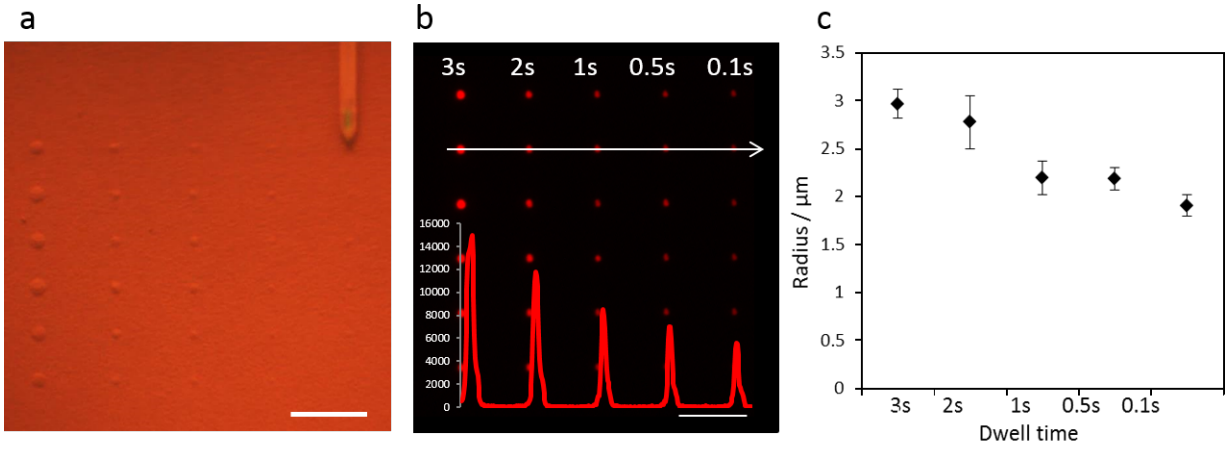


Figure 1: Phospholipid array on nanoporous HEMA-EDMA polymer. a) Phospholipid microcontact spotting on porous HEMA-EDMA with microchannel cantilevers imaged in situ on the lithography system. b) Fluorescence microscopy image of the DOPC phospholipid array doped with Rhodamine-PE (dwell times 3 to 0.1 s). The arrow indicates the intensity profile of dot features presented on the superimposed graph. Scale bar equals 50 µm. c) Relationship between spot radius and dwell time for the microarray shown in (b).

available biotin headgroups for protein binding [24]. After spotting, the arrays were blocked with 10% bovine serum albumin (BSA) to reduce unspecific binding of the protein to the polymer. Next, samples were washed and incubated for 1 h with 0.5 µg solution of STV-FITC in phosphate buffered saline (PBS). The observed STV-FITC fluorescence is homogenous over the whole arrays, indicating an even distribution of biotin headgroups embedded in the nanoporous HEMA-EDMA (Figure 2).

To assess the accessibility of lipid based allergen arrays on nanoporous HEM-EDMA A substrates to antibodies, we employed the established lipid/antibody pair DNP-cap-PE and anti-DNP IgE antibody. Previously, DNP-lipid recognition by a specific antibody was tested on glass supports [17], while on HEMA-EDMA polymer antibody binding was tested on covalently bound DNP-azide ink [10]. Here, allergen arrays were prepared by using 10 mol % admixture of DNP-cap-PE into DOPC lipid. As an optical reference DOPC doped with rhodamine was patterned in-between DNP-lipid structures (Figure 3a). After blocking with 10% BSA and subsequent washing, samples were incubated with anti-DNP IgE antibody labelled with Alexa 488 dye for direct visualization. Plotting of the mean fluorescence intensity against dwell time (Figure 3b) indicates a slight dependence of fluorescence intensity on dwell time (suggesting the infiltrated nature of the features as explained above). Though the difference between 2 s, 1 s and 0.5 s dwell time is not as strongly pronounced as in the case of the

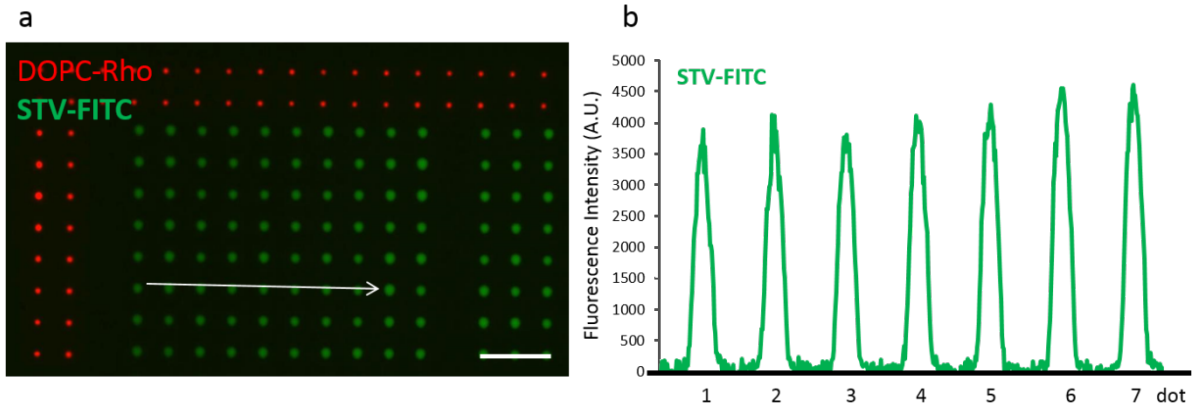


Figure 2: a) Fluorescence image of the STV-FITC binding Biotin-PE containing arrays on the nanoporous HEMA-EDMA substrate. DOPC doped with Rhodamine PE (red) was patterned around biotin array for optical reference with dwell time set to 1 s. Spotting dwell time for Biotin-PE containing arrays was set to 2 s. Scale bar equals 50 µm. b) The graph shows the fluorescence intensity after background subtraction of dots indicated by an arrow.

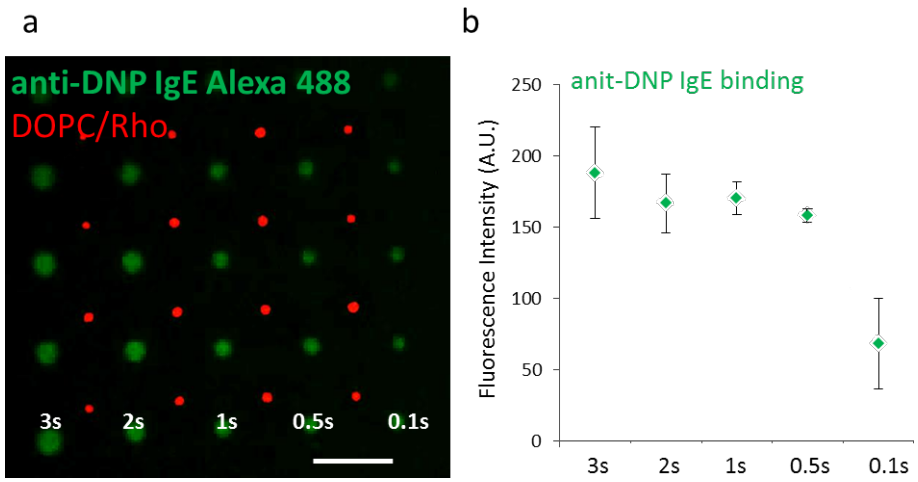


Figure 3: a) Fluorescence microscopy image of an anti-DNP IgE-Alexa 488 antibody (green) bound to an array of DNP-lipids on nanoporous HEMA-EDMA substrate. DOPC doped with Rhodamine-PE was patterned on the same sample as optical reference (red) with dwell time set to 1 s. Scale bar equals 50 µm. b) Fluorescence intensity of n = 5 dots features per dwell time of DNP-array (after background subtraction) presented in a) after binding the anti-DNP IgE-Alexa 488 antibody.

DOPC ink (Figure 1b), this dependency overall suggests that the antibody can access binding sites within the HEMA-EDMA substrate.

To test the binding of a more complex, functional protein on the HEMA-EDMA based lipid arrays, we chose AR^{biot}. Binding of AR^{biot} to the HEMA-EDMA membrane was performed in the presence of dihydrotestosterone hormone (DHT). The hormone addition is needed to assure receptor stability as the AR is known to be very unstable as an aporeceptor [25]. Firstly, biotin carrying arrays for AR^{biot} binding were prepared as described in the previous section with an admixing of 4 mol % biotin lipid into DOPC carrier. Next, after blocking with 10% BSA and binding of fluorescently labeled STV-Cy3, arrays were washed with PBS and blocked again with 10% BSA to prepare membranes for AR^{biot} binding. The coating of arrays with labeled STV allowed for direct visualization of the biotin arrays. In the last washing step after blocking with BSA dihydrotestosterone (DHT, 10^{-4} M) was added to the buffer in order to prepare the array for the binding of AR^{biot} onto the STV-Cy3–biotin arrays [25]. Next, freshly purified AR^{biot} was loaded onto the sample surface. After overnight incubation at 4 °C, arrays were washed with PBS containing 10^{-4} DHT to maintain the AR stability. Binding of AR^{biot} was detected via indirect immunofluorescence. First samples were blocked with fetal calf serum (FCS) for 1 h at room temperature (RT), then washed with PBS containing 10^{-4} DHT and loaded for 1 h with anti-AR antibody.

After another washing step, the sample was incubated with a secondary antibody labeled with FITC, for 15 min, washed with PBS containing 10^{-4} DHT and imaged with fluorescence microscope. Figure 4 shows biotin arrays after binding of STV-Cy3 (Texas Red channel) and AR^{biot}, detected with indirect immunofluorescence (FITC channel). Binding of STV-Cy3 served as an optical reference to easily localize the lipid arrays on the sample. Fluorescence signal after antibody binding on AR^{biot} coated arrays is homogenous, indicating an even distribution of the receptor bound to STV-biotin arrays embedded in the HEMA-EDMA (Figure 4, graph).

Conclusion

We present a novel platform for binding studies of functional molecules based on lipid arrays embedded in a nanoporous hydrophilic polymer substrate. The microcontact spotting approach used to pattern the functional lipid inks into arrays allows for the multiplexing of different inks into single arrays within the polymer mesh. Spotting with SPT probes on HEMA-EDMA polymer increases the spatial resolution of lipid pattern as compared to conventional spotting/ink jet printing on 3D substrates, such as PVDF or nitrocellulose membranes, from 50–300 µm in current commercial setups [26,27] to the presented average 6 µm features by µCS. The 3D nature of the spotted features (enabled by the infiltration of the ink into the nanoporous polymer) results in a higher signal intensity compared to similar arrays on strictly 2D substrates as glass [9,10]. As of now it is still unknown, just like in case of lipids spotted on PVDF membranes [7], how the polymer mesh accommodates lipid geometry and packaging, and how it affects the accessibility of the target lipid regions for the binding of proteins and antibodies. However, the infiltrated lipid arrays show high stability against washing steps, while still being accessible for protein and antibody binding. Even complex receptor pro-

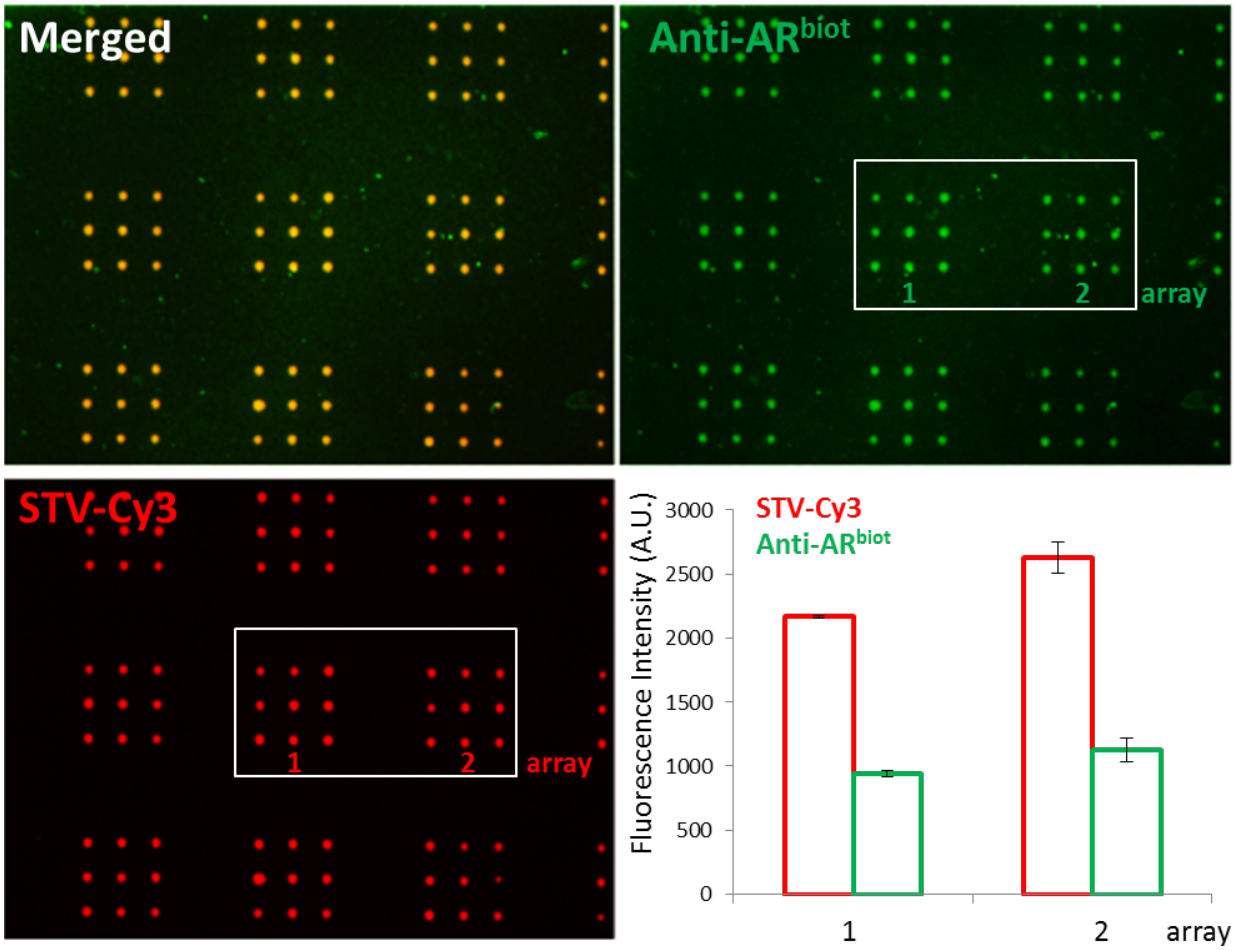


Figure 4: Fluorescence microscopy images of AR^{biot} binding onto STV-Cy3 coated biotin arrays on nanoporous HEMA-EDMA substrate. The STV-Cy3 was pre-bound onto biotin lipid spots (red), AR^{biot} was detected by immunostaining (green). Scale bars equal 50 µm. All arrays were spotted with a dwell time of 2 s. The graph presents intensity profiles of n = 9 dot features of two arrays, after STV-Cy3 (red points) and AR^{biot} binding (green points) (after background subtraction).

tein structures of AR^{biot} remain intact upon binding to the lipid arrays and are still accessible for the indirect immunofluorescence detection. The described model system and its demonstrated feasibility exhibit a high potential for follow-up studies. Even though the model is still very simplified, its ability to reduce the complexity of interactions for the study of specific aspects of AR function in protein complexes has been demonstrated. This setup may allow for the investigation of differences between various protein complexes isolated from pathological samples from mice models and patient samples. Antibody based detection approaches could be suitable to analyze the levels of AR proteins bound onto the lipid arrays. The described model system would thereby have a significant impact on the therapeutic treatment for breast and prostate cancer patients.

Keeping in mind previous applications of HEMA polymer in creating superhydrophilic–superhydrophobic micropatterned surfaces for cell patterning [28] and cell-screening applications [29,30], the addition of lipid arraying to the portfolio of HEMA polymer applications emphasizes the use of this solid substrate as a very attractive platform for a variety of biomedical applications. The combination of microfluidic settings and phospholipid arrays on solid supports like HEMA polymer may also prove fruitful for a multitude of sensing applications.

Experimental

Substrate preparation

Fabrication of alkyne HEMA-EDMA polymer film was described in our previous work [9,10]. Briefly, a 12.5 µm thin, hydrophilic porous polymer film was firstly prepared on a glass substrate by using photoinitiated copolymerization of 2-hydroxyethyl methacrylate and ethylene dimethacrylate in the presence of porogens (1-decanol and cyclohexanol) [29]. This procedure leads to the formation of a thin film of a highly cross-linked and porous (due to the presence of porogens) hydro-

philic polymethacrylate layer. The porous structure is a permeable network of interconnected polymer nanoglobules with pores of around 150 nm.

Microcontact spotting

The patterning of lipid arrays was performed on a NLP 2000 system (NanoInk, USA) with oxygen plasma activated (0.2 mbar O_2, 2 min) SPT probes (SPT-S-C10S, BioForce Nanosciences, USA). All lipids were purchased from Avanti Polar Lipids. Ink mixtures were prepared by admixing various lipids to DOPC carrier lipid: DOPC (20 mg/mL) and Rhodamine-PE (1 mg/mL) or Biotin-PE (1 mg/mL) or DNP-cap-PE (10 mg/mL) were used to prepare a 1 μM total lipid content ink mixture, sonicated together, air dried to remove the chloroform solvent and reconstituted with ethanol and glycerol (87%) in a 7:3 v/v ratio. Glycerol was added to prevent the premature drying of the ink on the SPT. Probes were filled with 0.5 μL ink, mounted onto the probe holder and used directly for spotting on unmodified poly(2-hydroxyethyl methacrylate-*co*-ethylene dimethacrylate) support (HEMA). Spotting was performed at 55–65% relative humidity. All patterning procedures were carried out with the sample stage tilted by 8° with respect to the SPT tip to minimize the probability of a contact between the ink reservoir and the sample surface. For all patterns, except the ones used for spot size versus dwell time analysis, a dwell time of 2 s was used for target patterns and 1 s for optical reference patterns.

Protein binding

Streptavidin-FITC (Streptavidin, Fluorescein Conjugate) was purchased from Calbiochem and Streptavidin-Cy3 (recombinant from *Streptomyces avidinii*, Cy3 labelled) was purchased from Sigma. Prior to protein binding on biotin lipid arrays, samples were blocked in 10% BSA (Sigma-Aldrich) solution in PBS (Gibco) for 20 min at room temperature. After washing with PBS, 0.5 μg solution of STV-Cy3 in PBS was incubated for 30 min on the substrate. Samples were typically washed with 100 μL PBS 3× and imaged under fluorescence microscope (Nikon Instruments Inc.).

AR^{biot} purification and binding was done as follows: Sf9 [23] cells were cultured with continuous shaking at 110 rpm at a density of 10^9 and a temperature of 27 °C in SF900 II medium (Invitrogen) supplemented with 5% fetal calf serum (FCS). One day prior to infection the medium was changed to serum-free SF900 II medium. Cells were infected with baculovirus stocks typically at MOIs of 5–7. 72 h post-infection cells were treated with DHT (10^{-4} M) for 3 h. The infected SF9 cells were lysed on ice in lysis buffer (20 mM HEPES pH 7.4, 400 mM NaCl, 1 mM β-mercaptoethanol, 1 mM $ZnCl_2$, 1 mM PMSF, 1 mM Na_2V0_3, 10 μL protease inhibitor cocktail (Roche Mannheim, Germany) per mL) with 10^{-4} M DHT and an equivalent amount of ethanol in a control purification. The lysates were then centrifuged for 10 min at 14,000*g* at 4 °C. Isolation of the biotin-tagged AR samples was performed on a streptavidin–mutein-matrix (Roche Mannheim, Germany) according to the manufacturer's instructions at 4 °C [18]. Freshly purified protein was quantified for total protein content. The concentration of the protein was measured at 280 nm by using the specific program 1 A/cm = 1 mg from the spectrophotometer Nanodrop Lite (Thermo Scientific) in duplicate and with a solution of elution buffer (10^{-4} DHT) as the blank. After blocking the sample surface with 10% BSA solution in PBS for 30 min at RT, samples were incubated with 0.5 μg solution of STV or STV-Cy3 in PBS for 30 min at room temperature. Next, samples were washed 2× with 100 μL PBS, and a final washing step was carried out with PBS containing 10^{-4} DHT. Then, 200 μL of freshly purified AR^{biot} (0.45 μg/μL) was loaded onto the sample. Samples were incubated over night at 4 °C for optimal protein binding. Samples were then washed 3 times with 100 μL PBS containing 10^{-4} M DHT and blocked again with 100 μL fetal bovine serum for 1 h at RT. Thereafter, samples were washed again 3 times with 100 μL PBS containing 10^{-4} M DHT and incubated with 100 μL primary anti-AR antibody (AR F39.4.1 from Santa Cruz Biotechnology, INC., sc-52309, 1:200 in PBS containing 10^{-4} M DHT) for 1–2 h at room temperature. Next, the samples were washed 3 times with 100 μL PBS containing 10^{-4} M DHT and incubated for 15 min. with 100 μL of the secondary antibody (Goat anti-Mouse IgG (H+L) Secondary Antibody, Alexa Fluor 488, ThermoFisher, A-11001, diluted in a ratio of 0.5:400 onto PBS containing 10^{-4} M DHT). Finally, the membranes were washed 3 times with PBS containig 10^{-4} DHT and imaged under upright fluorescence microscope (Nikon Instruments Inc.).

Antibody binding

DNP-lipid arrays were blocked with 10% BSA in PBS for 30 min at room temperature. After washing 3 times with PBS, 200 μL of 5 μg/mL of anti-DNP IgE-Alexa 488 antibody in PBS was applied. After 1 h incubation, samples were washed 3 times in PBS and imaged under fluorescence microscope (Nikon Instruments Inc.).

Fluorescence microscopy and quantification of signal

Fluorescence microscopy was carried out on an Eclipse 80i upright microscope (Nikon Instruments Inc.). Fluorescence images were taken with 10× or 20× objectives. Images were recorded with a CoolSNAP HQ2 camera (Photometrics). Patterns were aligned for imaging by using alignment markers scratched onto the polymer surface. The bleaching of fluorophores was minimized (especially for quantitative measurements) by first

focusing on the alignment mark before exposing the patterned area to light, and the lamp intensity was kept at a minimum. Fluorescence intensity profiles were generated by using NIS-AR software installed on the microscope PC (Nikon Instruments Inc.). For measurements the patterned areas of interest were marked, and fluorescence intensity was automatically recorded. Mean fluorescence intensity after background extraction was calculated using the onboard NIS-AR software as previously described in [17].

Acknowledgements

This work was partly carried out with the support of the Karlsruhe Nano Micro Facility (KNMF, http://www.knmf.kit.edu), a Helmholtz Research Infrastructure at the Karlsruhe Institute of Technology (KIT, http://www.kit.edu). PL thanks the Helmholtz Association's Initiative and Networking Fund (grant VH-NG-621).

References

1. Fodor, S. P.; Read, J. L.; Pirrung, M. C.; Stryer, L.; Lu, A. T.; Solas, D. *Science* **1991,** *251,* 767–773. doi:10.1126/science.1990438
2. Barbulovic-Nad, I.; Lucente, M.; Sun, Y.; Zhang, M.; Wheeler, A. R.; Bussmann, M. *Crit. Rev. Biotechnol.* **2006,** *26,* 237–259. doi:10.1080/07388550600978358
3. Sassolas, A.; Leca-Bouvier, B. D.; Blum, L. J. *Chem. Rev.* **2008,** *108,* 109–139. doi:10.1021/cr0684467
4. Weinrich, D.; Jonkheijm, P.; Niemeyer, C. M.; Waldmann, H. *Angew. Chem., Int. Ed.* **2009,** *48,* 7744–7751. doi:10.1002/anie.200901480
5. Yamada, M.; Imaishi, H.; Morigaki, K. *Langmuir* **2013,** *29,* 6404–6408. doi:10.1021/la400570h
6. Chen, Y.; Clegg, N. J.; Scher, H. I. *Lancet Oncol.* **2009,** *10,* 981–991. doi:10.1016/S1470-2045(09)70229-3
7. Brennan, K. M.; Galban-Horcajo, F.; Rinaldi, S.; O'Leary, C. P.; Goodyear, C. S.; Kalna, G.; Arthur, A.; Elliot, C.; Barnett, S.; Linington, C.; Bennett, J. L.; Owens, G. P.; Willison, H. J. *J. Neuroimmunol.* **2011,** *238,* 87–95. doi:10.1016/j.jneuroim.2011.08.002
8. Kanter, J. L.; Narayana, S.; Ho, P. P.; Catz, I.; Warren, K. G.; Sobel, R. A.; Steinman, L.; Robinson, W. H. *Nat. Med.* **2006,** *12,* 138–143. doi:10.1038/nm1344
9. Hirtz, M.; Lyon, M.; Feng, W.; Holmes, A. E.; Fuchs, H.; Levkin, P. A. *Beilstein J. Nanotechnol.* **2013,** *4,* 377–384. doi:10.3762/bjnano.4.44
10. Hirtz, M.; Feng, W.; Fuchs, H.; Levkin, P. A. *Adv. Mater. Interfaces* **2016,** *3,* 1500469. doi:10.1002/admi.201500469
11. Lenhert, S.; Sun, P.; Wang, Y.; Fuchs, H.; Mirkin, C. A. *Small* **2007,** *3,* 71–75. doi:10.1002/smll.200600431
12. Urtizberea, A.; Hirtz, M. *Nanoscale* **2015,** *7,* 15618–15634. doi:10.1039/C5NR04352B
13. Xu, J.; Lynch, M.; Huff, J. L.; Mosher, C.; Vengasandra, S.; Ding, G.; Henderson, E. *Biomed. Microdevices* **2004,** *6,* 117–123. doi:10.1023/B:BMMD.0000031748.13353.10
14. Davydova, M.; de los Santos Pereira, A.; Bruns, M.; Kromka, A.; Ukraintsev, E.; Hirtz, M.; Rodriguez-Emmenegger, C. *RSC Adv.* **2016,** *6,* 57820–57827. doi:10.1039/C6RA12194B
15. Hirtz, M.; Greiner, A. M.; Landmann, T.; Bastmeyer, M.; Fuchs, H. *Adv. Mater. Interfaces* **2014,** *1,* 1300129. doi:10.1002/admi.201300129
16. Helm, C. A.; Knoll, W.; Israelachvili, J. N. *Proc. Natl. Acad. Sci. U. S. A.* **1991,** *88,* 8169–8173. doi:10.1073/pnas.88.18.8169
17. Sekula-Neuner, S.; Maier, J.; Oppong, E.; Cato, A. C. B.; Hirtz, M.; Fuchs, H. *Small* **2012,** *8,* 585–591. doi:10.1002/smll.201101694
18. Juzumiene, D.; Chang, C.-y.; Fan, D.; Hartney, T.; Norris, J. D.; McDonnell, D. P. *Nucl. Recept. Signaling* **2005,** *3,* e001. doi:10.1621/nrs.03001
19. Jin, H.-J.; Kim, J.; Yu, J. *Transl. Androl. Urol.* **2013,** *2,* 158–177. doi:10.3978/j.issn.2223-4683.2013.09.01
20. Ni, M.; Chen, Y.; Lim, E.; Wimberly, H.; Bailey, S. T.; Imai, Y.; Rimm, D. L.; Liu, X. S.; Brown, M. *Cancer Cell* **2011,** *20,* 119–131. doi:10.1016/j.ccr.2011.05.026
21. Cortes, C. J.; Miranda, H. C.; Frankowski, H.; Batlevi, Y.; Young, J. E.; Le, A.; Ivanov, N.; Sopher, B. L.; Carromeu, C.; Muotri, A. R.; Garden, G. A.; La Spada, A. R. *Nat. Neurosci.* **2014,** *17,* 1180–1189. doi:10.1038/nn.3787
22. de Leon, J. T.; Iwai, A.; Feau, C.; Garcia, Y.; Balsiger, H. A.; Storer, C. L.; Suro, R. M.; Garza, K. M.; Lee, S.; Kim, Y. S.; Chen, Y.; Ning, Y.-M.; Riggs, D. L.; Fletterick, R. J.; Guy, R. K.; Trepel, J. B.; Neckers, L. M.; Cox, M. B. *Proc. Natl. Acad. Sci. U. S. A.* **2011,** *108,* 11878–11883. doi:10.1073/pnas.1105160108
23. Jochum, T.; Ritz, M. E.; Schuster, C.; Funderburk, S. F.; Jehle, K.; Schmitz, K.; Brinkmann, F.; Hirtz, M.; Moss, D.; Cato, A. C. B. *Biochim. Biophys. Acta* **2012,** *1822,* 1070–1078. doi:10.1016/j.bbadis.2012.02.006
24. Sekula, S.; Fuchs, J.; Weg-Remers, S.; Nagel, P.; Schuppler, S.; Fragala, J.; Theilacker, N.; Franzreb, M.; Wingren, C.; Ellmark, P.; Borrebaeck, C. A. K.; Mirkin, C. A.; Fuchs, H.; Lenhert, S. *Small* **2008,** *4,* 1785–1793. doi:10.1002/smll.200800949
25. Gregory, C. W.; Johnson, R. T.; Mohler, J. L., Jr.; French, F. S.; Wilson, E. M. *Cancer Res.* **2001,** *61,* 2892–2898.
26. Orth, R. N.; Kameoka, J.; Zipfel, W. R.; Ilic, B.; Webb, W. W.; Clark, T. G.; Craighead, H. G. *Biophys. J.* **2003,** *85,* 3066–3073. doi:10.1016/S0006-3495(03)74725-0
27. Saliba, A.-E.; Vonkova, I.; Deghou, S.; Ceschia, S.; Tischer, C.; Kugler, K. G.; Bork, P.; Ellenberg, J.; Gavin, A.-C. *Nat. Protoc.* **2016,** *11,* 1021–1038. doi:10.1038/nprot.2016.059
28. Efremov, A. N.; Stanganello, E.; Welle, A.; Scholpp, S.; Levkin, P. A. *Biomaterials* **2013,** *34,* 1757–1763. doi:10.1016/j.biomaterials.2012.11.034
29. Geyer, F. L.; Ueda, E.; Liebel, U.; Grau, N.; Levkin, P. A. *Angew. Chem., Int. Ed.* **2011,** *50,* 8424–8427. doi:10.1002/anie.201102545
30. Ueda, E.; Geyer, F. L.; Nedashkivska, V.; Levkin, P. A. *Lab Chip* **2012,** *12,* 5218–5224. doi:10.1039/c2lc40921f

License and Terms

This is an Open Access article under the terms of the Creative Commons Attribution License (http://creativecommons.org/licenses/by/4.0), which permits unrestricted use, distribution, and reproduction in any medium, provided the original work is properly cited.

The license is subject to the *Beilstein Journal of Nanotechnology* terms and conditions: (http://www.beilstein-journals.org/bjnano)

The definitive version of this article is the electronic one which can be found at: doi:10.3762/bjnano.8.75